ИНСТИТУТ ЗА ФИЗИКУ

ПРИМЉЕНО: 08. 10. 2021

Рад.јед.	Број	Арх.шифра	Прилог
0801	833/1		

Научном већу Института за физику у Београду

ПРЕДМЕТ: Молба за покретање поступка за стицање звања научни саветник

Молим Научно веће Института за физику да у складу са Правилником о поступку и начину вредновања и квантитативном исказивању научно-истраживачких резултата истраживача покрене поступак за мој избор у звање научни саветник. У прилогу достављам:

1. Мишљење руководиоца пројекта
2. Кратку биографију
3. Преглед научне активности
4. Елементе за квалитативну оцену научног доприноса
5. Елементе за квантитативну оцену научног доприноса
6. Списак објављених радова и њихове копије
7. Податке о цитираности
8. Копију решења о избору у претходно звање
9. Додатке

У Београду,
07. 10. 2021. године

С поштовањем,

др Ненад Лазаревић

Научном већу Института за физику у Београду

Предмет: Мишљење руководиоца

Др Ненад Лазаревић запослен је у Центру за физику чврстог стања и нове материјале Института за физику у Београду од 2008. године. Поред истраживања из области оптичке спектроскопије јако-корелисаних електронских система, са посебним акцентом на суперпроводнике на бази гвожђа, др Ненад Лазаревић је ангажован и на задатку развоја и одржавања лабораторија за Раманову спектроскопију. Руководио је или руководи четири пројекта и три докторске дисертације. Коаутор је преко четрдесет радова публикованих у међународним часописима највише репутације.

С обзиром да испуњава све услове предвиђене Правилником о поступку и начину вредновања и квантитативном исказивању научно-истраживачких резултата Министарства просвете, науке и технолошког развоја, велико ми је задовољство да предложим избор др Ненада Лазаревића у звање научни саветник. За чланове комисије предлажем:

1. Академик Зоран В. Поповић, научни саветник
2. др Дарко Танасковић, научни саветник
3. др Маја Шћепановић, научни саветник,
4. Академик Зоран Радовић, редовни професор у пензији

У Београду, 07.10.2021. године

Академик Зоран В. Поповић

1. Биографски и стручни подаци о кандидату

Др Ненад Лазаревић је рођен 31. 12. 1984. године у Јагодини, где је звршио основну школу и гимназију као ученик генерације. На такмичењима из физике за ученике средњих школа осваја многобројне прве награде, а 2003. године представља државу на Међународној олимпијади из физике. Исте године уписује основне студије на Физичком факултету Универзитета у Београду, смер Теоријска и експериментална физика. Дипломирао је 2008. године са радом под називом „*Фонон-фонон интеракције и дефектна стања у нанокристалима* $Ce_{0.85}Nd(Gd)_{0.15}O_{2-\delta}$ *проучавана методом Раман спектроскопије*". Просечна оцена током студија била је 9,96. Добитник је награде и стипендије др Ђорђе Живановић за 2007. годину. Од стране Универзитета у Београду проглашен је студентом генерације Физичког факултета. Добитник је Годишње награде Института за физику у Београду за 2021. годину.

Од 2008. године запослен је у Центру за физику чврстог стања и нове материјале Института за физику у Београду. Докторску дисертацију на тему „*Нееластично расејање светлости на јако-корелисаним електронским системима: антимониди и телуриди*“, под менторством академика Зорана В. Поповића, одбранио је на Физичком факултету Универзитета у Београду 2012. године. У звање виши научни сарадник изабран је 2017. године. Руководио је или руководи пројектима билатералне сарадње са Немачком „*Orbital-dependent correlation effects and phase relations in alkali-doped iron selenide superconductors*“, „*Fluctuations, magnetic frustrations and sub-dominant pairing in iron based superconductors*“ и „*Inelastic light scattering study of the strain tuned nematic and magnetic phases*“. Члан је менаџмент комитета COST акције „Nanoscale coherent hybrid devices for superconducting quantum technologies“.

Др Ненад Лазаревић је руководилац пројекта “*Strain effects in iron chalcogenide superconductors*” у оквиру ПРОМИС позива Фонда за науку Републике Србије. Био је ментор докторске дисертације др Ане Милосављевић, одбрањене 2021. на Физичком факултету, Универзитета у Београду и суштински је ментор докторске дисертације др Марка Опачића, одбрањене 2017. године на Електротехничком факултету Универзитета у Београду. Тренутно руководи израдом докторске дисертације Сање Ђурђић Мијин на Физичком факултету Универзитета у Београду. У досадашњем научно-истраживачком раду објавио је 41 научни рад у међународним часописима од којих је 31 категорије M21. Ови радови су до сада цитирани 509 пута уз h индекс 14 и i10 индекс 19 (Google Scholar), односно 390 од којих 286 без аутоцитата уз h индес 12 (Web of Science). Укупан импакт фактор током каријере износи 129,9, са просечним импакт фактором по раду већим од 3. Од 2016. године је ангажован као предавач на основним и докторским студијама (формирање курса) на Криминалистичко-полицијском универзитету, на смеру Форензичко инжењерство, где је изабран у звање доцента. Од 2021. ангажован је и на докторским студијама на Физичком факултету, Универзитета у Београду на предмету „Спектроскопске технике у физици кондензоване материје“. Године 2021. изабран је за председника Научног већа Института за физику у Београду.

2. Преглед научне активности

Фокус истраживања др Ненада Лазаревића у досадашњем раду био је усмерен на изучавање оптичких својстава различитих материјала методом Рамановe спектроскопије. У периоду **након** претходног избора у звање његова научно-истраживачка активност може се поделити у две целине:

- **Нееластично расејање светлости на материјалима са јаким електронским корелацијама**

Због својих необичних особина, нове генерације материјала са јаким електронским корелацијама привлаче пажњу науче заједнице не само са фундаменталног већ и са аспекта потенцијалне примене. Комплексна међуповезаност различитих степена слободе код ових материјала често захтева приступ проширеном фазном дијаграму. За потребе извођења експеримената (електронског) раманског расејања који су резултовали доле наведеним научним публикацијама, др Лазаревић извршио је различите модификације експерименталних поставки на Институту за физику знатно унапређујући њихову компетативност. У наведеном периоду започео је рад на експерименталној поставци која ће омогућити симултано мерење електронског раманског расејања, транспортних особина и напрезања у температурском опсегу 6 K – 320 K. Важно је напоменути да, иако је на први поглед слично „конвенционалном“ раманском расејању, електронско раманско расејање представља знатно комплекснију технику, како по питању експеримeнатлне поставке, тако и за тумачење података. Кроз своје активности, др Лазаревић успоставио је већи број сарадњи са међународно признатим научним институцијама, што је евидентирано кроз њихове доприносе на научним публикацијама.

1. A. Baum, H. N. Ruiz, **N. Lazarević**, YaoWang, T. Böhm, R. Hosseinian Ahangharnejhad, P. Adelmann, T.Wolf, Z. V. Popović, B. Moritz, T. P. Devereaux and R. Hackl, *Frustrated spin order and stripe fluctuations in FeSe,* Communications Physics, 2, 14 (2019). ИФ= 4.684 М21
2. A. Baum, A. Milosavljević**,** **N. Lazarević**, M. M. Radonjić, B. Nikolić, M. Mitschek, Z. Inanloo Maranloo, M. Šćepanović, M. Grujić-Brojčin, N. Stojilović, M. Opel, Aifeng Wang, C. Petrovic, Z. V. Popović, and R. Hackl, *Phonon anomalies in FeS,* Phys. Rev. B 97, 054306 (2018). ИФ= 3.836 М21

Због својих необичних особина, јединственим међу суперпроводницима на бази гвожђа, Fe(Se:S) привлачи огромну пажњу научне заједнице. Отворени проблеми који се односе на механизам спаривања, магнетно уређење и флуктуације дефинисани су у оквиру пројеката билатералне сарадње са Немачком, под руководством др Ненада Лазаевића и др Рудија Хакла (Валтер-Мајснер институт, Минхен): *„Fluctuations, magnetic frustrations and sub-dominant pairing in iron based superconductors*“ и „*Inelastic light scattering study of the strain tuned nematic and magnetic phases“*, као и пројекту Фонда за науку Републике Србије “*Strain effects in iron chalcogenide superconductors*”, такође под руководством колеге Лазаревића. Утврђено је присуство (спинских) флуктуација које достижу максимум на температури нематичног прелаза, као и екситација дво-магнонског типа на основу којих је предложено фрустрирано магнетно уређење код FeSe, јединствено код суперпроводника на бази гвожђа. Код FeS уочена је појачана електрон-фонон интеракција на ивици зоне, што је потенцијално указало на присуство конкурентног механизма спаривања.

3. A. Baum, Ying Li, M. Tomić, **N. Lazarević**, D. Jost, F. Löffler, B. Muschler, T. Böhm, J.- H. Chu, I. R. Fisher, R. Valentí, I. I. Mazin, and R. Hackl, *Interplay of lattice, electronic, and spin degrees of freedom in detwinned* $BaFe_2As_2$ *: A Raman scattering study,* Phys. Rev. B 98, 075113 (2018). ИФ= 3.836 M21
4. D. Jost, J.-R. Scholz, U. Zweck, W. R. Meier, A. E. Böhmer, P. C. Canfield, **N. Lazarević**, and R. Hackl, *Indication of subdominant d-wave interaction in superconducting* $CaKFe_4As_4$*,* Phys. Rev. B 98, 020504(R) (2018). ИФ= 3.836 M21

Праћењем резонантног Рамановог ефекта изучавана је међуповезаност спинских, електронских и фононских ексцитација у $BaFe_2As_2$. За потребе експеримента, конструисан је посебан носач у циљу уклањања појаве ефеката близанаца, који у значајној мери утиче на селекциона правила у овом материјалу. У суперпроводном стању монокристала $CaKFe_4As_4$ идентификовано је присуство Бардезис-Шиферових модова што указује на постојање више ортогоналних суб-доминантих канала спаривања.

5. **Nenad Lazarevic** and Rudi Hackl, *Fluctuations and pairing in Fe-based superconductors: light scattering experiments,* J. Phys.: Condens. Matter 32 413001 (2020). **(Review article)** ИФ= 2.711 M22
6. Marko Opačić, **Nenad Lazarević**, *Lattice dynamics of iron chalcogenides–Raman scattering study*, J. Serb. Chem. Soc. 82 (9), 957-983 (2017). ИФ= 1.015 M23

На основу публикованих резултата, припремљена су и два прегледа рада. Док се у другом сумирају резулати „класичне“ Раманове спектроскопије, први се искључиво базира на резултатима електронске Раманове спектроскопије и критички презентује досадашње резулатате из области, као и теоријске основе, неопходне за вршење експеримената и анализу добијених података.

7. Feng Jin, **Nenad Lazarević**, Changle Liu, Jianting Ji, Yimeng Wang, Shuna He, Hechang Lei, Cedomir Petrovic, Rong Yu, Zoran V. Popović, and Qingming Zhang, *Phonon anomalies and magnetic excitations in* $BaFe_2Se_2O$*,* Phys. Rev. B 99, 144419 (2019). ИФ= 3.813 M21

У оквиру билатералне сарадње са НР Кином извршен је низ експеримената раманског расејања у магнетном пољу у широком опсегу температура. Након анализе података пријављена је јака спин-фонон интеракције и резонанца између двомагнонског континуума и двомагнонског везаног стања код $BaFe_2Se_2O$.

8. S Đurđić Mijin, A Baum, J Bekaert, A Šolajić, J Pešić, Y Liu, Ge He, MV Milošević, C Petrovic, ZV Popović, R Hackl, **N Lazarević***, Probing charge density wave phases and Mott transition in 1T-TaS by inelastic light scattering,* Phys. Rev. B. 103, 245133 (2021). ИФ= 4.036 M21

Након експеримената раманског расејања велике резолуције у широком тепературком опсегу, праћена је еволуција *1T*-TaS кроз сукцесивна CDW стања. Анализом електронског континуума по први пут овом методом идентификован је Мотов процеп од око 180 mcV и праћена његова еволуција са температуром. За потребе интерпетације резултата, а на основу симетријске анализе, изведени су Раманови вертекси за хексагоналну структуру.

9. Sanja Djurdjić Mijin, AM Milinda Abeykoon, Andrijana Šolajić, Ana Milosavljević, Jelena Pešić, Yu Liu, Cedomir Petrovic, Zoran V Popović, **Nenad Lazarević**, *Short-Range Order in VI_3*, Inorg. Chem., 59, 22, 16265–16271 (2020). ИФ= 4.85 M21a
10. Ana Milosavljević, Andrijana Šolajić, Bojana Višić, Marko Opačić, Jelena Pešić, Yu Liu, Cedomir Petrovic, Zoran V Popović, **Nenad Lazarević**, *Vacancies and spin–phonon coupling in $CrSi_{0.8}Ge_{0.1}Te_3$, J Raman Spectrosc.* 51: 2153– 2160 (2020). ИФ= 2.809 M21
11. A. Milosavljević, A. Šolajić, S. Djurdjić-Mijin, J. Pešić, B. Višić, Yu Liu, C. Petrovic, **N. Lazarević**, Z. V. Popović, *Lattice dynamics and phase transitions in $Fe_{3-x}GeTe_2$*, Phys. Rev. B 99, 214304 (2019). ИФ= 3.813 M21
12. A. Milosavljević, A. Šolajić, J. Pešić, Yu Liu, C. Petrovic, **N. Lazarević**, and Z. V. Popović, *Evidence of spin-phonon coupling in $CrSiTe_3$*, Phys. Rev. B 98, 104306 (2018). ИФ= 3.836 M21
13. S. Djurdjić-Mijin, A. Šolajić, J. Pešić, M. Šćepanović, Y. Liu, A. Baum, C. Petrovic, **N. Lazarević**, and Z. V. Popović, *Lattice dynamics and phase transition in CrI_3 single crystals*, Phys. Rev. B 98, 104307 (2018). ИФ= 3.836 M21
14. M. Opačić, **N. Lazarević**, D. Tanasković, M. M. Radonjić, A. Milosavljević, Yongchang Ma, C. Petrovic, and Z. V. Popović, *Small influence of magnetic ordering on lattice dynamics in $TaFe_{1.25}Te_3$*, Phys. Rev. B 96, 174303 (2017). ИФ= 3.836 M21

Након прегледа литературе и на основу доступних узорака монокристала нове генерације магнетних (квази)дводимензионалних материјала, колега Лазаревић дефинише отворена питања и поставља експеримент у наведеној групи радова. Учествује у свим фазама истраживања, при чему подучава студенте докторских студија Сању Ђурђић Мијин (тема одбрањена 29.09.2021. године на Физичком факултету), Ану Милосављевић (дисертација одбрањена на Физичком факултету 06.04.2021. године) и Марка Опачића (дисертација одбрањена на Електротехничком факулету 18.06.2018. године) од поставке и калибрациије експеримента, преко обраде и анализе података, све до писања научног чланка и комуникације са уредницима и рецензентима. У радовима је анализирана кристална и магнета структура наведених материјала, као и њихова међуповезаност. Код VI_3 разрешене су, на први поглед, контрадикторности резултата различитих екесперименталних техника ревизијом кристалне структуре материјала. Код $CrSi_{0.8}Ge_{0.1}Te_3$ и $Fe_{3-x}GeTe_2$ пре свега, утврђено је присуство јаке спин-фонон интеракције, док код $TaFe_{1.25}Te_3$ она нема велики утицај на температурску еволуцију.

15. B. Colson, V. Fuentes, Z. Konstantinović, D. Colson, A. Forget, N. Lazarević, M. Šćepanović, Z.V. Popović, C. Frontera, Ll. Balcells, B. Martinez, A. Pomar, Mate. Self-assembled line network in $BiFeO_3$ thin films, J. Magn. Magn. Mater. 509, 166898 (2020). ИФ= 2.717 M22

У сарадњи са колегама из Института за материјале у Барселони, проучавани су самоорганизујући $BiFeO_3$ танки филмови на $LaAlO_3$. Након анализе спектара, узимајући у обзир ефекат близанаца, извршена је идентификација фаза $BiFeO_3$.

16. M Šćepanović, M Grujić-Brojčin, **N Lazarević**, ZV Popović, Temperature-Dependent Raman Study of Nanostructured and Multifunctional Materials, Physica Status Solidi (a), 216, 1800763, (2019). **(Review article)** ИФ= 1.795 M22

У овом прегледном раду, др Ненад Лазаревић активо учествује у припреми теоријског дела и формира део који се односи на суперпроводнике на бази гвожђа.

- **Примена Раманове спектроскопије у медицини, фармацији и форензици**

1. Lazarević JJ, Ralević U, Kukolj T, Bugarski D, Lazarević N, Bugarski B, Popović ZV, *Influence of chemical fixation process on primary mesenchymal stem cells evidenced by Raman spectroscopy*, Spectrochim Acta A Mol Biomol Spectrosc, 216, 173-178 (2019) ИФ= 3.232 M21
2. Lazarević JJ, Kukolj T, Bugarski D, Lazarević N, Bugarski B, Popović ZV, *Probing primary mesenchymal stem cells differentiation status by micro-Raman spectroscopy*, Spectrochim Acta A Mol Biomol Spectrosc, 213, 384-390 (2019) ИФ= 3.232 M21
3. M Krstic, J Djuris, O Petrovic, N Lazarevic, S Cvijic, S Ibric, Application of the melt granulation technique in development of lipid matrix tablets with immediate release of carbamazepine, J. Drug. Rug. Deliv. Sci. Tec., 39, 467-474 (2017). ИФ= 2.297 M22
4. Marko Krstic, Igor Lukic, Alma Busatlic, **Nenad Lazarevic**, Dragana Vasiljevic, *Solid dispersions with carbamazepine: optimization of formulation, characterization and examination of long-term stability*, Hem. Ind. 72, 191-205 (2018)

Поред истраживања које се односе на фундаменталну физику, др Ненад Лазаревић је активан и у области примена раманске спектроскопије у медицини, фармацији и форензици. У наведеним радовима, успостављен је интердисциплинарни тим у циљу испитивања промена насталих током процеса диференцијације ка хондрогеној, остеогеној и адипогеној лози на нивоу појединачних мезенхимских матичних ћелија пореклом из периодонцијума методом раманске спектроскопије. Поред тога, испитиван је и утицај хемијске фиксације, као најједноставнијег поступка трајног очувања биолошких узорака, на раманске спектре мезенхимских матичних ћелија. др Лазаревић је учествовао у постављању експеримената и његовој оптимизацији, а био је активан и током обраде и интерпретације података и априприме чланака.

3. Елементи за квалитативну оцену научног доприноса кандидата

3.1 Квалитет научних резултата

У периоду **након** избора у звање виши научни сарадник, др Ненад Лазаревић публиковао је укупно **20 научних радова** укупног **ИФ = 65.525**. Најзначајнији резултати представљени су на семинарима Центра за физику чврстог стања и нове материјале, Института за физику у Београду, као и на предавању по позиву.

3.1.1 Научни ниво и значај резултата, утицај научних радова

У периоду након претходног избора у звање истичу се следећи радови:

1. A. Baum, H. N. Ruiz, **N. Lazarević**, YaoWang, T. Böhm, R. Hosseinian Ahangharnejhad, P. Adelmann, T.Wolf, Z. V. Popović, B. Moritz, T. P. Devereaux and R. Hackl, *Frustrated spin order and stripe fluctuations in FeSe,* Communications Physics, 2, 14 (2019). ИФ= 4.684 M21
   DOI: https://doi.org/10.1038/s42005-019-0107-y
2. A. Baum, A. Milosavljević**, N. Lazarević**, M. M. Radonjić, B. Nikolić, M. Mitschek, Z. Inanloo Maranloo, M. Šćepanović, M. Grujić-Brojčin, N. Stojilović, M. Opel, Aifeng Wang, C. Petrovic, Z. V. Popović, and R. Hackl, *Phonon anomalies in FeS*, Phys. Rev. B 97, 054306 (2018). ИФ= 3.836 M21
   DOI: https://doi.org/10.1103/PhysRevB.97.054306

Због својих необичних особина, јединствених међу суперпроводницима на бази гвожђа, Fe(Se:S) привлачи огромну пажњу научне заједнице. Ненад Лазаревић је указао на могућности електронске раманске спектроскопије у разрешењу отворених проблема који се односе на присуство и порекло магнетног уређења и флуктуација код ове класе материјала. Отворена питања дефинисани су у оквиру пројеката билатералне сарадње са Немачком под руководством др Ненад Лазаевића и др Рудија Хакла (Валтер-Мајснер институт, Минхен): „*Fluctuations, magnetic frustrations and sub-dominant pairing in iron based superconductors*" и „*Inelastic light scattering study of the strain tuned nematic and magnetic phases*", као и пројекту Фонда за науку Републике Србије "*Strain effects in iron chalcogenide superconductors*", такође под руоводством др Лазаревића. У оквиру наведених публикације, др Ненад Лазаревић блиско сарађује са тада докторандом Андреасом Баумом (чија је докторска дисертација у потпуности заснована на заједничким резултатима) и студентом Аном Милосављевић која је одбранила дисертацију под његовим менторством. Након дефинисања проблема и параметара експеримента, колега Лазаревић учествује у постављању и извођењу истог, анализи података и писању научног чланка. Због комплексности проблема, проширена је мрежа научних институција које активно учествују у истраживању, а нумеричка истраживања FeSe представљају основу дисертације докторанда Харисона Руиза (Универзитет Станфорд, Калифорнија, САД). Утврђено је присуство (спинских) флуктуација које достижу максимум на температури нематичног прелаза, као и екситација дво-магнонског типа на основу којих је предложено фрустрирано магнетно уређење код FeSe, јединствено код суперпроводника на бази гвожђа. За разлику од FeSe, код FeS није установљено магнетно уређење, већ јака електрон-фонон интеракција што указује на потенцијално другачији механизам спаривања. Експерименти раманског расејања, извођени су на комплементарним поставкама у Београду и Минхену (током научних посета кадидата).

3. **Nenad Lazarevic** and Rudi Hackl, *Fluctuations and pairing in Fe-based superconductors: light scattering experiments*, J. Phys.: Condens. Matter 32 413001 (2020). **(Review article)** ИФ= 2.711 M22
   DOI: https://doi.org/10.1088/1361-648X/ab8849

На основу постигнутих резултата, Ненад Лазаревић у сарадњи са др Хаклом, формира прегледни чланак који сумира резултате добијене методом електронске раманске спектроскопије и даје теоријски основ за примену технике у изучавању комплексних суперпроводних материјала.

4. Sanja Djurdjić Mijin, AM Milinda Abeykoon, Andrijana Šolajić, Ana Milosavljević, Jelena Pešić, Yu Liu, Cedomir Petrovic, Zoran V Popović, **Nenad Lazarević**, *Short-Range Order in* VI_3, Inorg. Chem., 59, 22, 16265–16271 (2020). ИФ= 4.85 M21a
   DOI: 10.1021/acs.inorgchem.0c02060
5. S Đurđić Mijin, A Baum, J Bekaert, A Šolajić, J Pešić, Y Liu, Ge He, MV Milošević, C. Petrovic, Z.V. Popović, R. Hackl, **N. Lazarević**, *Probing charge density wave phases and Mott transition in 1T-TaS by inelastic light scattering*, Phys. Rev. B. 103, 245133 (2021). ИФ= 4.036 M21
   DOI: https://doi.org/10.1103/PhysRevB.103.245133

У наведеним публикацијама др Ненад Лазаревић поставља проблем, дефинише екесперимент и руководи целокупним истраживањем, при чему обучава докторанда Сању Ђурђић Мијин (тема одобрена на Физичком факултету). Већина експеримената раманског расејања извршена је у Београду уз додатне податке добијене у Минхену у оквиру пројеката билатералне сарадње. Код VI_3 разрешено је питање на први поглед контрадикорних резултата различитих експерименталних техника а у вези са кристалном структуром. У истраживању 1T-TaS, поред изучавања сукцесивних прелаза таласа густине електронских стања, по први пут је методом раманске спектроскопије уочено отварање Мотовог процепа и праћена његова еволуција са температуром.

3.1.2. Позитивна цитираност научних радова кандидата

Радови др Лазаревића су до сада цитирани 509 пута уз h индекс 14 и i10 индекс 19 (Google Scholar), односно 390 од којих 286 без аутоцитата уз h индес 12 (Web of Science). Укупан импакт фактор током каријере износи 129.9. (докази у прилогу)

3.1.3. Параметри квалитета радова и часописа

У досадашњој каријери др Лазаревић је публиковао 41 научни чланак од чега 31 (M21 и M21a), 7 M22 и 2 M23 просечног импкат фактора већег од 3. У периоду **након** последњег избора у звање публиковао је 20 научних чланака од чега 14 (M21 и M21a), 4 M22 и 2 M23 са укупним ИФ=65.526. У прилогу је листа научних радова са одговарајућом категоријом и ИФ.

	ИФ	M	СНИП
Укупно	65.526	140	20.76
Усредњено по чланку	3.2763	7	1.038
Усредњено по аутору	8.966	19.706	3.027

3.1.4. Степен самосталности и степен учешћа у реализацији радова у научним центрима у земљи и иностранству

Након претходног избора у звање, др Лазаревић руководи три пројекта и три докторске дисертације. Током боравака у више научних центара у Немачкој, Кини и Белгији шири мрежу научне сарадње што је евидетирано у претходно наведеним публикацијама.

3.1.5. Награде

У периоду **након** избора у претходно звање, др Лазаревић је добио Годишњу награду Института за физику за 2021. годину за резултате истраживања у области супрепроводника на бази гвожђа. (доказ у прилогу)

3.1.6. Елементи применљивости научних резултата

Научно-истраживаче активности др Лазаревића, пре свега, усмерене су на изучавање особина супервоводних и магнетних (квази)дводимензионалних материјала са великим потенцијалима примене у различитим областима. Поред тога, он активно ради на унапређењу методе рамански спектроскопије и њене примене у форензици.

3.2. Ангажованост у формирању научних кадрова

Др Лазаревић је руководио или руководи трима докторским дисерацијама:

1. др Марко Опачић (суштински ментор), "Nanoscale phase separation in iron-based superconductors investigated by Raman spectroscopy", Електротехнички факултет, Универзитет у Београду, 18.06.2018. (доказ у прилогу)
2. др Ана Милосављевић (ментор) „Electron-phonon and spin-phonon interaction in iron-based superconductors and quasi-2D materials studied by Raman spectroscopy“, Физички факултет, Универзитет у Београду 06.04.2021. (доказ у прилогу)
3. Сања Ђурђић Мијин (ментор), тема „Нееластично расејање светлости на квази-2Д материјалима“, Физички факултет 29.09.2021. (доказ у прилогу)

3.3. Нормирање броја коауторских радова, патената и техничких решења

Природа, као и сама комплексност истраживања неретко је захтевала учешће истраживача из различитих група. Укупан број бодова пре нормирања је 144,2, а када се узме у обзир број аутора, укупан број је смањен на 106,99. Вредности бодова након нормирања приказани су у листи публикација за сваки рад појединачно.

3.4. Руковођење пројектима, потпројектима и пројектним задацима

У периоду **након** претходног избора у звање др Лазаревић руководи пројектима **(докази у прилогу)**:

1. Билатерална сарадња са Немачком 2019-2020. „*Fluctuations, magnetic frustrations and sub-dominant pairing in iron based superconductors*“
2. Билатерална сарадња са Немачком 2021-2022. „*Inelastic light scattering study of the strain tuned nematic and magnetic phases*“.
3. ПРОМИС позив Фонда за науку Републике Србије “*Strain effects in iron chalcogenide superconductors*”
4. COST Action: CA16218 – Nanoscale coherent hybrid devices for superconducting quantum technologies (члан Комитета)

3.5. Активност у научним и научно-стручним друштвима

1. Председник Научног већа Института за физику,
2. Представник у Већу института Универзитета у Београду,
3. Представник у Већу групација природно-математичких наука Универзитата у Београду,
4. Резенцент у часописима APS-a, JRS-a и Analytical Methods (докази у прилогу),
5. Копредседавајући научног комитета BPU2021 (одложена за 2022. годину)

3.6. Утицај научних резултата

Видети 2 и 3.1.1.

3.7. Конкретан допринос кандидата у реализацији радова у научним центрима у земљи и иностранству

Видети 3.1.1.

3.8. Уводна предавања на конференцијама, друга предавања и активности

У периоду **након** претходног избора у звање, Ненад Лазаревић одржао је предавање по позиву (докази у прилогу):

1. **Nenad Lazarević**, Andreas Baum, Harrison N Ruiz, Yao Wang, Thomas Bohm, R Hosseinian Ahangharnejhad, Peter Adelmann, Thomas Wolf, Zoran V. Popović, Brian Moritz, Thomas P Devereaux, Rudi Hackl, *Frustration and fluctuations in FeSe: A Raman scattering study*, Vortex 2019, May 20 – 25, 2019, Antwerp, Belgium.

- Од 2016. године ангажован је као предавач на основним и докторским студијама (формирање курса) на Криминалистичко-полицијском универзитету, на смеру Форензичко инжењерство, где је изабран у звање доцента.
- Од 2021. године ангажован је на докторким студијама на Физичком факултету, Универзитета у Београду на предмету „Спектроскопске технике у физици кондензоване материје“.

4. Елементи за квантитативну оцену научног доприноса кандидата

		Потребно	Остварено	Нормирано
Научни саветник	Укупно	70	**144.2**	**106.99**
Обавезни(1)	M20 +M32	50	**140.4**	**104.48**
Обавезни(2)	M21+M22+M23	35	**140**	**104.28**

UNIVERZITET U BEOGRADU

FIZIČKI FAKULTET

Ana N. Milosavljević

Elektron-fonon i spin-fonon interakcija u superprovodnicima na bazi gvožđa i kvazi-2D materijalima izučavana metodom Ramanove spektroskopije

doktorska disertacija

Beograd, 2021

UNIVERSITY OF BELGRADE

FACULTY OF PHYSICS

Ana N. Milosavljević

Electron-phonon and spin-phonon interaction in iron-based superconductors and quasi-2D materials studied by Raman spectroscopy

doctoral dissertation

Belgrade, 2021

Članovi komisije:

Mentor:
Dr Nenad Lazarević
Viši naučni saradnik
Institut za fiziku Beograd
Univerzitet u Beogradu

Akademik Zoran V. Popović
Naučni savetnik
Institut za fiziku Beograd
Univerzitet u Beogradu

Prof. dr Đorđe Spasojević
Redovni profesor
Fizički fakultet
Univerzitet u Beogradu

Dr Božidar Nikolić
Vanredni profesor
Fizički fakultet
Univerzitet u Beogradu

Dr Zorica Popović
Docent
Fizički fakultet
Univerzitet u Beogradu

Zahvalnica

Ova disertacija rezultat je rada u Centru za fiziku čvrstog stanja i nove materijale, Instituta za fiziku, Beograd, Univerziteta u Beogradu. Istraživanje je finansirano od strane Ministarstva prosvete, nauke i tehnološkog razvoja u okviru projekata III45018 i Fonda za nauku Republike Srbije u okviru projekta StrainedFeSC, broj 6062656.

Na prvom mestu, želim da se zahvalim svom mentoru dr Nenadu Lazareviću na pruženoj podršci i pomoći, podjednako kao studentu i kao prijatelju. Zahvalila bih se na prenesenom znanju, strpljenju, uloženom trudu i optimizmu.

Akademiku Zoranu V. Popoviću se zahvaljujem najpre na ukazanoj prilici za rad u Centru za fiziku čvrstog stanja i nove materijale, i na savetima, sugestijama i pruženoj pomoći.

Kolegama iz Centra, dr Maji Šćepanović, dr Mirjani Grujić-Brojčin, dr Marku Opačiću i dr Bojani Višić se zahvaljujem na podršci i pomoći tokom mog rada u Centru i tokom izvođenja eksperimenta i na korisnim savetima i sugestijama .

Prof. dr Čedomiru Petroviću i njegovim saradnicima, dr Aifeng Wang-u i dr Yu Liu-u, se zahvaljujem na sintezi proučavanih uzoraka u okviru ove disertacije, eksperimentima, diskusijama i savetima.

Posebnu zahvalnost želim da izrazim prof. dr Rudi Hackl-u i dr Andreas Baum-u iz Valter Majsner instituta u Minhenu na izuzetnoj saradnji, eksperimentima, diskusijama, savetima i prenesenom znanju.

dr Milošu Radonjiću se zahvaljujem na teorijskim proračunima dinamike rešetke FeS sistema; dr Jeleni Pešić i Andrijani Šolajic na izvršenim proračunima za kvazi-dvodimenzione magnetne materijale; dr Božidaru Nikoliću na određivanju selekcionih pravila za dvo-fononske procese.

Zahvalila bih se i svom mentoru na master studijama dr Edibu Dobardžiću na pomoći i podrši tokom svih ovih godina.

dr Jasmini Lazarević zahvaljujem se na stalnoj podršci i drugarstvu tokom lepih i onih manje lepih trenutaka.

Koleginici Sanji Đurđić Mijin se zahvaljujem na više nego korektnoj saradnji i izdvojenom vremenu da ovu disertaciju pročita i da svoje sugestije.

Svom najboljem drugu Ivanu Despiću zahvaljujem se na svakoj vrsti podrške tokom izrade ove disertacije. Slavici Mastilović, Nataliji Resimić, Duši Vuković i Marjani Majsotorović, mojim najdivnijim drugaricama, zahvalna sam na strpljenju, ljubavi, podršci i ohrabrenju tokom svih ovih godina. Svojoj drugarici iz pandemijom izazvanog karantina, Dubravki Bunčić bih se zahvalila na uvek lepim i punim podrške rečima, i pozitivnom stavu.

Na kraju želim da se zahvalim svojoj porodici na beskonačnoj podršci i ljubavi.

Univerzitet u Beogradu

Elektrotehnički fakultet

Marko Opačić

Razdvajanje faza u superprovodnicima na bazi gvožđa korišćenjem Ramanove spektroskopije

Doktorska disertacija

Beograd, 2018.

University of Belgrade

School of Electrical Engineering

Marko Opačić

Nanoscale phase separation in iron-based superconductors investigated by Raman spectroscopy

PhD thesis

Belgrade, 2018.

Disertaciju posvećujem porodici i prijateljima

Ova disertacija je u potpunosti urađena u Centru za fiziku čvrstog stanja i nove materijale Instituta za fiziku Beograd. Istraživanje je finansirano od strane Ministarstva prosvete, nauke i tehnološkog razvoja Republike Srbije, u okviru projekata III45018 i ON171017. Numeričke simulacije vršene su na superračunaru PARADOX koji se nalazi u okviru Laboratorije za primenu računara u nauci Instituta za fiziku Beograd. Uzorci su sintetisani u Brukhejven Nacionalnoj Laboratoriji, Apton, SAD.

Prvenstveno želim da se zahvalim akademiku Zoranu V. Popoviću, formalnom mentoru ovog rada, na pruženoj šansi za rad na ovoj temi, veoma korisnim savetima i primedbama, učenju dobroj naučnoj praksi i stvorenim uslovima za rad.

Suštinskom mentoru dr Nenadu Lazareviću dugujem zahvalnost na uvođenju u veoma interesantnu oblast proučavanja vibracionih osobina novih materijala. Pored toga, veoma sam mu zahvalan na stalnoj podršci i pomoći tokom merenja, obrade rezultata, pisanja radova i na kraju pisanja ove teze, kao i na odnosu koji je više od kolegijalnog.

Duboku zahvalnost izražavam i kolegama sa kojima sam blisko sarađivao tokom izrade ove teze: dr Maji Šćepanović na pomoći i savetima vezanim za eksperimentalna merenja, dr Darku Tanaskoviću na saradnji vezanoj za numeričke simulacije i veoma iscrpnim diskusijama tokom pisanja radova, prof. dr Čedomiru Petroviću na pripremi uzoraka, dr Milošu Radonjiću na DFT proračunima dinamike rešetke razmatranih materijala i MSc Ani Milosavljević na saradnji i pomoći.

Prijateljska i pozitivna atmosfera u okruženju u mnogome je doprinela kvalitetu mog rada. Za to su zaslužne kolege iz kancelarije: Dimitrije, Nataša i Bojan, kao i ostale kolege iz Centra.

U mom profesionalnom i ljudskom usavršavanju značajnu ulogu su imali moja pokojna učiteljica Stoja Nikolić kao i profesori Pete beogradske gimnazije mr Eugen Vedral i Ljiljana Svorcan, te im i na ovaj način iskazujem zahvalnost. Zahvaljujem i

svim ostalim profesorima Pete beogradske gimnazije i Elektrotehničkog fakulteta koji su eksplicitno ili implicitno doprineli ovom radu.

Konačno, želim da pomenem dvoje svojih bliskih prijatelja, Bojanu Milošević i Marka Mladenovića, te da im zahvalim na prijateljstvu i podršci svih ovih godina.

Na kraju, iako ne najmanje važno, zahvaljujem porodici na ljubavi, strpljenju i beskonačnoj podršci.

Датум 06.07.2021.

Потпис ментора

Потпис студента

Мишљење Колегијума докторских студија

Након образложења теме докторске дисертације Колегијум докторских студија је тему

[✓ прихватио] ☒ није прихватио ☐

Датум

29.09.2021

Продекан за науку Физичког факултета

Стојадиновић

ДОКТОРСКЕ СТУДИЈЕ

ПРЕДЛОГ ТЕМЕ ДОКТОРСКЕ ДИСЕРТАЦИЈЕ КОЛЕГИЈУМУ ДОКТОРСКИХ СТУДИЈА

Школска година
2020/2021

Подаци о студенту

Име: Sanja

Презиме: Đurđić Mijin

Број индекса: 8017/2018

Научна област дисертације: Fizika kondenzovane materije

Подаци о ментору докторске дисертације

Име: Nenad

Презиме: Lazarević

Научна област: Fizika kondenzovane materije

Звање: Viši naučni saradnik

Институција: Institut za fiziku

Предлог теме докторске дисертације

Наслов: Neelastično rasejanje svetlosti na kvazi-2D materijalima

Уз пријаву теме докторске дисертације Колегијуму докторских студија, потребно је приложити следећа документа:

1. Семинарски рад (дужине до 10 страница)
2. Кратку стручну биографију писану у трећем лицу једнине
3. Фотокопију индекса са докторских студија

ИНСТИТУТ ЗА ФИЗИКУ

ПРИМЉЕНО: 04-02-2016

Рад.јед.	број	Арх.шифра	Прилог
0801	179/1		

Република Србија
МИНИСТАРСТВО ПРОСВЕТЕ,
НАУКЕ И ТЕХНОЛОШКОГ
РАЗВОЈА
Број: 451-03-01038/2015-09/11
Датум: 27.01.2016.
Београд, Немањина 22-26

Институт за физику
- Ненад Лазаревић -

Прегревица 118
<u>11 080 Београд</u>

Поштовани господине Лазаревићу,

Обавештавамо Вас да је у оквиру Програма билатералне научне и технолошке сарадње између Министарства просвете, науке и технолошког развоја Републике Србије и Немачке службе за академску размену (ДААД), а на основу спроведених процедура оцене пројеката у обе државе, усвојена листа за финансирање пројеката у двогодишњем периоду са почетком реализације од 1. јануара 2016. године.

Са задовољством Вас обавештавамо да је Ваш пројекат "*Орбитално зависно корелациони ефекти и фазна сепарација у допираним гвожђе-селенидним суперпроводницима*" одобрен за финансирање.

Желимо да напоменемо да сврха боравка истраживача у Републици Србији, односно Савезној Републици Немачкој, по овом Јавном позиву, треба да допринесе даљем унапређењу сарадње и конституисању пројектног тима, уз учешће младих истраживача, и генерисању новог пројектног предлога којим би се конкурисало у програму HORIZON 2020 или другим програмима са међународним финансирањем.

Захтеви за рефундацију трошкова путовања српских истраживача, односно трошкова боравка немачких истраживача, достављају се на обрасцу који можете преузети на интернет адреси Министарства, у огранку међународна научна сарадња, уз одговарајућу пратећу документацију.

Руководиоци одобрених пројеката за финансирање, дужни су да доставе годишњи и завршни извештај о реализацији пројекта, у року од 15 дана након завршетка пројектне године, односно након завршетка пројекта, у форми која се такође, налази на интернет адреси Министарства. Саставни део извештаја су и прилози који садрже резултате билатералног пројекта: листу учесника заједничке радионице и агенду; радну верзију апстракта пројекта са листом учесника, називом пројекта и називом потенцијалног програма или јавног позива на који се аплицира са овом темом; радну верзију или копију објављеног рада у међународном часопису.

Информација о свим одобреним пројектима објављена је на интернет страници Министарства просвете, науке и технолошког развоја.

Истовремено бих желео да Вам честитам на одобреном пројекту и пожелим успешну реализацију пројектних активности.

С поштовањем,

МИНИСТАР

Др Срђан Вербић

Република Србија
МИНИСТАРСТВО ПРОСВЕТЕ, НАУКЕ
И ТЕХНОЛОШКОГ РАЗВОЈА
Број: 451-03-01971/2018-09/13
Датум: 20.12.2018.
Београд, Немањина 22-26

Институт за физику
- Др Ненад Лазаревић -

Прегревица 118
11 080 Београд

Поштовани господине Лазаревићу,

Обавештавамо Вас да је у оквиру Програма билатералне научне и технолошке сарадње између Републике Србије и Савезне Републике Немачке, а на основу спроведених процедура оцене пројеката у обе државе, усвојена листа за финансирање пројеката у двогодишњем периоду са почетком реализације од 01. јануара 2019. године.

Са задовољством Вас обавештавамо да је Ваш пројекат *"Флуктуације, магнегтне фрустрације и субдоминантно спаривање у суперпроводницима на бази гвожђа"* одобрен за финансирање.

Сврха боравка истраживача у Републици Србији, односно Савезној Републици Немачкој, по овом Јавном позиву, треба да допринесе даљем унапређењу сарадње и конституисању пројектног тима, уз учешће младих истраживача, као и генерисању новог пројектног предлога којим би се конкурисало у програму HORIZON 2020 или другим програмима са међународним финансирањем.

У склопу овог Програма, Министарство просвете, науке и технолошког развоја Републике Србије, финансираће трошкове превоза српских истраживача између седишта институција које сарађују и трошкове смештаја и дневница за немачке истраживаче. На српској страни, максимална предвиђена издвајања по пројектном циклусу су у износу до 3.000 евра у динарској противвредности.

Немачка страна сносиће трошкове превоза немачких истраживача између седишта институција које сарађују и трошкове смештаја и дневница за српске истраживаче. На немачкој страни, максимална предвиђена издвајања по пројектном циклусу су у износу до 7.000 евра.

Захтеви за рефундацију трошкова путовања српских истраживача, односно трошкова боравка немачких истраживача, достављају се на обрасцу који можете преузети на интернет адреси Министарства, у огранку међународна научна сарадња, уз одговарајућу пратећу документацију.

Руководиоци одобрених пројеката за финансирање, дужни су да доставе годишњи и завршни извештај о реализацији пројекта, у року од 15 дана након завршетка пројектне године, односно након завршетка пројекта, у форми која се, такође, налази на интернет адреси Министарства. Саставни део извештаја су и прилози који садрже резултате билатералног пројекта нпр.: листа учесника заједничке радионице и агенда; апстракт са листом учесника, називом пројекта и називом потенцијалног програма или јавног позива на који се аплицира са темом која проистиче из ове сарадње; радна верзија или копија објављеног рада у међународном часопису и/или међународној конференцији, и др.

Информација о свим одобреним пројектима објављена је на интернет страници Министарства просвете, науке и технолошког развоја.

Истовремено бих желео да Вам честитам на одобреном пројекту и пожелим успешну реализацију пројектних активности.

С поштовањем,

МИНИСТАР

Младен Шарчевић

Annex I

Министарство просвете, науке и технолошког развоја Републике Србије и Немачка служба за академску размену – ДААД

Ministry of Education, Science and Technological Development of the Republic of Serbia and Deutcher Akademischer Austauschdienst - DAAD

Пројектни циклус / *Project years* 2021-2022

	Српски руководилац пројекта и српска институција	***Немачки руководилац пројекта и немачка институција*** ***German applicant and German institution***	***Назив пројекта*** ***Project title***
1.	Др Немања ТРИШОВИЋ Технолошко-металуршки факултет, Универзитет у Београду	Prof. Michael GIESE University of Duisburg-Essen, Essen	Халогено везивање као алатка за дизајнирање нових течних кристала савијене геометрије *Halogen bonding as a design tool for novel bent-shaped liquid crystals*
2.	Др Ненад ЛАЗАРЕВИЋ Институт за физику, Универзитет у Београду	Prof. Rudolf HACKL Walther Meissner Institut, München	Испитивање утицаја напрезања на нематичне и магнетне фазе методом нееластичног расејања светлости *Inelastic light scattering study of the strain tuned nematic and magnetic phases*
3.	Др Данијела СТАНИСАВЉЕВИЋ	PhD Наташа АТАНАСОВ	Утицај miR-219 и miR-221 на радиосензитивност глиобластома ћелија

	Институт за молекуларну генетику и генетичко инжењерство, Универзитет у Београду	Helmholtz Zentrum, München	*Effects of miR-219 and miR-221on radiosensitivity of glioblastoma cells*
4.	Др Дубравка РЕЛИЋ Хемијски факултет, Универзитет у Београду	Prof. Aleksander VOGEL Goethe University, Frankfurt	Извори и распрострањеност органофосфатних успоривача горења у спољашњој средини и затвореном простору у Немачкој и Србији – процена ризика по здравље људи и могуће методе деградације *Sources and occurrence of organophosphate flame retardants in indoor and outdoor environments in Germany and Serbia – human exposure assessment and possible degradation methods*
5.	Др Ивана ГАЂАНСКИ Институт Биосенс, Универзитет у Новом Саду	PhD Raffael OSEN Fraunhofer Institute for Process Engineering and Packaging IVV, Freising	Развој биљних јестивих микроносача и скафолда тј. 3Д носача за ћелије у циљу примене у ћелијској пољопривреди тј. производњи култивисаног меса путем ткивног инжењерства *Development of plant-based edible microcarriers and scaffolds for use in cellular agriculture i.e.*

			cultivated meat tissue engineering
6.	Проф. др Павле АНЂУС Биолошки факултет, Универзитет у Београду	Dr. David LUTZ Ruhr University, Bochum	Неурореперација протеолизом молекула ћелијске атхезије L1CAM у моделима спиналне повреде и ALS *Neurorepear by proteolysis of the cell adhesion molecule LICAM in ALS and spinal cord injury models*
7.	Др Данијела БАТАВЕЉИЋ Биолошки факултет, Универзитет у Београду	Dr. Dragomir MILOVANOVIĆ Charité – Universitätsmedizin Berlin, Berlin	Ефекат протеинских агрегата на динамику органела у ћелијским моделима АЛС *The effect of protein aggregation on organelle dynamics in cellular models of ALS*
8.	Др Весна ЦВЕТКОВИЋ Институт за хемију, технологију и металургију, Универзитет у Београду	Dr. Bernd FRIEDRICH RWTH Aachen University, Aachen	Рециклирање ретких земаља, Nd+Pr, из NdFeB магнетног отпада: Нови приступ *Recovery of rare earth, Nd+Pr, from end-of-life NdFeB magnets: A new approach to recycling*
9.	Др Владимир ПЕТРОВИЋ Институт за савремену историју, Универзитет у Београду	Dr. Danijel KEŽIĆ Lebniz-Institut für Ost- und Südosteuropaforschung, Regensburg	Отпорне инфраструктуре ? Испитивање континуитета током југословенског двадесетог века *Resilient Infrastructures? Exploring Continuities across the Yugoslav 20th Century*

10.	Др Мирјана БРДАР Технолошки факултет, Универзитет у Новом Саду	Dr. Sebastian FRANZ TU Dresden, Dresden	Сингуларно пертурбовани проблеми са више параметара *Singularly perturbed problems with multiple parameters*

For the Ministry of Education, Science and Technological Development of the Republic of Serbia

Dr. Aleksandar Jović, Assistant Minister

Date:

For the German Academic Exchange

Stephanie Knobloch

Project Funding for German Language and Research Mobility

Date:

Фонд за науку Републике Србије
Бр. 1538/2020
08.07. 2020. год.
БЕОГРАД, Немањина бр. 22-26

УНИВЕРЗИТЕТ У БЕОГРАДУ
ИНСТИТУТ ЗА ФИЗИКУ | БЕОГРАД
ИНСТИТУТ ОД НАЦИОНАЛНОГ ЗНАЧАЈА ЗА РЕПУБЛИКУ СРБИЈУ
www.ipb.ac.rs

Број 0801-585/1
Датум 16.07.2020. год.

У оквиру Програма за изврсне пројекте младих истраживача Фонда за науку Републике Србије на који је сагласност дала Влада РС решењем 05 број 660-02-5891/2019 од 13. јуна 2019. године („Службени гласник РС“, број 42/19), који се реализује у складу са Актом о циљевима, начину реализације и условима финансирања пројеката у оквиру Програма за изврсне пројекте младих истраживача број УО- 21-1/2019 од 04.06. 2019. године, а по јавном позиву Фонда за науку Републике Србије од 21. јуна 2019. године за пријаву научноистраживачких пројеката у оквиру Програма за изврсне пројекте младих истраживача – ПРОМИС и одлуке Управног одбора Фонда за науку број УО - 24/2020 од 27.02.2020. године о усвајању коначне листе Пројеката којима се одобрава за финансирање средствима Фонда за науку по Програму ПРОМИС (у даљем тексту: Одлука УО), закључује се

УГОВОР О ФИНАНСИРАЊУ

реализације научноистраживачког Пројекта под називом STRAIN EFFECTS IN IRON CHALCOGENIDE SUPERCONDUCTORS,

акроним StrainedFeSC, евиденциони број 6062656

у оквиру Програма за изврсне пројекте младих истраживача – ПРОМИС

Фонда за науку Републике Србије

између следећих уговорних страна:

1. **ФОНДА ЗА НАУКУ РЕПУБЛИКЕ СРБИЈЕ,** са регистрованим седиштем у Београду, ул. Немањина 22-26, и адресом обављања делатности у Ул. Масарикова 5/XIX, Београд, матични број 17921410, ПИБ 111343775, број рачуна КЈС 840-670723-30, кога заступа др Милица Ђурић-Јовичић, в.д. директора (у даљем тексту: **Фонд за науку**),

са једне стране,

и

2. Реализатора истраживања/корисника средстава одобрених за финансирање Пројекта (у даљем тексту свако од наведних појединачно означен као **Корисник средстава**, а сви заједнички означени као **Корисници средстава**):

   2.1. Акредитована научноистраживачка организација – НИО Институт за физику у Београду, Универзитет у Београду, са седиштем на адреси Прегревица 118, 11080 Београд, ПИБ: 100105980, матични број: 07018029, коју заступа др Александар Богојевић, директор, која је носилац реализације Пројекта (у даљем тексту: **Носилац Пројекта**);

3. **Ненад Лазаревић**, запослен у НИО Институт за физику у Београду, Универзитет у Београду Носиоцу Пројекта (у даљем тексту: **Руководилац Пројекта**),

са друге стране.

Уколико на пројекту учествује само једна НИО – Носилац Пројекта, за потребе овог Уговора, термин Учесник Пројекта се односи на НИО - Носилац Пројекта.

Термини изражени у овом Уговору у граматичком мушком роду подразумевају природни мушки и женски род лица на која се односе.

Please read COST Code of Conduct. In order to keep using e-COST, you have to declare to abide by its principles clicking here. ×

Open Call

COST Actions

e-COST The online platform of COST Association

Ongoing

There are no ongoing activities

Profile

ORCID iD encoded	✓
Affiliation encoded	✓
You are a COST Expert	
Expertise encoded	✓
Curriculum vitae added	✓

Roles

MC Member
From Serbia to COST Action CA16218

MC Substitute
From Serbia to Biomedicine and Molecular Biosciences BM1401

page displayed on: 20 September, 2021 at 12:16:57 – version: 2021.10.1

А. Листа научних радова др. Ненада Лазаревића након избора у звање виши научни сарадник

1. S Đurđić Mijin, A Baum, J Bekaert, A Šolajić, J Pešić, Y Liu, Ge He, MV Milošević, C Petrovic, ZV Popović, R Hackl, **N Lazarević**, *Probing charge density wave phases and Mott transition in 1T-TaS by inelastic light scattering*, Phys. Rev. B. 103, 245133 (2021). ИФ= 4.036 М21а М$^{\text{норм}}$ = 4

2. Ana Milosavljević, Andrijana Šolajić, Bojana Višić, Marko Opačić, Jelena Pešić, Yu Liu, Cedomir Petrovic, Zoran V Popović, **Nenad Lazarević**, *Vacancies and spin–phonon coupling in* CrSi$_{0.8}$Ge$_{0.1}$Te$_3$, *J Raman Spectrosc*. 51: 2153– 2160 (2020). ИФ= 3.133 М21 М$^{\text{норм}}$ = 5.7

3. Sanja Djurdjić Mijin, AM Milinda Abeykoon, Andrijana Šolajić, Ana Milosavljević, Jelena Pešić, Yu Liu, Cedomir Petrovic, Zoran V Popović, **Nenad Lazarević**, *Short-Range Order in* VI$_3$, Inorg. Chem., 59, 22, 16265–16271 (2020). ИФ= 5.165 М21а М$^{\text{норм}}$ =7.1

4. B. Colson, V. Fuentes, Z. Konstantinović, D. Colson, A. Forget, **N. Lazarević**, M. Šćepanović, Z.V. Popović, C. Frontera, Ll. Balcells, B. Martinez, A. Pomar, Mate. Self-assembled line network in BiFeO3 thin films, J. Magn. Magn. Mater. 509, 166898 (2020). ИФ= 2.993 М22 М$^{\text{норм}}$ = 2.5

5. **Nenad Lazarevic** and Rudi Hackl, *Fluctuations and pairing in Fe-based superconductors: light scattering experiments,* J. Phys.: Condens. Matter 32 413001 (2020). **(Review article)** ИФ= 2.711 М22 М$^{\text{норм}}$ = 5

6. A. Milosavljević, A. Šolajić, S. Djurdjić-Mijin, J. Pešić, B. Višić, Yu Liu, C. Petrovic, **N. Lazarević**, Z. V. Popović, *Lattice dynamics and phase transitions in* Fe$_{3-x}$GeTe$_2$, Phys. Rev. B 99, 214304 (2019). ИФ= 3.813 М21 М$^{\text{норм}}$ = 5.7

7. Lazarević JJ, Ralević U, Kukolj T, Bugarski D, **Lazarević N**, Bugarski B, Popović ZV, *Influence of chemical fixation process on primary mesenchymal stem cells evidenced by Raman spectroscopy,* Spectrochim Acta A Mol Biomol Spectrosc, 216, 173-178 (2019). ИФ= 3.232 М21 М$^{\text{норм}}$ = 8

8. Lazarević JJ, Kukolj T, Bugarski D, **Lazarević N**, Bugarski B, Popović ZV, *Probing primary mesenchymal stem cells differentiation status by micro-Raman spectroscopy,* Spectrochim Acta A Mol Biomol Spectrosc, 213, 384-390 (2019) ИФ= 3.232 М21 М$^{\text{норм}}$ = 8

9. Feng Jin, **Nenad Lazarević**, Changle Liu, Jianting Ji, Yimeng Wang, Shuna He, Hechang Lei, Cedomir Petrovic, Rong Yu, Zoran V. Popović, and Qingming Zhang, *Phonon anomalies and magnetic excitations in* BaFe$_2$Se$_2$O, Phys. Rev. B 99, 144419 (2019). ИФ= 3.813 М21 М$^{\text{норм}}$ = 4.4

10. A. Baum, H. N. Ruiz, **N. Lazarević**, YaoWang, T. Böhm, R. Hosseinian Ahangharnejhad, P. Adelmann, T.Wolf, Z. V. Popović, B. Moritz, T. P. Devereaux and R. Hackl, *Frustrated spin order and stripe fluctuations in FeSe*, Communications Physics, 2, 14 (2019). ИФ= 4.684 M21 $M^{норм}$ = 4

11. M Šćepanović, M Grujić-Brojčin, **N Lazarević**, ZV Popović, *Temperature-Dependent Raman Study of Nanostructured and Multifunctional Materials*, Physica Status Solidi (a), 216, 1800763, (2019). **(Review article)** ИФ= 1.795 M22 $M^{норм}$ = 5

12. A. Milosavljević, A. Šolajić, J. Pešić, Yu Liu, C. Petrovic, **N. Lazarević**, and Z. V. Popović, *Evidence of spin-phonon coupling in* $CrSiTe_3$, Phys. Rev. B 98, 104306 (2018). ИФ= 3.836 M21 $M^{норм}$ = 8

13. S. Djurdjić-Mijin, A. Šolajić, J. Pešić, M. Šćepanović, Y. Liu, A. Baum, C. Petrovic, **N. Lazarević**, and Z. V. Popović, *Lattice dynamics and phase transition in* CrI_3 *single crystals*, Phys. Rev. B 98, 104307 (2018). ИФ= 3.836 M21 $M^{норм}$ = 5.7

14. A. Baum, Ying Li, M. Tomić, **N. Lazarević**, D. Jost, F. Löffler, B. Muschler, T. Böhm, J.- H. Chu, I. R. Fisher, R. Valentí, I. I. Mazin, and R. Hackl, *Interplay of lattice, electronic, and spin degrees of freedom in detwinned* $BaFe_2As_2$ *: A Raman scattering study*, Phys. Rev. B 98, 075113 (2018). ИФ= 3.836 M21 $M^{норм}$ = 3.6

15. D. Jost, J.-R. Scholz, U. Zweck, W. R. Meier, A. E. Böhmer, P. C. Canfield, **N. Lazarević**, and R. Hackl, *Indication of subdominant d-wave interaction in superconducting* $CaKFe_4As_4$, Phys. Rev. B 98, 020504(R) (2018). ИФ= 3.836 M21 $M^{норм}$ = 6.7

16. A. Baum, A. Milosavljević**, N. Lazarević**, M. M. Radonjić, B. Nikolić, M. Mitschek, Z. Inanloo Maranloo, M. Šćepanović, M. Grujić-Brojčin, N. Stojilović, M. Opel, Aifeng Wang, C. Petrovic, Z. V. Popović, and R. Hackl, *Phonon anomalies in FeS*, Phys. Rev. B 97, 054306 (2018). ИФ= 3.836 M21 $M^{норм}$ = 3.1

17. M. Opačić, **N. Lazarević**, D. Tanasković, M. M. Radonjić, A. Milosavljević, Yongchang Ma, C. Petrovic, and Z. V. Popović, *Small influence of magnetic ordering on lattice dynamics in* $TaFe_{1.25}Te_3$, Phys. Rev. B 96, 174303 (2017). ИФ= 3.836 M21 $M^{норм}$ = 6.7

18. Marko Opačić, **Nenad Lazarević**, *Lattice dynamics of iron chalcogenides–Raman scattering study*, J. Serb. Chem. Soc. 82 (9), 957-983 (2017). ИФ= 1.015 M23 $M^{норм}$ = 3

19. M Krstic, J Djuris, O Petrovic, N Lazarevic, S Cvijic, S Ibric, Application of the melt granulation technique in development of lipid matrix tablets with immediate release of carbamazepine, J. Drug. Rug. Deliv. Sci. Tec., 39, 467-474 (2017). ИФ= 2.297 M22 $M^{норм}$ = 5

20. Marko Krstic, Igor Lukic, Alma Busatlic, **Nenad Lazarevic**, Dragana Vasiljevic, *Solid dispersions with carbamazepine: optimization of formulation, characterization and examination of long-term stability*, Hem. Ind. 72, 191-205 (2018) $M^{норм} = 3$

Б. Листа научних радова др Ненада Лазаревића до избора у звање виши научни сарадник

21. U. Ralević, **N. Lazarević**, A. Baum, H.-M. Eiter, R. Hackl, P. Giraldo-Gallo, I. R. Fisher, C. Petrovic, R. Gajić, and Z. V. Popović, *Charge density wave modulation and gap measurements in* $CeTe_3$, Phys. Rev. B 94, 165132 (2016)

22. M Opačić, **N Lazarević**, MM Radonjić, M Šćepanović, Hyejin Ryu, Aifeng Wang, D Tanasković, C Petrovic, ZV Popović, *Raman spectroscopy of* $K_xCo_{2-y}Se_2$ *single crystals near the ferromagnet-paramagnet transition*, Journal of Physics: Condensed Matter 28,485401 (2016)

23. Alberto Pomar, Zorica Konstantinović, Nuria Bagués, Jaume Roqueta, Laura López-Mir, Lluis Balcells, Carlos Frontera, Narcis Mestres, Araceli Gutiérrez-Llorente, Maja Šćepanović, **Nenad Lazarević**, Zoran V Popović, Felip Sandiumenge, Benjamín Martínez, José Santiso, *Formation of self-organized* Mn_3O_4 *nanoinclusions in* $LaMnO_3$ *films*, Frontiersin Physics 4, 41 (2016)

24. Hyejin Ryu, KefengWang, M. Opacic, **N. Lazarevic**, J. B.Warren, Z. V. Popovic, Emil S. Bozin, and C. Petrovic, *Sustained phase separation and spin glass in Co-doped* $K_xFe_{2-y}Se_2$ *single crystals*, Phys. Rev. B 92, 174522 (2015)

25. M Opačić, **N Lazarević**, M Šćepanović, Hyejin Ryu, Hechang Lei, C Petrovic, ZV Popović, *Evidence of superconductivity-induced phonon spectra renormalization in alkalidoped iron selenides*, Journal of Physics: Condensed Matter 27 (48), 485701 (2015)

26. Hyejin Ryu, Milinda Abeykoon, KefengWang, Hechang Lei, **N. Lazarevic**, J. B.Warren,E. S. Bozin, Z. V. Popovic, and C. Petrovic, *Insulating and metallic spin glass in Ni-doped* $K_xFe_{2-y}Se_2$ *single crystals*, Phys. Rev. B 91, 184503 (2015)

27. Z. V. Popović, M. Šćepanović, **N. Lazarević**, M. Opačić, M. M. Radonjić, D. Tanasković, Hechang Lei, and C. Petrovic, *Lattice dynamics of* $BaFe_2X_3$ *(X=S,Se) compounds*, Phys. Rev. B 91, 064303 (2015)

28. ZV Popović, **N Lazarević**, S Bogdanović, MM Radonjić, D Tanasković, Rongwei Hu, Hechang Lei, C Petrovic, *Signatures of the spin-phonon coupling in* $Fe_{1+y}Te_{1-x}Se_x$ *alloys*, Solid State Communications 193, 51-55 (2015)

29. **N. Lazarević**, E. S. Bozin, M. Šćepanović, M. Opačić, Hechang Lei, C. Petrovic, and Z. V. Popović, *Probing $IrTe_2$ crystal symmetry by polarized Raman scattering*, Phys. Rev. B 89, 224301 (2014)

30. Lazarević JJ, Uskoković-Marković S, Jelikić-Stankov M, Radonjić M, Tanasković D, **Lazarević N**, Popović ZV, *Intermolecular and low-frequency intramolecular Raman scattering study of racemic ibuprofen*, Spectrochim Acta A Mol Biomol Spectrosc, 126, 301- 305 (2014)

31. Z. V. Popović, M. Šćepanović, **N. Lazarević**, M. M. Radonjić, D. Tanasković, Hechang Lei, and C. Petrovic, *Phonon and magnetic dimer excitations in Fe-based S=2 spin-ladder compound $BaFe_2Se_2O$*, Phys. Rev. B 89, 014301 (2014)

32. **N. Lazarević**, M. Radonjić, M. Šćepanović, Hechang Lei, D. Tanasković, C. Petrovic, and Z. V. Popović, *Lattice dynamics of KNi_2Se_2*, Phys. Rev. B 87, 144305 (2013)

33. **N. Lazarević**, M. Abeykoon, P. W. Stephens, Hechang Lei, E. S. Bozin, C. Petrovic, and Z. V. Popović, *Vacancy-induced nanoscale phase separation in $K_xFe_{2-y}Se_2$ single crystals evidenced by Raman scattering and powder x-ray diffraction*, Phys. Rev. B 86, 054503 (2012)

34. **N Lazarević**, MM Radonjić, D Tanasković, Rongwei Hu, Cedomir Petrovic, ZV Popović, *Lattice dynamics of $FeSb_2$*, Journal of Physics: Condensed Matter 24 (25), 255402 (2012)

35. **N Lazarević**, MM Radonjić, Rongwei Hu, D Tanasković, C Petrovic, ZV Popović, *Phonon properties of $CoSb_2$ single crystals*, Journal of Physics: Condensed Matter 24 (13),135402 (2012)

36. S Aškrabić, Z Dohčević-Mitrović, A Kremenović, **N Lazarević**, V Kahlenberg, ZV Popović, *Oxygen vacancy-induced microstructural changes of annealed CeO_{2-x} nanocrystals*, Journal of Raman Spectroscopy 43, 76-81 (2012)

37. **N. Lazarević**, Hechang Lei, C. Petrovic, and Z. V. Popović, *Phonon and magnon excitations in block-antiferromagnetic $K_{0.88}Fe_{1.63}S_2$*, Phys. Rev. B 84, 214305 (2011)

38. **N. Lazarević**, Z. V. Popović, Rongwei Hu, and C. Petrovic, *Evidence of coupling between phonons and charge-density waves in $ErTe_3$*, Phys. Rev. B 83, 024302 (2011)

39. **N. Lazarević**, Z. V. Popović, Rongwei Hu, and C. Petrovic, *Evidence for electron-phonon interaction in $Fe_{1-x}M_xSb_2$ (M=Co and Cr; $0 \leq x \leq 0.5$) single crystals*, Phys. Rev. B 81, 144302 (2010)

40. **N. Lazarević**, Z. V. Popović, Rongwei Hu, and C. Petrovic, *Raman scattering study of the $Fe_{1-x}Co_xSb_2$ and $Fe_{1-x}Cr_xSb_2$ ($0 \leq x \leq 1$) single crystals*, Phys. Rev. B 80, 014302 (2009)

41. **Nenad Ž Lazarević**, Zorana D Dohčević-Mitrović, Mirjana U Grujić-Brojčin, Maja J Šćepanović, Marko B Radović, Zoran V Popović, *Defect states in* $Ce_{0.85}Nd(Gd)_{0.15}O_{2-\delta}$ *nano-crystals investigated by Raman spectroscopy*, Hem. Ind. 63, 221 (2008).

B. Листа публикација са конференција др Ненада Лазаревића након избора у звање виши научни сарадник

1. **Nenad Lazarević**, Andreas Baum, Harrison N Ruiz, Yao Wang, Thomas Bohm, R Hosseinian Ahangharnejhad, Peter Adelmann, Thomas Wolf, Zoran V. Popović, Brian Moritz, Thomas P Devereaux, Rudi Hackl, *Frustration and fluctuations in FeSe: A Raman scattering study*, Vortex 2019, May 20 – 25, 2019, Antwerp, Belgium p.91. M32 (доказ у прилогу)

2. Rudolf Hackl, Andreas Baum, Ying Li, **Nenad Lazarevic**, Daniel Jost, Jiun-Haw Chu, Ian Fisher, Roser Valenti, Igor Mazin, *Exploring the electronic structure of* $BaFe_2As_2$ *using resonant Raman scattering*, APS March Meeting 2020, March 2–6, 2020; Denver, Colorado, L61.00009. M34

3. Andreas Baum, Harrison Ruiz, **Nenad Lazarević**, Yao Wang, Thomas Boehm, Ramez Hosseinian Ahangharnejhad, Thomas Wolf, Brian Moritz, Thomas Devereaux, Rudolf Hackl, *Frustrated spin order in FeSe*, APS March Meeting 2020, March 2–6, 2020; Denver, Colorado, M61.00002. M34

4. Rudolf Hackl, Andreas Baum, Harrison Ruiz, **Nenad Lazarevic**, Yao Wang, Thomas Boehm, Thomas Wolf, Brian Moritz, Thomas Devereaux, *Orbital selective magnetism, nematicity, and fluctuations in FeSe*, March 4–8, APS March Meeting 2019; Boston, Massachusetts, S62.00003. M34

5. A. Baum, F. Kretzschmar, D. Jost, T. Böhm, L. Peis, U. Karahasanović, B. Muschler, J. Schmalian, S. Caprara, M. Grilli, C. Di Castro, J. G. Analytis, J.-H. Chu, I. R. Fisher, P. Gegenwart, J. Maiwald, R. Hosseinian Ahangharnejhad, P. Adelmann, T. Wolf, **N. Lazarević**, Z. Popović And R. Hackl, *NematicFluctuations In Iron Based System*, The 20th Symposium on Condensed Matter Physics, SFKM 2019, p. 7, October 7th -11th, 2019, Belgrade, Serbia, p.7. M34

6. S. Djurdjić-Mijin, A. Šolajić, J. Pešić, M. Šćepanović, Y. Liu, A. Baum, C. Petrovic, **N. Lazarević**, andZ. V. Popović, *The Vibrational Properties Of* CrI_3 *Single Crystal*, The 20th Symposium on Condensed Matter Physics, SFKM 2019, p. 21, October 7th -11th, 2019, Belgrade, Serbia, p.21. M34

7. B. Colson, V. Fuentes, Z. Konstantinovic, C. Frontera, D. Colson, A. Forget, **N. Lazarevic**, M. Scepanovic, Z. V. Popovic, Ll. Balcells, B. Martinez, A. Pomar,

Nanostructured $BiFeO_3$ *Thin Films*, The 20th Symposium on Condensed Matter Physics, SFKM 2019, p. 40, October 7th -11th, 2019, Belgrade, Serbia, p.45. M34

8. J. J. Lazarević, T. Kukolj, U. Ralević, D. Bugarski, **N. Lazarević**, B. Bugarski, and Z.V. Popović, *Raman Spectroscopy Study Of Primary Mesenchymal Stem Cells,* The 20th Symposium on Condensed Matter Physics, SFKM 2019, p. 48, October 7th -11th, 2019, Belgrade, Serbia, p.48. M34

9. A. Baum, A. Milosavljević, **N. Lazarević**, M.M. Radonjić, B.Nikolić, M. Mitschek,B, Z. I. Maranloo, M. Šćepanović, M.Grujić –Brojčin, N. Stojilović, M. Opel, Aifeng Wang, C. Petrovic, Z.V. Popović,H And R. Hackl, *Lattice Dynamics And Phonon Anomalies In FeS*, The 20th Symposium on Condensed Matter Physics, SFKM 2019, p. 54, October 7th -11th, 2019, Belgrade, Serbia, p.54. M34

10. A. Milosavljević, A. Šolajić, S. Djurdjić-Mijin, J. Pešić, B. Višić, Y. Liu, C. Petrovic, **N. Lazarević** and Z. V. Popović, *Lattice Dynamics And Phase Transitions In* $Fe_{3-x}GeTe_2$, The 20th Symposium on Condensed Matter Physics, SFKM 2019, p. 84, October 7th -11th, 2019, Belgrade, Serbia, p.84. M34

11. **N. Lazarević**, A. Baum, H. N. Ruiz, Yao Wan, T. Böhm, R. H. Ahanghamejhad, P. Adelmann, T. Wolf, Z. V. Popović, B. Moritz, T. P. Devereaux, R. Hackl, *Frustrated Spin Order and Fluctuations in FeSe: A Raman Scattering Study*, The 20th Symposium on Condensed Matter Physics, SFKM 2019, p. 49, October 7th -11th, 2019, Belgrade, Serbia, p.49. M34

12. M. Opačić, **N. Lazarević**, D. Tanasković, C. Petrović and Z.V.Popović, *Lattice dynamics of iron-based superconductors and related compounds*, The Seventh International School and Conference on Photonics, 26 August – 30 August 2019, Belgrade, Serbia, p.40. M34

13. A. Baum, H. N. Ruiz, **N. Lazarević**, Yao Wang, T. Böhm, R. Hosseinian Ahangharnejhad, P. Adelmann, T. Wolf, Z. V. Popović, B. Moritz, T. P. Devereaux and R. Hackl, *Frustrated spin order and orbital selectivity in FeSe*, SNS 2019, June 16 – 21, 2019, Tokyo, Japan, p.103. M34

14. Jasmina. J. Lazarević, Tamara Kukolj, Uroš Ralević, Diana Bugarski, **Nenad Lazarević**, Branko Bugarski, and Zoran V. Popović, *Single cell Raman scattering study of mesenchymal stem cells,* Eighteenth Young Researchers Conference-Materials Science and Engineering December 4-6, 2019, Belgrade, Serbia, p.7. M34

15. S. Djurdjić-Mijin, J. Bekaert, A. Šolajić, J. Pešić, Y. Liu, M. V. Milosevic, C. Petrovic, **N. Lazarević**, and Z. V. Popović, *Probing subsequent charge density waves in 1T-TaS2 by inelastic light scattering*, Eighteenth Young Researchers

Conference-Materials Science and Engineering December 4-6, 2019, Belgrade, Serbia, p.44. M34

16. Ana Milosavljević, A. Šolajić, J. Pešić, B. Višić, M. Opačić,Yu Liu, C. Petrovic, **N. Lazarević**, Z. V. Popović, *Spin-phonon coupling in* $CrSiTe_3$ *and* $CrSi_{0.8}Ge_{0.1}Te_3$, Eighteenth Young Researchers Conference – Materials Science and Engineering December 4-6, 2019, Belgrade, Serbia, p.64. M34

17. S. Djurdjić-Mijin, A. Šolajić, J. Pešić, M. Šćepanović, Y. Liu, A. Baum, C. Petrovic, **N. Lazarević** and Z. V. Popović, *Raman Spectroscopy Study on phase transition in* CrI_3 *single crystals*, Seventeenth Young Researchers Conference – Materials Science and Engineering, December 5-7, 2018, Belgrade, Serbia, p.70. M34

18. Rudolf Hackl, Andreas Baum, Harrison Ruiz, **Nenad Lazarevic**, Yao Wang, Thomas Boehm, Ramez Hosseinian Ahangharnejhad, Peter Adelmann, Thomas Wolf, Zoran Popovic, Brian Moritz, Thomas Devereaux, *Spin order and fluctuations in FeSe*, APS March Meeting 2018, March 5 – 9, 2018, Los Angeles, California, A14.00011. M34

19. Ana Milosavljević, Andreas Baum, **Nenad Lazarević**, Miloš M. Radonjić, Božidar Nikolić, Merlin Mitschek, Zahra Inanloo Maranloo, Maja Šćepanović, Nenad Stojilović, Matthias Opel, Aifeng Wang, Čedomir Petrović, Zoran V. Popović, Rudi Hackl, *Phonon anomalies in FeS*, Sixteenth Young Researchers-Materials Science and Engineering, December 6 – 8, 2017, Belgrade, Serbia, p.44. M34

20. Marko Opačić, **Nenad Lazarević**, Darko Tanasković, Miloš Radonjić, Ana Milosavljević, Yongchang Ma, Čedomir Petrović, Zoran V. Popović, *Small influence of magnetic ordering on lattice dynamics in* $TaFe_{1.25}Te_3$, Sixteenth Young Researchers Conference – Materials Science and Engineering, December 6 – 8, 2017, Belgrade, Serbia, p.42. M34

Citation Report

Publications
41
Total
From 1980 to 2021

Citing Articles
298 Analyze
Total
269 Analyze
Without self-citations

Times Cited
390
Total
9.51
Average per item
286
Without self-citations

12
H-Index

Times Cited and Publications Over Time

41 Publications

		Citations						
		2017	2018	2019	2020	2021	Average per year	Total
	Total	35	36	69	86	42	32.5	390
1	Oxygen vacancy-induced microstructural changes of annealed CeO2-x nanocrystals Askrabic, S; Dohcevic-Mitrovic, Z; (...); Popovic, ZV Jan 2012 | JOURNAL OF RAMAN SPECTROSCOPY 43 (1) , pp.76-81	7	2	7	4	6	4.9	49
2	Vacancy-induced nanoscale phase separation in KxFe2-ySe2 single crystals evidenced by Raman scattering and powder x-ray diffraction Lazarevic, N; Abeykoon, M; (...); Popovic, ZV Aug 6 2012 | PHYSICAL REVIEW B 86 (5)	2	3	5	1	0	4.3	43
3	Lattice dynamics and phase transition in CrI3 single crystals Djurdjic-Mijin, S; Solajic, A; (...); Popovic, ZV Sep 18 2018 | PHYSICAL REVIEW B 98 (10)	0	0	7	17	8	8	32
4	Evidence for electron-phonon interaction in Fe1-xMxSb2 (M=Co and Cr; 0 <= x <= 0.5) single crystals Lazarevic, N; Popovic, ZV; (...); Petrovic, C Apr 1 2010 | PHYSICAL REVIEW B 81 (14)	2	4	0	1	0	1.83	22
5	Evidence of spin-phonon coupling in CrSiTe3 Milosavljevic, A; Solajic, A; (...); Popovic, ZV Sep 18 2018 | PHYSICAL REVIEW B 98 (10)	0	0	5	13	2	5	20
6	Phonon and magnon excitations in block-antiferromagnetic K0.88Fe1.63S2 Lazarevic, N; Lei, HC; (...); Popovic, ZV Dec 12 2011 | PHYSICAL REVIEW B 84 (21)	1	2	1	0	0	1.55	17
7	Phonon anomalies in FeS Baum, A; Milosavljevic, A; (...); Hackl, R Feb 12 2018 | PHYSICAL REVIEW B 97 (5)	0	2	7	3	3	3.75	15
8	Lattice dynamics of KNi2Se2 Lazarevic, N; Radonjic, M; (...); Popovic, ZV Apr 22 2013 | PHYSICAL REVIEW B 87 (14)	2	2	1	1	0	1.67	15
9	Frustrated spin order and stripe fluctuations in FeSe Baum, A; Ruiz, HN; (...); Hackl, R Feb 4 2019 | COMMUNICATIONS PHYSICS 2	0	0	2	6	6	4.67	14
10	Signatures of the spin-phonon coupling in Fe1+yTe1-xSex alloys Popovic, ZV; Lazarevic, N; (...); Petrovic, C Sep 2014 | SOLID STATE COMMUNICATIONS 193 , pp.51-55	4	3	2	2	1	1.75	14
11	Evidence of coupling between phonons and charge-density waves in ErTe3 Lazarevic, N; Popovic, ZV; (...); Petrovic, C Jan 24 2011 | PHYSICAL REVIEW B 83 (2)	3	2	3	2	0	1.27	14
12	Lattice dynamics of BaFe2X3(X = S, Se) compounds Popovic, ZV; Scepanovic, M; (...); Petrovic, C Feb 27 2015 | PHYSICAL REVIEW B 91 (6)	3	2	3	3	0	1.71	12
13	Probing IrTe2 crystal symmetry by polarized Raman scattering Lazarevic, N; Bozin, ES; (...); Popovic, ZV Jun 16 2014 | PHYSICAL REVIEW B 89 (22)	1	4	3	3	0	1.38	11
14	Intermolecular and low-frequency intramolecular Raman scattering study of racemic ibuprofen Lazarevic, JJ; Uskokovic-Markovic, S; (...); Popovic, ZV May 21 2014 | SPECTROCHIMICA ACTA PART A-MOLECULAR AND BIOMOLECULAR SPECTROSCOPY 126 , pp.301-305	2	2	2	3	1	1.38	11
15	Interplay of lattice, electronic, and spin degrees of freedom in detwinned BaFe2As2: A Raman scattering study Baum, A; Li, Y; (...); Hackl, R Aug 7 2018 | PHYSICAL REVIEW B 98 (7)	0	0	4	5	0	2.25	9
16	Application of the melt granulation technique in development of lipid matrix tablets with immediate release of carbamazepine Krstic, M; Djuris, J; (...); Ibric, S Jun 2017 | JOURNAL OF DRUG DELIVERY SCIENCE AND TECHNOLOGY 39 , pp.467-474	0	2	1	3	3	1.8	9
17	Lattice dynamics of FeSb2 Lazarevic, N; Radonjic, MM; (...); Popovic, ZV Jun 27 2012 | JOURNAL OF PHYSICS-CONDENSED MATTER 24 (25)	0	1	1	0	0	0.9	9
18	Lattice dynamics and phase transitions in Fe3-xGeTe2 Milosavljevic, A; Solajic, A; (...); Popovic, ZV Jun 17 2019 | PHYSICAL REVIEW B 99 (21)	0	0	0	6	2	2.67	8
19	Indication of subdominant d-wave interaction in superconducting CaKFe4As4 Jost, D; Scholz, JR; (...); Hackl, R Jul 13 2018 | PHYSICAL REVIEW B 98 (2)	0	1	1	5	1	2	8
20	Insulating and metallic spin glass in Ni-doped KxFe2-ySe2 single crystals Ryu, H; Abeykoon, M; (...); Petrovic, C May 4 2015 | PHYSICAL REVIEW B 91 (18)	1	1	2	0	0	1	7
21	Phonon and magnetic dimer excitations in Fe-based S = 2 spin-ladder compound BaFe2Se2O Popovic, ZV; Scepanovic, M; (...); Petrovic, C Jan 3 2014 | PHYSICAL REVIEW B 89 (1)	1	0	3	0	0	0.88	7
22	Raman scattering study of the Fe1-xCoxSb2 and Fe1-xCrxSb2 (0 < x < 1) single crystals Lazarevic, N; Popovic, ZV; (...); Petrovic, C Jul 2009 | PHYSICAL REVIEW B 80 (1)	0	0	1	0	0	0.46	6
23	Evidence of superconductivity-induced phonon spectra renormalization in alkali-doped iron selenides Opacic, M; Lazarevic, N; (...); Popovic, ZV Dec 9 2015 | JOURNAL OF PHYSICS-CONDENSED MATTER 27 (48)	2	1	0	0	0	0.71	5
24	Probing primary mesenchymal stem cells differentiation status by micro-Raman spectroscopy Lazarevic, JJ; Kukolj, T; (...); Popovic, ZV Apr 15 2019 | SPECTROCHIMICA ACTA PART A-MOLECULAR AND BIOMOLECULAR SPECTROSCOPY 213 , pp.384-390	0	0	0	2	2	1.33	4
25	Raman spectroscopy of KxCo2-ySe2 single crystals near the ferromagnet-paramagnet transition Opacic, M; Lazarevic, N; (...); Popovic, ZV Dec 7 2016 | JOURNAL OF PHYSICS-CONDENSED MATTER 28 (48)	2	0	1	1	0	0.67	4
26	Formation of Self-Organized Mn3O4 Nanoinclusions in LaMnO3 Films Pomar, A; Konstantinovic, Z; (...); Santiso, J Sep 20 2016 | FRONTIERS IN PHYSICS 4	0	0	0	0	4	0.67	4
27	Sustained phase separation and spin glass in Co-doped KxFe2-ySe2 single crystals Ryu, H; Wang, KF; (...); Petrovic, C Nov 19 2015 | PHYSICAL REVIEW B 92 (17)	1	1	1	0	0	0.57	4
28	Lattice dynamics of iron chalcogenides: Raman scattering study Opacic, MR and Lazarevic, NZ 2017 | JOURNAL OF THE SERBIAN CHEMICAL SOCIETY 82 (9) , pp.957-983	1	1	1	0	0	0.6	3
29	Charge density wave modulation and gap measurements in CeTe3 Ralevic, U; Lazarevic, N; (...); Popovic, ZV Oct 14 2016 | PHYSICAL REVIEW B 94 (16)	0	0	2	1	0	0.5	3
30	Phonon properties of CoSb2 single crystals Lazarevic, N; Radonjic, MM; (...); Popovic, ZV Apr 4 2012 | JOURNAL OF PHYSICS-CONDENSED MATTER 24 (13)	0	0	2	0	0	0.3	3
31	Fluctuations and pairing in Fe-based superconductors: light scattering experiments Lazarevic, N and Hackl, R Sep 2020 | JOURNAL OF PHYSICS-CONDENSED MATTER 32 (41)	0	0	0	0	2	1	2
32	Phonon anomalies and magnetic excitations in BaFe2Se2O Jin, F; Lazarevic, N; (...); Zhang, QM Apr 22 2019 | PHYSICAL REVIEW B 99 (14)	0	0	0	1	1	0.67	2
33	Solid dispersions with carbamazepine: optimization of formulation, characterization and examination of long-term stability Krstic, M; Lukic, I; (...); Vasiljevic, D 2018 | HEMIJSKA INDUSTRIJA 72 (4) , pp.191-204	0	0	0	2	0	0.5	2
34	Influence of chemical fixation process on primary mesenchymal stem cells evidenced by Raman spectroscopy Lazarevic, JJ; Ralevic, U; (...); Popovic, ZV Jun 5 2019 | SPECTROCHIMICA ACTA PART A-MOLECULAR AND BIOMOLECULAR SPECTROSCOPY 216 , pp.173-178	0	0	0	1	0	0.33	1
35	Small influence of magnetic ordering on lattice dynamics in TaFe1.25Te3 Opacic, M; Lazarevic, N; (...); Popovic, ZV Nov 16 2017 | PHYSICAL REVIEW B 96 (17)	0	0	1	0	0	0.2	1
36	Probing charge density wave phases and the Mott transition in 1T-TaS2I by inelastic light scattering Mijin, SD; Baum, A; (...); Lazarevic, N Jun 22 2021 | PHYSICAL REVIEW B 103 (24)	0	0	0	0	0	0	0
37	Short-Range Order in VI3 Mijin, SD; Abeykoon, AMM; (...); Lazarevic, N Nov 16 2020 | INORGANIC CHEMISTRY 59 (22) , pp.16265-16271	0	0	0	0	0	0	0
38	Self-assembled line network in BiFeO3 thin films Colson, B; Fuentes, V; (...); Pomar, A Sep 1 2020 | JOURNAL OF MAGNETISM AND MAGNETIC MATERIALS 509	0	0	0	0	0	0	0
39	Vacancies and spin-phonon coupling in CrSi0.8Ge0.1Te3 Milosavljevic, A; Solajic, A; (...); Lazarevic, N Nov 2020 | Aug 2020 (Early Access) | JOURNAL OF RAMAN SPECTROSCOPY 51 (11) , pp.2153-2160	0	0	0	0	0	0	0
40	Temperature-Dependent Raman Study of Nanostructured and Multifunctional Materials Scepanovic, M; Grujic-Brojcin, M; (...); Popovic, ZV Jul 2019 | PHYSICA STATUS SOLIDI A-APPLICATIONS AND MATERIALS SCIENCE 216 (13)	0	0	0	0	0	0	0
41	DEFECT STATES IN Ce0.85Nd(Gd)(0.15)O2-delta NANO-CRYSTALS INVESTIGATED BY RAMAN SPECTROSCOPY Lazarevic, NZ; Dohcevic-Mitrovic, ZD; (...); Popovic, ZV 7th Seminar of Young Researchers May-jun 2009 | HEMIJSKA INDUSTRIJA 63 (3) , pp.221-226	0	0	0	0	0	0	0

Citation Report Publications Table

Nenad Lazarevic

Institute of Physics Belgrade
Solid State Physics

	All	Since 2016
Citations	509	393
h-index	14	13
i10-index	19	17

2 articles	17 articles
not available	available

Based on funding mandates

TITLE	CITED BY	YEAR
Oxygen vacancy-induced microstructural changes of annealed CeO2−x nanocrystals S Aškrabić, Z Dohčević-Mitrović, A Kremenović, N Lazarević, ... Journal of Raman Spectroscopy 43 (1), 76-81	59	2012
Vacancy-induced nanoscale phase separation in KxFe2−ySe2 single crystals evidenced by Raman scattering and powder x-ray diffraction N Lazarević, M Abeykoon, PW Stephens, H Lei, ES Bozin, C Petrovic, ... Physical Review B 86 (5), 054503	55	2012
Lattice dynamics and phase transition in CrI_3 single crystals S Djurdjić-Mijin, A Šolajić, J Pešić, M Šćepanović, Y Liu, A Baum, ... Physical Review B 98 (10), 104307	36	2018
Evidence for electron-phonon interaction in Fe1−xMxSb2 (M= Co and Cr; 0≤ x≤ 0.5) single crystals N Lazarević, ZV Popović, R Hu, C Petrovic Physical Review B 81 (14), 144302	26	2010
Frustrated spin order and stripe fluctuations in FeSe A Baum, HN Ruiz, N Lazarević, Y Wang, T Böhm, RH Ahangharnejhad, ... Communications Physics 2 (1), 1-7	22	2019
Evidence of spin-phonon coupling in CrSiTe_3 A Milosavljević, A Šolajić, J Pešić, Y Liu, C Petrovic, N Lazarević, ... Physical Review B 98 (10), 104306	22	2018
Phonon anomalies in FeS A Baum, A Milosavljević, N Lazarević, MM Radonjić, B Nikolić, M Mitschek, ... Physical Review B 97 (5), 054306	22	2018
Lattice dynamics of KNi 2 Se 2 N Lazarević, M Radonjić, M Šćepanović, H Lei, D Tanasković, C Petrovic, ... Physical Review B 87 (14), 144305	21	2013
Phonon and magnon excitations in block-antiferromagnetic K0.88Fe1.63S2 N Lazarević, H Lei, C Petrovic, ZV Popović Physical Review B 84 (21), 214305	21	2011
Evidence of coupling between phonons and charge-density waves in ErTe3 N Lazarević, ZV Popović, R Hu, C Petrovic Physical Review B 83 (2), 024302	20	2011
Application of the melt granulation technique in development of lipid matrix tablets with immediate release of carbamazepine M Krstic, J Djuris, O Petrovic, N Lazarevic, S Cvijic, S Ibric Journal of Drug Delivery Science and Technology 39, 467-474	16	2017
Intermolecular and low-frequency intramolecular Raman scattering study of racemic ibuprofen JJ Lazarević, S Uskoković-Marković, M Jelikić-Stankov, M Radonjić, ...	16	2014

TITLE	CITED BY	YEAR
Spectrochimica Acta Part A: Molecular and Biomolecular Spectroscopy 126, 301-305		
Indication of subdominant d-wave interaction in superconducting $\mathrm{CaKFe_4As_4}$ D Jost, JR Scholz, U Zweck, WR Meier, AE Böhmer, PC Canfield, ... Physical Review B 98 (2), 020504	15	2018
Probing Ir Te 2 crystal symmetry by polarized Raman scattering N Lazarević, ES Bozin, M Šćepanović, M Opačić, H Lei, C Petrovic, ... Physical Review B 89 (22), 224301	14	2014
Interplay of lattice, electronic, and spin degrees of freedom in detwinned $\mathrm{BaFe_2As_2}$: A Raman scattering study A Baum, Y Li, M Tomić, N Lazarević, D Jost, F Löffler, B Muschler, T Böhm, ... Physical Review B 98 (7), 075113	13	2018
Lattice dynamics of BaFe 2 X 3 (X= S, Se) compounds ZV Popović, M Šćepanović, N Lazarević, M Opačić, MM Radonjić, ... Physical Review B 91 (6), 064303	13	2015
Signatures of the spin-phonon coupling in Fe1+ yTe1− xSex alloys ZV Popović, N Lazarević, S Bogdanović, MM Radonjić, D Tanasković, ... Solid State Communications 193, 51-55	13	2014
Phonon and magnetic dimer excitations in Fe-based S= 2 spin-ladder compound BaFe2Se2O ZV Popović, M Šćepanović, N Lazarević, MM Radonjić, D Tanasković, ... Physical Review B 89 (1), 014301	13	2014
Lattice dynamics of FeSb2 N Lazarević, MM Radonjić, D Tanasković, R Hu, C Petrovic, ZV Popović Journal of Physics: Condensed Matter 24 (25), 255402	10	2012
Evidence of superconductivity-induced phonon spectra renormalization in alkali-doped iron selenides M Opačić, N Lazarević, M Šćepanović, H Ryu, H Lei, C Petrovic, ... Journal of Physics: Condensed Matter 27 (48), 485701	9	2015
Lattice dynamics and phase transitions in $\mathrm{Fe_{3-x}GeTe_2}$ A Milosavljević, A Šolajić, S Djurdjić-Mijin, J Pešić, B Višić, Y Liu, ... Physical Review B 99 (21), 214304	8	2019
Insulating and metallic spin glass in Ni-doped K x Fe 2− y Se 2 single crystals H Ryu, M Abeykoon, K Wang, H Lei, N Lazarevic, JB Warren, ES Bozin, ... Physical Review B 91 (18), 184503	8	2015
Charge density wave modulation and gap measurements in CeTe 3 U Ralević, N Lazarević, A Baum, HM Eiter, R Hackl, P Giraldo-Gallo, ... Physical Review B 94 (16), 165132	7	2016
Formation of self-organized Mn3O4 nanoinclusions in LaMnO3 films A Pomar, Z Konstantinović, N Bagués, J Roqueta, L López-Mir, L Balcells, ... Frontiers in Physics 4, 41	7	2016
Probing primary mesenchymal stem cells differentiation status by micro-Raman spectroscopy JJ Lazarević, T Kukolj, D Bugarski, N Lazarević, B Bugarski, ZV Popović Spectrochimica Acta Part A: Molecular and Biomolecular Spectroscopy 213, 384-390	6	2019

TITLE	CITED BY	YEAR
Raman scattering study of the Fe1−xCoxSb2 and Fe1−xCrxSb2 (0≤ x≤ 1) single crystals N Lazarević, ZV Popović, R Hu, C Petrovic Physical Review B 80 (1), 014302	6	2009
Lattice dynamics of iron chalcogenides–Raman scattering study M Opačić, N Lazarević Journal of the Serbian Chemical Society 82 (9), 957-983	5	2017
Sustained phase separation and spin glass in Co-doped K x Fe 2− y Se 2 single crystals H Ryu, K Wang, M Opacic, N Lazarevic, JB Warren, ZV Popovic, ES Bozin, ... Physical Review B 92 (17), 174522	5	2015
Fluctuations and pairing in Fe-based superconductors: light scattering experiments N Lazarevic, RU Hackl Journal of Physics: Condensed Matter	4	2020
Raman spectroscopy of K x Co2− y Se2 single crystals near the ferromagnet–paramagnet transition M Opačić, N Lazarević, MM Radonjić, M Šćepanović, H Ryu, A Wang, ... Journal of Physics: Condensed Matter 28 (48), 485401	4	2016
Phonon anomalies and magnetic excitations in $\mathrm{BaFe_2Se_2O}$ F Jin, N Lazarević, C Liu, J Ji, Y Wang, S He, H Lei, C Petrovic, R Yu, ... Physical Review B 99 (14), 144419	3	2019
Phonon properties of CoSb2 single crystals N Lazarević, MM Radonjić, R Hu, D Tanasković, C Petrovic, ZV Popović Journal of Physics: Condensed Matter 24 (13), 135402	3	2012
Solid dispersions with carbamazepine: Optimization of formulation, characterization and examination of long-term stability K Marko, L Igor, B Alma, L Nenad, V Dragana Hemijska Industrija 72 (4), 191	2	2018
Small influence of magnetic ordering on lattice dynamics in $\mathrm{TaFe_{1.25}Te_3}$ M Opačić, N Lazarević, D Tanasković, MM Radonjić, A Milosavljević, ... Physical Review B 96 (17), 174303	2	2017
Vacancies and spin–phonon coupling in CrSi$_{0.8}$Ge$_{0.1}$Te$_3$ A Milosavljević, A Šolajić, B Višić, M Opačić, J Pešić, Y Liu, C Petrovic, ... Journal of Raman Spectroscopy 51 (11), 2153-2160	1	2020
Self-assembled line network in BiFeO3 thin films B Colson, V Fuentes, Z Konstantinović, D Colson, A Forget, N Lazarević, ... Journal of Magnetism and Magnetic Materials 509, 166898	1	2020
Influence of chemical fixation process on primary mesenchymal stem cells evidenced by Raman spectroscopy JJ Lazarević, U Ralević, T Kukolj, D Bugarski, N Lazarević, B Bugarski, ... Spectrochimica Acta Part A: Molecular and Biomolecular Spectroscopy 216, 173-178	1	2019
Probing charge density wave phases and Mott transition in $1T$-TaS$_2$ by inelastic light scattering S Đurđić Mijin, A Baum, J Bekaert, A Šolajić, J Pešić, Y Liu, G He, ... arXiv e-prints, arXiv: 2102.04821		2021

TITLE	CITED BY	YEAR
Short-Range Order in VI$_3$ S Djurdjić Mijin, AMM Abeykoon, A Šolajić, A Milosavljević, J Pešić, ... Inorganic Chemistry 59 (22), 16265-16271		2020
Superconducting Order from Local Disorder A Wang, E Stavitski, M Naamneh, VN Ivanovski, M Abeykoon, ... arXiv preprint arXiv:2009.06623		2020
Exploring the electronic structure of BaFe$_2$As$_2$ using resonant Raman scattering R Hackl, A Baum, Y Li, N Lazarevic, D Jost, JH Chu, I Fisher, R Valenti, ... Bulletin of the American Physical Society 65		2020
Frustrated spin order in FeSe A Baum, H Ruiz, N Lazarević, Y Wang, T Boehm, ... Bulletin of the American Physical Society 65		2020
Self-assembled network of nanostructures in BiFeO3 thin films B Colson, V Fuentes, Z Konstantinović, C Frontera, J Santiso, ...		2019
Temperature-Dependent Raman Study of Nanostructured and Multifunctional Materials M Šćepanović, M Grujić-Brojčin, N Lazarević, ZV Popović physica status solidi (a), 1800763		2019
Orbital selective magnetism, nematicity, and fluctuations in FeSe R Hackl, A Baum, H Ruiz, N Lazarevic, Y Wang, T Boehm, T Wolf, B Moritz, ... APS March Meeting Abstracts 2019, S62. 003		2019
Cvrste disperzije sa karbamazepinom: optimizacija formulacija, karakterizacija i ispitivanje dugorocne stabilnosti M Krstic, I Lukic, A Busatlic, N Lazarevic, D Vasiljevic Hemijska Industrija 72 (4), 191-205		2018
Spin order and fluctuations in FeSe R Hackl, A Baum, H Ruiz, N Lazarevic, Y Wang, T Boehm, ... APS March Meeting Abstracts 2018, A14. 011		2018
Neelastično rasejanje svetlosti na jako korelisanim elektronskim sistemima-antimonidi i teluridi NŽ Lazarević Univerzitet u Beogradu, Fizički fakultet		2012
Defect states in Ce0. 85Nd (Gd) 0.15 O2-δ nano-crystals investigated by Raman spectroscopy NŽ Lazarević, ZD Dohčević-Mitrović, MU Grujić-Brojčin, MJ Šćepanović, ... Hemijska industrija 63 (3), 221-226		2009

Subject **How you contributed to quality peer review in 2020**
From Emma Wilson <publishing@rsc.org>
To <nenad.lazarevic@ipb.ac.rs>
Date 2021-02-11 13:31

Online version

Dear Dr Lazarevic

We want to take a moment and thank you for your work as a peer reviewer for our journals in 2020.

As a society, and with your support, we can continue to advance excellence in the chemical sciences – to improve the lives of people around the world now and in the future.

Your contributions to peer review in 2020:

Total number of reviews completed: 1

By journal:

Analytical Methods 1

Please check your reviewer account

Have any of your details, research interests or contact preferences changed recently?

I would be grateful if you could check your account to ensure that we send you papers relevant to your expertise.

Once you have logged in, select 'Edit Account' at the top of the screen to update your information. You can learn how we protect the information you share with us in our privacy statement.

Make an update

Support for your contributions

Track and boost your impact as a reviewer. Read about our partnership with Publons and set up a profile – you can do this easily via our review submission system.
If you are relatively new to peer review, take a look at our peer review infographic to better understand our peer review process.

For more advice and information, take a trip to our online reviewer hub.

Thank you once again for your commitment and support. The whole publishing team looks forward to working with you once again in 2021.

Emma Wilson

Director of Publishing
Royal Society of Chemistry

The Royal Society of Chemistry, Thomas Graham House, Science Park, Cambridge CB4 0WF, United Kingdom.
Registered charity number: 207890.

Subject **Referee update Lazarevic 875626**
From <office@aps.org>
To <nenadl@ipb.ac.rs>
Date 2020-08-30 06:59

Dr. Nenad Lazarevic
University of Belgrade
Belgrade
SERBIA
nenadl@ipb.ac.rs

Dear Dr. Lazarevic,

Thank you for your help as a referee for the Physical Review journals and Reviews of Modern Physics. We understand that your time is valuable and have therefore made your record available via our referee server (https://referees.aps.org/) so that you can make changes quickly and easily at any time.

We recognize that your availability to review manuscripts may fluctuate throughout the year and suggest that you visit this site whenever necessary to update your relevant information. Please be reminded that to access our referee server you will need to have an active APS Journal account. For more information and to create an account please go to https://journals.aps.org/signup.

Providing us with up to date and accurate information helps the refereeing process run smoothly and ensures that we only ask you to review appropriate material, when you are able to, and that we do not contact you unnecessarily.

Thank you for your assistance.

Sincerely,

Michael Thoennessen
Editor in Chief
American Physical Society

☰ Journal of Raman Spectroscopy

Home

Author

Review

Reviewer View Manuscripts

0 Review and Score

3 Scores Submitted

Invitations

Legacy Instructions

Scores Submitted

[illegible]eted

Select...

11-Jul-2019

JRS-19-0101.R1

Characterization of 2D materials from Raman spectral data
Files archived

Minor Revision (12-Jul-2019) a revision has been submitted
Archiving completed on 31-Oct-2019

Select...

02-Apr-2019

JRS-19-0101

Characterization of 2D materials from Raman spectral data
Files archived

Major Revision (03-Apr-2019) a revision has been submitted
Archiving completed on 31-Oct-2019

Select...

04-Nov-2018

JRS-18-0305

Raman Spectroscopic Study of the Influence of Voltage-Time on Titania Growth-Fast Anodized Nanostructures.
Files archived

Reject - unsuitable for referral (11-Nov-2018)
Archiving completed on 16-Jan-2019

НАУКЕ И ТЕХНОЛОШКОГ РАЗВОЈА
Комисија за стицање научних звања

Број: 660-01-00006/77
24.05.2017. године
Београд

На основу члана 22. став 2. члана 70. став 5. Закона о научноистраживачкој делатности ("Службени гласник Републике Србије", број 110/05, 50/06 – исправка, 18/10 и 112/15), члана 3. ст. 1. и 3. и члана 40. Правилника о поступку, начину вредновања и квантитативном исказивању научноистраживачких резултата истраживача ("Службени гласник Републике Србије", број 24/16, 21/17 и 38/17) и захтева који је поднео

Институт за физику у Београду

Комисија за стицање научних звања на седници одржаној 24.05.2017. године, донела је

ОДЛУКУ
О СТИЦАЊУ НАУЧНОГ ЗВАЊА

Др Ненад Лазаревић

стиче научно звање

Виши научни сарадник

у области природно-математичких наука - физика

ОБРАЗЛОЖЕЊЕ

Институт за физику у Београду

утврдио је предлог број 177/1 од 07.02.2017. године на седници Научног већа Института и поднео захтев Комисији за стицање научних звања број 198/1 од 13.02.2017. године за доношење одлуке о испуњености услова за стицање научног звања ***Виши научни сарадник***.

Комисија за стицање научних звања је по претходно прибављеном позитивном мишљењу Матичног научног одбора за физику на седници одржаној 24.05.2017. године разматрала захтев и утврдила да именовани испуњава услове из члана 70. став 5. Закона о научноистраживачкој делатности ("Службени гласник Републике Србије", број 110/05, 50/06 – исправка,18/10 и 112/15), члана 3. ст. 1. и 3. и члана 40. Правилника о поступку, начину вредновања и квантитативном исказивању научноистраживачких резултата истраживача ("Службени гласник Републике Србије", број 24/16, 21/17 и 38/17) за стицање научног звања ***Виши научни сарадник***, па је одлучила као у изреци ове одлуке.

Доношењем ове одлуке именовани стиче сва права која му на основу ње по закону припадају.

Одлуку доставити подносиоцу захтева, именованом и архиви Министарства просвете, науке и технолошког развоја у Београду.

ПРЕДСЕДНИК КОМИСИЈЕ
С. Стошић-Грујичић
Др Станислава Стошић-Грујичић,
научни саветник

МИНИСТАР
Младен Шарчевић

Република Србија
КРИМИНАЛИСТИЧКО-ПОЛИЦИЈСКИ
УНИВЕРЗИТЕТ
28 Бр. 85/1-4-2020
16.03.2020.
Београд

На основу члана 68. став 6. тачка 1. Статута Криминалистичко-полицијског универзитета (18 бр. 72/4-2-2018 од 17.07.2019. године), а у вези члана 74. став 8. и члана 75. став 4. Закона о високом образовању ("Службени гласник РС" број 88/17, 27/18-др. закон и 73/18),

Веће научних области природно-математичких и техничко-технолошких студија Криминалистичко-полицијског универзитета, на седници одржаној 16.03.2020. године, доноси

ОДЛУКУ
О ИЗБОРУ НАСТАВНИКА У ЗВАЊЕ И НА РАДНО МЕСТО

1. **др Ненад Лазаревић**, бира се у звање и на радно место доцент, за ужу научну област *Електротехничко инжењерство,* за наставни предмет **Оптички и спектроскопски уређаји** -на период у трајању од 5 година;
2. Права, обавезе и одговорности из радног односа именованог уредиће се посебним решењем.

Образложење

На основу Одлуке ректора 01 број 535/1 од 25.12.2019. године, Криминалистичко-полицијски универзитет објавио је у огласним новинама Националне службе за запошљавање *Послови,* од 31. децембар 2019. године, конкурс за стицање звања и заснивање радног односа једног наставника, са пуним радним временом, у звању доцента за ужу научну област *Електротехничко инжењерство* за наставни предмет Оптички и спектроскопски уређаји -на период у трајању од 5 година.

Веће Департмана форензичког инжењерства, донело је Одлуку 25 број 82/11-4-2019 од 30.12.2019. године, којом је образована Комисија за припрему извештаја о пријављеним кандидатима, у саставу: др Стево Јаћимовски, редовни професор, Криминалистичко-полицијски универзитет, др Радован Радовановић, редовни професор, Криминалистичко-полицијски универзитет и др Зоран Поповић, академик, редовни професор, Институт за физику Универзитета у Београду.

Комисија је прегледала конкурсни материјал, сачинила Извештај који је доставила Изборном већу Криминалистичко-полицијског универзитета, које је донело Одлуку о утврђивању предлога (26 бр. 83/1-7-2020 од 16.03.2020. године) и исти доставила Већу научних области ради доношења одлуке.

Веће научних области је, након разматрања извештаја комисије и Одлуке о утврђивању предлога Изборног већа, донело одлуку о избору др Ненада Лазаревића у звање и на радно место доцента за ужу научну област *Електротехничко инжењерство* за наставни предмет Оптички и спектроскопски уређаји.

Сходно томе, одлучено је као у изреци.

ПРЕДСЕДНИК ВЕЋА
проф. др Стево Јаћимовски

ДОСТАВИТИ:

⇒ именованом
⇒ персонални досије
⇒ архива

Институт за физику у Београду

на основу одлуке Жирија о додељивању Годишње награде додељује:

ГОДИШЊУ НАГРАДУ ИНСТИТУТА ЗА ФИЗИКУ ЗА 2021. ГОДИНУ

др Ненаду Лазаревићу

за његов значајан допринос разумевању комплексне међуповезаности фононских, електронских и магнетних степена слободе код суперпроводника на бази гвожђа

др Жељка Никитовић
председница
Научног већа

Београд
31. август 2021.

др Александар Богојевић
директор
Института за физику

Mobility Agreement
Staff Mobility For Teaching[1]

Planned period of the teaching activity: from *20/05/2019* till *24/05/2019*

Duration (days) – excluding travel days: 5

The teaching staff member

Last name (s)	**Lazarević**	First name (s)	**Nenad**
Seniority[2]	Intermediate	Nationality[3]	**Serbian**
Sex [*M/F*]	M	Academic year	2018/2019
E-mail	nenadl@ipb.ac.rs		

The Sending Institution/Enterprise[4]

Name	Institute of Physics Belgrade/ University of Belgrade		
Erasmus code[5] (if applicable)	RS-BELGRADE	Faculty/Department	Institute of Physics Belgrade
Address	Belgrade	Country/ Country code[6]	**Serbia**
Contact person name and position	Ljubica Dimitrijevic	Contact person e-mail / phone	stamlj@rect.bg.ac.rs
Type of enterprise:	University	Size of enterprise (if applicable)	☐<250 employees ☐>250 employees

The Receiving Institution

Name	University of Antwerp	Faculty/Department	Sciences / / Physics
Erasmus code (if applicable)	B ANTWERP01		
Address	Antwerp	Country/ Country code	Belgium
Contact person name and position	Sarah Verberckmoes	Contact person e-mail / phone	Sarah. verberckmoes @uantwerpen. be

For guidelines, please look at the end notes on page 3.

Section to be completed BEFORE THE MOBILITY

I. PROPOSED MOBILITY PROGRAMME

Main subject field[7]: Physics

Level (select the main one): Short cycle (EQF level 5) ☐; Bachelor or equivalent first cycle (EQF level 6) ☐; Master or equivalent second cycle (EQF level 7) ☒; Doctoral or equivalent third cycle (EQF level 8) ☒

Number of students at the receiving institution benefiting from the teaching programme: 10

Number of teaching hours: 8

Language of instruction: English

Overall objectives of the mobility:

Establishing a collaboration between the respective partner institutions and exchange of knowledge.

Added value of the mobility (in the context of the modernisation and internationalisation strategies of the institutions involved):

Through the proposed programme the researchers of the partner institutions will gain deeper insight into the research activities of the respective partners, thus defining common grounds for future collaboration. At the same time young scientists will be given the chance to establish networks as a basis for future cooperation in both science and industry.

Content of the teaching programme:

The programme will be realised through the hands-on course on Raman spectroscopy. In the first part a thorough introduction to the theoretical aspects of inelastic light scattering will be given, including the scattering mechanisms for various types of excitations. Additionally, the experimental challenges in obtaining high quality data are discussed. The second part focus on recent results of Raman spectroscopy in the field of Fe-based superconductors. In addition, a talk entitled "Frustration and fluctuations in FeSe: A Raman scattering study" will be presented.

Expected outcomes and impact (e.g. on the professional development of the teaching staff member and on the competences of students at both institutions):

Through the realisation of the proposed programme teaching staff member(s) will tend to establish scientific collaboration with the partner institution thereby raising competitiveness and laying ground for joint application for future EU projects. Within planned activities, students will be introduced to the basic and advanced concepts of the Raman spectroscopy and its application in the field of high temperature superconductors. The opportunities for the student exchange will also be promoted.

II. COMMITMENT OF THE THREE PARTIES

By signing[6] this document, the teaching staff member, the sending institution/enterprise and the receiving institution confirm that they approve the proposed mobility agreement.

The sending higher education institution supports the staff mobility as part of its modernisation and internationalisation strategy and will recognise it as a component in any evaluation or assessment of the teaching staff member.

The teaching staff member will share his/her experience, in particular its impact on his/her professional development and on the sending higher education institution, as a source of inspiration to others.

The teaching staff member and the beneficiary institution commit to the requirements set out in the grant agreement signed between them.

The teaching staff member and the receiving institution will communicate to the sending institution/enterprise any problems or changes regarding the proposed mobility programme or mobility period.

The teaching staff member

Name: Nenad Lazarevic

Signature: Date: 03.05.2019.

The sending institution/enterprise

Name of the responsible person: Prof. Dr Nenad Zrnić, Vice Rector

Signature: Date: 13 MAY 2019

Name of the responsible person: Dr Antun Balaž, Deputy Director, Institute of Physics Belgrade

Signature: Date:

The receiving institution

Name of the responsible person: Sarah Verberckmoes

Signature: Date: 14/05/2019

Universiteit Antwerpen

---

[1] In case the mobility combines teaching and training activities, **this template** should be used and adjusted to fit both activity types.

[2] **Seniority:** Junior (approx. < 10 years of experience), Intermediate (approx. > 10 and < 20 years of experience) or Senior (approx. > 20 years of experience).

[3] **Nationality:** Country to which the person belongs administratively and that issues the ID card and/or passport.

[4] All refererences to "**enterprise**" are only applicable to mobility for staff between Programme Countries or within Capacity Building projects.

[5] **Erasmus Code:** A unique identifier that every higher education institution that has been awarded with the Erasmus Charter for Higher Education receives. It is only applicable to higher education institutions located in Programme Countries.

[6] **Country code:** ISO 3166-2 country codes available at: https://www.iso.org/obp/ui/#search.

[7] The ISCED-F 2013 search tool (available at http://ec.europa.eu/education/tools/isced-f_en.htm) should be used to find the ISCED 2013 detailed field of education and training.

[8] Circulating papers with original signatures is not compulsory. Scanned copies of signatures or electronic signatures may be accepted, depending on the national legislation of the country of the sending institution (in the case of mobility with Partner Countries: the national legislation of the Programme Country). Certificates of attendance can be provided electronically or through any other means accessible to the staff member and the sending institution.

PHYSICAL REVIEW B **103**, 245133 (2021)

Probing charge density wave phases and the Mott transition in $1T$-TaS$_2$ by inelastic light scattering

S. Djurdjić Mijin,[1] A. Baum,[2] J. Bekaert,[3] A. Šolajić,[1] J. Pešić,[1] Y. Liu,[4,*] Ge He,[2] M. V. Milošević,[3] C. Petrovic,[4]
Z. V. Popović,[1,5] R. Hackl,[2] and N. Lazarević[1]
[1] *Center for Solid State Physics and New Materials, Institute of Physics Belgrade, University of Belgrade, Pregrevica 118, RS-11080 Belgrade, Serbia*
[2] *Walther Meissner Institut, Bayerische Akademie der Wissenschaften, D-85748 Garching, Germany*
[3] *Department of Physics, University of Antwerp, Groenenborgerlaan 171, B-2020 Antwerp, Belgium*
[4] *Condensed Matter Physics and Materials Science Department, Brookhaven National Laboratory, Upton, New York 11973-5000, USA*
[5] *Serbian Academy of Sciences and Arts, Knez Mihailova 35, RS-11000 Belgrade, Serbia*

(Received 10 March 2021; revised 14 June 2021; accepted 16 June 2021; published 22 June 2021)

We present a polarization-resolved, high-resolution Raman scattering study of the three consecutive charge density wave (CDW) regimes in $1T$-TaS$_2$ single crystals, supported by *ab initio* calculations. Our analysis of the spectra within the low-temperature commensurate (C-CDW) regime shows $P\bar{3}$ symmetry of the system, thus excluding the previously proposed triclinic stacking of the "star-of-David" structure, and promoting trigonal or hexagonal stacking instead. The spectra of the high-temperature incommensurate (IC-CDW) phase directly project the phonon density of states due to the breaking of the translational invariance, supplemented by sizable electron-phonon coupling. Between 200 and 352 K, our Raman spectra show contributions from both the IC-CDW and the C-CDW phases, indicating their coexistence in the so-called nearly commensurate (NC-CDW) phase. The temperature dependence of the symmetry-resolved Raman conductivity indicates the stepwise reduction of the density of states in the CDW phases, followed by a Mott transition within the C-CDW phase. We determine the size of the Mott gap to be $\Omega_{\text{gap}} \approx$ 170–190 meV, and track its temperature dependence.

DOI: 10.1103/PhysRevB.103.245133

I. INTRODUCTION

Quasi-two-dimensional transition metal dichalcogenides (TMDs), such as the various structures of TaSe$_2$ and TaS$_2$, have been in the focus of various scientific investigations over the last 30 years, mostly due to the plethora of charge density wave (CDW) phases [1,2]. Among all TMD compounds $1T$-TaS$_2$ stands out because of its unique and rich electronic phase diagram [3–6]. It experiences phase transitions at relatively high temperatures, making it easily accessible for investigation and, mainly for the hysteresis effects, attractive for potential applications such as data storage [7], information processing [8], or voltage-controlled oscillators [9].

The cascade of phase transitions as a function of temperature includes the transition from the normal metallic to the incommensurate CDW (IC-CDW) phase, the nearly commensurate CDW (NC-CDW) phase, and the commensurate CDW (C-CDW) phase occurring at around $T_{\text{IC}} = 554$ K, $T_{\text{NC}} = 355$ K, and in the temperature range from $T_{\text{C}\downarrow} = 180$ K to $T_{\text{C}\uparrow} = 230$ K, respectively. Recent studies indicate the possibility of yet another phase transition in $1T$-TaS$_2$ at $T_H = 80$ K, named the hidden CDW state [10–12]. This discovery led to a new boost in attention for $1T$-TaS$_2$.

Upon lowering the temperature to $T_{\text{IC}} = 554$ K, the normal metallic state structure, described by the space group $P\bar{3}m1$ (D_{3d}^d) [13], transforms into the IC-CDW state. As will be demonstrated here, the IC-CDW domains shrink upon further temperature reduction until they gradually disappear, giving place to the C-CDW ordered state. This region in the phase diagram between 554 and roughly 200 K is characterized by the coexistence of the IC-CDW and C-CDW phases and is often referred to as NC-CDW. At the transition temperature T_C, IC-CDW domains completely vanish [14] and a new lattice symmetry is established. There is a general consensus about the formation of "star-of-David" clusters with in-plane $\sqrt{13}a \times \sqrt{13}a$ lattice reconstruction, whereby 12 Ta atoms are grouped around the 13th Ta atom [15,16]. In the absence of any external strain fields, this can be achieved in two equivalent ways (by either clockwise or counterclockwise rotations) thus yielding domains [17]. Despite extensive investigations, both experimental and theoretical, it remains an open question whether the stacking of star-of-David clusters is triclinic, trigonal, hexagonal, or a combination thereof [15,16,18–20]. The C-CDW phase is believed to be an insulator [3,21–23] with a gap of around 100 meV [13]. Very recent theoretical studies based on density-functional theory (DFT) find an additional ordering pattern along the crystallographic c axis. The related gap has a width of approximately 0.5 eV along k_z and becomes gapped at the Fermi energy E_{F} in the C-CDW phase [24,25].

Nearly all of the previously reported results for optical phonons in $1T$-TaS$_2$ are based on Raman spectroscopy on the C-CDW phase and on temperature-dependent measurements in a narrow range around the NC-CDW to C-CDW phase transition [13,15,18–20]. In this paper we present temperature-dependent polarization-resolved Raman

---

[*] Present address: Los Alamos National Laboratory, Los Alamos, New Mexico 87545, USA.

measurements in the temperature range from 4 to 370 K covering all three CDW regimes of $1T$-TaS$_2$. Our analysis of the C-CDW phase confirms the symmetry to be $P\bar{3}$, while the NC-CDW phase is confirmed as a mixed regime of commensurate and incommensurate domains. The Raman spectra of the IC-CDW phase mainly project the phonon density of states due to the breaking of translation invariance and sizable electron-phonon coupling. The growth of the CDW gap upon cooling, followed by the opening of the Mott gap, is traced via the initial slope of the symmetry-resolved spectra. The size of 170–190 meV and the temperature dependence of the Mott gap are directly determined from high-energy Raman data.

II. EXPERIMENTAL AND NUMERICAL METHODS

The preparation of the studied $1T$-TaS$_2$ single crystals is described elsewhere [26–29]. Calibrated customized Raman scattering equipment was used to obtain the spectra. Temperature-dependent measurements were performed with the sample attached to the cold finger of a He-flow cryostat. The sample was cooled down to the lowest temperature and then heated. In either case the rates were less than ± 1 K/min. All measurements were performed in a high vacuum of approximately 5×10^{-5} Pa.

The 575-nm laser line of a diode-pumped Coherent GENESIS MX-SLM solid state laser was used as an excitation source. Additional measurements with the 458- and 514-nm laser lines were performed with a Coherent Innova 304C argon ion laser. The absorbed power was set at 4 mW. All spectra shown are corrected for the sensitivity of the instrument and the Bose factor, yielding the imaginary part of the Raman susceptibility $R\chi''$, where R is an experimental constant. An angle of incidence of $\Theta_i = 66.0 \pm 0.4^\circ$ and atomically flat cleaved surfaces enable us to measure at energies as low as 5 cm^{-1} without a detectable contribution from the laser line since the directly reflected light does not reach the spectrometer. The corresponding laser spot has an area of roughly 50×100 μm^2 which prevents us from observing the possible emergence of the domains [17,30]. The inelastically scattered light is collected along the surface normal (crystallographic c axis) with an objective lens having a numerical aperture of 0.25. In the experiments presented here, the linear polarizations of the incident and scattered light are denoted as $\mathbf{e}_\mathrm{i}$ and $\mathbf{e}_\mathrm{s}$, respectively. For $\mathbf{e}_\mathrm{i}$ horizontal to the plane of incidence there is no projection on the crystallographic c axis. For the low numerical aperture of the collection optics $\mathbf{e}_\mathrm{s}$ is always perpendicular to the c axis. Low-energy data up to 550 cm^{-1} were acquired in steps of $\Delta\Omega = 1$ cm^{-1} with a resolution of $\sigma \approx 3$ cm^{-1}. The symmetric phonon lines were modeled using Voigt profiles where the width of the Gaussian part is given by σ. For spectra up to higher energies the step width and resolution were set at $\Delta\Omega = 50$ cm^{-1} and $\sigma \approx 20$ cm^{-1}, respectively. The Raman tensors for the D_{3d} point group are given in Table I. Accordingly, parallel linear polarizations project both A_{1g} and E_g symmetries, while crossed linear polarizations only project E_g. The pure A_{1g} response then can be extracted by subtraction.

TABLE I. Raman tensors for trigonal systems (point group D_{3d}).

$$A_{1g} = \begin{pmatrix} a & 0 & 0 \\ 0 & a & 0 \\ 0 & 0 & b \end{pmatrix} \quad {}^1E_g = \begin{pmatrix} c & 0 & 0 \\ 0 & -c & d \\ 0 & d & 0 \end{pmatrix} \quad {}^2E_g = \begin{pmatrix} 0 & -c & -d \\ -c & 0 & 0 \\ -d & 0 & 0 \end{pmatrix}$$

We have performed DFT calculations as implemented in the ABINIT package [31]. We have used the Perdew-Burke-Ernzerhof (PBE) functional, an energy cutoff of 50 Ha for the plane-wave basis, and we have included spin-orbit coupling by means of fully relativistic Goedecker pseudopotentials [32,33], where Ta-$5d^36s^2$ and S-$3s^23p^4$ states are treated as valence electrons. The crystal structure was relaxed so that forces on each atom were below 10 μeV/Å and the total stress on the unit cell below 1 bar, yielding lattice parameters $a = 3.44$ Å and $c = 6.83$ Å. Subsequently, the phonons and the electron-phonon coupling (EPC) were obtained from density-functional perturbation theory (DFPT) calculations, also within ABINIT [34]. Here, we have used an $18 \times 18 \times 12$ **k**-point grid for the electron wave vectors and a $6 \times 6 \times 4$ **q**-point grid for the phonon wave vectors. For the electronic occupation we employed Fermi-Dirac smearing with broadening factor $\sigma_\mathrm{FD} = 0.01$ Ha, which is sufficiently high to avoid unstable phonon modes related to the CDW phases.

III. RESULTS AND DISCUSSION

A. Lattice dynamics of the charge-density wave regimes

Temperature-dependent symmetry-resolved Raman spectra of $1T$-TaS$_2$ are presented in Fig. 1. It is obvious that their evolution with temperature is divided into three distinct ranges (IC-CDW, NC-CDW, and C-CDW) as indicated. The lattice dynamics for each of these ranges will be treated separately in the first part of the section. In the second part we address the electron dynamics.

1. C-CDW phase

At the lowest temperatures $1T$-TaS$_2$ exists in the commensurate C-CDW phase. Here, the atoms form so-called star-of-David clusters. Different studies report either triclinic stacking of these clusters leading to $P\bar{1}$ unit cell symmetry [16], or trigonal or hexagonal stacking and $P\bar{3}$ unit cell symmetry [15,18–20]. A factor group analysis predicts 57 A_g Raman-active modes with an identical polarization dependence for $P\bar{1}$ unit cell symmetry, and alternatively 19 A_g+19 E_g Raman-active modes for $P\bar{3}$ unit cell symmetry [13] Our polarized Raman scattering measurements at $T = 4$ K, measured in two scattering channels, together with the corresponding cumulative fits are shown in Fig. 2. As it can be seen, we have observed modes of two different symmetries in the related scattering channels. This result indicates trigonal or hexagonal stacking of the star-of-David clusters. The symmetric phonon lines can be described by Voigt profiles, the best fit of which is shown as blue (for parallel light polarizations) and red (crossed polarizations) lines. After fitting Voigt profiles to the Raman spectra, 38 phonon modes were singled out. Following the selection rules for A_g and E_g symmetry modes, 19 were assigned as A_g and 19 as E_g symmetry, meaning all expected modes could be identified. The contribution from each mode to the cumulative fit is presented in Fig. 2 as green

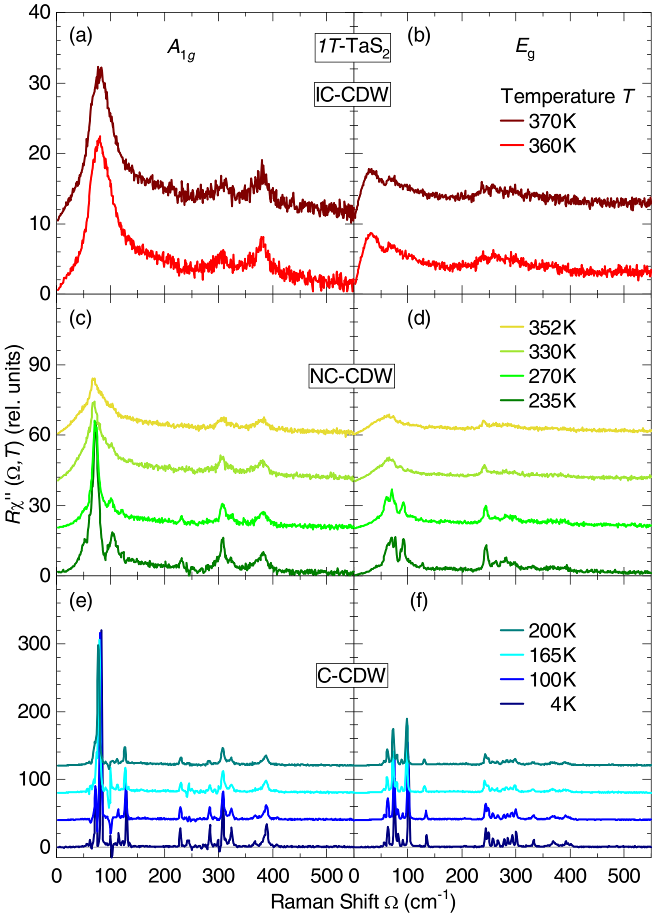

FIG. 1. Symmetry-resolved Raman spectra of $1T$-TaS$_2$ at temperatures as indicated. Both C-CDW (blue lines) and IC-CDW (red lines) domains yield significant contributions to the Raman spectra of the NC-CDW phase (green lines).

TABLE II. A_{1g} and E_g Raman mode energies experimentally obtained at $T = 4$ K.

n_o	ω_{A_g} (cm^{-1})	ω_{E_g} (cm^{-1})
1	62.6	56.5
2	73.3	63.3
3	83.4	75.3
4	114.9	82.0
5	121.9	90.5
6	129.5	101.1
7	228.7	134.8
8	244.1	244.0
9	271.9	248.9
10	284.2	257.5
11	298.6	266.6
12	307.2	278.3
13	308.2	285.0
14	313.0	292.9
15	321.2	300.5
16	324.2	332.7
17	332.0	369.2
18	367.2	392.6
19	388.4	397.7

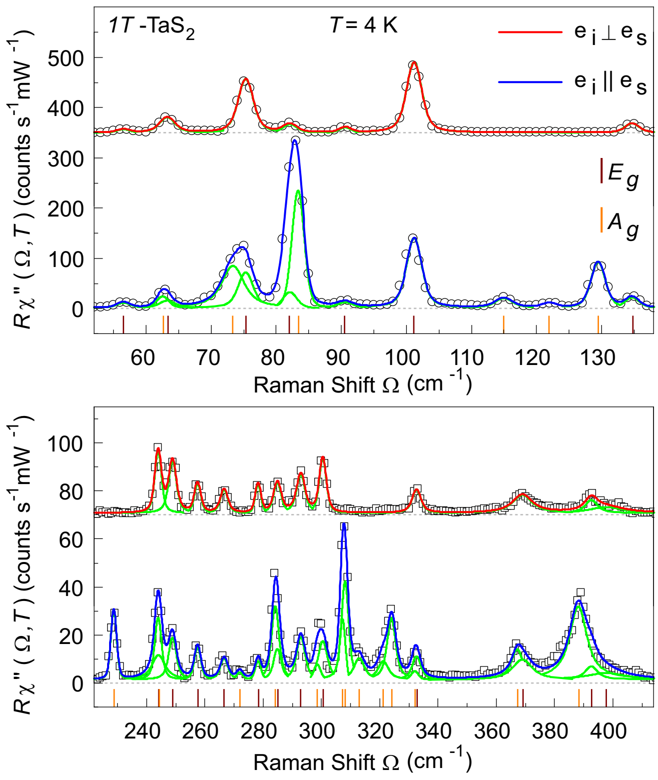

FIG. 2. Raman spectra at $T = 4$ K, i.e., in the C-CDW phase, for parallel and crossed light polarizations. Red and blue solid lines represent fits of the experimental data using Voigt profiles. Spectra are offset for clarity. The short vertical lines depict central frequencies obtained from the data analysis. The exact energy values are presented in Table II.

lines, whereas the complete list of the corresponding phonon energies can be found in Table II.

2. *IC-CDW phase*

At the highest experimentally accessible temperatures $1T$-TaS$_2$ adopts the IC-CDW phase. Data collected by Raman scattering at $T = 370$ K, containing all symmetries, are shown as a blue solid line in Fig. 3. As $1T$-TaS$_2$ is metallic in this phase [25] we expect the phonon lines to be superimposed on a continuum of electron-hole excitations which we approximate using a Drude spectrum shown as a dashed line [35,36].

Since the IC-CDW phase arises from the normal metallic phase, described by space group $P\bar{3}m1$ [13,37], it is interesting to compare our Raman results on the IC-CDW phase to an *ab initio* calculation of the phonon dispersion in the normal phase, shown as an inset in Fig. 3. Four different optical modes were obtained at Γ: E_u at 189 cm^{-1} (double degenerate), E_g at 247 cm^{-1} (double degenerate), A_{2u} at 342 cm^{-1}, and A_{1g} at 346 cm^{-1}. A factor group analysis shows that two of these are Raman active, namely E_g and A_{1g} [13].

We observe that the calculated phonon eigenvalues of the simple metallic phase at Γ do not closely match the observed peaks in the experimental spectra of the IC-CDW phase. Rather, these correspond better to the calculated phonon density of states (PDOS), depicted in Fig. 3. There are essentially three different ways to project the PDOS in a Raman

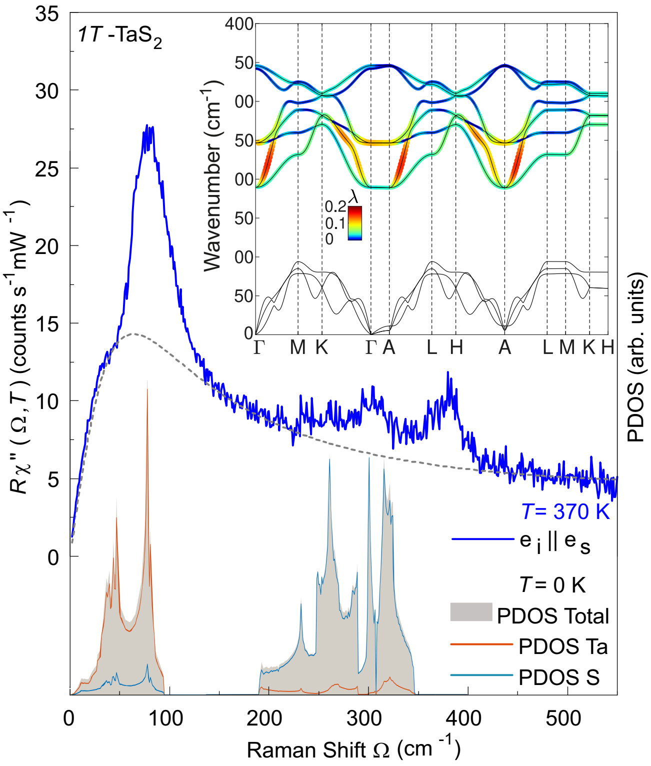

FIG. 3. Raman response for parallel light polarizations in the IC-CDW phase at 370 K (blue line). The dashed line depicts the possible electronic continuum. The contributions of the Ta (dark brown) and S atoms (light brown) to the calculated PDOS (gray area) are shown below. The inset shows the calculated phonon dispersion of $1T$-TaS$_2$ in the simple metallic phase, with the electron-phonon coupling (λ) of the optical branches indicated through the color scale.

experiment and to overcome the $q \approx 0$ selection given by the small momentum of visible light: (i) scattering on impurities [38], (ii) enhanced electron-phonon coupling [39], and (iii) breaking of the translational symmetry in the IC-CDW phase. (i) We rule out chemical impurity scattering, expected to exist at all temperatures, as the low-temperature spectra (Fig. 2) show no signs thereof. (ii) The additional scattering channel may come from the electron-phonon coupling (EPC). The calculated EPC, λ, in the optical modes (inset of Fig. 3) is limited, yet not negligible, reaching maxima of $\sim$0.2 in the lower optical branches around the Brillouin zone (BZ) points Γ and A. The calculated atom-resolved PDOS shows the acoustic modes to be predominantly due to Ta and the optical modes due to S, as a result of their difference in atomic mass. The acoustic modes display several dips that are signatures of the latent CDW phases, for which the EPC cannot be reliably determined. Significant EPC in the optical modes of $1T$-TaS$_2$ is furthermore supported by experimental results linking a sharp increase in the resistivity above the IC-CDW transition temperature to the EPC [37]. It also corroborates calculated [14] and experimentally obtained [13] values of the CDW gap, which correspond to intermediate to strong EPC [37]. (iii) Although EPC certainly contributes we believe that the majority of the additional scattering channels can be traced back to the incommensurate breaking of the translational invariance upon entering IC-CDW. Thus the "weighted" PDOS is projected into the Raman spectrum [see Figs. 1(a) and 1(b)]. These "weighting" factors depend on the specific symmetries along the phonon branches as well as the "new periodicity" and go well beyond the scope of this paper.

3. *NC-CDW phase*

The nearly commensurate phase is seen as a mixed phase consisting of regions of commensurate and incommensurate CDWs [40,41]. This coexistence of high- and low-temperature phases is observable in our temperature-dependent data as shown in Fig. 1. The spectra for the IC-CDW (red curves) and C-CDW phase (blue curves) are distinctly different, as also visible in the data shown above (Figs. 2 and 3). The spectra of the NC-CDW phase (235 K $< T <$ 352 K) comprise contributions from both phases. As 352 K is the highest temperature at which the contributions from the C-CDW phase can be observed in the spectra, we suggest that the phase transition temperature from IC-CDW to NC-CDW phase is somewhere in between 352 and 360 K. This conclusion is in good agreement with experimental results regarding this transition [4–6].

B. Gap evolution

The opening of a typically momentum-dependent gap in the electronic excitation spectrum is a fundamental property of CDW systems which has also been observed in $1T$-TaS$_2$ [13,37,42]. Here, in addition to the CDW, a Mott transition at the onset of the C-CDW phase leads to an additional gap opening in the bands close to the Γ point [21,43]. Symmetry-resolved Raman spectroscopy can provide additional information here using the momentum resolution provided by the selection rules. To this end, we look at the initial slopes of the electronic part of the spectra.

As shown in Figs. 4(a)–4(c), different symmetries project individual parts of the BZ [36,44]. The vertices given by the hexagonal symmetry of $1T$-TaS$_2$ are derived in Appendix C. The A_{1g} vertex mainly highlights the area around the Γ point while the E_g vertices predominantly project the BZ boundaries. The opening of a gap at the Fermi level reduces N_F, leading to an increase of the resistivity in the case of $1T$-TaS$_2$. This reduction of N_F manifests itself also in the Raman spectra which, to zeroth order, are proportional to N_F [35,44]. As a result, the initial slope changes as shown Figs. 4(d) and 4(e), which zoom in on the low-energy region of the spectra from Fig. 1. The initial slope of the Raman response is $R \lim_{\Omega\to 0} \frac{\partial \chi''}{\partial \Omega} \propto N_\mathrm{F}\tau_0$, where R incorporates only experimental factors [44]. The electronic relaxation $\Gamma_0^* \propto (N_\mathrm{F}\tau_0)^{-1}$ is proportional to the dc resistivity $\rho(T)$ [45]. If a gap opens up there is vanishing intensity at $T = 0$ below the gap edge for an isotropic gap. At finite temperature there are thermally excited quasiparticles which scatter. Thus, there is a linear increase at low energies [35]. The black lines in Figs. 4(d)–4(g) represent the initial slopes and their temperature dependences. The lines comprise carrier relaxation and gap effects, and we focus only on the relative changes.

Starting in the IC-CDW phase at $T = 370$ K [Fig. 4(d)] the initial slope is higher for the E_g spectrum than for A_{1g} symmetry. While the CDW gap started to open already at

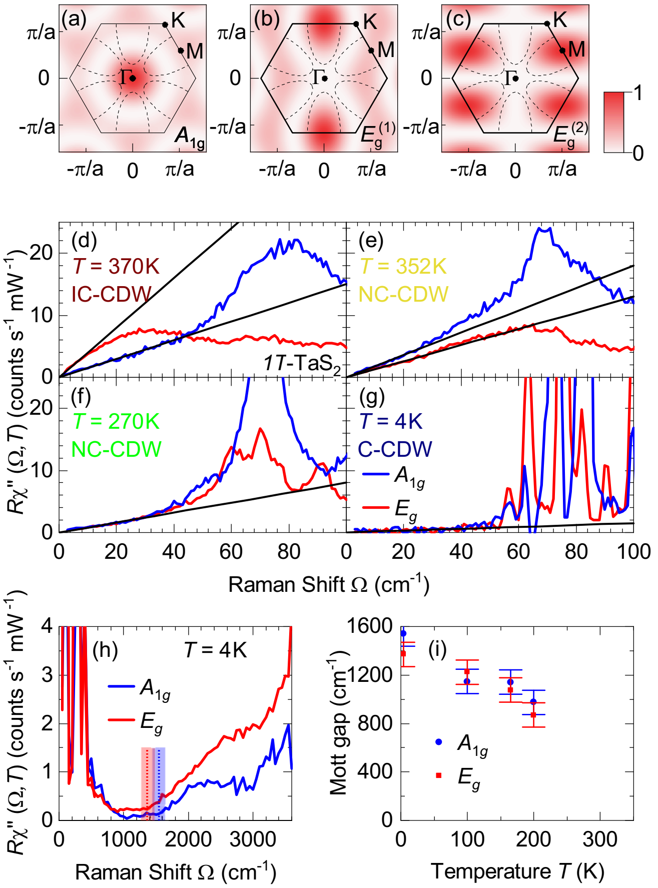

FIG. 4. Evolution of the gaps. (a)–(c) Squared Raman vertices and Fermi surface of $1T$-TaS$_2$ for the indicated symmetries in the normal phase above $T_{\rm IC}$. The derivation of Raman vertices is presented in Appendix C. (d)–(g) Low-energy Raman spectra for A_{1g} symmetry (blue) and E_g symmetries (red) at temperatures as indicated. The spectra shown are zooms on the data shown in Fig. 1. The black lines highlight the initial slope of the spectra. (h) High-energy spectra at 4 K. Vertical dashed lines and colored bars indicate the approximate size and error bars of the Mott gap for the correspondingly colored spectrum. (i) Temperature dependence of the Mott gap Δ_μ ($\mu = A_{1g}, E_g$).

554 K around the M points [43], which are highlighted by the E_g vertex, the Fermi surface projected by the E_g vertex continues to exist. Thus, we may interpret the different slopes as a manifestation of a momentum-dependent gap in the IC-CDW phase and assume overall intensity effects to be symmetry independent for all temperatures. At $T = 352$ K [Fig. 4(e)] the slope for E_g symmetry is substantially reduced to below the A_{1g} slope due to a strong increase of the CDW gap in the commensurate regions [43] which emerge upon entering the NC-CDW phase. Further cooling also decreases the slope for the A_{1g} spectrum, as the Mott gap around the Γ point starts to open within the continuously growing C-CDW domains [40,41]. Below $T = 270$ K the initial slopes are identical for both symmetries and decrease with temperature. Apparently, the Mott gap opens up on the entire Fermi surface in direct correspondence with the increase of the resistivity by approximately an order of magnitude [3]. Finally, at the lowest temperature close to 4 K the initial slopes drop to almost zero [Fig. 4(g)], indicating vanishing conductivity or fully gapped bands in the entire BZ.

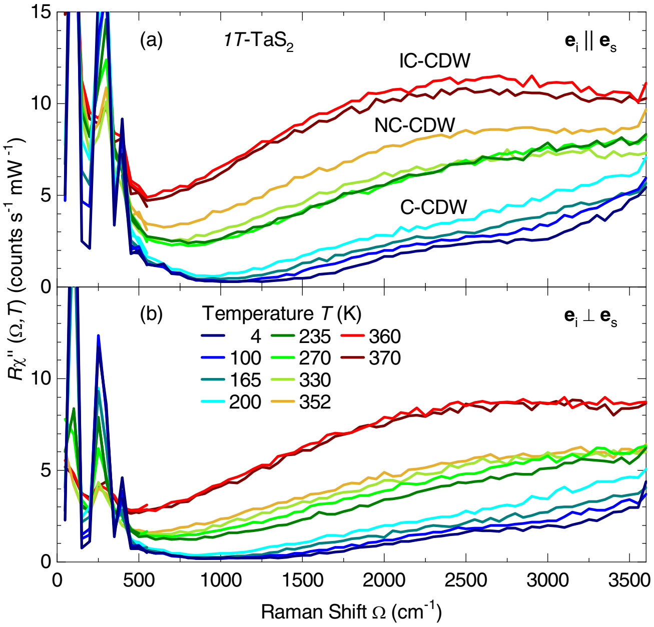

FIG. 5. Raman spectra up to high energies for (a) parallel and (b) crossed polarizations of the incident and scattered light at temperatures as given in the legend.

Concomitantly, and actually more intuitive for the opening of a gap, we observe the loss of intensity in the Raman spectra below a threshold at an energy $\Omega_{\rm gap}$. Below 30 cm^{-1} the intensity is smaller than 0.2 counts(mW s)$^{-1}$ [Fig. 4(g)] and still smaller than 0.3 counts(mW s)$^{-1}$ up to 1500 cm^{-1} [Fig. 4(h)]. For a superconductor or a CDW system the threshold is given by 2Δ, where Δ is the single-particle gap, and a pileup of intensity for higher energies, $\Omega > 2\Delta$ [44]. A pileup of intensity cannot be observed here. Rather, the overall intensity is further reduced with decreasing temperature as shown in Figs. 5 and 6 in Appendixes A and B. In particular, the reduction occurs in distinct steps between the phases and continuous inside the phases with the strongest effect in the C-CDW phase below approximately 210 K (Fig. 5). In a system as clean as $1T$-TaS$_2$ the missing pileup in the C-CDW phase is surprising and argues for an alternative interpretation.

In a Mott system, the gap persists to be observable but the pileup is not a coherence phenomenon and has not been observed yet. In fact, the physics is quite different, and the conduction band is split symmetrically about the Fermi energy $E_{\rm F}$ into a lower and a upper Hubbard band. Thus in the case of Mott-Hubbard physics the experimental signatures are more such as those expected for an insulator or semiconductor having a small gap, where at $T = 0$ there is a range without intensity and an interband onset with a band-dependent shape. At finite temperature there are thermal excitations inside the gap. For $1T$-TaS$_2$ at the lowest accessible temperature, both symmetries exhibit a flat, nearly vanishing electronic continuum below a slightly symmetry-dependent threshold (superposed by the phonon lines at low energies). Above the threshold a weakly structured increase is observed. We interpret this onset as the distance of the lower

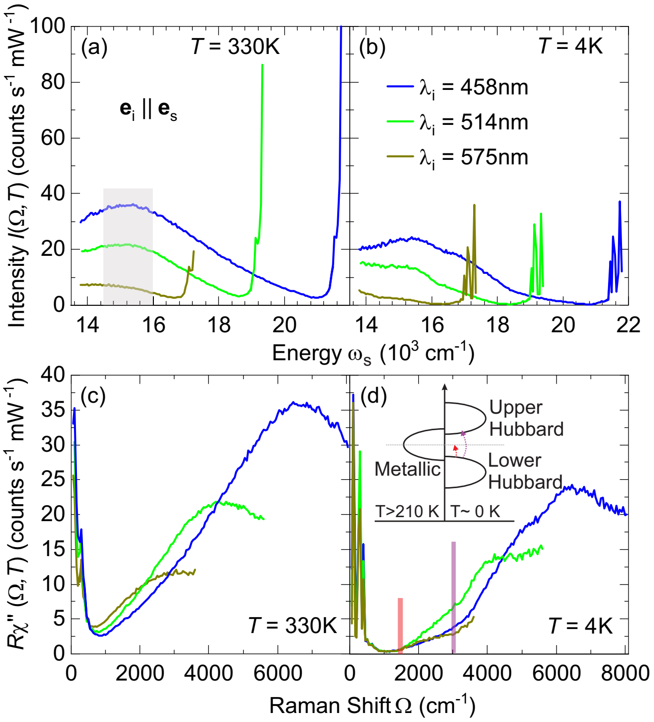

FIG. 6. Luminescence contribution to the Raman data. (a), (b) Intensity as a function of the absolute frequency for (a) $T = 330$ K and (b) $T = 4$ K. The approximate peak maximum of the contribution attributed to luminescence is highlighted by the gray shaded area. (c), (d) Raman susceptibility calculated from (a) and (b), respectively, shown as a function of frequency (Raman) shift. The luminescence peak appears at different Raman shifts depending on the wavelength of the laser light. At $T = 4$ K the spectra are identical up to 1600 cm^{-1} for all laser light wavelengths.

Hubbard band from the Fermi energy E_F or half of the distance between the lower and the upper Hubbard band, shown as vertical dashed lines at 1350–1550 cm^{-1} $\equiv$ 170–190 meV [Fig. 4(h)]. The energy is in good agreement with gap obtained from the in-plane angle-resolved photoemission spectroscopy (ARPES) [43], scanning tunneling spectroscopy [46], and infrared spectroscopy [13] which may be compared directly with our Raman results measured with in-plane polarizations. Upon increasing the temperature the size of the gap shrinks uniformly in both symmetries [Fig. 4(i)] and may point to an onset above the C-CDW phase transition, consistent with the result indicated by the initial slope. However, we cannot track the development of the gap into the NC-CDW phase as an increasing contribution of luminescence (see Appendix B) overlaps with the Raman data.

Recently, it was proposed on the basis of DFT calculations that 1T-TaS$_2$ orders also along the c axis perpendicular to the planes in the C-CDW state [24,25]. This quasi-one-dimensional (1D) coupling is unexpectedly strong and the resulting metallic band is predicted to have a width of approximately 0.5 eV. For specific relative ordering of the star of David patterns along the c axis this band develops a gap of 0.15 eV at E_F [25], which is intriguingly close to the various experimental observations. However, since our light polarizations are strictly in plane, we have to conclude that the gap observed here (and presumably in the other experiments) is an in-plane gap. Our experiment cannot detect an out-of-plane gap. Thus, neither a quasimetallic dispersion along the c axis nor a gap in this band along k_z may be excluded in the C-CDW phase. However, there is compelling evidence for a Mott-like gap in the layers rather than a CDW gap.

IV. CONCLUSIONS

We have presented a study of the various charge density wave regimes in 1T-TaS$_2$ by inelastic light scattering, supported by *ab initio* calculations. The spectra of lattice excitations in the commensurate CDW (C-CDW) phase determine the unit cell symmetry to be $P\bar{3}$, indicating trigonal or hexagonal stacking of the “star-of-David” structure. The high-temperature spectra of the incommensurate CDW (IC-CDW) state are dominated by a projection of the phonon density of states caused by either a significant electron-phonon coupling or, more likely, the superstructure. The intermediate nearly commensurate (NC-CDW) phase is confirmed to be a mixed regime of commensurate and incommensurate regions contributing to the phonon spectra below an onset temperature $T_{NC} \approx 352$–360 K, in good agreement with previously reported values. At the lowest measured temperatures, the observation of a virtually clean gap without a redistribution of spectral weight from low to high energies below T_C argues for the existence of a Mott metal-insulator transition at a temperature of order 100 K. The magnitude of the gap is found to be $\Omega_{gap} \approx 170$–190 meV and has little symmetry, thus momentum, dependence, in agreement with earlier ARPES results [37]. At 200 K, on the high-temperature end of the C-CDW phase, the gap shrinks to ~60% of its low-temperature value. Additionally, the progressive filling of the CDW gaps by thermal excitations is tracked via the initial slope of the spectra, and indicates that the Mott gap opens primarily on the parts of the Fermi surface closest to the Γ point.

Our results demonstrate the potential of using inelastic light scattering to probe the momentum dependence and energy scale of changes in the electronic structure driven by low-temperature collective quantum phenomena. This opens perspectives to investigate the effect of hybridization on collective quantum phenomena in heterostructures composed of different 2D materials, e.g., alternating T and H monolayers as in the 4Hb-TaS$_2$ phase [47].

ACKNOWLEDGMENTS

The authors acknowledge funding provided by the Institute of Physics Belgrade through the grant by the Ministry of Education, Science and Technological Development of the Republic of Serbia. The work was supported by the Science Fund of the Republic of Serbia, PROMIS, No. 6062656, StrainedFeSC, and by Research Foundation-Flanders (FWO). J.B. acknowledges support of a postdoctoral fellowship of the FWO, and of the Erasmus + program for staff mobility and training (KA107, 2018) for a research stay at the Institute of Physics Belgrade, during which part of the work was carried out. The computational resources and services used for the first-principles calculations in this work were provided by the VSC (Flemish Supercomputer Center), funded by the

FWO and the Flemish Government – department EWI. Work at Brookhaven is supported by the U.S. DOE under Contract No. DESC0012704. A.B. and R.H. acknowledge support by the German research foundation (DFG) via Projects No. Ha2071/12-1 and No. 107745057 – TRR 80 and by the DAAD via the project-related personal exchange program PPP with Serbia Grant No. 57449106.

APPENDIX A: RAW DATA

Figure 5 shows Raman spectra at temperatures ranging from $T = 4$ to 370 K for parallel [Fig. 5(a)] and crossed [Fig. 5(b)] in-plane light polarizations. The spectra were measured in steps of $\Delta\Omega = 50\ \mathrm{cm}^{-1}$ and a resolution of $\sigma \approx 20\ \mathrm{cm}^{-1}$. Therefore neither the shapes nor the positions of the phonon lines below 500 cm^{-1} may be resolved. All spectra reach a minimum in the range from 500 to 1600 cm^{-1}. At energies above 500 cm^{-1} the overall intensities are strongly temperature dependent and decreasing with decreasing temperature. Three clusters of spectra are well separated according to the phases they belong to.

In the C-CDW phase ($T \leqslant 200$ K, blue lines) the spectra start to develop substructures at 1500 and 3000 cm^{-1}. The spectra at 200 K increase almost linearly with energy. The spectra of the NC- and IC-CDW phases exhibit a broad maximum centered in the region of 2200–3200 cm^{-1} which may be attributed to luminescence (see Appendix B). For clarification we measured a few spectra with various laser lines for excitation.

APPENDIX B: LUMINESCENCE

Figure 6 shows Raman spectra measured with parallel light polarizations for three different wavelengths λ_{i} of the incident laser light. Figures 6(a) and 6(b) depict the measured intensity I (without the Bose factor) as a function of the absolute frequency $\tilde{\nu}$ of the scattered light.

At high temperature [$T = 330$ K, Fig. 6(a)] a broad peak can be seen for all λ_{i} which is centered at a fixed frequency of 15 200 cm^{-1} of the scattered photons (gray shaded area). The peak intensity decreases for increasing λ_{i} (decreasing energy). Correspondingly, this peak's center depends on the laser wavelength in the spectra shown as a function of the Raman shift [Fig. 6(c)]. This behavior indicates that the origin of this excitation is likely to be luminescence where transitions at fixed absolute final frequencies are expected.

At low temperature [Fig. 6(b)] we can no longer find a structure at a fixed absolute energy. Rather, as already indicated in the main part, the spectra develop additional, yet weak, structures which are observable in all spectra but are particularly pronounced for blue excitation. For green and yellow excitation the spectral range of the spectrometer, limited to 732 nm, is not wide enough for a deeper insight into the luminescence contributions (at energies different from those at high temperature) and no maximum common to all three spectra is observed. If these spectra are plotted as a function of the Raman shift, the changes in slope at 1500 and 3000 cm^{-1} are found to be in the same position for all λ_{i}, values thus arguing for inelastic scattering rather than luminescence. Since we do currently not have the appropriate experimental tools for an in-depth study, our interpretation is preliminary although supported by the observations in Fig. 6(d).

As shown in the inset of Fig. 6(d) we propose a scenario on the basis of Mott physics. In the C-CDW phase the reduced bandwidth is no longer the largest energy and the Coulomb repulsion U becomes relevant [22] and splits the conduction band into a lower and upper Hubbard band. We assume that the onset of scattering at 1500 cm^{-1} corresponds to the distance of the highest energy of the lower Hubbard band to the Fermi energy E_{F}. The second onset corresponds then to the distance between the highest energy of the lower Hubbard band and the lowest energy of the upper Hubbard band. An important question needs to be answered: Into which unoccupied states right above E_{F} does the first process scatter electrons? We may speculate that some DOS is provided by the metallic band dispersing along k_z or by the metallic domain walls between the different types of ordering patterns along the c axis observed recently by tunneling spectroscopy [46]. These quasi-1D domain walls would provide the states required for the onset of scattering at high energy but are topologically too small for providing enough density of states for a measurable intensity at low energy [Fig. 4(g)] in a location-integrated experiment such as Raman scattering.

APPENDIX C: DERIVATION OF THE RAMAN VERTICES

Phenomenologically, the Raman vertices can be derived based on lattice symmetry, which are proportional to the Brillouin zone harmonics. They are a set of functions that exhibit the symmetry and periodicity of the lattice structure proposed by Allen [48]. These functions make the k-space sums and energy integrals more convenient than that of the Cartesian basis or the spherical harmonics basis, especially for those materials who have anisotropic and/or multiple Fermi pockets. The three Cartesian components of the Fermi velocity v_k are recommended to generate this set of functions since they inherit the symmetry and periodicity of the crystal lattice naturally. However, in most cases, we do not know the details of band dispersion. A phenomenological method is needed to construct such a set of basis functions. Here, we demonstrate a method based on the group theory. The Brillouin zone harmonics can be obtained by the projection operation on specific trial functions.

For a certain group G with symmetry elements R and symmetry operators $\hat{P}_R$, it can be described by several irreducible representations Γ_n, where n labels the representation. For each irreducible representation, there are corresponding basis functions $\Phi^{j}_{\Gamma_n}$ that can be used to generate representation matrices for a particular symmetry. Here, j labels the component or partner of the representations. For an arbitrary function F, we have

$$F = \sum_{\Gamma_n} \sum_{j} f_j^{\Gamma_n} \Phi^{j}_{\Gamma_n}. \tag{C1}$$

According to the group theory, we can always define a projection operator by the relation [49]

$$\hat{P}^{\Gamma_n} = \frac{d}{N} \sum_{R} \chi^{\Gamma_n}(R) * \hat{P}_R, \tag{C2}$$

TABLE III. Symmetry operations $\hat{P}_R$ and corresponding character table of theD_{3d} point group.

$\hat{P}_R$	x'	y'	z'	$\chi^{\Gamma_n}(R)$	
				A_{1g}	E_g
E	x	y	z	1	2
C_3^1	$-\frac{1}{2}x+\frac{\sqrt{3}}{2}y$	$-\frac{\sqrt{3}}{2}x-\frac{1}{2}y$	z	1	-1
C_3^{-1}	$-\frac{1}{2}x-\frac{\sqrt{3}}{2}y$	$\frac{\sqrt{3}}{2}x-\frac{1}{2}y$	z	1	-1
C_2'	x	$-y$	$-z$	1	0
C_2''	$-\frac{1}{2}x+\frac{\sqrt{3}}{2}y$	$\frac{\sqrt{3}}{2}x+\frac{1}{2}y$	$-z$	1	0
C_2'''	$-\frac{1}{2}x-\frac{\sqrt{3}}{2}y$	$-\frac{\sqrt{3}}{2}x+\frac{1}{2}y$	$-z$	1	0
I	$-x$	$-y$	$-z$	1	2
S_6^1	$\frac{1}{2}x-\frac{\sqrt{3}}{2}y$	$\frac{\sqrt{3}}{2}x+\frac{1}{2}y$	$-z$	1	-1
S_6^{-1}	$\frac{1}{2}x+\frac{\sqrt{3}}{2}y$	$-\frac{\sqrt{3}}{2}x+\frac{1}{2}y$	$-z$	1	-1
σ_v'	$-x$	y	z	1	0
σ_v''	$\frac{1}{2}x-\frac{\sqrt{3}}{2}y$	$-\frac{\sqrt{3}}{2}x-\frac{1}{2}y$	z	1	0
σ_v'''	$\frac{1}{2}x+\frac{\sqrt{3}}{2}y$	$\frac{\sqrt{3}}{2}x-\frac{1}{2}y$	z	1	0

that satisfies the relation

$$\hat{P}^{\Gamma_n}F=\sum_j f_j^{\Gamma_n}\Phi^j_{\Gamma_n}, \tag{C3}$$

where d is the dimensionality of the irreducible representation Γ_n, N is the number of symmetry operators in the group, and $\chi^{\Gamma_n}(R)$ is the character of the matrix of symmetry operator R in irreducible representation Γ_n. By projection operation on a certain irreducible representation Γ_n, we can directly get its basis functions $\Phi^j_{\Gamma_n}$.

The basis functions are not unique. In specific physical problems, it is useful to use physical insight to guess an appropriate arbitrary function to find the basis functions for specific problems. $1T$-TaS$_2$ belongs to the D_{3d} point group. There are 12 symmetry operators in this group, i.e., E, C_3^1, C_3^{-1}, C_2', C_2'', C_2''', I, S_6^1, S_6^{-1}, σ_v', σ_v'', σ_v'''. The coordinate transformations after symmetry operations and the corresponding character table are listed in Table III.

In order to simulate the periodicity of the Brillouin zone, trigonometric functions are used as trial functions. According to the parity of the irreducible representations, we can choose an appropriate trigonometric function, e.g., a sine function for odd parity representation and cosine function for even parity representation. The combinations of them are also available.

Here, we use $F=\cos(k_xa)$ as a trial function, where a is the in-plane crystal constant. The basis function of A_{1g} can be derived as

$$\Phi_{A_{1g}}(\mathbf{k})=\frac{1}{3}\left[\cos(k_xa)+2\cos\left(\frac{1}{2}k_xa\right)\cos\left(\frac{\sqrt{3}}{2}k_ya\right)\right]. \tag{C4}$$

With the same method, we obtain a basis function of E_g as

$$\Phi_{E_g^1}(\mathbf{k})=\frac{2}{3}\left[\cos(k_xa)-\cos\left(\frac{1}{2}k_xa\right)\cos\left(\frac{\sqrt{3}}{2}k_ya\right)\right]. \tag{C5}$$

Since the E_g is a two-dimensional representation, the projection operation provides only one of the two basis functions of the corresponding subspace. The second function is found based on the subspace invariance under the symmetry operations (e.g., if we operate $\Phi_{E_g^1}$ with C_3^1 symmetry, the result can be presented as a linear combination of $\Phi_{E_g^1}$ and $\Phi_{E_g^2}$). Thus we obtain

$$\Phi_{E_g^2}(\mathbf{k})=2\sin\left(\frac{1}{2}k_xa\right)\sin\left(\frac{\sqrt{3}}{2}k_ya\right). \tag{C6}$$

---

[1] J. C. Tsang, J. E. Smith, M. W. Shafer, and S. F. Meyer, Raman spectroscopy of the charge-density-wave state in $1T$- and $2H$-TaSe$_2$, Phys. Rev. B **16**, 4239 (1977).

[2] C. J. Sayers, H. Hedayat, A. Ceraso, F. Museur, M. Cattelan, L. S. Hart, L. S. Farrar, S. Dal Conte, G. Cerullo, C. Dallera, E. Da Como, and E. Carpene, Coherent phonons and the interplay between charge density wave and Mott phases in $1T$-TaSe$_2$, Phys. Rev. B **102**, 161105(R) (2020).

[3] A. J. Wilson, J. F. D. Salvo, and S. Mahajan, Charge-density waves and superlattices in the metallic layered transition metal dichalcogenides, Adv. Phys. **24**, 117 (1975).

[4] C. B. Scruby, P. M. Williams, and G. S. Parry, The role of charge density waves in structural transformations of $1T$-TaS$_2$, Philos. Mag. **31**, 255 (1975).

[5] R. E. Thomson, B. Burk, A. Zettl, and J. Clarke, Scanning tunneling microscopy of the charge-density-wave structure in $1T$-TaS$_2$, Phys. Rev. B **49**, 16899 (1994).

[6] W. Wen, C. Dang, and L. Xie, Photoinduced phase transitions in two-dimensional charge-density-wave $1T$-TaS$_2$, Chin. Phys. B **28**, 058504 (2019).

[7] D. Svetin, I. Vaskivskyi, S. Brazovskii, Mertelj, and D. Mihailovic, Three-dimensional resistivity and switching between correlated electronic states in $1T$-TaS$_2$, Sci. Rep. **7**, 46048 (2017).

[8] D. Svetin, I. Vaskivskyi, P. Sutar, E. Goreshnik, J. Gospodaric, T. Mertelj, and D. Mihailovic, Transitions between photoinduced macroscopic quantum states in $1T$-TaS$_2$ controlled by substrate strain, Appl. Phys. Express **7**, 103201 (2014).

[9] G. Liu, B. Debnath, T. R. Pope, T. T. Salguero, R. K. Lake, and A. A. Balandin, A charge-density wave oscillator based on an integrated tantalum disulfide-boron nitride-graphene device operating at room temperature, Nat. Nanotechnol. **11**, 845 (2016).

[10] R. Salgado, A. Mohammadzadeh, F. Kargar, A. Geremew, C.-Y. Huang, M. A. Bloodgood, S. Rumyantsev, T. T. Salguero, and A. A. Balandin, Low-frequency noise spectroscopy of charge-density-wave phase transitions in vertical quasi-2D $1T$-TaS$_2$ devices, Appl. Phys. Express **12**, 037001 (2019).

[11] Z. X. Wang, Q. M. Liu, L. Y. Shi, S. J. Zhang, T. Lin, T. Dong, D. Wu, and N. L. Wang, Photoinduced hidden CDW state and relaxation dynamics of $1T$-TaS$_2$ probed by time-resolved terahertz spectroscopy, arXiv:1906.01500.

[12] L. Stojchevska, I. Vaskivskyi, T. Mertelj, P. Kusar, D. Svetin, S. Brazovskii, and D. Mihailovic, Ultrafast switching to a stable

hidden quantum state in an electronic crystal, Science **344**, 177 (2014).

[13] L. V. Gasparov, K. G. Brown, A. C. Wint, D. B. Tanner, H. Berger, G. Margaritondo, R. Gaál, and L. Forró, Phonon anomaly at the charge ordering transition in $1T$-TaS$_2$, Phys. Rev. B **66**, 094301 (2002).

[14] O. R. Albertini, R. Zhao, R. L. McCann, S. Feng, M. Terrones, J. K. Freericks, J. A. Robinson, and A. Y. Liu, Zone-center phonons of bulk, few-layer, and monolayer $1T$-TaS$_2$: Detection of commensurate charge density wave phase through Raman scattering, Phys. Rev. B **93**, 214109 (2016).

[15] S. Uchida and S. Sugai, Infrared and raman studies on a commensurate CDW states in transition metal dichalcogenides, Physica B+C **105**, 393 (1981).

[16] R. Brouwer and F. Jellinek, The low-temperature superstructures of $1T$-TaSe$_2$ and $2H$-TaSe$_2$, Physica B+C **99**, 51 (1980).

[17] A. Zong, X. Shen, A. Kogar, L. Ye, C. Marks, D. Chowdhury, T. Rohwer, B. Freelon, S. Weathersby, R. Li, J. Yang, J. Checkelsky, X. Wang, and N. Gedik, Ultrafast manipulation of mirror domain walls in a charge density wave, Sci. Adv. **4**, eaau5501 (2018).

[18] J. R. Duffay and R. D. Kirby, Raman scattering from $1T$-TaS$_2$, Solid State Commun. **20**, 617 (1976).

[19] T. Hirata and F. S. Ohuchi, Temperature dependence of the Raman spectra of $1T$-TaS$_2$, Solid State Commun. **117**, 361 (2001).

[20] S. L. L. M. Ramos, R. Plumadore, J. Boddison-Chouinard, S. W. Hla, J. R. Guest, D. J. Gosztola, M. A. Pimenta, and A. Luican-Mayer, Suppression of the commensurate charge density wave phase in ultrathin $1T$-TaS$_2$ evidenced by Raman hyperspectral analysis, Phys. Rev. B **100**, 165414 (2019).

[21] B. Sipos, A. F. Kusmartseva, A. Akrap, H. Berger, L. Forró, and E. Tutis, From Mott state to superconductivity in $1T$-TaS$_2$, Nat. Mater. **7**, 960 (2008).

[22] P. Fazekas and E. Tosatti, Electrical, structural and magnetic properties of pure and doped $1T$-TaS$_2$, Philos. Mag. B **39**, 229 (1979).

[23] E. Martino, A. Pisoni, L. Ćirić, A. Arakcheeva, H. Berger, A. Akrap, C. Putzke, P. J. W. Moll, I. Batistić, E. Tutiš, L. Forró, and K., Preferential out-of-plane conduction and quasi-one-dimensional electronic states in layered $1T$-TaS$_2$, npj 2D Mater. Appl. **4**, 7 (2020).

[24] P. Darancet, A. J. Millis, and C. A. Marianetti, Three-dimensional metallic and two-dimensional insulating behavior in octahedral tantalum dichalcogenides, Phys. Rev. B **90**, 045134 (2014).

[25] S.-H. Lee, J. S. Goh, and D. Cho, Origin of the Insulating Phase and First-Order Metal-Insulator Transition in $1T$-TaS$_2$, Phys. Rev. Lett. **122**, 106404 (2019).

[26] Y. Ma, Y. Hou, C. Lu, L. Li, and C. Petrovic, Possible origin of nonlinear conductivity and large dielectric constant in the commensurate charge-density-wave phase of $1T$-TaS$_2$, Phys. Rev. B **97**, 195117 (2018).

[27] L. J. Li, W. J. Lu, X. D. Zhu, L. S. Ling, Z. Qu, and Y. P. Sun, Fe-doping induced superconductivity in the charge-density-wave system $1T$-TaS$_2$, Europhys. Lett. **98**, 29902 (2012).

[28] Y. Liu, R. Ang, W. J. Lu, W. H. Song, L. J. Li, and Y. P. Sun, Superconductivity induced by Se-doping in layered charge-density-wave system $1T$-TaS$_{2-x}$Se$_x$, Appl. Phys. Lett. **102**, 192602 (2013).

[29] R. Ang, Y. Miyata, E. Ieki, K. Nakayama, T. Sato, Y. Liu, W. J. Lu, Y. P. Sun, and T. Takahashi, Superconductivity and bandwidth-controlled Mott metal-insulator transition in $1T$-TaS$_{2-x}$Se$_x$, Phys. Rev. B **88**, 115145 (2013).

[30] M. Bovet, D. Popović, F. Clerc, C. Koitzsch, U. Probst, E. Bucher, H. Berger, D. Naumović, and P. Aebi, Pseudogapped Fermi surfaces of $1T$-TaS$_2$ and $1T$-TaSe$_2$: A charge density wave effect, Phys. Rev. B **69**, 125117 (2004).

[31] X. Gonze, B. Amadon, P.-M. Anglade, J.-M. Beuken, F. Bottin, P. Boulanger, F. Bruneval, D. Caliste, R. Caracas, M. Côté, T. Deutsch, L. Genovese, P. Ghosez, M. Giantomassi, S. Goedecker, D. Hamann, P. Hermet, F. Jollet, G. Jomard, S. Leroux *et al.*, ABINIT: First-principles approach to material and nanosystem properties, Comput. Phys. Commun. **180**, 2582 (2009).

[32] S. Goedecker, M. Teter, and J. Hutter, Separable dual-space Gaussian pseudopotentials, Phys. Rev. B **54**, 1703 (1996).

[33] M. Krack, Pseudopotentials for H to Kr optimized for gradient-corrected exchange-correlation functionals, Theor. Chem. Acc. **114**, 145 (2005).

[34] X. Gonze, D. C. Allan, and M. P. Teter, Dielectric Tensor, Effective Charges, and Phonons in α-Quartz by Variational Density-Functional Perturbation Theory, Phys. Rev. Lett. **68**, 3603 (1992).

[35] A. Zawadowski and M. Cardona, Theory of Raman scattering on normal metals with impurities, Phys. Rev. B **42**, 10732 (1990).

[36] N. Lazarević and R. Hackl, Fluctuations and pairing in Fe-based superconductors: Light scattering experiments, J. Phys.: Condens. Matter **32**, 413001 (2020).

[37] K. Rossnagel, On the origin of charge-density waves in select layered transition-metal dichalcogenides, J. Phys.: Condens. Matter **23**, 213001 (2011).

[38] R. Shuker and R. W. Gammon, Raman-Scattering Selection-Rule Breaking and the Density of States in Amorphous Materials, Phys. Rev. Lett. **25**, 222 (1970).

[39] A. Baum, A. Milosavljević, N. Lazarević, M. M. Radonjić, B. Nikolić, M. Mitschek, Z. I. Maranloo, M. Šćepanović, M. Grujić-Brojčin, N. Stojilović, M. Opel, A. Wang, C. Petrovic, Z. V. Popović, and R. Hackl, Phonon anomalies in FeS, Phys. Rev. B **97**, 054306 (2018).

[40] A. Spijkerman, J. L. de Boer, A. Meetsma, G. A. Wiegers, and S. van Smaalen, X-ray crystal-structure refinement of the nearly commensurate phase of $1T$-TaS$_2$ in $(3+2)$-dimensional superspace, Phys. Rev. B **56**, 13757 (1997).

[41] R. He, J. Okamoto, Z. Ye, G. Ye, H. Anderson, X. Dai, X. Wu, J. Hu, Y. Liu, W. Lu, Y. Sun, A. N. Pasupathy, and A. W. Tsen, Distinct surface and bulk charge density waves in ultrathin $1T$-TaS$_2$, Phys. Rev. B **94**, 201108(R) (2016).

[42] G. Grüner, The dynamics of charge-density waves, Rev. Mod. Phys. **60**, 1129 (1988).

[43] C. Sohrt, A. Stange, M. Bauer, and K. Rossnagel, How fast can a Peierls–Mott insulator be melted?, Faraday Discuss. **171**, 243 (2014).

[44] T. P. Devereaux and R. Hackl, Inelastic light scattering from correlated electrons, Rev. Mod. Phys. **79**, 175 (2007).

[45] M. Opel, R. Nemetschek, C. Hoffmann, R. Philipp, P. F. Müller, R. Hackl, I. Tüttő, A. Erb, B. Revaz, E. Walker, H. Berger, and L. Forró, Carrier relaxation, pseudogap, and superconducting

gap in high-T_c cuprates: A Raman scattering study, Phys. Rev. B **61**, 9752 (2000).

[46] J. Skolimowski, Y. Gerasimenko, and R. Žitko, Mottness Collapse without Metallization in the Domain Wall of the Triangular-Lattice Mott Insulator $1T$-TaS$_2$, Phys. Rev. Lett. **122**, 036802 (2019).

[47] A. Ribak, R. M. Skiff, M. Mograbi, P. K. Rout, M. H. Fischer, J. Ruhman, K. Chashka, Y. Dagan, and A. Kanigel, Chiral superconductivity in the alternate stacking compound $4Hb$-TaS$_2$, Sci. Adv. **6**, eaax9480 (2020).

[48] P. B. Allen, Fermi-surface harmonics: A general method for nonspherical problems. Application to Boltzmann and Eliashberg equations, Phys. Rev. B **13**, 1416 (1976).

[49] M. S. Dresselhaus, G. Dresselhaus, and A. Jorio, *Group Theory* (Springer, Berlin, 2008).

Received: 14 May 2020 | Revised: 15 July 2020 | Accepted: 22 July 2020
DOI: 10.1002/jrs.5962

RESEARCH ARTICLE

Journal of RAMAN SPECTROSCOPY WILEY

Vacancies and spin–phonon coupling in $CrSi_{0.8}Ge_{0.1}Te_3$

Ana Milosavljević[1] | Andrijana Šolajić[1] | Bojana Višić[1] | Marko Opačić[1] | Jelena Pešić[1] | Yu Liu[2] | Cedomir Petrovic[2] | Zoran V. Popović[1,3] | Nenad Lazarević[1]

[1]Institute of Physics Belgrade, University of Belgrade, Pregrevica 118, Belgrade, 11080, Serbia

[2]Condensed Matter Physics and Materials Science Department, Brookhaven National Laboratory, Upton, New York, 11973-5000, USA

[3]Serbian Academy of Sciences and Arts, Knez Mihailova 35, Belgrade, 11000, Serbia

Correspondence
Ana Milosavljević, Institute of Physics Belgrade, University of Belgrade, Pregrevica 118, 11080 Belgrade, Serbia.
Email: ana.milosavljevic@ipb.ac.rs

Funding information
Serbian Academy of Sciences and Arts, Grant/Award Number: F-134; Slovenian Research Agency, Grant/Award Number: P1-0099; Ministry of Education, Science and Technological Development of the Republic of Serbia U.S. DOE-BES, Division of Materials Science and Engineering, Grant/Award Number: DE-SC0012704

Abstract

We report temperature-dependent Raman scattering and magnetization studies of van der Waals ferromagnetic compound $CrSi_{0.8}Ge_{0.1}Te_3$. Magnetic susceptibility measurements revealed dominant ferromagnetic interactions below T_C which shift to the lower values due to the presence of vacancies. A Raman active mode, additional to the ones predicted by symmetry in the parent compounds, has been observed. This A_g symmetry mode most likely emerges as a consequence of the atomic vacancies on Si/Ge site. Presence of the strong spin–phonon coupling at temperature around 210 K is indicated by deviations from conventional phonon self-energy temperature dependence of all analysed modes.

KEYWORDS

magnetism, phonons, raman spectroscopy, van der Waals materials

1 | INTRODUCTION

Considerable progress has been made in the field of material science through developing new materials and revealing their properties in the last decade. Namely, in the recent years, large family of van der Waals materials with inherent magnetism became the focus of experimental and theoretical research, because they seem suitable for numerous technical applications.[1-7] The family includes $Fe_{3-x}GeTe_2$ metallic materials with high magnetic transition temperature,[8-10] semiconductors $CrXTe_3$ (X = Si, Ge, Sn) and CrX_3 (X = Cl, Br, I) monolayers[2,11-13] and heterostructures.[14]

$CrSiTe_3$ and $CrGeTe_3$ are ferromagnetic (FM) semiconductors with band gap of 0.4 and 0.7 eV and Curie temperatures (T_C) of 32 and 61 K, respectively.[15-18] Twinning of $CrSiTe_3$ single crystals along *c*-axes was revealed by X-ray diffraction experiment as well as Cr^{3+} ions magnetic order.[15] Recently, through high-resolution angle-resolved photoemission spectroscopy (ARPES), it was possible to identify full electronic structure near the Fermi level. Due to spin–orbit coupling, $CrSiTe_3$ is a Mott-type FM insulator.[19] Electronic structure of $CrGeTe_3$ single crystals was also investigated by ARPES.[20] It was shown that the low-lying valence bands are centred around the Γ point and are mainly formed from Te 5*p* orbitals.

Raman scattering studies of $CrSiTe_3$ reveal strong spin–lattice coupling in the paramagnetic phase[15,21] as a consequence of a short-range magnetic order in this compound. In addition to renormalization of energies and linewidths of observed Raman active modes, coupling of doubly degenerate E_g mode with magnetic continuum was found.[21] The coupling results in an asymmetric phonon line shape up to 180 K. Besides the splitting of two low-energy E_g modes in the magnetic phase of $CrGeTe_3$ and unconventional behaviour of phonon properties around transition temperature, experimental results indicate spin–phonon coupling effect with magnetic quasi-elastic scattering.[22] Pressure-dependent Raman scattering study of $CrGeTe_3$ showed a decrease in bond length, the deviation of Cr–Te–Cr angle, and reduction of phase transition temperature.[23]

Change of the carrier concentration plays an important role in the physics of semiconducting materials as it can lead to surprising physical properties. Very small variations in dopant concentrations can lead to structural modifications and considerable changes in magnetic transition temperature. Here, we report a Raman scattering and magnetization studies of $CrSi_{0.8}Ge_{0.1}Te_3$. Our scanning electron microscopy (SEM) measurements reveal 10% of Ge atoms concentration and 10% of vacancies. Vacancies induced a decrease in T_C was detected within magnetic susceptibility measurements. In the Raman scattering results, we identified three A_g and four E_g symmetry modes. Additional peak of the A_g symmetry is also observed in our spectra. This mode may be traced to vacancies and possible inhomogeneous distribution of Ge atoms substitution on Si atomic site at nano-scale. Energies of modes predicted by symmetry analysis are found between the experimental values of parent compounds $CrSiTe_3$ and $CrGeTe_3$, reported previously in Milosavljevi et al..[21] The presence of the strong spin–phonon interaction at temperature around 210 K is indicated in small deviations from conventional temperature-dependent behaviour of the observed modes energies and linewidths, including additional one.

2 | EXPERIMENT AND NUMERICAL METHOD

$CrSi_{0.8}Ge_{0.1}Te_3$ single crystals were grown as described previously.[24] Magnetic properties were measured in a Quantum Design MPMS-XL5 system.

SEM measurements were performed using FEI HeliosNanolab 650. This microscope is equipped with an Oxford Instruments energy dispersive spectroscopy (EDS) system with an X-max SSD detector operating at 20 kV. Measurements were performed on as-cleaved samples deposited on a graphite tape. The elemental composition EDS mapping was obtained on crystals that appeared to be uniform for several tens of microns. The maps show the presence of Cr, Ge, Te and Si.

For Raman scattering experiment, Tri Vista 557 spectrometer was used in the subtractive backscattering micro-Raman configuration. The combination of gratings was 1800/1800/2400 grooves/mm and the entrance slit of 80 μm. Solid state laser with 532-nm line was used as an excitation source. In our scattering configuration, plane of incidence is *ab*-plane, where $|a| = |b|$ $(\measuredangle(a, b) = 120^\circ)$, with incident (scattered) light propagation direction along *c*-axes. Samples were cleaved in the air before being placed in vacuum. All measurements were performed in high vacuum (10^{-6} mbar) using a KONTI CryoVac continuous Helium flow cryostat with 0.5-mm thick window. Laser beam focusing was achieved using microscope objective with ×50 magnification. All spectra were corrected for Bose factor.

Spin-polarized density functional theory calculations were performed in Quantum Espresso software package,[25] based on plane waves and pseudopotentials, using Perdew–Burke–Ernzerhof (PBE) exchange-correlation functional[26] and projector augmented wave (PAW) pseudopotentials.[27,28] The cutoff for wavefunctions and the charge density of 85 and 425 Ry were chosen, respectively. The *k*-point were sampled using the Monkhorst-Pack scheme, on $8 \times 8 \times 8$ Γ centred grid used for both structures. Optimization of the lattice parameters and atomic positions in unit cell was performed until the interatomic forces were minimized down to 10^{-6} Ry/Å. Treatment of the van der Waals interactions is included using the Grimme-D2 correction, in order to obtain the lattice parameters more accurately. Phonon wave numbers were calculated within the linear response method, as implemented in PHonon part of Quantum Espresso.

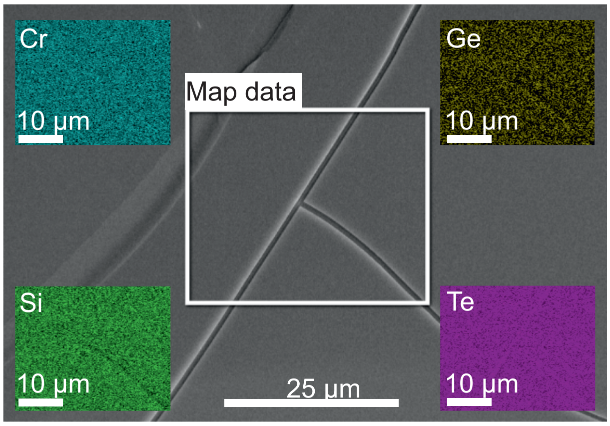

FIGURE 1 Energy dispersive spectroscopy (EDS) mapping on a $CrSi_{0.8}Ge_{0.1}Te_3$ single crystal [Colour figure can be viewed at wileyonlinelibrary.com]

3 | RESULTS AND DISCUSSION

In order to investigate uniformity and elemental composition of $CrSi_{0.8}Ge_{0.1}Te_3$ sample, SEM measurements were performed on as-cleaved crystals. EDS mapping presented in Figure 1 shows that the ratio of Cr:Si:Ge:Te (averaged over 10 measurements) is 1:0.8:0.1:3. This result reveals the presence of 10% Ge atomic vacancies in the sample.

Figure 2a,b presents the temperature dependence of zero-field cooling (ZFC) magnetic susceptibility $\chi(T) = M(T)/H$ measured in 1-kOe magnetic field applied parallel to a (a) and c (b) crystallographic axes. Curie–Weiss law $\chi = \frac{C}{T-\theta}$ fit at high temperatures yields Weiss temperatures θ_a = 61(2) K, θ_c = 70(2) K and high temperature paramagnetic moments $\mu_{eff,a} = 4.14(2)\mu_B$ and $\mu_{eff,c} = 3.91(2)\mu_B$ for $CrSi_{0.8}Ge_{0.1}Te_3$, consistent with dominant FM interactions below T_c and in line with the observed FM T_c and magnetic hystheresis loops.[13,24] The approximate T_c value can be determined from the minima of the $d\chi/dT$ curves insets in Figure 2(a,b). It should be noted that, instead of monotonous rise, there is a weak but discernible shift to lower temperature in $d\chi/dT$ in $CrSi_{0.8}Ge_{0.1}Te_3$ when compared with $CrSiTe_3$. This small reduction in FM transition temperature is likely induced by the presence of vacancies, as suggested by the EDS data. The presence of vacancies in this class of materials usually disarrange magnetic exchange due to disorder increment, which leads to the reduction of T_C.[29]

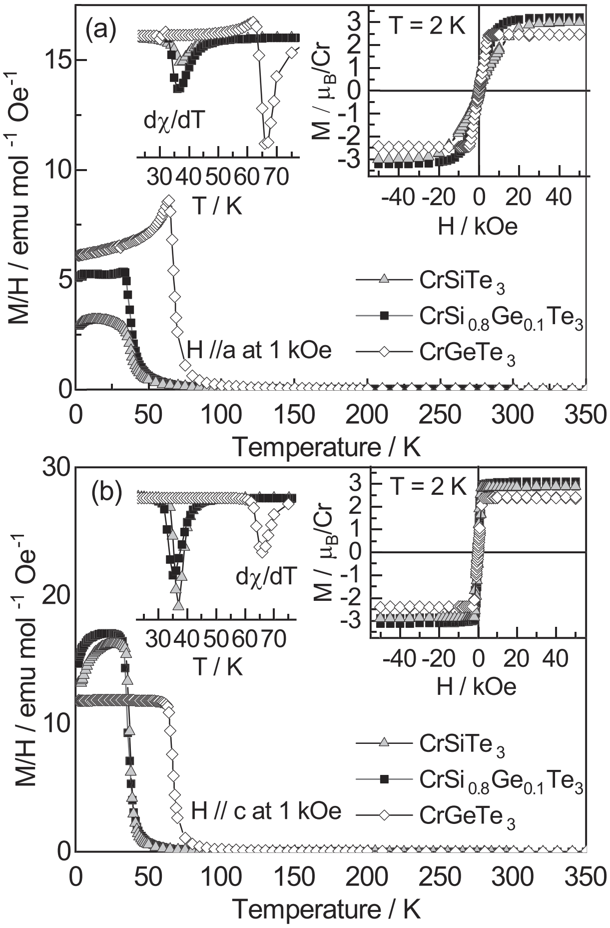

FIGURE 2 Temperature dependence of zero-field cooling (ZFC) χ=M/H for $CrSiTe_3$, $CrSi_{0.8}Ge_{0.1}Te_3$ and $CrGeTe_3$ in 1-kOe magnetic field applied in-plane (a) and along the c-axis (b). Insets show transition temperatures of ferromagnetic orders (dχ/dT) and magnetic hystheresis loops taken at 2 K

Isostructural parent compounds $CrSiTe_3$ and $CrGeTe_3$ crystallize in the rhombohedral crystal structure, described with space group $R\bar{3}$ (C_{3i}^2).[30] According to factor group analysis, five A_g and five double degenerate E_g symmetry modes are expected to be observed in the light scattering experiment. Detailed symmetry analysis, phonon mode distribution and selection rules for parent compounds ($CrSiTe_3$ and $CrGeTe_3$) can be found in Milosavljević et al.[21] In our scattering configuration, the plane of incidence is ab plane, where $|a| = |b|$ ($\measuredangle(a,b) = 120^\circ$) (inset in Figure 3), and the direction of incident (scattered) light propagation is along c-axes. According to the selection rules for this scattering configuration,[21] all Raman active modes may be observed, having in mind that A_g symmetry modes can be detected only in parallel polarization configuration. The E_g symmetry modes are expected to appear in both the parallel and cross polarization configurations. Raman spectra of $CrSi_{0.8}Ge_{0.1}Te_3$, obtained by continuous change of the angle between polarization vectors of incident and

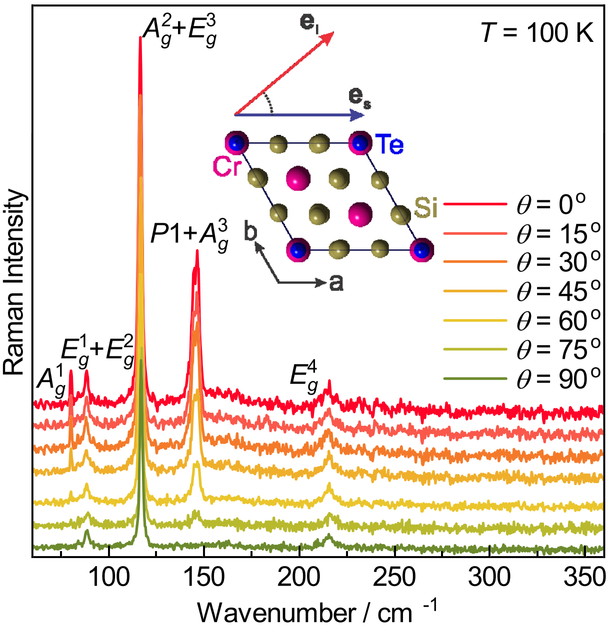

FIGURE 3 Raman spectra of $CrSi_{0.8}Ge_{0.1}Te_3$ single crystal, measured at 100 K, as a function of angle θ, between incident and scattered light polarization. Inset: schematic representation of the incident and scattered light polarization with respect to the crystal orientation [Colour figure can be viewed at wileyonlinelibrary.com]

scattered light, $\theta = \measuredangle(\mathbf{e}_\mathrm{i}, \mathbf{e}_\mathrm{s})$, $(0^\circ \leqslant \theta \leqslant 90^\circ)$ at 100 K, are shown in Figure 3. It can be seen that by changing this angle, starting from $\theta = 0^\circ$, the intensities of the peaks at energies 80.2, 116.4 and 145.5 cm^{-1} continuously decrease and completely vanish for polarization angle of 90°. Therefore, these excitations obey pure A_g symmetry. On the other hand, the peaks at energies of 84.5, 88.3, 117.2 and 215.0 cm^{-1} are not influenced by change of polarization angle, so they can be identified as E_g symmetry modes.

Here, one should note that the feature observed at around 117 cm^{-1} in both scattering configurations is actually a two-peak structure comprising of 116.4-cm^{-1} A_g and 117.2-cm^{-1} E_g symmetry modes. Detailed analysis of the structure for two scattering configurations is presented in Figure A1 of Appendix. Furthermore, closer inspection of the data revealed that peak at energy of 145.5 cm^{-1}, which obeys pure A_g symmetry, is also composed of two modes, $P1$ (144.6 cm^{-1}) and A_g^3 (146.7 cm^{-1}), as shown in Figure A2 of Appendix.

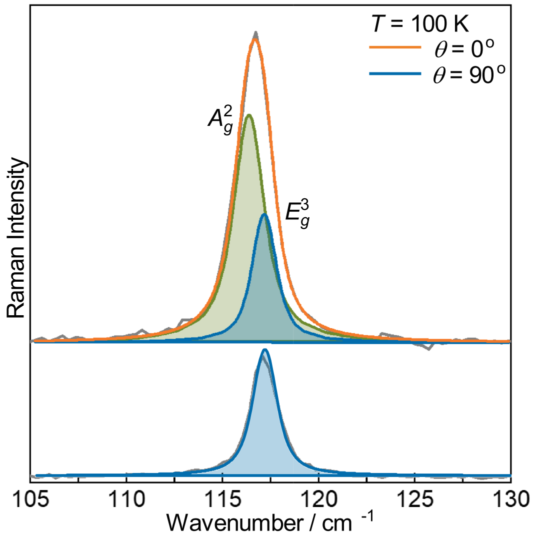

FIGURE A1 Decomposition of unresolved A_g^2 and E_g^3 symmetry modes obtained by simultaneous modelling in parallel and cross polarization configuration. Grey line represents the measured data, Voigt line of A_g^2 mode is shown by green, and blue lines represent the E_g^3 symmetry mode in parallel (upper panel) and cross (lower panel) polarization. The orange line is the superposition of these two lines [Colour figure can be viewed at wileyonlinelibrary.com]

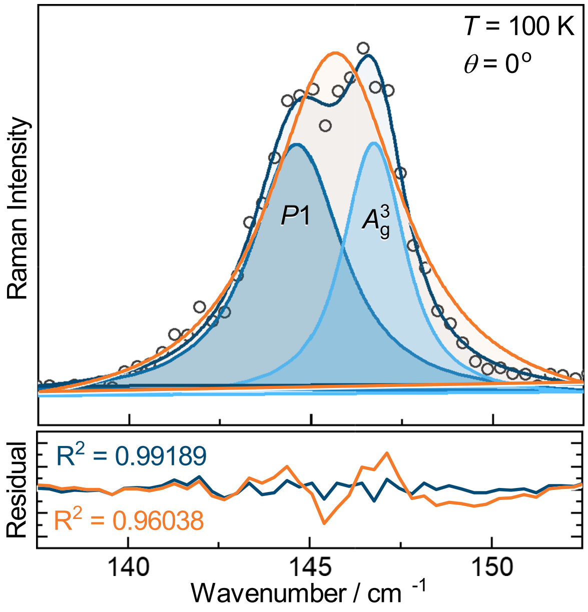

FIGURE A2 Decomposition of phonon mode in parallel scattering configuration on two A_g symmetry modes. Open circles represent the measured data and the blue one sum of two Voigt profile line shapes. Data modelled with one Voigt profile line shape (orange line) deviates significantly from measured data [Colour figure can be viewed at wileyonlinelibrary.com]

Calculated optical phonon wavenumbers of the parent compounds, $\mathrm{CrSiTe_3}$ and $\mathrm{CrGeTe_3}$, together with their experimental Raman active values as well as Raman mode energies of $\mathrm{CrSi_{0.8}Ge_{0.1}Te_3}$, are compiled in Table 1. As expected, experimental values of $\mathrm{CrSi_{0.8}Ge_{0.1}Te_3}$ Raman active modes are found between the values of the observed modes in parent compounds.[21] Figure 4a shows compositional evolution of the peaks with highest intensity, assigned as E_g^3 and A_g^3 symmetry modes in parent compounds. The E_g^3 mode energy changes almost linearly (Figure 4b), as a consequence of change in lattice parameters and "change of mass" effect. The observed energy shift is followed by doubling of the linewidth, dominantly induced by the significant crystalline disorder. The similar type of behaviour, with somewhat larger increase in the linewidth, was also observed for the A_g^3 symmetry mode. The most striking feature was the additional A_g symmetry mode (denoted as $P1$, see Figure A2 of the Appendix), observed in the doped sample. Generally, both the substitutional defects and vacancies may have similar impact on the Raman modes energy and linewidth. Here, the appearance of $P1$ peak can be understood as a consequence of the presence of vacancies on Si/Ge atomic site and their inharmonious distribution at nano-scale. The mode "splitting" is detected only for the A_g^3 but not for other observed modes, due to the fact that different nature of these vibrations results in different values of energy shifts. In the case of other modes, the difference between the shifts for corresponding domains is smaller than the spectral resolution of the instrument (~1.8 cm^{-1}), and therefore, the separate modes can not be resolved.

Figure 5 shows $\mathrm{CrSi_{0.8}Ge_{0.1}Te_3}$ Raman scattering spectra measured at various temperatures. For clarity, spectra obtained for cross polarization configuration are

TABLE 1 Phonon symmetry, calculated ($T = 0$ K) and experimental ($T = 100$ K) Raman active phonon wavenumbers of parent compounds $CrSiTe_3$ and $CrGeTe_3$.[21] Experimental values for Raman active phonons of $CrSi_{0.8}Ge_{0.1}Te_3$ at 100 K are shown in the last column

Raman active modes					
	Calculations		**Experiment**		
Symmetry	**$CrSiTe_3$**	**$CrGeTe_3$**	**$CrSiTe_3$**	**$CrGeTe_3$**	**$CrSi_{0.8}Ge_{0.1}Te_3$**
A_g^1	88.2	84.2	—	—	80.2
E_g^1	93.5	82.0	88.9	83.5	84.5
E_g^2	96.9	90.8	—	—	88.3
E_g^3	118.3	114.2	118.2	112.2	117.2
A_g^2	122.0	105.9	—	—	116.4
A_g^3	148.0	134.8	147.4	137.9	146.7
A_g^4	208.7	200.3	—	—	—
E_g^4	219.5	209.6	217.2	217.5	215.0
E_g^5	357.4	229.8	—	—	—
A_g^5	508.9	290.7	—	296.6	—

Note: All values are given in cm^{-1}.

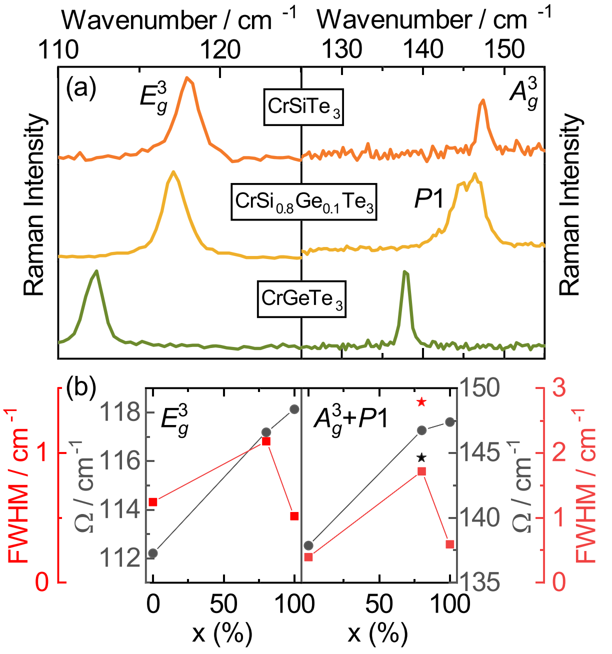

FIGURE 4 (a) Raman scattering spectra of E_g^3 and A_g^3 phonon modes of $CrSiTe_3$ (orange line), $CrSi_{0.8}Ge_{0.1}Te_3$ (yellow line) and $CrGeTe_3$ (green line) at $T = 100$ K measured in cross (left panel) and parallel (right panel) scattering configuration, respectively. (b) Energy (grey line) and linewidth (red line) of these two modes with respect to the percentage of Si atoms concentration. Energy and linewidth of $P1$ mode are marked with black and red star, respectively [Colour figure can be viewed at wileyonlinelibrary.com]

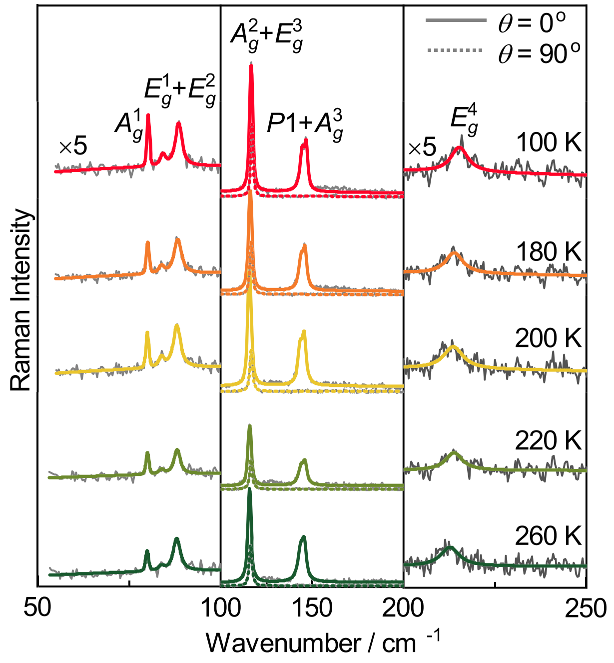

FIGURE 5 Raman spectra of $CrSi_{0.8}Ge_{0.1}Te_3$ single crystal measured at various temperatures. The spectra were analysed by using multiple Voigt peak functions and a single $\chi''_{cont} = a\Gamma\omega/(\Gamma^2 + \omega^2) + b\omega$ function, for parallel ($\theta = 0°$, solid coloured lines) and cross ($\theta = 90°$, dashed coloured lines) scattering configuration. For clarity, higher and lower energy ranges (left and right panel) are multiplied by the factor of five [Colour figure can be viewed at wileyonlinelibrary.com]

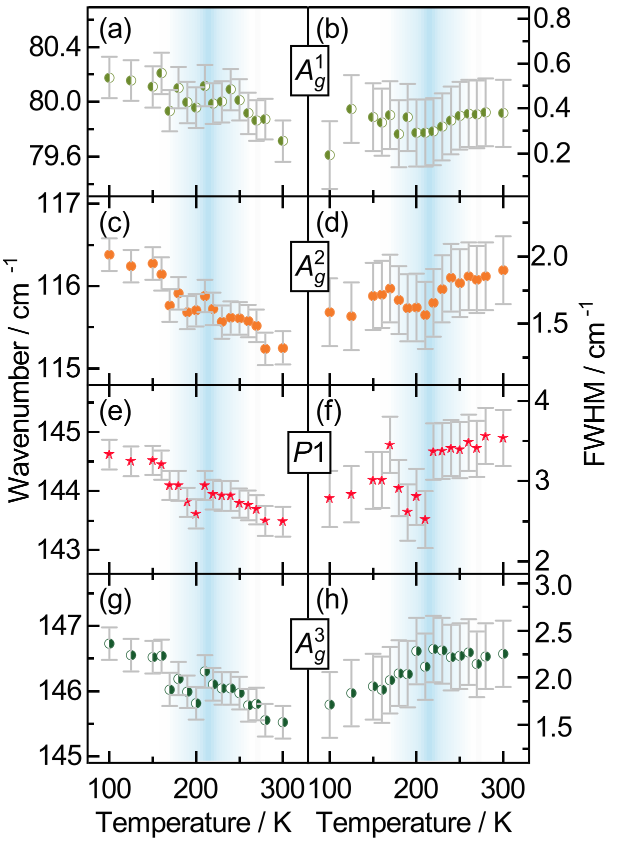

FIGURE 6 Energy and linewidth temperature dependence of A_g^1 (a,b), A_g^2 (c,d), $P1$ (e,f) and A_g^3 (g,h) Raman modes [Colour figure can be viewed at wileyonlinelibrary.com]

only shown for the mid-energy range. Temperature dependence of energies and linewidths of all the observed A_g symmetry modes, including $P1$, are presented in Figure 6. By heating the sample from 100 K to approximately 210 K, monotonous decrease in energy of all the A_g symmetry modes is present, dominantly driven by thermal expansion.[31] In the temperature region around 210 K, these modes' energy exhibit small deviation, followed by a continuous decrease up to room temperature. In the same temperature region, deviation from expected anharmonic type of behaviour is observed for all the A_g symmetry modes linewidth. This effect is more pronounced for higher energy modes where the anharmonicity is expected to be higher. Similar response of analysed E_g symmetry modes is present and shown in Figure 7.

Concerning previously reported strong spin–phonon coupling in $CrSiTe_3$,[15,21] which persists up to 180 K, we believe that this unconventional behaviour of energies and linewidths can be attributed to the coupling of the phonon modes to the spin system.[32] Due to the doping and presence of vacancies, strong magnetic correlations in $CrSi_{0.8}Ge_{0.1}Te_3$ are sustained up to 210 K.

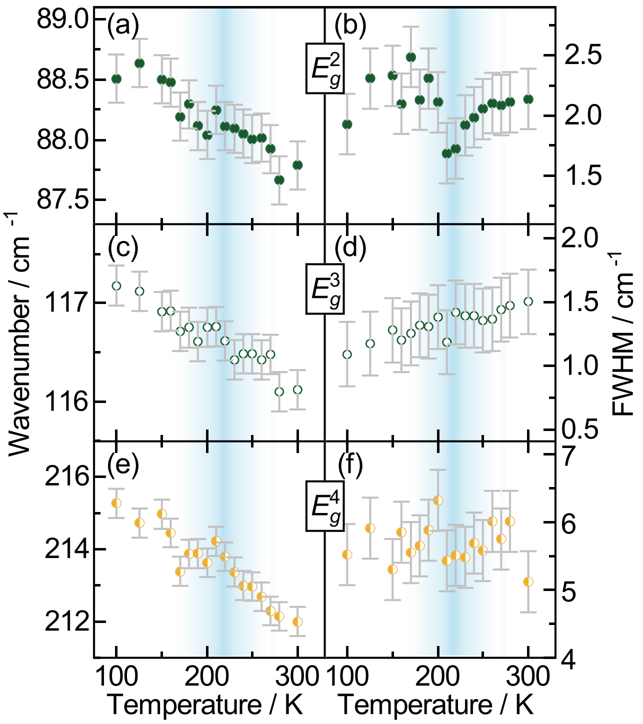

FIGURE 7 Energy and linewidth temperature dependence of E_g^2 (a,b), E_g^3 (c,d) and E_g^4 (e,f) symmetry modes [Colour figure can be viewed at wileyonlinelibrary.com]

4 | CONCLUSIONS

In summary, we presented temperature-dependent Raman scattering and magnetization studies of doped van der Waals ferromagnet $CrSi_{0.8}Ge_{0.1}Te_3$. SEM measurements revealed the presence of 10% vacancies on Si/Ge atomic site. As a consequence, magnetization measurements detected small but clear decrease in T_C. Seven out of 10 Raman active modes have been assigned in our Raman spectra. Temperature dependence of all the observed modes shows the persistence of magnetic correlations up to 210 K. In addition, the results revealed the appearance of the peak that obey pure A_g symmetry, which is attributed to the possible inhomogeneous distribution of Ge atoms and vacancies at nano-scale. This study provides an insight into the impact of doping and presence of vacancies on magnetic and lattice properties in this class of materials.

ACKNOWLEDGEMENTS

This work was supported by the Ministry of Education, Science and Technological Development of the Republic of Serbia and project no F-134 of the Serbian Academy of Sciences and Arts. DFT calculations were performed using computational resources at Johannes Kepler University, Linz, Austria. Electron microscopy was performed at Jozef Stefan Institute, Ljubljana, Slovenia, under Slovenian Research Agency contract P1-0099 (B. V.). Work at BNL (crystal synthesis and magnetic characterization) was supported by the U.S. DOE-BES, Division of Materials Science and Engineering, under Contract No. DE-SC0012704.

ORCID

Ana Milosavljević https://orcid.org/0000-0002-8654-0475

REFERENCES

[1] F. Hellman, A. Hoffmann, Y. Tserkovnyak, G. S. Beach, E. E. Fullerton, C. Leighton, A. H. MacDonald, D. C. Ralph, D. A. Arena, H. A. Dürr, P. Fischer, *Rev. Mod. Phys.* **2017**, *89*, 025006.

[2] N. Sivadas, M. W. Daniels, R. H. Swendsen, S. Okamoto, D. Xiao, *Phys. Rev. B.* **2015**, *91*, 235425.

[3] K. S. Novoselov, A. K. Geim, S. V. Morozov, D. Jiang, Y. Zhang, S. V. Dubonos, I. V. Grigorieva, A. A. Firsov, *Science* **2004**, *306*(5696), 666.

[4] Q. H. Wang, K. Kalantar-Zadeh, A. Kis, J. N. Coleman, M. S. Strano, *Nat. Nanotechnol.* **2012**, *7*, 699.

[5] G. Cheng, L. Lin, L. Zhenglu, J. Huiwen, S. Alex, X. Yang, C. Ting, B. Wei, W. Chenzhe, W. Yuan, Z. Q. Qiu, R. J. Cava, G. L. Steven, X. Jing, Z. Xiang, *Nature* **2017**, *546*, 265.

[6] B. Huang Bevin, G. Clark, E. Navarro-Moratalla, D. R. Klein, R. Cheng, K. L. Seyler, D. Zhong, E. Schmidgall, M. A. McGuire, D. H. Cobden, W. Yao, *Nature* **2017**, *546*, 270.

[7] K. S. Burch, D. Mandrus, J.-G. Park, *Nature* **2018**, *563* (7729), 47.

[8] J.-X. Zhu, M. Janoschek, D. Chaves, S. J. C. Cezar, T. Durakiewicz, F. Ronning, Y. Sassa, M. Mansson, B. L. Scott, N. Wakeham, E. D. Bauer, J. D. Thompson, *Phys. Rev. B.* **2016**, *93*, 144404.

[9] B. Chen, J. H. Yang, H. D. Wang, M. Imai, H. Ohta, C. Michioka, K. Yoshimura, M. H. Fang, *J. Phys. Soc. Japan* **2013**, *82*(12), 124711.

[10] A. Milosavljević, A. Šolajić, S. Djurdjić-Mijin, J. Pešić, B. Višić, Y. Liu, C. Petrovic, N. Lazarević, Z. V. Popović, *Phys. Rev. B.* **2019**, *99*, 214304.

[11] M. A. McGuire, H. Dixit, V. R. Cooper, B. C. Sales, *Chem. Mat.* **2015**, *27*(2), 612.

[12] H. L. Zhuang, Y. Xie, P. R. C. Kent, P. Ganesh, *Phys. Rev. B.* **2015**, *92*, 035407.

[13] G. T. Lin, H. L. Zhuang, X. Luo, B. J. Liu, F. C. Chen, J. Yan, Y. Sun, J. Zhou, W. J. Lu, P. Tong, Z. G. Sheng, *Phys. Rev. B.* **2017**, *95*, 245212.

[14] M. Gibertini, M. Koperski, A. F. Morpurgo, K. S. Novoselov, *Nat. Nanotech.* **2019**, *14*(5), 408.

[15] L. D. Casto, A. J. Clune, M. O. Yokosuk, J. L. Musfeldt, T. J. Williams, H. L. Zhuang, M.-W. Lin, K. Xiao, R. G. Hennig, B. C. Sales, J.-Q. Yan, D. Mandrus, *APL Mat.* **2015**, *3*(4), 041515.

[16] X. Zhang, Y. Zhao, Q. Song, S. Jia, J. Shi, W. Han, *JJpn. J. Appl. Phys.* **2016**, *55*(3), 033001.

[17] B. Siberchicot, S. Jobic, V. Carteaux, P. Gressier, G. Ouvrard, *Phys. J. Chem.* **1996**, *100*(14), 5863.

[18] V. Carteaux, F. Moussa, M. Spiesser, *EPL.* **1995**, *29*(3), 251.

[19] J. Zhang, X. Cai, W. Xia, A. Liang, J. Huang, C. Wang, L. Yang, H. Yuan, Y. Chen, S. Zhang, Y. Guo, *Phys. Rev. Lett.* **2019**, *123*, 047203.

[20] Y. F. Li, W. Wang, W. Guo, C. Y. Gu, H. Y. Sun, L. He, J. Zhou, Z. B. Gu, Y. F. Nie, X. Q. Pan, *Phys. Rev. B.* **2018**, *98*, 125127.

[21] A. Milosavljević, A. Šolajić, J. Pešć, Y. Liu, C. Petrovic, N. Lazarević, Z. V. Popović, *Phys. Rev. B.* **2018**, *98*, 104306.

[22] Y. Tian, M. J. Gray, H. Ji, R. J. Cava, K. S. Burch, *2D Mater.* **2016**, *3*(2), 025035.

[23] Y. Sun, R. C. Xiao, G. T. Lin., R. R. Zhang, L. S. Ling, Z. W. Ma, X. Luo, W. J. Lu, Y. P. Sun, Z. G. Sheng, *Appl. Phys. Lett.* **2018**, *112*(7), 072409.

[24] Y. Liu, C. Petrovic, *Phys. Rev. Mater.* **2019**, *3*, 014001.

[25] P. Giannozzi, S. Baroni, N. Bonini, M. Calandra, R. Car, C. Cavazzoni, D. Ceresoli, G. L. Chiarotti, M. Cococcioni, I. Dabo, A. Dal Corso, *J. Phys. Condens. Matter.* **2009**, *21*(39), 395502.

[26] J. P. Perdew, K. Burke, M. Ernzerhof, *Phys. Rev. Lett.* **1996**, *77*, 3865.

[27] P. E. Blöchl, *Phys. Rev. B.* **1994**, *50*, 17953.

[28] G. Kresse, D Joubert, *Phys. Rev. B.* **1999**, *59*, 1758.

[29] F. A. May, S. Calder, C. Cantoni, H. Cao, M. A. McGuire, *Phys. Rev. B* **2016**, *93*, 014411.

[30] R. E. Marsh, *J. Solid State Chem.* **1988**, *77*(1), 190.

[31] M. Opačić, N. Lazarević, M. Šćepanović, H. Ryu, H. Lei, C. Petrovic, Z. V. Popović, *J. Phys. Condens. Matter.*, *48*(27), 485701.

[32] F. Feng, N. Lazarević, C. Liu, J. Ji, Y. Wang, S. He, H. Lei, C. Petrovic, R. Yu, Z. V. Popović, Q. Zhang, *Phys. Rev. B.* **2019**, *99*, 144419.

How to cite this article: Milosavljević A, Šolajić A, Višić B, et al. Vacancies and spin–phonon coupling in CrSi$_{0.8}$Ge$_{0.1}$Te$_3$. *J Raman Spectrosc*. 2020;1–8. https://doi.org/10.1002/jrs.5962

APPENDIX: A DECOMPOSITION OF UNRESOLVED MODES

Analysing the spectra of CrSi$_{0.8}$Ge$_{0.1}$Te$_3$ single crystal, in different polarization configurations (Figure 3), in the energy range around 117 cm^{-1}, becomes clear that lower energy part completely disappears in cross polarization configuration, whereas higher energy part persists. Enlarged part of this energy region is shown in Figure A1, in parallel and cross polarization configuration at temperature of 100 K. After simultaneous modelling of these spectra becomes clear that they consist of the A_g^2 and E_g^3 modes, at energies 116.4 and 117.2 cm^{-1}, respectively. This is completely supported with theoretical calculations presented in Table 1.

On the other hand, existence of $P1$ is not predicted by theoretical calculations, as Raman active peak. Only closer inspection and detailed analysis, presented in Figure A2, shows that much better agreement with experimental results gives modelling as a superposition of two Voigt lines.

Inorganic Chemistry

pubs.acs.org/IC Article

Short-Range Order in VI_3

Sanja Djurdjić Mijin, A. M. Milinda Abeykoon, Andrijana Šolajić, Ana Milosavljević, Jelena Pešić, Yu Liu, Cedomir Petrovic, Zoran V. Popović, and Nenad Lazarević*

Cite This: https://dx.doi.org/10.1021/acs.inorgchem.0c02060 Read Online

ABSTRACT: We present a detailed investigation of the crystal structure of VI_3, a two-dimensional van der Waals material of interest for studies of low-dimensional magnetism. As opposed to the average crystal structure that features $R\overline{3}$ symmetry of the unit cell, our Raman scattering and X-ray atomic pair distribution function analysis supported by density functional theory calculations point to the coexistence of short-range ordered $P\overline{3}1c$ and long-range ordered $R\overline{3}$ phases. The highest-intensity peak, A_{1g}^3, exhibits a moderate asymmetry that might be traced back to the spin−phonon interactions, as in the case of CrI_3.

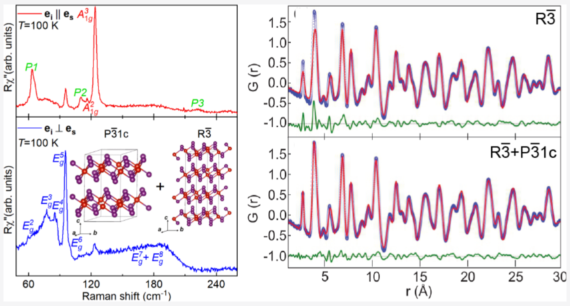

■ INTRODUCTION

A well-known family of transition metal trihalides (TMTs) MX_3 (X = Cr, B, or I) have received a great deal of attention due to potential existence of two-dimensional (2D) ferromagnetism,[1−6] which has been confirmed in CrI_3.[7,8] The similar crystal structure and magnetic properties of CrI_3 and VI_3 fostered a belief that the same might be found in the latter. In fact, magnetization measurements revealed the 2D ferromagnetic nature of VI_3 with a Currie temperature (T_c) of around 50 K.[9,10] Contrary to a layer-dependent ferromagnetism in CrI_3,[11] the first-principles calculations predict that ferromagnetism in VI_3 persists down to a single layer,[9] making it a suitable candidate for engineering 2D spintronic devices. Resistivity measurements showed VI_3 is an insulator with an optical band gap of ∼0.6 eV.[9,12]

Whereas laboratory X-ray diffraction studies reported three possible high-temperature VI_3 unit cell symmetries,[9,12−14] high-resolution synchrotron X-ray diffraction confirmed a rhombohedral $R\overline{3}$ space group.[10] A very recently published Raman spectroscopy study indicated that the VI_3 crystal structure can be described within the C_{2h} point group.[15] All results agree on the existence of a phase transition at a temperature of 79 K. However, the subtle[12] structural changes below 79 K are still under debate.

The long-range magnetic order in ultrathin 2D van der Waals (vdW) crystals stems from strong uniaxial anisotropy, in contrast to materials with isotropic exchange interactions where order parameters are forbidden.[16−18] 2D vdW magnetic materials are of interest both as examples of exotic magnetic order[19] and for potential applications in spintronic technology.[2,4,20,21]

Atomically thin flakes of $CrCl_3$ have a magnetic transition temperature that is different from that of bulk crystals possibly due to the different crystal structure of the monolayer and ultrathin crystals when compared to bulk.[22,23] Similar observations were made on CrI_3 monolayers.[22,24,25] It has been proposed[23] that the second anomaly in heat capacity in bulk $CrCl_3$ arises due to regions close to the surface that host a different crystal structure when compared to bulk;[26,27] however, due to the substantial mass fraction detected in heat capacity measurements, this could also reflect differences between the short-range order and long-range crystallographic order of Bragg planes. The short-range order is determined by the space group that is energetically favorable for a monolayer or a few layers, whereas the long-range crystallographic order is established over large packing lengths.

In this paper, we present an experimental Raman scattering study of the bulk VI_3 high-temperature structure, supported by density functional theory (DFT) calculations and the X-ray atomic pair distribution function (PDF) analysis. The comparison between the Raman experiment and DFT calculations for each of the previously reported space groups suggested that the high-temperature lattice vibrations of bulk VI_3 are consistent with a $P\overline{3}1c$ trigonal structure. Nine ($2A_{1g}$ + $7E_g$) of 12 observed peaks were assigned on the basis of factor group analysis (FGA) and DFT calculations. The PDF analysis indicated the coexistence of two crystallographic phases at two different interatomic distances, short-range ordered $P\overline{3}1c$ and

Received: July 12, 2020

long-range ordered $R\overline{3}$, as two segregated phases and/or as randomly distributed short-range ordered $P\overline{3}1c$ domains in the long-range ordered $R\overline{3}$ lattice. Raman data displayed a moderate asymmetry of the A_{1g}^3 phonon line. This behavior was attributed to the spin−phonon interaction, similar to the case for CrI_3. The additional peaks in our spectra obey A_g selection rules and can be described in terms of overtones, as well as the A_{2g} silent modes "activated" by the symmetry breaking.

■ EXPERIMENTAL AND COMPUTATIONAL DETAILS

The preparation of single-crystal VI_3 samples used in this study is presented elsewhere.[10] For the Raman scattering experiment, a Tri Vista 557 spectrometer was used in the backscattering micro-Raman configuration with a 1800/1800/2400 grooves/mm diffraction grating combination. A Coherent Ar^+/Kr^+ ion laser with a 514 nm line was used as an excitation source. Laser beam focusing was achieved through the microscope objective with 50× magnification. The direction of the incident (scattered) light coincides with the crystallographic c axis. The sample, cleaved in open air, was held inside a KONTI CryoVac continuous helium flow cryostat with a 0.5 mm thick window. Raman scattering measurements were performed under high vacuum (10^{-6} mbar). All of the obtained Raman spectra were corrected by the Bose factor. The spectrometer resolution is comparable to the Gaussian width of 1 cm^{-1}.

PDF and wide-angle X-ray scattering measurements were carried out in capillary transmission geometry using a PerkinElmer amorphous silicon area detector placed 206 and 983 mm downstream from the sample, respectively, at beamline 28-ID-1 (PDF) of National Synchrotron Light Source II at Brookhaven National Laboratory. The setup utilized a 74.3 keV (λ = 0.1668 Å) X-ray beam.

Two-dimensional diffraction data were integrated using the Fit2D software package.[28] Data reduction was performed to obtain experimental PDFs (Q_{max} = $26A^{-1}$) using the xPDFsuite software package.[29] The Rietveld and PDF analyses were carried out using GSAS-II[30] and PDFgui[31] software packages, respectively.

Density functional theory calculations were performed using the Quantum Espresso software package,[32] employing the PBE exchange-correlation functional[33] and PAW pseudopotentials.[34,35] All calculations are spin-polarized. The cutoff for wave functions and the charge density were set to 48 and 650 Ry, respectively. The k-points were sampled using the Monkhorst−Pack scheme, on a 6 × 6 × 6 Γ-centered grid for $R\overline{3}$ and $C2/m$ structures and a 12 × 12 × 8 grid for the $P\overline{3}1c$ structure. Optimization of the lattice parameters and atomic positions in the unit cell was performed until the interatomic forces were $<10^{-6}$ Ry/Å. To obtain more accurate lattice parameters, treatment of the van der Waals interactions is included using the Grimme-D2 correction. The correlation effects are treated with the Hubbard U correction (LDA+U), using a rotationally invariant formulation implemented in QE,[36] where U = 3.68 eV. Band structure plots are calculated at 800 k-points on the chosen path over high-symmetry points. Phonon frequencies were calculated with the linear response method, as implemented in the -honon part of Quantum Espresso.

■ RESULTS AND DISCUSSION

The first reported results for VI_3, dating from the 1950s,[37−39] indicated that VI_3 adopts a honeycomb layer-type BiI_3 structure described with space group $R\overline{3}$, which is a structure common in TMTs, also found in the low-temperature phase of CrI_3.[6,40]

There have been several proposed unit cell symmetries for VI_3 in the literature: $R\overline{3}$,[12,13] $C2/m$,[14] and $P\overline{3}1c$.[9] Schematic representations of the $P\overline{3}1c$, $R\overline{3}$, and $C2/m$ crystal structures are depicted in Figure 1. The corresponding crystallographic unit cell parameters, previously reported, are listed in Table 1.

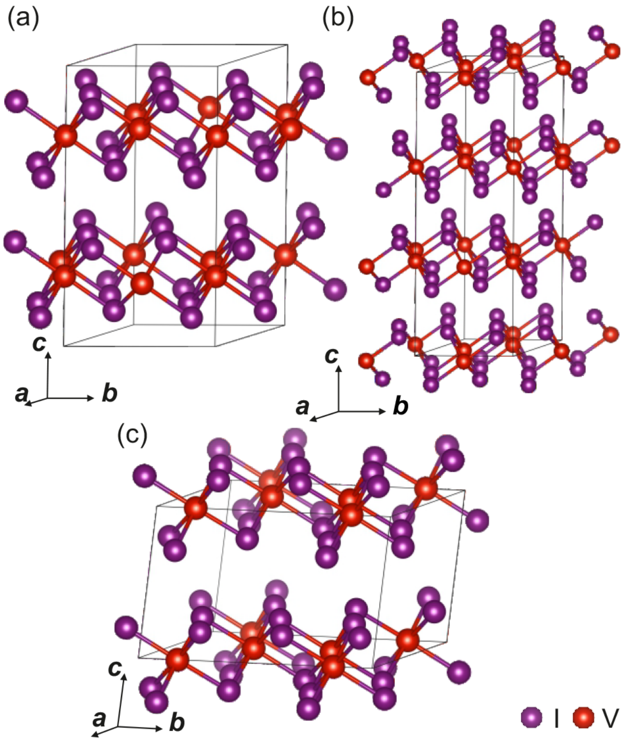

Figure 1. Schematic representation of the high-temperature (a) $P\overline{3}1c$, (b) $R\overline{3}$, and (c) $C2/m$ structures of VI_3. Black solid lines represent unit cells.

Each of the suggested symmetries implies a different distribution of Raman active modes.

According to FGA, eight ($4A_g + 4E_g$), 11 ($3A_{1g} + 8E_g$), and 12 ($6A_g + 6B_g$) Raman active modes are expected to be observed in the light scattering experiment for $R\overline{3}$, $P\overline{3}1c$, and $C2/m$ crystal structures, respectively. Wyckoff positions, irreducible representations, and corresponding tensors of Raman active modes for each space group are listed in Table 2.

The first step in determining the crystal symmetry from the light scattering experiment is to compare the expected and observed Raman active modes, shown in Figure 2. The red solid line represents the spectrum measured in the parallel polarization configuration, whereas the blue line corresponds to the cross polarization configuration. Five of 12 observed peaks emerge only in parallel, whereas five peaks and a broad peak-like structure can be observed for both polarization configurations. The emergence of the 123.4 cm^{-1} peak in the cross polarization can be understood as a "leakage" of the A_{1g}^3 mode due to a possible finite c axis projection and/or the presence of defects.

Now the peaks that appear only for the parallel polarization configuration can be assigned as either A_{1g} or A_g symmetry modes, assuming the light polarization direction along the main crystal axis of the $C2/m$ structure for the later. On the basis of the FGA for possible symmetry group candidates, the remaining Raman active modes can be either of E_g or B_g symmetry. The selection rules (Table 2) do not allow observation of the B_g symmetry modes for the parallel polarization configuration. Consequently, the peaks that can be observed in both scattering channels were recognized as E_g modes. The absence of B_g modes in the Raman spectra rules out the possibility of the $AlCl_3$ type of structure (space group $C2/m$). Two possible remaining crystal symmetries ($R\overline{3}$ and

Table 1. Previously Reported Experimental and Calculated Unit Cell Parameters for $P\bar{3}1c$, $R\bar{3}$, and $C2/m$ Structures of VI_3

	$P\bar{3}1c$		$R\bar{3}$		$C2/m$	
	calcd	exp.[9]	calcd	exp.[12]	calcd	exp.[14]
a (Å)	6.87	6.89(10)	6.69	6.89(3)	7.01	6.84(3)
b (Å)	6.87	6.89(10)	6.69	6.89(3)	12.14	11.83(6)
c (Å)	13.224	13.289(1)	19.81	19.81(9)	7.01	6.95(4)
α (deg)	90	90	90	90	90	90
β (deg)	90	90	90	90	109.05	108.68
γ (deg)	120	120	120	120	90	90
cell volume (Å^3)	559.62	547.74(10)	767.71	814.09(8)	563.33	533.66(36)

Table 2. Wyckoff Positions of Atoms and Their Contributions to the Γ-Point Phonons for the $R\bar{3}$, $C2/m$, and $P\bar{3}1c$ Structures and the Raman Tensors for the Corresponding Space Groups

space group $P\bar{3}1c$		space group $R\bar{3}$		space group $C2/m$	
atom	irreducible representation	atom	irreducible representation	atom	irreducible representation
V (2a)	$A_{2g} + A_{2u} + E_g + E_u$	V (3a)		V (4g)	$A_g + A_u + 2B_g + 2B_u$
V (2c)	$A_{2g} + A_{2u} + E_g + E_u$	V (6c)	$A_g + A_u + E_g + E_u$	I (4i)	$2A_g + A_u + B_g + 2B_u$
I (12i)	$3A_{1g} + 3A_{1u} + 3A_{2g} + 3A_{2u} + 6E_g + 6E_u$	I (18f)	$3A_g + 3A_u + 3E_g + 3E_u$	I (8j)	$3A_g + 3A_u + 3B_g + 3B_u$
$A_{1g} = \begin{pmatrix} a & & \\ & a & \\ & & b \end{pmatrix}$		$A_g = \begin{pmatrix} a & & \\ & a & \\ & & b \end{pmatrix}$		$A_g = \begin{pmatrix} a & & d \\ & c & \\ d & & b \end{pmatrix}$	
${}^1E_g = \begin{pmatrix} c & & \\ & -c & d \\ & d & \end{pmatrix}$ ${}^2E_g = \begin{pmatrix} & -c & -d \\ -c & & \\ d & & \end{pmatrix}$		${}^1E_g = \begin{pmatrix} c & d & e \\ d & -c & f \\ e & f & \end{pmatrix}$ ${}^2E_g = \begin{pmatrix} d & -c & -f \\ -c & -d & e \\ -f & e & \end{pmatrix}$		$B_g = \begin{pmatrix} & e & \\ e & & f \\ & f & \end{pmatrix}$	

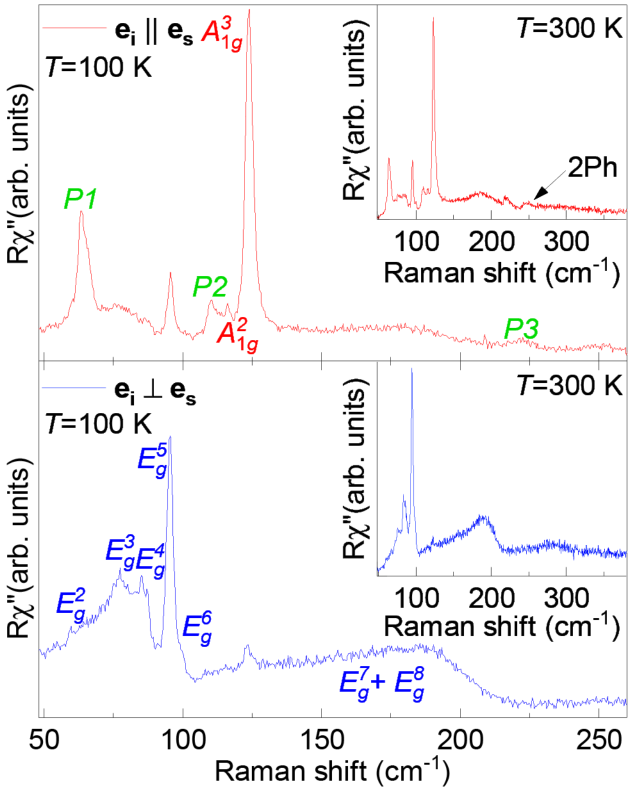

Figure 2. Raman spectra of the high-temperature VI_3 single-crystal structure measured in parallel (red solid line) and cross (blue solid line) polarization configurations at 100 K. Peaks observed in both spectra were identified as E_g modes, whereas peaks observed only in the red spectrum were assigned as A_{1g} modes. Additional peaks that obey pure A_{1g} symmetry are marked as $P1-P3$.

$P\bar{3}1c$) are difficult to single out on the basis of the Raman data symmetry analysis alone. To overcome this obstacle, the DFT method was applied for each of the suggested structures.

It was reported in the literature that $P\bar{3}1c$ VI_3 can have two possible electronic states[9,14,41−43] that both can be obtained using DFT+U calculations by varying the smearing and mixing parameters. This approach resulted in a Mott-insulator state having a lower energy making it the electronic ground state of VI_3. However, the total energy difference of these two states is small and will not be mentioned further because it is outside of the scope of our analysis. For the sake of completeness, both sets of phonon energies obtained through DFT calculations for these electronic states of the $P\bar{3}1c$ structure are listed in Table 3 together with the results for the $R\bar{3}$ and $C2/m$ space groups as well as the experimental results measured at 100 K.

Now one can see that, even though the Raman mode symmetries for the case of the $R\bar{3}$ crystal structure can describe our Raman spectra, there is a stronger mismatch in calculated and experimentally determined phonon energies when compared to the results obtained for the $P\bar{3}1c$ structure. The deviation is largest for the calculated A^1_g mode. The closest mode in energy, which obeys the same symmetry rules as the calculated A^1_g, is a peak at ~64.1 cm^{-1}, yielding a deviation of ~30%. Also, the calculated energy of the A^4_g mode could not be identified within our spectrum, with the closest experimental A_g peaks being within 20%. Such deviation in theory and experiment, >20%, indicates that the room-temperature phonon vibrations in VI_3 do not originate predominantly from the BiI_3 structure type either, leaving $P\bar{3}1c$ as the only candidate. This indication is further reinforced by the inability to connect the experimentally observed E_g modes at ~77 and ~86 cm^{-1} with the $R\bar{3}$-calculated modes.

Our experimental data (Table 3) are mostly supported by the phonon energies obtained for possible electronic states of

Table 3. Comparison between Calculated Values of Raman Active Phonon Energies for Insulating and Half-Metallic States of the $P\bar{3}1c$ Structure and Experimentally Obtained Values (left)[a] and Phonon Symmetries and Calculated Phonon Energies for the $R\bar{3}$ and $C2/m$ Structures of VI_3[b]

space group $P\bar{3}1c$				space group $R\bar{3}$		space group $C2/m$	
symmetry	calcd (cm^{-1})	calcd (cm^{-1})	exp. (cm^{-1})	symmetry	calcd (cm^{-1})	symmetry	calcd (cm^{-1})
E_g^1	17.2	15.2	–	E_g^1	45.2	A_g^1	58.1
A_{2g}^1 (silent)	35.0	56.8		E_g^2	69.9	B_g^1	60.0
E_g^2	62.2	61.6	59.8	A_g^1	99.3	A_g^2	82.7
A_{2g}^2 (silent)	69.4	72.3		E_g^3	99.8	B_g^2	82.9
E_g^3	74.1	75.9	77.2	A_g^2	105.1	A_g^3	85.7
A_{1g}^1	83.3	84.2	–	A_g^3	135.5	B_g^3	88.9
E_g^4	84.9	86.6	86.7	A_g^4	167.9	A_g^4	99.3
E_g^5	91.5	98.4	95.2	E_g^4	176.8	B_g^4	99.3
A_{2g}^3 (silent)	92.2	96.3				A_g^5	122.3
E_g^6	97.4	108.3	100.4			B_g^5	149.9
A_{1g}^2	113.2	119.3	116.8			B_g^6	161.0
A_{1g}^3	117.1	123.9	123.4			A_g^6	164.0
A_{2g}^4 (silent)	121.3	147.8					
E_g^7	132.2	151.9	c				
E_g^8	149.4	166.9	c				
A_{2g}^5 (silent)	185.9	212.1					

[a] The experimental values were determined at 100 K. The experimental uncertainty is 0.3 cm^{-1}. [b] All calculations were performed at 0 K. [c] See the text for an explanation.

the $P\bar{3}1c$ trigonal structure with deviations of around 10% and 15%. Nine of 11 Raman modes were singled out and identified, with E_g^1 being not observable in our experimental setup due to its low energy. The A_{1g}^1 mode might be missing due to its low intensity and/or the finite spectrometer resolution. The most striking was the observation of the broad feature at ∼180 cm^{-1}, persisting up to 300 K in both scattering channels. Whereas its line shape resembles those of the two-magnon type of excitation, we believe that scenario is unlikely for a ferromagnetic material. The energy region where the feature was observed may also suggest the possibility of a two-phonon type of excitation. However, their scattering cross sections are usually small and dominated by overtones, thus mostly observed for the parallel scattering configuration.[45] For example, such an excitation was observed at ∼250 cm^{-1} (Figure 2). Finally, the observed feature also falls into the energy region where, as suggested by the numerical calculations, observation of the E_g^7 and E_g^8 modes is expected. We believe that it is actually a complex structure comprising E_g^7 and E_g^8 Raman modes, significantly broadened by the spin−phonon interaction, that is particularly strong on these phonon branches. The proximity of the two very broad, presumably asymmetric peaks hampers their precise assignment.

Closer inspection of other Raman peaks revealed that some of them also exhibit an asymmetric line shape. To further demonstrate this virtue, we have quantitatively analyzed the highest-intensity peak, A_{1g}^3, using the symmetric Voigt line shape and convolution of a Fano profile and a Gausian.[44−46] The asymmetric line shape (with a Fano parameter of $|q| = 12.3$) gives a slightly better agreement with the experimental data, as depicted in Figure 3. Considering that the observed asymmetry in similar materials was shown to reflect the spin−phonon interaction,[46,47] we propose it as a possible scenario in VI_3, as well.

Our findings, based on the inelastic light scattering experiments, at first glance differ from those presented in ref 10. To resolve this discrepancy, we used synchrotron X-ray Rietveld and PDF analysis. Typically, the short-range order (SRO) contributes to diffuse scattering under the long-range order (LRO) Bragg peaks when they coexist. Because the diffuse scattering is subtracted as part of the background in the Rietveld refinement, this method is more sensitive to the average structure of materials. In contrast, PDF analysis is performed on the sine Fourier transform of the properly corrected diffraction patten, including both Bragg and diffuse

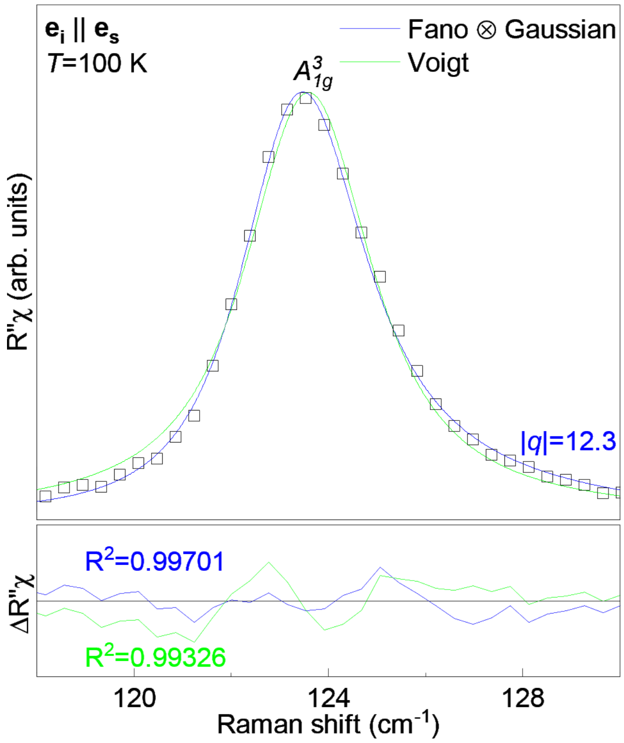

Figure 3. Quantitative analysis of the A_{1g}^3 mode. The blue solid line represents the line shape obtained as a convolution of the Fano line shape and the Gaussian, whereas the green one represents a Voigt profile fitted to experimental data (□). For details, see refs 44 and 45.

components. PDF is a real space function that provides a histogram of interatomic distances, which contain information regarding all length scales.[48−51] The 1−10 and 11−30 Å PDF length scales are more sensitive to SRO and LRO, respectively. For the VI_3 system, the best Rietveld fit was obtained using the $R\bar{3}$ space group (Figure 4a), in agreement with that previously observed.[10] Not surprisngly, LRO obtained from the Rietveld refinement showed a good agreement on the PDF length scale of 10−30 Å. However, the $R\bar{3}$ space group gave a poor fit on the length scale of 1.5−15 Å with refined $\delta 1$ to account for correlated motion (Figure 4b). In contrast, $P\bar{3}1c$ gave a better fit to SRO, but a poor fit to LRO. The best PDF fits were obtained by refining a weighted two-phase structural model containing ∼25 wt % SRO $P\bar{3}1c$ and ∼75 wt % LRO $R\bar{3}$ phases. The refined correlation length of the SRO is ∼15−20 Å (Figure 4c). These results suggest two possible seanarios: (1) coexistence of two segregated phases, LRO $R\bar{3}$ and SRO $P\bar{3}1c$, and (2) randomly distributed short-range ordered $P\bar{3}1c$ domains in the long-range ordered $R\bar{3}$ lattice. A detailed structural analysis is required to pinpoint scenario 1 and/or 2, which is beyond the scope of this work.

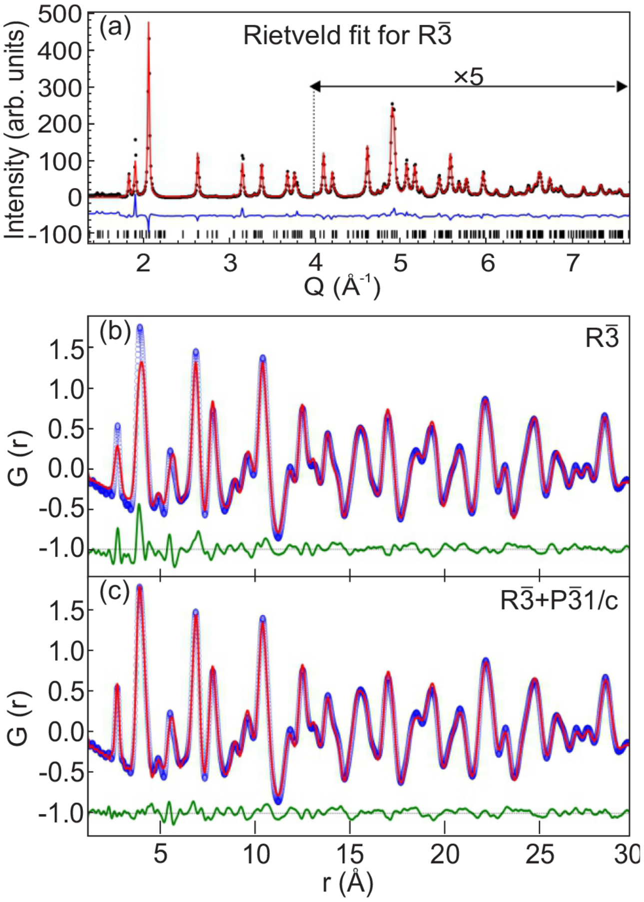

Figure 4. Best structural model fits to diffraction data. (a) Rietveld fit using the $R\bar{3}$ space group with black vertical bars indicating calculated peak positions. (b) PDF fit using the $R\bar{3}$ space group. (c) Two-phase PDF fit using $R\bar{3}$ and $P\bar{3}1c$ space groups to fit LRO and SRO, respectively. Black dots (XRD) and blue dots (PDF) represent experimental data, and red solid lines represent the model-based fits. The fit residues are shown at the bottom of each plot.

In addition to the peaks already assigned to Γ-point Raman active phonons of the $P\bar{3}1c$ crystal structure (Table 2), three additional peaks at 64.2 cm^{-1} ($P1$), 110.1 cm^{-1} ($P2$), and 220.6 cm^{-1} ($P3$) are observed (see Figure 2). According to the results of DFT, energies of these modes correspond well to those calculated for silent A_{2g}^2, A_{2g}^3, and A_{2g}^5 modes. Their observability in Raman data may come from the release of the symmetry selection rules by breaking of the (translation) symmetry as suggested by the PDF in both scenarios.[52−55] However, as previously discussed, these peaks obey A_{1g} selection rules, indicating the possibility for them to be overtones in nature. In this less likely scenario, the phonon−phonon coupling is enhanced by the spin−phonon interaction and/or by the structural imperfections, thus enhancing the Raman scattering rate for the two-phonon processes.[45] Hence, the observed Raman modes reflect the symmetry of phonon vibrations related to the SRO.[56,57] It is interesting to note that, besides a possible short-range crystallography that is different from the average, VI_3 might also feature short-range magnetic order above 79 K.[14]

CONCLUSION

In summary, room-temperature phonon vibrations of VI_3 stem from the $P\bar{3}1c$ symmetry of the unit cell. The PDF analysis suggested the coexistence of two phases, short-range ordered $P\bar{3}1c$ and long-range ordered $R\bar{3}$, as two segregated phases and/or as randomly distributed short-range ordered $P\bar{3}1c$ domains in the long-range ordered $R\bar{3}$ lattice. Nine of 12 observed peaks in the Raman spectra were assigned in agreement with $P\bar{3}1c$ symmetry calculations. Three additional peaks, which obey A_{1g} symmetry rules, could be explained as either overtones or as activated A_{2g} silent modes caused by a symmetry breaking. The asymmetry of one of the A_{1g} phonon modes, together with the anomalous behavior of E_g^7 and E_g^8, indicates strong spin−phonon coupling, which has already been reported in similar 2D materials.[46,58]

AUTHOR INFORMATION

Corresponding Author

Nenad Lazarević − *Institute of Physics Belgrade, University of Belgrade, 11080 Belgrade, Serbia;* orcid.org/0000-0001-6310-9511; Email: nenadl@ipb.ac.rs

Authors

Sanja Djurdjić Mijin − *Institute of Physics Belgrade, University of Belgrade, 11080 Belgrade, Serbia*

A. M. Milinda Abeykoon − *National Synchrotron Light Source II, Brookhaven National Laboratory, Upton, New York 11973, United States*

Andrijana Šolajić − *Institute of Physics Belgrade, University of Belgrade, 11080 Belgrade, Serbia*

Ana Milosavljević − *Institute of Physics Belgrade, University of Belgrade, 11080 Belgrade, Serbia*

Jelena Pešić − *Institute of Physics Belgrade, University of Belgrade, 11080 Belgrade, Serbia*

Yu Liu − *Condensed Matter Physics and Materials Science Department, Brookhaven National Laboratory, Upton, New York 11973-5000, United States;* orcid.org/0000-0001-8886-2876

Cedomir Petrovic − *Condensed Matter Physics and Materials Science Department, Brookhaven National Laboratory, Upton, New York 11973-5000, United States;* orcid.org/0000-0001-6063-1881

Zoran V. Popović − *Institute of Physics Belgrade, University of Belgrade, 11080 Belgrade, Serbia; Serbian Academy of Sciences and Arts, 11000 Belgrade, Serbia*

Complete contact information is available at:
https://pubs.acs.org/10.1021/acs.inorgchem.0c02060

Notes

The authors declare no competing financial interest.

■ ACKNOWLEDGMENTS

The authors acknowledge funding provided by the Institute of Physics Belgrade, through a grant from the Ministry of Education, Science and Technological Development of the Republic of Serbia, Project F-134 of the Serbian Academy of Sciences and Arts, and the Science Fund of the Republic of Serbia, PROMIS, 6062656, StrainedFeSC. DFT calculations were performed using computational resources at Johannes Kepler University (Linz, Austria). Materials synthesis was supported by the U.S. DOE-BES, Division of Materials Science and Engineering, under Contract DE-SC0012704 (BNL). This research used beamline 28-ID-1 of National Synchrotron Light Source II, a U.S. DOE Office of Science User Facility operated for the DOE Office of Science by Brookhaven National Laboratory under Contract DE-S.

■ REFERENCES

(1) Seyler, K. L.; Zhong, D.; Klein, D. R.; et al. Ligand-field helical luminescence in a 2D ferromagnetic insulator. *Nat. Phys.* **2018**, *14*, 277−281.

(2) Klein, D. R.; MacNeill, D.; Lado, J. L.; Soriano, D.; Navarro-Moratalla, E.; Watanabe, K.; et al. Probing magnetism in 2D van der Waals crystalline insulators via electron tunneling. *Science* **2018**, *360*, 1218−1222.

(3) Huang, B.; Clark, G.; Klein, D. R.; MacNeill, D.; Navarro-Moratalla, E.; Seyler, K. L.; et al. Electrical control of 2D magnetism in bilayer CrI_3. *Nat. Nanotechnol.* **2018**, *13*, 544−548.

(4) Jiang, S.; Li, L.; Wang, Z.; Mak, K. F.; Shan, J. Controlling magnetism in 2D CrI_3 by electrostatic doping. *Nat. Nanotechnol.* **2018**, *13*, 549−553.

(5) McGuire, M. A.; Clark, G.; KC, S.; Chance, W. M.; Jellison, G. E.; Cooper, V. R.; Xu, X.; Sales, B. C. Magnetic behavior and spin-lattice coupling in cleavable van der Waals layered $CrCl_3$ crystals. *Phys. Rev. Materials* **2017**, *1*, 014001.

(6) Djurdjic-Mijin, S. D.; Šolajić, A.; Pešić, J.; Šćepanović, M.; Liu, Y.; Baum, A.; et al. Lattice dynamics and phase transition in CrI_3 single crystals. *Phys. Rev. B: Condens. Matter Mater. Phys.* **2018**, *98*, 104307.

(7) Thiel, L.; Wang, Z.; Tschudin, M.; Rohner, D.; Gutierrez-Lezama, I. G.; Ubrig, N.; et al. Probing magnetism in 2D materials at the nanoscale with single-spin microscopy. *Science* **2019**, *364*, 973−976.

(8) Lin, G. T.; Luo, X.; Chen, F. C.; Yan, J.; Gao, J. J.; Sun, Y.; et al. Critical behavior of two-dimensional intrinsically ferromagnetic semiconductor CrI_3. *Appl. Phys. Lett.* **2018**, *112*, 072405.

(9) Son, S.; Coak, M. J.; Lee, N.; Kim, J.; Kim, T. Y.; Hamidov, H.; et al. Bulk properties of the van der Waals hard ferromagnet VI_3. *Phys. Rev. B: Condens. Matter Mater. Phys.* **2019**, *99*, 041402.

(10) Liu, Y.; Abeykoon, M.; Petrovic, C. Critical behavior and magnetocaloric effect in VI_3. *Phys. Rev. Research* **2020**, *2*, 013013.

(11) Huang, B.; Clark, G.; Navarro-Moratalla, E.; Klein, D. R.; Cheng, R.; Seyler, K. L.; et al. Layer-dependent ferromagnetism in a van der Waals crystal down to the monolayer limit. *Nature* **2017**, *546*, 270−273.

(12) Kong, T.; Stolze, K.; Timmons, E. I.; Tao, J.; Ni, D.; Guo, S.; et al. VI_3 − a New Layered Ferromagnetic Semiconductor. *Adv. Mater.* **2019**, *31*, 1808074.

(13) Doležal, P.; Kratochvílová, M.; Holý, V.; Čermak, P.; Sechovský, V.; Dušek, M.; et al. Crystal structures and phase transitions of the van der Waals ferromagnet VI_3. *Phys. Rev. Materials* **2019**, *3*, 121401.

(14) Tian, S.; Zhang, J.-F.; Li, C.; Ying, T.; Li, S.; Zhang, X.; et al. Ferromagnetic van der Waals Crystal VI_3. *J. Am. Chem. Soc.* **2019**, *141*, 5326−5333.

(15) Wang, Y.-M.; Tian, S.-J.; Li, C.-H.; Jin, F.; Ji, J.-T.; Lei, H.-C.; Zhang, Q.-M. Raman scattering study of two-dimensional magnetic van der Waals compound VI_3. *Chin. Phys. B* **2020**, *29*, 056301.

(16) Lee, I.; Utermohlen, F. G.; Weber, D.; Hwang, K.; Zhang, C.; van Tol, J.; Goldberger, J. E.; Trivedi, N.; Hammel, P. C. Fundamental Spin Interactions Underlying the Magnetic Anisotropy in the Kitaev Ferromagnet CrI_3. *Phys. Rev. Lett.* **2020**, *124*, 017201.

(17) Xu, C.; Feng, J.; Xiang, H.; Bellaiche, L. Interplay between Kitaev interaction and single ion anisotropy in ferromagnetic CrI_3 and $CrGeTe_3$ monolayers. *npj Comput. Mater.* **2018**, *4*, 57.

(18) Mermin, N. D.; Wagner, H. Absence of Ferromagnetism or Antiferromagnetism in One- or Two-Dimensional Isotropic Heisenberg Models. *Phys. Rev. Lett.* **1966**, *17*, 1133−1136.

(19) Pershoguba, S. S.; Banerjee, S.; Lashley, J. C.; Park, J.; Ågren, H.; Aeppli, G.; Balatsky, A. V. Dirac Magnons in Honeycomb Ferromagnets. *Phys. Rev. X* **2018**, *8*, 011010.

(20) Liu, J.; Shi, M.; Mo, P.; Lu, J. Electrical-field-induced magnetic Skyrmion ground state in a two-dimensional chromium tri-iodide ferromagnetic monolayer. *AIP Adv.* **2018**, *8*, 055316.

(21) Jiang, S.; Li, L.; Wang, Z.; Shan, J.; Mak, K. Spin tunnel field-effect transistors based on two-dimensional van der Waals heterostructures. *Nature Electronics* **2019**, *2*, 159.

(22) Klein, D. R.; MacNeill, D.; Song, Q.; Larson, D. T.; Fang, S.; Xu, M.; Ribeiro, R. A.; Canfield, P. C.; Kaxiras, E.; Comin, R.; Jarillo-Herrero, P. Enhancement of interlayer exchange in an ultrathin two-dimensional magnet. *Nat. Phys.* **2019**, *15*, 1255−1260.

(23) Wang, Z.; Gibertini, M.; Dumcenco, D.; Taniguchi, T.; Watanabe, K.; Giannini, E.; Morpurgo, A. Determining the phase diagram of atomically thin layered antiferromagnet $CrCl_3$. *Nat. Nanotechnol.* **2019**, *14*, 1116.

(24) Ubrig, N.; Wang, Z.; Teyssier, J.; Taniguchi, T.; Watanabe, K.; Giannini, E.; Morpurgo, A. F.; Gibertini, M. Low-temperature monoclinic layer stacking in atomically thin CrI_3 crystals. *2D Mater.* **2020**, *7*, 015007.

(25) Sun, Z.; et al. Giant nonreciprocal second-harmonic generation from antiferromagnetic bilayer CrI_3. *Nature* **2019**, *572*, 497−501.

(26) McGuire, M. A.; Clark, G.; KC, S.; Chance, W. M.; Jellison, G. E.; Cooper, V. R.; Xu, X.; Sales, B. C. Magnetic behavior and spin-lattice coupling in cleavable van der Waals layered $CrCl_3$ crystals. *Phys. Rev. Materials* **2017**, *1*, 014001.

(27) Kuhlow, B. Magnetic Ordering in $CrCl_3$ at the Phase Transition. *physica status solidi (a)* **1982**, *72*, 161−168.

(28) Hammersley, A. P.; Svensson, S. O.; Hanfland, M.; Fitch, A. N.; Hausermann, D. Two-dimensional detector software: From real detector to idealised image or two-theta scan. *High Pressure Res.* **1996**, *14*, 235−248.

(29) Yang, X.; Juhas, P.; Farrow, C. L.; Billinge, S. J. L. *xPDFsuite: an end-to-end software solution for high throughput pair distribution function transformation, visualization and analysis*; 2014.

(30) Toby, B. H.; Von Dreele, R. B. *GSAS-II*: the genesis of a modern open-source all purpose crystallography software package. *J. Appl. Crystallogr.* **2013**, *46*, 544−549.

(31) Farrow, C. L.; Juhas, P.; Liu, J. W.; Bryndin, D.; Božin, E. S.; Bloch, J.; Proffen, T.; Billinge, S. J. L. PDFfit2 and PDFgui: computer programs for studying nanostructure in crystals. *J. Phys.: Condens. Matter* **2007**, *19*, 335219.

(32) Giannozzi, P.; et al. QUANTUM ESPRESSO: a modular and open-source software project for quantum simulations of materials. *J. Phys.: Condens. Matter* **2009**, *21*, 395502.

(33) Perdew, J. P.; Burke, K.; Ernzerhof, M. Generalized Gradient Approximation Made Simple. *Phys. Rev. Lett.* **1996**, *77*, 3865−3868.

(34) Blöchl, P. E. Projector augmented-wave method. *Phys. Rev. B: Condens. Matter Mater. Phys.* **1994**, *50*, 17953−17979.

(35) Kresse, G.; Joubert, D. From ultrasoft pseudopotentials to the projector augmented-wave method. *Phys. Rev. B: Condens. Matter Mater. Phys.* **1999**, *59*, 1758−1775.

(36) Cococcioni, M.; de Gironcoli, S. Linear response approach to the calculation of the effective interaction parameters in the LDA + U method. *Phys. Rev. B: Condens. Matter Mater. Phys.* **2005**, *71*, 035105.

(37) Juza, D.; Giegling, D.; Schäfer, H. Über die Vanadinjodide VJ_2 und VJ_3. *Z. Anorg. Allg. Chem.* **1969**, *366*, 121−129.

(38) Berry, K. O.; Smardzewski, R. R.; McCarley, R. E. Vaporization reactions of vanadium iodides and evidence for gaseous vanadium-(IV) iodide. *Inorg. Chem.* **1969**, *8*, 1994−1997.

(39) Klemm, W.; Krose, E. Die Kristallstrukturen von $ScCl_3$, $TiCl_3$ und VCl_3. *Z. Anorg. Chem.* **1947**, *253*, 218−225.

(40) Liu, Y.; Petrovic, C. Three-dimensional magnetic critical behavior in CrI_3. *Phys. Rev. B: Condens. Matter Mater. Phys.* **2018**, *97*, 014420.

(41) He, J.; Ma, S.; Lyu, P.; Nachtigall, P. Unusual Dirac half-metallicity with intrinsic ferromagnetism in vanadium trihalide monolayers. *J. Mater. Chem. C* **2016**, *4*, 2518−2526.

(42) Wang, Y.-P.; Long, M.-Q. Electronic and magnetic properties of van der Waals ferromagnetic semiconductor VI_3. *Phys. Rev. B: Condens. Matter Mater. Phys.* **2020**, *101*, 024411.

(43) Li, Y.; Liu, Y.; Wang, C.; Wang, J.; Xu, Y.; Duan, W. Electrically tunable valleytronics in quantum anomalous Hall insulating transition metal trihalides. *Phys. Rev. B: Condens. Matter Mater. Phys.* **2018**, *98*, 201407.

(44) Lazarević, N.; Popović, Z. V.; Hu, R.; Petrovic, C. Evidence for electron-phonon interaction in $Fe_{1-x}M_xSb_2$ (M = Co and Cr $0 \leq x \leq 0.5$) single crystals. *Phys. Rev. B: Condens. Matter Mater. Phys.* **2010**, *81*, 144302.

(45) Baum, A.; Milosavljević, A.; Lazarević, N.; Radonjić, M. M.; Nikolić, B.; Mitschek, M.; Maranloo, Z. I.; Šćepanović, M.; Grujić-Brojčin, M.; Stojilović, N.; Opel, M.; Wang, A.; Petrovic, C.; Popović, Z. V.; Hackl, R. Phonon anomalies in FeS. *Phys. Rev. B: Condens. Matter Mater. Phys.* **2018**, *97*, 054306.

(46) Milosavljević, A.; Šolajic, A.; Pešić, J.; Liu, Y.; Petrovic, C.; Lazarević, N.; Popović, Z. V. Evidence of spin-phonon coupling in $CrSiTe_3$. *Phys. Rev. B: Condens. Matter Mater. Phys.* **2018**, *98*, 104306.

(47) McCarty, K. F.; Radousky, H. B.; Hinks, D. G.; Zheng, Y.; Mitchell, A. W.; Folkerts, T. J.; Shelton, R. N. Electron-phonon coupling in superconducting $Ba_{0.6}K_{0.4}BiO_3$: A Raman scattering study. *Phys. Rev. B: Condens. Matter Mater. Phys.* **1989**, *40*, 2662−2665.

(48) Proffen, T.; Page, K. L.; McLain, S. E.; Clausen, B.; Darling, T. W.; TenCate, J. A.; Lee, S.-Y.; Ustundag, E. Atomic pair distribution function analysis of materials containing crystalline and amorphous phases. *Z. Kristallogr.* **2005**, *220*, 1002−1008.

(49) Bordet, P. Application of the pair distribution function analysis for the study of cultural heritage materials. *C. R. Phys.* **2018**, *19*, 561−574.

(50) Bozin, E. S.; Yin, W. G.; Koch, R. J.; Abeykoon, M.; Hor, Y. S.; Zheng, H.; Lei, H. C.; Petrovic, C.; Mitchell, J. F.; Billinge, S. J. L. Local orbital degeneracy lifting as a precursor to an orbital-selective Peierls transition. *Nat. Commun.* **2019**, *10*, 3638.

(51) Egami, T.; Billinge, S. J. L. *Underneath the Bragg Peaks: Structural Analysis of Complex Materials*; 2003; p 16.

(52) Jin, F.; Lazarević, N.; Liu, C.; Ji, J.; Wang, Y.; He, S.; Lei, H.; Petrovic, C.; Yu, R.; Popović, Z. V.; Zhang, Q. Phonon anomalies and magnetic excitations in $BaFe_2Se_2O$. *Phys. Rev. B: Condens. Matter Mater. Phys.* **2019**, *99*, 144419.

(53) Moskovits, M.; Dilella, D. Surface-enhanced Raman spectroscopy of benzene and benzene-d6 adsorbed on silver. *J. Chem. Phys.* **1980**, *73*, 6068−6075.

(54) Dubroka, A.; Humlíček, J.; Abrashev, M. V.; Popović, Z. V.; Sapiña, F.; Cantarero, A. Raman and infrared studies of $La_{1-y}Sr_yMn_{1-x}M_xO_3$ (M = Cr,Co,Cu,Zn,Sc or Ga): Oxygen disorder and local vibrational modes. *Phys. Rev. B: Condens. Matter Mater. Phys.* **2006**, *73*, 224401.

(55) Souza Filho, A. G.; Faria, J. L. B.; Guedes, I.; Sasaki, J. M.; Freire, P. T. C.; Freire, V. N.; Mendes Filho, J.; Xavier, M. M.; Cabral, F. A. O.; de Araújo, J. H.; da Costa, J. A. P. Evidence of magnetic polaronic states in $La_{0.70}Sr_{0.30}Mn_{1-x}Fe_xO_3$manganites. *Phys. Rev. B: Condens. Matter Mater. Phys.* **2003**, *67*, 052405.

(56) Lekgoathi, M.; Kock, L. Effect of short and long range order on crystal structure interpretation: Raman and powder X-ray diffraction of $LiPF_6$. *Spectrochim. Acta, Part A* **2016**, *153*, 651−654.

(57) Wolverton, C.; Zunger, A.; Lu, Z.-W. Long-versus short-range order in Ni_3V and Pd_3V alloys. *Phys. Rev. B: Condens. Matter Mater. Phys.* **1994**, *49*, 16058.

(58) Webster, L.; Liang, L.; Yan, J.-A. Distinct spin-lattice and spin-phonon interactions in monolayer magnetic CrI_3. *Phys. Chem. Chem. Phys.* **2018**, *20*, 23546−23555.

Journal of Magnetism and Magnetic Materials 509 (2020) 166898

Contents lists available at ScienceDirect

Journal of Magnetism and Magnetic Materials

journal homepage: www.elsevier.com/locate/jmmm

Self-assembled line network in $BiFeO_3$ thin films

B. Colson[a], V. Fuentes[a], Z. Konstantinović[b,*], D. Colson[c], A. Forget[c], N. Lazarević[b], M. Šćepanović[b], Z.V. Popović[b], C. Frontera[a], Ll. Balcells[a], B. Martinez[a], A. Pomar[a]

[a] Institut de Ciencia de Materials de Barcelona, ICMAB-CSIC, Campus UAB, 08193 Bellaterra, Spain
[b] Center for Solid State Physics and New Materials, Institute of Physics Belgrade, Pregrevica 118, University of Belgrade, Serbia
[c] SPEC, CEA, CNRS UMR 3680, Université Paris-Saclay, 91191 Gif sur Yvette Cedex, France

ARTICLE INFO

Keywords:
Multiferroic thin films
Long-range ordered nanostructures
Growth kinetic
Mixed phase nanodomains

ABSTRACT

In this work we report on the controlled fabrication of a self-assembled line network in highly epitaxial $BiFeO_3$ thin films on top of $LaAlO_3$ in the kinetically limited grown region by RF sputtering. As previously shown in the case of manganite thin films, the remarkable degree of ordering is achieved using vicinal substrates with well-defined step-terrace morphology. Nanostructured $BiFeO_3$ thin films show mixed-phase morphology. Besides typical formation following (100) and (010) axes, some mixed phase nanodomains are detected also in-between the regular line network. These particular microstructures open a playground for future applications in multiferroic nanomaterials.

1. Introduction

Bismuth ferrite $BiFeO_3$ (BFO) is a very active research domain due to environment friendly room-temperature multiferroic character with wide range of potential applications, from the low-power spintronic to optical devices [1,2]. The very large electrical polarization [3,4], coupling between the polarization and magnetic easy plane [5–7] and its strong sensitivity on the epitaxial strain are crucial parameters for applications and for understanding their fundamental properties in general [8,9]. The control over the ferroelectric polarization through the structural strain and the miscut angle of underlying substrates rapidly gain interest [10], additionally enhanced with the discovery of mixed phase nanodomains [9,11–13]. In addition, it has been recently shown that the kinetic growth conditions allow synthesizing high quality films with selective ferroelectric domains [14].

Self-organization of long-range ordered nanostructures of transition metal oxide thin films is of major relevance for both, the study of enhanced or novel physical properties at the nanoscale (from enhanced magneto-resistive properties to unexpected interfacial effects) and for developing a new generation of devices [15,16]. This bottom-up nanostructural approach presents an alternative to the more conventional top-down lithography-based methods with numerous advantages ranging from rapid preparation of low-cost and large surface oxide nanotemplates to the formation of nanoobjects with size and densities beyond actual possibilities [17]. Finally, ferroelectric BFO thin films crystallize in the very similar rhombohedral structure as previously studied LSMO thin films [15,17] and open a huge playground for the formation of nanostructured networks at the surface.

In this paper, we report on the formation of regular nanostructures in ferroelectric BFO thin films grown on top of $LaAlO_3$ (LAO) substrates by RF sputtering. The nanostructuration of BFO thin films is directly induced by structural and morphological features of the underlying substrate (lattice parameter inducing strain conditions on the one side and step-terrace morphology and chemical affinity on the other side). In addition to regular network, stripe-like features are detected and analyzed by X-ray, Raman and AFM spectroscopy.

2. Experimental

BFO thin films were grown by RF magnetron sputtering on top of $LaAlO_3$ (0 0 1) substrates under an oxygen partial pressure of 0.19 Pa using commercial stoichiometric target (Kurt J. Lesker Company). Growth conditions (growth rate of $F \sim 0.03$ ML/s and high growth temperature) were adjusted to promote self-organized surface nanostructures in the kinetic growth regime, i.e. far away from thermodynamic relaxation mechanisms, that have been previously studied in detail in GeSi semiconductors [18]. By a fine tuning of the growth kinetic pathway, the surface diffusion was reduced (but not completely suppressed), taking advantage of the unusual misfit strain relaxation in presence of stepped substrate [17]. Substrates were previously washed in milliQ water and thermally treated at 1000 °C to assure the presence of terrace-step morphology with unit cell height. The thickness value, *t*,

---

[*] Corresponding author.
E-mail address: zorica.konstantinovic@ipb.ac.rs (Z. Konstantinović).

https://doi.org/10.1016/j.jmmm.2020.166898
Received 16 October 2019; Received in revised form 6 April 2020; Accepted 14 April 2020

of the different BFO/LAO films presented in this study is in the range of 40 nm $< t <$ 50 nm.

The surface morphology of the films was studied using Atomic Force Microscopy (AFM) and Scanning Electron Microscopy (SEM). AFM images were obtained in a MFP3D Asylum AFM while SEM images were obtained with a QUANTA FEI 200 FEG-ESEM. The crystal structure was characterized by X-ray diffraction (XRD) and reflectivity techniques (XRR) using a Siemens D5000 diffractometers with Kα-Cu radiation.

Magnetic characterization was performed at room temperature (in-plane configuration $H \perp (100)$ and out-of-plane configuration $H \perp (100)$) with a superconducting quantum interference device magnetometer (Quantum Design). In order to estimate the magnetization of the film, the diamagnetic background of substrates was subtracted (estimated from negative slope of M(H) at high magnetic field, $10000 < H < 50000$ Oe).

Raman scattering measurements were performed using a Jobin Yvon T64000 Raman system in μ-Raman configuration. A Coherent VerdiG solid state laser with 532 nm line was used as an excitation source. Laser beam focusing was accomplished by a microscope objective with × 50 magnification.

3. Results and discussion

$BiFeO_3$ presents, at room temperature, a rhombohedral structure in bulk form (lattice constant $a_{\text{bulk}} = 3.964$ Å) [3,5]. In thin films, structural and functional properties of this multiferroic compound can be drastically modified due to presence of the structural strain induced by the selected substrate [19]. Particularly, the epitaxial growth of BFO on top of LAO substrate induces huge compressive in-plane strain, which allows stabilizing the tetragonal phase, correlated with theoretically predicted giant ferroelectric polarization [20]. In this study, the films were grown under large compressive strain of $\varepsilon = (a_{\text{LAO}}\text{-}a_{\text{BFO}})/a_{\text{BFO}} = -4.62\%$, giving rise to a significantly larger perpendicular cell parameter compared to bulk counterpart (see below).

Fig. 1 shows the formation of the long range ordered line network on top of the BFO surface during crystal growth. Fast Fourier Transform (FFT) (Fig. 1(b)) of topographic AFM image (Fig. 1(a)) indicate long-range order of grooves along one specific direction (see two high intensity dots in circles) with a separation around $1/k_\perp \sim 150$ nm. Two additional dots (see arrows) are also visible (doubled distance in k space) in possible correlation with the formation of the polarization nano-domains (see below). The regular lines, i.e. grooves have typical depth of around 6 ± 2 nm (Fig. 1(c)).

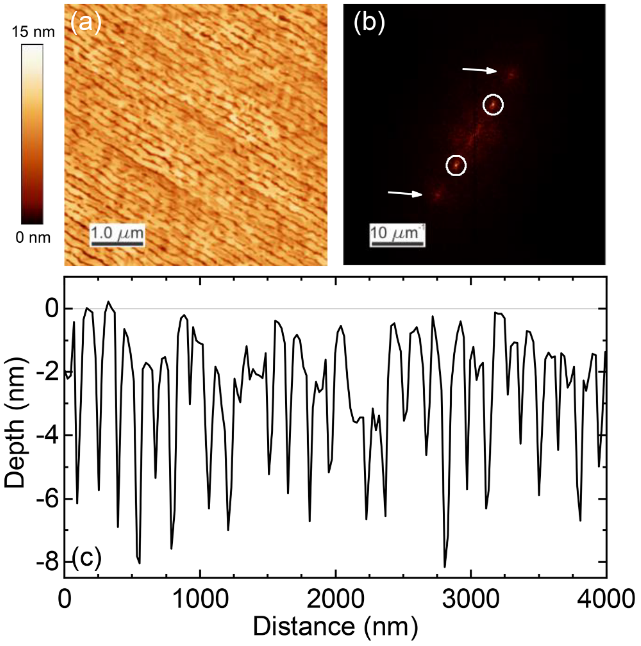

Fig. 1. (a) Topographic AFM image (4x4 μm^2) of $BiFeO_3$ film (thickness, t = 45 nm) grown on top of LAO and (b) corresponding Fast Fourier Transform (c) Typical line profile of regular grooves.

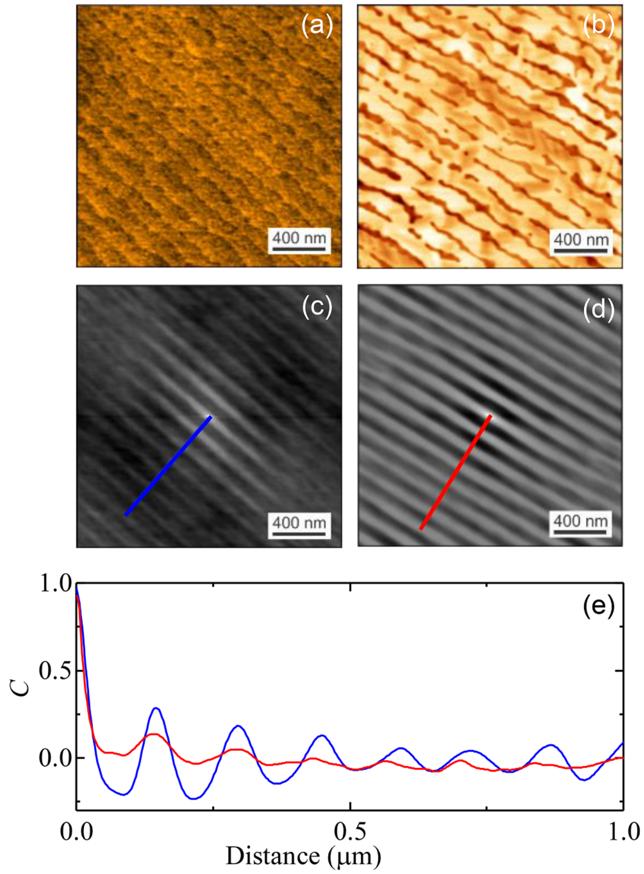

Fig. 2. (a) Topographic AFM images (2 × 2 μm^2) of (a) $LaAlO_3$ substrates (α ~ 0.155°) and (b) $BiFeO_3$ film (thickness, t = 45 nm) grown on top of it. The corresponding height -height correlation functions of the topographic surfaces are shown in (c) and (d) respectively. (e) Corresponding profile lines of LAO (blue) and of BFO (red).

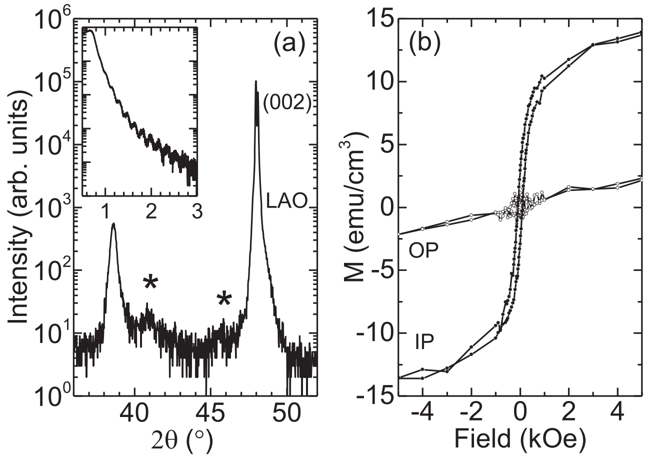

Fig. 3. (a) θ-2θ XRD scans of the (0 0 2) reflections for BFO/LAO thin film. In the inset, corresponding XRR data with thickness values of 45 nm. (b) Magnetization versus field corrected with the diamagnetic slope for the in-plane (IP) and out-of-plane field (OP) at room temperature.

In order to further clarify the structural arrangement of the regular lines the topography of BFO thin films (Fig. 2(b)) is compared directly

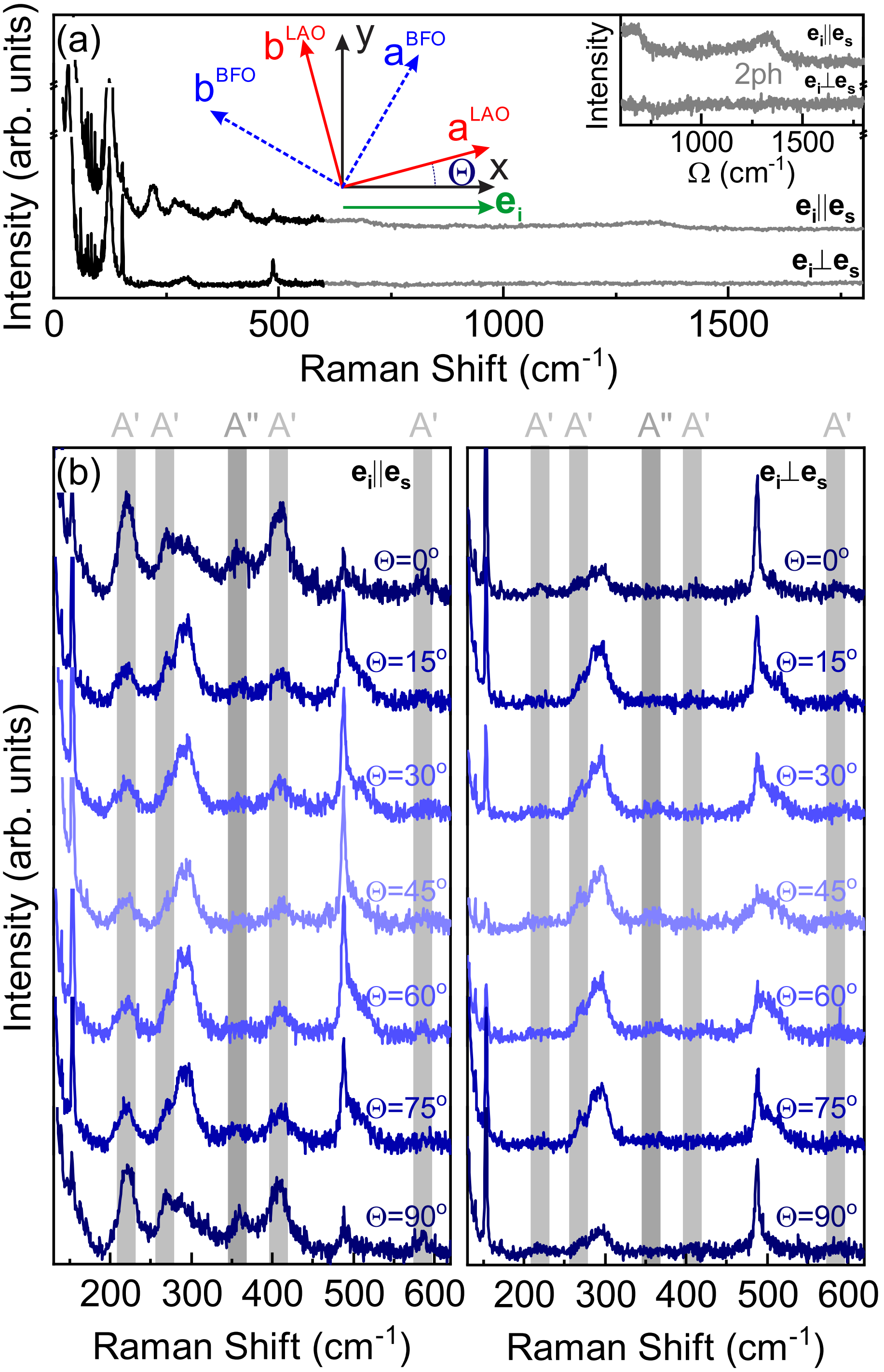

Fig. 4. (a) Raman spectra measured in parallel and cross polarization configurations for $\Theta = 0$. xy is the laboratory system at room temperature. Black and grey lines represent spectra obtained with binning 1 and 2 respectively. Inset: High energy region of the BFO/LAO Raman spectra. (b) BFO/LAO Raman spectra measured in parallel and cross polarization configurations for various sample orientations.

with the topography of the underlying LAO substrate (Fig. 2(a)). The corresponding height-height autocorrelation functions are shown in Fig. 2(c) for LAO and (d) for BFO topography. The regular line pattern is visible at the overall surface in both cases, also as non-vanishing oscillations in the corresponding profile perpendicular to lines. A clear correlation between the two patterns is evident from the corresponding profile lines in Fig. 2(e), demonstrating a typical separation between ordered nanostructured lines of $l \sim 140$ nm, in agreement with the underlying terrace-step morphology of the LAO substrate with a miscut angle of $\alpha \sim 0.155^\circ$.

The structural properties have been investigated by θ-2θ X-ray diffraction (XRD), Fig. 3(a) shows scans around (0 0 2) LAO reflection. The strongest peak in Fig. 3(a) corresponds to the LAO substrate ($2\theta = 48.05^\circ$ with lattice parameter of $c = 3.787$ Å). Besides this, a dominant peak ($2\theta = 38.62^\circ$) and two small intensity peaks are also detected ($2\theta = 40.87^\circ$ and $2\theta = 45.74^\circ$, see stars in Fig. 3(a)). Dominant peak corresponds to an out-of-plane parameter of $c_{perp} = 4.66(2)$ Å, much larger than the pseudocubic cell parameter of bulk BFO and it is associated with hyper strained tetragonal phase.

The position of the two small peaks suggests the presence of two

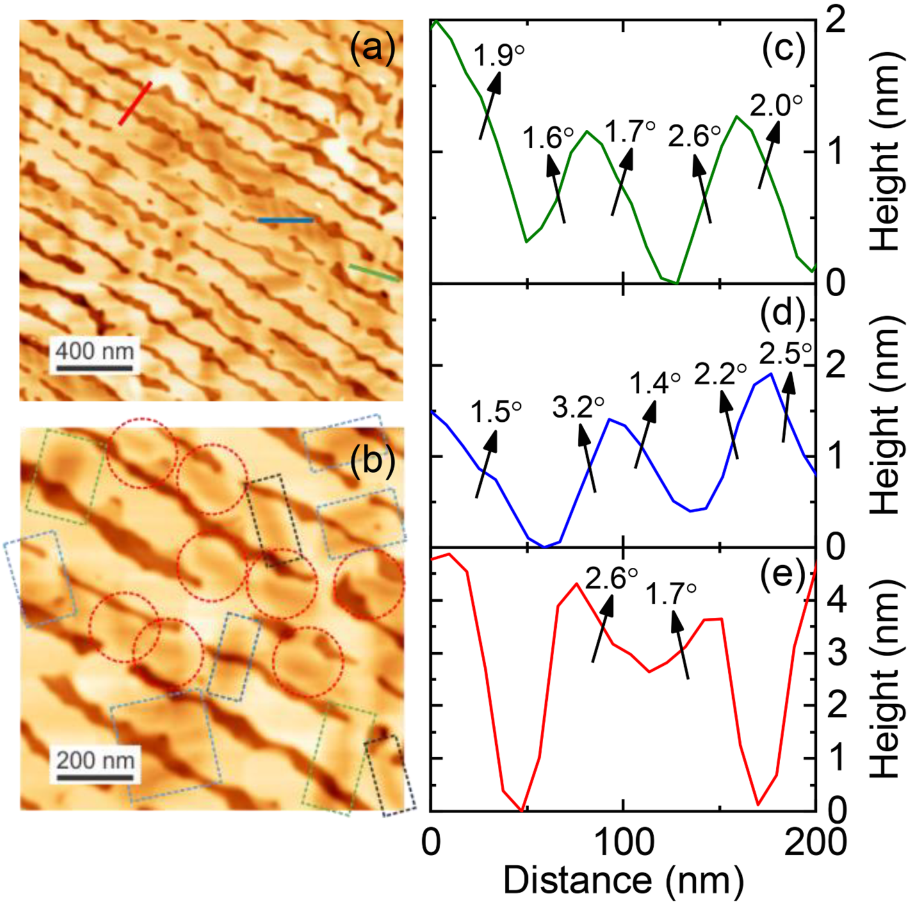

Fig. 5. The formation of nanodomains in the presence of regular line network. (a) AFM topography (2 × 2 μm^2) with profile lines. (b) Small area AFM topography (1 × 1 μm^2) with different orientation of detected nanodomains (expected orientation in blue and green rectangles and new nanodomains induced by line network in red circles). (c)-(e) Profile lines of nanodomains from (a).

additional phases with out-of-plane parameters in the order of $c_{\text{perp1}} = 4.41(6)$ Å and $c_{\text{perp2}} = 3.96(7)$ Å, which are ascribed to the intermediate monoclinic structure and the rhombohedral phase respectively. While the intermediate monoclinic phase is associated to the formation of nanodomains [9,12] the rhombohedral phase is the residue of the bulk counterpart phase [3]. Thickness value of the BFO/LAO film (t ~ 45 nm) is determined from XRR curve (inset of Fig. 3(a)). No magnetic impurity phases are detected, in agreement with the weak ferromagnetic moment measured at room-temperature (Fig. 3(b)).

Raman spectra of BFO film with ordered connected pits morphology are shown in Fig. 4. Due to the fact that the film thickness is much smaller than the penetration depth of the beam, significant contribution from the LAO substrate is clearly observable in the BFO/LAO Raman spectra (Fig. 4(a)). For the purpose of probing the crystal structure of the BFO film, Raman spectra were collected for different sample orientation (as presented in Fig. 4) in two polarization configurations.

Detailed analysis of the Raman intensity angular dependence [21] taking into account the twinning effects, indicates that Raman features observed at about 227, 273, 417 and 587 cm^{-1} correspond to the A' symmetry modes, whereas peak at 368 cm^{-1} correspond to A'' symmetry mode of the monoclinic Cc crystal structure. These findings are in accordance with the density-functional calculations predicting that BFO structure under strain values higher than 4% become tetragonal-like with larger c/a ratio [22]. According to the first principles calculations, this structure has Cc symmetry with the base centered unit cell containing four formula) units, for which the factor group analysis predicts the existence of $13A' + 14A''$ Raman-active phonon modes [22]. Note that, a large number of modes ascribed to the Cc structure have been experimentally observed in the low-temperature Raman spectra of BiFeO$_3$ films commensurately grown on LaAlO$_3$ substrates and subjected to ~4.4% compressive strain, wherein it was indicated that 13 most intense modes (including those at 237, 282, 415, and 605 cm^{-1}) could be referred to the A' symmetry [23]. However, Himcinschi et al. [23] suggested that the modes at 225, 263 and 367 cm^{-1} in the Raman spectrum of highly strained BiFeO$_3$ epitaxial films deposited on LaAlO$_3$ may correspond to A“ symmetry mode of the Cc monoclinic structure [23]. Therefore, there is no doubt that BFO/LAO film whose Raman spectra are shown in Fig. 4 has Cc structure, but small differences in the positions of the identified modes in comparison with those referred in the literature [23] indicate that the structure of the film investigated here is monoclinically distorted in a specific way.

More details of the formation of the mixed-phase structures in the middle of the regular network line can be obtained from AFM topography shown in Fig. 5. The thin strip-line patterns could be visualized in Fig. 5(a), known in literature as asymmetric “saw-tooth” surface structure and identified as intimated mixture between highly distorted monoclinic phase (monoclinic version of highly tetragonal phase with $c/a = 1.23$), detected by Raman scattering in Fig. 4 and an intermediate monoclinic phase ($c/a = 1.17$), detected as small peak by XRD in Fig. 3(a). The profile line of these strip-like patterns can be found in Fig. 5(c)-(e). Typical strip-like patterns, disoriented around ~1° from the in-plane (100) and (010) axes, could be seen in green and blue squares in Fig. 5(b). Corresponding AFM profile line indicate that they are tilted away from the surface normal for about 2.5–3° (intermediate monoclinic phase) and 1.5–2° (highly distorted monoclinic phase), in agreement with previous reports [9,12]. The typical height difference between different phases (around 3 nm) [9,24] is not always observed, as strongly perturbed with formation of regular grooved (for more details see Fig. S1 in supplementary material). In addition, the stripe-like formation could be observed also in our case between regular line-network and disoriented around ~150° from the in-plane (100) axes (red circles in Fig. 5(b)) with very similar profile line (Fig. 5(e)).

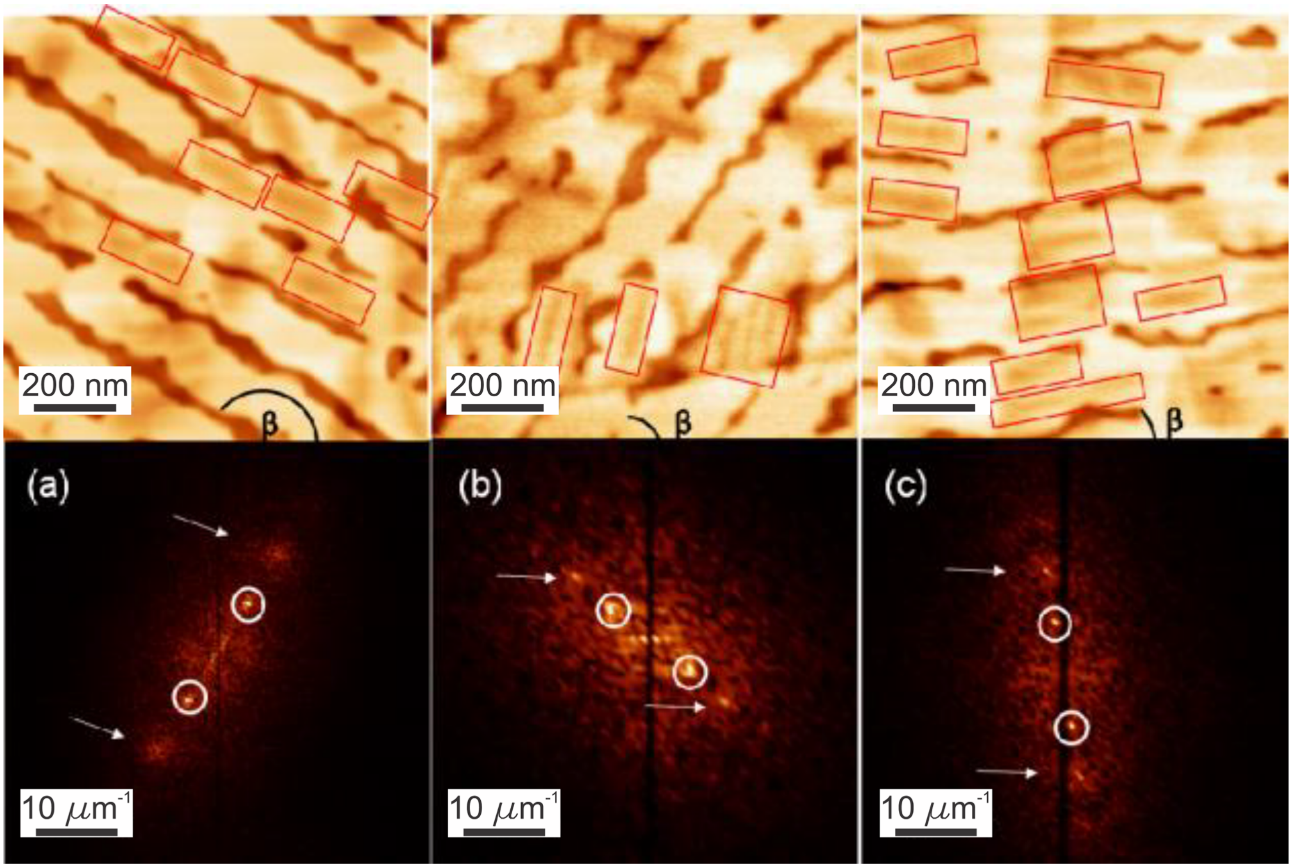

Fig. 6. AFM of BFO films grown on the top of LAO with similar miscut angle ($0.12^\circ < \alpha < 0.16^\circ$) with different orientation of nanostructured lines respected to [1 0 0] direction (a) β ~ 150°, (b) 52° and (c) 6°. The corresponding FFT images are given below.

Finally, the formation of the mixed-phase structures in the middle of the regular network is followed for different network orientations respected to [100] direction. In Fig. 6, AFM topography with corresponding Fast Fourier Transform is shown for BFO thin films grown on LAO with similar terrace width but with different orientation respected to substrate edges ($6^\circ < \beta < 150^\circ$). FFT of topographic images indicate the long-range order coming from of formation of groove network (two high intensity dots in circles in all cases). In addition, as mentioned before, two additional points (see arrows) are visible at doubled distance in k space, suggesting the presence of additional structures in-between the regular line network. In all cases, the presence of "saw-tooth" surface structures in between the grooves could be identified in the corresponding AFM topography (see red rectangles and Fig. S1 in supplementary). Noticeably, in the case of network line slightly disoriented from the in-plane (100) axes (β ~ 6°), the nanodomains form more easily in-between the grooves (see Fig. 6(c)) as it is closer to their spontaneous configuration [9,12,24].

4. Conclusion

In summary, a regular nanostructured network is grown on the surface of BFO films, in close correlation with the step-terraces morphology of the underlying LAO substrate (miscut angle $0.12^\circ < \alpha < 0.16^\circ$). Raman scattering detected the dominant contribution from the monoclinic version of highly strained tetragonal phase. XRD spectra also indicate the presence of additional polymorphs, rhombohedral and intermediate monoclinic phases. The stripe-like patterns, formed by intimate mixture between two monoclinic polymorphs, are visualized by AFM topography. Beside typical formation following (100) and (010) axes, some stripe-like patterns are also detected in-between the regular line network. Finally, the observed self-nanostructuration of the BFO surface opens a playground for tailoring structural polymorphs with strong potential interest for future applications in multiferroic nanomaterials.

5. Author statement

B. Colson: thin film preparation and characterization, Z. Konstantinović: design and leading the research, manuscript preparation, D. Colson, A. Forget: ferroelectric properties, N. Lazarević, M. Šćepanović, Z. V. Popović: Raman measurements, V. Fuentes, C. Frontera: X-ray diffraction characterization, D. Colson, Ll. Balcells, B. Martinez, A. Pomar: Reviewing and editing manuscript.

Declaration of Competing Interest

The authors declare that they have no known competing financial interests or personal relationships that could have appeared to influence the work reported in this paper.

Acknowledgements

This work has received funding from the European Union's Horizon 2020 research and innovation under the Marie Sklodowska-Curie grant agreement No. 645658 (DAFNEOX Project). A.P., V. F. and Z.K. thank Senzor-INFIZ (Serbia) for the cooperation provided during their respective secondments. E. P.-M. acknowledge financial support from the Spanish Ministry of Economy and Competitiveness through the "Severo Ochoa" Programme for Centres of Excellence in R&D (SEV-2015- 0496), and project MAT2015-71664 and SPINCURIOX (RTI2018-099960-B-I00). N. L., M. S., Z. K. and Z.V.P. acknowledge the support of the Serbian Ministry of Education, Science and Technological Development (Projects No III45018).

Appendix A. Supplementary data

Supplementary data to this article can be found online at https://doi.org/10.1016/j.jmmm.2020.166898.

References

[1] G. Catalan, J.F. Scott, Physics and applications of bismuth ferrite, Adv. Mater. 21 (2009) 2463.

[2] D. Sando, A. Barthelemy, M. Bibes, BiFeO3 epitaxial thin films and devices: past, present and future, J. Phys.: Condens. Matter 26 (2014) 473201.

[3] D. Lebeugle, D. Colson, A. Forget, M. Viret, P. Bonville, J.F. Marucco, S. Fusil, Room temperature coexistence of large electric polarization and magnetic order in $BiFeO_3$ single crystals, Phys. Rev. B 76 (2007) 024116.

[4] D. Lebeugle, D. Colson, A. Forget, M. Viret, Very large spontaneous electric polarization in $BiFeO_3$ single crystals at room temperature and its evolution under cycling fields, Appl. Phys. Lett. 91 (2007) 022907.

[5] D. Lebeugle, D. Colson, A. Forget, M. Viret, A.M. Bataille, A. Gukasov, Electric Field-Induced Spin Flop in $BiFeO_3$ single crystals at room temperature, Phys. Rev. Lett. 100 (2008) 227602.

[6] T. Zhao, A. Scholl, F. Zavaliche, K. Lee, M. Barry, A. Doran, M.P. Cruz, Y.H. Chu, C. Ederer, N.A. Spaldin, R.R. Das, D.M. Kim, S.H. Baek, C.B. Eom, R. Ramesh, Electrical control of antiferromagnetic domains in multiferroic $BiFeO_3$ films at room temperature, Nature Mater. 5 (2006) 823.

[7] S. Lee, W. Ratcliff, S.W. Cheong, V. Kiryukhin, Electric field control of the magnetic state in $BiFeO_3$ single crystals, Appl. Phys. Lett. 92 (2006) 192906.

[8] C. Ederer, N.A. Spaldin, Effect of epitaxial strain on the spontaneous polarization of thin film ferroelectrics, Phys. Rev. Lett. 95 (2005) 257601.

[9] A.R. Damodaran, J.C. Agar, S. Pandya, Z. Chen, L. Dedon, R. Xu, B. Apgar, S. Saremi, L.W. Martin, New modalities of strain-control of ferroelectric thin films, J. Phys.: Condens. Matter 28 (2016) 263001.

[10] Y.-H. Chu, M.P. Cruz, C.-H. Yang, L.W. Martin, P.-L. Yang, J.-X. Zhang, K. Lee, P. Yu, L.-Q. Chen, R. Ramesh, Domain control in multiferroic $BiFeO_3$ through substrate vicinality, Adv. Mater. 19 (2007) 2662.

[11] J.X. Zhang, Q. He, M. Trassin, W. Luo, D. Yi, M.D. Rossell, P. Yu, L. You, C.H. Wang, C.Y. Kuo, J.T. Heron, Z. Hu, R.J. Zeches, H.J. Lin, A. Tanaka, C.T. Chen, L.H. Tjeng, Y.-H. Chu, R. Ramesh, Microscopic origin of the giant ferroelectric polarization in tetragonal-like $BiFeO_3$, Phys. Rev. Lett. 107 (2011) 147602.

[12] L. You, Z. Chen, X. Zou, H. Ding, W. Chen, L. Chen, G. Yuan, J. Wang, Characterization and manipulation of mixed phase nanodomains in highly strained $BiFeO_3$ thin films, ACS Nano 6 (2012) 5388.

[13] A. Kumar, S. Denev, R.J. Zeches, E. Vlahos, N.J. Podraza, A. Melville, D.G. Schlom, R. Ramesh, V. Gopalan, Probing mixed tetragonal/rhombohedral-like monoclinic phases in strained, bismuth ferrite films by optical second harmonic generation, Appl. Phys. Lett. 97 (2010) 112903;
J. Seidel, M. Trassin, Y. Zhang, P. Maksymovych, T. Uhlig, P. Milde, D. Köhler, A.P. Baddorf, S.V. Kalinin, L.M. Eng, X. Pan, R. Ramesh, Electronic properties of isosymmetric phase boundaries in highly strained Ca-doped $BiFeO_3$, Adv. Mater. 26 (2014) 4376.

[14] A. Solmaz, M. Huijben, G. Koster, R. Egoavil, N. Gauquelin, G. Van Tendeloo, J. Verbeeck, B. Noheda, G. Rijnders, Domain selectivity in $BiFeO_3$, thin films by modified substrate termination, Adv. Funct. Mater. 26 (2016) 2882.

[15] Z. Konstantinovic, J. Santiso, Ll. Balcells, B. Martınez, Strain-driven self-assembled network of antidots in complex oxide thin films, Small 5 (2009) 265.

[16] Y. Zhao, Z. Yin, X. Zhang, Z. Fu, J. Wu, Formation and local conduction of nanopits in $BiFeO_3$ epitaxial films, J. Mater. Chem. C 3 (2015) 11250.

[17] Z. Konstantinovic, F. Sandiumenge, J. Santiso, Ll. Balcells, B. Martınez, Self-assembled pit arrays as templates for the integration of Au nanocrystals in oxide surfaces, Nanoscalle 5 (2013) 1001.

[18] J.L. Grey, R. Hull, C.-H. Lam, P. Sutter, J. Means, J.A. Floro, Beyond the hetero-epitaxial quantum dot: self-assembling complex nanostructures controlled by strain and growth kinetics, Phys. Rev. B 72 (2005) 155323.

[19] H. Bea, B. Dupe, S. Fusil, R. Mattana, E. Jacquet, B. Warot-Fonrose, F. Wilhelm, A. Rogalev, S. Petit, V. Cros, A. Anane, F. Petroff, K. Bouzehouane, G. Geneste, B. Dkhil, S. Lisenkov, I. Ponomareva, L. Bellaiche, M. Bibes, A. Barthelemy, Evidence for room-temperature multiferroicity in a compound with a giant axial ratio, Phys. Rev. Lett. 102 (2009) 217603.

[20] B. Colson, «Elaboration et caractérisation de films minces de $BiFeO_3$ nanostructurés», DUT Mesures Physiques, IUT d'Orsay, Université Paris-Sud, 2016.

[21] D.R. Palai, H. Schmid, J.F. Scott, R.S. Katiyar, Raman spectroscopy of single-domain multiferroic $BiFeO_3$, Phys. Rev. B – Condens. Matter Mater. Phys. 81 (2010) 064110.

[22] J. Hatt, N.A. Spaldin, C. Ederer, Strain-induced isosymmetric phase transition in $BiFeO_3$, Phys. Rev. B – Condens. Matter Mater. Phys. 81 (2010) 054109.

[23] C. Himcinschi, A. Bhatnagar, A. Talkenberger, M. Barchuk, D.R.T. Zahn, D. Rafaja, J. Kortus, M. Alexe, Optical properties of epitaxial $BiFeO_3$ thin films grown on $LaAlO_3$, Appl. Phys. Lett. 106 (2015) 012908.

[24] R.J. Zeches, M.D. Rossell, J.X. Zhang, A.J. Hatt, Q. He, C.-H. Yang, A. Kumar, C.H. Wang, A. Melville, C. Adamo, G. Sheng, Y.-H. Chu, J.F. Ihlefeld, R. Erni, C. Ederer, V. Gopalan, L.Q. Chen, D.G. Schlom, N.A. Spaldin, L.W. Martin, R. Ramesh, A strain-driven morphotropic phase boundary in $BiFeO_3$, Science 326 (2009) 977.

Journal of Physics: Condensed Matter

Fluctuations and pairing in Fe-based superconductors: light scattering experiments

To cite this article: N Lazarevi and R Hackl 2020 *J. Phys.: Condens. Matter* **32** 413001

OPEN ACCESS
IOP Publishing
Journal of Physics: Condensed Matter
J. Phys.: Condens. Matter **32** (2020) 413001 (29pp)
https://doi.org/10.1088/1361-648X/ab8849

Topical Review

Fluctuations and pairing in Fe-based superconductors: light scattering experiments

N Lazarević[1] **and R Hackl**[2]

[1] Center for Solid State Physics and New Materials, Institute of Physics Belgrade, University of Belgrade, Pregrevica 118, 11080 Belgrade, Serbia
[2] Walther Meissner Institut, Bayerische Akademie der Wissenschaften, 85748 Garching, Germany

E-mail: nenadl@ipb.ac.rs and hackl@wmi.badw.de

Received 14 October 2019, revised 24 February 2020
Accepted for publication 9 April 2020
Published 15 July 2020

Abstract

Inelastic scattering of visible light (Raman effect) offers a window into properties of correlated metals such as spin, electron and lattice dynamics as well as their mutual interactions. In this review we focus on electronic and spin excitations in Fe-based pnictides and chalcogenides, in particular but not exclusively superconductors. After a general introduction to the basic theory including the selection rules for the various scattering processes we provide an overview over the major experimental results. In the superconducting state below the transition temperature T_c the pair-breaking effect can be observed, and the gap energies may be derived and associated with the gaps on the electron and hole bands. In spite of the similarities of the overall band structures the results are strongly dependent on the family and may even change qualitatively within one family. In some of the compounds strong collective modes appear below T_c. In $Ba_{1-x}K_xFe_2As_2$, which has the most isotropic gap of all Fe-based superconductors, there are indications that these modes are exciton-like states appearing in the presence of a hierarchy of pairing tendencies. The strong in-gap modes observed in Co-doped NaFeAs are interpreted in terms of quadrupolar orbital excitations which become undamped in the superconducting state. The doping dependence of the scattering intensity in $Ba(Fe_{1-x}Co_x)_2As_2$ is associated with a nematic resonance above a quantum critical point and interpreted in terms of a critical enhancement at the maximal T_c. In the normal state the response from particle–hole excitations reflects the resistivity. In addition, there are strongly temperature-dependent contributions from presumably critical fluctuations in the energy range of k_BT which can be compared to the elastic properties. Currently it is not settled whether the fluctuations observed by light scattering are related to spin or charge. Another controversy relates to putative two-magnon excitations, typically in the energy range below 0.5 eV. Whereas this response presumably originates from charge excitations in most of the Fe-based compounds theory and experiment suggest that the excitations in the 60 meV range in FeSe stem from localized spins in a nearly frustrated system.

Keywords: superconductivity, Fe-based compounds, light scattering

(Some figures may appear in colour only in the online journal)

---

1. Introduction

Superconductivity in iron-based compounds (FeBCs) came as a big surprise when first reported by Kamihara and coworkers [1, 2]. The FeBCs consist of quadratically coordinated Fe planes sandwiched between layers of pnictogen (As, P) or chalcogen (S, Se, Te) atoms as shown in figure 1(a). The rest of the structure is rather variable as can be seen from the sum formulae in table 1. For this variability and the relative change in the band structures the FeBCs are a laboratory for studying the interrelation of magnetism, fluctuations and superconductivity or strong versus weak-coupling effects as summarized in excellent reviews including [3–8].

FeBCs typically have a magnetically ordered phase at zero nominal doping. Upon elemental substitution or application of pressure, magnetism can be suppressed and superconductivity (SC) may appear (figure 1(b)). In contrast to the cuprates, all phases are metallic. The order at zero doping is a stripe-like antiferromagnetic spin-density wave (SDW) and widely believed to originate from the nesting properties of the hole- and electron-like Fermi surfaces encircling the $(0, 0)$ (Γ) and the $(\pm\pi, 0)/(0, \pm\pi)$ (X/Y) points in the idealized 1 Fe Brillouin zone. Similarly, the topology of the Fermi surface is considered important for superconductivity [9]. Although the Fermi surfaces are always centered at Γ and X/Y there are substantial variations in shape and character across the families and as a function of doping [10]. However, this variation is not necessarily and exclusively at the origin of the differences in the superconducting ground states. Already on the level of local-density approximation (LDA) [11] a variety of nearly degenerate superconducting ground states is expected [6, 12].

In addition to the SDW and SC phase transitions, nematic order, with the rotational symmetry broken but the translational symmetry preserved, and wide temperature ranges with fluctuations are observed [14]. For studying this plethora of instabilities, a wide variety of experimental methods has been applied. Inelastic light scattering is a useful technique, since relevant information on practically all phases and their fluctuations can be obtained.

It will be the purpose of this review to present typical results, provide a snapshot of the current status of the field and outline possible future developments. First, we briefly describe the experiment and the theoretical background and then summarize the most relevant results obtained from light scattering with the focus placed on electronic and spin excitations.

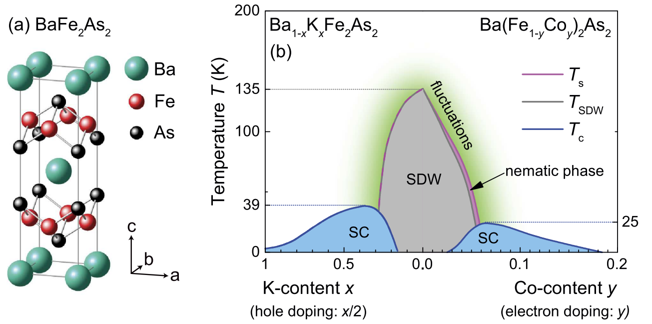

Figure 1. Crystal structure and phase diagram. (a) Crystal structure of BaFe$_2$As$_2$. Thin gray lines indicate the edges of the unit cell (2 Fe per layer), I4/mmm. Gray connecting lines between Fe and As illustrate covalent Fe-As bonds. (b) Phase diagram. The spin density wave (SDW) and the superconducting (SC) ranges are indicated in gray and blue, respectively. The dashed magenta-grey line indicates a simultaneous structural transition at T_S and SDW transition at T_{SDW}. The nematic phase is shaded magenta. The green shaded area indicates the existence of fluctuations next to the SDW transition. Note that the scales in x (hole doping) and y (electron doping) differ. Reproduced with permission from [13].

2. Raman experiment

Shown in figure 2 is a schematic view of the experimental setup of a typical macro Raman experiment *in vacuo* and in a diamond anvil cell (inset) on opaque samples. In the macro setup the incident light with polarization $\hat{\mathbf{e}}_I$ impinges on the surface at an angle of incidence $\vartheta_I \sim 70^\circ$ in order to prevent the directly reflected light from entering the optics and the spectrometer. For this 'pseudo-Brewster' angle the reflection is minimal for $\hat{\mathbf{e}}_I$ parallel to the plane of incidence. The scattered light is collected along the surface normal. Photons having a selected polarization state $\hat{\mathbf{e}}_S$ enter the spectrometer. A charge-coupled device (CCD) detector registers the number of transmitted photons per unit time $\dot{N}_{I,S}(\Omega)$ ('Raman spectrum') for a given energy shift $\Omega = \omega_I - \omega_S$ and polarization combination $(\hat{\mathbf{e}}_I, \hat{\mathbf{e}}_S)$, where $\omega_{I,S}$ are the energies of the photons. The differential light scattering cross-section is proportional to the Raman spectrum,

$$\frac{\mathrm{d}^2\sigma_{I,S}}{\mathrm{d}\Omega_S \mathrm{d}\omega_S} = \hbar r_0^2 \frac{\omega_S}{\omega_I} \frac{1}{\pi} \{1 + n(\Omega, T)\} R_{I,S} \chi''_{I,S}(\mathbf{q}, \Omega, T). \tag{1}$$

Here Ω_S is the solid angle into which the photons are scattered, and $R_{I,S}$ absorbs matrix element effects and experimental factors, $\chi_{I,S}(\mathbf{q}, \Omega, T) = \chi'_{I,S} + i\chi''_{I,S}$ is the typically non-resonant response function, $n(\Omega, T) = [\exp(\hbar\Omega/k_\mathrm{B}T) - 1]^{-1}$ is the Bose–Einstein occupation number and $r_0 = \mathrm{e}^2/(4\pi\varepsilon_0 mc^2)$ the Thomson electron radius, thus equation (1) describes the cross section per electron. From linear combinations of the spectra, pure symmetries μ can be derived (for details see section 4.9).

3. Materials

Most of the existing FeBCs were studied by Raman scattering. In the beginning the phonons were in the main focus [16–22]. With the advent of high-quality single crystals of

Table 1. Materials studied by Raman scattering. The table includes only materials for which electronic properties (spin, charge, fluctuations) were studied. In the second column typical acronyms are listed which will be used occasionally in the text. The main subject of the respective experiments are listed in the second to last column.

Material	Acronym	Substitution	Subject	Reference
$BaFe_2As_2$	BFA/Ba122	No	SDW	[27, 32]
$SrFe_2As_2$	Sr122	No	SDW, fluctuations	[29, 33]
$EuFe_2As_2$	Eu122	No	SDW, fluctuations	[33, 34]
$CaFe_2As_2$	Ca122	No	SDW	[34]
LaFeAsO	1111	No	SDW	[35]
$Ba(Fe_{1-x}Co_x)_2As_2$	BFCA	$x = 0.061, 0.085$	SC gap	[25]
$Ba(Fe_{1-x}Co_x)_2As_2$	BFCA	$x = 0.061$	Gap, vertex	[36]
$Ba(Fe_{1-x}Co_x)_2As_2$	BFCA	$x = 0.08$	Gap	[37]
$Ba(Fe_{1-x}Co_x)_2As_2$	BFCA	$0 \leqslant x \leqslant 0.045$	SDW	[26]
$Ba(Fe_{1-x}Co_x)_2As_2$	BFCA	$0 \leqslant x \leqslant 0.20$	Fluctuations	[30]
$Ba(Fe_{1-x}Co_x)_2As_2$	BFCA	$0.055 \leqslant x \leqslant 0.10$	SC gap	[38]
$Ba(Fe_{1-x}Co_x)_2As_2$	BFCA	$0 \leqslant x \leqslant 0.10$	SC gap-nematicity	[39]
$Ba(Fe_{1-x}Co_x)_2As_2$	BFCA	$x = 0, 0.025, 0.051$	Fluctuations	[40]
$Ba(Fe_{1-x}Co_x)_2As_2$	BFCA	$0.045 \leqslant x \leqslant 0.085$	Fluctuations and SC gap	[41]
$Ca(Fe_{1-x}Co_x)_2As_2$		$x = 0.03$	Crystal field	[42]
$Sr(Fe_{1-x}Co_x)_2As_2$		$x = 0, 0.04, 0.20$	SDW	[43, 44]
$Ba(Fe_{1-x}Au_x)_2As_2$		$x = 0, 0.012, 0.014, 0.031$	Fluctuations	[45]
$Ba_{1-x}K_xFe_2As_2$	BKFA	$x = 0.4$	SC gap and pairing	[46]
$Ba_{1-x}K_xFe_2As_2$	BKFA	$x = 0.4$	SC gap and pairing	[47]
$Ba_{1-x}K_xFe_2As_2$	BKFA	$0.22 \leqslant x \leqslant 0.70$	Fluctuations and SC gap	[41]
$Ba_{1-x}K_xFe_2As_2$	BKFA	$x = 0.25, 0.4, 0.6$	Fluctuations and SC gap	[48]
$BaFe_2(As_{1-x}P_x)_2$	BFAP	$x = 0.5$	Fluctuations and SC gap	[48]
$NaFe_{1-x}Co_xAs$	Na111	$0 \leqslant x \leqslant 0.08$	Fluctuations and SC gap	[49]
$CaKFe_4As_4$	CKFA/1144	No	SC gap and pairing	[50, 51]
$Fe_{1+\delta}Te_{1-x}Se_x$		$x = 0, 0.4$	SC gap, phonon, magnon	[52]
FeSe	11	No	Fluctuations	[15, 53, 54]
FeSe	11	No	2-Magnon	[55]
$FeSe_{0.82}$	11	No	Crystal field	[56]
$FeSe_{1-x}S_x$		$x = 0, 0.04, 0.08, 0.15, 0.20$	Fluctuations	[57]
$K_{0.75}Fe_{1.75}Se_2$		No	Gap	[58]
$Rb_{0.8}Fe_{1.6}Se_2$		No	Gap	[46]
$A_{0.8}Fe_{1.6}Se_2$		$A =$ K, Rb, Cs, Tl	2-Magnon	[59]

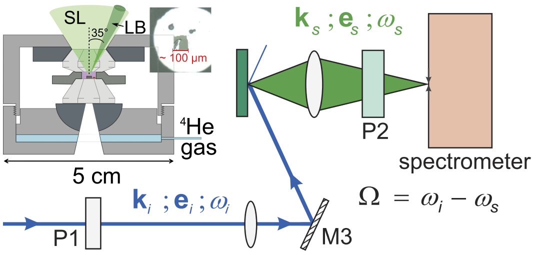

Figure 2. Schematic representation of a Raman experiment. The polarized monochromatic photons hit the sample at a large angle of incidence. The scattered photons are collected along the surface normal and pass the analyzer before entering the spectrometer. Inset: side view of a Raman pressure cell. The laser beam (LB) enters from the right, the scattered light (SL) is collected along the normal of the sample surface. Reprinted figure with permission from [15], Copyright (2018) by the American Physical Society.

the 122 family [23], being a result of FeAs self-flux growth [24], the study of electronic properties by light scattering became promising, and the superconducting gap was studied successfully in $Ba(Fe_{1-x}Co_x)_2As_2$ for two doping levels [25]. Soon thereafter the redistribution of spectral weight in the SDW state of $BaFe_2As_2$ was reported [26, 27]. Finally, the fluctuations above the magneto-structural transformation, inferred from transport [28], were observed [29, 30]. Although there are reports on spectra in the range 1000 cm^{-1} to 4000 cm^{-1} (the energy range of two-magnon excitations) [31], their interpretation remains controversial.

The materials for which data on the spin, charge and orbital response exist are compiled in table 1.

4. Theoretical background

The analysis of the results in the FeBCs requires insight into the theoretical background, including both standard knowledge and modern developments. We give a brief historical summary and sketch the underlying theory with the emphasis placed on metallic systems.

4.1. Historical remarks

Raman scattering studies of excitations of localized spins started in the 1960s on insulating antiferromagnets [60] and experienced a renaissance with the advent of the cuprates [61]. The theoretical framework was set by the seminal work of Elliot, Fleury and Loudon [62] which still represents the basis of contemporary analyses [63] even in the case of metallic systems such as the FeBCs [31, 64, 65].

Light scattering from conduction electrons was first discussed in the context of superconductors [66]. It took almost 20 years to observe the effect experimentally in the layered compound 2H-NbSe$_2$ [67]. In NbSe$_2$ superconductivity competes with a charge density wave (CDW) for area on the Fermi surface (FS), and the spectral features observed below T_c cannot directly be traced back to the superconducting energy gap in contrast to those for selected symmetries in the A15 compounds V$_3$Si and Nb$_3$Sn [68, 69] or in the cuprates [63, 70, 71]. Hence, only in special cases the Raman spectra of superconductors can be described satisfactorily in terms of lowest order weak coupling theory as developed between 1961 and 1984 [66, 72, 73]. In all other cases, including the FeBCs, lowest order is insufficient, although it still captures the plain vanilla such as the strong momentum dependence of the gap if the symmetries of the response are properly taken into account [74].

In normal metals, contributions from particle–hole excitations were observed and discussed for doped semiconductors [75, 76], but in-depth studies started only in the cuprates [77–81]. Similarly as in the superconducting state, the major contribution from Raman scattering, in addition to what was known from optical spectroscopy, was the observation of a polarization dependent relaxation of the carriers which could be mapped on the electronic momentum [74, 82].

Important new developments include the observation and analysis of critical fluctuations in both cuprates [83, 84] and FeBCs [29, 30, 49, 85–87]. In the superconducting state an anisotropic pairing potential [73, 88–92], amplitude ('Higgs') fluctuations of the superconducting order parameter [93, 94], number-phase fluctuations in multiband systems (Leggett modes [95]) [96–100] or a nematic resonance [39] need to be included. Whereas the interpretation of the results in NbSe$_2$ in terms of coupled gap excitations and amplitude fluctuations in a coupled SC-CDW system seems to converge [101, 102] the discussion of the E_g symmetry contributions in the A15 materials [68, 69, 89, 102, 103], the B_{1g} response in the cuprates [104–109] or the in-gap modes in the FeBCs [39, 41, 46, 47, 49] remains controversial. In addition to the weak-coupling description of the superconducting state at $T = 0$ a lot more work is needed to arrive at a coherent picture for the normal and superconducting states in the presence of collisions, fluctuations and strong coupling. Only a few special cases have been studied theoretically so far [77, 83, 85–87, 110–116]. More details can be found in references [63, 82] and, for recent developments, in [41, 64, 65, 85–87, 91, 92, 99, 100, 115–118].

4.2. Light scattering

Photons in the visible or x-ray range do not directly scatter off low-energy excitations. Rather, high-energy electron–hole pairs having energies of the incoming photons ($1.6 \leqslant \hbar\omega_I \leqslant 3.5$ eV for the visible) are created and couple to excitations in the range $\hbar\Omega = 1, \ldots, 200$ meV such as phonons, fluctuations, particle–hole, gap or spin excitations [119]. After scattering, the electron–hole pairs recombine and emit photons with energies $\hbar\omega_S = \hbar\omega_I \mp \hbar\Omega$. The mechanism works whether or not the intermediate electronic states are eigenstates. If they are eigenstates the cross-section is resonantly enhanced, but most of the results were successfully analysed in terms of non-resonant scattering. In systems with a high correlation energy $U = \mathcal{O}(\hbar\omega_I)$ there are no well-defined eigenstates, and the resonances are in fact found to be mild in most of the cases.

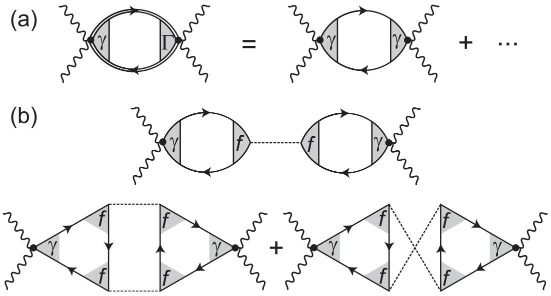

Figure 3. Feynman diagrams for (non-resonant) light scattering. (a) Raman response of particle–hole excitations in the presence of interactions and (b) scattering processes involving one and two bosonic excitations. Wavy lines represent incident and scattered photons whereas solid lines are electronic propagators. The bosonic excitation or fluctuation propagators are represented by dashed lines. The bare and renormalized Raman vertices γ and, respectively, Γ describe the interaction of light and electrons and f describes the interaction of electrons and other excitations, e.g. bosons.

Given these considerations, equation (1) is most naturally derived from scattering matrix elements in third order perturbation theory such as in the case of phonons or spin excitations [62, 119]. For electrons the Raman susceptibility or response function $\chi(\Omega, T)$ is almost always derived in the non-resonant limit using either diagrammatic techniques [63, 66, 73, 77] or the kinetic equation [82, 120]. Since $\chi(\Omega, T)$ is not a pure density or current correlation function there is no general sum rule such as the f-sum rule in optical conductivity [121]. Usually[3] for this reason, the Raman cross section may be a superposition of independent contributions, for example particle–hole excitations (electronic continuum) and magnons or phonons. Occasionally, some of the excitations may be interrelated, for instance phonons and particle–hole excitations leading to the Fano effect (not discussed in this review) or gap formation and excitations in density-wave or superconducting states and the continuum playing an important role below.

The Raman response of all types of excitations is causal implying that $\chi^*_{I,S}(-\Omega) = \chi_{I,S}(\Omega)$ where * denotes the complex conjugate. Thus $\chi''_{I,S}(\Omega)$ is anti-symmetric with respect to the origin, and its expansion contains only odd powers of Ω.

In figure 3, Feynman diagrams for Raman scattering are displayed. γ and Γ are the bare and the renormalized

---

[3] Special cases [107, 122] are beyond the scope of this review.

vertices, respectively, for the interaction between light and electrons [63]. They depend on the light polarization and on momenta and determine the selection rules. In panel (a) particle–hole excitations are described. The bare vertex γ is an approximation where properties of the intermediate states are neglected assuming that all photon energies are smaller than any band gap, $\hbar\omega_{I,S} < |\varepsilon_c - \varepsilon_\nu|$, where the subscripts c and ν refer to electrons in the conduction bands and those in other bands, respectively. Γ is a renormalized vertex in the spirit of the Bethe–Salpeter equation [123]. In panel (b) scattering from bosons via electrons is described. f is the vertex for the interaction between electrons and other excitations.

4.3. Charged systems

In general, visible light cannot transfer substantial momentum to a crystal since the lattice constant a is much smaller than the wavelengths $\lambda_{I,S}$ of the incoming and outgoing photons, and all unit cells are excited in phase. This is usually called the $q = 0$ selection rule of Raman scattering in crystals. In the case of (resonant) inelastic x-ray scattering [(R)IXS] with $\lambda = \mathcal{O}(a)$ most of the Brillouin zone can be accessed [124]. Metals have a small penetration depth for light $a < \delta_0 < \lambda_{I,S}$. As a consequence, the momentum transfer in a metal is bigger than in an insulator, $|\mathbf{q}| = q \sim \delta_0^{-1}$, where $100\ \text{Å} < \delta_0 < 1000\ \text{Å}$ for typical metals, as pointed out first by Abrikosov and Fal'kovskii [66]. Yet, the available momentum is still much smaller than π/a, and for exciting a non-interacting conduction electron from an occupied (i) to an unoccupied (f) state the maximal energy is limited by $\hbar\Omega_{\max} = \epsilon_{\mathbf{k}}^{(f)} - \epsilon_{\mathbf{k}}^{(i)} \approx \hbar v_{\mathrm{F}}\delta_0^{-1}$ where $\epsilon_{\mathbf{k}}$ is the electronic dispersion. In the FeBCs the relevant in-plane Fermi velocity is of order $10^6\ \mathrm{cm\ s^{-1}}$, and the penetration depth is close to 1000 Å yielding $\hbar\Omega_{\max} \lesssim 1\ \mathrm{meV} \equiv 8\ \mathrm{cm^{-1}}$.

Due to charge conservation and screening all isotropic charge excitations are pushed up to the plasma frequency Ω_{pl} [125], and there is no scattering in the range of $k_{\mathrm{B}}T$ in non-interacting systems with a strictly quadratic electron dispersion. What looks like a disadvantage at first glance is the origin of the selection rules for electronic Raman scattering [72]. Loosely speaking, one cannot move charges from one unit cell to another one but the charges can only be redistributed in phase inside all unit cells (quadrupolar-type of excitations). This is the origin of the form factors, and the light does not scatter from the charge density but from a weighted charge density [72, 73, 89],

$$\tilde{\rho}_{\mathbf{q}} = \frac{1}{N}\sum_{n}\sum_{\mathbf{k},\sigma}\gamma_n(\mathbf{k},\mathbf{q})c^{\dagger}_{n,\mathbf{k}+\mathbf{q},\sigma}c_{n,\mathbf{k},\sigma}. \qquad (2)$$

n is the band index, and $\gamma_n(\mathbf{k},\mathbf{q})$ is a form factor which is related to the Raman vertex $\gamma_{\alpha,\beta}(\mathbf{k},\mathbf{q})$ through the polarization directions $\hat{\mathbf{e}}_{I,S}$,

$$\gamma_n(\mathbf{k},\mathbf{q}) = \sum_{\alpha,\beta} e_I^{\alpha}\gamma_{n,\alpha,\beta}(\mathbf{k},\mathbf{q})e_S^{\beta}. \qquad (3)$$

The bare response $\tilde{\chi}(\mathbf{q},\Omega)$ is the commutator of $\tilde{\rho}_{\mathbf{q}}$,

$$\tilde{\chi}(\mathbf{q},\Omega) = \langle\langle\left[\tilde{\rho}_{\mathbf{q}}(t),\tilde{\rho}_{-\mathbf{q}}(0)\right]\rangle\rangle_{\Omega} = \tilde{\chi}' + i\tilde{\chi}'', \qquad (4)$$

where $\langle\langle\ldots\rangle\rangle_{\Omega}$ denotes the thermodynamic average and the Fourier transformation, and $\tilde{\chi}'$ and $\tilde{\chi}''$ are the real and imaginary part of $\tilde{\chi}$, respectively. Equation (4) includes a sum over the Brillouin zone and the bands through equation (2), and can be recast as [82],

$$\tilde{\chi}_{a,b}(\mathbf{q},\Omega) = \frac{1}{N}\sum_{n}\sum_{\mathbf{k}}a_{\mathbf{k}}b_{\mathbf{k}}\Theta_n(\mathbf{k},\Omega). \qquad (5)$$

$a = a_{\mathbf{k}}$ and $b = b_{\mathbf{k}}$ are generalized vertices that stand for either an isotropic (1) or Raman ($\gamma(\mathbf{k},\mathbf{q})$) or renormalized Raman ($\Gamma(\mathbf{k},\mathbf{q})$) vertex. $\Theta_n(\mathbf{k},\Omega)$ is the response kernel, examples of which will be presented below.

The bare response is not gauge invariant, and charge conservation and screening lead to the final—exact and gauge-invariant—result for the response [89, 120, 126],

$$\chi_{\gamma,\gamma} = \tilde{\chi}_{\gamma,\gamma} - \frac{\tilde{\chi}_{1,\gamma}\tilde{\chi}_{\gamma,1}}{\tilde{\chi}_{1,1}}\left(1 - \frac{1}{\varepsilon}\right). \qquad (6)$$

The projected structure of the first two terms is a result of charge conservation. The polarization-dependent vertex is written down explicitly as a subscript in equation (6), and ε in the third term is the dielectric function which originates from screening alone. Since a constant vertex can be pulled in front of the sum of equation (2) the first two terms of equation (6) cancel for constant γ (corresponding to lowest order A_{1g} symmetry and/or strictly parabolic dispersion), and only the last term survives but is suppressed as $q^2/\Omega_{\mathrm{pl}}^2$ in a charged system. In the fully symmetric channel having A_{1g} symmetry in the D_{4h} space group, applicable for most of the FeBCs, the response is at least partially screened.

4.4. Weakly interacting systems

The scattering from free electrons cuts off at $\hbar\Omega_{\max}$ [127]. In a realistic normal metal with a single conduction band either impurities or interactions can maintain the $q = 0$ selection rule and facilitate the occurrence of broad continua extending to energies well above $\hbar\Omega_{\max}$ [77, 128]. Obviously this is the case in all materials of interest with interactions including the FeBCs, the cuprates, the A15 compounds, $\mathrm{MgB_2}$ and many others. However, only in the cuprates the argumentation is straightforward since there is one conduction band in the single-layer compounds with one $\mathrm{CuO_2}$ plane per unit cell, for instance $\mathrm{La_{2-x}Sr_xCuO_4}$. Somewhat surprisingly, the response is nearly identical in the double-layer compounds (two neighboring $\mathrm{CuO_2}$ planes) such as $\mathrm{YBa_2Cu_3O_{6+y}}$ to that in materials with just one $\mathrm{CuO_2}$ plane. It was in fact shown that the contributions from individual bands in multi-band systems just add up to a good approximation not only in the cuprates [129] but also in the FeBC [117] allowing one, as a starting point, to treat the response in a band basis and neglect inter-band transition.

If we disregard spurious contributions to the cross section such as luminescence (being a good approximation at low energies; see, however, reference [57]) only (dynamic) interactions can produce the broad continua observed [81, 130]. Impurities are present but irrelevant in high-quality single crystals as can be seen directly below T_{c} since impurities reduce the effect of pair breaking in the Raman spectra. As shown by

Klein and Dierker [73] the response of a clean isotropic superconductor has a square root singularity at the gap edge 2Δ in the limit $q=0$. In the presence of impurities (and similarly for finite q [73]) the singularity disappears and the response at 2Δ becomes finite and scales as $\Delta\tau_0$, where τ_0 is the impurity scattering time [110–112]. In all realistic cases the difference between the normal and superconducting spectra cannot be observed any further for $\hbar\tau_0^{-1}\to\Delta$. Therefore, the continuum in superconductors essentially comes from dynamical interactions between the conduction electrons and other excitations which are gapped out below T_c for $\hbar\Omega\lesssim 2\Delta$. In nearly all superconductors which have been studied by light scattering this conclusion holds. The only exception is the A_{1g} response in A15 compounds where the normal state intensity vanishes [103, 131].

Although the normal state continuum generally signals the presence of strong interactions, it is impossible to describe the superconducting response in terms of strong-coupling theory so long as the microscopic origin of the relevant interactions is unknown. Only in the case of spin fluctuations both the normal and the superconducting spectra have been modelled microscopically on equal footing [113]. In a few cases phenomenological descriptions on the basis of Eliashberg theory were applied [112, 132–134].

In the majority of cases, the weak-coupling result [73] is used since it is sufficient to capture the generic properties of the superconducting state. The response kernel is given by the Tsuneto–Maki (TM) function [135],

$$\Theta''_{\mathbf{k},\mathrm{TM}}(\Omega,T)=\frac{\pi}{2}\frac{|2\Delta_\mathbf{k}|^2}{\Omega\sqrt{\Omega^2-|2\Delta_\mathbf{k}|^2}};\quad \Omega>|2\Delta_\mathbf{k}|. \tag{7}$$

It is the result of a superposition of particle excitations across the gap from an occupied into an unoccupied state and pair breaking. Both contributions have a square-root singularity at $|2\Delta_\mathbf{k}|$ and, because of the coherence factors, add constructively in the case of light scattering and destructively in the case of the (real part of the) optical (IR) conductivity $\sigma'(\Omega)$ [136].

In the case of a charge or spin density wave the functional form of the response close to the density-wave gap $|2\Delta_\mathrm{DW}|$ is also described by equation (7) [137] if the material is insulating below the transition. In a metal the best way of describing the response is the superposition of a normal metallic response (see next section) and a condensate in the spirit of a two-fluid model [82]. In all metallic cases there is an incomplete redistribution of spectral weight from low to high energies starting abruptly at the transition temperature. The line shape is comparable to that of a superconductor having an anisotropic gap with $\mathrm{BaFe_2As_2}$ being a prototypical example for SDW formation in the pnictides [38].

4.5. Collision limited regime

The simplest type of response in the normal state in systems with vanishingly small $\hbar v_\mathrm{F}q$ results from the presence of (heavy) impurities. Here the electrons change only their momentum but not their energy (Drude model). The gauge-invariant kernel was derived by Zawadowski and Cardona [77],

$$\Theta''_{\mathbf{k},\mathrm{D}}(\Omega)=\frac{\pi}{2}\frac{\hbar\Omega\Gamma^*_\mathbf{k}}{(\hbar\Omega)^2+(\Gamma^*_\mathbf{k})^2}, \tag{8}$$

where $\Gamma^*_\mathbf{k}=\hbar(\tau^*_\mathbf{k})^{-1}$. $\tau^*_\mathbf{k}$ is not identical to the electronic relaxation time but is renormalized by a (presumably small) channel-dependent vertex correction, similarly as in ordinary transport where the vertex corrections ensure (among other things) that forward scattering does not contribute to the resistivity. $\Gamma^*_\mathbf{k}$ is temperature and energy independent.

If the electrons scatter from excitations in the energy range of $k_\mathrm{B}T$ such as phonons, spin fluctuations or among themselves they transfer both momentum and energy. As a consequence they become dressed quasi-particles, and the relaxation rate depends now on energy, momentum and temperature. Due to these interaction effects, the electron velocity gets reduced and the mass increases by the same factor $1+\lambda_\mathbf{k}(\Omega,T)$, and the extended Drude response reads [81]

$$\Theta''_{\mathbf{k},\mathrm{eD}}(\Omega,T)=\frac{\pi}{2}\frac{\hbar\Omega\Gamma^*_\mathbf{k}(\Omega,T)}{(\hbar\Omega[1+\lambda_\mathbf{k}(\Omega,T)])^2+[\Gamma^*_\mathbf{k}(\Omega,T)]^2}. \tag{9}$$

The energy and temperature dependent projected parameters $\Gamma^*_\mathbf{k}(\Omega,T)$ and $1+\lambda_\mathbf{k}(\Omega,T)$ can be derived if $\Theta''_{\mathbf{k},\mathrm{eD}}(\Omega,T)$ is known for a sufficiently wide energy interval [81]. The zero-energy extrapolation value of $\Gamma_0(T)=\Gamma^*_\mathbf{k}(\Omega\to 0,T)$ can be compared with ordinary or optical transport, for instance. Shastry and Shraiman [138] noticed that the relation between the Raman response and the real part of the optical conductivity, $\Theta''_{\mathbf{k},\mathrm{(e)D}}(\Omega,T)\propto\Omega\sigma'(\Omega,T)$, is a good approximation in many cases, in particular if the momentum dependence is weak[4]. In this sense $\Theta''_{\mathbf{k},\mathrm{(e)D}}(\Omega,T)/\Omega$ is a momentum dependent 'Raman conductivity'.

An expression equivalent to equation (9) can be derived for the superconducting or a density-wave state in terms of Eliashberg theory. It is considerably more complicated, and the normal state continuum and the gap excitations are closely interrelated [113]. Since this analysis was not used in the case of the FeBCs so far we do not reproduce it here. The interested reader can consult references [132, 134]. Qualitatively, the continuum is gapped out below $|2\Delta|$ for zero temperature and increases continuously for $0<T\leqslant T_\mathrm{c(DW)}$ due to the presence of thermal excitations. In the zero-energy limit $\chi''\propto\Omega$, and the initial slope reflects the anomalous (Nambu) Raman relaxation rate $\Gamma^\mathrm{SC(DW)}_{0,\mu}$ inside the gap being similarly difficult to analyze as the relaxation rates in NMR, microwave or ultrasound absorption experiments, in particular in unconventional systems.

All results summarized here are essentially lowest-order response theory. However, the experiments in $\mathrm{Ba_{1-x}K_xFe_2As_2}$ and $\mathrm{Na(Fe_{1-x}Co_x)As_2}$ show [41, 46, 47, 49] that higher order corrections may be necessary for the proper interpretation

---

[4] The reason is that σ' is always an average over the entire Fermi surface whereas $\Theta''_{\mathbf{k},\mathrm{(e)D}}$ is not (see below).

and for extracting relevant information on the pairing in the superconducting state [47, 90, 91, 115, 118].

4.6. Beyond lowest order

Equation (7) is the lowest-order approximation of the response and is not gauge invariant as already pointed out by Klein and Dierker [73]. The controversy as to whether or not the resulting vertex corrections are relevant for the interpretation in the A15 materials is still not settled [73, 89, 94, 103, 139]. A similar narrow in-gap mode as in the E_g response of the A15s was observed recently in BKFA where it is well separated from the pair-breaking peak [46]. A mode in the $d_{x^2-y^2}$ channel (1 Fe unit cell) with this property was predicted by Scalapino and Devereaux [91] for a two-band model applicable to the FeBCs. Chubukov and coworkers [90] predicted an A_{1g} mode originating from the same type of mechanism for a different hierarchy of pairing instabilities.

The existence of in-gap modes in a superconductor was first noticed by Bardasis and Schrieffer (BS) [140]. They studied the effect of final state interaction in the presence of an anisotropic pairing potential $V_{\mathbf{k},\mathbf{k}'}$ and found undamped modes below the gap edge, $\hbar\Omega_{L,M} < 2\Delta$, which are characterized by quantum numbers L and M corresponding to the expansion of $V_{\mathbf{k},\mathbf{k}'}$ into spherical harmonics. These collective excitations, usually called BS modes, are similar to excitons in semiconductors with binding energy $E_{b,L,M} = 2\Delta - \hbar\Omega_{L,M}$. For simplicity they may be referred to as $E_{\mathrm{BS},\alpha}$ labelled by α in consecutive order. The result was adopted for light scattering in superconductors [89] and is formally similar to light scattering from roton pairs in superfluid ^{4}He [88, 141]. The predictions include symmetry selection rules and the dependence of $E_{\mathrm{BS},\alpha}$ and the strength of the pole $Z_{\mathrm{BS},\alpha}$ on the relative coupling strength of the sub-leading channels $\alpha > 1$ with respect to the ground state $\alpha = 1$, λ_α/λ_1. As pointed out in references [90, 91] the analysis of these excitons would help in clarifying the so far elusive pairing mechanism in the FeBCs.

The functional form of the response additional to lowest order (equation (7)) reads [91],

$$\Delta\tilde{\chi}''(\Omega) = \frac{8}{\Omega^2}\,\Im\left\{\frac{\langle\gamma(\mathbf{k})g(\mathbf{k})\Delta(\mathbf{k})\bar{P}(\Omega,\mathbf{k})\rangle^2}{\left(\lambda_d^{-1} - \lambda_s^{-1}\right) - \langle g^2\bar{P}(\Omega,\mathbf{k})\rangle}\right\}, \tag{10}$$

where $\gamma(\mathbf{k})$ is the usual Raman vertex, $g(\mathbf{k})$ is the d-wave-like form factor on the electron bands for making the interaction between them separable, and $\bar{P}(\Omega,\mathbf{k})$ is the complex superconducting response kernel the imaginary part of which is given in equation (7). Equation (10) was used in reference [47] for estimating the value of the sub-leading $d_{x^2-y^2}$ coupling parameter λ_d from the electronic Raman spectra of BKFA for a given s-wave coupling strength λ_s. Identical expressions with redefined coupling parameters were derived for explaining the nematic resonance [39]. Similarly as in the case of excitons, there may be more than one BS mode in the presence of several sub-leading coupling channels. This possibility was considered recently in a theoretical study [92].

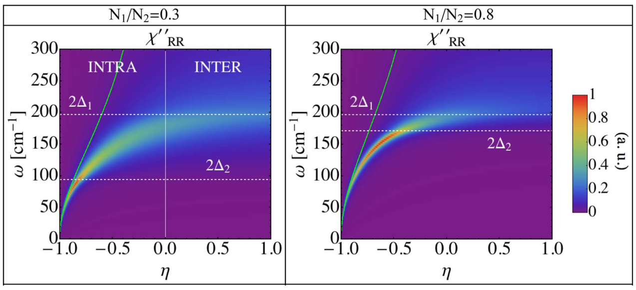

Figure 4. Response from Leggett modes in a two-gap system. N_i is the density of states on band i. η encodes the ratio of intra- to inter-band coupling with $\eta = -1$ and $\eta = 1$ representing pure intra- and inter-band coupling, respectively. The mode's energy saturates at the maximal gap. The damping starts above the smaller gap. Reprinted figure with permission from [99], Copyright (2016) by the American Physical Society.

In a system with more than one band there is an additional contribution to the response from number-phase oscillations between the bands in momentum space comparable to the Josephson effect in real space [95]. It must be included to make the response gauge invariant, as pointed out recently by Cea and Benfatto [99]. Usually, for instance in the cases studied theoretically by Suhl and coworkers [142], which is possibly realized in MgB$_2$, the main contribution to superconductivity comes from coupling in the individual bands having strength $\lambda_{i,i}$. The inter-band coupling $\lambda_{i,j}$ is weaker but leads to an increase of T_{c} to values above the maximum of the individual bands. It is widely believed that the main contribution to pairing in the FeBC has its origin in inter-band [9] or inter-orbital [143] coupling and that the intra-band pairing is weak. The effect of weak inter-band coupling was investigated already earlier in the context of MgB$_2$ [96, 97] whereas strong inter-band coupling was addressed only recently in the context of the FeBCs [98–100]. The symmetry properties of the Leggett modes depend sensitively on the orbital content [98, 100].

For weak inter-band coupling, the mode related to the number-phase fluctuations is below the gap energy and increases essentially linearly with $\lambda_{i,j}$. For $\lambda_{i,i} \ll \lambda_{i,j}$ the Legget mode is in the continuum above 2Δ and is therefore overdamped. Figure 4 shows the transition between the two coupling regimes and demonstrates the damping effect. In addition, it could be shown that the energy saturates at the maximal gap energy.

4.7. Spin excitations

For spin excitations the Elliot–Fleury–Loudon Hamiltonian [62] is the simplest nonresonant interaction operator which describes scattering in a Heisenberg model with nearest-neighbour exchange coupling J,

$$\hat{H}_{\mathrm{EFL}} = J\sum_{<i,\hat{\delta}>}(\hat{\delta}\cdot\hat{\mathbf{e}}_I)(\hat{\delta}\cdot\hat{\mathbf{e}}_S)(\mathbf{S}_{\mathbf{r}(i)}\cdot\mathbf{S}_{\mathbf{r}(i)+\hat{\delta}a}). \tag{11}$$

$\mathbf{S}_{\mathbf{r}(i)}$ is a spin at site $\mathbf{r}(i)$, a is the distance between the sites and $\hat{\delta}$ is a unit vector pointing towards one of the nearest neighbors. $\langle i, \hat{\delta} \rangle$ is a restricted sum to avoid double counting. The spectral shape can either be determined in terms of spin-wave theory [62], by numerical [64] or field theoretical methods [144]. In the thermodynamic limit (infinitely large systems) of a spin-only model the low-energy limit is characterized by an Ω^3 variation of the response [144–147]. If there exist itinerant electrons in addition to localized spins, such as proposed for FeSe for instance [148–150], the spin response may be superimposed on an electronic continuum. Possible interrelation effects have not been explored yet.

In anisotropic systems two-magnon excitations may be observed well above T_N. Then the evolution of the two-magnon line is continuous over large temperature ranges below and above T_N [151]. Thus the line shape and the temperature dependence of the response allows one to clearly distinguish the scattering from localized and itinerant spins as described at the end of section 4.4.

Screening may become relevant in metallic systems such as the FeBCs in which the spins forming the SDW are itinerant as opposed to the cuprates which are Mott insulators at low doping. However, there is no analytic treatment yet dealing with the problem of light scattering from spin polarized conduction electrons beyond SDW formation or the nearly antiferromagnetic Fermi liquid [152]. Doped cuprates were studied using quantum Monte Carlo methods [153, 154]. Considerations along these lines may surface when analyzing the differences between the pnictides and chalcogenides where the magnetism is believed to be predominantly itinerant and localized, respectively, at least for some orbitals [149, 155–158]. However, this rather general problem cannot be solved here and the controversial discussion on spin excitations in the FeBCs requires additional work.

4.8. Fluctuations

In the case of fluctuations, there are three possibilities to deal with the $q = 0$ selection rule. (i) A fluctuation can have zero momentum. This case applies if all unit cells have the same excitation pattern as for the case of ferro-orbital fluctuations [49]. (ii) A fluctuation with finite critical wave vector such as $\mathbf{q}_c = (\pi, \pi)$ or $\mathbf{q}_c = (\pi, 0)$ for incipient Néel type or stripe-like antiferromagnetic order, respectively, can exchange momentum with another excitation or a defect. The case of moderately high defect concentrations was studied by Gallais and Paul [116]. The momentum transferred by the photons is certainly insufficient for large critical momenta (see section 4.3). (iii) Two fluctuations with opposite momenta are exchanged. It is exactly what happens in the case of two-magnon excitations in a system with long-ranged order [62, 159]. The same type of scattering may also occur in partially ordered systems [160] or in the presence of critical fluctuations [83]. This type of diagrams were first studied by Aslamazov and Larkin in the context of paraconductivity above the superconduction transition [161].

For the FeBCs there are various theoretical studies on the Raman response of fluctuations [85–87, 115, 118]. Although spin, orbital, and charge degrees of freedom are not independent, the question as to the leading instability remains relevant and crucial for the understanding of the FeBCs [40, 49, 115, 116, 118, 162–166].

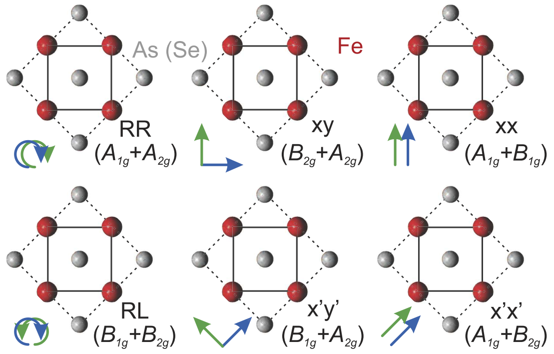

Figure 5. Scattering geometry and symmetries for the *ab* plane of FeBCs. Incoming and scattered photon polarizations are indicated as blue and green arrows. In backscattering configuration, the arrows corresponding to R and L polarization of the scattered light should be interchanged. The symmetries refer to the 1 Fe unit cell (full line) which is relevant (and frequently used) for electronic and spin excitations. Phonons have the right symmetry in the crystallographic or 2 Fe unit cell (broken line) where B_{1g} and B_{2g} are interchanged with respect to the 1 Fe cell.

4.9. Selection rules

In an inelastic light scattering experiment, all selection rules must be compatible with the direct product of two dipole transitions in the relevant crystal structure [119]. Figure 5 shows the main scattering geometries and the related sums of projected symmetries μ of the D_{4h} point group relevant for FeBCs (and cuprates). The pure symmetries can only be obtained by linear combinations of the spectra measured in appropriate geometries. The symmetry selection rules are generally valid and well known for, e.g., phonons. We now consider those for spin and charge excitations.

4.9.1. Particle–hole and gap excitations.

In the simplest approximation the vertices relevant for the projections in the Brillouin zone can be expanded into crystal harmonics of the respective point group [167]. Figure 6 shows the related symmetry form factors μ.

In first order approximation selection rules can be derived on the basis of symmetry alone since $\gamma_\mu(\mathbf{k}, \mathbf{q} \to 0)$ can be expanded into the set of basis functions $\Phi_\mu(\mathbf{k})$ [82]. Figure 6 shows schematic representations of the first and second order basis functions (crystal harmonics) of each symmetry to which the Raman vertices γ_μ are proportional. For particle–hole excitations, symmetry-resolved Raman vertices can be derived from the band structure within the effective mass approximation,

$$\gamma_{n,A_{1g}}(\mathbf{k}, \mathbf{q} \to 0) \propto \frac{1}{2}\left(\frac{\partial^2 \varepsilon_n(\mathbf{k})}{\partial k_x k_x} + \frac{\partial^2 \varepsilon_n(\mathbf{k})}{\partial k_y k_y}\right) \qquad (12)$$

$$\gamma_{n,B_{1g}}(\mathbf{k}, \mathbf{q} \to 0) \propto \frac{1}{2}\left(\frac{\partial^2 \varepsilon_n(\mathbf{k})}{\partial k_x k_x} - \frac{\partial^2 \varepsilon_n(\mathbf{k})}{\partial k_y k_y}\right) \qquad (13)$$

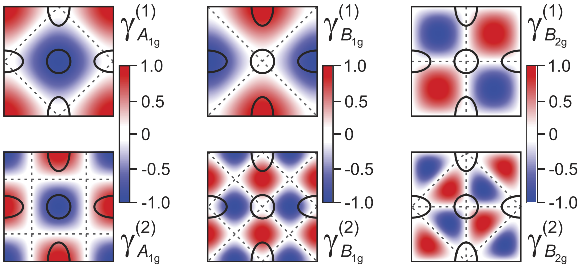

Figure 6. Symmetry properties and momentum dependences of the Raman vertices γ_μ. Shown are the first and second order vertices (form factors) for the symmetries $\mu = A_{1g}$, B_{1g} and B_{2g} of the D_{4h} point group. The zeroth order A_{1g} vertex is just a constant and is entirely screened. Higher order A_{1g} vertices are only partially screened. The solid lines represent an idealized two-band Fermi surface of FeSCs in the 1Fe unit cell. For the symmetry properties of the band structure in the FeBCs the screening in A_{1g} symmetry is almost negligible [117].

$$\gamma_{n,B_{2g}}(\mathbf{k},\mathbf{q}\to 0) \propto \left(\frac{\partial^2\varepsilon_n(\mathbf{k})}{\partial k_x k_y}\right), \qquad (14)$$

where n is the band index. The vertex for each symmetry μ is obtained by summing over all bands crossing E_F.

The first-order diagram on the right-hand side of figure 3(a) describes particle–hole excitations above and below T_c upon using the propagators for either the normal or the superconducting state. The evaluation yields the Raman response which depends quadratically on $\gamma_\mu(\mathbf{k})$. The vertices for $\mathrm{Ba(Fe_{1-x}Co_x)_2As_2}$ and $\mathrm{Ba_{1-x}K_xFe_2As_2}$ were calculated in references [36, 47] yielding $\gamma^{(2)}_{A_{1g}}$ rather than $\gamma^{(1)}_{A_{1g}}$ to be relevant for presumably most of the FeBCs. As can be seen from figure 6, in the B_{1g} symmetry ($\gamma^{(1)}_{B1g}$) one may expect to probe electron pockets, whereas both electron and hole pockets may be probed in A_{1g} symmetry ($\gamma^{(2)}_{A1g}$). The dependence of the Raman response on $\gamma^2_\mu(\mathbf{k})$ directly explains the selectivity in k-space.

4.9.2. Bardasis-Schrieffer modes. The selection rules for BS modes depend on the symmetry of the sub-leading interaction. The first proposals considered a ground state being driven by spin fluctuations thus having an $s_\pm$-wave gap with opposite sign on the electron and hole bands. Then, if the sub-leading channel originates from orbital fluctuations, predominantly along the $(\pi, 0)$ direction [143], the BS mode is expected in the A_{1g} channel [90]. Alternatively, the next strongest pairing interactions can have the same origin as the ground state resulting from spin fluctuations between the electron bands along (π, π) thus entailing a BS mode in B_{1g} symmetry.

4.9.3. Leggett modes. The symmetry selection rules for the Leggett modes depend on the interactions included and thus on the band structure and the coupling. If two concentric bands or interactions with wave-vector $(\pi, 0)$ are included the Leggett mode appears in the fully symmetric A_{1g} channel [99]. In the case when (π, π) interactions have to be considered, in particular if the central hole band is missing, the Leggett modes appear in B_{1g} symmetry [100]. In the case of fluctuations between the d_{xz} and d_{yz} orbitals Leggett modes may also appear in B_{1g} symmetry so long as they are not overdamped [98].

4.9.4. Fluctuations. Fluctuation contributions to the Raman response may arise from one and/or two fluctuations (see figure 3(b)). As can be seen from the diagrams, the first order term is non-vanishing only if the symmetry of the fluctuation is that of the Raman vertex. On the other hand, second order diagrams include electronic loops $\Lambda^0_\mu(\mathbf{q})$ which depend linearly on γ and quadratically on f. Consequently, for a given critical vector $\mathbf{q}_c$ and a set of FS hot spots $\mathbf{k}_0$ which are connected by $\mathbf{q}_c$, the selection rules for the second order term read $\Lambda^0_\mu(\mathbf{q}_c) \propto \sum_{\mathbf{k}_0}\gamma_\mu(\mathbf{q}_c)$ [83]. It states that a finite response in symmetry channel μ is expected only if $\mathbf{q}_c$ connects hot-spots in which γ_μ does not change sign. As opposed to the first order term, γ_μ does not necessarily reflect the symmetry of the fluctuation for second order processes.

5. Instabilities beyond superconductivity

The phase diagram (figure 1) shows that the FeBCs have a multitude of instabilities beyond superconductivity. Their interrelation amongst each other and with superconductivity is a main focus of research. For certain ranges of doping and/or applied pressure all FeBCs exhibit long range magnetism while remaining metallic in contrast to undoped cuprates. Some of the FeBCs like FeSe display only short-ranged magnetic order at finite temperature [157, 168]. Not surprisingly, the nature of the magnetism is still under discussion. It was shown recently that the degree of localization of electrons and thus spins may depend on the orbital and varies between the materials [149].

Above the magnetic ordering temperature there are various structural transitions which typically go along with electronic anisotropies such as substantial differences in the resistivities measured along inequivalent directions [28] or orbital order, specifically of the d_{xz} and d_{yz} orbitals [169]. Yet, how can the origin of these differences be pinned down?

5.1. Excitations from localized spins

While itinerant and localized magnetism cannot easily be distinguished by neutron scattering, Raman scattering offers clear criteria [55] which are outlined in sections 4.4 and 4.7. The main arguments are the temperature, doping and symmetry dependences and line shapes.

Early experiments on Fe chalcogenides and pnictides reported excitations in the range 2000–4000 cm^{-1} in all symmetries. The results were interpreted in terms of local spins [27, 31], and the energies are in fact compatible with the exchange coupling $J \approx 120$ meV found by neutron scattering or density functional theory (DFT) [170]. With the improvement of the sample quality, the peaks in this range faded away and may be traced back to luminescence with high probability [43].

Recent experiments in FeSe support scattering from localized spins. The B_{1g} spectra at high (300 K) and low (20 K) temperature are dominated by a broad peak centered at approximately 500 cm^{-1}, whereas near T_S an additional sharp peak appears in the range 100–200 cm^{-1} [53, 55, 57] which we disregard here but discuss in detail below in the context of fluctuations. The main peak in B_{1g} symmetry at 500 cm^{-1} depends continuously on temperature [55] and survives low doping with sulfur [57]. For FeS the excitation is completely gone. In contrast to Massat *et al* [53] and Zhang *et al* [57], Baum and coworkers [55] assign this peak to a two-magnon excitation of nearly frustrated spins.

There are experimental and theoretical arguments for this assessment. Very generally, antiferromagnetically ordered local spins give rise to two-magnon excitations close to $3J$ [62] whereas SDW order in a metallic system leads to instantaneously appearing coherence effects close to the gap energy in the electronic excitation spectrum similar to those in a superconductor (see section 4.4). In FeSe, the pronounced excitation in B_{1g} symmetry on top of the particle–hole continuum builds up gradually [53, 55]. Thus the temperature dependence of the scattering intensity is compatible with that of a quasi two-dimensional Néel antiferromagnet, e.g., $YBa_2Cu_3O_6$ [151]. However, the energy of the B_{1g} peak is too small by approximately a factor of five, suggesting frustrated magnetism, as studied theoretically already in pnictides and chalcogenides [64], expected from LDA results [170], and explored recently for FeSe using exact diagonalization [171].

On a square lattice, frustration can occur in the presence of interactions beyond nearest-neighbour coupling. In this case, a variety of ordering patterns or wave vectors may be realized. A possible model is the J_1–J_2–J_3–K Heisenberg model [170] where nearest, next-nearest and next–next-nearest neighbor exchange couplings are taken into account. K is the coefficient of the bilinear interaction proportional to $(\mathbf{S}_i \cdot \mathbf{S}_j)^2$ which, depending on the sign (de)stabilizes long-range order. For $J_2 \approx 0.5J_1$ Néel (π, π) and stripe $(\pi, 0)$ order occur with similar probability for $J_3 \rightarrow 0$ and are separated by a $(\pi, \pi/2)$ phase for $J_3 > 0$ [170]. In all cases, little energy is required for flipping a spin, and the maximum of the two-magnon excitation moves to zero energy in the classical limit ($S \rightarrow \infty$) and to approximately $0.5J_1$ for $S = 1/2$ as opposed to $2.84J_1$ when J_1 dominates [144]. The near degeneracy of the Néel and the stripe state going along with short range order in FeSe was not only predicted by LDA studies [170] but also observed recently by neutron scattering [157].

The B_{1g} response in FeSe was studied theoretically for zero and finite temperature by diagonalizing a 4×4 cluster carrying spin 1 using $J_2 = 0.528J_1$ and $J_3 = 0$ [55, 171]. The observed agreement between theory and experiment is semi-quantitative for all symmetries. The conclusions are in agreement with those of the neutron scattering experiments [157] and support the existence of local spins. How are local spins compatible with metallic transport in FeSe and why is FeSe different from the pnictides? Before discussing this question in section 5.4 the SDW systems and fluctuations will be reviewed.

5.2. Spin density wave order

Signatures of the SDW in the Raman spectra of BFA were first discussed by Chauvière *et al* [26]. Figure 7 compares the low and high temperature B_{1g} Raman response. Spectral weight is redistributed from energies below to above the SDW gap upon entering the SDW state. The Raman spectra exhibit two distinct features: A peak at about 900 cm^{-1} appearing only in B_{1g} symmetry and a step-like increase at about 400 cm^{-1} in all channels [26].

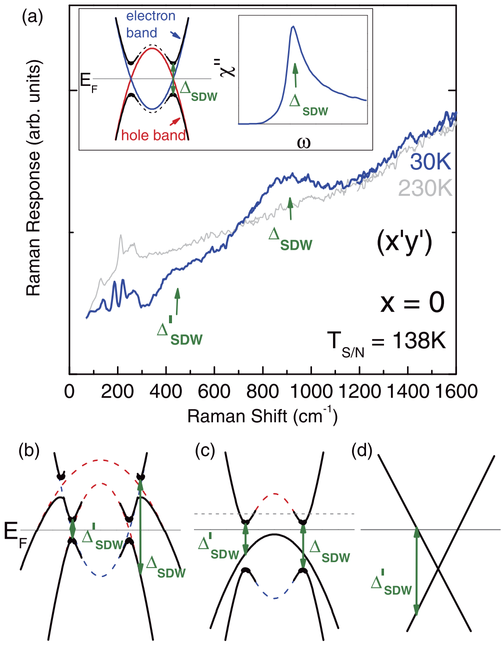

Figure 7. Effect of SDW formation on the Raman response of BFA. (a) High- and low-temperature Raman response in $x'y'$ configuration. The spectra show two spectral features at Δ_{SDW} and Δ'_{SDW}. The inset shows the anti-crossing of the hole and electron band and the related opening of Δ_{SDW}. The Raman response (right) is given by Equation (7). (b) If one electron band and two hole bands anti-cross Δ_{SDW} is much larger than Δ'_{SDW}. (c) If one of the hole bands does not reach the Fermi level the two gaps are expected to have similar magnitude. For phase-space reasons the response at Δ'_{SDW} has higher spectral weight than that at Δ_{SDW} in case (b) in comparison to case (c). (d) In the presence of a Dirac cone (non-interacting bands) Δ'_{SDW} should be characterized by very small spectral weight, and Δ_{SDW} is not expected to be observable. Reprinted figure with permission from [26], Copyright (2011) by the American Physical Society.

The B_{1g} selection rules for inter-orbital transitions would be compatible with a transition $d_{x^2-y^2} \leftrightarrow d_{z^2}$ to correspond to the peak at 900 cm^{-1}. Yet, this straightforward explanation is in conflict with band-structure calculations which find the dominant contribution to the states at the Fermi surface to originate from d_{xz}, d_{yz}, and d_{xy} orbitals. Thus intensity can only be redistributed among these orbitals. Consequently, a band-folding picture was suggested with two types of electronic transitions in the SDW state: (a) a high-energy transition between electron and hole bands anti-crossing after back-folding and (b) a low-energy transition involving either interacting or noninteracting bands. Upon Co substitution, the peak observed in B_{1g} symmetry disappears due to the increase of the Fermi energy and the related filling of the unoccupied states at the anti-crossing points [26].

A much more pronounced redistribution of spectral weight was reported for Sr122 [43] with a suppression at low

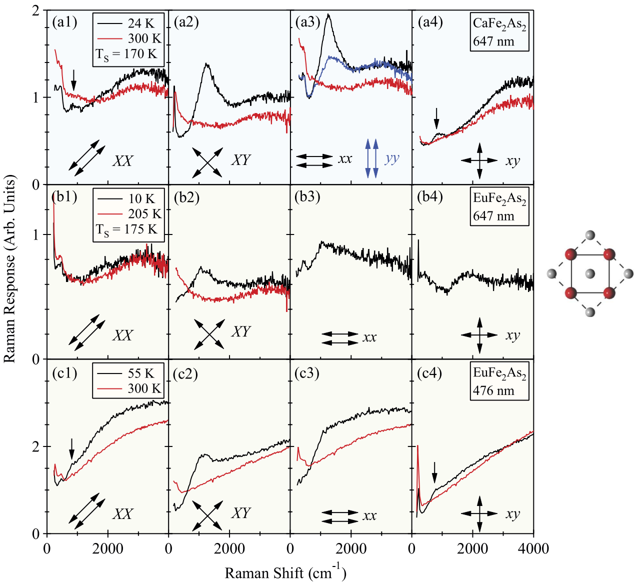

Figure 8. Effect of SDW order in the Raman spectra of $CaFe_2As_2$ and $EuFe_2As_2$. The unit cell on the right which the polarizations in the panels refer to is added to the original figure for clarity. Note the notations $X \equiv x'$ and $Y \equiv y'$. (a1)–(a4) Spectra of $CaFe_2As_2$ measured with 647 nm laser excitation in the normal state (300 K, red) and in the SDW phase (24 K, black/blue) of a twin-free sample. (b1)–(b4) Raman response of $EuFe_2As_2$ in the normal state (205 K, red) and the SDW state (10 K, black) of a twinned sample. (c1)–(c4) Same as (b1)–(b4) with 476 nm laser excitation. Reprinted figure with permission from [34], Copyright (2016) by the American Physical Society.

energies and three distinct peaks at 820 cm^{-1}, 1140 cm^{-1} and 1420 cm^{-1} appearing in B_{1g} symmetry. The peak at 820 cm^{-1} is also present in B_{2g} symmetry. In A_{1g} symmetry no peaks can be resolved. On the basis of the symmetry selection rules the authors argue that the peaks at 1140 cm^{-1} and 1420 cm^{-1} originate from anti-crossing bands in the presence of imperfect nesting rendering the X and Y points inequivalent. The peak at 1420 cm^{-1} appears only well below T_{SDW} and was explained in terms of a temperature dependent Fermi surface topology and the disappearance of a hole-like Fermi surface pocket very close to the chemical potential in the reconstructed SDW electronic structure. The peak at 820 cm^{-1} is assigned to an optical transition between folded bands away from the Γ–X and Γ–Y directions which are probed in xy configuration.

Recently Zhang *et al* [34] reported spectral weight redistribution in twinned Eu122 and detwinned mono-domain Ca122 single-crystals in the SDW phase, as shown in figure 8. In the $x'y'[\equiv XY]$ configuration, spectral weight is transferred from low energy to above 800 cm^{-1} with the development of a peak at 1220 cm^{-1} and 1060 cm^{-1} for Ca122 and Eu122, respectively (see panels (a2) and (b2) in figure 8). For de-twinned Ca122 a large intensity anisotropy of the 1220 cm^{-1} peak is observed in xx and yy scattering configurations (see panel (a3) in figure 8). In addition, a weak spectral feature is observed at 830 cm^{-1} in $x'x'[\equiv XX]$ and xy scattering configurations as indicated by arrows. The authors derive the selection rules for inter- and intra-orbital transitions on the basis of the D_{2h} group for the high symmetry points in the Brillouin zone. The symmetry analysis, augmented by an orbital-resolved DFT + DMFT study [34], suggests that the peak at 1200 cm^{-1} in the A_g symmetry channel originates from an intra-orbital transition at the Z point induced by the SDW band folding, whereas the peak at 830 cm^{-1} in the B_{1g} channel arises from the $d_{xz} \leftrightarrow d_{yz}$ transition at the Γ point.

The analysis of the Raman spectra in the SDW state shows that the typical gaps induced by ordering of the magnetic moments of itinerant electrons are in the range of 100–150 meV or 8 k_BT_{SDW}. This ratio is in the same range as that of the superconducting gap, and one cannot conclude that T_{SDW} is suppressed by fluctuations as, for instance, in the tritellurides [137]. Rather, the large value may indicate strong coupling. Whether or not the $a - b$ anisotropy of the gap energy found in Ca122 [34] is a generic feature of all pnictides cannot be decided on the basis of the material at hand. However, a strong electronic anisotropy was also found in the energy range of 2–3 eV in Ba122 below T_{SDW} when studying resonance effects of the A_g arsenic phonon [172]. Thus, anisotropies in the electronic structure were identified by Raman scattering at low and high energies in the magnetically ordered phase.

5.3. *Fluctuations above the ordering transitions*

There are various types of instabilities in the FeSCs which can drive the phase transitions. While some groups consider magnetic ordering the dominant interaction [9, 173], Kontani *et al* see orbital ordering in the driver's seat [174]. These basic considerations were studied in some detail and refined recently. A tendency towards charge-driven or Pomeranchuk-type order was found for FeSe using either Hubbard models with strong coupling between spin and orbitals [163] or renormalization group (RG) schemes on model band structures [164, 165] or orbital-dependent nesting properties [166]. For the pnictides these studies favor spin-driven nematicity and explain, on a qualitative basis, the proximity of the nematic and the magnetic transitions and the absence of magnetism in the chalcogenides. This rather incomplete selection of theoretical work already highlights the importance of experimental studies for clarifying the issue.

Since strong fluctuations precede the structural transitions in many compounds, experimental access to the fluctuations is highly desirable. Raman spectroscopy is among the handful of techniques available but does not probe the fluctuations alone. Rather, since the FeBCs are metals the contribution is always superimposed on the particle–hole continuum which needs to be taken into account for quantitative analyses.

A contribution from fluctuations to the Raman spectra of FeBCs were first reported by Choi *et al* [29]. They observed a pronounced build up of the low energy Raman response in Sr122 upon cooling towards T_S and suggested a magnetic nature of the fluctuations. The similar build up of the low-energy signal in the B_{1g} channel was also observed for Ba122 by Sugai *et al* [27, 32] as presented in figure 9. The authors attributed the low-energy $x'x'[\equiv aa]$ and xy spectra to excitations near Dirac nodes where the bands intersect without interacting (circles in figure 9(b)) and the xx and $x'y'[\equiv ab]$ spectra to the 'anti-nodal' excitations where the back-folded

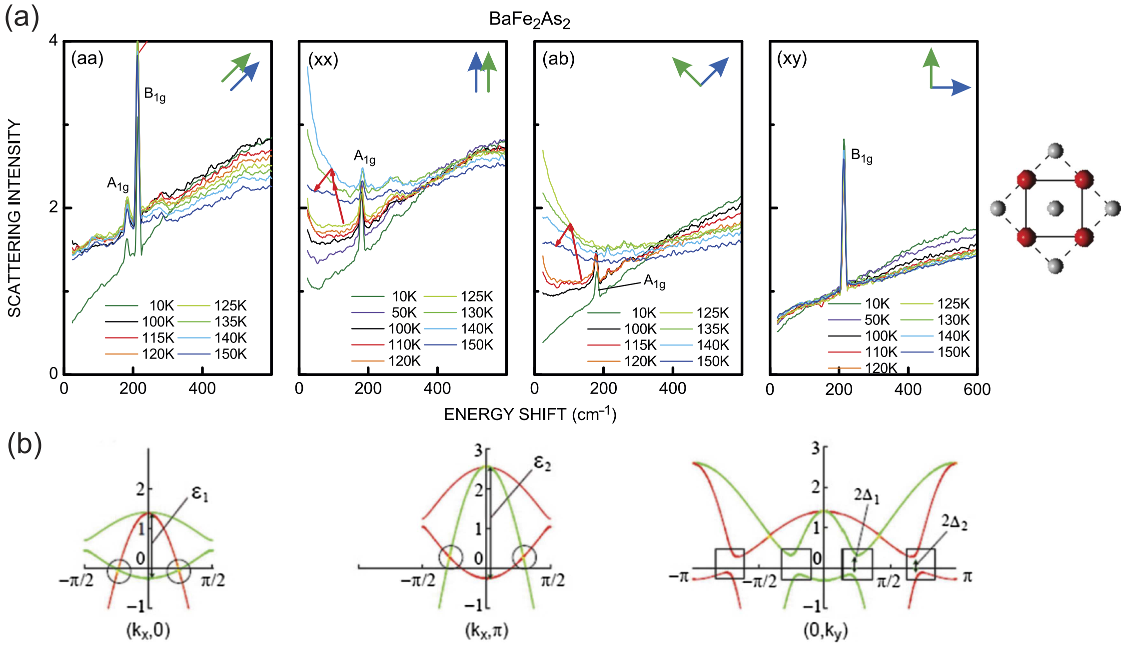

Figure 9. (a) Low-energy Raman spectra of $BaFe_2As_2$ at temperatures as indicated. The pictograms displaying the unit cell and the polarizations are added to the original figure for clarity. The two central panels (xx) and $(ab)[\equiv x'y']$ show contributions from fluctuations at low energy and the redistribution of spectral weight from below to above 350 cm^{-1} upon cooling through $T_{\mathrm{SDW}} \approx 135$ K as indicated by red arrows. Reprinted from [27], with the permission of AIP Publishing. (b) Electron dispersions in $(k_x, 0)$, (k_x, π), and $(0, k_y)$ direction. The circles denote the Dirac nodes, and the squares denote the 'anti-nodes' where the electrons interact. Reprinted by permission from Springer Nature Customer Service Centre GmbH: Springer, Journal of Superconductivity and Novel Magnetism, [32] (2019).

bands interact (squares in figure 9(b)). The increase of the low-energy scattering intensity was interpreted in terms of critical fluctuations related to the opening of the anti-nodal gap.

Several detailed studies of fluctuations in both pnictides and chalcogenides were presented more recently in references [30, 33, 35, 40, 44, 49, 53, 116, 175, 176]. As discussed in section 4.8, one and/or two fluctuations may contribute to the Raman spectra via distinct scattering processes. Gallais and Paul [116] and Thorsmølle *et al* [49] point out that the first order term has a non-zero contribution only in the presence of momentum scattering processes (or, equivalently, finite $v_{\mathrm{F}}q$). On the other hand, the second order AL diagrams may include contributions having $q \gg 0$.

Gallais and coworkers suggested to use the static limit of the real part of the response, $\chi'_{B1g}(\Omega = 0, T)$, for analyzing the Raman data and comparing them to the results of other quasi-static methods such as NMR or elasticity. $\chi'_{B1g}(\Omega = 0, T)$ was directly extracted from $\chi''_{B1g}(\Omega, T)$ via Kramers–Kronig transformation, $\chi'_{B1g}(\Omega = 0, T) = \pi^{-1}\int \mathrm{d}\Omega\chi''_{B1g}(\Omega, T)/\Omega$, where $\chi''_{\mu}(\Omega, T)/\Omega$ has the meaning of a channel dependent Raman conductivity. This procedure requires an extrapolation of $\chi''_{B1g}(\Omega, T)$ to zero energy and the selection of a high-energy cutoff since $\chi''_{B1g}(\Omega \to \infty, T) \approx c$ where c is a constant. The method was applied to the analysis of the data of BFCA [30, 116] (see next paragraph) and subsequently of Eu/Sr122 [33, 44], BKFA [176], and Na111 [49]. Thorsmølle *et al* demonstrated the scaling of the static susceptibility obtained from Raman scattering and NMR data for Na111. Consequently, low energy quasi-elastic scattering was related to $d^{\pm}$ quadrupolar nematic fluctuations which became critical on approaching a Pomeranchuk instability with a deformation of the Fermi surface [177, 178].

The low-energy Raman response in differently doped BFCA was extensively studied by Gallais *et al* [30, 116]. The authors argue that the nematic susceptibility is observable in the B_{1g} channel and originates from charge fluctuations for symmetry reasons since inelastic light scattering couples preferably to the charge. They observe a strong enhancement of the B_{1g} response $\chi''_{B1g}(\Omega \approx k_BT, T)$ upon cooling towards T_{S} and a collapse thereof in the orthorhombic/SDW state, whereas the B_{2g} response is essentially temperature independent. First, $\chi'_{B1g}(\Omega = 0, T)$ was determined. Second, it is shown that this quantity is equal to the quasi-static nematic susceptibility and, in fact, compares well to the Young modulus $c_{66}(T)$ derived from thermal expansion [116, 179]. Interestingly, neither $c_{66}(T)$ nor $\chi'_{B1g}(\Omega = 0, T)$ diverge at T_{S} due to the coupling of the electronic/spin degrees of freedom to the lattice [30, 116, 180]. As a consequence, the divergence of $\chi'_{B1g}(\Omega = 0, T)$ derived from a Curie–Weiss fit occurs always below the structural transition, $T_0 < T_{\mathrm{S}}$.

Kretzschmar *et al* [40] focused their attention on BFCA at finite doping where the magnetic ordering temperature and the structural transition are separated ($T_{\mathrm{SDW}} < T_{\mathrm{S}}$) as shown in figure 10. The memory function method [81] was used for extracting the static Raman relaxation rates $\Gamma_0(T)$ in A_{1g} and B_{1g} symmetry and for facilitating the identification of the cross-over temperature T_{f} below which the contributions from fluctuations become detectable in the B_{1g} channel.

The fluctuations and the particle–hole continuum can only be considered additive if they get excited through independent

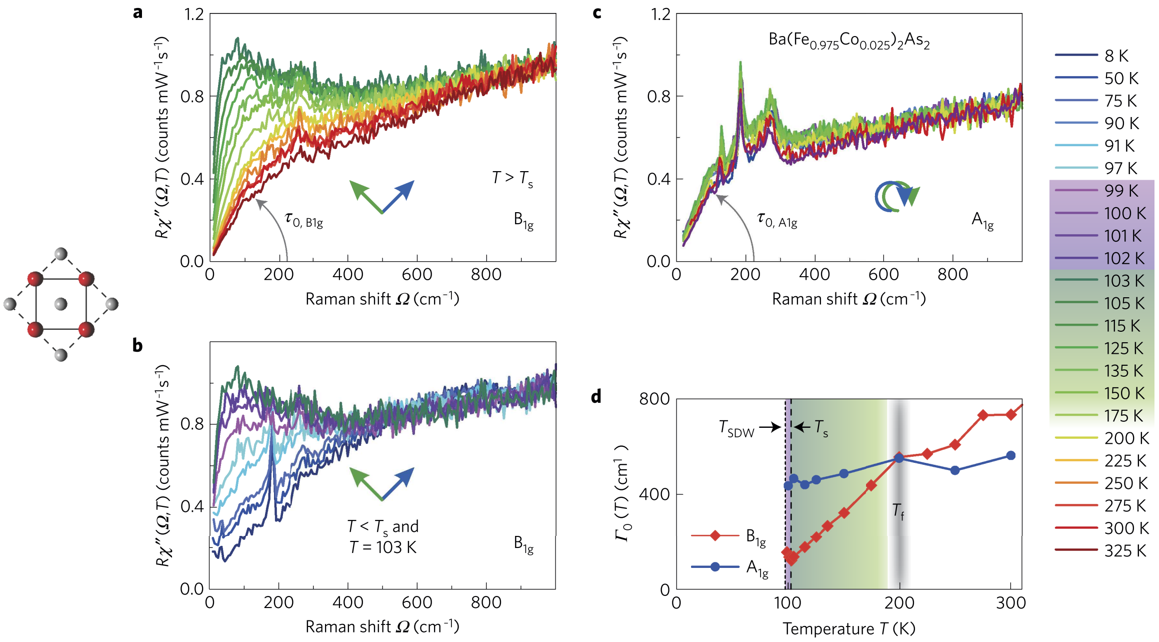

Figure 10. Polarization-resolved Raman results for Ba$(\mathrm{Fe}_{0.975}\mathrm{Co}_{0.025})_2\mathrm{As}_2$. (a)–(c) Response $R\chi''(\Omega, T)$ at temperatures as indicated. The pictograms for the polarizations were added. (a) B_{1g} spectra above and (b) below T_S. (c) A_{1g} response. The initial slopes defined in (a) and (c) by gray arrows are proportional to the static two-particle lifetime $\tau_{0,\mu}$ in symmetry $\mu = A_{1g}, B_{1g}$. (d) Raman relaxation rates $\Gamma_{0,\mu}(T) = \hbar/\tau_{0,\mu}(T)$, in A_{1g} (blue circles) and B_{1g} (red diamonds) symmetry as a function of temperature. The A_{1g} and B_{1g} data above T_f closely follow the resistivity. The fluctuation range $T_\mathrm{S} < T < T_\mathrm{f}$ and the nematic phase $T_\mathrm{SDW} < T < T_\mathrm{S}$ are shaded green and magenta, respectively. Reprinted by permission from Macmillan Publishers Ltd: [Nature Physics] [40], Copyright (2016).

scattering channels such as, e.g., phonons and charge excitations. If two fluctuations are excited simultaneously (AL mechanism) the response from fluctuations exists independent of other excitations, otherwise the excitations are entangled. In order to separate the fluctuation contribution, the high temperature particle–hole continuum ($T > T_\mathrm{f}$) was extrapolated down to low temperatures by varying $\Gamma_0(T)$ in a way that the initial slope of the spectra matches the transport results and was subtracted from the respective total Raman response.

It is considered the key observation of that paper that the fluctuations do not disappear directly below T_S but continuously lose spectral weight with the peak maximum staying pinned. This indicates a nearly constant correlation length between T_S and T_SDW. The persistence of the fluctuations down to T_SDW and their immediate disappearance below T_SDW favors their magnetic origin.

For LaFeAsO and Sr$(\mathrm{Fe}_{1-x}\mathrm{Co}_x)_2\mathrm{As}_2$ the analysis arrives at slightly different conclusions for the temperature dependence but similar ones for the origin of the fluctuations [35, 44]. In both compounds the maxima of the fluctuation response do not coincide with the structural transition temperature, and in Sr$(\mathrm{Fe}_{0.8}\mathrm{Co}_{0.2})_2\mathrm{As}_2$ the fluctuations do not disappear right below the magnetic ordering temperature. Some of the discrepancies may be related to the time scale of the fluctuations relative to that of the phonons. In fact, the peak positions indicate much slower dynamics in Sr$(\mathrm{Fe}_{0.8}\mathrm{Co}_{0.2})_2\mathrm{As}_2$ than in the other materials. In addition, inhomogeneities in the Co content may contribute. It is certainly necessary to study more doping levels before concluding finally.

The spectral shape of the fluctuations can be described quantitatively in terms AL-type of diagrams if electron–phonon interaction is included [83]. Otherwise the decay on the high-energy side is too slow [115, 118]. The corresponding selection rules (see section 4.9) yield $\mathbf{q}_c = (\pi, 0)$ as the wave vector of the critical fluctuations. Furthermore, it was demonstrated that the initial slope of the fluctuation response χ''_fluct exhibits qualitative agreement with the temperature dependence of the nematic susceptibility in the tetragonal and the nematic phase, as expected from a Ginzburg–Landau type of consideration. A comparison of BFCA and BKFA and details of the analysis are further discussed in reference [181].

In FeSe, having a structural transition at $T_\mathrm{S} \approx 90$ K and short-ranged but no long-ranged magnetic order above 4 K [157, 168], the fluctuations survive down to temperatures right above $T_\mathrm{c} \approx 9$ K [53, 55, 57]. The experimental results, of the three groups of authors agree with each other in the energy and temperature range where they can be compared. We show the results of Massat *et al* in figure 11 and describe those in B_{1g} symmetry in detail. At 295 K (upper part of panel (a)) a broad peak at 50 meV is observed which is unique for FeSe (and $\mathrm{FeSe}_{1-x}\mathrm{S}_x$ for $x \leqslant 0.2$). In the pnictides or in pure FeS it is absent, the spectra are nearly flat and the overall intensity in all symmetry projections is similar. Upon cooling, this peak first gains intensity. Below 200 K an additional structure starts to appear at some 20 meV which becomes clearly discernible in the yellow spectrum at 142 K (see also and panel (b)). At $T_\mathrm{S} = 90$ K (black) it peaks at 4–5 meV and has maximal intensity. The peak at 50 meV stays nearly pinned and has now almost twice the intensity as at 295 K. Below 90 K (panel (c)) the low energy peak survives down to at least 45 K (Baum *et al* [55] can resolve it even at 20 K) and moves to lower energies reaching some 2 meV directly above T_c while losing most of its intensity. The redistribution of spectral weight in the superconducting state shows directly that the remaining intensity below 15 meV originates from particle–hole excitations as in the pnictides. Concomitantly, the peak at 50 meV hardens slightly and increases further. Baum *et al* [55] argue that the persistence of the fluctuations well below T_S is supportive of spin fluctuations similar to those in BFCA, whereas Massat *et al* [53] assign the fluctuations to charge and/or orbital physics and the peak at 50 meV to interband transitions. Zhang *et al* [57] interpret the quasi-elastic peak at low-energy in terms of ferro-quadrupole fluctuations of a d-wave Pomeranchuk instability at $q = 0$ and assign the reduction of the intensity below 50 meV and T_S to the opening of a gap in the electronic excitation spectrum following the lattice distortion.

In a recent preprint [87] Udina *et al* present a detailed gauge-invariant study of the charge part of the low-energy Raman response in FeSe and assign the temperature dependence of the spectra to the relative shift of the Fe $3d_{xz}$ and $3d_{yz}$ orbitals in the nematic phase. The authors predict the variation of the spectral shape below T_S and find that the energy of the quasi-elastic peak increases with decreasing temperature if an order-parameter-like variation of the orbital splitting is assumed (see figure 3 of reference [87]). This variation leads to a gap-like suppression of the intensity at low energies and resembles the temperature dependent intensity of the fluctuation peak, whereas the energy of the quasi-elastic peak increases below T_S at variance with the experimental findings (see last preceding paragraph).

Massat and coworkers apply an analysis similar to that in BFCA for studying FeSe at ambient [53] and applied pressure [15], as shown in figure 11. The spectra for $P = 0$ exhibit a pronounced temperature dependence in the B_{1g} channel (figure 11(a)–(c)). The real part of the static Raman susceptibility $\chi'_{B1g}(\Omega = 0, T)$, as derived from the 'Raman conductivity' $\chi''_{B1g}(\Omega, T)/\Omega$, follows a Curie–Weiss law with T_0 significantly lower than T_S for reasons discussed above in agreement with the stiffness data. With increasing pressure (figure 11(e)) T_S decreases, and above 2 GPa the SDW is the dominating phase with T_SDW reaching 45 K at approximately 5 GPa (figure 11(d)) [182]. With the appearance of the SDW phase above 2 GPa the Curie–Weiss-type variation of $\chi'_{B1g}(\Omega = 0, T)$, as determined from the spectra in figure 11(f), disappears as opposed to the observations in BFCA. Apparently, the magnetism in FeSe has aspects different from those in the pnictides.

5.4. Origin of the excitations: spin or charge?

There is no consensus yet on the leading instability in the FeBCs, and there are arguments in favor of both orbital and spin ordering. This controversy characterizes also the interpretation of the Raman data, in particular those of the fluctuation response. It is true that photons couple to the charge, and if the vertex has the same symmetry as the fluctuations, there is coupling. However, this does not exclude other types of fluctuations to couple to the light; in other words, the selection rules and the coupling argument are not sufficient for deciding between spin and charge[5].

Selection rules similar to those of charge excitations can also be derived for spin fluctuations owing to the specific band structure of the FeBCs [40, 83]. Given the issue with the selection rules, the temperature dependence may be used as another criterion, since critical fluctuations are expected to disappear immediately at the corresponding ordering temperature. This disappearance is observed directly at $T_\mathrm{S} \approx T_\mathrm{SDW}$ in BFA [39, 40], at $T_\mathrm{SDW} < T_\mathrm{S}$ in BFCA [40], and not at all in FeSe without long-ranged order [53, 55]. $\chi'_{B1g}(\Omega = 0, T)$ as an energy-integrated quantity possibly obscures this important detail to some extent. Therefore, we argue that spin fluctuations dominate the low-energy Raman spectra in most of the FeBCs but would not go so far as to say that there is evidence beyond reasonable doubt. However, we believe that the issue can be settled, presumably by light scattering, using a wide range of excitation energies in the visible range for tracking the resonance behavior or by resonant inelastic x-ray scattering (RIXS) [183].

The second open question pertains to the nature of the short- or long-ranged spin ordering (which exists beyond any doubt): in the pnictides the spins of itinerant electrons order because of a Fermi surface instability [9, 184, 185], whereas the spins or at least some of the spins in the chalcogenides are more localized than in the pnictides [149, 186]. The signatures of these different types of order in the Raman spectra are relatively clear as can be directly seen by comparing the Raman response in cuprates to that in Ba122, for instance. However, it was argued that the band at 500 cm^{-1} in FeSe originates from incoherent intra-band scattering [53] rather than spin excitations [55]. Yet, there are two considerations which are hard to reconcile with charge (particle–hole) excitations: (i) since the energy of the band does not vary significantly upon cooling from 300 to 4 K, only momentum scattering having a scattering rate of approximately 500 cm^{-1} and a temperature independent intensity [77] can be at its origin. (ii) With the scattering rate being an order of magnitude larger than the superconducting gap the gap excitations would be entirely suppressed [110, 111] as opposed to the experimental results [53, 55, 57].

On the other hand, the semi-quantitative agreement of the spectra in all symmetries with simulations [55, 171] provides an attractive explanation for the observed spectra. While the dependence (or independence) of the B_{1g} peak on S substitution [57] still needs to be clarified it does not seem to be a killer argument [187]. The orbital dependent localization [149, 156] provides the necessary explanation for the differences between

---

[5] Coupling to the charge does not mean that the photons couple directly to low-energy charge excitations. Rather, the effective scattering Hamiltonian for particle–hole excitations close to E_F is an approximation derived for photon energies much smaller than the gaps in the band structure [63]. Why this approximation works quite well in the FeBCs and in the cuprates in the presence of low-lying bands is not entirely clear. It may have its origin in strong correlation effects which broaden all electronic states away from E_F and thus reduce resonances.

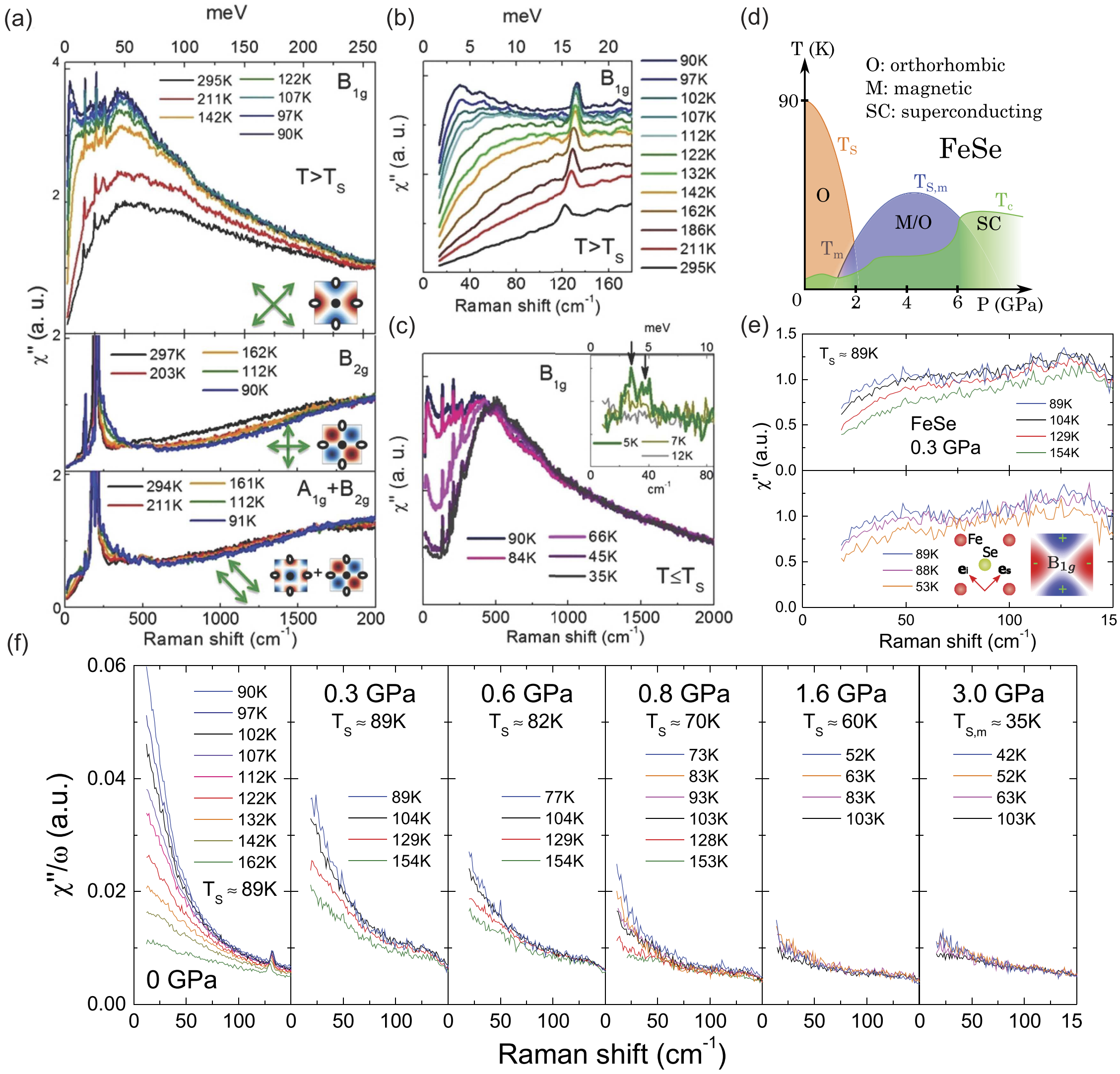

Figure 11. Light scattering in FeSe. (a)–(c) Symmetry-dependent Raman spectra of FeSe above $T_S = 87$ K using photons at 2.33 eV. The sharp peaks superimposed on the electronic continuum are due to Raman active optical phonons. The insets display the Raman form factors in different symmetries (blue and red colors indicate positive and negative amplitudes, respectively), and the polarization configurations used to select them. (b) Temperature dependence of the low energy B_{1g} spectra above T_S. (c) Evolution of the B_{1g} spectra across T_S. The inset shows the spectra across the superconducting transition at $T_c = 8.5$ K. The arrows indicate the peaks associated with 2Δ. Panels (a)–(c) reproduced with permission from [53]. (d) Pressure–temperature phase diagram of FeSe. (e) B_{1g} response at $P = 0.3$ GPa and temperatures as indicated. (f) $\chi''(\omega)/\omega$ in B_{1g} symmetry for pressure values and temperatures as indicated. Panels (d)–(f) reprinted with permission from [15], Copyright (2018) by the American Physical Society.

the pnictides and chalcogenides, including the experimentally observed near localization of the electrons in the d_{xy} orbitals in FeSe as opposed to the by and large orbital-independent itineracy of the electrons in all bands in the pnictides [188]. RIXS as a rapidly developing technique may help to pin down the orbital character of the differently localized electrons [189].

In spite of all these arguments the problem is not settled, and the type of fluctuations and the leading instability may be different in the pnictides and chalcogenides as outlined in the beginning of section 5.3. Thus further criteria for the analysis of the B_{1g} Raman data were proposed recently including scaling arguments for the slope of the spectra in the zero-energy limit and for the real part of the static susceptibility [86]. Klein *et al* analyzed data of FeSe, Ba122 and NaFe$_{1-x}$Co$_x$As and found support for a Pomeranchuk-type charge instability in FeSe and for spin fluctuations in the pnictides. Close to a quantum critical point being ubiquitous in the pnictides and chalcogenides energy power laws for the response were derived but were not tested yet against experiments [85].

6. Superconductivity

The identification of the pairing mechanism remains one of the major challenges in all unconventional superconductors. The momentum dependence of the gap magnitude (and phase, if possible) is among the important observables for addressing this question since $\Delta_{\mathbf{k}}$ and the pairing potential $V_{\mathbf{k},\mathbf{k}'}$ are interrelated via the BCS gap equation [190]. Therefore, a large variety of methods has been applied to derive properties of the energy gap in the iron-based materials with the goal to understand $V_{\mathbf{k},\mathbf{k}'}$ and the coupling [7]. Raman spectroscopy allows access to the magnitude of the gap [66, 73, 74], its number-phase fluctuations [95–97] and bound in-gap states encoding the anisotropy of $V_{\mathbf{k},\mathbf{k}'}$ [89–91, 140].

6.1. Gap spectroscopy

6.1.1. Results from canonical methods. From the beginning, a substantial band and momentum dependence of the energy gap was observed. Yet, sign changes of the gap on individual bands or between the bands could not be pinned down unambiguously although tunneling experiments with an applied magnetic field [191] and neutron scattering experiments [192] supported unconventional order parameters in Fe(Se,Te) and BKFA, respectively. More pieces need to be added to solve the puzzle and clarify the type of pairing in the ground state.

Further complication arises since the gaps vary strongly between the families and with elemental substitution [12, 210, 211]. In BKFA at optimal doping band dependent gaps with little variation on the individual Fermi surfaces are observed by angle-resolved photoemission spectroscopy (ARPES) [201, 212], while the gaps vary rather strongly around the electron and hole pockets and along the k_z reciprocal axis in BFCA and overdoped BKFA [196, 199, 213, 214]. As a general feature, the maximal gaps observed across the families are in the range 6–8 in units of k_BT_c similar to those in cuprates.

In table 2 we compile characteristic results found by ARPES, specific heat (c_{el}), neutron scattering (INS) and tunneling spectroscopy (STS) and compare them to Raman results. It is instructive to have this overview in addition to the light scattering results which are usually more subject to controversy than the canonical methods, since data analysis is more difficult due to the appearance of additional electronic excitations close to or below the gap energy (cf section 4.6).

6.1.2. Raman results. Momentum- and band-resolved Raman results for the energy gap were first presented and discussed by Muschler *et al* [25] and are shown in figure 12. They reported data of a complete symmetry analysis in the normal and superconducting states of optimally doped $\mathrm{Ba(Fe_{1-x}Co_x)_2As_2}$ ($x = 0.061$). For the symmetry analysis the 2 Fe unit cell was used, and the related projections in the Brillouin zone were discussed subsequently on the basis of an LDA band structure [36]. For comparison with figure 5 the B_{1g} and B_{2g} symmetries must be interchanged. The effect of superconductivity is best seen by comparing spectra taken well below and slightly above T_c similarly as in the case of an SDW (see figure 7).

In $\mathrm{Ba(Fe_{1-x}Co_x)_2As_2}$, differences between the spectra above and below T_c which are associated with the opening of the superconducting gap are observed only in A_{1g} and B_{1g} symmetry. In A_{2g} the intensity is generally low for the absence of excitations having the right symmetry. In B_{2g} symmetry little spectral weight is expected since the vertices are small close to the Fermi surface crossings of the bands. Surprisingly, the intensity becomes comparable to that in A_{1g} and B_{1g} symmetry at approximately 300 $\mathrm{cm^{-1}}$ but there are no indications of an energy gap. There are essentially three explanations for the absence of gap structures: (a) The intensity originates from excitations other than electron–hole pairs such as spins. The slow increase of the B_{2g} intensity indicates either that (b) states far away from the Fermi surface are projected consistent with the vertices or that (c) the relaxation rate is much higher than expected from transport. Such an anisotropy may occur if the quasi-particle relaxation is strongly momentum dependent for the presence of Co scatterers in the Fe plane. Then the gap excitations are suppressed for specific symmetry projections [112]. We consider (c) the most likely explanation since spin excitations are already very weak at optimal doping and B_{2g} gap features indeed appear in $\mathrm{Ba_{1-x}K_xFe_2As_2}$ where the substitution generates only out-of-plane defects [46].

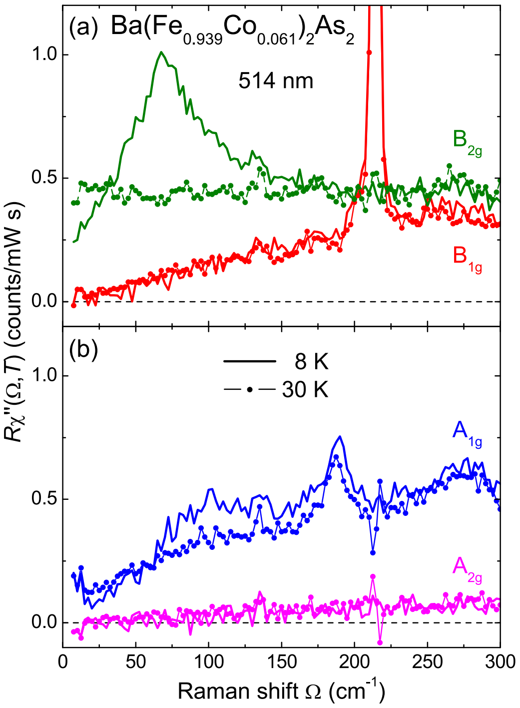

Figure 12. Symmetry-resolved Raman response of $\mathrm{Ba(Fe_{1-x}Co_x)_2As_2}$ ($x = 0.061$) for in-plane light polarizations right above (points) and well below T_c (full lines). The redistribution of intensity typical for superconductivity is observed only in (a) B_{2g} and (b) A_{1g} symmetry. (a) In this study, the 2 Fe unit cell was used for the symmetry assignment implying that the out-of-phase Fe phonon at 214 $\mathrm{cm^{-1}}$ is observed in the proper B_{1g} symmetry. (b) In A_{1g} symmetry there is a small increase for $\Omega \to 0$ from insufficient rejection of the laser light. The A_{2g} signal can safely be neglected at low energies. Reprinted with permission from [25], Copyright (2009) by the American Physical Society.

In superconducting BFCA [25], the broad maximum close to 100 $\mathrm{cm^{-1}}$ and the well-defined peak at around 70 $\mathrm{cm^{-1}}$ in A_{1g} and B_{1g} symmetry, respectively, correspond to gap excitations in the hole and the electron band. Finite spectral weight observed down to very small energies indicates vanishingly small gaps. The $\sqrt{\Omega}$ dependence in B_{1g} symmetry suggests accidental nodes [215].

Similar spectra were reported for doping levels in the range $0.045 \leqslant x \leqslant 0.10$ [37, 38, 181, 216] where broad pair-breaking peaks appear in A_{1g} symmetry between 50 $\mathrm{cm^{-1}}$ and 160 $\mathrm{cm^{-1}}$. The B_{1g} spectra generally peak at lower energy than those in A_{1g} symmetry. In both symmetries the spectral changes upon entering the superconducting state become less pronounced below and above optimal doping [38, 181, 216]. In A_{1g} symmetry the peak maxima scale approximately as $6k_{\rm B}T_{\rm c}$ in agreement with $2\Delta_{\rm max}$ from other methods. The B_{1g} spectra peak at $4k_{\rm B}T_{\rm c}$ at optimal doping and at $3k_{\rm B}T_{\rm c}$ for $x < 0.055$.

The discussion about the details of the interpretation of the spectral shape in superconducting BFCA is not finally settled although the data agree and the basic features are clear. Chauvière *et al* [38] interpret their B_{1g} results for optimally doped and underdoped samples in terms of a two-gap scenario with a maximal gap $2\Delta_{\rm max} \approx 75{\rm cm}^{-1}$ and a small but finite gap $2\Delta_{\rm min} \approx 15{\rm cm}^{-1}$ (see table 2). The maximal superconducting gap appears in the same location in momentum space as the SDW gap and is thus suppressed rapidly below optimal doping by the opening of the larger SDW gap, $2\Delta_{\rm SDW} > 2\Delta_{\rm max}$, and only the feature related to $2\Delta_{\rm min}$ survives. The spectral shape in B_{1g} symmetry may also be reproduced with a strong k_z dependence of $\Delta_{\mathbf{k}}$ but the disappearance of the structure at $2\Delta_{\rm max}$ in underdoped samples can only be explained with an in-plane anisotropy.

Muschler *et al* [25] argue that the $\sqrt{\Omega}$ variation of the low-energy B_{1g} spectra can be explained with accidental nodes or near-nodes on the outer electron band. This would be in agreement with the results from heat transport [217] and theoretical considerations [36]. Sugai *et al* find support from band structure calculations for the B_{1g} intensity (1 Fe cell) to originate from the hole bands [37]. The latter conclusion is at variance with symmetry arguments (cf figure 5) and the LDA results of Mazin *et al* [36]. As a matter of fact, the gap in BFCA is very anisotropic at all doping levels and may even vanish for certain momenta. The maximum is in the range $2\Delta_{\rm max} \approx 6k_{\rm B}T_{\rm c}$. Below optimal doping there is an interaction with the SDW gap.

The observation of gap features in other pnictides and in chalcogenides was delayed by sample and surface issues. In chalcogenides the observation of pair breaking succeeded first in $\rm Rb_{0.8}Fe_{1.6}Se_2$ after cleaving the sample *in situ* at low temperature [46]. Differences between normal and superconducting spectra were only found in B_{1g} symmetry. Since $\rm Rb_{0.8}Fe_{1.6}Se_2$ has presumably no hole pockets, the B_{1g} selection rule supports the symmetry assignment of references [25, 36] as reproduced in section 4.9. The observed gap appears to be almost constant on the electron pockets, being compatible with either a simple s- or a d-wave state without nodes on the Fermi surface and a sign change between the pockets. From what we shall see below d-wave symmetry is more likely but cannot be distinguished from an s-wave gap on the basis of the light scattering experiment. As in the case of BFCA, it is difficult to explain the intensities in other symmetries which do not show features induced by superconductivity. As a hypothesis which needs to be worked out in more detail we assign the continua in A_{1g} and B_{2g} symmetry to excitations in lower lying bands and/or the tails of the numerous phonon lines.

In $\rm Ba_{0.6}K_{0.4}Fe_2As_2$ continua and gap structures are observed in all symmetries and are by and large in agreement with the results from other methods [46] as shown in table 2. Since the hole-like Fermi surfaces are more extended in the Brillouin zone, the relevant electronic states are well sampled by all vertices. Second, the simulations using the effective mass approximation arrive at a semi-quantitative explanation of the spectra [47]. Third, the effect of defects induced by K doping in the Ba layer is expected to be weak. Finally, resonance effects may contribute [41, 49, 65] although they were found to be mild in BFCA [36].

The spectra of $\rm Ba_{0.6}K_{0.4}Fe_2As_2$ clearly show a small but true gap of approximately 30 $\rm cm^{-1}$ indicating, among other things, that the contributions from luminescence are negligible here. The largest gaps reside on the middle hole band and on the electron bands and are rather sharp as opposed to BFCA. The gap maximum $2\Delta_{\rm max}$ reaches almost 10 in units of $k_{\rm B}T_{\rm c}$ [46, 47]. This large ratio exceeds the ARPES results and, in particular, the gap ratio derived from the electronic specific heat as a typical bulk method [199]. However, thermally activated behavior is generally sensitive to the small gaps on the individual bands. These minimal gap energies are typically 180 $\rm cm^{-1}$ or 6.8 in units of $k_{\rm B}T_{\rm c}$ in the phenomenological analysis [41, 47] thus reconciling Raman scattering and thermodynamic measurements.

In addition to the pair-breaking features, the B_{1g} spectra show unexpected structures below $2\Delta_{\rm max}$ which, as opposed to the pair-breaking features, have a nearly resolution limited width and will be discussed in detail in the following section. Here we first wrap up observations of the energy gaps by Raman scattering in other compounds.

A pair-breaking peak was also observed in the A_{1g} spectrum of $\rm BaFe_2(As_{0.5}P_{0.5})_2$ [48] with the spectral weight decreasing linearly towards low frequencies indicating the presence of nodes in agreement with recent ARPES results for optimally doped $\rm BaFe_2(As_{0.65}P_{0.35})_2$ [207] but, at first glance, not with thermodynamic results on a material with comparable doping [208] (see table 2). However, the small value of the thermodynamically derived gap indicates a substantial anisotropy also for $\rm BaFe_2(As_{0.5}P_{0.5})_2$ which may be concealed by the notion of a single (average) gap.

Very recently, pair-breaking features were observed in $\rm CaKFe_4As_4$ [50, 51]. Depending on the incoming photon energy, gap features are observed either in all symmetries [50] or only in B_{1g} symmetry (1 Fe unit cell corresponding to B_{2g} in the 2 Fe cell used by Zhang *et al* [51]). The gap energies derived from the A_{1g} and B_{2g} (1 Fe) Raman data are compatible with those determined by ARPES [205] if the entire energy range given by Mou *et al* is considered (see also table 2). The B_{1g} maximum (1 Fe) appears at a substantially smaller energy, has a sharp onset and is clearly peaked [50]. Zhang *et al* [51] identify all features observed in B_{1g} symmetry with pair breaking while Jost *et al* [50], based on the results in three symmetries, propose that the B_{1g} peak at 134 $\rm cm^{-1}$ originates from a collective mode similar to that in slightly underdoped BKFA [41]. This—controversial—point of view would indicate a sub-leading interaction having $d_{x^2-y^2}$ symmetry which is to be discussed in more detail now.

6.2. Collective modes

The lowest order gap excitations in the electronic Raman spectra essentially reflect the magnitude of the energy gap.

Table 2. Compilation of gap energies in Fe-based superconductors as observed by angle-resolved photoemission (ARPES), tunneling (STS), optical (IR) and Raman spectroscopy. For selected cases we show also the results of thermodynamic measurements (c_{el}) and neutron scattering (INS) revealing local gap minima and, respectively, the spin resonance energy which are typically below the maximal gap. In the third last column the maximal gap of each method is given in units of $k_{\mathrm{B}}T_{\mathrm{c}}$. A similar compilation of the results and a discussion may be found in references [8, 193]. In particular in the case of ARPES but also for some of the thermodynamic and Raman measurements the entries are not exhaustive and display only typical values. In some Raman studies the data of B_{1g} symmetry were fitted using one, two or three gap scenarios as indicated. For four samples of BKFA the data of all symmetries were fitted simultaneously using a phenomenology including collective modes [41, 47]. In some cases the peak frequencies alone are reproduced. For the analysis of the IR spectra the theory by Mattis and Bardeen [136] was applied. The BFCA sample used for STS [194] had a nominal doping of $x = 0.10$ but the T_{c} is more compatible with optimal doping.

Material	T_{c} (K)	Method	$2\Delta_i$ (meV)	$2\Delta_i$ (cm^{-1})	$2\Delta_{\max}$ ($k_{\mathrm{B}}T_{\mathrm{c}}$)	Ref.	Comment
Ba(Fe$_{1-x}$Co$_x$)$_2$As$_2$							
$x = 0.051$	19	ARPES	8.0/11.6		7.1	[195]	el/h band
$x = 0.051$	18	Raman	3.7…7.4/9.9	40…60/80	6.4	[181]	B_{1g}/A_{1g} peaks
$x = 0.052$	20	c_{el}	3.1/7.1		4.1	[196]	Min/max gap
$x = 0.055$	20.5	Raman	5.0	41		[38]	B_{1g}; 1-gap
$x = 0.055$	23	Raman	8.7/12.4	65/105	5.9	[181]	B_{1g}/A_{1g} peaks
$x = 0.060$	24	Raman	4.1/9.3	33/75	4.5	[38]	B_{1g}; 2-gaps
$x = 0.061$	24	Raman	8.7/12.4	70/100	5.9	[25]	B_{1g}/A_{1g}; aniso.
$x = 0.060$	25	c_{el}	4.3/10.8		5.0	[196]	Min/max gap
$x = 0.065$	24.5	Raman	1.9/8.9	15/72	4.2	[38]	B_{1g}; 2-gaps
$x = 0.067$	25	INS	8.0 ± 1			[195]	Spin resonance
$x = 0.067$	25	ARPES	9.2/13.0		6.0	[195]	el/h band
$x = 0.075$	25.5	ARPES	10/13.8		6.2	[197]	el/h band; isotropic
$x = 0.075$	23.5	Raman	9.7	78	4.8	[38]	B_{1g}; 1-gap
$x = 0.085$	23	c_{el}	4.0/8.7		4.4	[196]	Min/max gap
$x = 0.085$	22	Raman	9.3/11.8	75/95	6.2	[25]	B_{1g}/A_{1g} peaks
$x = 0.095$	19	ARPES	9.2/11.2		6.8	[195]	el/h band
$x = 0.100$	25.3	STS	12.5 ± 3.0		5.7	[194]	Average; OPT?
$x = 0.100$	20	Raman	9.8	79	5.7	[38]	B_{1g}; 1-gap
Ba$_{1-x}$K$_x$Fe$_2$As$_2$							
$x = 0.22$	24.6	Raman	3.1…13.7	25…110	6.5	[41]	Only B_{1g} peaks
$x = 0.25$	26	ARPES	7.8/15.7		7.0	[198]	el/h bands
$x = 0.25$	31	c_{el}	1.9/16.0		6.0	[199]	Min/max gap
$x = 0.25$	31	Raman	6.0, 20.0	48, 161	7.5	[48]	B_{1g} peaks
$x = 0.25$	30.9	Raman	7.4, 18.6	60, 150 ± 20	7.0	[41]	B_{1g} peaks
$x = 0.27$	31	IR	13.7/27.1	110/218	10.1	[200]	Mattis–Bardeen
$x = 0.35$	38.9	Raman	9.9…31.8	80…256	9.5	[41]	Phenomenology
$x = 0.40$	38	INS	14			[192]	Spin resonance
$x = 0.40$	38	ARPES	12/24		7.5	[201]	Min/max gap
$x = 0.40$	38	ARPES	8/24		7.5	[202]	Min/max gap; k_z
$x = 0.40$	38	ARPES	7.2/20.4		6.2	[203]	Min/max gap; k_z
$x = 0.40$	37	STS	30		$\approx$9.4	[204]	
$x = 0.40$	39.0	IR	18.6/31.0	157/263	9.7	[200]	Mattis–Bardeen
$x = 0.40$	38.5	Raman	8.4…32.0	68…258	9.6	[46, 47]	Phenomenology
$x = 0.42$	38.5	c_{el}	2.3/24.2		7.3	[199]	Min/max gap
$x = 0.43$	36.7	Raman	6.2…31.0	50…250	9.8	[41]	Phenomenology
$x = 0.48$	34.3	Raman	4.0…20.0	32…161	6.8	[41]	Phenomenology
$x = 0.51$	34.2	c_{el}	2.1/17.7		6.0	[199]	Min/max gap
$x = 0.62$	26.6	Raman	7.4…13.7	60…110 ± 10	6.0	[41]	Peak energies
$x = 0.70$	22	c_{el}	2.1/9.1		4.8	[199]	Min/max gap
$x = 0.70$	21.6	Raman	6.2…11.2	50…90 ± 10	6.0	[41]	Peak energies
CaKFe$_4$As$_4$	35	ARPES	16/24		8.0	[205]	el/h band
CaKFe$_4$As$_4$	35	Raman	15.5/26.7	125/215	8.8	[50]	All symmetries
CaKFe$_4$As$_4$	35	Raman	13.6/16.8/20.2	110/135/162	6.7	[51]	B_{1g}; 3-gaps
BaFe$_2$(As$_{0.65}$P$_{0.35}$)$_2$	30	ARPES	4		3	[206]	Isotropic
BaFe$_2$(As$_{0.7}$P$_{0.3}$)$_2$	30	ARPES	12/15.2		5.9	[207]	Nodal gap
BaFe$_2$(As$_{0.5}$P$_{0.5}$)$_2$	18.2	c_{el}	4.8		3.1	[208]	Average gap
BaFe$_2$(P$_{0.5}$As$_{0.5}$)$_2$	16	Raman	6.7	54	4.9	[176]	B_{1g}
FeSe	9	STS	5.0/7.0		9.0	[209]	
FeSe	8.5	Raman	3.6/4.7	29…38	6.4	[53]	B_{1g}
FeSe	8.9	Raman	3.0…4.6	24…37	6.0	[57, 55]	B_{1g}

Yet, some caution is appropriate when numbers are to be derived (see table 2). Similar as in the ARPES or tunneling spectra neither the onset of the enhanced intensity nor the peak maxima are directly related to the gap 2Δ. Only in the clean limit, for $q = 0$, and an isotropic superconductor a square-root singularity is expected at 2Δ [73]. In all other cases the maximum is at higher energies [73, 74, 110, 112], and numbers can only be extracted via theoretical models. Specifically in multiband systems, such as the FeBCs or in the presence of higher order corrections (final state interactions), only a model analysis leads to useful conclusions as outlined in section 4.6. Yet, since a host of additional information can in principle be derived from the spectra in general and from higher order contributions specifically it is worth the effort.

There is general consensus that collective modes exist in at least some of the pnictides having sufficiently clean gaps [41, 46, 47, 49, 50]. Indications of collective modes were also reported for the chalcogenide $K_{0.75}Fe_{1.75}Se_2$ and discussed along with a theoretical model [58] but we are not aware of a comprehensive symmetry analysis or an in-depth study. Including this report, collective modes were observed mainly in B_{1g} (1 Fe) or B_{2g} (2 Fe) symmetry (which are equivalent). An A_{1g} collective mode, as predicted by Chubukov *et al* [90], was observed as part of a broad spectrum but not as an isolated line [49].

There is a lively discussion on how the collective modes are to be explained in terms of one of the essentially four possibilities (see also section 6.4): (i) amplitude (Higgs) fluctuations of the order parameter (ii) Leggett modes, (iii) fluctuation modes which become undamped in the presence of a gap and (vi) BS modes. Here, the distinction between particle–particle and particle–hole modes [49] was introduced only recently, and both of them were actually coined excitons in the original paper of Bardasis and Schrieffer [140]. We adopt this nomenclature in the following. The essential difference is that particle–particle and particle–hole bound states are expected for attractive and, respectively, repulsive contributions to an attractive pairing potential and vice versa. From an experimental point of view a distinction is difficult or impossible.

6.2.1. Amplitude fluctuations of the order parameter. Were discussed mainly for systems where superconductivity competes with other ordering phenomena such as a CDW [67, 94, 101] which break the particle–hole symmetry. Otherwise the coupling to the amplitude mode is weak [218]. Currently it is not clear whether or not amplitude fluctuations can be observed in the FeSCs. The only chance would be in $Ba_{1-x}K_xFe_2As_2$ below $x < 0.25$ where the gap is sufficiently clean and $T_{SDW} > T_c$. So far we are not aware of related reports.

6.2.2. Leggett modes. [95] were first discussed for MgB_2 [96, 97] where the intra-band interaction dominates and the Leggett modes are below the gap edge. In FeBCs there is a wide agreement that the intra-band interaction is weaker than the inter-band interaction [9, 219], and the Leggett modes are expected to be pushed towards the continuum and overdamped. They may contribute to the Raman intensity at the gap edge and are thus indistinguishable from the pair-breaking effect [98, 99]. Consequently, they are unlikely to augment the information derived from gap spectroscopies, although interesting conclusions about the pairing symmetry could be derived in special cases of chalcogenides without a central Fermi surface [100]. Here the Leggett modes are predicted to appear in B_{1g} symmetry, whereas, in the presence of a Fermi surface encircling the Γ point, as in all pnictides and in bulk FeSe, the Leggett modes are expected to be observed in A_{1g} symmetry [99]. This argument needs to be qualified if the orbital content of the bands is taken into account [98]. An experimental study thereof does not exist and seems difficult. Only resonance effects may be a viable approach.

6.2.3. Quadrupole modes. In $NaFe_{1-x}Co_xAs$, when excited with blue light (476 nm), a very strong and narrow B_{2g} mode (B_{1g} in the 1 Fe unit cell) appears below T_c at approximately 56 cm^{-1} close to the gap edge derived from ARPES [49]. As shown in figure 13, 56 cm^{-1} is close to the maximum of the fluctuation peak observed above T_c. The continuous temperature dependence across T_c, the narrowing below T_c and the independence of the mode energy of T_c support the interpretation in terms of a quadrupolar fluctuation of charges between the electron and hole bands which becomes undamped inside the superconducting gap.

In A_{1g} symmetry a broad peak is observed which cuts off softly below the maximum located at approximately 70 cm^{-1} thus indicating a finite density of states inside the gap. The maximum—as an integral part of the peak—is interpreted in terms of the particle–hole collective Bardasis–Schrieffer mode predicted by Chubukov, Eremin, and Korshunov [90] for the case of an $s_\pm$ ground state, where the gap has opposite sign on the electron and hole bands and an s_{++} subleading instability without a sign change induced by orbital fluctuations [143]. Since the relatively broad peak includes several excitations, the gap energy can be extracted only with difficulties from the smoothed A_{1g} spectra. For $x = 0.0175$ and 0.05 the humps on the high-energy side are close to the ARPES gaps.

The authors also used red photons (646 nm) for excitation but show only B_{2g} spectra, making a comparison with the spectra obtained for blue light less stringent. For 646 nm, the B_{2g} excitation at 56 cm^{-1} becomes much weaker in the underdoped range, $x \leqslant 0.0175$, and two new modes appear. These modes are compared to the BS mode in the A_{1g} spectrum measured with excitation at 476nm and are tentatively assigned to p–h and p–p collective modes without experimental substantiation or a phenomenological theory. Therefore, more work is needed to disentangle the complex but very interesting Raman spectra of $NaFe_{1-x}Co_xAs$.

Whereas the normal-state data of $NaFe_{1-x}Co_xAs$ are rather similar to those of BFCA several differences are observed below T_c. For instance, the gap anisotropy on the individual bands is larger in BFCA than in $NaFe_{1-x}Co_x$ as can be inferred from the Raman spectra [25, 38, 49] or, similarly, from other experiments [213, 220, 221]. Given the rather anisotropic gap in BFCA, it is not surprising that no sharp in-gap modes comparable to those in $NaFe_{1-x}Co_xAs$ are observed. On the other

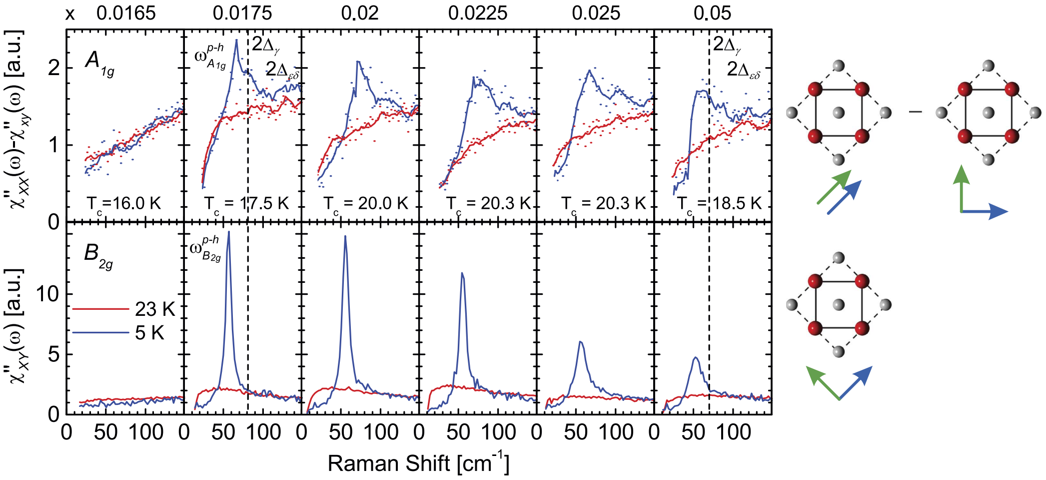

Figure 13. Raman susceptibilities of Na(Fe$_{1-x}$Co$_x$)As$_2$ in the normal (red) and superconducting (blue) states for excitation with blue photons (476 nm). Reprinted with permission from [49], Copyright (2016) by the American Physical Society. The pictograms were added by the authors for clarity. (a) $\chi''_{XX}(\omega)$-$\chi''_{xy}(\omega)$ (top row) and $\chi''_{XY}(\omega)$ (bottom row) in the superconducting (5 K) and normal (23 K) states at doping levels as indicated. The vertical dashed lines, shown for $x = 0.0175$ and 0.05, indicate the lowest superconducting gaps $2\Delta_\gamma \simeq 10$ meV and 9 meV, respectively, determined by ARPES. B_{2g} symmetry in the figure corresponds to B_{1g} used in this review.

hand, the peak maximum in B_{1g} symmetry is quite sharp in optimally doped BFCA and may be interpreted alternatively in terms of a nematic resonance near a quantum critical point [39, 116]. In BFCA, both the enhancement of the spectral weight of the B_{1g} pair-breaking peak upon approaching optimal doping, $x \approx 0.065$, and its scaling with the nematic response above T_c (figure 14) argue in favor of the nematic resonance. Yet, a similar doping dependence is also observed in A_{1g} symmetry and qualifies this conclusion [181].

Na111 and BFCA seem to be the two material classes with the strongest interaction between superconductivity and nematic fluctuations. In contrast, the fluctuations can hardly be observed in BKFA [48, 181] or CKFA [51], and a detailed comparison of these material classes seems highly desirable.

6.2.4. BS modes. Finally, we discuss the possibility of subleading pairing interactions having $d_{x^2-y^2}$ symmetry and the related BS modes inside the gap in the B_{1g} Raman spectra. The BS modes display various properties which distinguish them from other collective modes (see Equation (10)).

(a) In a clean gap the BS modes are resolution limited. The energy, $\Omega_{\rm BS}(T)$, is directly linked to the gap parameter [89], as opposed to the maximum of the pair-breaking peak $\Omega_{\rm pb}(T)$ which depends on both the gap $\Delta_{\rm max}(T)$ and the quasi-particle relaxation rate $\Gamma_{\rm qp}(T)$ as $\Omega_{\rm pb}(T) \approx 2\sqrt{|\Delta_{\rm max}(T)|^2 + \Gamma^2_{\rm qp}(T)}$ [110–113]. Thus the temperature dependence of the BS modes rather than that of $\Omega_{\rm pb}(T)$ is expected to be determined by that of the single particle gap, $\Omega_{\rm BS} \propto \Delta_{\rm max}(T)$.

(b) The BS mode drains spectral weight from the pair-breaking peak, but there is no sum rule. Rather, the intensity in the pair-breaking maximum is reduced rapidly, whereas the spectral weight in the BS mode increases first with increasing interaction strength λ_α, with α indexing the eigenvalues (see section 6.3), and then decreases towards zero [41]. In isotropic systems the intensity in the pair-breaking maximum is reduced in the entire energy range. In systems with anisotropic

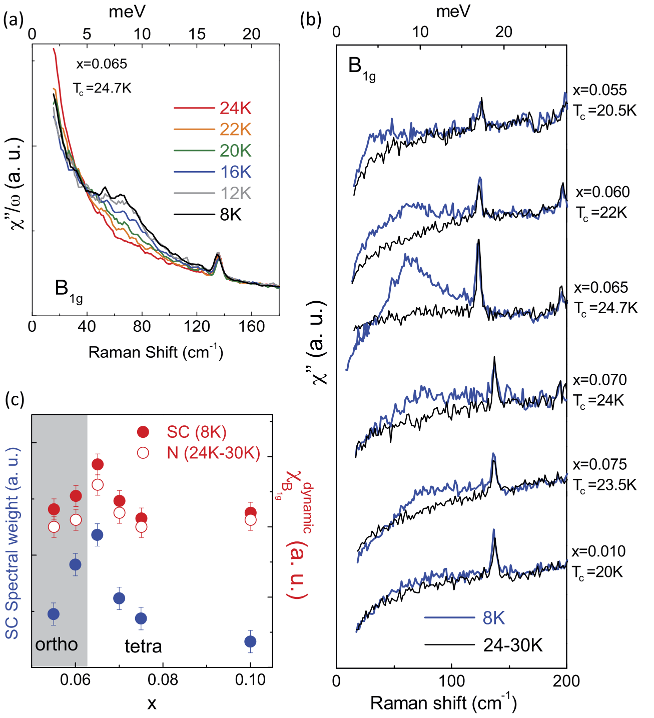

Figure 14. Doping dependence of the Raman spectra of Ba(Fe$_{1-x}$Co$_x$)$_2$As$_2$. (a) Evolution of the B_{1g} Raman conductivity χ''/ω across T_c for $x = 0.065$. (b) B_{1g} Raman response well below (blue) and right above T_c (black) as a function of Co doping as indicated. (c) Integrated SC spectral weight of the Raman response χ'' (blue) as a function of Co doping. The corresponding nematic susceptibilities $\chi^{\rm dynamic}_{B1g}$ both slightly above $T_{\rm c}$ (N) and well below T_c (SC) are also shown (open and, respectively, full red symbols). Reproduced from [116]. CC BY 4.0.

interactions $V_{\mathbf{k},\mathbf{k}'}$ only parts of the pair-breaking peak are depleted depending on the channel-specific components of $V_{\mathbf{k},\mathbf{k}'}$. This behavior can be modeled phenomenologically [47] or on the basis of the eigenvectors $g_\alpha(\mathbf{k})$ which determine the momentum dependence of the gap $\Delta_\alpha(\mathbf{k})$ and, to some extent, reflect the variation of $V_{\mathbf{k},\mathbf{k}'}$ by virtue of the BCS gap equation [41, 92].

(c) The binding energies of the BS modes, $E_{\mathrm{BS},\alpha} = 2\Delta_{\max} - \Omega_{\mathrm{BS},\alpha}$, are related to the coupling strengths of the sub-leading channels λ_α ($\alpha > 1$) with respect to that of the ground state λ_1. For $\lambda_1 \approx 1$ the relationship is given by $\sqrt{E_{\mathrm{BS},\alpha}/2\Delta_{\max}} \approx \lambda_\alpha/\lambda_1$ and is thus much simpler than that of the intensities [41].

All B_{1g} peaks observed in $\mathrm{Ba_{0.6}K_{0.4}Fe_2As_2}$ were suggested to be BS modes [46] following the phenomenology for anisotropic gaps proposed by Scalapino and Devereaux [91]. The detailed study of the temperature dependence performed later [47] is shown in figure 15 and requires this assignment to be revisited. The inset demonstrates the scaling of $\Omega_{\mathrm{BS}}(T)$ at 140 $\mathrm{cm^{-1}}$ and $\Delta_{\max}(T)$ as directly observed by ARPES [212], while the maximum at 170 $\mathrm{cm^{-1}}$ stays pinned. Apparently, the two strongest modes depend distinctly differently on temperature suggesting the mode at 170 $\mathrm{cm^{-1}}$ to be related to pair breaking and that at 140 $\mathrm{cm^{-1}}$ to a sub-leading channel. The comparison of all symmetries shows that intensity is in fact drained from the B_{1g} pair-breaking maximum although part of the peak survives indicating highly anisotropic interactions.

Maiti *et al* [92] pointed out that there may be more than one BS mode in the presence of a hierarchy of sub-leading coupling channels in addition to the $s_\pm$-wave ground state. Although there is a candidate peak at 70 $\mathrm{cm^{-1}}$ (see figure 15), this proposal can only be addressed by studying differently doped samples.

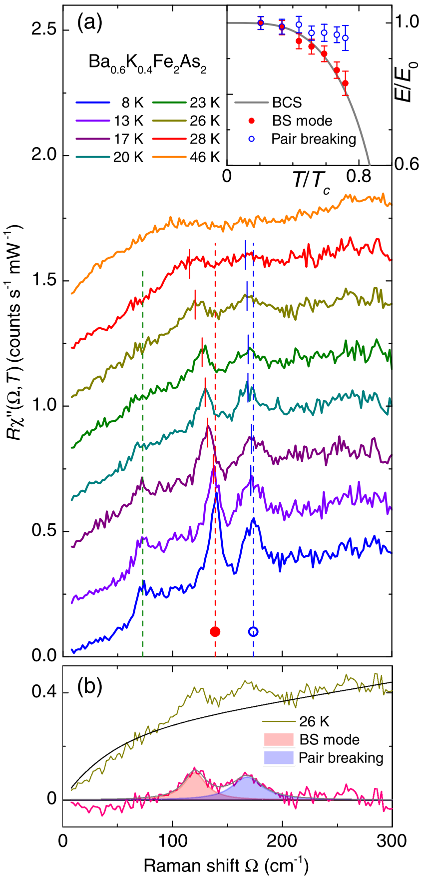

Figure 15. Temperature dependence of the Raman spectra of $\mathrm{Ba_{0.6}K_{0.4}Fe_2As_2}$ in $\mathrm{B_{1g}}$ symmetry. (a) The spectra measured above 8 K are consecutively shifted up by 0.2 units. The pair-breaking features (open symbols) and the collective mode (full circles) depend differently on temperature, as shown in the inset (where zero energy is suppressed). The pair-breaking maximum exhibits a temperature dependence which is different from the BCS prediction due to interaction effects. (b) The peak energies are determined by fitting the spectra with two Lorentzians and a smooth phenomenological background (black curve). Reproduced from [47]. CC BY 4.0.

6.3. Doping

Doping x or pressure P can be used as non-thermal control parameters in the context of quantum phase transitions. Here, doping x proves useful for the assignment of the in-gap modes and for scrutinizing the anisotropy of the pairing potential $V_{\mathbf{k},\mathbf{k}'}$ through the evolution with x of the related in-gap modes in BKFA. This will be the main focus of this subsection, but prior to this discussion the results on BFCA and BFAP will be summarized. For Na111 the reader is referred to section 6.2.

The parent compound Ba122 can be driven superconducting in various ways. Both chemical substitution, using isovalent phosphorus substitution for arsenic, and applied pressure lead to T_c values in the 30 K range [222, 223]. Currently there are no Raman studies of pressure-induced superconductivity in BFA. However, BFAP can be considered to fill this gap at least as a proxy [176]. For $x = 0.5$ BFAP has a T_c of 16 K and displays a broad pair-breaking peak in A_{1g} symmetry having a maximum at $\Omega_{\mathrm{pb}}(T) \approx 2\Delta_{\max} = 6.7$ meV or 4.9 $k_{\mathrm{B}}T_{\mathrm{c}}$ (see table 2 and section 6.1). The nearly linear energy dependence of the spectra below the peak maximum indicates a much broader gap distribution than in BKFA and suggests line nodes of the gap. If the peak is identified with the gap maximum of 4.9 $k_{\mathrm{B}}T_{\mathrm{c}}$, it falls below the ratio in the range of 6–8 $k_{\mathrm{B}}T_{\mathrm{c}}$ for other compounds [8]. There are no gap structures in the other symmetries and no collective modes in any symmetry. Thus from all aspects BFAP is closer to BFCA than BKFA.

Due to the doping dependent changes of the band structure, (π, π) scattering is expected to gain strength in BFCA in comparison to BKFA, and one would expect enhanced subdominant coupling channels. Rather, the anisotropy of the gaps grows, and the resulting density of states below the gap maximum leads to overdamping of potential in-gap modes similar to what has theoretically been shown to happen for d-wave gaps [120]. Therefore no collective modes can be resolved in BFCA, and the doping dependence is limited to intensity variations of the pair-breaking features described above. Consequently, only BKFA and the related CKFA [50] facilitate the study of changes of $V_{\mathbf{k},\mathbf{k}'}$ as a function of doping or, more appropriately, of the Fermi surface topology.

In what follows we assume that the modes observed below the maximal gap in BKFA are excitonic in origin [140]. This interpretation is not entirely accepted, although many criteria were tested experimentally (see above) and found to be in agreement with the theoretical prediction whereas counterarguments have not been presented yet. The doping dependence adds another piece of evidence to this assignment.

Although BKFA is superconducting for $0.1 < x \leqslant 1$ the range without magnetic order or changes of the Fermi surface topology is rather small, $0.25 < x < 0.6$. For $x < 0.25$ BKFA develops an SDW which gaps out part of the Fermi surface. For $x > 0.6$ the Fermi energy dives below the bottom of the inner electron band and for $x > 0.7$ hole-like bands appear around the X points [224]. It is still under debate which doping level should be associated with the Lifshitz transition but, as a matter of fact, one electron band is lost at $x \approx 0.6$.

The doping dependence of the Raman spectra in superconducting BKFA was studied by two groups. Wu and coworkers [48] looked at three doping levels, $x = 0.25$, 0.4, and 0.6 and, for $x = 0.4$, reproduced earlier results [46]. Three peaks were observed in B_{1g} symmetry at 50, 120, and 168 cm^{-1} and at 70, 140, and 172 cm^{-1} for the first and the second cleave, respectively, of the same crystal. Sample-dependent differences at optimal doping were also observed by Kretzschmar and collaborators [46] but the variations were much smaller, in particular the peak energies were nearly and the overall intensities entirely identical. We find it difficult to explain that the results obtained from two successive cleaves of the same crystal differ substantially, while the local T_c values or doping concentrations x are not reported to be different. For $x = 0.25$ Wu *et al* observe spectra which are qualitatively different from those at optimal doping and similar to what was found later by Böhm *et al* [41] in comparable samples. The spectra of Wu's overdoped BKFA, having nominally $x = 0.6$ and $T_\mathrm{c} = 25$ K, are closer to the results found for $x = 0.43, \ldots, 0.48$ in reference [41] although the T_c values differ by at least 10 K. An explanation of these discrepancies without directly comparing the magnetization measurements of the samples studied cannot be a subject of this review.

Regarding the experiments in the doping range $0.35 \leqslant x \leqslant 0.48$ studied in reference [41] only samples without indications of secondary transitions and with $\Delta T_\mathrm{c} < 1.3$ K were selected. In this relatively small doping range which is sufficiently far away from the SDW and from changes in the Fermi surface topology the Raman spectra of all symmetries depend continuously on x. The highest peak energies in all symmetries follow T_c to within ±12%. In general, the A_{1g} and B_{2g} energies are close to $(8 \pm 1)k_\mathrm{B}T_\mathrm{c}$ (see table 2) and thus higher than those in B_{1g} symmetry which scale roughly as $6.2k_\mathrm{B}T_\mathrm{c}$ as shown in figure 16 which displays raw and difference spectra in B_{1g} symmetry. There are two other maxima in B_{1g} symmetry at lower energy which are clearly resolved in all data sets and scale as $1 - x$ rather than T_c (figure 16(e)). The comparison of all symmetries and doping levels demonstrates that there are only very weak or no maxima in A_{1g} and B_{2g} symmetry in the range of the low-energy B_{1g} peaks. In addition, the low-energy peaks are nearly resolution limited and depend on temperature as $\Delta(T)$ [47].

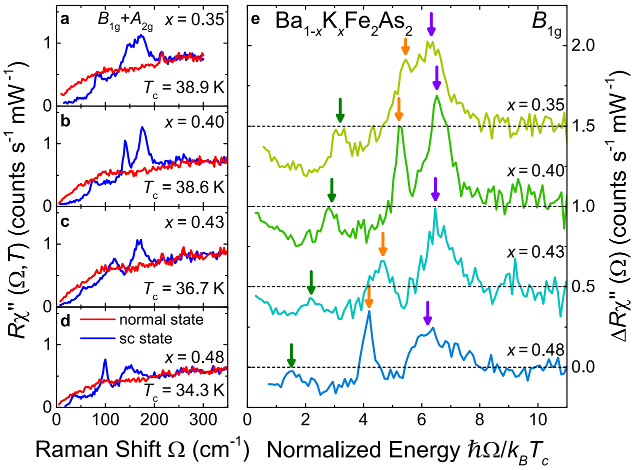

Figure 16. B_{1g} Raman spectra of BKFA for doping levels as indicated. (a)–(d) Raw data (after division by the Bose–Einstein factor) slightly above (red) and well below T_c (blue). (e) Difference spectra $\Delta R\chi''(\Omega) = R\chi''(\Omega, T \approx 8\mathrm{K}) - R\chi''(\Omega, T \gtrsim T_\mathrm{c})$. Here all temperature independent features drop out. Apparently, there are no temperature-dependent phonons. As an artifact, the intensity becomes negative inside the gap. Zero-intensity is indicated by horizontal lines (dashes). Reproduced from [41]. CC BY 4.0.

For $0.35 \leqslant x \leqslant 0.48$ the spectra of all symmetries can be described consistently [41] in terms of the phenomenology outlined in reference [91] and further elaborated on by Böhm *et al* [47] for $x = 0.4$. This approach starts from a realistic electronic structure [11], and the doping is accounted for by a shift of the Fermi energy. The Raman vertices are derived from the band structure (see equation (12)–(14)). The A_{1g} and B_{2g} spectra are used for determining the band and momentum dependent gap values compatible with ARPES studies. After some iterations the bare B_{1g} spectra (without final state interaction) become consistent with the experimental B_{1g} spectra. Here, consistent does not mean that the entire B_{1g} spectra can be reproduced. Rather, there are three features which by no combination of gaps can be explained: the two sharp lines below the gap edge and the missing intensity above the B_{1g} pair-breaking maximum which is expected according to the A_{1g} and B_{2g} spectra. With the final state interaction 'switched on' this part of the calculated B_{1g} spectrum is suppressed and reappears in the narrow modes. An explicit calculation was performed only for the stronger mode which was then found to acquire too much spectral weight for the coupling strength λ_d derived from the energy position (see equation (10)).

This discrepancy was solved later when theoretical considerations suggested the existence of two sub-leading channels rather than one [41, 92]. The two sub-leading channels ($\alpha = 2, 3$ ordered by strength) were derived from two independent microscopic approaches and were found to have second and first order $d_{x^2-y^2}$ (B_{1g}) symmetry (see figure 6 center). Having the higher binding energy $E_{\mathrm{BS}(2)} > E_{\mathrm{BS}(3)}$ the intensity of the BS mode at lower absolute energy (higher binding energy) is much smaller but still high enough for being the strongest spectral feature in the respective energy range. Unfortunately, the gap energies of the outer hole bands are in the same range [199], motivating Wu *et al* to assign the mode to that gap at $x = 0.4$ [176]. Yet, both the phenomenology and the experimental results in A_{1g} and B_{2g} symmetry show that the B_{1g} mode is at least an order of magnitude too strong for justifying an explanation in terms of direct gap excitations [41] thus furnishing further evidence for the excitonic character of the two narrow in-gap modes.

Very recently, CKFA was studied. CKFA is a stoichiometric version of BKFA since the Ca and K layers alternate in a regular fashion for the substantial size difference of the Ca and K ions. From the viewpoint of valence count CKFA should be slightly overdoped, and the T_c values are indeed close to the maximum found for BKFA. The ARPES [205] and Raman experiments [50, 51] find gaps similar to those of BKFA. The features appearing below T_c are relatively strong in B_{1g} symmetry. In A_{1g} and B_{2g} symmetry they are weak and can only be observed for $\hbar\omega_I = 2.16$ eV [50] but not for $\hbar\omega_I = 1.92$ eV [51]. The weak structures in A_{1g} and B_{2g} symmetry are compatible with the gaps derived from ARPES. The B_{1g} spectra have substructures similar to those found for $x = 0.35$ in BKFA. There is agreement that the mode at 134 cm^{-1} may be a collective excitation and that the hump at 160 cm^{-1} is a remainder from pair breaking. The very weak structure at 50 cm^{-1}, tentatively assigned to a second BS mode in reference [50], remains controversial.

Even though there is no full agreement among the experimental groups about the details of the interpretation and, in particular, the doping dependence in BKFA, the question arises as to whether or not the idea of competing pairing channels may be a relevant contribution from Raman scattering to directly support the microscopic considerations. For addressing this question the hierarchy of pairing interactions was studied.

6.4. Possible conclusions for Cooper pairing

In conventional superconductors, the ground state has a much lower energy than potential competing pairing tendencies. Unconventional superconductors have typically various instabilities in close proximity, all of which may be intertwined with Cooper pairing. The ways to study the related phase diagrams include Hubbard-like models [143], the spin-fluctuation scenario which is studied in the random phase approximation (RPA) [9, 225], and the functional renormalization group (fRG) scheme [12, 210, 226, 227] which, as opposed to RPA, treats all possible interactions on equal footing.

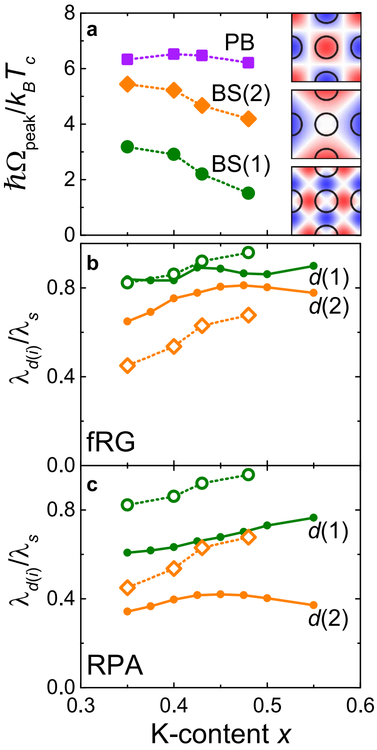

Figure 17. Doping dependence of the pairing strength in BKFA. (a) The positions of the pair-breaking maxima scale approximately as T_c whereas the energies of the BS modes decrease monotonously with increasing doping in the range $0.35 \leqslant x \leqslant 0.48$ indicating increasing coupling in the sub-leading channels. The insets show the eigenvectors $g_\alpha(\mathbf{k})$ of the three channels. (b) and (c) The coupling strength of the two sub-leading $d_{x^2-y^2}$-wave channels relative to the $s_\pm$-wave ground state, $\lambda_{d(i)}/\lambda_s$ (s, $d(1)$, and $d(2)$ correspond to $\alpha = 1, 2$, and 3, respectively), is predicted to increase with doping (full symbols) in qualitative agreement with experiment (open symbols). $\lambda_{d(i)}/\lambda_s$ is derived from the binding energies in (a) as described in section 6.2. The results on the basis of fRG and RPA are similar. Reproduced from [41]. CC BY 4.0.

In contrast to the Hubbard–Holstein model, which predicts an s_{++} ground state [143], both RPA and fRG find an $s_\pm$ ground state for the specific band structure of the FeBCs where the energy gap has the same magnitude on the electron and hole bands but opposite sign [9, 12, 210, 226, 227]. Upon using a realistic band structure [11] and a rigid band model for simulating the doping, the hierarchy of pairing interactions was studied with RPA and fRG schemes. The results are similar in both cases and show that the ground state has $s_\pm$ symmetry followed by two $d_{x^2-y^2}$ pairing tendencies. The solution of the eigenvalue equations yields the eigenvectors $g_\alpha(\mathbf{k})$ and eigenvalues λ_α in channel α. $g_\alpha(\mathbf{k})$ and λ_α describe the variation with $\mathbf{k}$ of the energy gap and, respectively, the coupling strength in channel α. On this basis the positions of the BS modes can be predicted and compared with the experiments as shown in figure 17.

The agreement of experiment and theory is remarkable in the case of fRG and still qualitative for RPA. The RPA results are offset to lower coupling strengths by 10%–20%. Since RPA neglects contributions other than spin-fluctuations, the observed discrepancy may indicate the existence of weak contributions from other coupling mechanisms such as charge fluctuations [41]. Yet, the similarity of the fRG and RPA results for the hierarchy of pairing channels supports spin-fluctuation-induced superconductivity in BKFA in the doping range studied. CKFA appears to fit into this picture although the weakness of the putative low-energy BS mode, the proximity of the second BS mode to the pair-breaking maximum [50], and the resulting controversy in the interpretation [51] qualify this conclusion and call for further experiments.

Whereas the recent RPA and fRG studies favor spin fluctuations, an $s_{\pm}$-wave gap and two sub-leading pairing channels having $d_{x^2-y^2}$ symmetry, the Hubbard–Holstein model leads to different conclusions and finds an s_{++} ground state driven by electron–phonon coupling and orbital fluctuations [143]. For the construction of the model sub-leading channels were not identified. However, if the sub-leading interactions in this model would be identified to have $d_{x^2-y^2}$ symmetry the resulting Raman spectra would be indistinguishable from those observed in BKFA and CKFA. Thus the case for spin fluctuation induced pairing depends crucially on the reliability of the hierarchy of pairing tendencies derived from fRG and RPA. Other experimental probes such as the study of quasi-particle interference effects in magnetic fields [191] or in the presence of impurities [228, 229] by scanning tunneling spectroscopy may help to clarify the symmetry of the ground state.

7. Conclusions

Raman scattering in iron pnictides and chalcogenides has provided a host of information on the electronic, magnetic and lattice properties of these systems. We focused on the spin and charge degrees of freedom in this review.

In all cases the spectra consist of a superposition of several types of excitations. To which extent *luminescence* (as an *a priori* undesired contribution) plays a role is not entirely clear, but the comparison of a large amount of results shows that luminescence decreases substantially with improved sample quality and may be neglected at least at low energies.

Particle–hole excitations are important in all compounds and for all doping levels. They are partially gapped out in the SDW state (section 5.2) where the materials remain metallic and are fully gapped out, for instance, in superconducting BKFA when the surfaces are sufficiently clean (see section 6.1 and reference [46]). In the normal state, the particle–hole excitations in A_{1g} symmetry depend on temperature as expected from the static resistivity (cf figure 10(d)).

In B_{1g} symmetry, a strong contribution from *fluctuations* (see section 5.3) is observed below room temperature at energies of order k_BT which softens with decreasing temperature, has the strongest spectral weight directly at the structural transition T_S, and loses intensity below T_S without, however vanishing so long as the material does not order magnetically. Raman scattering is particularly useful here since other spectroscopies have generic difficulties in observing the fluctuations: in the case of neutron scattering, the fluctuations appear only in the notoriously weak four-particle correlation, and NMR spectroscopy covers only a small energy range well below k_BT. The same holds true for thermodynamic methods [230] or transport measurements [231] both of which probe fluctuations only indirectly. We argue that the temperature dependence identifies the Raman response as critical fluctuations which are expected to vanish at the related transition temperature. The persistence of the excitations below T_S is therefore considered an indication of spin rather than charge fluctuations. Yet, there is no consensus in the published literature on this point. However, if the controversy was settled the driving force behind the phase transitions could be identified.

In all pnictides, the response of the spin density wave (SDW) is clearly observed (section 5.2). Although the gap energies are in the range 6–8 k_BT_{SDW}, the spectra are by and large described by weak-coupling physics including band reconstruction in the ordered state. This indicates that the magnetism here results from a Fermi surface instability of itinerant electrons. The relevant gap energies are in the range 100–150 meV in the parent compounds and decrease with doping or substitution along with the gradual suppression of the magnetically ordered phase.

In the chalcogenide Fe(Se$_{1-x}$S$_x$) the B_{1g} response is distinctly different from that in the pnictides at all temperatures [55, 57]. In the range 60 meV, a broad excitation is observed for $x \lesssim 0.2$ which gains spectral weight by a factor of approximately two upon cooling without moving by more than a few percent. This temperature (and doping) dependence is not expected for quasi-particle scattering from impurities. Rather, the peak was associated with *two-magnon excitations of nearly localized moments in a frustrated magnet* (see sections 5.1 and 5.4) in agreement with neutron scattering experiments [157], LDA predictions for the exchange parameters J_1 and J_2 [170], and simulations using exact diagonalization [55, 171]. The response from fluctuations entirely fills the gap below 60 meV in the temperature range around T_S and persists down to $T \approx 20$ K. Indications of an SDW were not found. It is argued that orbital dependent localization of electrons as expected in Hund's metals with $J \sim U$ may be at the origin of this dichotomy between the pnictides and chalcogenides [149, 156].

In the *superconducting state gap excitations* are observed in all sufficiently clean systems independent of the concentration of substitutional atoms (see section 6.1). Only Co substitution gradually suppresses the pair-breaking features. In all FeBCs there is a strong band dependence of the gaps. In FeSe the gap can be resolved in the Raman spectra but its small magnitude prevents a reliable analysis. In BFCA, the gaps on the electron bands exhibit a strong modulation with momentum and may even have accidental nodes at optimal doping. Here, Raman scattering and transport measurements arrive at similar conclusions [25, 36, 217]. In BKFA and presumably CKFA, the gaps on the individual bands are nearly constant. This fact, first derived from ARPES [205, 212], manifests itself in sharp gap edges in the Raman spectra.

Below the gap edges narrow, nearly *resolution-limited lines* are observed in the B_{1g} spectra of BKFA [47] (see sections 6.2 and 6.3). These lines display a BCS-like temperature dependence, vary as $1-x$ with doping and steal spectral weight from the pair-breaking features. The pair-breaking features scale with T_c and barely depend on temperature. These criteria are predicted only for BS modes that result from sub-leading pairing interactions competing with the ground state.

Microscopic model calculations using fRG and RPA (see section 6.4) show that the pnictides have indeed a hierarchy of pairing channels with very similar eigenvalues, an $s_{\pm}$ ground state, and two sub-leading $d_{x^2-y^2}$ instabilities of different order [41]. The Raman experiments agree semi-quantitatively with these predictions concerning doping dependence but cannot pin down the sign change of the ground state. Tunneling experiments in samples with different impurity concentration [232] and with applied field [191] or RIXS experiments [233] may settle this point. Yet, the doping dependence of the sub-leading channels in BKFA and presumably the results in CKFA as well make a strong case for spin fluctuations to contribute partially or predominantly to the Cooper pairing in the pnictides.

In summary, the most significant contributions from light scattering experiments to the physics of the FeBCs pertain to the analysis of fluctuations and of the superconducting pairing states. The fluctuations can be compared to the evolution of the elasticity [116, 181] and of the spin-lattice relaxation as obtained from NMR studies [49]. While the interrelation of the various methods is obvious several aspects of the interpretation remain controversial, in particular the origin of the fluctuations. Concerning superconductivity the derivation of the gap energies is of specific relevance. Table 2 shows that the results from light scattering fit very well into the concert of the other methods if the data are read properly. Reading properly means, in particular, understanding the respective observables and including collective excitations which reveal details of the pairing potential $V_{\mathbf{k},\mathbf{k}'}$. In many cases the Raman response contributes information which cannot easily or not at all be obtained by other methods. Thus, part of the understanding of the pnictides and chalcogenides may rest on light scattering results, in particular if the remaining challenges in the interpretation can be settled. Additional insight is expected from novel x-ray techniques [124] which may help to settle, e.g., the sign problem of the order parameter [233] and from experiments under extreme conditions, specifically pressure. Here, the problem of the luminescence in the diamond anvils is a particular challenge if continuous spectra rather than narrow phonon lines have to be analyzed quantitatively.

Acknowledgments

We gratefully acknowledge discussions with A Baum, L Benfatto, G Blumberg, A Chubukov, T P Devereaux, Y Gallais, M Grilli, W Hanke, F Hardy, P Hirschfeld, D Jost, M Khodas, S Lederer, S Maiti, C Meingast, B Moritz, Z V Popović, R Thomale, and I Tüttő. Financial support came from the German Research Foundation (DFG) via the Priority Program SPP1458 (Grant-no Ha2071/7), the Transregional Collaborative Research Center TRR80 (Project ID 107745057), from the Serbian Ministry of Education, Science and Technological Development under Project III45018 and by the Science Fund of the Republic of Serbia (Project 'StrainedFe'). We acknowledge support by the DAAD through the bilateral project between Serbia and Germany (Grant Numbers 57335339 and 57449106).

ORCID iDs

R Hackl https://orcid.org/0000-0002-6751-0879

References

[1] Kamihara Y, Hiramatsu H, Hirano M, Kawamura R, Yanagi H, Kamiya T and Hosono H 2006 *J. Am. Chem. Soc.* **128** 10012

[2] Kamihara Y, Watanabe T, Hirano M and Hosono H 2008 *J. Am. Chem. Soc.* **130** 3296

[3] Paglione J and Greene R L 2010 *Nat. Phys.* **6** 645

[4] Johnston D C 2010 *Adv. Phys.* **59** 803

[5] Stewart G R 2011 *Rev. Mod. Phys.* **83** 1589

[6] Hirschfeld P J, Korshunov M M and Mazin I I 2011 *Rep. Prog. Phys.* **74** 125508

[7] Hirschfeld P J 2016 *Compt. Rendus Phys.* **17** 197

[8] Korshunov M M 2018 *Phys. Rev.* B **98** 104510

[9] Mazin I I, Singh D J, Johannes M D and Du M H 2008 *Phys. Rev. Lett.* **101** 057003

[10] Kordyuk A A, Zabolotnyy V B, Evtushinsky D V, Yaresko A N, Büchner B and Borisenko S V 2013 *J. Supercond. Nov. Magnetism* **26** 2837

[11] Graser S, Maier T, Hirschfeld P and Scalapino D 2009 *New J. Phys.* **11** 025016

[12] Thomale R, Platt C, Hanke W and Bernevig B A 2011 *Phys. Rev. Lett.* **106** 187003

[13] Böhm T 2017 The case for spin-fluctuation induced pairing in $Ba_{1-x}K_xFe_2As_2$ *PhD Thesis* (Technische Universität München)

[14] Fernandes R M, Chubukov A V and Schmalian J 2014 *Nat. Phys.* **10** 97

[15] Massat P, Quan Y, Grasset R, Méasson M A, Cazayous M, Sacuto A, Karlsson S, Strobel P, Toulemonde P, Yin Z and Gallais Y 2018 *Phys. Rev. Lett.* **121** 077001

[16] Hadjiev V G, Iliev M N, Sasmal K, Sun Y Y and Chu C W 2008 *Phys. Rev.* B **77** 220505

[17] Litvinchuk A P, Hadjiev V G, Iliev M N, Lv B, Guloy A M and Chu C W 2008 *Phys. Rev.* B **78** 060503

[18] Rahlenbeck M, Sun G L, Sun D L, Lin C T, Keimer B and Ulrich C 2009 *Phys. Rev.* B **80** 064509

[19] Um Y J, Park J T, Min B H, Song Y J, Kwon Y S, Keimer B and Le Tacon M 2012 *Phys. Rev.* B **85** 012501

[20] Lazarević N, Popović Z V, Hu R and Petrovic C 2011 *Phys. Rev.* B **83** 024302

[21] Lazarević N, Abeykoon M, Stephens P W, Lei H, Bozin E S, Petrovic C and Popović Z V 2012 *Phys. Rev.* B **86** 054503

[22] Zhang A M, Liu K, Xiao J H, He J B, Wang D M, Chen G F, Normand B and Zhang Q M 2012 *Phys. Rev.* B **85** 024518

[23] Rotter M, Tegel M and Johrendt D 2008 *Phys. Rev. Lett.* **101** 107006

[24] Sefat A S, Jin R, McGuire M A, Sales B C, Singh D J and Mandrus D 2008 *Phys. Rev. Lett.* **101** 117004

[25] Muschler B, Prestel W, Hackl R, Devereaux T P, Analytis J G, Chu J H and Fisher I R 2009 *Phys. Rev.* B **80** 180510

[26] Chauvière L, Gallais Y, Cazayous M, Méasson M A, Sacuto A, Colson D and Forget A 2011 *Phys. Rev.* B **84** 104508

[27] Sugai S, Mizuno Y, Watanabe R, Kawaguchi T, Takenaka K, Ikuta H, Takayanagi Y, Hayamizu N and Sone Y 2012 *J. Phys. Soc. Japan* **81** 024718

[28] Chu J H, Analytis J G, Greve K D, McMahon P L, Islam Z, Yamamoto Y and Fisher I R 2010 *Science* **329** 824

[29] Choi K Y, Lemmens P, Eremin I, Zwicknagl G, Berger H, Sun G L, Sun D L and Lin C T 2010 *J. Phys.: Condens. Matter.* **22** 115802

[30] Gallais Y, Fernandes R M, Paul I, Chauvière L, Yang Y X, Méasson M A, Cazayous M, Sacuto A, Colson D and Forget A 2013 *Phys. Rev. Lett.* **111** 267001

[31] Okazaki K, Sugai S, Niitaka S and Takagi H 2011 *Phys. Rev.* B **83** 035103

[32] Sugai S, Mizuno Y, Watanabe R, Kawaguchi T, Takenaka K, Ikuta H, Kiho K, Nakajima M, Lee C H, Iyo A, Eisaki H and Uchida S 2013 *J. Supercond. Nov. Magnetism* **26** 1179

[33] Zhang W L, Richard P, Ding H, Sefat A S, Gillett J, Sebastian S E, Khodas M and Blumberg G 2014 On the origin of the electronic anisotropy in iron pnicitde superconductors (arXiv:1410.6452)

[34] Zhang W L, Yin Z P, Ignatov A, Bukowski Z, Karpinski J, Sefat A S, Ding H, Richard P and Blumberg G 2016 *Phys. Rev.* B **93** 205106

[35] Kaneko U F, Gomes P F, García-Flores A F, Yan J Q, Lograsso T A, Barberis G E, Vaknin D and Granado E 2017 *Phys. Rev.* B **96** 014506

[36] Mazin I I, Devereaux T P, Analytis J G, Chu J H, Fisher I R, Muschler B and Hackl R 2010 *Phys. Rev.* B **82** 180502

[37] Sugai S, Mizuno Y, Kiho K, Nakajima M, Lee C H, Iyo A, Eisaki H and Uchida S 2010 *Phys. Rev.* B **82** 140504

[38] Chauvière L, Gallais Y, Cazayous M, Méasson M A, Sacuto A, Colson D and Forget A 2010 *Phys. Rev.* B **82** 180521

[39] Gallais Y, Paul I, Chauvière L and Schmalian J 2016 *Phys. Rev. Lett.* **116** 017001

[40] Kretzschmar F, Böhm T, Karahasanović U, Muschler B, Baum A, Jost D, Schmalian J, Caprara S, Grilli M, Di Castro C, Analytis J H, Chu J H, Fisher I R and Hackl R 2016 *Nat. Phys.* **12** 560

[41] Böhm T, Kretzschmar F, Baum A, Rehm M, Jost D, Hosseinian Ahangharnejhad R, Thomale R, Platt C, Maier T A, Hanke W, Moritz B, Devereaux T P, Scalapino D J, Maiti S, Hirschfeld P J, Adelmann P, Wolf T, Wen H H and Hackl R 2018 *npj Quant. Mater.* **3** 48

[42] Kumar P, Muthu D V S, Harnagea L, Wurmehl S, Buchner B and Sood A K 2014 *J. Phys.: Condens. Matter.* **26** 305403

[43] Yang Y X, Gallais Y, Rullier-Albenque F, Méasson M A, Cazayous M, Sacuto A, Shi J, Colson D and Forget A 2014 *Phys. Rev.* B **89** 125130

[44] Kaneko U F, Piva M M, Jesus C, Saleta M, Urbano R, Pagliuso P G and Granado E 2019 *J. Phys.: Condens. Matter.* **31** 495402

[45] Wu S F, Zhang W L, Li L, Cao H, Kung H H, Sefat A, Ding H, Richard P and Blumberg G 2017 On the origin of critical nematic fluctuations in pnictide superconductors (arXiv:1712.06066)

[46] Kretzschmar F, Muschler B, Böhm T, Baum A, Hackl R, Wen H H, Tsurkan V, Deisenhofer J and Loidl A 2013 *Phys. Rev. Lett.* **110** 187002

[47] Böhm T, Kemper A F, Moritz B, Kretzschmar F, Muschler B, Eiter H M, Hackl R, Devereaux T P, Scalapino D J and Wen H H 2014 *Phys. Rev.* X **4** 041046

[48] Wu S F, Richard P, Ding H, Wen H H, Tan G, Wang M, Zhang C, Dai P and Blumberg G 2017 *Phys. Rev.* B **95** 085125

[49] Thorsmølle V K, Khodas M, Yin Z P, Zhang C, Carr S V, Dai P and Blumberg G 2016 *Phys. Rev.* B **93** 054515

[50] Jost D, Scholz J R, Zweck U, Meier W R, Böhmer A E, Canfield P C, Lazarević N and Hackl R 2018 *Phys. Rev.* B **98** 020504

[51] Zhang W L, Meier W R, Kong T, Canfield P C and Blumberg G 2018 *Phys. Rev.* B **98** 140501

[52] Okazaki K, Sugai S, Niitaka S and Takagi H 2011 *Phys. Rev.* B **83** 035103

[53] Massat P, Farina D, Paul I, Karlsson S, Strobel P, Toulemonde P, Méasson M A, Cazayous M, Sacuto A, Kasahara S, Shibauchi T, Matsuda Y and Gallais Y 2016 *Proc. Natl Acad. Sci.* **113** 9177

[54] Glamazda A, Lemmens P, Ok J M, Kim J S and Choi K Y 2019 *Phys. Rev.* B **99** 075142

[55] Baum A, Ruiz H N, Lazarević N, Wang Y, Böhm T, Hosseinian Ahangharnejhad R, Adelmann P, Wolf T, Popović Z V, Moritz B, Devereaux T P and Hackl R 2019 *Commun. Phys.* **2** 14

[56] Kumar P, Kumar A, Saha S, Muthu D, Prakash J, Patnaik S, Waghmare U, Ganguli A and Sood A 2010 *Solid State Commun.* **150** 557

[57] Zhang W L, Wu S F, Kasahara S, Shibauchi T, Matsuda Y and Blumberg G 2017 Stripe quadrupole order in the nematic phase of FeSe$_{1-x}$ S$_x$ (arXiv:1710.09892)

[58] Khodas M, Chubukov A V and Blumberg G 2014 *Phys. Rev.* B **89** 245134

[59] Zhang A M, Xiao J H, Li Y S, He J B, Wang D M, Chen G F, Normand B, Zhang Q M and Xiang T 2012 *Phys. Rev.* B **85** 214508

[60] Fleury P A, Porto S P S, Cheesman L E and Guggenheim H J 1966 *Phys. Rev. Lett.* **17** 84

[61] Lyons K B, Sulewski P E, Fleury P A, Carter H L, Cooper A S, Espinosa G P, Fisk Z and Cheong S W 1989 *Phys. Rev.* B **39** 9693

[62] Fleury P A and Loudon R 1968 *Phys. Rev.* **166** 514

[63] Devereaux T P and Hackl R 2007 *Rev. Mod. Phys.* **79** 175

[64] Chen C C, Jia C J, Kemper A F, Singh R R P and Devereaux T P 2011 *Phys. Rev. Lett.* **106** 067002

[65] Baum A, Milosavljević A, Lazarević N, Radonjić M M, Nikolić B, Mitschek M, Maranloo Z I, Šćepanović M, Grujić-Brojčin M, Stojilović N, Opel M, Wang A, Petrovic C, Popović Z V and Hackl R 2018 *Phys. Rev.* B **97** 054306

[66] Abrikosov A A and Fal'kovskii L A 1961 *Zh. Eksp. Teor. Fiz.* **40** 262
Abrikosov A A and Fal'kovskii L A 1961 *Sov. Phys - JETP* **13** 179

[67] Sooryakumar R and Klein M V 1980 *Phys. Rev. Lett.* **45** 660

[68] Dierker S B, Klein M V, Webb G W and Fisk Z 1983 *Phys. Rev. Lett.* **50** 853

[69] Hackl R, Kaiser R and Schicktanz S 1983 *J. Phys. C: Solid State Phys.* **16** 1729

[70] Cooper S L, Klein M V, Pazol B G, Rice J P and Ginsberg D M 1988 *Phys. Rev.* B **37** 5920

[71] Hackl R, Gläser W, Müller P, Einzel D and Andres K 1988 *Phys. Rev.* B **38** 7133

[72] Abrikosov A and Genkin V 1973 *Zh. Eksp. Teor. Fiz.* **65** 842
Abrikosov A and Genkin V 1974 *Sov. Phys - JETP* **38** 417

[73] Klein M V and Dierker S B 1984 *Phys. Rev.* B **29** 4976

[74] Devereaux T P, Einzel D, Stadlober B, Hackl R, Leach D H and Neumeier J J 1994 *Phys. Rev. Lett.* **72** 396

[75] Chandrasekhar M, Cardona M and Kane E O 1977 *Phys. Rev.* B **16** 3579–95

[76] Ipatova I, Subashiev A and Voitenko V 1981 *Solid State Commun.* **37** 893

[77] Zawadowski A and Cardona M 1990 *Phys. Rev.* B **42** 10732

[78] Staufer T, Hackl R and Müller P 1990 *Solid State Commun.* **75** 975

[79] Slakey F, Klein M V, Rice J P and Ginsberg D M 1991 *Phys. Rev.* B **43** 3764

[80] Hackl R, Opel M, Müller P F, Krug G, Stadlober B, Nemetschek R, Berger H and Forró L 1996 *J. Low Temp. Phys.* **105** 733

[81] Opel M, Nemetschek R, Hoffmann C, Philipp R, Müller P F, Hackl R, Tüttő I, Erb A, Revaz B, Walker E, Berger H and Forró L 2000 *Phys. Rev.* B **61** 9752

[82] Einzel D and Hackl R 1996 *J. Raman Spectrosc.* **27** 307

[83] Caprara S, Di Castro C, Grilli M and Suppa D 2005 *Phys. Rev. Lett.* **95** 117004

[84] Tassini L, Venturini F, Zhang Q M, Hackl R, Kikugawa N and Fujita T 2005 *Phys. Rev. Lett.* **95** 117002

[85] Klein A, Lederer S, Chowdhury D, Berg E and Chubukov A 2018 *Phys. Rev.* B **97** 155115

[86] Klein A, Lederer S, Chowdhury D, Berg E and Chubukov A 2018 *Phys. Rev.* B **98** 041101

[87] Udina M, Grilli M, Benfatto L and Chubukov A V 2020 *Phys. Rev. Lett.* **120** 197602

[88] Zawadowski A, Ruvalds J and Solana J 1972 *Phys. Rev.* A **5** 399

[89] Monien H and Zawadowski A 1990 *Phys. Rev.* B **41** 8798–810

[90] Chubukov A V, Eremin I and Korshunov M M 2009 *Phys. Rev.* B **79** 220501

[91] Scalapino D J and Devereaux T P 2009 *Phys. Rev.* B **80** 140512

[92] Maiti S, Maier T A, Böhm T, Hackl R and Hirschfeld P J 2016 *Phys. Rev. Lett.* **117** 257001

[93] Littlewood P B and Varma C M 1981 *Phys. Rev. Lett.* **47** 811

[94] Littlewood P B and Varma C M 1982 *Phys. Rev.* B **26** 4883

[95] Leggett A J 1966 *Prog. Theor. Phys.* **36** 901

[96] Blumberg G, Mialitsin A, Dennis B S, Klein M V, Zhigadlo N D and Karpinski J 2007 *Phys. Rev. Lett.* **99** 227002

[97] Klein M V 2010 *Phys. Rev.* B **82** 014507

[98] Burnell F J, Hu J, Parish M M and Bernevig B A 2010 *Phys. Rev.* B **82** 144506

[99] Cea T and Benfatto L 2016 *Phys. Rev.* B **94** 064512

[100] Huang W, Sigrist M and Weng Z Y 2018 *Phys. Rev.* B **97** 144507

[101] Méasson M A, Gallais Y, Cazayous M, Clair B, Rodière P, Cario L and Sacuto A 2014 *Phys. Rev.* B **89** 060503

[102] Pekker D and Varma C 2015 *Annu. Rev. Condens. Matter Phys.* **6** 269

[103] Hackl R, Kaiser R and Gläser W 1989 *Physica* C **162-164** 431

[104] Kendziora C and Rosenberg A 1995 *Phys. Rev.* B **52** 9867

[105] Chen X K, Naeini J G, Hewitt K C, Irwin J C, Liang R and Hardy W N 1997 *Phys. Rev.* B **56** R513

[106] Sugai S and Hosokawa T 2000 *Phys. Rev. Lett.* **85** 1112

[107] Le Tacon M, Sacuto A, Georges A, Kotliar G, Gallais Y, Colson D and Forget A 2006 *Nat. Phys.* **2** 537

[108] Munnikes N, Muschler B, Venturini F, Tassini L, Prestel W, Ono S, Ando Y, Peets D C, Hardy W N, Liang R, Bonn D A, Damascelli A, Eisaki H, Greven M, Erb A and Hackl R 2011 *Phys. Rev.* B **84** 144523

[109] Li Y, Le Tacon M, Matiks Y, Boris A V, Loew T, Lin C T, Chen L, Chan M K, Dorow C, Ji L, Barišić N, Zhao X, Greven M and Keimer B 2013 *Phys. Rev. Lett.* **111** 187001

[110] Devereaux T P 1992 *Phys. Rev.* B **45** 12965

[111] Devereaux T P 1993 *Phys. Rev.* B **47** 5230

[112] Devereaux T P 1995 *Phys. Rev. Lett.* **74** 4313

[113] Manske D 2004 *Theory of Unconventional Superconductors* (Springer Tracts in Modern Physics 202) (Heidelberg: Springer)

[114] Caprara S, Colonna M, Di Castro C, Hackl R, Muschler B, Tassini L and Grilli M 2015 *Phys. Rev.* B **91** 205115

[115] Karahasanovic U, Kretzschmar F, Böhm T, Hackl R, Paul I, Gallais Y and Schmalian J 2015 *Phys. Rev.* B **92** 075134

[116] Gallais Y and Paul I 2016 *Compt. Rendus Phys.* **17** 113

[117] Boyd G R, Devereaux T P, Hirschfeld P J, Mishra V and Scalapino D J 2009 *Phys. Rev.* B **79** 174521

[118] Khodas M and Levchenko A 2015 *Phys. Rev.* B **91** 235119

[119] Hayes W and Loudon R 2005 *Scattering of Light by Crystals* (New York: Dover)

[120] Devereaux T P and Einzel D 1995 *Phys. Rev.* B **51** 16336

[121] Kosztin J and Zawadowski A 1991 *Solid State Commun.* **78** 1029

[122] Freericks J K, Devereaux T P, Moraghebi M and Cooper S L 2005 *Phys. Rev. Lett.* **94** 216401

[123] Salpeter E E and Bethe H A 1951 *Phys. Rev.* **84** 1232–42

[124] Ament L J P, van Veenendaal M, Devereaux T P, Hill J P and van den Brink J 2011 *Rev. Mod. Phys.* **83** 705–67

[125] Pines D and Nozières P 1966 *The Theory of Quantum Liquids: Normal Fermi Liquids* (Reading, MA: Benjamin)

[126] Maiti S, Chubukov A V and Hirschfeld P J 2017 *Phys. Rev.* B **96** 014503

[127] Platzman P M 1965 *Phys. Rev.* **139** A379

[128] Kostur V N 1992 *Z. Phys. B Condens. Matter* **89** 149–59

[129] Devereaux T P, Virosztek A and Zawadowski A 1996 *Phys. Rev.* B **54** 12523

[130] Muschler B, Prestel W, Tassini L, Hackl R, Lambacher M, Erb A, Komiya S, Ando Y, Peets D, Hardy W, Liang R and Bonn D 2010 *Eur. Phys. J. Spec. Top.* **188** 131

[131] Hackl R and Kaiser R 1988 *J. Phys. C: Solid State Phys.* **21** L453

[132] Cuk T, Lu D H, Zhou X J, Shen Z X, Devereaux T P and Nagaosa N 2005 *Phys. Status Solidi* b **242** 11

[133] Inosov D S, Borisenko S V, Eremin I, Kordyuk A A, Zabolotnyy V B, Geck J, Koitzsch A, Fink J, Knupfer M, Büchner B, Berger H and Follath R 2007 *Phys. Rev.* B **75** 172505

[134] Prestel W, Venturini F, Muschler B, Tüttő I, Hackl R, Lambacher M, Erb A, Komiya S, Ono S, Ando Y, Inosov D, Zabolotnyy V B and Borisenko S V 2010 *Eur. Phys. J. Spec. Top.* **188** 163

[135] Tsuneto T 1960 *Phys. Rev.* **118** 1029–35

[136] Mattis D C and Bardeen J 1958 *Phys. Rev.* **111** 412

[137] Eiter H M, Lavagnini M, Hackl R, Nowadnick E A, Kemper A F, Devereaux T P, Chu J H, Analytis J G, Fisher I R and Degiorgi L 2013 *Proc. Natl. Acad. Sci.* **110** 64

[138] Shastry B S and Shraiman B I 1990 *Phys. Rev. Lett.* **65** 1068

[139] Varma C M 2002 *J. Low Temp. Phys.* **126** 901

[140] Bardasis A and Schrieffer J R 1961 *Phys. Rev.* **121** 1050–62

[141] Greytak T J and Yan J 1969 *Phys. Rev. Lett.* **22** 987

[142] Suhl H, Matthias B T and Walker L R 1959 *Phys. Rev. Lett.* **3** 552

[143] Kontani H and Onari S 2010 *Phys. Rev. Lett.* **104** 157001

[144] Weidinger S A and Zwerger W 2015 *Eur. Phys. J.* B **88** 237

[145] Podolsky D, Auerbach A and Arovas D P 2011 *Phys. Rev.* B **84** 174522

[146] Gazit S, Podolsky D and Auerbach A 2013 *Phys. Rev. Lett.* **110** 140401

[147] Chelwani N, Baum A, Böhm T, Opel M, Venturini F, Tassini L, Erb A, Berger H, Forró L and Hackl R 2018 *Phys. Rev.* B **97** 024407

[148] de' Medici L, Hassan S R, Capone M and Dai X 2009 *Phys. Rev. Lett.* **102** 126401

[149] Yin Z P, Haule K and Kotliar G 2011 *Nat. Mater.* **10** 932

[150] Leonov I, Skornyakov S L, Anisimov V I and Vollhardt D 2015 *Phys. Rev. Lett.* **115** 106402

[151] Knoll P, Thomsen C, Cardona M and Murugaraj P 1990 *Phys. Rev.* B **42** 4842

[152] Devereaux T P and Kampf A P 1999 *Phys. Rev.* B **59** 6411

[153] Moritz B, Johnston S, Devereaux T P, Muschler B, Prestel W, Hackl R, Lambacher M, Erb A, Komiya S and Ando Y 2011 *Phys. Rev.* B **84** 235114

[154] Jia C J, Nowadnick E A, Wohlfeld K, Kung Y F, Chen C C, Johnston S, Tohyama T, Moritz B and Devereaux T P 2014 *Nat. Commun.* **5** 3314

[155] Georges A, de' Medici L and Mravlje J 2013 *Annu. Rev. Condens. Matter Phys.* **4** 137

[156] Si Q, Yu R and Abrahams E 2016 *Nat. Rev. Mater.* **1** 16017

[157] Wang Q, Shen Y, Pan B, Zhang X, Ikeuchi K, Iida K, Christianson A D, Walker H C, Adroja D T, Abdel-Hafiez M, Chen X, Chareev D A, Vasiliev A N and Zhao J 2016 *Nat. Commun.* **7** 12182

[158] Skornyakov S L, Anisimov V I, Vollhardt D and Leonov I 2017 *Phys. Rev.* B **96** 035137

[159] Sulewski P E, Fleury P A, Lyons K B and Cheong S W 1991 *Phys. Rev. Lett.* **67** 3864

[160] Venturini F, Michelucci U, Devereaux T P and Kampf A P 2000 *Phys. Rev.* B **62** 15204

[161] Aslamasov L G and Larkin A I 1968 *Sov. Phys. Solid State* **10** 875

[162] Fernandes R M and Schmalian J 2012 *Supercond. Sci. Technol.* **25** 084005

[163] Yamakawa Y, Onari S and Kontani H 2016 *Phys. Rev.* X **6** 021032

[164] Chubukov A V, Khodas M and Fernandes R M 2016 *Phys. Rev.* X **6** 041045

[165] Classen L, Xing R Q, Khodas M and Chubukov A V 2017 *Phys. Rev. Lett.* **118** 037001

[166] Fanfarillo L, Benfatto L and Valenzuela B 2018 *Phys. Rev.* B **97** 121109

[167] Allen P B 1976 *Phys. Rev.* B **13** 1416

[168] Baek S H, Efremov D V, Ok J M, Kim J S, van den Brink J and Büchner B 2014 *Nat. Mater.* **14** 210

[169] Yi M, Lu D, Chu J H, Analytis J G, Sorini A P, Kemper A F, Moritz B, Mo S K, Moore R G, Hashimoto M, Lee W S, Hussain Z, Devereaux T P, Fisher I R and Shen Z X 2011 *Proc. Natl Acad. Sci.* **108** 6878

[170] Glasbrenner J K, Mazin I I, Jeschke H O, Hirschfeld P J, Fernandes R M and Valentí R 2015 *Nat. Phys.* **11** 953

[171] Ruiz H, Wang Y, Moritz B, Baum A, Hackl R and Devereaux T P 2019 *Phys. Rev.* B **99** 125130

[172] Baum A, Li Y, Tomić M, Lazarević N, Jost D, Löffler F, Muschler B, Böhm T, Chu J H, Fisher I R, Valentí R, Mazin I I and Hackl R 2018 *Phys. Rev.* B **98** 075113

[173] Fernandes R M, Chubukov A V, Knolle J, Eremin I and Schmalian J 2012 *Phys. Rev.* B **85** 024534

[174] Kontani H, Saito T and Onari S 2011 *Phys. Rev.* B **84** 024528

[175] Gnezdilov V, Pashkevich Y G, Lemmens P, Wulferding D, Shevtsova T, Gusev A, Chareev D and Vasiliev A 2013 *Phys. Rev.* B **87** 144508

[176] Wu S F, Zhang W L, Hu D, Kung H H, Lee A, Mao H C, Dai P C, Ding H, Richard P and Blumberg G 2016 Collective excitations of dynamic Fermi surface deformations in $\mathrm{BaFe_2(As_{0.5}P_{0.5})_2}$ (arXiv:1607.06575)

[177] Yamase H and Zeyher R 2011 *Phys. Rev.* B **83** 115116

[178] Yamase H and Zeyher R 2013 *Phys. Rev.* B **88** 125120

[179] Yoshizawa M, Kimura D, Chiba T, Simayi S, Nakanishi Y, Kihou K, Lee C H, Iyo A, Eisaki H, Nakajima M and Uchida S i 2012 *J. Phys. Soc. Japan* **81** 024604

[180] Kontani H and Yamakawa Y 2014 *Phys. Rev. Lett.* **113** 047001

[181] Böhm T, Hosseinian Ahangharnejhad R, Jost D, Baum A, Muschler B, Kretzschmar F, Adelmann P, Wolf T, Wen H H, Chu J H, Fisher I R and Hackl R 2017 *Phys. Status Solidi* b **254** 1600308

[182] Sun J P, Matsuura K, Ye G Z, Mizukami Y, Shimozawa M, Matsubayashi K, Yamashita M, Watashige T, Kasahara S, Matsuda Y, Yan J Q, Sales B C, Uwatoko Y, Cheng J G and Shibauchi T 2016 *Nat. Commun.* **7** 12146

[183] Jia C, Wohlfeld K, Wang Y, Moritz B and Devereaux T P 2016 *Phys. Rev.* X **6** 021020

[184] de la Cruz C, Huang Q, Lynn J W, Li J, Ratcliff II W, Zarestky J L, Mook H A, Chen G F, Luo J L, Wang N L and Dai P 2008 *Nature* **453** 899

[185] Chu J H, Analytis J G, Kucharczyk C and Fisher I R 2009 *Phys. Rev.* B **79** 014506

[186] Yi M, Liu Z K, Zhang Y, Yu R, Zhu J X, Lee J, Moore R, Schmitt F, Li W, Riggs S, Chu J H, Lv B, Hu J, Hashimoto M, Mo S K, Hussain Z, Mao Z, Chu C, Fisher I, Si Q, Shen Z X and Lu D 2015 *Nat. Commun.* **6** 7777

[187] Coldea A I, Blake S F, Kasahara S, Haghighirad A A, Watson M D, Knafo W, Choi E S, McCollam A, Reiss P, Yamashita T, Bruma M, Speller S C, Matsuda Y, Wolf T, Shibauchi T and Schofield A J 2019 *npj Quant. Mater.* **4** 2

[188] Yi M, Zhang Y, Shen Z X and Lu D 2017 *npj Quant. Mater.* **2** 57

[189] Yao D W and Li T 2019 *Europhys. Lett.* **125** 37002

[190] Bardeen J, Cooper L N and Schrieffer J R 1957 *Phys. Rev.* **106** 162

[191] Hanaguri T, Niitaka S, Kuroki K and Takagi H 2010 *Science* **328** 474

[192] Christianson A D, Goremychkin E A, Osborn R, Rosenkranz S, Lumsden M D, Malliakas C D, Todorov I S, Claus H, Chung D Y, Kanatzidis M G, Bewley R I and Guidi T 2008 *Nature* **456** 930

[193] Korshunov M M, Shestakov V A and Togushova Y N 2017 *J. Magn. Magn Mater.* **440** 133

[194] Yin Y, Zech M, Williams T L, Wang X F, Wu G, Chen X H and Hoffman J E 2009 *Phys. Rev. Lett.* **102** 097002

[195] Wang M, Yi M, Sun H L, Valdivia P, Kim M G, Xu Z J, Berlijn T, Christianson A D, Chi S, Hashimoto M, Lu D H, Li X D, Bourret-Courchesne E, Dai P, Lee D H, Maier T A and Birgeneau R J 2016 *Phys. Rev.* B **93** 205149

[196] Hardy F, Burger P, Wolf T, Fisher R A, Schweiss P, Adelmann P, Heid R, Fromknecht R, Eder R, Ernst D, von Löhneysen H and Meingast C 2010 *Europhys. Lett.* **91** 47008

[197] Terashima K, Sekiba Y, Bowen J H, Nakayama K, Kawahara T, Sato T, Richard P, Xu Y M, Li L J, Cao G H, Xu Z A, Ding H and Takahashi T 2009 *Proc. Natl Acad. Sci.* **106** 7330

[198] Nakayama K, Sato T, Richard P, Xu Y M, Kawahara T, Umezawa K, Qian T, Neupane M, Chen G F, Ding H and Takahashi T 2011 *Phys. Rev.* B **83** 020501

[199] Hardy F, Böhmer A E, de' Medici L, Capone M, Giovannetti G, Eder R, Wang L, He M, Wolf T, Schweiss P, Heid R, Herbig A, Adelmann P, Fisher R A and Meingast C 2016 *Phys. Rev.* B **94** 205113

[200] Xu B, Dai Y M, Xiao H, Shen B, Wen H H, Qiu X G and Lobo R P S M 2017 *Phys. Rev.* B **96** 115125

[201] Ding H, Richard P, Nakayama K, Sugawara K, Arakane T, Sekiba Y, Takayama A, Souma S, Sato T, Takahashi T, Wang Z, Dai X, Fang Z, Chen G F, Luo J L and Wang N L 2008 *Europhys. Lett.* **83** 47001

[202] Zhang Y, Yang L X, Chen F, Zhou B, Wang X F, Chen X H, Arita M, Shimada K, Namatame H, Taniguchi M, Hu J P, Xie B P and Feng D L 2010 *Phys. Rev. Lett.* **105** 117003

[203] Evtushinsky D V, Zabolotnyy V B, Kim T K, Kordyuk A A, Yaresko A N, Maletz J, Aswartham S, Wurmehl S, Boris A V, Sun D L, Lin C T, Shen B, Wen H H, Varykhalov A, Follath R, Büchner B and Borisenko S V 2014 *Phys. Rev.* B **89** 064514

[204] Wray L, Qian D, Hsieh D, Xia Y, Li L, Checkelsky J G, Pasupathy A, Gomes K K, Parker C V, Fedorov A V, Chen G F, Luo J L, Yazdani A, Ong N P, Wang N L and Hasan M Z 2008 *Phys. Rev.* B **78** 184508

[205] Mou D, Kong T, Meier W R, Lochner F, Wang L L, Lin Q, Wu Y, Bud'ko S L, Eremin I, Johnson D D, Canfield P C and Kaminski A 2016 *Phys. Rev. Lett.* **117** 277001

[206] Shimojima T, Sakaguchi F, Ishizaka K, Ishida Y, Kiss T, Okawa M, Togashi T, Chen C T, Watanabe S, Arita M, Shimada K, Namatame H, Taniguchi M, Ohgushi K, Kasahara S, Terashima T, Shibauchi T, Matsuda Y, Chainani A and Shin S 2011 *Science* **332** 564

[207] Zhang Y, Ye Z R, Ge Q Q, Chen F, Jiang J, Xu M, Xie B P and Feng D L 2012 *Nat. Phys.* **8** 371

[208] Diao Z, Campanini D, Fang L, Kwok W K, Welp U and Rydh A 2016 *Phys. Rev.* B **93** 014509

[209] Kasahara S, Watashige T, Hanaguri T, Kohsaka Y, Yamashita T, Shimoyama Y, Mizukami Y, Endo R, Ikeda H, Aoyama K, Terashima T, Uji S, Wolf T, von Löhneysen H, Shibauchi T and Matsuda Y 2014 *Proc. Natl Acad. Sci.* **111** 16309

[210] Thomale R, Platt C, Hu J, Honerkamp C and Bernevig B A 2009 *Phys. Rev.* B **80** 180505

[211] Thomale R, Platt C, Hanke W, Hu J and Bernevig B A 2011 *Phys. Rev. Lett.* **107** 117001

[212] Evtushinsky D V, Inosov D S, Zabolotnyy V B, Koitzsch A, Knupfer M, Büchner B, Viazovska M S, Sun G L, Hinkov V, Boris A V, Lin C T, Keimer B, Varykhalov A, Kordyuk A A and Borisenko S V 2009 *Phys. Rev.* B **79** 054517

[213] Tanatar M A, Ni N, Martin C, Gordon R T, Kim H, Kogan V G, Samolyuk G D, Bud'ko S L, Canfield P C and Prozorov R 2009 *Phys. Rev.* B **79** 094507

[214] Tanatar M A, Ni N, Thaler A, Bud'ko S L, Canfield P C and Prozorov R 2010 *Phys. Rev.* B **82** 134528

[215] Hirschfeld P 2009 *J. Phys.* **2** 100

[216] Muschler B 2012 Carrier dynamics of $\mathrm{Ba(Fe_{1-x}Co_x)_2As_2}$ as a function of doping *PhD Thesis* (Technical University Munich)

[217] Tanatar M A, Reid J P, Shakeripour H, Luo X G, Doiron-Leyraud N, Ni N, Bud'ko S L, Canfield P C, Prozorov R and Taillefer L 2010 *Phys. Rev. Lett.* **104** 067002

[218] Cea T, Castellani C and Benfatto L 2016 *Phys. Rev.* B **93** 180507

[219] Boeri L, Dolgov O V and Golubov A A 2008 *Phys. Rev. Lett.* **101** 026403

[220] Liu C, Palczewski A D, Dhaka R S, Kondo T, Fernandes R M, Mun E D, Hodovanets H, Thaler A N, Schmalian J, Bud'ko S L, Canfield P C and Kaminski A 2011 *Phys. Rev.* B **84** 020509

[221] Ge Q Q, Ye Z R, Xu M, Zhang Y, Jiang J, Xie B P, Song Y, Zhang C L, Dai P and Feng D L 2013 *Phys. Rev.* X **3** 011020

[222] Colombier E, Bud'ko S L, Ni N and Canfield P C 2009 *Phys. Rev.* B **79** 224518

[223] Analytis J G, Kuo H H, McDonald R D, Wartenbe M, Rourke P M C, Hussey N E and Fisher I R 2014 *Nat. Phys.* **10** 194

[224] Xu N, Richard P, Shi X, van Roekeghem A, Qian T, Razzoli E, Rienks E, Chen G F, Ieki E, Nakayama K, Sato T, Takahashi T, Shi M and Ding H 2013 *Phys. Rev.* B **88** 220508

[225] Maier T A, Graser S, Scalapino D J and Hirschfeld P J 2009 *Phys. Rev.* B **79** 224510

[226] Chubukov A V, Efremov D V and Eremin I 2008 *Phys. Rev.* B **78** 134512

[227] Platt C, Hanke W and Thomale R 2014 *Adv. Phys.* **62** 453–562

[228] Hirschfeld P J, Altenfeld D, Eremin I and Mazin I I 2015 *Phys. Rev.* B **92** 184513

[229] Böker J, Volkov P A, Hirschfeld P J and Eremin I 2019 *New J. Phys.* **21** 083021

[230] Böhmer A E and Meingast C 2016 *Compt. Rendus Phys.* **17** 90

[231] Chu J H, Kuo H H, Analytis J G and Fisher I R 2012 *Science* **337** 710–2

[232] Martiny J H J, Kreisel A, Hirschfeld P J and Andersen B M 2017 *Phys. Rev.* B **95** 184507

[233] Marra P, van den Brink J and Sykora S 2016 *Sci. Rep.* **6** 25386

Lattice dynamics and phase transitions in $Fe_{3-x}GeTe_2$

A. Milosavljević,[1] A. Šolajić,[1] S. Djurdjić-Mijin,[1] J. Pešić,[1] B. Višić,[1] Yu Liu (刘育),[2] C. Petrovic,[2]
N. Lazarević,[1] and Z. V. Popović[1,3]
[1]*Center for Solid State Physics and New Materials, Institute of Physics Belgrade, University of Belgrade, Pregrevica 118, 11080 Belgrade, Serbia*
[2]*Condensed Matter Physics and Materials Science Department, Brookhaven National Laboratory, Upton, New York 11973-5000, USA*
[3]*Serbian Academy of Sciences and Arts, Knez Mihailova 35, 11000 Belgrade, Serbia*

(Received 23 April 2019; published 17 June 2019)

We present Raman spectroscopy measurements of the van der Waals bonded ferromagnet $Fe_{3-x}GeTe_2$, together with lattice dynamics. Four out of eight Raman active modes are observed and assigned, in agreement with numerical calculations. The energies and linewidths of the observed modes display an unconventional temperature dependence at about 150 and 220 K, followed by the nonmonotonic evolution of the Raman continuum. Whereas the former can be related to the magnetic phase transition, the origin of the latter anomaly remains an open question.

DOI: 10.1103/PhysRevB.99.214304

I. INTRODUCTION

A novel class of magnetism hosting van der Waals bonded materials has recently become of great interest, since the materials are suitable candidates for numbers of technical applications [1–5]. Whereas $CrXTe_3$ (X = Si, Ge, Sn) and CrX_3 (X = Cl, Br, I) classes maintain low phase transition temperatures [1,6–9] even in a monolayer regime [10], $Fe_{3-x}GeTe_2$ has a high bulk transition temperature, between 220 and 230 K [11,12], making it a promising applicant.

The $Fe_{3-x}GeTe_2$ crystal structure consists of $Fe_{3-x}Ge$ sublayers stacked between two sheets of Te atoms, and a van der Waals gap between neighboring Te layers [13,14]. Although the structure contains two different types of Fe atoms, it is revealed that vacancies take place only in the Fe2 sites [13,15].

Neutron diffraction, thermodynamic and transport measurements, and Mössbauer spectroscopy were used to analyze the magnetic and functional properties of $Fe_{3-x}GeTe_2$, with an Fe atom deficiency of $x \approx 0.1$ and $T_C = 225$ K. It is revealed that at a temperature of 1.5 K, magnetic moments of $1.95(5)\mu_B$ and $1.56(4)\mu_B$ are directed along the easy magnetic c axes [16]. In chemical vapor transport (CVT) grown Fe_3GeTe_2 single crystals, besides the ferromagnetic (FM)-paramagnetic (PM) transition at a temperature of 214 K, FM layers order antiferromagnetically at 152 K [17]. Close to a ferromagnetic transition temperature of 230 K, a possible Kondo lattice behavior, i.e., coupling of traveling electrons and periodically localized spins, is indicated at $T_K = 190 \pm 20$ K, which is in good agreement with theoretical predictions of 222 K [18].

Lattice parameters, as well as the magnetic transition temperature, vary with Fe ion concentration. Lattice parameters a and c follow the opposite trend, whereas the Curie temperature T_C decreases with an increase of Fe ion concentration [15]. For flux-grown crystals, the critical behavior was investigated by bulk dc magnetization around the ferromagnetic phase transition temperature of 152 K [13]. The anomalous Hall effect was also studied, where a significant amount of defects produces bad metallic behavior [19].

Theoretical calculations predict a dynamical stability of Fe_3GeTe_2 single-layer, uniaxial magnetocrystalline anisotropy that originates from spin-orbit coupling [20]. Recently, anomalous Hall effect measurements on single-crystalline metallic Fe_3GeTe_2 nanoflakes with different thicknesses are reported, with a T_C near 200 K and strong perpendicular magnetic anisotropy [21].

We report $Fe_{3-x}GeTe_2$ single-crystal lattice dynamic calculations, together with Raman spectroscopy measurements. Four out of eight Raman active modes were observed and assigned. Phonon energies are in a good agreement with theoretical predictions. Analyzed phonon energies and linewidths reveal fingerprint of a ferromagnetic phase transition at a temperature around 150 K. Moreover, discontinuities in the phonon properties are found at temperatures around 220 K. Consistently, in the same temperature range, the Raman continuum displays nonmonotonic behavior.

II. EXPERIMENT AND NUMERICAL METHOD

$Fe_{3-x}GeTe_2$ single crystals were grown by the self-flux method as previously described [13]. Samples for scanning electron microscopy (SEM) were cleaved and deposited on graphite tape. Energy dispersive spectroscopy (EDS) maps were collected using a FEI Helios NanoLab 650 instrument equipped with an Oxford Instruments EDS system, equipped with an X-max SSD detector operating at 20 kV. The surface of the as-cleaved $Fe_{3-x}GeTe_2$ crystal appears to be uniform for several tens of microns in both directions, as shown in Fig. 4 of Appendix A. Additionally, the elemental composition maps of Fe, Ge, and Te show a distinctive homogeneity of all the three elements (Fig. 5 of Appendix A).

For Raman scattering experiments, a Tri Vista 557 spectrometer was used in the backscattering micro-Raman configuration. As an excitation source, a solid state laser with a 532 nm line was used. In our scattering configuration, the plane of incidence is the ab plane, where $|a| = |b|$ ($\measuredangle(a, b) = 120^\circ$), with the incident (scattered) light propagation direction

TABLE I. Top panel: The type of atoms, Wyckoff positions, each site's contribution to the phonons in the Γ point, and corresponding Raman tensors for the $P6_3/mmc$ space group of $Fe_{3-x}GeTe_2$. Bottom panel: Phonon symmetry, calculated optical Raman active phonon frequencies (in cm^{-1}) for the magnetic (M) phase, and experimental values for Raman active phonons at 80 K.

Space group $P6_3/mmc$ (No. 194)

Fe1 (4*e*)	$A_{1g} + E_{1g} + E_{2g} + A_{2u} + E_{1u}$
Fe2 (2*c*)	$E_{2g} + A_{2u} + E_{1u}$
Ge (2*d*)	$E_{2g} + A_{2u} + E_{1u}$
Te (2*c*)	$A_{1g} + E_{1g} + E_{2g} + A_{2u} + E_{1u}$

Raman tensors

$$A_{1g} = \begin{pmatrix} a & 0 & 0 \\ 0 & a & 0 \\ 0 & 0 & b \end{pmatrix} \qquad E_{1g} = \begin{pmatrix} 0 & 0 & -c \\ 0 & 0 & c \\ -c & c & 0 \end{pmatrix} \qquad E_{2g} = \begin{pmatrix} d & -d & 0 \\ -d & -d & 0 \\ 0 & 0 & 0 \end{pmatrix}$$

Raman active modes

Symmetry	Calculations (M)	Experiment (M)
E_{2g}^1	50.2	
E_{1g}^1	70.3	
E_{2g}^2	122.2	89.2
A_{1g}^1	137.2	121.1
E_{1g}^2	209.5	
E_{2g}^3	228.6	214.8
A_{1g}^2	233.4	239.6
E_{2g}^4	334.3	

along the *c* axes. Samples were cleaved in the air, right before being placed in the vacuum. All the measurements were performed in the high vacuum (10^{-6} mbar) using a KONTI CryoVac continuous helium flow cryostat with a 0.5 mm thick window. To achieve laser beam focusing, a microscope objective with ×50 magnification was used. A Bose factor correction of all spectra was performed. More details can be found in Appendix C.

Density functional theory (DFT) calculations were performed with the QUANTUM ESPRESSO (QE) software package [22]. We used the projector augmented-wave (PAW) pseudopotentials [23,24] with the Perdew-Burke-Ernzerhof (PBE) exchange-correlation functional [25]. The electron wave function and charge density cutoffs of 64 and 782 Ry were chosen, respectively. The *k* points were sampled using the Monkhorst-Pack scheme, with an 8 × 8 × 4 Γ-centered grid. Both magnetic and nonmagnetic calculations were performed, using the experimentally obtained lattice parameters and the calculated values obtained by relaxing the theoretically proposed structure. In order to obtain the lattice parameters accurately, a treatment of the van der Waals interactions is introduced. The van der Waals interaction was included in all calculations using the Grimme-D2 correction [26]. Phonon frequencies in the Γ point are calculated within the linear response method implemented in QE.

III. RESULTS AND DISCUSSION

$Fe_{3-x}GeTe_2$ crystallizes in a hexagonal crystal structure, described with the $P6_3/mmc$ (D_{6h}^4) space group. The atom type, site symmetry, each site's contribution to the phonons in the Γ point, and corresponding Raman tensors for the $P6_3/mmc$ space group are presented in Table I.

Calculated displacement patterns of Raman active modes, which can be observed in our scattering configuration, are presented in Fig. 1(a). Since the Raman tensor of the E_{1g} mode contains only the *z* component (Table I), by selection rules, it cannot be detected when measuring from the *ab* plane in the backscattering configuration. Whereas A_{1g} modes include vibrations of Fe and Te ions along the *c* axis, E_{2g} modes include in-plane vibrations of all four atoms. The Raman spectra of $Fe_{3-x}GeTe_2$ in the magnetic phase (M), at 80 K, and nonmagnetic phase (NM), at 280 K, in a parallel scattering configuration ($\mathbf{e}_i \parallel \mathbf{e}_s$), are presented in Fig. 1 (b). As it can be seen, four peaks at 89.2, 121.1, 214.8, and 239.6 cm^{-1} can be clearly observed at 80 K. According to numerical calculations (see Table I), peaks at 89.2 and 239.6 cm^{-1} correspond to two out of four E_{2g} modes, whereas peaks at 121.1 and 239.6 cm^{-1} can be assigned as two A_{1g} symmetry modes. One should note that numerical calculations performed by using experimentally obtained lattice parameters in the magnetic phase yield a better agreement with experimental values. This is not surprising since the calculations are performed for the stoichiometric compound as opposed to the nonstoichiometry of the sample. Furthermore, it is known that lattice parameters strongly depend on the Fe atom deficiency [15]. All calculated Raman and infrared phonon frequencies, for the magnetic and nonmagnetic phase of $Fe_{3-x}GeTe_2$, using relaxed and experimental lattice parameters, together with experimentally observed Raman active modes, are summarized in Table II of Appendix D.

After assigning all observed modes we focused on their temperature evolution. Having in mind finite instrumental

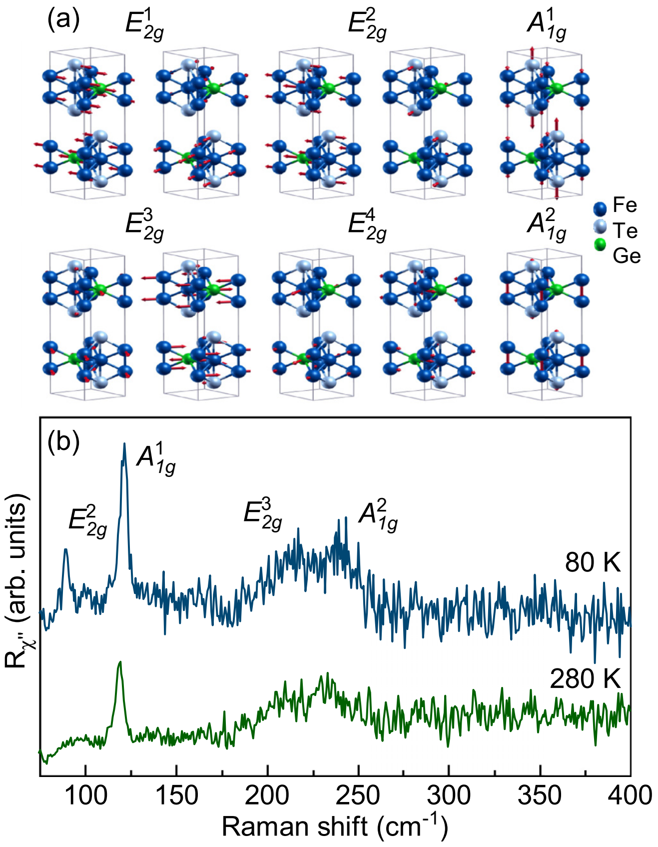

FIG. 1. (a) Displacement patterns of A_{1g} and E_{2g} symmetry modes. (b) Raman spectra of $Fe_{3-x}GeTe_2$ single crystal measured at different temperatures in a parallel polarization configuration.

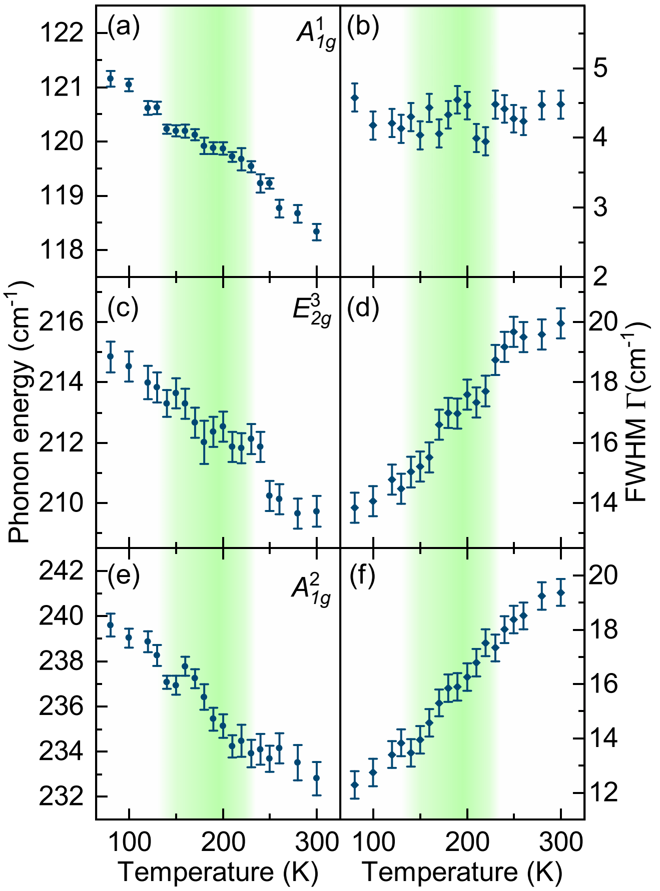

FIG. 2. Energy and linewidth temperature dependence of A_{1g}^1 [(a) and (b)], E_{2g}^3 [(c) and (d)], and A_{1g}^2 [(e) and (f)] phonon modes in $Fe_{3-x}GeTe_2$.

broadening, the Voigt line shape was used for the data analysis [27,28]. The modeling procedure is described in detail in Appendix B and presented in Fig. 6. Figure 2 shows the temperature evolution of the energy and linewidth of the A_{1g}^1, E_{2g}^3, and A_{1g}^2 modes between 80 and 300 K. Upon heating the sample, both the energy and linewidth of A_{1g}^1 and A_{1g}^2 symmetry modes exhibit a small but sudden discontinuity at about 150 K [Figs. 2(a) and 2(e)]. An apparent discontinuity in energy of all analyzed Raman modes is again present at temperatures around 220 K. In the same temperature range the linewidths of these Raman modes show a clear deviation from the standard anharmonic behavior [27–31].

Apart from the anomalies in the phonon spectra, a closer inspection of the temperature-dependent Raman spectra measured in the parallel polarization configuration reveals a pronounced evolution of the Raman continuum [Fig. 3(a)]. For the analysis we have used a simple model including a damped Lorentzian and linear term, $\chi''_{\text{cont}} \propto a\Gamma\omega/(\omega^2 + \Gamma^2) + b\omega$ [32], where a, b, and Γ are temperature-dependent parameters. Figure 3(b) summarizes the results of the analysis with the linear term omitted (most likely originating from a luminescence). At approximately the same temperatures, where phonon properties exhibit discontinuities, the continuum temperature dependence manifests nonmonotonic behavior. The maximum positions of the curve were obtained by integrating those shown in Fig. 3(b). The inset of Fig. 3(b) shows the temperature evolution of their displacements. This analysis confirms the presence of discontinuities in the electronic continuum at temperatures around 150 and 220 K, which leaves a trace in the phonon behavior around these temperatures (Fig. 2). While we do not have evidence for the Kondo effect in the $Fe_{3-x}GeTe_2$ crystals we measured, a modification of the electronic background at FM ordering due to localization or the Kondo effect cannot be excluded.

The temperature evolutions of the phonon self-energies and the continuum observed in the Raman spectra of $Fe_{3-x}GeTe_2$ suggest the presence of phase transition(s). Magnetization measurements of the samples were performed as described in Ref. [13], revealing a FM-PM transition at 150 K. Thus, the discontinuity in the observed phonon properties around this temperature can be traced back to the weak to moderate spin-phonon coupling. The question remains open regarding the anomaly observed at about 220 K. As previously reported, the Curie temperature of the $Fe_{3-x}GeTe_2$ single crystals grown by the CVT method is between 220 and 230 K [11,12,14], varying with the vacancy concentration, i.e., a decrease in the vacancy content will result an increment of T_C [15]. On the other hand, the $Fe_{3-x}GeTe_2$ crystals grown by the self-flux method usually have a lower Curie temperature, since the

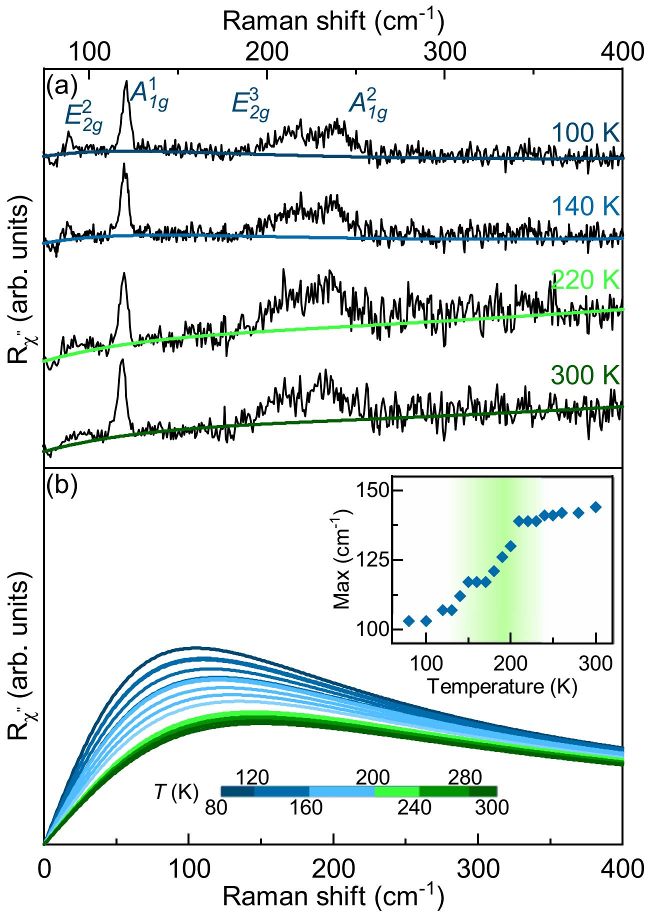

FIG. 3. (a) Raman spectra of $Fe_{3-x}GeTe_2$ at four temperatures measured in a parallel polarization configuration. Solid lines represent the theoretical fit to the experimental data. (b) Temperature evolution of the electronic continuum after omitting the linear term. Inset: Displacement of the maximum of fitted curves.

vacancy content is higher [13,15]. Crystals used in the Raman scattering experiment presented here were grown by the self-flux method with a Fe vacancy content of $x \approx 0.36$ [13]. This is in good agreement with our EDS results of $x = 0.4 \pm 0.1$, giving rise to the FM-PM transition at 150 K. Nevertheless, an inhomogeneous distribution of vacancies may result the formation of vacancy depleted “islands” which in turn would result in an anomaly at 220 K similar to the one observed in our Raman data. However, the EDS data (see Fig. 5) do not support this possibility. At this point we can only speculate that while the long-range order temperature is shifted to a lower temperature by the introduction of vacancies, short-range correlations may develop at 220 K.

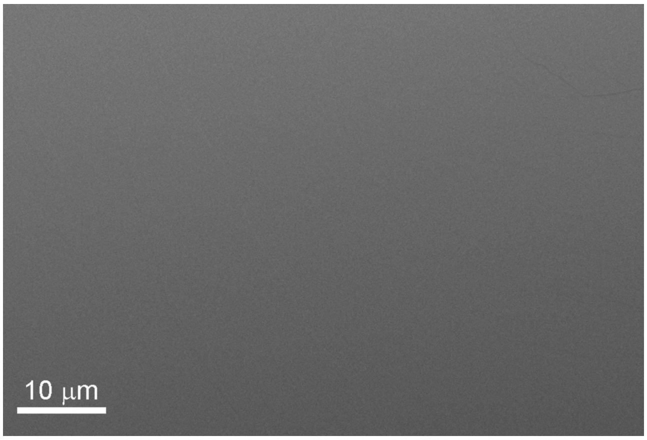

FIG. 4. SEM image of a $Fe_{3-x}GeTe_2$ single crystal.

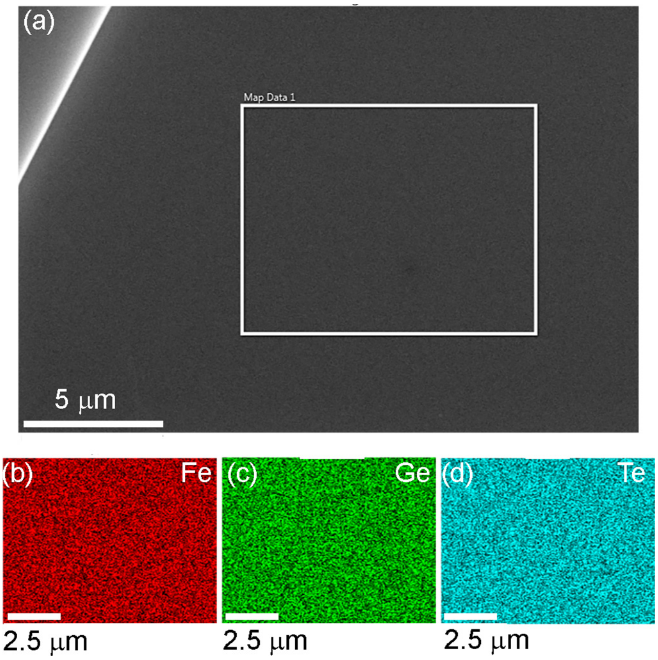

FIG. 5. EDS mapping on a $Fe_{3-x}GeTe_2$ single crystal. (a) Secondary electron image of the crystal with the mapping performed within the rectangle. (b)–(d) Associated EDS maps for Fe, Ge, and Te, respectively.

IV. CONCLUSION

We have studied the lattice dynamics of flux-grown $Fe_{3-x}GeTe_2$ single crystals by means of Raman spectroscopy and DFT. Four out of eight Raman active modes, two A_{1g} and two E_{2g}, have been observed and assigned. DFT calculations are in good agreement with experimental results. The temperature dependence of the A^1_{1g}, E^3_{2g}, and A^2_{1g} mode properties reveals a clear fingerprint of spin-phonon coupling, at a temperature of around 150 K. Furthermore, the anomalous behavior in the energies and linewidths of the observed phonon modes is present in the Raman spectra at temperatures around 220 K with the discontinuity also present in the electronic continuum. Its origin still remains an open question, and requires further analysis.

ACKNOWLEDGMENTS

The work was supported by the Serbian Ministry of Education, Science and Technological Development under Projects No. III45018 and No. OI171005. DFT calculations were performed using computational resources at Johannes Kepler University, Linz, Austria. Materials synthesis was supported

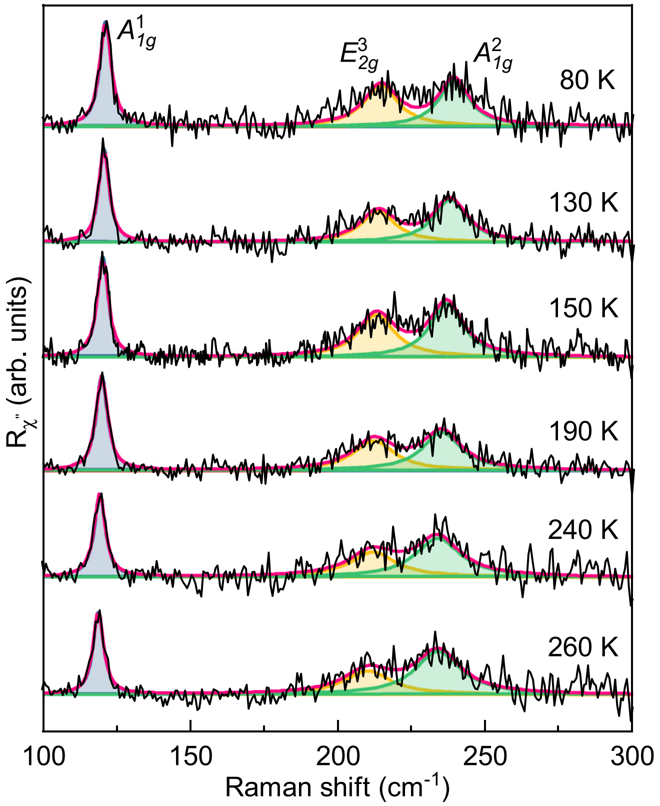

FIG. 6. Modeled Raman spectra of $Fe_{3-x}GeTe_2$ single crystal, after subtracting continuum contributions, obtained at various temperatures. For experimental data modeling, the Voigt line shape was used.

TABLE II. Top panel: Comparison of calculated energies of Raman active phonons using relaxed (R) and experimental [nonrelaxed (NR)] lattice parameters for the magnetic (M) and nonmagnetic phase (NM), given in cm^{-1}. Obtained experimental values in the magnetic phase at a temperature of 80 K are given in the last column. Bottom panel: Comparison of calculated energies of infrared optical phonons of $Fe_{3-x}GeTe_2$.

Raman active modes					
	Calculations				
Sym.	NM-R	M-R	NM-NR	M-NR	Experiment (M)
E^1_{2g}	28.4	49.6	33.9	50.2	
E^1_{1g}	79.2	70.2	71.7	70.3	
E^2_{2g}	115.5	121.0	100.0	122.2	89.2
A^1_{1g}	151.7	139.2	131.7	137.2	121.1
E^2_{1g}	225.5	206.0	194.3	209.5	
E^3_{2g}	238.0	232.6	204.9	228.6	214.8
A^2_{1g}	272.0	262.6	235.7	233.4	239.6
E^4_{2g}	362.0	337.6	315.4	334.7	
Infrared active modes					
A^1_{2u}	70.7	96.6	73.5	92.7	
E^1_{1u}	112.5	121.2	89.4	121.6	
A^2_{2u}	206.0	162.5	183.1	153.7	
E^2_{1u}	226.4	233.6	192.1	231.3	
A^3_{2u}	271.8	248.6	240.8	241.0	
E^3_{1u}	361.1	336.6	314.7	334.7	

by the US Department of Energy, Office of Basic Energy Sciences as part of the Computation Material Science Program (Y.L. and C.P.). Electron microscopy was performed at Jozef Stefan Institute, Ljubljana, Slovenia under Slovenian Research Agency Contract No. P1-0099 (B.V.). This work has received funding from the European Union's Horizon 2020 research and innovation program under the Marie Sklodowska-Curie Grant Agreement No. 645658 (DAFNEOX Project).

APPENDIX A: ELECTRON MICROSCOPY

In order to examine the uniformity of $Fe_{3-x}GeTe_2$, Scanning electron microscopy (SEM) was performed on as-cleaved crystals. It can be seen from Fig. 4 that the crystals maintain uniformity for several tens of microns. Furthermore, the elemental composition was obtained using EDS mapping, as shown in Fig. 5. The atomic percentage, averaged over ten measurements, is 47%, 17%, and 36% (±2%) for Fe, Ge, and Te, respectively, with the vacancy content $x = 0.4 \pm 0.1$. The maps associated with the selected elements appear homogeneous, as they are all present uniformly with no apparent islands or vacancies.

APPENDIX B: DATA MODELING

In order to obtain the temperature dependence of the energies and linewidths of the observed $Fe_{3-x}GeTe_2$ phonon modes, the Raman continuum, shown in colored lines in Fig. 3(a), was subtracted for simplicity from the raw Raman susceptibility data (black line). The spectra obtained after the subtraction procedure are presented in Fig. 6 (black line) for various temperatures. Because of the finite resolution of the spectrometer and the fact that line shapes of all the observed phonons are symmetric, the Voigt line shape ($\Gamma_G = 0.8$ cm^{-1}) was used for data modeling. Blue, yellow, and green lines in Fig. 6 represent fitting curves for A^1_{1g}, E^3_{2g}, and A^2_{1g} phonon modes, respectively, whereas the overall spectral shape is shown in the red line.

APPENDIX C: EXPERIMENTAL DETAILS

Before being placed in a vacuum and being cleaved, the sample was glued to a copper plate with GE varnish in order to achieve good thermal conductivity and prevent strain effects. Silver paste, as a material with high thermal conductivity, was used to attach the copper plate with the sample to the cryostat. The laser beam spot, focused through an Olympus long-range objective of × 50 magnification, was approximately 6 μm in size, with a power less than 1 mW at the sample surface. A TriVista 557 triple spectrometer was used in the subtractive mode, with a diffraction grating combination of 1800/1800/2400 grooves/mm and the entrance and second intermediate slit set to 80 μm, in order to enhance stray light rejection and attain good resolution.

APPENDIX D: CALCULATIONS

In Table II the results of DFT calculations are presented for magnetic (M) and nonmagnetic (NM) relaxed and experimental lattice parameters. For comparison, the experimental results are shown in the last column. Since the lattice parameters strongly depend on the Fe atom deficiency, the best agreement with experimental results gives the magnetic nonrelaxed solution.

[1] N. Sivadas, M. W. Daniels, R. H. Swendsen, S. Okamoto, and D. Xiao, Magnetic ground state of semiconducting transition-metal trichalcogenide monolayers, Phys. Rev. B **91**, 235425 (2015).

[2] K. S. Novoselov, A. K. Geim, S. V. Morozov, D. Jiang, Y. Zhang, S. V. Dubonos, I. V. Grigorieva, and A. A. Firsov, Electric field rffect in atomically thin carbon films, Science **306**, 666 (2004).

[3] Q. H. Wang, K. Kalantar-Zadeh, A. Kis, J. N. Coleman, and M. S. Strano, Electronics and optoelectronics of two-dimensional transition metal dichalcogenides, Nat. Nanotechnol. **7**, 699 (2012).

[4] C. Gong, L. Li, Z. Li, H. Ji, A. Stern, Y. Xia, T. Cao, W. Bao, C. Wang, Y. Wang, Z. Q. Qiu, R. J. Cava, S. G. Louie, J. Xia, and X. Zhang, Discovery of intrinsic ferromagnetism in two-dimensional van der Waals crystals, Nature (London) **546**, 265 (2017).

[5] B. Huang, G. Clark, E. Navarro-Moratalla, D. R. Klein, R. Cheng, K. L. Seyler, D. Zhong, E. Schmidgall, M. A. McGuire, D. H. Cobden, W. Yao, D. Xiao, P. Jarillo-Herrero, and X. Xu, Layer-dependent ferromagnetism in a van der Waals crystal down to the monolayer limit, Nature (London) **546**, 270 (2017).

[6] M. A. McGuire, H. Dixit, V. R. Cooper, and B. C. Sales, Coupling of crystal structure and magnetism in the layered, ferromagnetic insulator CrI_3, Chem. Mater. **27**, 612 (2015).

[7] H. L. Zhuang, Y. Xie, P. R. C. Kent, and P. Ganesh, Computational discovery of ferromagnetic semiconducting single-layer $CrSnTe_3$, Phys. Rev. B **92**, 035407 (2015).

[8] G. T. Lin, H. L. Zhuang, X. Luo, B. J. Liu, F. C. Chen, J. Yan, Y. Sun, J. Zhou, W. J. Lu, P. Tong, Z. G. Sheng, Z. Qu, W. H. Song, X. B. Zhu, and Y. P. Sun, Tricritical behavior of the two-dimensional intrinsically ferromagnetic semiconductor $CrGeTe_3$, Phys. Rev. B **95**, 245212 (2017).

[9] L. D. Casto, A. J. Clune, M. O. Yokosuk, J. L. Musfeldt, T. J. Williams, H. L. Zhuang, M.-W. Lin, K. Xiao, R. G. Hennig, B. C. Sales, J.-Q. Yan, and D. Mandrus, Strong spin-lattice coupling in $CrSiTe_3$, APL Mater. **3**, 041515 (2015).

[10] M.-W. Lin, H. L. Zhuang, J. Yan, T. Z. Ward, A. A. Puretzky, C. M. Rouleau, Z. Gai, L. Liang, V. Meunier, B. G. Sumpter, P. Ganesh, P. R. C. Kent, D. B. Geohegan, D. G. Mandrus, and K. Xiao, Ultrathin nanosheets of $CrSiTe_3$: A semiconducting two-dimensional ferromagnetic material, J. Mater. Chem. C **4**, 315 (2016).

[11] J.-X. Zhu, M. Janoschek, D. S. Chaves, J. C. Cezar, T. Durakiewicz, F. Ronning, Y. Sassa, M. Mansson, B. L. Scott, N. Wakeham, E. D. Bauer, and J. D. Thompson, Electronic correlation and magnetism in the ferromagnetic metal Fe_3GeTe_2, Phys. Rev. B **93**, 144404 (2016).

[12] B. Chen, J. H. Yang, H. D. Wang, M. Imai, H. Ohta, C. Michioka, K. Yoshimura, and M. H. Fang, Magnetic properties of layered itinerant electron ferromagnet Fe_3GeTe_2, J. Phys. Soc. Jpn. **82**, 124711 (2013).

[13] Y. Liu, V. N. Ivanovski, and C. Petrovic, Critical behavior of the van der Waals bonded ferromagnet $Fe_{3-x}GeTe_2$, Phys. Rev. B **96**, 144429 (2017).

[14] H.-J. Deiseroth, K. Aleksandrov, C. Reiner, L. Kienle, and R. K. Kremer, Fe_3GeTe_2 and Ni_3GeTe_2 - Two new layered transition-metal compounds: Crystal structures, HRTEM investigations, and magnetic and electrical properties, Eur. J. Inorg. Chem. **2006**, 1561 (2006).

[15] A. F. May, S. Calder, C. Cantoni, H. Cao, and M. A. McGuire, Magnetic structure and phase stability of the van der Waals bonded ferromagnet $Fe_{3-x}GeTe_2$, Phys. Rev. B **93**, 014411 (2016).

[16] V. Yu. Verchenko, A. A. Tsirlin, A. V. Sobolev, I. A. Presniakov, and A. V. Shevelkov, Ferromagnetic order, strong magnetocrystalline anisotropy, and magnetocaloric effect in the layered telluride $Fe_{3-\delta}GeTe_2$, Inorg. Chem. **54**, 8598 (2015).

[17] J. Yi, H. Zhuang, Q. Zou, Z. Wu, G. Cao, S. Tang, S. A. Calder, P. R. C. Kent, D. Mandrus, and Z. Gai, Competing antiferromagnetism in a quasi-2D itinerant ferromagnet: Fe_3GeTe_2, 2D Mater. **4**, 011005 (2016).

[18] Y. Zhang, H. Lu, X. Zhu, S. Tan, W. Feng, Q. Liu, W. Zhang, Q. Chen, Y. Liu, X. Luo, D. Xie, L. Luo, Z. Zhang, and X. Lai, Emergence of Kondo lattice behavior in a van der Waals itinerant ferromagnet, Fe_3GeTe_2, Sci. Adv. **4**, eaao6791 (2018).

[19] Y. Liu, E. Stavitski, K. Attenkofer, and C. Petrovic, Anomalous Hall effect in the van der Waals bonded ferromagnet $Fe_{3-x}GeTe_2$, Phys. Rev. B **97**, 165415 (2018).

[20] H. L. Zhuang, P. R. C. Kent, and R. G. Hennig, Strong anisotropy and magnetostriction in the two-dimensional Stoner ferromagnet Fe_3GeTe_2, Phys. Rev. B **93**, 134407 (2016).

[21] C. Tan, J. Lee, S.-G. Jung, T. Park, S. Albarakati, J. Partridge, M. R. Field, D. G. McCulloch, L. Wang, and C. Lee, Hard magnetic properties in nanoflake van der Waals Fe_3GeTe_2, Nat. Commun. **9**, 1554 (2018).

[22] P. Giannozzi *et al.*, QUANTUM ESPRESSO: A modular and open-source software project for quantum simulations of materials, J. Phys.: Condens. Matter **21**, 395502 (2009).

[23] P. E. Blöchl, Projector augmented-wave method, Phys. Rev. B **50**, 17953 (1994).

[24] G. Kresse and D. Joubert, From ultrasoft pseudopotentials to the projector augmented-wave method, Phys. Rev. B **59**, 1758 (1999).

[25] J. P. Perdew, K. Burke, and M. Ernzerhof, Generalized Gradient Approximation Made Simple, Phys. Rev. Lett. **77**, 3865 (1996).

[26] S. Grimme, Semiempirical GGA-type density functional constructed with a long-range dispersion correction, J. Comput. Chem. **27**, 1787 (2006).

[27] A. Milosavljević, A. Šolajić, J. Pešić, Y. Liu, C. Petrovic, N. Lazarević, and Z. V. Popović, Evidence of spin-phonon coupling in $CrSiTe_3$, Phys. Rev. B **98**, 104306 (2018).

[28] A. Baum, A. Milosavljević, N. Lazarević, M. M. Radonjić, B. Nikolić, M. Mitschek, Z. I. Maranloo, M. Šćepanović, M. Grujić-Brojčin, N. Stojilović, M. Opel, A. Wang,

C. Petrovic, Z. V. Popović, and R. Hackl, Phonon anomalies in FeS, Phys. Rev. B **97**, 054306 (2018).

[29] M. Opačić, N. Lazarević, M. M. Radonjić, M. Šćepanović, H. Ryu, A. Wang, D. Tanasković, C. Petrovic, and Z. V. Popović, Raman spectroscopy of $K_xK_{2-y}Se_2$ single crystals near the ferromagnet–paramagnet transition, J. Phys.: Condens. Matter **28**, 485401 (2016).

[30] Z. V. Popović, N. Lazarević, S. Bogdanović, M. M. Radonjić, D. Tanasković, R. Hu, H. Lei, and C. Petrovic, Signatures of the spin-phonon coupling in $Fe_{1+y}Te_{1-x}Se_x$ alloys, Solid State Commun. **193**, 51 (2014).

[31] Z. V. Popović, M. Šćepanović, N. Lazarević, M. Opačić, M. M. Radonjić, D. Tanasković, H. Lei, and C. Petrovic, Lattice dynamics of $BaFe_2X_3$ (X = S, Se) compounds, Phys. Rev. B **91**, 064303 (2015).

[32] T. P. Devereaux and R. Hackl, Inelastic light scattering from correlated electrons, Rev. Mod. Phys. **79**, 175 (2007).

Spectrochimica Acta Part A: Molecular and Biomolecular Spectroscopy 216 (2019) 173–178

Contents lists available at ScienceDirect

Spectrochimica Acta Part A: Molecular and Biomolecular Spectroscopy

journal homepage: www.elsevier.com/locate/saa

Influence of chemical fixation process on primary mesenchymal stem cells evidenced by Raman spectroscopy

J.J. Lazarević[a], U. Ralević[a], T. Kukolj[b], D. Bugarski[b], N. Lazarević[a,*], B. Bugarski[c], Z.V. Popović[a,d]

[a] Center for Solid State Physics and New Materials, Institute of Physics Belgrade, University of Belgrade, Pregrevica 118, Belgrade 11080, Serbia
[b] Laboratory for Experimental Hematology and Stem Cells, Institute for Medical Research, University of Belgrade, Belgrade 11000, Serbia
[c] Department of Chemical Engineering, Faculty of Technology and Metallurgy, University of Belgrade, Karnegijeva 4, Belgrade 11060, Serbia
[d] Serbian Academy of Sciences and Arts, Knez Mihailova 35, Belgrade 11000, Serbia

ARTICLE INFO

Article history:
Received 7 December 2018
Received in revised form 6 March 2019
Accepted 6 March 2019
Available online 9 March 2019

Keywords:
Raman spectroscopy
Stem cells
Chemical fixation

ABSTRACT

In investigation of (patho)physiological processes, cells represent frequently used analyte as an exceptional source of information. However, spectroscopic analysis of live cells is still very seldom in clinics, as well as in research studies. Among others, the reasons are long acquisition time during which autolysis process is activated, necessity of specified technical equipment, and inability to perform analysis in a moment of sample preparation. Hence, an optimal method of preserving cells in the existing state is of extreme importance, having in mind that selection of fixative is cell lineage dependent. In this study, two commonly used chemical fixatives, formaldehyde and methanol, are used for preserving primary mesenchymal stem cells extracted from periodontal ligament, which are valuable cell source for reconstructive dentistry. By means of Raman spectroscopy, cell samples were probed and the impact of these fixatives on their Raman response was analyzed and compared. Different chemical mechanisms are the core processes of formaldehyde and methanol fixation and certain Raman bands are shifted and/or of changed intensity when Raman spectra of cells fixed in that manner are compared. In order to get clearer picture, comprehensive statistical analysis was performed.

1. Introduction

Mesenchymal stem cells (MSCs) are heterogenous group of adult stem cells originally discovered in bone marrow, but present in all tissues and organs, with the purpose to keep tissue homeostasis, regeneration and renewal. These acts are performed not only through multipotent differentiation potential (toward chondrogenic, adipogenic, and osteogenic lineages), but also through their ability to modulate immune response (directly or indirectly) [1-5]. Although MSCs posses common cellular features, it is overall accepted that these cells still exhibit variable regenerative capacity due to different tissue origin, donor diversity, and variations in culture conditions [6,7]. Human MSCs investigated in this study originate from periodontal ligament, a fibrous, cellular, and vascular soft connective tissue. The main role of periodontal ligament is to anchor tooth to the alveolar bone, maintain mineralisation level and alleviate mechanical forces associated with the process of mastication [8-10]. Previously, it was demonstrated that human periodontal ligament stem cells (hPDLSCs) investigated in this experiment fulfill criteria for MSCs identification and characterization, set by The International Society for Cell Therapy (ISCT) [11,12]. Minimal criteria for characterization of human MSCs, set by ISCT, include plastic adhesion, with expression of CD73, CD90, CD105 surface markers and lack of hematopoietic markers CD34−, CD45−, CD14−, CD79α −, HLA-DR−; and multilineage differentiation potential into osteoblasts, adipocytes, and chondroblasts [13]. However, MSCs nature, including hPDLSCs, is still elusive. Therefore, the exploration of hPDLSCs, as a cell source for reconstructive dentistry, is of great importance for the novel therapeutic strategies related to recovery of periodontium and curing dental defects [14].

Taking into account the heterogeneity of MSCs, it is crucial for these cells to be adequately characterized during the lifespan, before further manipulation. Although many techniques are available in this field, including mass spectroscopy, flow cytometry, and immunocytochemistry, most of them are destructive, invasive, time consuming or require expensive cell-specific labels [15,16]. However, a light scattering technique, Raman spectroscopy, is able to overrun these issues due to its unique properties: it is non-invasive, non-destructive, fast, label-free, and complex sample preparation is not required. It operates with low sample volume even in aqueous

---

* Corresponding author.
E-mail address: nenadl@ipb.ac.rs (N. Lazarević).

https://doi.org/10.1016/j.saa.2019.03.012
1386-1425/

solutions and provide a plenty of biochemical information as an outcome. Raman spectroscopy is a type of vibrational spectroscopy, based on Raman effect [17], in which an inelastically scattered component of the visible light bears the information of the analyte. Raman scattering experiment results in vibrational spectrum, a fingerprint of a sample, which carries the information about chemical composition and structure of a sample, on a submolecular level. Typically, it comprises vibrational modes of the highest Raman scattering cross section [16, 18-20].

Spectroscopic analysis of live cells is still very seldom, both in clinical and research conditions, particularly due to the longevity of the processes, when autolysis is inevitable. On the other hand, it is not always possible to investigate a sample in a moment of acquiring. The crucial and fundamental step in cell biology, for obtaining sensitive and reproducible results, is a process called fixation, which maintain the localization of biomolecules. It is used for preserving a cell in a physiological state, by preventing cell shrinkage or swelling caused by osmotic pressure initiated with air-drying, as well as autolysis by activating lysosomal enzymes, which includes denaturation of proteins, dephosphorylation of mononucleotides, phospholipids and proteins, chromatin compaction, nuclear fragmentation, and cytoplasmic condensation and fragmentation [21]. However, it is known that selection of a fixative is very much dependent on a cell nature when it comes to Raman spectroscopy and can significantly distort experimental data [22]. In the past decade, investigations of different fixatives' influence on Raman spectra of numerous cell lineages were reported, with an aim to clarify the best option for each cell lineage. One of the studies investigated the effect of formaldehyde and ethanol fixation on CARS (Coherent Anti-Stokes Raman Spectroscopy) signal of proteins and lipids in different cellular compartments of glial and neuronal cells, concluding that formaldehyde fixation is preferable method of preservation of these cells [22]. Also, the effect of chemical fixation procedures on the Raman spectra of normal and leukemia cells was characterized [23]. When compared to the spectra of unfixed cells, the fixed cell spectra showed changes in the intensity of specific Raman markers, and latter statistical analysis suggested that methanol provokes greater changes in Raman spectra when compared to paraformaldehyde. Further, micro-Raman spectroscopy was employed for chemical fixation mechanism study in three cell lines (normal skin, normal bronchial epithelium, and lung adenocarcinoma) [24]. Nucleic acid degradation, protein denaturation, and lipid leaching was observed with all fixatives (formalin, Carnoy's fixative, and methanol-acetic acid) and for all cell lines, but to varying degrees. Also, the authors suggested that formalin best preserves cellular integrity and gives the closest spectral content to that in live cells. The next study monitored the impact of fixation by formalin, desiccation, and air-drying on *in vitro* cell culture lines [25]. The results indicate that the choice of fixation methodology significantly influences the quality and reproducibility of the resulting spectral data. Formalin showed inconsistency in sample preservation and a loss of signal intensity, while air-drying appears to be inconsistent in terms of spectral reproducibility. Desiccation showed good spectral reproducibility and good signal-to-noise ratio [25].

Although numerous Raman studies of fixative process' spectral influence have been performed [22-25], according to our knowledge, no such research has been performed on primary mesenchymal stem cells originating from periodontal ligament. We used micro-Raman spectroscopy in order to probe fixed hPDLSCs and investigate the effects of two most frequently used chemical fixatives which have different chemical mechanisms of preservation (formaldehyde and methanol), and then compared those effects. Formaldehyde reacts extensively with amino groups to form methylene bridges and cross-links molecules, which alters, but stabilizes them [26]. Further, formaldehyde does not appear to perturb tertiary structure very much. On the other hand, methanol replaces water in cell environment, disrupts hydrophobic and hydrogen bonding, and consequently alters tertiary structure of proteins [27,28]. Although fixation substantially alters composition and appearance, it is possible to produce consistent chemical and physical properties by selection of suitable preparation conditions. Nevertheless, standardization of Raman spectroscopy regarding fixative selection could provide valuable additional information in many biological tests that require cell fixation and also indicate the existence of fine differences in the fixative effect that are necessary to be taken into consideration during standard biological protocols.

2. Experiment

2.1. Isolation and Cultivation of Human Periodontal Ligament Stem Cells

After getting the informed consent from healthy patients (age 18), subjected to the procedure of tooth extraction for orthodontic reasons, at the Department of Oral Surgery of the Faculty of Dental Medicine, the University of Belgrade, human periodontal ligament tissues from normal impacted third molars were collected. Immediately after, tissues were placed in sterile cell culturing conditions. As previously reported [11], human PDLSCs were isolated, characterized and expanded. For hPDLSCs isolation, periodontal tissues were carefully detached from the mid-third of the root surface, cut into small pieces and placed in a 25 cm^2 flask with Dulbecco's modified Eagle's medium (DMEM; Sigma-Aldrich St. Louis, MO, USA) supplemented with 10% fetal bovine serum (FBS; Capricorn-Scientific, Germany), 100 U/ml penicillin and 100 mg/ml streptomycin (Gibco, Thermo Fisher Scientific, USA). Standard cultivation conditions included 37 °C temperature, humidified atmosphere containing 5% CO_2, while medium was exchanged two times per week. After reaching 80% to 90% confluence, cells were detached regularly in growth medium (GM-DMEM with 10% FBS) using 0.05% trypsin with 1 mM EDTA (Gibco, Thermo Fisher Scientific, USA). In order to demonstrate the universality of experimental results for MSCs, cells from third and sixth passages were used, divided into two batches. Moreover, hPDLSCs were characterized based on immunophenotype and multipotent differentiation potential toward osteogenic, chondrogenic and adipogenic lineages as it has been described before [11]. All treatments were performed according to the approved ethical guidelines set by Ethics Committee of the Faculty of Dental Medicine, University of Belgrade and Declaration of Helsinki.

2.2. Sample Preparation

For the Raman experiment, hPDLSCs were seeded on rounded CaF_2 slides in 24-well plate (5×10^3 cells per slide) and cultivated in GM in standard cultivation conditions during 24 h. Following the adhesion, hPDLSCs were washed with saline buffer and fixed with 3.7% formaldehyde or methanol for 10 min at room temperature. Right before Raman spectroscopy was performed, samples were washed with distilled water.

2.3. μ-Raman Spectroscopy

In most of the cases, the Raman spectroscopy independently probes single vibrations within a molecule or a crystal, but in a complex biological systems composed of various types of macromolecules, only vibrational bands consisting of numerous vibrations of the same type, rather than a single vibration, could be distinguished. Consequently, the changes of biological system composition may result with a change of certain Raman bands line-shapes and/or intensities.

The Raman scattering experiment was performed using NTegra Spectra from NTMDT. The 532 nm line of a semiconductor laser was used as an excitation source. The laser power was set to 2 mW

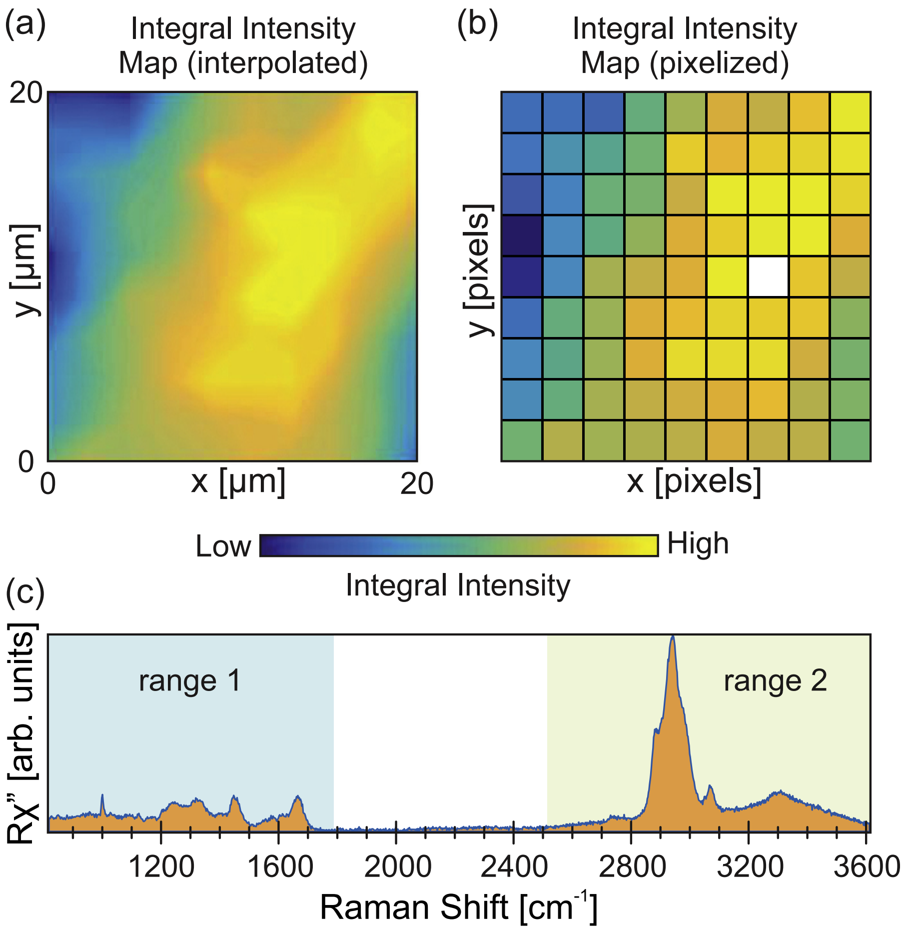

Fig. 1. A single PDLSC Raman (a) interpolated integral intensity map, and (b) pixelized integral intensity map. (c) Human PDLSC Raman scattering spectrum acquired on a pixel marked in white.

and focused on the area of about 1 µm, in order to provide a reasonable Raman intensity for a 60 s long acquisition. Under these conditions, the sample associated Raman bands, acquired sequentially at the same position, were found to be stable in terms of both the band intensity and spectral position. In other words, no visible laser induced modifications of the cells were observed upon repeating the signal acquisition for a few times at any of the acquisition points.

Due to very complex inner structure of a cell, there may be small variations in Raman spectra for the data collected at different positions. Consequently, suitable methodology must be applied in order to achieve the needed level of sample representation. In other words, the applied method has to be robust. Here, two batches of cells treated with methanol and formaldehyde were examined by spatially mapping the Raman scattering signal on 20 cells per batch. The spectra were collected at 10 × 10 or 11 × 11 matrices of spatial points separated by a distance larger than the estimated focus diameter of ≈1 µm. The distance between adjacent spatial points, or the spatial resolution, was varied between 2 µm and 3 µm depending on the cell size. The example of an interpolated spectral map of a single methanol fixed cell is presented in Fig. 1(a). Fig. 1(b) shows the same map with the actual pixels omitting the interpolation for clarity. The x and y represent spatial coordinates in which a spectrum is acquired. The intensity of a pixel, labeled white in Fig. 1(b), is obtained by integrating the Raman spectra collected at that pixel. The value of the integral is equal to the area below the acquired signal as illustrated by shaded (orange) area below the typical hPDLSC Raman spectra in Fig. 1(c). It is characterized by clearly visible Raman bands in two spectral regions marked in Fig. 1(c). The first spectral region spans from 800 cm^{-1} to 1770 cm^{-1}, whereas the second starts at 2500 cm^{-1} and ends at 3600 cm^{-1}.

2.4. Data Processing and Analysis

In addition to typical PDLSCs Raman spectra [Fig. 1(c)], a few (in total) significantly different spectra, having an extremely high

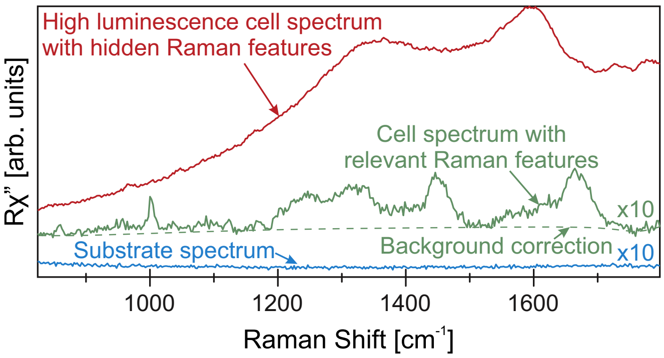

Fig. 2. A typical PDLSCs, substrate, and high luminescence points Raman spectra in the range from 800 cm^{-1} to 1800 cm^{-1}, depicting spectral selection and preprocessing.

luminescence contribution, were observed as well. The example of such a spectrum truncated to the spectral region from 800 cm^{-1} to 1770 cm^{-1} is shown in Fig. 2. Clearly, extremely strong luminescence masks the relevant Raman bands, making them misleading. Consequently, the high luminescence spectra were omitted from the analysis. The relevant Raman spectra were preprocessed before further manipulation. In the initial step, the background, modelled as a polynomial function of the fourth degree, was subtracted (see Fig. 2). Upon background removal, the spectra were normalized to the value of the integral intensity, calculated within the considered spectral region and then subjected to the analysis.

Besides the direct comparison of the Raman spectra of the cells fixed with formaldehyde and methanol, a multivariate statistical method, principal component analysis (PCA), was applied [15,18,29,30]. Thereby, the dimensionality of the experimental data set is reduced, by transforming to a new set of variables, the principal components, which are uncorrelated and ordered in a way that the first few retain most of the variation present in all of the original variables [31]. The outcome of this analysis is distinct grouping of Raman spectra based on their mutual features [18,29].

3. Results and Discussion

Regarding biological background of our samples, it is well known that primary mesenchymal stem cell cultures represent heterogenic cellular populations, thus the intrinsic heterogeneity of primary cells should be taken into consideration. Moreover, cellular features of these cells are highly prone to modifications during standard cultivation process [32,33]. Therefore, in order to get reproducible results, we analyzed cells from different passages (passage 3 in Batch 1 and passage 6 in Batch 2).

It is known that the effect of fixation process is cell type and fixative dependent [25]. Different chemical mechanisms may result in variations of the respective Raman spectra. Whereas depletion of certain component will result in reduction of corresponding Raman bands' intensities, various perturbations of the electronic cloud will lead to the changes of bands energy and linewidth. The second does not exclude the possibility of variations of the Raman intensities since the change in electronic structure may impact probability of the inelastic light scattering processes. In our data, the most pronounced changes are occurring in two spectral regions [Fig. 1], ranging from 800 cm^{-1} to 1770 cm^{-1} and from 2500 cm^{-1} to 3600 cm^{-1}. In the statistical treatment, these regions were analyzed independently due to the intrinsic imperfections of the spectrometer.

In Fig. 3, 2D Raman spectra map, averaged spectra, their difference and PCA of Batch 1 and Batch 2 of formaldehyde and methanol fixed PDLSCs, are presented respectively, for spectral region between 800 cm^{-1} and 1770 cm^{-1}. Closer inspection of formaldehyde and methanol fixed PDLSCs 2D Raman spectra map [Fig. 3(a) and (c)] already reveals significant difference between two groups. Relative change of intensity and/or energy shift can be clearly observed for multiple Raman bands. This is even more evident in the difference of formaldehyde and methanol fixed PDLSCs average Raman spectra [Fig. 3(a) and (c)]. It can be seen that phenylalanine peaks at 1002 cm^{-1} and 1030 cm^{-1} are of higher intensity in methanol fixed PDLSCs Raman spectra compared to formaldehyde fixed ones.

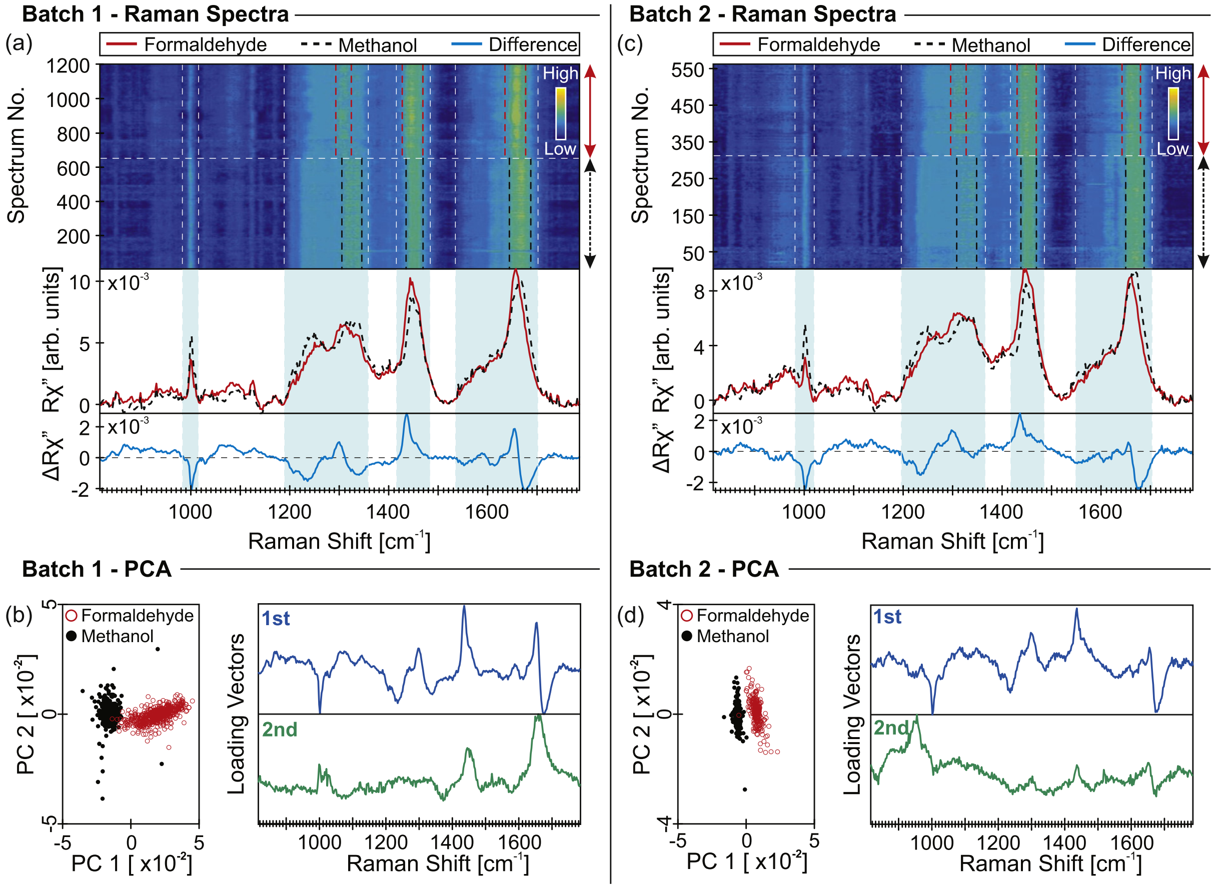

Fig. 3. 2D Raman spectra map obtained from PDLSCs (see Supplementary information), fixed with formaldehyde and methanol, their mean spectra, as well as their difference for the spectral region from 800 cm^{-1} to 1770 cm^{-1}; PCA score plots calculated for these two groups of cells, and PCA loading vectors for (a)–(b) Batch 1 and (c)–(d) Batch 2, respectively. Percentage of variance PC1–PC2: for Batch 1 19.85%–5.76%; for Batch 2 17.95%–7.43%.

The DNA bands at 1095 cm^{-1}, 1130 cm^{-1}, and 1330 cm^{-1} are of higher intensity in formaldehyde fixed PDLSCs spectra whereas the band at about 1330 cm^{-1} is also slightly shifted. Amide III band at about 1260 cm^{-1} is significantly shifted and of higher intensity in methanol fixed spectra. When it comes to lipid band at 1450 cm^{-1}, it is of noticeable higher intensity and shifted in formaldehyde fixed spectra, as well as the Amide I band at about 1660 cm^{-1}.

The observed behaviour is consistent with the biochemical picture in which the protein content is larger in methanol fixed cells. This is evidenced by more pronounced phenylalanine peak. On the other hand, the secondary structure is more preserved in formaldehyde fixed samples (Amide I band). Modification of native proteins by formaldehyde does not perturb the secondary structure very much. Lipid content is maintained greatly in formaldehyde fixed sample, which is in a good agreement with the literature, due to methanol-caused leaching of lipids through deteriorated cell membrane. As a consequence of cross-linking mechanism of fixation, DNA level is maintained in greater moiety in formaldehyde fixed PDLSCs Raman spectrum [27,28,34].

Spectra of averaged formaldehyde and methanol fixed PDLSCs spectra, and their difference spectrum, from Batch 2 are given in Fig. 3(c). The only observable difference, in comparison to Batch 1, is lower intensity of Amide I band at 1660 cm^{-1} in formaldehyde fixed PDLSCs Raman spectrum, relative to methanol fixed PDLSCs spectrum.

The same procedure is repeated for spectral region from 2500 cm^{-1} to 3600 cm^{-1}. In Fig. 4, 2D Raman spectra map, averaged spectra, their difference, and PCA of Batch 1 and Batch 2 of formaldehyde and methanol fixed PDLSCs, are presented respectively. Again, formaldehyde and methanol fixed PDLSCs Raman spectra are compared in this spectral region which reflects protein, lipid, and water content. In Fig. 4(a) and (c), it is observable from averaged spectra of difference that the bands at 2860 cm^{-1} and 2890 cm^{-1}, are more intense in formaldehyde fixed PDLSCs Raman spectra. These two bands present CH_2 and CH_3 symmetric stretch in lipids and proteins [35]. Raman band at 2940 cm^{-1} is assigned to CH vibrations in lipids and proteins and is more pronounced in methanol fixed PDLSCs Raman spectra. This confirms above-mentioned statements that formaldehyde better maintains the level of lipids with regard to methanol. On the other hand, methanol keeps protein levels.

Further, PCA is applied for the treatment of the spectral data, and the outcome is presented in Figs. 3 (b), (d) and 4(b), (d) for Batch 1 and Batch 2, respectively. Analyzing PCA score plots, clear assemblage of cells fixed with the same fixative is observable and, as expected, in all cases, PC1 is the component that makes the difference [Figs. 3(b), (d), and 4(b), (d)]. Only a few overlapping points have been observed due to the heterogeneity of the samples and/or variable signal-to-noise ratio. For illustration, PC2s and corresponding loading vectors are also presented. They represent intra- and inter-cellular variations, within the group of cells fixed with the same fixative. PC1 loading vectors are consistent with discrepancies directly observable in Raman spectra of differences, as discussed above. This is not surprising, having in mind the nature of this principal component and the algorithms applied.

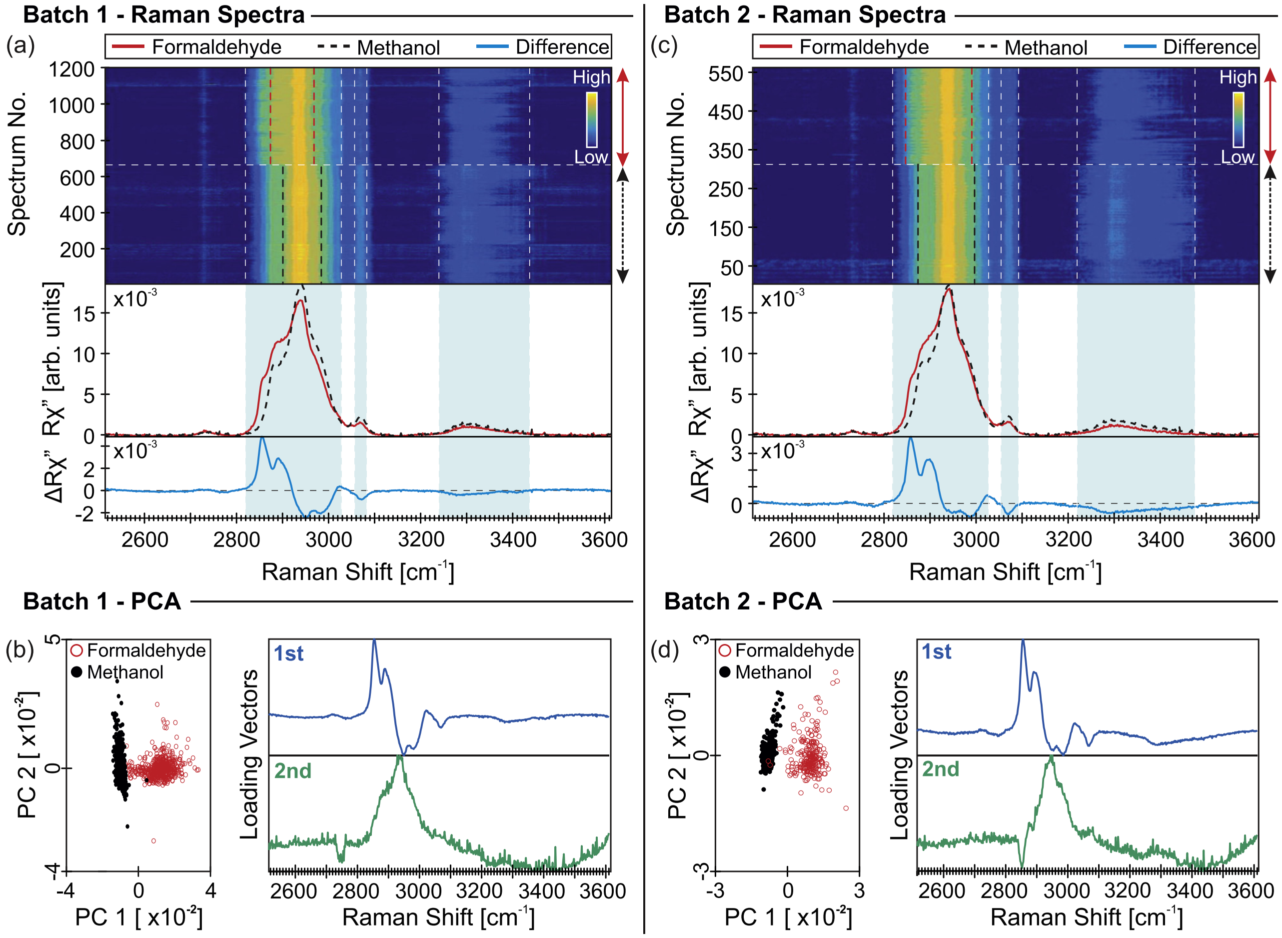

Fig. 4. 2D Raman spectra map obtained from PDLSCs (see Supplementary information), fixed with formaldehyde and methanol, their mean spectra, as well as their difference for spectral region from 2500 cm^{-1} to 3600 cm^{-1}; PCA score plots calculated for these two groups of cells, and PCA loading vectors for (a)–(b) Batch 1 and (c)–(d) Batch 2, respectively. Percentage of variance PC1–PC2: for Batch 1 64.09%–12.59%; for Batch 2 60.08%–14.64%.

Closer inspection of PCA score plots [Figs. 3(b), (d), and 4(b), (d)] reveals greater spread along PC1 for Batch 1, in particular for the spectral region from 800 cm^{-1} to 1770 cm^{-1} of formaldehyde fixed cells. This is most likely a consequence of heterogeneity of these primary cells. Depending on the nature of the inter-/intracellular variations, fixation process may enhance and/or suppress their Raman spectra signatures [22-26]. Detailed comparison between batches for both fixatives is presented in the Supplementary information.

4. Conclusion

Fixatives cause dramatic changes for all cell types but to varying extent. It is crucial to have a clear idea of what is expected from the sample when choosing the fixative agent. Preservation of cells by formaldehyde and methanol treatment represents standard procedures in most laboratory protocols. In this study, we investigated the effects of these two chemicals on Raman spectra of primary cell lineage, PDLSCs. Both procedures provided quantitatively and qualitatively close Raman spectra that can be considered as fingerprint spectra for this cell lineage. Through the direct comparison of the Raman spectra, as well as the statistical treatment, subtle differences have been observed between two groups that can be traced back to the variations in lipid and protein content. Consequently, when choosing the fixation method, the purpose of investigation has to be kept in mind. When it comes to Raman spectroscopy of hPDLSCs, both formaldehyde and methanol are acceptable choices,but with unlike sensitivity for tracing different biochemical composition.

Acknowledgments

We gratefully acknowledge M. Miletić and M. Andrić for supplying the periodontal ligament tissue. This work was supported by the Ministry of Education, Science, and Technological Development of the Republic of Serbia under Projects Nos. III46010, III45018, ON175062, and OI171005.

Appendix A. Supplementary Data

Supplementary data to this article can be found online at https://doi.org/10.1016/j.saa.2019.03.012.

References

[1] M. Gazdic, V. Volarevic, N. Arsenijevic, M. Stojkovic, Mesenchymal stem cells: a friend or foe in immune-mediated diseases, Stem Cell Rev. Rep. 11 (2) (2015) 280–287.

[2] Y. Sato, H. Araki, J. Kato, K. Nakamura, Y. Kawano, M. Kobune, T. Sato, K. Miyanishi, T. Takayama, M. Takahashi, et al. Human mesenchymal stem cells xenografted directly to rat liver are differentiated into human hepatocytes without fusion, Blood 106 (2) (2005) 756–763.

[3] R.O. Oreffo, C. Cooper, C. Mason, M. Clements, Mesenchymal stem cells, Stem Cell Rev. 1 (2) (2005) 169–178.

[4] A.R. Williams, J.M. Hare, Mesenchymal stem cells biology, pathophysiology, translational findings, and therapeutic implications for cardiac disease, Circ. Res. 109 (8) (2011) 923–940.

[5] J. Lazarević, T. Kukolj, D. Bugarski, N. Lazarević, B. Bugarski, Z. Popović, Probing primary mesenchymal stem cells differentiation status by micro-raman spectroscopy, Spectrochim. Acta A Mol. Biomol. Spectrosc. **213**, 384–390.

[6] R. Hass, C. Kasper, S. Böhm, R. Jacobs, Different populations and sources of human mesenchymal stem cells (msc): a comparison of adult and neonatal tissue-derived msc, Cell Commun. Signal 9 (1) (2011) 12.

[7] D.G. Phinney, Functional heterogeneity of mesenchymal stem cells: implications for cell therapy, J. Cell. Biochem. 113 (9) (2012) 2806–2812.

[8] I.C. Gay, S. Chen, M. MacDougall, Isolation and characterization of multipotent human periodontal ligament stem cells, Orthod. Craniofacial Res. 10 (3) (2007) 149–160.

[9] S. Ivanovski, S. Gronthos, S. Shi, P. Bartold, Stem cells in the periodontal ligament, Oral Dis. 12 (4) (2006) 358–363.

[10] M. Shimono, T. Ishikawa, H. Ishikawa, H. Matsuzaki, S. Hashimoto, T. Muramatsu, K. Shima, K.I. Matsuzaka, T. Inoue, Regulatory mechanisms of periodontal regeneration, Microsc. Res. Tech. 60 (5) (2003) 491–502.

[11] A. Miletić, S. Mojsilović, I. Okić-Djordjević, T. Kukolj, A. Jauković, J. Santibanez, G. Jovčić, D. Bugarski, Mesenchymal stem cells isolated from human periodontal ligament, Arch. Biol. Sci. 66 (1) (2014) 261–271.

[12] T. Kukolj, D. Trivanović, I.O. Djordjević, J. Mojsilović, J. Krstić, H. Obradović, S. Janković, J.F. Santibanez, A. Jauković, D. Bugarski, Lipopolysaccharide can modify differentiation and immunomodulatory potential of periodontal ligament stem cells via ERK1, 2 signaling, J. Cell. Physiol. 233 (1) (2018) 447–462.

[13] A. Klimczak, U. Kozlowska, Mesenchymal stromal cells and tissue-specific progenitor cells: their role in tissue homeostasis, Stem Cells Int. 2016 (2016) 1–11.

[14] H. Egusa, W. Sonoyama, M. Nishimura, I. Atsuta, K. Akiyama, Stem cells in dentistry—part II: clinical applications, J. Prosthodont. Res. 56 (4) (2012) 229–248.

[15] A. Downes, R. Mouras, A. Elfick, Optical spectroscopy for noninvasive monitoring of stem cell differentiation, BioMed Res. Int. 2010 (2010) 1–10.

[16] A. Downes, R. Mouras, P. Bagnaninchi, A. Elfick, Raman spectroscopy and CARS microscopy of stem cells and their derivatives, J. Raman Spectrosc. 42 (10) (2011) 1864–1870.

[17] C.V. Raman, K.S. Krishnan, A new type of secondary radiation, Nature 121 (3048) (1928) 501.

[18] J.W. Chan, D.K. Lieu, Label-free biochemical characterization of stem cells using vibrational spectroscopy, J. Biophotonics 2 (11) (2009) 656–668.

[19] A.F. Palonpon, J. Ando, H. Yamakoshi, K. Dodo, M. Sodeoka, S. Kawata, K. Fujita, Raman and SERS microscopy for molecular imaging of live cells, Nat. Protoc. 8 (4) (2013) 677–692.

[20] I. Notingher, I. Bisson, A.E. Bishop, W.L. Randle, J.M. Polak, L.L. Hench, In situ spectral monitoring of mrna translation in embryonic stem cells during differentiation in vitro, Anal. Chem. 76 (11) (2004) 3185–3193.

[21] F. Lyng, E. Gazi, P. Gardner, Preparation of Tissues and Cells for Infrared and Raman Spectroscopy and Imaging, Biomedical Applications of Synchrotron Infrared Microspectroscopy: A Practical Approach, Royal Society of Chemistry, Cambridge, 2010, 147–191.

[22] S.M. Levchenko, X. Peng, L. Liu, J. Qu, The impact of cell fixation on CARS signal intensity in neuronal and glial cell lines, J. Biophotonics (2018) e201800203.

[23] J.W. Chan, D.S. Taylor, D.L. Thompson, The effect of cell fixation on the discrimination of normal and leukemia cells with laser tweezers Raman spectroscopy, Biopolymers Original Res. Biomol. 91 (2) (2009) 132–139.

[24] A.D. Meade, C. Clarke, F. Draux, G.D. Sockalingum, M. Manfait, F.M. Lyng, H.J. Byrne, Studies of chemical fixation effects in human cell lines using Raman microspectroscopy, Anal. Bioanal. Chem. 396 (5) (2010) 1781–1791.

[25] M.M. Mariani, P. Lampen, J. Popp, B.R. Wood, V. Deckert, Impact of fixation on in vitro cell culture lines monitored with Raman spectroscopy, Analyst 134 (6) (2009) 1154–1161.

[26] E.A. Hoffman, B.L. Frey, L.M. Smith, D.T. Auble, Formaldehyde crosslinking: a tool for the study of chromatin complexes, J. Biol. Chem. (2015)jbc-R115.

[27] M. Noguchi, J.S. Furuya, T. Takeuchi, S. Hirohashi, Modified formalin and methanol fixation methods for molecular biological and morphological analyses, Pathol. Int. 47 (10) (1997) 685–691.

[28] J. Shaham, Y. Bomstein, A. Meltzer, Z. Kaufman, E. Palma, J. Ribak, DNA-protein crosslinks, a biomarker of exposure to formaldehyde-in vitro and in vivo studies, Carcinogenesis 17 (1) (1996) 121–126.

[29] T. Ichimura, K.F. Liang-da Chiu, S. Kawata, T.M. Watanabe, T. Yanagida, H. Fujita, Visualizing cell state transition using Raman spectroscopy, PloS One 9 (1) (2014) 1–8.

[30] E. Brauchle, K. Schenke-Layland, Raman spectroscopy in biomedicine—non-invasive in vitro analysis of cells and extracellular matrix components in tissues, Biotechnol. J. 8 (3) (2013) 288–297.

[31] I. Jolliffe, Principal component analysis, International Encyclopedia of Statistical Science, Springer. 2011, pp. 1094–1096.

[32] W. Wagner, P. Horn, M. Castoldi, A. Diehlmann, S. Bork, R. Saffrich, V. Benes, J. Blake, S. Pfister, V. Eckstein, et al. Replicative senescence of mesenchymal stem cells: a continuous and organized process, PloS One 3 (5) (2008) e2213.

[33] Y.H.K. Yang, C.R. Ogando, C.W. See, T.Y. Chang, G.A. Barabino, Changes in phenotype and differentiation potential of human mesenchymal stem cells aging in vitro, Stem Cell Res. Ther. 9 (1) (2018) 131.

[34] E. Gazi, J. Dwyer, N.P. Lockyer, J. Miyan, P. Gardner, C. Hart, M. Brown, N.W. Clarke, Fixation protocols for subcellular imaging by synchrotron-based Fourier transform infrared microspectroscopy, Biopolymers Original Res. Biomol. 77 (1) (2005) 18–30.

[35] A.C.S. Talari, Z. Movasaghi, S. Rehman, I.U. Rehman, Raman spectroscopy of biological tissues, Appl. Spectrosc. Rev. 50 (1) (2015) 46–111.

Spectrochimica Acta Part A: Molecular and Biomolecular Spectroscopy 213 (2019) 384–390

Contents lists available at ScienceDirect

Spectrochimica Acta Part A: Molecular and Biomolecular Spectroscopy

journal homepage: www.elsevier.com/locate/saa

Probing primary mesenchymal stem cells differentiation status by micro-Raman spectroscopy

J.J. Lazarević[a], T. Kukolj[b], D. Bugarski[b], N. Lazarević[a,*], B. Bugarski[c], Z.V. Popović[a,d]

[a] Center for Solid State Physics and New Materials, Institute of Physics Belgrade, University of Belgrade, Pregrevica 118, Belgrade 11080, Serbia
[b] Laboratory for Experimental Hematology and Stem Cells, Institute for Medical Research, University of Belgrade, Belgrade 11000, Serbia
[c] Department of Chemical Engineering, Faculty of Technology and Metallurgy, University of Belgrade, Karnegijeva 4, Belgrade 11060, Serbia
[d] Serbian Academy of Sciences and Arts, Knez Mihailova 35, Belgrade 11000, Serbia

ARTICLE INFO

Article history:
Received 17 September 2018
Accepted 21 January 2019
Available online 29 January 2019

Keywords:
Raman spectroscopy
Stem cells
Differentiation

ABSTRACT

We have employed micro-Raman spectroscopy to get insight into intrinsic biomolecular profile of individual mesenchymal stem cell isolated from periodontal ligament. Furthermore, these cells were stimulated towards adipogenic, chondrogenic, and osteogenic lineages and their status of differentiation was assessed using micro-Raman spectroscopy. In both cases, glass coverslips were used as substrates, due to their wide availability and cost effectiveness. In all sample groups, the same type of behavior was observed, manifested as changes in Raman spectra: the increase of relative intensity of protein/lipid bands and decrease of nucleic acid bands. Comprehensive statistical analysis in the form of principal component analysis was performed, which revealed noticeable grouping of cells with the similar features. Despite the inhomogeneity of primary stem cells and their differentiated lineages, we demonstrated that micro-Raman spectroscopy is sufficient for distinguishing cells' status, which can be valuable for medical and clinical application.

1. Introduction

In the era of regenerative medicine development, stem cells are in the center of attention, bringing hope for treating conditions and diseases presently incurable. In general, these expectations arise from unique qualities of these cells, which include self-renewal and multilineage differentiation potential *in vitro*. When it comes to potential clinical application of stem cells, from the aspect of differentiation capacity, embryonic stem cells (ESCs) and induced pluripotent stem cells (iPSCs) provide the greatest possibilities. However, it is well documented that both ESCs and iPSCs can form teratoma which directly restricts their therapeutic application. On the other hand, considering relatively simple isolation procedures, without ethical issues that follow manipulation of ESCs, mesenchymal stem cells (MSCs) have advantage over ESCs and iPSCs. Therefore, MSCs are promising agents in cell therapy and tissue engineering [1,2]. More than forty years ago, MSCs were discovered in bone marrow, but today it is known that this heterogenous population of cells resides in tissues and organs throughout the adult organism, where their primary role is maintenance of tissue regeneration and tissue homeostasis [3,4]. According to The International Society for Cellular Therapy, minimal criteria for characterisation of human MSCs are plastic adhesion with expression of CD73, CD90, and CD105 surface markers and lack of hematopoietic markers CD34-, CD45-, CD14-, CD79α-, HLA-DR-, and multilineage differentiation potential into osteoblasts, adipocytes, and chondroblasts [5]. Even though MSCs posses common cellular features, it is generally accepted that, due to tissue origin, donor age, culture conditions, these cells exhibit variable regenerative capacity [6,7]. Along with differentiation potential, an important part in considering MSCs as possible new therapeutic agents is their ability of immune response modulation (directly, through cell-to-cell contact or indirectly, by secretion of soluble factors) [8]. Originally, it was reported that MSCs can alter immune response in hypoimmunogenic manner, but their role in immunity is still the subject of extensive research [9].

Within regenerative dentistry, there is a great interest in development of novel therapeutic strategies related to the recovery of periodontium. As tooth supportive tissue, periodontium is directly responsible for appropriate incorporation of synthetic implants which today represents one of the main methods of medical treatment for curing dental defects. However, damaged periodontal tissue has limited capacity for regeneration and is often influenced by inflammation that can severely hamper periodontal structure,

---

[*] Corresponding author.
E-mail address: nenadl@ipb.ac.rs.

https://doi.org/10.1016/j.saa.2019.01.069
1386-1425/© 2019 Published by Elsevier B.V.

disabling implantation and tooth restoration. Periodontal ligament is a soft connective tissue which anchors tooth to the alveolar bone. Hence, the exploration of human periodontal ligament stem cells (hPDLSCs), as potential cell source for reconstructive dentistry, strongly contributes to the improvement of periodontal therapies [10-12]. Previously is demonstrated that PDLSCs fulfill criteria for MSCs identification and characterisation [13,14], set by International Society for Cellular Therapy [5,15]. Keeping in mind that the origin tissue of PDLSCs is periodontal ligament and that the main role of cells within this tissue is maintenance of mineralization level [16,17], it is expected for PDLSCs to be more osteogenic than adipogenic committed when compared to MSCs derived from other sources [18,19].

Regarding heterogeneity of MSCs, carefully performed characterisation of these cells and thoroughly monitored process of their differentiation, before further manipulation, is of great significance for their usage [20]. Various techniques are available in this field, such as immunocytochemistry, flow cytometry, mass spectrometry or gene expression analyses. However, these methods mostly imply disruption of cell integrity and, at the same time, they can be time consuming and require expensive biomarkers for each cell type [21]. Destructiveness comes out as the dominant drawback of these techniques. This gives rise to a need for non-invasive, non-destructive and fast technique, which would be able to monitor stem cells behavior, including differentiation process [20,21]. Owing to its features, Raman spectroscopy appears to be a promising candidate. Regarding clinical applicability, no sample preparation or a minimal preparation, is important feature of Raman spectroscopy. It is also suitable for measurements in aqueous solutions. The outcome of Raman scattering measurement is a vibrational spectrum in which macromolecules, such as proteins, nucleic acids, carbohydrates, and lipids, are presented with the most pronounced vibration modes of different chemical bonds. Interactions of molecules are also visible. Accordingly, Raman spectrum is a fingerprint of the analysed sample. In past decade, the interest in performing this type of analysis on stem cells is well documented [21-30].

Currently, advanced Raman setups are used in biomedical researches [31]. Most of the studies in the field of stem cells biology were performed with more experimentally demanding Raman spectroscopy experiments, such as Coherent anti-Stokes Raman spectroscopy (CARS), Raman tweezers, Tip enhanced Raman spectroscopy (TERS), or Surface enhanced Raman spectroscopy (SARS), due to their higher sensitivity. As far as we know, great number of these studies were focused on live murine and human ESCs [22-26], and spectral mapping of live and apoptotic ESCs [27], but the interest in mesenchymal stem cells is also noticeable [28,29,21]. One of the Raman studies on MSCs was performed to characterise the Raman spectra of bone marrow-derived MSCs and to study the effect of different inducers on their differentiation towards osteogenic lineage [30]. Further, Raman spectroscopy was assessed as the analytical tool which could be used for characterisation and identification of rhesus monkey mesenchymal stem cells from different age groups (fetal to juvenile) [32]. Moreover, Raman spectroscopy was used to map the distribution of different biomolecules within two types of stem cells: adult human bone marrow-derived MSCs and human ESCs, and to identify Raman spectral characteristics which distinguish genetically abnormal and transformed stem cell from normal ones [33]. Another study was dedicated to viability transitions detection of umbilical cord mesenchymal stem cells (hUC-MSCs) by micro-Raman spectroscopy, where the authors proposed that the viability of hUC-MSCs can be described with three peaks of certain energies [28].

Although numerous Raman studies of different stem cell lineages have been performed [22-26], it is still unclear whether Raman spectroscopy can unambiguously distinguish differentiation status of primary stem cells such as hPDLSCs. In order to address this matter, Raman scattering study of undifferentiated and differentiated hPDLSCs (osteogenic, chondrogenic, and adipogenic cells) has been performed. To assure multilineage mesenchymal differentiation capacity of hPDLSCs, standard biological detection of adipogenesis, chondrogenesis, and osteogenesis was conducted.

In general, the widespread applicability of this technique demands simplicity of the experimental setup and the availability of used substrates. In medicine, the most commonly used substrates are made of glass, which may be challenging for Raman spectroscopy, due to contributions to the sample spectrum. Besides limiting the spectral region that can be probed in the light scattering experiment it also hinders signal to noise ratio. The aim of this work was to determine the analytical ability of micro-Raman spectroscopy in commonly available experimental configuration, in order to assess differentiation status of hPDLSCs, with minimal sample processing, on glass substrates. Direct comparison of the primary hPDLSCs and differentiated hPDLSCs Raman spectra, as well as statistical analysis, revealed clear distinction between these groups. This approach could vastly simplify diagnostics and promote clinical application of MSCs.

2. Experiment

2.1. Isolation and Cultivation of Human Periodontal Ligament Stem Cells

Human PDLSCs were isolated from normal impacted third molars, as described elsewhere [14]. In brief, following the informed consent, tissues were collected from healthy patients aging 18–25 years, subjected to the procedure of tooth extraction for orthodontic reasons, at the Department of Oral Surgery of the Faculty of Dental Medicine, the University of Belgrade. All treatments were performed according to the approved ethical guidelines set by Ethics Committee of the Faculty of Dental Medicine, the University of Belgrade and Declaration of Helsinki. Directly after tooth extraction, periodontal tissues were carefully detached from the mid-third of the root surface, minced into small pieces and placed in a 25 cm^2 flask with Dulbecco's modified Eagle's medium (DMEM; PAA Laboratories, Pasching, Austria) supplemented with 10% fetal bovine serum (FBS; PAA Laboratories), 100 U/ml penicillin and 100 μg/ml streptomycin (PAA Laboratories), and cultured at 37 °C in a humidified atmosphere containing 5% CO_2, with medium exchange every third day. When the 80% to 90% confluence was reached, the cells were passaged regularly in growth medium (GM-DMEM with 10% FBS) using 0.05% trypsin with 1 mM EDTA (PAA Laboratories) and for this study cells from third to sixth passages were used. Further on, considering the minimal criteria for characterisation of MSC [5] immunophenotype of hPDLSCs and their multipotent differentiation capacity towards osteogenic, chondrogenic, and adipogenic lineages were confirmed as previously reported [14].

2.2. Sample Preparation

For Raman measurements, hPDLSCs were seeded on rounded glass coverslips in 24-well plate (2×10^4 cells per well) and grown in standard cultivation conditions. Simultaneously, cells were seeded in 24-well plate (2×10^4 cells per well) to follow differentiation by regular *in vitro* staining. When the confluence was reached, cells were induced to differentiate into osteogenic, chondrogenic and adipogenic lineages by specific differentiation medium. Osteogenic differentiation medium contained DMEM supplemented with 5% FBS, 100 U/ml penicillin/streptomycin, 50 μM ascorbic acid-2-phosphate and 10 mM β-glycerophosphate (both from Sigma-Aldrich). Chondrogenic medium contained DMEM with 5% FBS, 2 ng/ml of transforming growth factor-β1 (TGF-β; R&D Systems, Minneapolis, MN, USA), 50 µM ascorbic acid-2-phosphate, 10 nM dexamethasone, 100 U/ml penicillin/streptomycin. Adipogenic medium contained 5% FBS in DMEM, 100 U/ml penicillin/streptomycin, 100 µg/ml isobutyl-methyl xanthine (IBMX; Sigma-Aldrich), 1 µM dexamethasone and 10 µg/ml insulin (Sigma-Aldrich). With regular medium exchange, osteogenesis and chondrogenesis were evaluated after three weeks of cultivation, whereas adipogenesis was induced during four weeks. As for the control samples, cells were cultivated in GM with 5% FBS during the corresponding time. After this period, hPDLSCs were washed with saline buffer, fixed with methanol for 10 min at room temperature and washed with distilled water just before Raman spectroscopy was performed. Standard *in vitro* examination of differentiation process was performed after cells had been fixed and stained with specific dye. Intracellular lipid droplets were observed by Oil Red O (Merck Chemicals, Darmstadt, Germany) staining, while Safranin O confirmed cartilage-specific proteoglycan formation. Alizarin red was used to visualize calcium deposition and mineralization of extracellular matrix (see Fig. 1). Optical microscope with digital camera was used for cell morphology analysis and imaging.

2.3. *µ-Raman Spectroscopy*

Raman scattering measurements were performed using TriVista 557 Raman system in backscattering *µ*-Raman configuration. As an excitation source, 532 nm laser line of the Coherent VerdiG laser was used. The focusing on the sample was achieved by using ×100 microscope objective, $NA = 0.80$. The laser spot diameter in our experimental configuration was ≈4µm. In order to avoid any possible sample damage and/or temperature related effect, the laser power at the sample plain was kept at low levels, ≈ 1 mW. Acquisition time was 900 s. More details on Raman scattering experiment can be found in the Section S1 of the Supplementary Information.

From the aspects of vibrational spectroscopy, which can independently probe a single vibration within a molecule or a crystal, biological samples consisting of various types of macro-molecules, represent rather complicated systems. In these systems, only vibrational bands, consisting of numerous vibrations of the same type, can be taken into consideration, rather than a single vibration. Consequently, the changes of biological system (e.g. single cell) composition, may result in a change of certain Raman bands intensities.

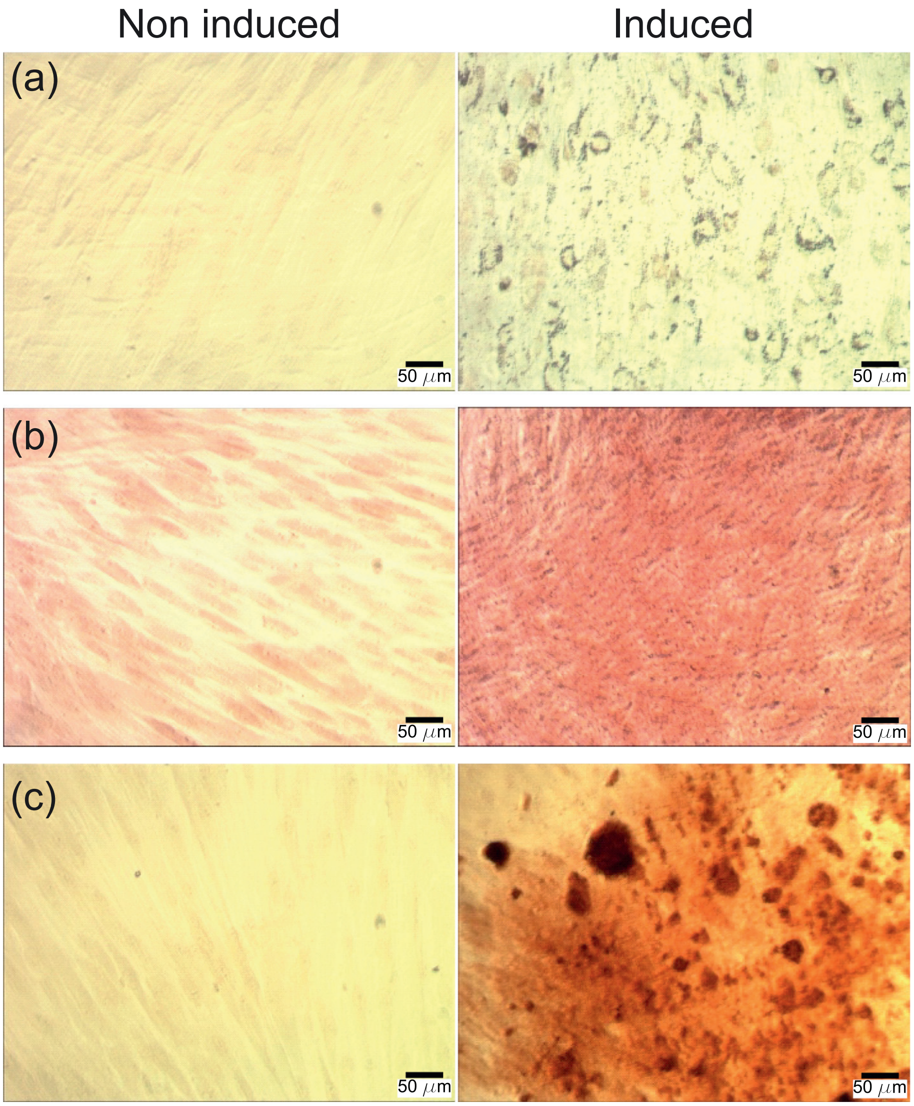

Fig. 1. Multilineage differentiation potential of hPDLSCs. (a) Oil Red O staining showed presence of intracytoplasmatic lipid droplets confirming adipogenic differentiation. (b) Chondrogenic differentiation was demonstrated by positive staining of proteoglycans with Safranin O. (c) Positive Alizarin red staining of extracellular matrix mineralization confirmed osteogenic differentiation.

It should be taken into account that when probing a single cell, due to its complex inner structure, there might be small variations in Raman spectra for the data collected at different positions. To obtain single spectra representative for each of the cells, recorded spectra were averaged. The preliminary experiment involved investigation of 54 cells of Batch 1. For every cell lineage, 9 hPDLSCs and 9 differentiated cells were analysed by probing each cell at 10 randomly chosen positions. The results of the analysis performed on the full set of data as well as on the sub-set including three random positions, revealed no qualitative difference. This implies that for our experimental configuration and for the samples under investigation, three randomly chosen positions are sufficient to make qualitative conclusions. Having in mind statistical treatment of the results, a total of 1080 spectra from 360 cells were recorder and analysed in the main experiment.

2.4. Data Processing and Analysis

Prior to the analysis, all Raman spectra were processed by subtracting the contributions from substrate (see Fig. 2 (a)), as well as biological fluorescence. No spectral smoothing of the samples spectra has been performed. On the other hand, the substrate spectrum was obtained separately with greater acquisition time and statistics and post-processed by Savitzky–Golay filter. Right inset on Fig. 2 (a) compares the substrate and the mean of 540 hPDLSCs Raman spectra. Significantly smaller noise level of the (glass) substrate spectrum indicates absence of its contribution to hPDLSCs spectra statistics. Due to the substantial increase of the substrate spectral weight at lower energies, our analysis was limited to the region above 1000 cm^{-1}.

The absolute value of Raman intensity is not usually a reliable quantity. Even small variations in the experimental conditions may produce the " artificial" variations of Raman intensity. In order to exclude this possible uncertainty, all spectra were normalised onto the peak at about 1660 cm^{-1}, which is present with high intensity in all obtained spectra.

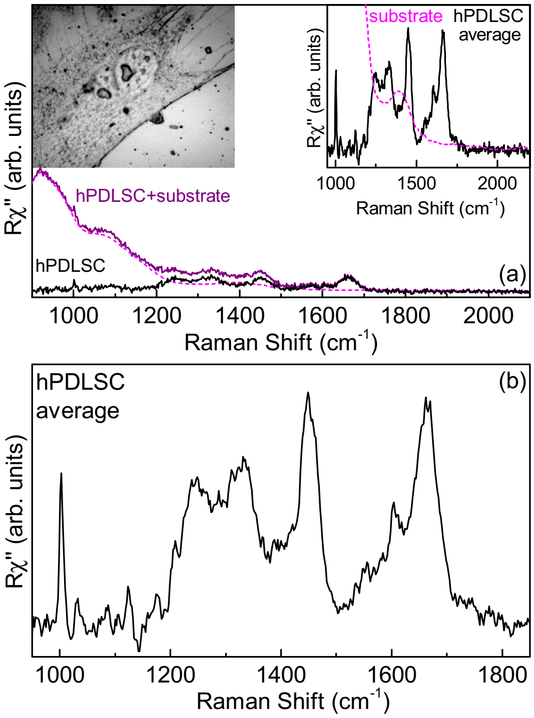

Fig. 2. (a) Raman scattering spectra of hPDLSCs on glass, glass substrate and their difference. Left inset: Image of hPDLSCs. Right inset: Comparison between the substrate and the mean of 540 hPDLSCs Raman spectra. (b) The mean of 540 hPDLSCs Raman spectra.

Besides the direct comparison of spectra obtained from stem cells and differentiated cells, a multivariate statistical method, principal component analysis (PCA), was employed [40,20,25,22]. The main goal of PCA is to reduce the effective dimensionality of the experimental data set by determining the orthonormal basis of loading vectors in a way that the greatest variance is projected onto the first coordinate, the second greatest variance is projected onto the second coordinate, and so on. The outcome of this analysis is clear grouping of Raman spectra according to their mutual features. Prior to performing PCA, the spectral data were subtracted by the mean spectrum and divided by its standard deviation [40,22].

3. Results and Discussion

To get insight on how hPDLSCs differentiation status reflects on Raman spectra, three sets of Raman experiments were performed. The samples were set in two batches. For every lineage, spectra were obtained for 30 hPDLSCs and 30 differentiated cells (hPDLSC grown in standard cultivation medium for the corresponding time for each differentiation). The spectrum of every cell was measured three times on each of three randomly chosen positions within the cell in order to incorporate possible variations within a single cell and test the approach sufficiency for observing the difference between cell lineages.

Fig. 2 (b) shows Raman spectrum of hPDLSCs obtained by averaging spectra of all control samples. The main contribution to the hPDLSCs Raman spectrum for the region under consideration comes from nucleic acids, proteins and lipids [24,28,41,23,37-39]. Spectral features of nucleic acids originate from the individual purine and pyrimidine bases (adenine, thymine, guanine, cytosine, and uracil), as well as from backbone structure of DNA and RNA, whereas protein spectral features include contributions from aromatic amino acids (phenylalanine, tryptophan, and tyrosine), amide groups of secondary protein structures (α-helices, β-sheets, and random coils), and various vibrations of carbon atoms bonded with nitrogen and/or other carbon atoms [38]. Different vibrations within the hydrocarbon chain (e.g. C—C stretching, CH_2 and CH_3 scissoring and twisting) present specific features of lipids in Raman spectra [35]. Principally, various contributions may overlap, making the determination of the potential changes in Raman spectra of undifferentiated and differentiated hPDLSCs a formidable task. As can be seen from Fig. 2 (b), numerous vibrational bands have been observed in hPDLSCs Raman spectrum. The most pronounced bands are assigned according to the literature [24,28,41,23, 34-39] and summarized in Table 1.

Fig. 3 (a)–(c) shows averaged hPDLSCs Raman spectra of control samples, differentiated cells (adipocytes, chondroblasts, and osteoblasts, respectively) of both batches, as well as corresponding pairs' differences. Although the overall spectral features in these pairs of spectra look almost the same, after the subtraction, the difference is more pronounced. General conclusion, consistent with the literature data [22,25], is that relative intensities (with regard to 1660 cm^{-1} peak structure intensity) of nucleic acids and proteins, are able to distinguish stem cells from more mature cells. In the case of adipogenic differentiation, a slight decrease of the relative intensity of the band at 1100 cm^{-1} and increase of the relative intensity of peaks at about 1353 cm^{-1}, 1447 cm^{-1}, and 1590 cm^{-1} (see Fig. 3 (a)) is observed. According to Table 1, this might be understood as slight reduction of nucleic acids and enhancement of proteins and lipids. On the other hand, the possible increase of the band at 1735 cm^{-1}, assigned to lipids (esters), is absent. Explanation for this lies in the fact that these cells do not originate from

Table 1
Vibrations in hPDLSCs and their energies noticed in Raman spectrum. (A) adenine, (U) uracil, (C) cytosine, (T) thymine, (G) guanine, (Phe) phenylalanine, (Trp) tryptophan, (Tyr) tyrosine, (vib) vibration, (bg) bending, (br) breathing, (bk) backbone,(def) deformation, (tw) twist, (sym) symmetric, (asym) asymmetric, and (str) stretch [28,23,34-39].

Energy (cm^{-1})	Assignment
1004	Phe
1032	Phe
1061	C—N and C—C str
1080	PO_2^- sym str
1085	C—O str
1105	PO_2^- str (sym)
1130	C—N and C—C asym str
1155	C—C and C—N str of proteins
1165	C—O str, COH bg
1172	G ring str
1178	CH ben Tyr
1209	C-C_6H_5 str, Phe, Trp
1228	Asym phosphate str
1250	T, amide III_β
1260	N—H and C—H bg (amide III/distorted)
1265	Amide III_α
1315	G, CH def.
1332	DNA purine bases (CH_3CH_2 wagging mode of polynucleotide chain)
1450	CH_2 str def of methylene group in lipids
1456	CH def.
1556	Amide II
1604	Phe, Tyr
1654	Amide I, α helix
1670	Amide I, β sheet

adipose tissue [18,19]. When it comes to the case of chondrogenic differentiation, higher relative intensities of the peaks at 1065 cm^{-1}, 1250–1450 cm^{-1}, and 1630 cm^{-1} are exhibited (Fig. 3 (b)). These changes arise from higher content of proteins and proteoglycans [42,43]. Regarding the osteogenic differentiation, spectral changes between hPDLSCs and their differentiated pairs (Fig. 3 (c)) originate from the lower relative intensities of the bands in the region from 1170 cm^{-1} to 1220 cm^{-1} and from 1450 cm^{-1} to 1490 cm^{-1}, and higher relative intensities at about 1045 cm^{-1}, 1070 cm^{-1}, and 1600 cm^{-1}. These changes are caused by decrease in amino acids and likely lipids, and increase in carbonates and phosphates, as expected. This decrease of the band intensity in the region that most likely correspond to lipids, might be understood as a change in proteins to lipids ratio. Typical spectral marker for this type of cells is hydroxyapatite, but due to spectral interference from the substrate (glass), it is out of spectral range of interest in this study [43]. Consistently observed spectral changes during the differentiation process (the increase of protein bands and decrease of nucleic acid bands in differentiated cells) are in accordance with the literature [22,25]. The possible explanation for this behavior is that, as cells differentiate, they gradually begin to use up the pool of mRNA to support the synthesis of new, cell lineage specific proteins [22].

Although the direct comparison between hPDLSCs and their differentiated lineages Raman spectra gave us means to distinguish cell differentiation status, it is demanding and require detailed analysis of the spectra. However, if we utilize the Raman spectra as characteristic fingerprints of the cells under investigation, PCA can be employed for pattern recognition and grouping. Fig. S1 of the Supplementary information summarizes loading vectors for the main PCs. It is noticeable that a certain loading vector or their linear combination fully describe corresponding difference spectra shown in Fig. 3 (a)–(c). Consequently, the same conclusions can be made as in previous paragraph. Fig. 3 (d)–(f) shows score plots calculated independently using PCA for three groups of control hPDLSCs samples and their differentiated lineages'

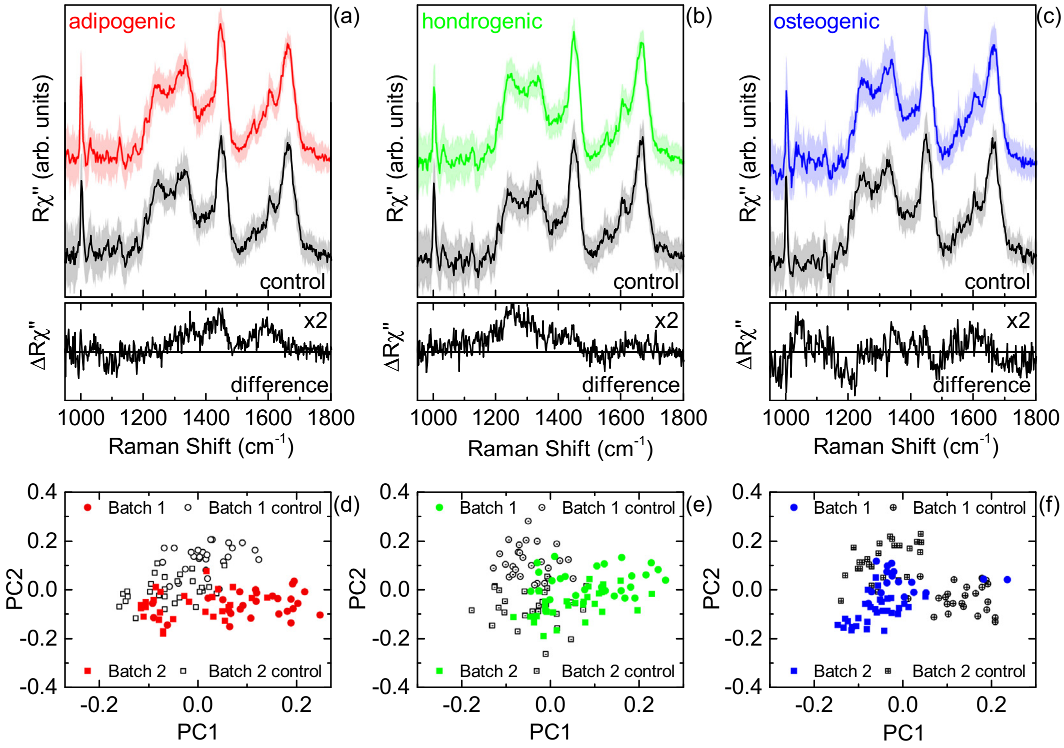

Fig. 3. (a)–(c) Averaged Raman spectra (black lines) of hPDLSCs (control samples), differentiated hPDLSCs (adipogenic, chondrogenic, and osteogenic lineages) and difference spectrum between these two groups of cells. Standard deviation for each lineage and control group is presented with the colored areas. (d)–(f) Score plots calculated independently using PCA for three groups of control hPDLSCs and differentiated hPDLSCs Raman spectra.

Raman spectra. In all three cases, two groups can be observed, with each grouping corresponding to a particular cell lineage. Furthermore, within each grouping, sub-groupings are noticed, indicating variations and inhomogeneity between the batches. In fact, this is not surprising since these are primary cells and the higher level of inhomogeneity is expected. In the following paragraphs, the attention will be focused on the analysis within the batches.

Fig. 4 summarizes adipogenic, chondrogenic, and osteogenic lineages score plots for Batches 1 and 2. Although the separation between data point groupings can be observed for both batches, it is more pronounced for Batch 1. Most likely, this is a consequence of higher inhomogeneity within the Batch 2.

In the next step, we wanted to test whether the same approach can be used to distinguish different types of differentiated cells (adipocytes, chondroblasts, and osteoblasts). For this purpose, the data from all three sets of experiments had been combined and PCA performed, for both batches. The obtained score plots are presented in Fig. 5. Shaded areas represent 1σ 2D confidence level. Remarkably, very good grouping of the different cell lineages has been observed for Batch 1. Less separation of different cell groups was observed for Batch 2, in agreement with the results presented in Fig. 4. Additionally, PCA indicates the variations within hPDLSCs (in particular for Batch 2) although this was not so obvious in direct comparison. When PCA was applied on hPDLSCs from all three control groups and compared with differentiated hPDLSCs data, it could be noticed that even though small variations are present, control hPDLSCs retain characteristics of stem cells, suggesting these cell populations are not homogeneous. Keeping that in mind, spectral analyses of hPDLSCs are in accordance with data obtained by traditional MSCs characterisation methods that also emphasize heterogeneity of MSCs population. As being primary cells, cellular diversity of MSCs is a result of isolation methods and culture conditions. Further, the absence of unique MSCs biomarkers makes these cells still highly difficult for molecular identification and characterisation [5,44]. Thus, our results suggest the possibility of the Raman spectroscopy application in characterisation of MSCs.

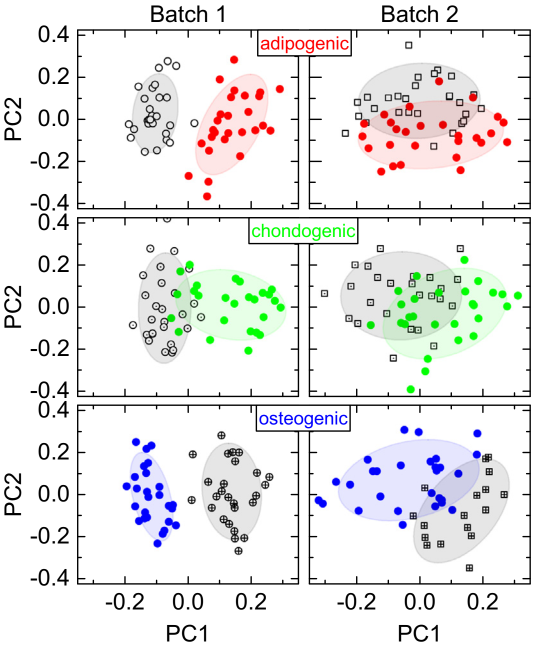

Fig. 4. Score plots calculated independently using PCA for three groups of control (black) and differentiated (adipogenic, chondogenic, and osteogenic lineages) hPDLSCs samples Raman spectra in two batches. Shaded areas represent 1σ 2D confidence level.

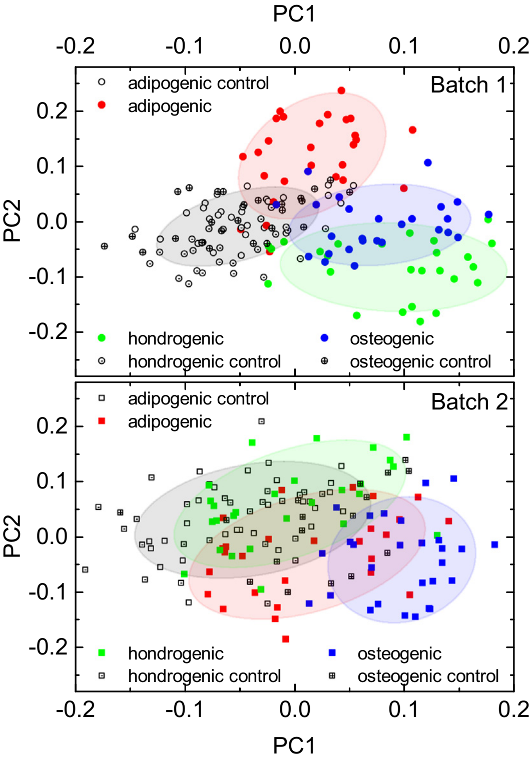

Fig. 5. PCA performed on all obtained Raman spectra of four groups of cells including nondifferentiated hPDLSCs (control) and differentiated hPDLSCs (osteogenic, chondrogenic and adipogenic lineages) for different batches. Shaded areas represent 1σ 2D confidence level.

4. Conclusion

In this study, the applicability of micro-Raman spectroscopy for probing primary hPDLSCs differentiation status on glass substrate was demonstrated. In direct comparison of hPDLSCs and differentiated cells Raman spectra, the difference in the relative intensities of certain marker bands has been observed. Additionally, statistical analysis of fingerprint Raman spectra of the cells using PCA, revealed distinct groupings based on the similar features. This gives a possibility of devising the procedure not only for fast and simple detection of different mesenchymal stem cell lineages, but also for the variations within. Furthermore, due to minimal preparation requirements and independency on the reagents that are necessary in standard biological techniques, Raman spectroscopy can be used as an additional method in MSCs characterisation. From the standpoint of MSCs utilization in biomedicine, simplification of the procedures in cell identification could significantly facilitate research in the field of stem cell biology.

Acknowledgments

We gratefully acknowledge M. Miletić and M. Andrić for supplying the periodontal ligament tissue and Dr. N. Paunović for constructive discussions on the subject. This work was supported by the Ministry of Education, Science, and Technological Development of the Republic of Serbia, Serbia under Projects No. III46010, III45018, and ON175062.

Appendix A. Supplementary data

Supplementary data to this article can be found online at https://doi.org/10.1016/j.saa.2019.01.069.

References

[1] X. Wei, X. Yang, Z. p. Han, F. f. Qu, L. Shao, Y. f. Shi, Mesenchymal stem cells: a new trend for cell therapy, Acta Pharmacol. Sin. 34 (6) (2013) 747–754.
[2] D. Howard, L.D. Buttery, K.M. Shakesheff, S.J. Roberts, Tissue engineering: strategies, stem cells and scaffolds, J. Anat. 213 (1) (2008) 66–72.
[3] Y. Sato, H. Araki, J. Kato, K. Nakamura, Y. Kawano, M. Kobune, T. Sato, K. Miyanishi, T. Takayama, M. Takahashi, et al. Human mesenchymal stem cells xenografted directly to rat liver are differentiated into human hepatocytes without fusion, Blood 106 (2) (2005) 756–763.
[4] C. Toma, M.F. Pittenger, K.S. Cahill, B.J. Byrne, P.D. Kessler, Human mesenchymal stem cells differentiate to a cardiomyocyte phenotype in the adult murine heart, Circulation 105 (1) (2002) 93–98.
[5] M. Dominici, K. Le Blanc, I. Mueller, I. Slaper-Cortenbach, F. Marini, D. Krause, R. Deans, A. Keating, D. Prockop, E. Horwitz, Minimal criteria for defining multipotent mesenchymal stromal cells. The International Society for Cellular Therapy position statement, Cytotherapy 8 (4) (2006) 315–317.
[6] R. Hass, C. Kasper, S. Böhm, R. Jacobs, D. Populations, Sources of human mesenchymal stem cells (msc). A comparison of adult and neonatal tissue-derived msc, Cell Commun. Signal 9 (1) (2011) 12.
[7] D.G. Phinney, Functional heterogeneity of mesenchymal stem cells: implications for cell therapy, J. Cell. Biochem. 113 (9) (2012) 2806–2812.
[8] M. Gazdic, V. Volarevic, N. Arsenijevic, M. Stojkovic, Mesenchymal stem cells: a friend or foe in immune-mediated diseases, Stem Cell Rev. Rep. 11 (2) (2015) 280–287.
[9] R. Abdi, P. Fiorina, C.N. Adra, M. Atkinson, M.H. Sayegh, Immunomodulation by mesenchymal stem cells: a potential therapeutic strategy for type 1 diabetes, Diabetes 57 (7) (2008) 1759–1767.
[10] S. Shi, P. Bartold, M. Miura, B. Seo, P. Robey, S. Gronthos, The efficacy of mesenchymal stem cells to regenerate and repair dental structures, Orthod. Craniofac. Res. 8 (3) (2005) 191–199.
[11] E.A.A. Neel, W. Chrzanowski, V.M. Salih, H.W. Kim, J.C. Knowles, Tissue engineering in dentistry, J. Dent. 42 (8) (2014) 915–928.
[12] H. Egusa, W. Sonoyama, M. Nishimura, I. Atsuta, K. Akiyama, Stem cells in dentistry-part ii: clinical applications, J. Prosthodont. Res. 56 (4) (2012) 229–248.
[13] T. Kukolj, D. Trivanović, I.O. Djordjević, S. Mojsilović, J. Krstić, H. Obradović, S. Janković, J.F. Santibanez, A. Jauković, D. Bugarski, Lipopolysaccharide can modify differentiation and immunomodulatory potential of periodontal ligament stem cells via erk1,2 signaling, J. Cell. Physiol. 233 (1) (2018) 447–462.
[14] M. Miletić, S. Mojsilović, I. Okić-Djordjević, T. Kukolj, A. Jauković, J. Santibacez, G. Jovčić, D. Bugarski, Mesenchymal stem cells isolated from human periodontal ligament, Arch. Biol. Sci. 66 (1) (2014) 261–271.
[15] A. Klimczak, U. Kozlowska, Mesenchymal stromal cells and tissue-specific progenitor cells: their role in tissue homeostasis, Stem Cells Int. 2016 (2016) 1–11.
[16] M. Shimono, T. Ishikawa, H. Ishikawa, H. Matsuzaki, S. Hashimoto, T. Muramatsu, K. Shima, K.I. Matsuzaka, T. Inoue, Regulatory mechanisms of periodontal regeneration, Microsc. Res. Tech. 60 (5) (2003) 491–502.
[17] A. Nanci, D.D. Bosshardt, Structure of periodontal tissues in health and disease, Periodontol. 2000 40 (1) (2006) 11–28.
[18] T. Iwata, M. Yamato, Z. Zhang, S. Mukobata, K. Washio, T. Ando, J. Feijen, T. Okano, I. Ishikawa, Validation of human periodontal ligament-derived cells as a reliable source for cytotherapeutic use, J. Clin. Periodontol. 37 (12) (2010) 1088–1099.
[19] D. Trivanović, A. Jauković, B. Popović, J. Krstić, S. Mojsilović, I. Okić-Djordjević, T. Kukolj, H. Obradović, J.F. Santibanez, D. Bugarski, Mesenchymal stem cells of different origin: comparative evaluation of proliferative capacity, telomere length and pluripotency marker expression, Life Sci. 141 (2015) 61–73.
[20] A. Downes, R. Mouras, A. Elfick, Optical spectroscopy for noninvasive monitoring of stem cell differentiation, Biomed. Res. Int. 2010 (2010) 1–10.
[21] A. Downes, R. Mouras, P. Bagnaninchi, A. Elfick, Raman spectroscopy and cars microscopy of stem cells and their derivatives, J. Raman Spectrosc. 42 (10) (2011) 1864–1870.
[22] J.W. Chan, D.K. Lieu, Label-free biochemical characterization of stem cells using vibrational spectroscopy, J. Biophotonics 2 (11) (2009) 656–668.
[23] I. Notingher, I. Bisson, A.E. Bishop, W.L. Randle, J.M. Polak, L.L. Hench, In situ spectral monitoring of mrna translation in embryonic stem cells during differentiation in vitro, Anal. Chem. 76 (11) (2004) 3185–3193.
[24] C. Aksoy, F. Severcan, Role of vibrational spectroscopy in stem cell research, J. Spectrosc. 27 (3) (2012) 167–184.
[25] E. Brauchle, K. Schenke-Layland, Raman spectroscopy in biomedicine-non-invasive in vitro analysis of cells and extracellular matrix components in tissues, Biotechnol. J. 8 (3) (2013) 288–297.
[26] H.G. Schulze, S.O. Konorov, N.J. Caron, J.M. Piret, M.W. Blades, R.F. Turner, Assessing differentiation status of human embryonic stem cells noninvasively using Raman microspectroscopy, Anal. Chem. 82 (12) (2010) 5020–5027.
[27] A. Ghita, F.C. Pascut, V. Sottile, C. Denning, I. Notingher, Applications of Raman micro-spectroscopy to stem cell technology: label-free molecular discrimination and monitoring cell differentiation, EPJ Techniques Instrum. 2 (1) (2015) 1–14.
[28] H. Bai, P. Chen, H. Fang, L. Lin, G. Tang, G. Mu, W. Gong, Z. Liu, H. Wu, H. Zhao, et al. Detecting viability transitions of umbilical cord mesenchymal stem cells by Raman micro-spectroscopy, Laser Phys. Lett. 8 (1) (2011) 78–84.
[29] H.K. Chiang, F.Y. Peng, S.C. Hung, Y.C. Feng, In situ Raman spectroscopic monitoring of hydroxyapatite as human mesenchymal stem cells differentiate into osteoblasts, J. Raman Spectrosc. 40 (5) (2009) 546–549.
[30] E. Azrad, D. Zahor, R. Vago, Z. Nevo, R. Doron, D. Robinson, L.A. Gheber, S. Rosenwaks, I. Bar, Probing the effect of an extract of elk velvet antler powder on mesenchymal stem cells using Raman microspectroscopy: enhanced differentiation toward osteogenic fate, J. Raman Spectrosc. 37 (4) (2006) 480–486.
[31] C. Krafft, J. Popp, The many facets of Raman spectroscopy for biomedical analysis, Anal. Bioanal. Chem. 407 (3) (2015) 699–717.
[32] B.S. Kim, C.C.I. Lee, J.E. Christensen, T.R. Huser, J.W. Chan, A.F. Tarantal, Growth, differentiation, and biochemical signatures of rhesus monkey mesenchymal stem cells, Stem Cells Dev. 17 (1) (2008) 185–198.
[33] L. Harkness, S.M. Novikov, J. Beermann, S.I. Bozhevolnyi, M. Kassem, Identification of abnormal stem cells using Raman spectroscopy, Stem Cells Dev. 21 (12) (2012) 2152–2159.
[34] A. Rygula, K. Majzner, K.M. Marzec, A. Kaczor, M. Pilarczyk, M. Baranska, Raman spectroscopy of proteins: a review, J. Raman Spectrosc. 44 (8) (2013) 1061–1076.
[35] K. Czamara, K. Majzner, M. Pacia, K. Kochan, A. Kaczor, M. Baranska, Raman spectroscopy of lipids: a review, J. Raman Spectrosc. 46 (1) (2015) 4–20.
[36] K. Maquelin, C. Kirschner, L.-P. Choo-Smith, N. van den Braak, H. Endtz, D. Naumann, G. Puppels, Identification of medically relevant microorganisms by vibrational spectroscopy, J. Microbiol. Methods 51 (3) (2002) 255–271.
[37] G. Clemens, J.R. Hands, K.M. Dorling, M.J. Baker, Vibrational spectroscopic methods for cytology and cellular research, Analyst 139 (18) (2014) 4411–4444.
[38] Q. Matthews, A. Jirasek, J. Lum, X. Duan, A.G. Brolo, Variability in Raman spectra of single human tumor cells cultured in vitro: correlation with cell cycle and culture confluency, Appl. Spectrosc. 64 (8) (2010) 871–887.
[39] Z. Movasaghi, S. Rehman, I.U. Rehman, Raman spectroscopy of biological tissues, Appl. Spectrosc. Rev. 42 (5) (2007) 493–541.
[40] T. Ichimura, K.F. Liang-da Chiu, S. Kawata, T.M. Watanabe, T. Yanagida, H. Fujita, Visualizing cell state transition using Raman spectroscopy, PloS one 9 (1) (2014) 1–8.
[41] E. Brauchle, S. Noor, E. Holtorf, C. Garbe, K. Schenke-Layland, C. Busch, Raman spectroscopy as an analytical tool for melanoma research, Clin. Exp. Dermatol. 39 (5) (2014) 636–645.
[42] M. Pudlas, E. Brauchle, T.J. Klein, D.W. Hutmacher, K. Schenke-Layland, Non-invasive identification of proteoglycans and chondrocyte differentiation state by Raman microspectroscopy, J. Biophotonics 6 (2) (2013) 205–211.
[43] G.S. Mandair, M.D. Morris, Contributions of Raman spectroscopy to the understanding of bone strength, BoneKEy Reports 4 (620) (2015) 1–8.
[44] J. Kobolak, A. Dinnyes, A. Memic, A. Khademhosseini, A. Mobasheri, Mesenchymal stem cells: identification, phenotypic characterization, biological properties and potential for regenerative medicine through biomaterial micro-engineering of their niche, Methods 99 (2016) 62–68.

PHYSICAL REVIEW B **99**, 144419 (2019)

Phonon anomalies and magnetic excitations in $BaFe_2Se_2O$

Feng Jin,[1] Nenad Lazarević,[2] Changle Liu,[3] Jianting Ji,[4] Yimeng Wang,[1] Shuna He,[1] Hechang Lei,[1] Cedomir Petrovic,[5]
Rong Yu,[1] Zoran V. Popović,[2,6] and Qingming Zhang[4,7,*]

[1]*Department of Physics and Beijing Key Laboratory of Opto-electronic Functional Materials & Micro-nano Devices, Renmin University of China, Beijing 100872, China*
[2]*Center for Solid State Physics and New Materials, Institute of Physics Belgrade, University of Belgrade, Pregrevica 118, 11080 Belgrade, Serbia*
[3]*State Key Laboratory of Surface Physics and Department of Physics, Fudan University, Shanghai 200433, China*
[4]*Beijing National Laboratory for Condensed Matter Physics, Institute of Physics, Chinese Academy of Sciences, Beijing 100190, China*
[5]*Condensed Matter Physics and Materials Science Department, Brookhaven National Laboratory, Upton, New York 11973-5000, USA*
[6]*Serbian Academy of Sciences and Arts, Knez Mihailova 35, Belgrade 11000, Serbia*
[7]*School of Physical Science and Technology, Lanzhou University, Lanzhou 730000, China*

(Received 6 March 2019; revised manuscript received 4 April 2019; published 22 April 2019)

We report a temperature- and magnetic-field-dependent Raman-scattering study of the spin-ladder compound $BaFe_2Se_2O$. Temperature evolution of the B_{1g} mode self-energies revealed anomalous behavior at about 100 and 240 K with strong temperature-dependent Fano asymmetry. Furthermore, the A_g modes integrated intensity exhibits an additional change in tendency at about 50 K. All the observed anomalies can be traced back to spin-phonon interaction contributions as well as multiple magnetic phase transitions present in $BaFe_2Se_2O$ also detected in the Raman continuum induced by the spin fluctuations. Moreover, the absence of magnetic-field dependence of the magnetic mode observed at 436 cm^{-1} and the small linewidth and high intensity are different from the magnetic modes at about 650 cm^{-1}. This suggests a two-magnon continuum and a two-magnon bound state resonance for this mode.

DOI: 10.1103/PhysRevB.99.144419

I. INTRODUCTION

Quantum spin ladders have attracted much interest because of their fascinating properties and their possible relevance to the phase diagram of high-temperature superconducting cuprates [1–4]. The ground-state properties and the quasiparticle spectrum of the two-leg spin ladder have been studied theoretically [5–9] and experimentally [10–14]. Generally these systems may host various competing magnetic phases that are in close proximity.

Raman scattering offers a unique and powerful tool for probing lattice, spin, and charge excitations as well as interplay between them [4]. In the undoped spin ladder compound $La_6Ca_8Cu_{24}O_{41}$, the ladders contribute to a very broad two-triplet Raman line shape whose position is slightly different for leg-leg and rung-rung polarizations [15] in accordance with theoretical models [16]. However, in the spin-ladder and charge-ordered compound $Sr_{14}Cu_{24}O_{41}$, only a particularly sharp peak is observed at the same frequency for both polarizations [12,15]. Here, the spin-ladder (antiferromagnetic dimer) structure magnon related modes appear in the form of singularities of one-dimensional density of two-magnon states [11].

The iron-based compound $BaFe_2Se_2O$ is an experimental realization of a two-leg ladder structure [17–19]. In this compound, all iron ions are in the Fe^{2+} oxidation state with a high spin $S = 2$. The Fe_2Se_2O planes containing weakly coupled ladders are stacked along the c crystallographic axis. The ladder legs and rungs are along the b and a crystallographic axis, respectively. The basic magnetic properties of $BaFe_2Se_2O$ have been characterized by magnetic susceptibility and specific-heat measurements [17,18]. The magnetic susceptibility shows a broad maximum at $T_{\max} \approx 450$ K and three successive magnetic phase transitions at $T \approx 240$, 115, and 43 K with $T_{\max}$ explained as due to the short-range correlation of the local moments [17] and the three magnetic phase transitions explained as either due to the antiferromagnetic phase transition (240 K) or due to the formation of spin-singlet dimers (115 and 43 K) [18]. Surprisingly, the specific-heat measurements indicate that the magnetic entropy up to 300 K is much smaller than the expected value. Local-spin-density-approximation calculations [17] suggest that the interaction along the rungs J is more than three times stronger than the interladder interaction J', whereas the interaction along the legs J'' can be neglected. A lattice dynamics study of $BaFe_2Se_2O$ was recently reported by Popović *et al.* [19]. They also observed a magnetic excitation related structure in the form of a magnon continuum with peaks corresponding to the singularities in the one-dimensional density of magnon states. In order to clarify the unusually large intensity of the lower-energy (magnon) peak and the origin of the B_{1g} modes line-shape asymmetry, a systematic Raman study, particularly in magnetic fields, is highly required.

In this paper, we report temperature- and field-dependent Raman-scattering measurements on $BaFe_2Se_2O$. The

---

[*] Corresponding author: qmzhang@ruc.edu.cn

temperature-dependent Raman spectra indicate the absence of a structural phase transition between 10 and 300 K, consistent with a moderate spin-phonon coupling. The Raman continuum observed only in the parallel polarization suggests strong spin fluctuations, and allows us to identify magnetic phase transitions at about 50, 100, and 240 K. The intensity of the sharp magnetic mode at 436 cm^{-1} exhibits a strong nonmonotonic field-dependent behavior with no observable energy shift with external magnetic fields up to 9 T. It is interpreted in terms of the two-magnon continuum and a two-magnon bound state resonance. The present study provides the fundamental lattice and spin dynamics information on $\text{BaFe}_2\text{Se}_2\text{O}$ and deepens the understanding of magnetic excitations in low-dimensional spin systems.

II. EXPERIMENTS

The $\text{BaFe}_2\text{Se}_2\text{O}$ single crystals used in this study were grown using the self-flux method. The details of crystal growth can be found elsewhere [18]. The average stoichiometry was checked using energy-dispersive x-ray spectroscopy (EDS; Oxford X-Max 50). The average atomic ratios determined from EDS are Ba:Fe:Se =1.0:1.9(2):2.0(2), close to the ratio of stoichiometric $\text{BaFe}_2\text{Se}_2\text{O}$. The presence of oxygen was confirmed for $\text{BaFe}_2\text{Se}_2\text{O}$, but the exact amount could not be quantified because of experimental limitations.

Freshly cleaved samples of (001) orientation were transferred into a UHV cryostat with a vacuum of better than 10^{-8} mbar. Temperature-dependent Raman spectra were collected with a Jobin Yvon LabRam HR800 spectrometer equipped with a volume Bragg grating low-wave-number suite, a liquid-nitrogen-cooled back-illuminated charge-coupled device detector, and a 633-nm laser (Melles Griot) with $\Gamma_\sigma < 0.1\ \text{cm}^{-1}$. The laser was focused into a spot of $\sim 5\ \mu\text{m}$ in diameter on the sample surface, with a power $< 100\ \mu\text{W}$, to avoid overheating. Magnetic-field-dependent Raman spectra were collected with a Jobin Yvon T64000 spectrometer also equipped with a liquid-nitrogen-cooled back-illuminated CCD. A 532-nm diode-pumped solid-state laser (Torus 532; Laser Quantum) was used as an excitation source. The laser was focused onto the samples with a spot size of 5–10 μm in diameter. The laser power was maintained at a level of 300 μW and monitored with a power meter (Coherent Inc.). Magnetic fields were generated up to 9 T using a superconducting magnet (Cryomagnetics) that has a room-temperature bore that is suitable for a microscope lens. The magnetic-field direction was perpendicular to the (001) plane of the sample.

In this paper, the Porto notation $i(jk)l$ is used for the scattering geometry, where i and l denote the direction and j and k the polarization of the incident and scattered light, respectively, and u stands for unpolarized light.

III. RESULTS AND DISCUSSION

A. Lattice dynamics and spin-phonon coupling

$\text{BaFe}_2\text{Se}_2\text{O}$ crystallizes in the orthorhombic crystal structure, described with space group *Pmmm*, with Ba and O atoms having C_{2v} site symmetry, whereas Fe and Se atoms have C_s site symmetry [19]. The symmetry analysis yields a total of 18 Raman-active modes $\Gamma_{\text{Raman}} = 6A_g + 2B_{1g} + 6B_{2g} + 4B_{3g}$, out of which, according to the Raman tensors below and the selection rules, only eight ($6A_g + 2B_{1g}$) are observable for our scattering geometry.

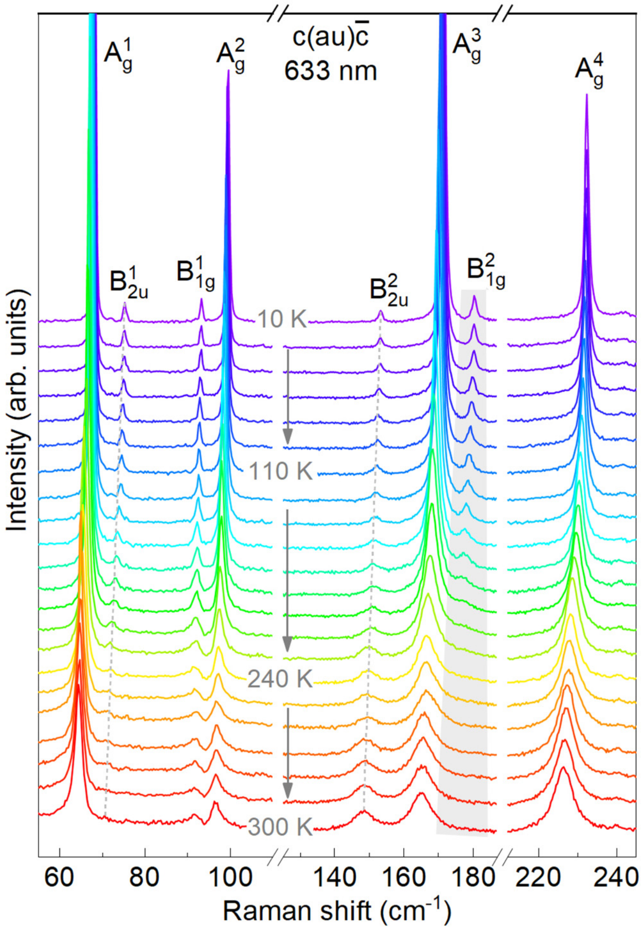

FIG. 1. Identification and temperature dependence of phonon modes in $\text{BaFe}_2\text{Se}_2\text{O}$. No change of crystal structure fingerprint was observed in the phonon spectra down to 10 K.

$$A_g = \begin{pmatrix} a & 0 & 0 \\ 0 & b & 0 \\ 0 & 0 & c \end{pmatrix},\ B_{1g} = \begin{pmatrix} 0 & d & 0 \\ d & 0 & 0 \\ 0 & 0 & 0 \end{pmatrix},$$

$$B_{2g} = \begin{pmatrix} 0 & 0 & e \\ 0 & 0 & 0 \\ e & 0 & 0 \end{pmatrix},\ B_{3g} = \begin{pmatrix} 0 & 0 & 0 \\ 0 & 0 & f \\ 0 & f & 0 \end{pmatrix}.$$

Figure 1 shows the temperature evolution of the $\text{BaFe}_2\text{Se}_2\text{O}$ Raman spectra in the temperature range between 10 and 300 K, in which eight phonon modes are observed. According to the lattice dynamical calculations [19], four A_g and two B_{1g} modes can be well assigned, as shown in Fig. 1. In addition to the A_g and B_{1g} symmetry modes, two peaks at about 75.2 and 153.3 cm^{-1} were also observed, which we previously attributed to new phonon modes due to the possible change of crystal symmetry accompanying the magnetic phase transition at $T_N = 240$ K [19]. As can be seen in Fig. 1, these peaks are also observable in our data even above T_N, indicating different origin. Energies are consistent with B_{2u}^1 and B_{2u}^2 infrared-active phonon modes, theoretically

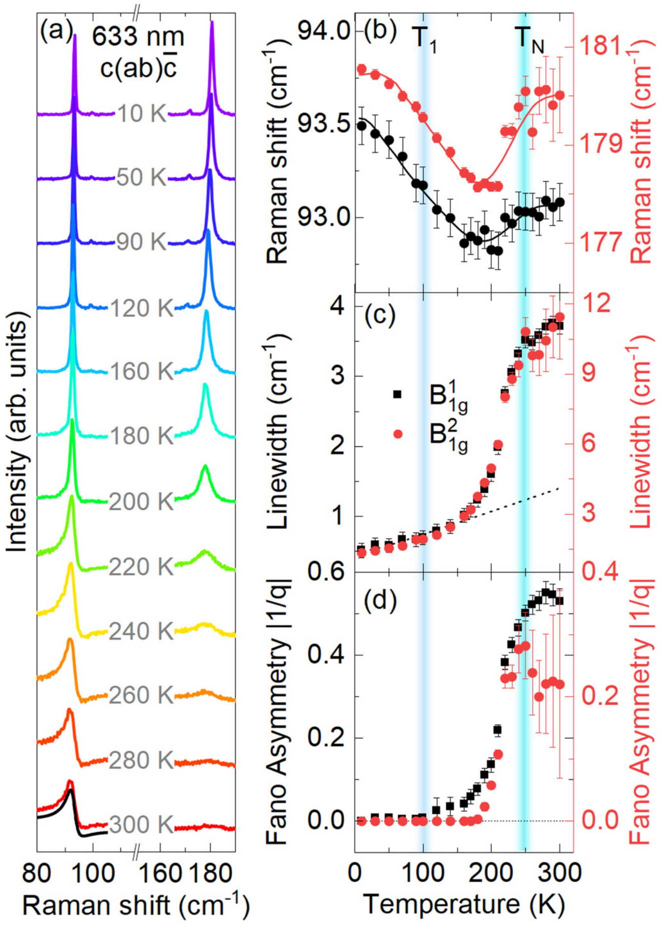

FIG. 2. Anomalies of B_{1g} modes induced by spin-lattice coupling. (a) Temperature dependence of Raman spectra for the $c(ab)\bar{c}$ polarization configuration, in which only the B_{1g} modes can be observed. The solid black line is a fit to a Fano line shape. Temperature dependence of the (b) frequency shift, (c) linewidth, and (d) Fano asymmetry parameters $|1/q|$ of B_{1g}^1 (left axis, black) and B_{1g}^2 (right axis, red) modes. The solid lines in (b) represent a fit to Eq. (1) and the dotted line in (c) represents the behavior expected from anharmonicity.

predicted by density functional theory calculations [19], and we assign them accordingly. Their observability in Raman data may stem from the release of symmetry selection rule by the structural imperfections. In our previous paper [18], Mössbauer data suggested oxygen deficiency, i.e., O_{1-x} composition for $BaFe_2Se_2O$. This might be the source of structural imperfections.

First, we focus on B_{1g} phonon modes, which display a pronounced asymmetry at high temperatures ($T > T_N$) that is suppressed at low temperatures ($T \ll T_N$), as can be seen in Fig. 2(a). Having in mind small instrumental broadening, the analysis of the line shape was preformed by using Fano function alone [20,21]: $I(\omega) = I_0(q+\varepsilon)^2/(1+\varepsilon^2)$, where $\varepsilon = (\omega - \omega_0)/\Gamma$, ω_0 is the bare phonon frequency, Γ is the linewidth, and q is the asymmetry parameter [22]. Frequency shift, linewidth, and Fano asymmetry parameter $|1/q|$ for both modes as a function of temperature are presented in Figs. 2(b), 2(c), and 2(d), respectively. Whereas they exhibit very similar temperature dependence, upon heating from 10 K a small deviation from the "standard" anharmonic type of behavior can be noticed at about $T_1 = 100$ K accompanied by the appearance of the line-shape asymmetry. Further heating results in a significant renormalization of the phonon self-energies around T_N with the Fano asymmetry parameters reaching maximum value in the same temperature region.

The pronounced Fano asymmetry observed for the B_{1g} modes above T_N [Fig. 2(d)] indicates strong coupling to a continuum of excitations. Here we attribute the continuum to the magnetic scattering stemming from the spin fluctuation, which will be further discussed below. In comparison, an electronic mechanism for the continuum is unlikely as $BaFe_2Se_2O$ is electrically insulating with a transport gap of 1.86 eV [17]. According to the lattice dynamical calculations [19], the B_{1g} modes are mainly due to the vibration of Fe and Se atoms along the b axis which mediate the magnetic interaction. Therefore, one could expect B_{1g} modes to couple to the magnetic scattering.

The coupling of B_{1g} modes to the spin system is also reflected in the abnormal behaviors of their linewidth. To demonstrate this, we have included in Fig. 2(c) plots of the behavior expected from anharmonicity, $\Gamma(T) = \Gamma_0[1 + 2/(e^{\hbar\omega/2k_BT} - 1)]$. The fit strongly deviates already around 170 K, implying an additional relaxation mechanism which we ascribe to spin-phonon coupling. Such coupling is very pronounced in low-dimensional spin dimer systems, as well as in two- and three-dimensional frustrated spin systems [23–25].

In order to estimate the spin-phonon coupling constant in $BaFe_2Se_2O$, we may approximate phonon frequency temperature dependence as

$$\omega(T) = \omega(0) - C\left(1 + \frac{2}{e^x - 1}\right) + \lambda\langle S_i S_j\rangle, \tag{1}$$

where $\omega(0)$ is the harmonic frequency of an optical mode at zero temperature, $x = \hbar\omega(0)/2k_BT$, λ is the spin-phonon coupling constant, $\langle S_i S_j\rangle$ represents the spin-spin correlation function, and C is an anharmonic constant. The second term in Eq. (1) describes the anharmonic phonon contribution based on symmetrical optical phonon decay into acoustic phonons [26], whereas the third term represents the contribution from the spin-phonon coupling based on the Baltensperger and Helman model [27,28]. If we take into account only the nearest-neighbor interactions, the spin-spin correlation function $\langle S_i S_j\rangle_\chi$ can be written as [25]

$$\langle S_i S_j\rangle_\chi = \frac{k_B T \chi_m(T)}{N_A g^2 \mu_B^2} - \frac{S(S+1)}{3}, \tag{2}$$

where $g = 2$, $S = 2$, and the magnetic susceptibility $\chi_m(T)$ is given in Ref. [18]. We can now analyze the B_{1g} symmetry modes frequency temperature dependance within Eq. (1) [see solid lines in Fig. 2(b)]. This yields the spin-phonon coupling constants $\lambda(B_{1g}^1) = 1.8\ \text{cm}^{-1}$, $\lambda(B_{1g}^2) = 12.8\ \text{cm}^{-1}$, and the anharmonic constant $C(B_{1g}^1) = 0.33\ \text{cm}^{-1}$, $C(B_{1g}^2) = 4.76\ \text{cm}^{-1}$. The individual contribution due to anharmonic and spin-phonon coupling can be found in Fig. 5 in Appendix A. Obtained spin-phonon coupling constants are smaller than those in the spin-Peierls system $CuGeO_3$, where spin-phonon

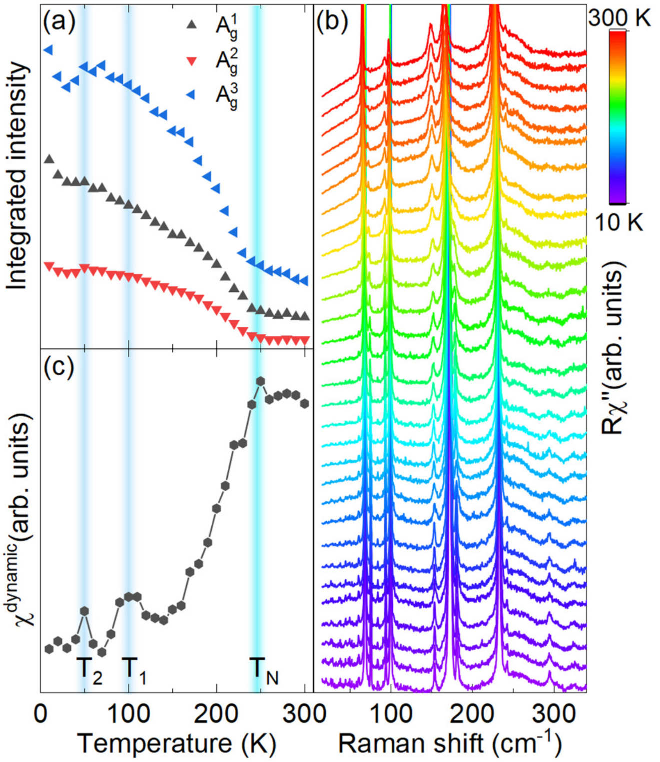

FIG. 3. (a) Integrated intensity of the A_g^1, A_g^2, and A_g^3 symmetry modes as a function of temperature. (b) Temperature evolution of Raman susceptibility data for $BaFe_2Se_2O$ obtained in parallel scattering configuration. The pronounced Raman continuum evolution is observable only in parallel [i.e., (*aa*) or (*bb*)] and absent in cross polarization configurations [i.e., (*ab*) or (*ba*)] (not shown). (c) Temperature dependence of dynamical susceptibility $\chi^{\text{dynamic}}(T)$ obtained from the Raman data.

coupling constants of $\lambda_{103} = -10\ \text{cm}^{-1}$, $\lambda_{215} = 40\ \text{cm}^{-1}$, $\lambda_{366} = -21\ \text{cm}^{-1}$, and $\lambda_{812} = -8\ \text{cm}^{-1}$ were found [29]. Thus moderate spin-phonon coupling constants in $BaFe_2Se_2O$ may account for the absence of a structural phase transition at the magnetic phase transition.

Now we turn our attention to the A_g symmetry modes. As can be seen from Fig. 3(a), the integrated intensity temperature dependence of the analyzed A_g modes exhibits clear discontinuity at T_N. In addition, another change in tendency has been observed at about $T_2 = 50$ K.

Whereas the phonon anomalies at T_N can be directly traced back to the spin dynamics, the origin of the phonon anomalies at T_1 and T_2 is not clear. To clarify this, we analyze the Raman continuum that nonmonotonically develops in the A_{1g} channel with temperature [see Fig. 3(a)], as expected for the (quasi-) one-dimensional spin systems [30–32]. Directly from the Raman data, dynamic Raman susceptibility [33] can be calculated using the Kramers-Kronig relation $\chi^{\text{dynamic}} = \lim_{\omega\to 0}\chi(q=0,\omega) \propto \int_0^\infty \frac{\chi''}{\omega} d\omega$. Since we do not attempt to quantitatively analyze the spin-fluctuation contributions, which falls beyond the scope of our work, but to pinpoint possible magnetic phase transition, we approximate $\chi^{\text{dynamic}}(T)$ as an integral of the Raman conductivity data after excluding the contributions from phonons. As can be seen in Fig. 3(c), $\chi^{\text{dynamic}}(T)$ strongly increases upon approaching T_N after which it saturates in the paramagnetic phase where the spins are not correlated. At low temperatures it develops two peak-like features coinciding with observed anomalies in the lattice dynamic thus indicating their spin dynamics related origin. Furthermore, $\chi^{\text{dynamic}}(T)$ exhibits good agreement with the previously reported magnetic susceptibility data [18], indicating additional magnetic phase transitions in $BaFe_2Se_2O$ at low temperatures.

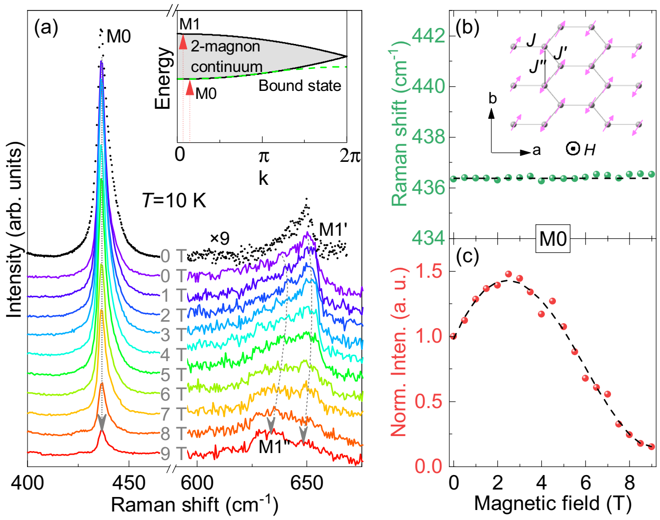

FIG. 4. Identification of magnetic excitations in $BaFe_2Se_2O$. (a) Field-dependent Raman spectra, measured at 10 K with 532-nm laser line (solid lines). The spectrum (dotted line) collected at 0 T with a 633-nm laser are also shown for comparison. Inset: Schematic spin excitation spectrum of $BaFe_2Se_2O$. The green dashed line represents a possible two-magnon bound state. Field dependence of the (b) energy and (c) intensity of the *M*0 mode. Inset of (b): Schematic representation of the periodic magnetic structure in the (*ab*) plane. *J* represents Fe-O-Fe antiferromagnetic (AFM) exchange interaction along the rungs; *J*′ is the interladder Fe-Se-Fe AFM exchange interaction. *J*″ is the ferromagnetic Fe-Se-Fe exchange interaction along the ladder legs and can be neglected.

B. Two-magnon Raman scattering

The two asymmetric peaks at 436 and 653 cm^{-1} (see Fig. 4) have been reported before and assigned as a magnetic excitation related structure due to their special polarization and temperature-dependent characterizations [19]. However, the extremely high intensity of the 436 cm^{-1} (*M*0) mode suggests an additional mechanism that comes into play, other than those manifested with the 653 cm^{-1} mode. In particular, compared with the linewidth of two-magnon modes in other two-dimensional (2D) spin systems, the *M*0 linewidth of only ~5 cm^{-1} at 15 K is quite unusual for a 2D spin-ladder system. For example, the linewidth of the two-magnon mode is ~800 cm^{-1} for $Sr_2Cu_2O_2Cl_2$ [34], whereas it is ~500 cm^{-1} in $La_6Ca_8Cu_{24}O_{41}$ [13]. To the best of our knowledge, the sharpest two-magnon mode so far was found in CaV_2O_5 with a width of more than 50 cm^{-1} [10], still one order of magnitude larger than that in $BaFe_2Se_2O$.

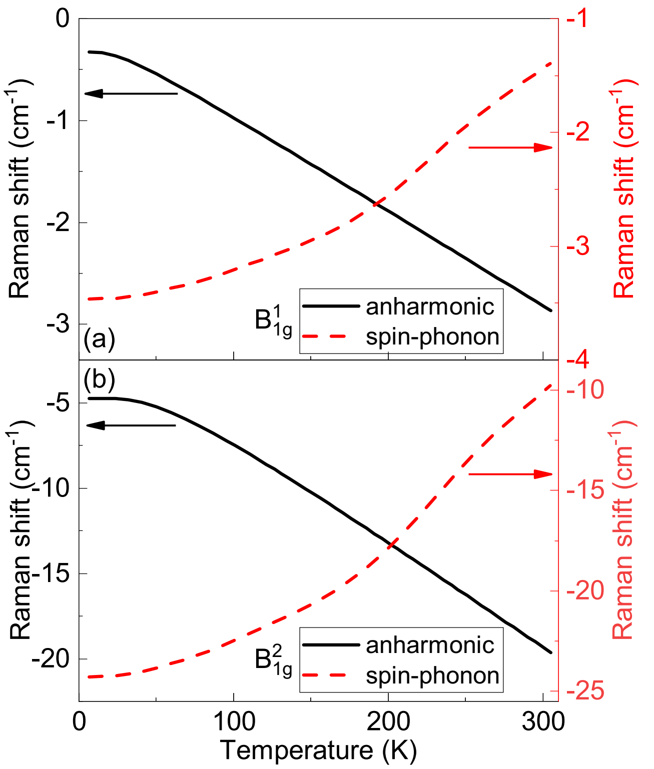

FIG. 5. Anharmonic (solid line) and spin-phonon (dashed line) contribution to the temperature dependence of the energy of (a) B^1_{1g} and (b) B^2_{1g} phonon modes obtained by fitting Eq. (1) to the experimental data.

To clarify the origin of the unusual $M0$ mode, the magnetic-field- and temperature-dependent Raman experiments have been performed on $\mathrm{BaFe_2Se_2O}$ crystals [Fig. 4(a) and Fig. 6 in Appendix B]. The field dependence of the energy and intensity of the $M0$ mode are summarized in Figs. 4(b) and 4(c). It can be seen that both the $M0$ energy and the linewidth are nearly field independent, whereas the intensity exhibits a strong nonmonotonic field dependence. The intensity slightly increases with magnetic fields below 3 T, but quickly drops down above 3 T and almost vanishes for $B = 9$ T. A closer inspection of the 653-cm^{-1} peak magnetic-field-dependent spectra reveals its two-peak nature ($M1'$ and $M1''$; see Fig. 4). Both peaks harden up to 3 T after which they soften. Whereas the $M1'$ intensity follows the $M0$ mode behavior, $M1''$ experiences a constant gain of intensity. The strong field dependence of $M0$, $M1'$, and $M1''$ as well as their special polarization and temperature-dependent characterizations [19] confirms that these modes are indeed magnon related, but not due to some structural imperfections.

In general, several theoretical scenarios can be considered to account for the strength and sharpness of the magnon modes in the 2D system: (i) backfolding of the triplet dispersion due to charge ordering [13]; (ii) large anisotropy of the magnetic exchanges along rung and leg directions [35]; and (iii) the resonance between the two-magnon continuum and a two-magnon bound state [16,36]. In $\mathrm{BaFe_2Se_2O}$, the origin of dispersion backfolding can be excluded because of its electrically insulating nature. Although the large anisotropy between J'' and J explains the observation of the $M0$ mode at the given energy, it alone cannot account for the intensity and its magnetic-field dependence. This kind of behavior can be observed in the presence of the resonance between the two-magnon continuum and a two-magnon bound state.

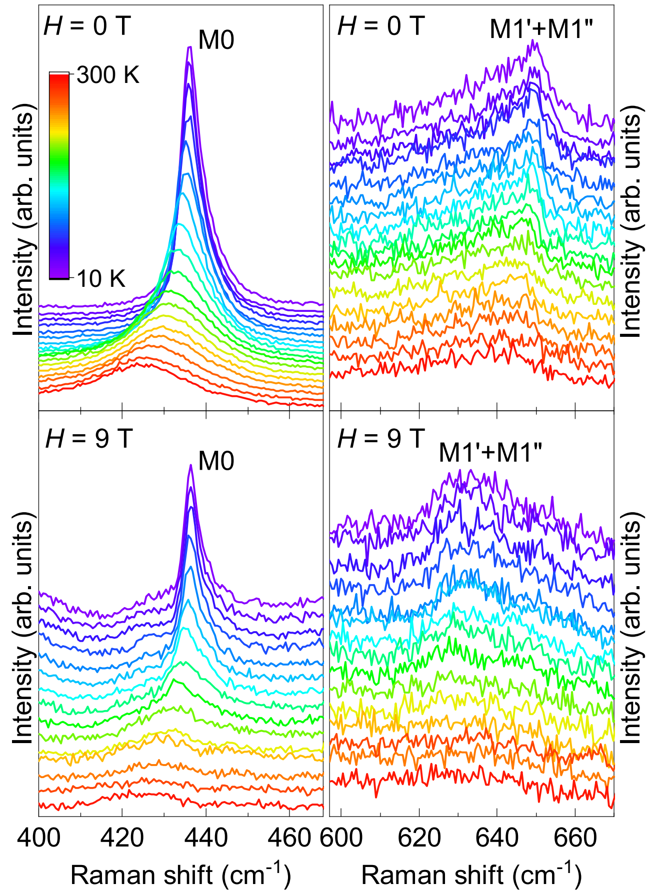

FIG. 6. Temperature-dependent spectra of the $M0$, $M1'$, and $M1''$ modes at 0 and 9 T.

In low-dimensional antiferromagnets, a strong magnon-magnon interaction induces a magnetic bound state [31,37–40] that merges with the two-magnon continuum at zero momentum (schematically shown in Fig. 4). This allows a resonance at the bottom of the continuum and contributes to the asymmetric line shape [36]. Such a resonance can well explain the strength, sharpness, and asymmetry of the $M0$ mode. The field dependence of the $M0$ mode intensity provides further support for the picture. External magnetic fields usually lead to a spin canting or even a spin flop/flip transition [41] and consequently modulate the magnon excitation spectrum. In $\mathrm{BaFe_2Se_2O}$, the modulation of the magnon excitation spectrum is evidenced by the energy shift of the $M1'$ and$M1''$ modes (Fig. 4). A quantitative understanding of the $M0$, $M1'$, and $M1''$ modes magnetic-field dependence requires more theoretical work in the future and goes beyond the scope of this paper.

IV. SUMMARY

In summary, a $\mathrm{BaFe_2Se_2O}$ temperature- and field-dependent Raman-scattering study has been performed. The temperature evolution of the Raman-active modes indicates that there is no structural phase transition accompanying the magnetic phase transitions. Observed anomalies in the phonon spectra can be traced back to moderate spin-phonon interaction contributions as well as multiple magnetic phase transitions present in $\mathrm{BaFe_2Se_2O}$ also detected in the Raman continuum induced by the spin fluctuations. The anomalous intensity of the $M0$ peak is attributed to the contribution from the two-magnon continuum and a two-magnon bound state resonance. The present study provides the fundamental lattice and spin dynamics information on $\mathrm{BaFe_2Se_2O}$ and is of significance for the understanding of magnetic excitations in low-dimensional spin systems.

ACKNOWLEDGMENTS

This work was supported by the National Natural Science Foundation of China, the Ministry of Science and Technology of China, the Fundamental Research Funds for the Central Universities, the Research Funds of Renmin University of China and Serbian Ministry of Education, Science and Technological Development under Project III45018. The work at Brookhaven National Laboratory was supported by the U.S. DOE under Contract No. DE-SC0012704 (material synthesis).

APPENDIX A: ANHARMONIC AND SPIN-PHONON CONTRIBUTIONS TO PHONON MODE ENERGIES

In this Appendix, we show the individual contribution of anharmonic and spin-phonon terms to the temperature dependence of the energy of the two B1g modes (Fig. 5), which are obtained by fitting Eq. (1) to the experimental data.

APPENDIX B: TEMPERATURE- AND FIELD-DEPENDENT RAMAN SPECTRA

To explore the origin of the magnetic scattering modes, we performed temperature-dependent Raman experiments and the collected spectra of the M0 M1' and M1" modes at 0 and 9 T are shown in Fig. 6. One can see that these modes exhibit distinctive temperature dependent behaviors, namely, a characteristic decrease in energy and intensity, and an increase in linewidth, with increasing temperature, reflecting the renormalization of magnon energies and lifetimes by thermally excited carriers.

[1] P. W. Anderson, Science **235**, 1196 (1987).

[2] E. Dagotto and T. M. Rice, Science **271**, 618 (1996).

[3] E. Dagotto, Rep. Prog. Phys. **62**, 1525 (1999).

[4] P. Lemmens, G. Güntherodt, and C. Gros, Phys. Rep. **375**, 1 (2003).

[5] T. Barnes, E. Dagotto, J. Riera, and E. S. Swanson, Phys. Rev. B **47**, 3196 (1993).

[6] T. Barnes and J. Riera, Phys. Rev. B **50**, 6817 (1994).

[7] S. R. White, R. M. Noack, and D. J. Scalapino, Phys. Rev. Lett. **73**, 886 (1994).

[8] S. Gopalan, T. M. Rice, and M. Sigrist, Phys. Rev. B **49**, 8901 (1994).

[9] D. G. Shelton, A. A. Nersesyan, and A. M. Tsvelik, Phys. Rev. B **53**, 8521 (1996).

[10] M. J. Konstantinović, Z. V. Popović, M. Isobe, and Y. Ueda, Phys. Rev. B **61**, 15185 (2000).

[11] Z. V. Popović, M. J. Konstantinović, V. A. Ivanov, O. P. Khuong, R. Gajić, A. Vietkin, and V. V. Moshchalkov, Phys. Rev. B **62**, 4963 (2000).

[12] A. Gozar, G. Blumberg, B. S. Dennis, B. S. Shastry, N. Motoyama, H. Eisaki, and S. Uchida, Phys. Rev. Lett. **87**, 197202 (2001).

[13] K. P. Schmidt, C. Knetter, M. Grüninger, and G. S. Uhrig, Phys. Rev. Lett. **90**, 167201 (2003).

[14] A. Gößling, U. Kuhlmann, C. Thomsen, A. Löffert, C. Gross, and W. Assmus, Phys. Rev. B **67**, 052403 (2003).

[15] S. Sugai and M. Suzuki, Phys. Status Solidi B **215**, 653 (1999).

[16] K. P. Schmidt, C. Knetter, and G. S. Uhrig, Europhys. Lett. **56**, 877 (2001).

[17] F. Han, X. Wan, B. Shen, and H.-H. Wen, Phys. Rev. B **86**, 014411 (2012).

[18] H. Lei, H. Ryu, V. Ivanovski, J. B. Warren, A. I. Frenkel, B. Cekic, W.-G. Yin, and C. Petrovic, Phys. Rev. B **86**, 195133 (2012).

[19] Z. V. Popović, M. Šćepanović, N. Lazarević, M. M. Radonjić, D. Tanasković, H. Lei, and C. Petrovic, Phys. Rev. B **89**, 014301 (2014).

[20] A. Baum, A. Milosavljević, N. Lazarević, M. M. Radonjić, B. Nikolić, M. Mitschek, Z. I. Maranloo, M. Šćepanović, M. Grujić-Brojčin, N. Stojilović, M. Opel, A. Wang, C. Petrovic, Z. V. Popović, and R. Hackl, Phys. Rev. B **97**, 054306 (2018).

[21] A. Milosavljević, A. Šolajić, J. Pešić, Y. Liu, C. Petrovic, N. Lazarević, and Z. V. Popović, Phys. Rev. B **98**, 104306 (2018).

[22] U. Fano, Phys. Rev. **124**, 1866 (1961).

[23] M. Braden, B. Hennion, W. Reichardt, G. Dhalenne, and A. Revcolevschi, Phys. Rev. Lett. **80**, 3634 (1998).

[24] K.-Y. Choi, Y. G. Pashkevich, K. V. Lamonova, H. Kageyama, Y. Ueda, and P. Lemmens, Phys. Rev. B **68**, 104418 (2003).

[25] C. Kant, J. Deisenhofer, T. Rudolf, F. Mayr, F. Schrettle, A. Loidl, V. Gnezdilov, D. Wulferding, P. Lemmens, and V. Tsurkan, Phys. Rev. B **80**, 214417 (2009).

[26] J. Menéndez and M. Cardona, Phys. Rev. B **29**, 2051 (1984).

[27] W. Baltensperger and J. S. Helman, Helv. Phys. Acta **41**, 668 (1968).

[28] W. Baltensperger, J. Appl. Phys. **41**, 1052 (1970).

[29] R. Werner, C. Gros, and M. Braden, Phys. Rev. B **59**, 14356 (1999).

[30] T. Sekine, M. Jouanne, C. Julien, and M. Balkanski, Phys. Rev. B **42**, 8382 (1990).

[31] P. Lemmens, M. Grove, M. Fischer, G. Güntherodt, V. N. Kotov, H. Kageyama, K. Onizuka, and Y. Ueda, Phys. Rev. Lett. **85**, 2605 (2000).

[32] K. Y. Choi, J. W. Hwang, P. Lemmens, D. Wulferding, G. J. Shu, and F. C. Chou, Phys. Rev. Lett. **110**, 117204 (2013).

[33] A. Glamazda, P. Lemmens, S. H. Do, Y. S. Choi, and K. Y. Choi, Nat. Commun. **7**, 12286 (2016).

[34] G. Blumberg, P. Abbamonte, M. V. Klein, W. C. Lee, D. M. Ginsberg, L. L. Miller, and A. Zibold, Phys. Rev. B **53**, R11930 (1996).

[35] K. P. Schmidt, A. Gössling, U. Kuhlmann, C. Thomsen, A. Löffert, C. Gross, and W. Assmus, Phys. Rev. B **72**, 094419 (2005).

[36] C. Jurecka, V. Grützun, A. Friedrich, and W. Brenig, Eur. Phys. J. B **21**, 469 (2001).

[37] O. P. Sushkov and V. N. Kotov, Phys. Rev. Lett. **81**, 1941 (1998).

[38] G. Bouzerar, A. P. Kampf, and G. I. Japaridze, Phys. Rev. B **58**, 3117 (1998).

[39] M. Windt, M. Grüninger, T. Nunner, C. Knetter, K. P. Schmidt, G. S. Uhrig, T. Kopp, A. Freimuth, U. Ammerahl, B. Büchner, and A. Revcolevschi, Phys. Rev. Lett. **87**, 127002 (2001).

[40] C. Knetter, K. P. Schmidt, M. Grüninger, and G. S. Uhrig, Phys. Rev. Lett. **87**, 167204 (2001).

[41] S. Blundell, in *Magnetism in Condensed Matter* (Oxford University Press, New York, 2001).

COMMUNICATIONS
PHYSICS

ARTICLE

https://doi.org/10.1038/s42005-019-0107-y OPEN

Frustrated spin order and stripe fluctuations in FeSe

A. Baum[1,2], H.N. Ruiz[3,4], N. Lazarević[5], Yao Wang[3,6,10], T. Böhm[1,2,11], R. Hosseinian Ahangharnejhad[1,2,12], P. Adelmann[7], T. Wolf[7], Z.V. Popović[5,8], B. Moritz[3], T.P. Devereaux[3,9] & R. Hackl[1]

The charge and spin dynamics of the structurally simplest iron-based superconductor, FeSe, may hold the key to understanding the physics of high temperature superconductors in general. Unlike the iron pnictides, FeSe lacks long range magnetic order in spite of a similar structural transition around 90 K. Here, we report results of Raman scattering experiments as a function of temperature and polarization and simulations based on exact diagonalization of a frustrated spin model. Both experiment and theory find a persistent low energy peak close to 500 cm^{-1} in B_{1g} symmetry, which softens slightly around 100 K, that we assign to spin excitations. By comparing with results from neutron scattering, this study provides evidence for nearly frustrated stripe order in FeSe.

---

[1] Walther Meissner Institut, Bayerische Akademie der Wissenschaften, 85748 Garching, Germany. [2] Fakultät für Physik E23, Technische Universität München, 85748 Garching, Germany. [3] Stanford Institute for Materials and Energy Sciences, SLAC National Accelerator Laboratory, 2575 Sand Hill Road, Menlo Park, CA 94025, USA. [4] Department of Physics, Stanford University, Stanford, CA 94305, USA. [5] Center for Solid State Physics and New Materials, Institute of Physics Belgrade, University of Belgrade, Pregrevica 118, 11080 Belgrade, Serbia. [6] Department of Applied Physics, Stanford University, Stanford, CA 94305, USA. [7] Karlsruher Institut für Technologie, Institut für Festkörperphysik, 76021 Karlsruhe, Germany. [8] Serbian Academy of Sciences and Arts, Knez Mihailova 35, 11000 Belgrade, Serbia. [9] Geballe Laboratory for Advanced Materials, Stanford University, Stanford, CA 94305, USA. [10] Present address: Lyman Laboratory 336, Harvard University, 17 Oxford St. Cambridge, 02138 MA, USA. [11] Present address: TNG Technology Consulting GmbH, Beta-Straße, 85774 Unterföhring, Germany. [12] Present address: School of Solar and Advanced Renewable Energy, Department of Physics and Astronomy, University of Toledo, Toledo, OH 43606, USA. Correspondence and requests for materials should be addressed to R.H. (email: hackl@wmi.badw.de)

Fe-based pnictides and chalcogenides, similar to cuprates, manganites or some heavy fermion compounds, are characterized by the proximity and competition of various phases including magnetism, charge order, and superconductivity. Specifically the magnetism of Fe-based systems has various puzzling aspects which do not straightforwardly follow from the Fe valence or changes in the Fermi surface topology[1–4]. Some systems have a nearly ordered localized moment close to $2\mu_B$[5], such as FeTe or rare-earth iron selenides, whereas the moments of AFe$_2$As$_2$-based compounds (A = Ba, Sr, Eu or Ca) are slightly below $1\mu_B$[6] and display aspects of itinerant spin-density-wave (SDW) magnetism with a gap in the electronic excitation spectrum[7]. In contrast others do not order down to the lowest temperatures, such as FeSe[8] or LaFePO[9].

The material specific differences are a matter of intense discussion, and low- as well as high-energy electronic and structural properties determine the properties[1,2,4,10–13]. At the Fermi energy E_F, the main fraction of the electronic density of states originates from t_{2g} Fe orbitals, but a substantial part of the Fe–Fe hopping occurs via the pnictogen or chalcogen atoms, hence via the xz, yz, and p_z orbitals. For geometrical reasons, the resulting exchange coupling energies between nearest (J_1) and next nearest neighbor (J_2) iron atoms have the same order of magnitude, and small changes in the pnictogen (chalcogen) height above the Fe plane influence the ratio J_2/J_1, such that various orders are energetically very close[12].

The reduced overlap of the in-plane xy orbitals decreases the hopping integral t and increases the influence of the Hund's rule interactions and the correlation energy U, even though they are only in the range of 1–2 eV. Thus the electrons in the xy orbitals have a considerably higher effective mass m^* and smaller quasiparticle weight Z than those of the xz and yz orbitals. This effect was coined orbital selective Mottness[14–16] and was observed by photoemission spectroscopy (ARPES) in Fe-based chalcogenides[17]. It is similar in spirit to what was found by Raman scattering in the cuprates as a function of momentum[18]. In either case some of the electron wave functions are more localized than others. This paradigm may explain why the description remains difficult and controversial in all cases.

Therefore we address the question as to whether systematic trends can be found across the families of the Fe-based superconductors, how the spin excitations are related to other highly correlated systems, and how they can be described appropriately.

As an experimental tool we use Raman scattering since the differences expected theoretically[1,3] and indicated experimentally in the electronic structure[7] can be tracked in both the charge and the spin channel. Another advantage is the large energy range of approximately 1 meV to 1 eV (8–8000 cm^{-1}) accessible by light scattering[19].

Early theoretical work on Fe-based systems considered the Heisenberg model the most appropriate approach[20], and the high-energy maxima observed by Raman scattering in BaFe$_2$As$_2$ were interpreted in terms of localized spins[21,22]. On the other hand, the low-energy spectra are reminiscent of charge density wave (CDW) or SDW formation[22–25]. In principle, both effects can coexist if the strength of the correlations varies for electrons from different orbitals, where itinerant electrons form a SDW, while those on localized orbitals give rise to a Heisenberg-like response.

In contrast to the AFe$_2$As$_2$-based compounds, FeSe seems to be closer to localized order with a larger mass renormalization than in the iron pnictides[1]. Apart from low lying charge excitations, the remaining, presumably spin, degrees of freedom in FeSe may be adequately described by a spin-1 J_1-J_2-J_3-K Heisenberg model[12] which provides also a consistent description of our results shown in this work and allows for the presence of different spin orders. Since various types of spin order are energetically in close proximity[12,26,27], frustration may quench long-range order down to the lowest temperatures[8], even though neutron scattering experiments in FeSe find large values for the exchange energies[27,28].

Recent experiments on FeSe focused on low-energies and B_{1g} ($x^2 - y^2$) symmetry, and the response was associated with particle-hole excitations and critical fluctuations[29]. Here, we obtain similar experimental results below 1500 cm^{-1}. Those in the range 50–200 cm^{-1} show similarities with the other Fe-based systems while those above 200 cm^{-1} are distinctly different but display similarities with the cuprates[30,31]. In addition to previous work, we analyze all symmetries at higher energies up to 3500 cm^{-1}, to uncover crucial information about the behavior of the spin degrees of freedom.

By comparing experimental and simulated Raman data we find a persistent low-energy peak at roughly 500 cm^{-1} in B_{1g} symmetry, which softens slightly around 100 K. We assign the B_{1g} maximum and the related structures in A_{1g} and B_{2g} symmetry to spin excitations. The theoretical simulations also aim at establishing a link between light and neutron scattering data with respect to the spin degrees of freedom and to furnish evidence for nearly frustrated stripe order at low temperature. We arrive at the conclusion that frustrated order of localized spins dominates the physics in FeSe, while critical spin and/or charge fluctuations are not the main focus of the paper.

Results

Experiments. Symmetry-resolved Raman spectra of single-crystalline FeSe (see Methods) in the energy range up to 0.45 eV (3600 cm^{-1}) are shown in Fig. 1. The spectra are linear combinations of the polarization dependent raw data (see Methods and Supplementary Fig. 1 in Supplementary Note 1). For B_{1g} symmetry (Fig. 1a) we plot only two temperatures, 40 and 300 K, to highlight the persistence of the peak at ~500 cm^{-1}. The full temperature dependence will be shown below. For A_{1g}, A_{2g}, and B_{2g} symmetry we show spectra at 40, 90, and 300 K (Fig. 1b–d). Out of the four symmetries, the A_{1g}, B_{1g}, and B_{2g} spectra display Raman active phonons, magnons or electron-hole excitations, while the A_{2g} spectra are weak and vanish below 500–1000 cm^{-1}. As intensity in A_{2g} symmetry appears only under certain conditions not satisfied in the present study, we ignore it here.

In the high-energy limit the intensities are smaller in all symmetries than those in other Fe-based systems such as BaFe$_2$As$_2$ (see Supplementary Fig. 2 in Supplementary Note 2). However, in the energy range up to ~3000 cm^{-1} there is a huge additional contribution to the B_{1g} cross section in FeSe (Fig. 1a). The response is strongly temperature dependent and peaks at 530 cm^{-1} in the low-temperature limit. Between 90 and 40 K the A_{1g} and B_{2g} spectra increase slightly in the range around 700 and 3000 cm^{-1}, respectively (indicated as blue shaded areas in Fig. 1b, d). The overall intensity gain in the A_{1g} and B_{2g} spectra in the shaded range is a fraction of ~5% of that in B_{1g} symmetry. The B_{2g} spectra exhibit a reduction in spectral weight in the range from 600 to 1900 cm^{-1} (shaded red) which is already fully developed at the structural transition at T_s = 89.1 K in agreement with earlier work[29]. In contrast to A_{1g} and B_{2g} symmetry, the temperature dependence of the B_{1g} intensity is strong, whereas the peak energy changes only weakly, displaying some similarity with the cuprates[32]. This similarity, along with the considerations of Glasbrenner et al.[12], motivated us to explore a spin-only, Heisenberg-like model for describing the temperature evolution of the Raman scattering data.

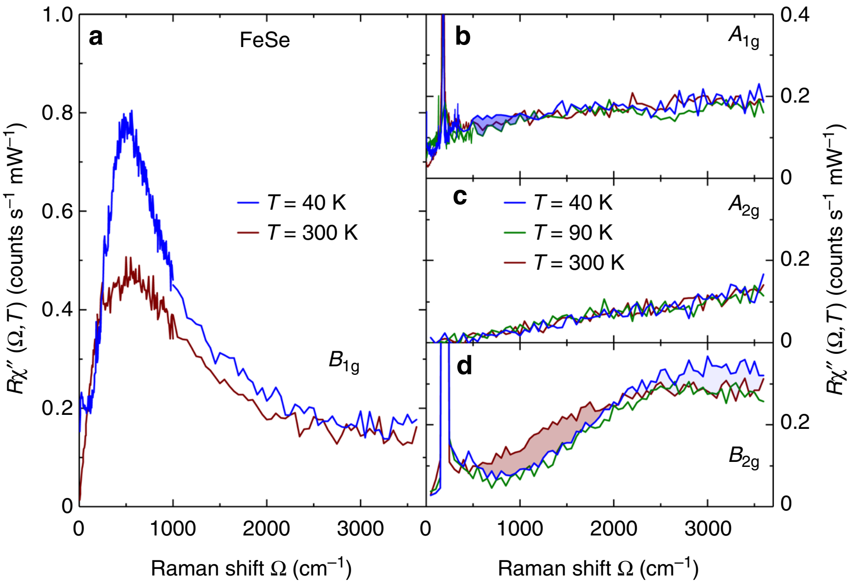

Fig. 1 Symmetry-resolved Raman spectra of FeSe at various temperatures for large energy transfers. **a** B_{1g} spectra at temperatures as indicated. The spectrum at 90 K is omitted here for clarity but is displayed in a separate figure below The weak structure at $T = 40$ K in the range 20–25 cm^{-1} is left over from the fluctuation peak which is most pronounced right above T_s as shown below. **b** A_{1g}, **c** A_{2g}, and **d** B_{2g} spectra at temperatures as indicated. In A_{1g} and B_{2g} symmetry particle-hole excitations dominate the response. In agreement with the simulations weak additional peaks from spin excitations appear at low temperature (blue shaded areas). B_{2g} shows a loss of spectral weight (shaded red). The narrow lines close to 200 cm^{-1} are the A_{1g} and B_{1g} phonons. In the 1 Fe unit cell used here the B_{1g} phonon appears in B_{2g} symmetry since the axes are rotated by 45° with respect to the crystallographic (2 Fe) cell. The A_{2g} intensity vanishes below 500 cm^{-1} and the cross section is completely temperature independent

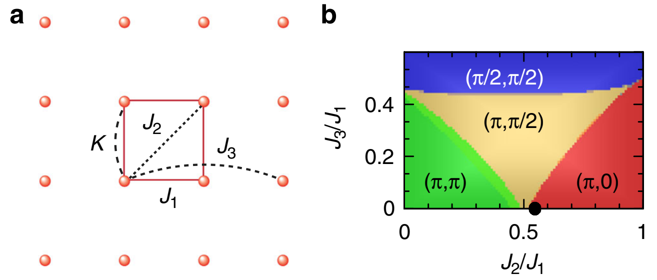

Fig. 2 Model and resulting phase diagram. **a** A 4 × 4 cluster was used for the simulations. The red spheres represent the Fe atoms, each of which carries localized spin $\mathbf{S}_i$, with $S = 1$. The nearest, next-nearest, and next-next-nearest neighbor interactions J_1, J_2, and J_3, respectively, are indicated. K is the coefficient of the biquadratic term proportional to $(\mathbf{S}_i \cdot \mathbf{S}_j)^2$. **b** $J_2 - J_3$ phase diagram as obtained from our simulations at $T = 0$ and for $K = 0.1$. The black dot shows the parameters at which temperature-dependent simulations have been performed

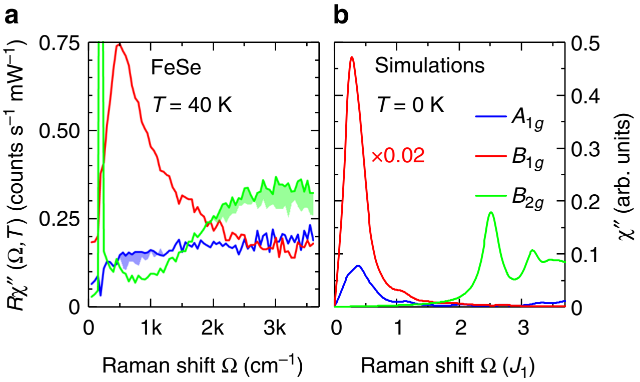

Fig. 3 Symmetry-resolved Raman spectra of FeSe for large energy shifts at low temperature. **a** Experimental results for symmetries as indicated at 40 K. The B_{1g} peak at 500 cm^{-1} dominates the spectrum. In A_{1g} and B_{2g} symmetry the electron-hole continua dominate the response, and the magnetic excitations yield only small additional contributions at approximately 700 and 3000 cm^{-1}, respectively. **b** Simulated Raman spectra at $T = 0$ K including only magnetic contributions. The A_{1g} and B_{1g} symmetries have peaks solely at low energies whereas the B_{2g} contributions are at high energies only. The B_{1g} response is multiplied by a factor of 0.02

Simulations at zero temperature. We performed numerical simulations at zero temperature for a frustrated spin-1 system on the basis of a J_1-J_2-J_3-K Heisenberg model[12] on a 16-points cluster as shown in Fig. 2a and described in the Methods section. Figure 2b shows the resulting phase diagram as a function of J_2 and J_3. K was set at 0.1 (repulsive) in order to suppress ordering tendencies on the small cluster. The parameter set for the simulations of the Raman and neutron data at finite temperature is indicated as a black dot.

In Fig. 3 we show the low-temperature data (Fig. 3a) along with the simulations (Fig. 3b). The energy scale for the simulations is given in units of J_1 which has been derived[12] to be 123 meV or 990 cm^{-1}, allowing a semi-quantitative comparison with the experiment. As already mentioned, the experimental A_{1g} and B_{2g} spectra are not dominated by spin excitations and we do not attempt to further analyze the continua extending to energies in excess of 1 eV, considering them a background. The opposite is true for B_{1g} symmetry, also borne out in the simulations. For the selected values of $J_1 = 123$ meV, $J_2 = 0.528J_1$, $J_3 = 0$, and $K = 0.1J_1$, the positions of the spin excitations in the three symmetries and the relative intensities are qualitatively reproduced. The choice of parameters is motivated by the previous use of the J_1-J_2 Heisenberg model, with $J_1 = J_2$ to describe the stripe phase of iron pnictides[20]. Here we use a value of J_2 smaller than J_1 to enhance competition between Néel and stripe orders when describing

FeSe. This approach and choice of parameters is strongly supported in a recent neutron scattering study[27].

The comparison of the different scattering symmetries, the temperature dependence, and our simulations indicate that the excitation at 500 cm^{-1} is an additional scattering channel superimposed on the particle-hole continuum and fluctuation response, as shown in Supplementary Note 3 with Supplementary Figs. 3 and 4. Here we focus on the peak centered at ~500 cm^{-1} which, in agreement with the simulations, originates from two-magnon excitations in a highly frustrated spin system, although the features below 500 cm^{-1} also are interesting and were interpreted in terms of quadrupolar orbital fluctuations[29].

Temperature dependence. It is enlightening to look at the B_{1g} spectra across the whole temperature range as plotted in Fig. 4. The well-defined two-magnon peak centered at ~500 cm^{-1} in the low temperature limit loses intensity, and becomes less well-defined with increasing temperature up to the structural transition $T_s = 89.1$ K. Above the structural transition, the spectral weight continues to decrease and the width of the two-magnon feature grows, while the peak again becomes well-defined and the energy increases slightly approaching the high temperature limit of the study. What may appear as a gap opening at low temperature is presumably just the reduction of spectral weight in a low-energy feature at ~22 cm^{-1}. The intensity of this lower energy response increases with temperature, leading to a well-formed peak at an energy around 50 cm^{-1} near the structural transition. Above the structural transition this feature rapidly loses spectral weight, hardens, and becomes indistinguishable from the two-magnon response in the high temperature limit. This low-energy feature develops in a fashion very similar to that found in $Ba(Fe_{1-x}Co_x)_2As_2$ for $x > 0$[33–35].

Now we compare the measurements with numerical simulations for the temperature dependence of the Raman B_{1g} susceptibility in Fig. 5a, b, respectively. For the simulations (Fig. 5b) we use the same parameters as at $T = 0$ (black dot in Fig. 3). At zero temperature the simulations show a single low energy B_{1g} peak around $0.3J_1$. As temperature increases, a weak shoulder forms on the low-energy side of the peak, and the whole peak softens slightly and broadens over the simulated temperature range. Except for the additional intensity at low energies, $\Omega < 200$ cm^{-1} (Fig. 5a), there is good qualitative agreement between theory and experiment. As shown in Supplementary Fig. 5 in Supplementary Note 4, a similar agreement between experiment and simulations is obtained for the temperature dependence in A_{1g} and B_{2g} symmetries, indicating that both the gain in intensity (blue shaded areas in Fig. 1) as well as the reduction in spectral weight in B_{2g} from 600 to 1900 cm^{-1} (shaded red in Fig. 1d) can be attributed to the frustrated localized magnetism.

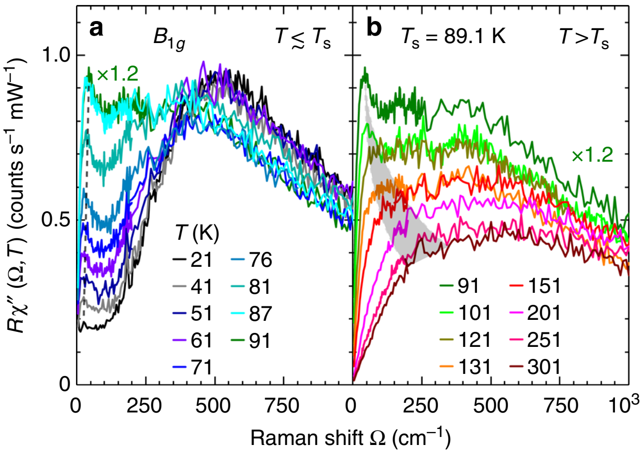

Fig. 4 Raman spectra in B_{1g} symmetry at temperatures **a** below and **b** above $T_s = 89.1$ K. The spectrum at 91 K appears in both panels for better comparison. The black dashed line in **a** and the gray shaded area in **b** indicate the approximate positions of the low-energy peak resulting from critical fluctuations. The peak centered close to 500 cm^{-1} results from excitations of neighboring spins which are studied here. A tentative decomposition is shown in Supplementary Fig. 4

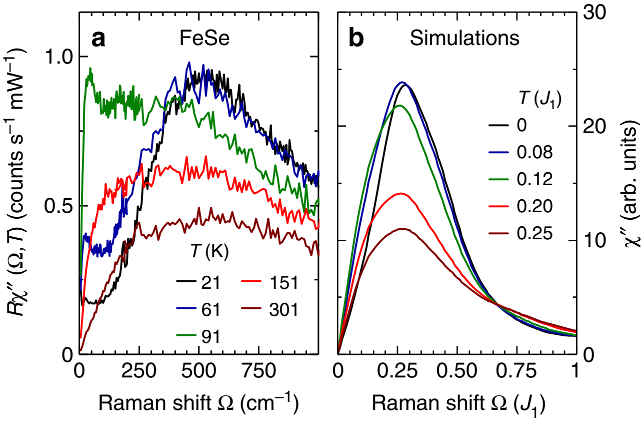

Fig. 5 Temperature dependence of the B_{1g} response. **a** Experimental spectra at selected temperatures as indicated. The spectra include several excitations the decomposition of which is shown in Supplementary Fig. 4. **b** Simulated Raman response at temperatures as indicated. Only magnetic excitations are included. The coupling constant was derived as $J_1 = 123$ meV in ref. [12]

Connection to the spin structure factor. To support our explanation of the Raman data, we simulated the dynamical spin structure factor $S(\mathbf{q}, \omega)$ and compared the findings to results of neutron scattering experiments[27]. While clearly not observing long-range order, above the structural transition neutron scattering finds similar intensity at finite energy for several wave vectors along the line $(\pi, 0) - (\pi, \pi)$. Upon cooling, the spectral weight at these wave vectors shifts away from (π, π) to directions along $(\pi, 0)$, although the respective peaks remain relatively broad. In Fig. 6a, b we show the results of the simulations for two characteristic temperatures. As the temperature decreases, spectral weight shifts from (π, π) toward $(\pi, 0)$ in agreement with the experiment[27]. In Fig. 6c we show the evolution of the spectral weights around (π, π) and $(\pi, 0)$ in an energy window of $(0.4 \pm 0.1)J_1$ as a function of temperature, similar to the results shown in ref. [27]. In the experiment, the temperature where the integrated dynamical spin structure factor changes most dramatically is close to the structural transition. From our simulations, the temperature where similar changes occur in comparison to neutron scattering corresponds to the temperature at which the simulated B_{1g} response (Fig. 5) shows the most pronounced shoulder, and the overall intensity begins to decrease. Not surprisingly, the low-energy peak in the Raman scattering experiment is also strongest near the structural transition.

Discussion

The agreement of experiment with theory in both neutron and Raman scattering suggests that a dominant contribution to the FeSe spectra comes from frustrated magnetism of essentially local spins. The differences between the classes of ferro-pnictides and -chalcogenides, in particular the different degrees of itineracy, may then originate in a subtle orbital differentiation across the families[1].

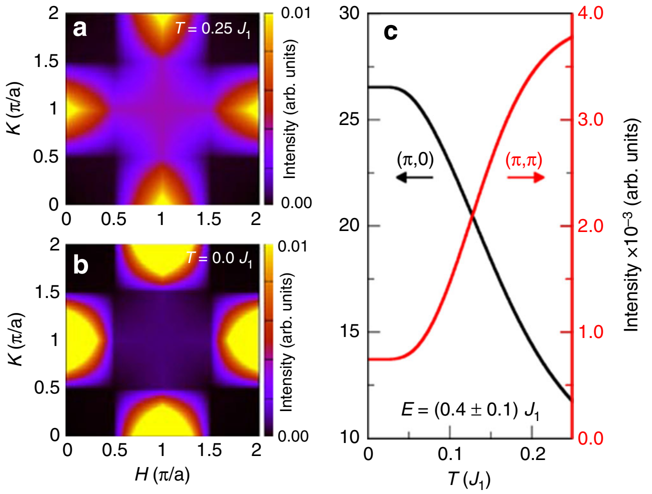

Fig. 6 Simulations of the dynamical structure factor $S(\mathbf{q}, \omega)$ of localized spin excitations integrated over an energy window of $(0.4 \pm 0.1)J_1$. **a**, **b** display cuts through the first Brillouin zone at $T = 0.25$ and $0J_1$, respectively. At high temperature there is intensity at (π, π) indicating a tendency toward Néel order. At low temperature the intensity at (π, π) is reduced and the stripe-like antiferromagnetism with $(\pi, 0)$ ordering wave vector becomes stronger. **c** $S(\mathbf{q}, \omega)$ integrated over an energy window $(0.4 \pm 0.1)J_1$ for fixed momenta (π, π) and $(\pi, 0)$ intensities as a function of temperature

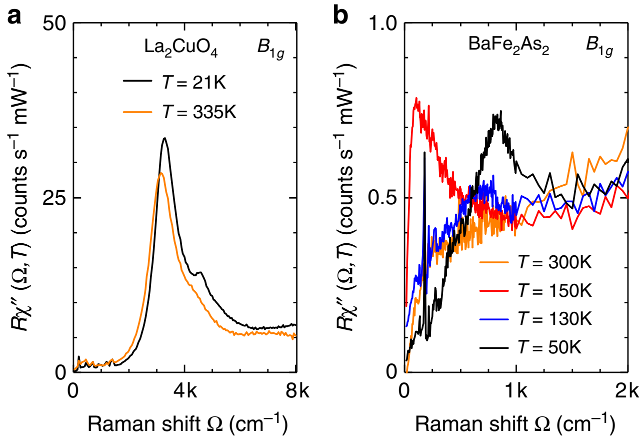

Fig. 7 Examples of localized and itinerant magnets. **a** B_{1g} Raman spectra of La_2CuO_4. From ref. [31]. **b** B_{1g} spectra of $BaFe_2As_2$ at four characteristic temperatures as indicated

If FeSe were frustrated, near such a phase boundary between magnetic states, then its behavior would be consistent with the observed sensitivity to intercalation[36,37], layer thickness[38], and pressure[39], which could affect the exchange interactions through the hopping. Relative to the theoretical results below 200 cm^{-1}, critical fluctuations of any origin, which are characterized by a diverging correlation length close to the transition, can neither be described nor distiguished in such a small cluster calculation. Here, only experimental arguments can be applied similar to those in ref. [35], but will not be further discussed, since they are not the primary focus of the analysis. A brief summary may be found in the Supplementary Note 3.

It is remarkable how clearly the Raman spectra of an SDW state originating from a Fermi surface instability and a magnet with local moments can be distingiuished. For comparison, Fig. 7 shows B_{1g} Raman spectra for La_2CuO_4 and $BaFe_2As_2$ at characteristic temperatures. La_2CuO_4 (Fig. 7a) is an example of a material with local moments on the Cu sites[30,31] having a Néel temperature of $T_N = 325$ K. The well-defined peak at ~$2.84J_1$[40,41] possesses a weak and continuous temperature dependence across T_N[32]. The origin of the scattering in La_2CuO_4 and other insulating cuprates[42] can thus be traced back to Heisenberg-type physics of local moments[43], which, for simplicity, need only include the nearest-neighbor exchange interaction J_1.

In contrast, most iron-based superconductors are metallic antiferromagnets in the parent state exhibiting rather different Raman signatures. In $BaFe_2As_2$ (Fig. 7b) abrupt changes are observed in B_{1g} symmetry upon entering the SDW state: the fluctuation peak below 100 cm^{-1} vanishes, a gap develops below some 500–600 cm^{-1}, and intensity piles up in the range 600–1500 cm^{-1} (ref. [22,44]), the typical behavior of an SDW or CDW[24] in weak-coupling, resulting from Fermi surface nesting. Yet, even for itinerant systems such as these, longer range exchange interactions can become relevant and lead to magnetic frustration[45].

In summary, the Raman response of FeSe was measured in all symmetries and compared to simulations of a frustrated spin-1 system. The experimental data were decomposed in order to determine which parts of the spectra originate from particle-hole excitations, fluctuations of local spins, and low energy critical fluctuations. Comparison of the decomposed experimental data with the simulations gives evidence that the dominant contribution of the Raman spectra comes from magnetic competition between $(\pi, 0)$ and (π, π) ordering vectors. These features of the Raman spectra, which agree qualitatively with a spin-only model, consist of a dominant peak in B_{1g} symmetry around 500 cm^{-1} along with a peak at similar energy but lower intensity in A_{1g} and at higher energy in B_{2g} symmetry. These results will likely help to unravel the mechanism behind the superconducting phase found in FeSe.

Methods

Experiment. The FeSe crystals were prepared by the vapor transport technique. Details of the crystal growth and characterization are described elsewhere[46]. Before the experiment the samples were cleaved in air and the exposure time was minimized. The surfaces obtained in this way have several atomically flat regions allowing us to measure spectra down to 5 cm^{-1}. At the tetragonal-to-orthorhombic transition T_s twin boundaries appear and become clearly visible in the observation optics. As described in detail by Kretzschmar et al.[35] the appearance of stripes can be used to determine the laser heating ΔT_L and T_s to be (0.5 ± 0.1) K m W^{-1} and (89.1 ± 0.2) K, respectively.

Calibrated Raman scattering equipment was used for the experiment. The samples were attached to the cold finger of a He-flow cryostat having a vacuum of ~5×10^{-5} Pa (5×10^{-7} mbar). For excitation we used a diode-pumped solid state laser emitting at 575 nm (Coherent GENESIS MX-SLM 577-500) and various lines of an Ar ion laser (Coherent Innova 304). The angle of incidence was close to 66° for reducing the elastic stray light entering the collection optics. Polarization and power of the incoming light were adjusted in a way that the light inside the sample had the proper polarization state and, respectively, a power of typically $P_a = 4$ mW independent of polarization. For the symmetry assignment we use the 1 Fe unit cell (axes x and y parallel to the Fe–Fe bonds) which has the same orientation as the magnetic unit cell in the cases of Néel or single-stripe order (4 Fe cell). The orthorhombic distortion is along these axes whereas the crystallographic cell assumes a diamond shape with the length of the tetragonal axes preserved. Because of the rotated axes in the 1 Fe unit cell the Fe B_{1g} phonon appears in the B_{2g} spectra. Spectra at low to medium energies were measured with a resolution $\sigma \approx 5$ cm^{-1} in steps of $\Delta\Omega = 2.5$ or 5 cm^{-1} below 250 cm^{-1} and steps of 10 cm^{-1} above where no sharp peaks need to be resolved. Spectra covering the energy range up to 0.5–1 eV were measured with a resolution $\sigma \approx 20$ cm^{-1} in steps of $\Delta\Omega = 50$ cm^{-1}.

Simulations. We use exact diagonalization to study a Heisenberg-like model on a 16-site square lattice, which contains the necessary momentum points and is small enough that exact diagonalization can reach high enough temperatures to find agreement with the temperature dependence in the experiment. This was solved using the parallel Arnoldi method[47]. The Hamiltonian is given by

$$\begin{aligned}\mathcal{H} = \sum_{\mathrm{nn}}\left[J_1\mathbf{S}_i\cdot\mathbf{S}_j + K\left(\mathbf{S}_i\cdot\mathbf{S}_j\right)^2\right] \\ + \sum_{\mathrm{2nn}} J_2\mathbf{S}_i\cdot\mathbf{S}_j + \sum_{\mathrm{3nn}} J_3\mathbf{S}_i\cdot\mathbf{S}_j\end{aligned} \tag{1}$$

where $\mathbf{S}_i$ is a spin-1 operator reflecting the observation that the local moments of iron chalcogenides are close to $2\mu_B$[48]. The sum over nn is over nearest neighbors, the sum over 2nn is over next nearest neighbors, and the sum over 3nn is over next next nearest neighbors.

We determine the dominant order according to the largest static spin structure factor, given by

$$S(\mathbf{q}) = \frac{1}{N}\sum_l \mathrm{e}^{i\mathbf{q}\cdot\mathbf{R}_l}\sum_i\left\langle \mathbf{S}_{\mathbf{R}_i+\mathbf{R}_l}\cdot\mathbf{S}_{\mathbf{R}_i}\right\rangle. \tag{2}$$

Due to the possible spontaneous symmetry breaking we adjust the structure factor by the degeneracy of the momentum. To characterize the relative strength of the dominant fluctuations we project the relative intensity of the dominant static structure factor onto the range [0, 1] using the following

$$\text{Intensity} = 1 - \frac{d_{\mathbf{q}_{\mathrm{sub}}}S(\mathbf{q}_{\mathrm{sub}})}{d_{\mathbf{q}_{\max}}S(\mathbf{q}_{\max})} \tag{3}$$

where $d_\mathbf{q}$ is the degeneracy of momentum $\mathbf{q}$, $\mathbf{q}_{\max}$ is the momentum with the largest $d_\mathbf{q}S_\mathbf{q}$, and $\mathbf{q}_{\mathrm{sub}}$ is the momentum with the second largest (subdominant) $d_\mathbf{q}S_\mathbf{q}$.

The Raman susceptibilities for B_{1g}, B_{2g}, and A_{1g} symmetries for non-zero temperatures were calculated using the Fleury-Loudon scattering operator[20] given by

$$\mathcal{O} = \sum_{i,j} J_{ij}\left(\widehat{\mathbf{e}}_{\mathrm{in}}\cdot\widehat{\mathbf{d}}_{ij}\right)\left(\widehat{\mathbf{e}}_{\mathrm{out}}\cdot\widehat{\mathbf{d}}_{ij}\right)\mathbf{S}_i\cdot\mathbf{S}_j \tag{4}$$

where J_{ij} are the exchange interaction values used in the Hamiltonian, $\widehat{\mathbf{d}}_{ij}$ is a unit vector connecting sites i and j and $\widehat{\mathbf{e}}_{\mathrm{in/out}}$ are the polarization vectors. For the symmetries calculated we use the polarization vectors

$$\begin{aligned}\widehat{\mathbf{e}}_{\mathrm{in}} = \tfrac{1}{\sqrt{2}}(\widehat{\mathbf{x}}+\widehat{\mathbf{y}}),\ \widehat{\mathbf{e}}_{\mathrm{out}} = \tfrac{1}{\sqrt{2}}(\widehat{\mathbf{x}}+\widehat{\mathbf{y}})\ \text{for}\ A_{1g}\oplus B_{2g}, \\ \widehat{\mathbf{e}}_{\mathrm{in}} = \widehat{\mathbf{x}},\ \widehat{\mathbf{e}}_{\mathrm{out}} = \widehat{\mathbf{y}}\ \text{for}\ B_{2g}, \\ \widehat{\mathbf{e}}_{\mathrm{in}} = \tfrac{1}{\sqrt{2}}(\widehat{\mathbf{x}}+\widehat{\mathbf{y}}),\ \widehat{\mathbf{e}}_{\mathrm{out}} = \tfrac{1}{\sqrt{2}}(\widehat{\mathbf{x}}-\widehat{\mathbf{y}})\ \text{for}\ B_{1g},\end{aligned} \tag{5}$$

(where $\widehat{\mathbf{x}}$ and $\widehat{\mathbf{y}}$ point along the Fe–Fe directions). We use this operator to calculate the Raman response $R(\omega)$ using the continued fraction expansion[49], where $R(\omega)$ is given by

$$R(\omega) = -\frac{1}{\pi Z}\sum_n \mathrm{e}^{-\beta E_n}\,\mathrm{Im}\left(\langle\Psi_n|\mathcal{O}^\dagger\frac{1}{\omega+E_n+i\epsilon-\mathcal{H}}\mathcal{O}|\Psi_n\rangle\right) \tag{6}$$

with Z the partition function. The sum traverses over all eigenstates Ψ_n of the Hamiltonian $\mathcal{H}$ having eigenenergies $E_n < E_0 + 2J_1$ where E_0 is the ground state energy. The Raman susceptibility is given by $\chi''(\omega) = \frac{1}{2}[R(\omega) - R(-\omega)]$. The dynamical spin structure factor was calculated using the same method with $\mathcal{O}$ replaced with $S^z_\mathbf{q} = \frac{1}{\sqrt{N}}\sum_l \mathrm{e}^{i\mathbf{q}\cdot\mathbf{R}_l}S^z_l$. **Note added in proof:** More details about the numerical study of the model can be found in ref. [50].

Data availability

Data are available upon reasonable request from the corresponding author.

Received: 18 June 2018 Accepted: 21 December 2018

References

1. Yin, Z. P., Haule, K. & Kotliar, G. Kinetic frustration and the nature of the magnetic and paramagnetic states in iron pnictides and iron chalcogenides. *Nat. Mater.* **10**, 932–935 (2011).
2. Georges, A., de' Medici, L. & Mravlje, J. Strong correlations from Hund's coupling. *Annu. Rev. Cond. Mat. Phys.* **4**, 137–178 (2013).
3. Si, Q., Yu, R. & Abrahams, E. High-temperature superconductivity in iron pnictides and chalcogenides. *Nat. Rev. Mater.* **1**, 16017 (2016).
4. Skornyakov, S. L., Anisimov, V. I., Vollhardt, D. & Leonov, I. Effect of electron correlations on the electronic structure and phase stability of FeSe upon lattice expansion. *Phys. Rev. B* **96**, 035137 (2017).
5. Li, S. et al. First-order magnetic and structural phase transitions in $\mathrm{Fe}_{1+y}\mathrm{Se}_x\mathrm{Te}_{1-x}$. *Phys. Rev. B* **79**, 054503 (2009).
6. Johnston, D. C. The puzzle of high temperature superconductivity in layered iron pnictides and chalcogenides. *Adv. Phys.* **59**, 803 (2010).
7. Yi, M., Zhang, Y., Shen, Z.-X. & Lu, D. Role of the orbital degree of freedom in iron-based superconductors. *npj Quantum Mater.* **2**, 57 (2017).
8. Baek, S.-H. et al. Orbital-driven nematicity in FeSe. *Nat. Mater.* **14**, 210–214 (2014).
9. Taylor, A. E. et al. Absence of strong magnetic fluctuations in FeP-based systems LaFePO and $\mathrm{Sr_2ScO_3FeP}$. *J. Phys. Condens. Matter* **25**, 425701 (2013).
10. Mazin, I. I. & Johannes, M. D. A key role for unusual spin dynamics in ferropnictides. *Nat. Phys.* **5**, 141 (2009).
11. Stadler, K. M., Yin, Z. P., von Delft, J., Kotliar, G. & Weichselbaum, A. Dynamical mean-field theory plus numerical renormalization-group study of spin-orbital separation in a three-band Hund metal. *Phys. Rev. Lett.* **115**, 136401 (2015).
12. Glasbrenner, J. K. et al. Effect of magnetic frustration on nematicity and superconductivity in iron chalcogenides. *Nat. Phys.* **11**, 953–958 (2015).
13. Baum, A. et al. Interplay of lattice, electronic, and spin degrees of freedom in detwinned $\mathrm{BaFe_2As_2}$: a Raman scattering study. *Phys. Rev. B* **98**, 075113 (2018).
14. Anisimov, V. I., Nekrasov, I. A., Kondakov, D. E., Rice, T. M. & Sigrist, M. Orbital-selective Mott-insulator transition in $\mathrm{Ca}_{2-x}\mathrm{Sr}_x\mathrm{RuO}_4$. *Eur. Phys. J. B* **25**, 191–201 (2002).
15. de'Medici, L., Hassan, S. R., Capone, M. & Dai, X. Orbital-selective Mott transition out of band degeneracy lifting. *Phys. Rev. Lett.* **102**, 126401 (2009).
16. de' Medici, L. Hund's induced fermi-liquid instabilities and enhanced quasiparticle interactions. *Phys. Rev. Lett.* **118**, 167003 (2017).
17. Yi, M. et al. Observation of universal strong orbital-dependent correlation effects in iron chalcogenides. *Nat. Commun.* **6**, 7777 (2015).
18. Venturini, F. et al. Observation of an unconventional metal-insulator transition in overdoped $\mathrm{CuO_2}$ compounds. *Phys. Rev. Lett.* **89**, 107003 (2002).
19. Devereaux, T. P. & Hackl, R. Inelastic light scattering from correlated electrons. *Rev. Mod. Phys.* **79**, 175 (2007).
20. Chen, C.-C., Jia, C. J., Kemper, A. F., Singh, R. R. P. & Devereaux, T. P. Theory of Two-Magnon Raman Scattering in Iron Pnictides and Chalcogenides. *Phys. Rev. Lett.* **106**, 067002 (2011).
21. Okazaki, K., Sugai, S., Niitaka, S. & Takagi, H. Phonon, two-magnon, and electronic Raman scattering of $\mathrm{Fe}_{1+y}\mathrm{Te}_{1-x}\mathrm{Se}_x$. *Phys. Rev. B* **83**, 035103 (2011).
22. Sugai, S. et al. Spin-density-wave gap with Dirac nodes and two-magnon Raman scattering in $\mathrm{BaFe_2As_2}$. *J. Phys. Soc. Jpn.* **81**, 024718 (2012).
23. Chauvière, L. et al. Raman scattering study of spin-density-wave order and electron-phonon coupling in $\mathrm{Ba(Fe}_{1-x}\mathrm{Co}_x)_2\mathrm{As}_2$. *Phys. Rev. B* **84**, 104508 (2011).
24. Eiter, H.-M. et al. Alternative route to charge density wave formation in multiband systems. *Proc. Natl Acad. Sci. USA* **110**, 64–69 (2013).
25. Yang, Y.-X. et al. Temperature-induced change in the Fermi surface topology in the spin density wave phase of $\mathrm{Sr(Fe}_{1-x}\mathrm{Co}_x)_2\mathrm{As}_2$. *Phys. Rev. B* **89**, 125130 (2014).
26. Wang, F., Kivelson, S. A. & Lee, D.-H. Nematicity and quantum paramagnetism in FeSe. *Nat. Phys.* **11**, 959–963 (2015).
27. Wang, Q. et al. Magnetic ground state of FeSe. *Nat. Commun.* **7**, 12182 (2016).
28. Rahn, M. C., Ewings, R. A., Sedlmaier, S. J., Clarke, S. J. & Boothroyd, A. T. Strong $(\pi, 0)$ spin fluctuations in $\beta-$FeSe observed by neutron spectroscopy. *Phys. Rev. B* **91**, 180501 (2015).
29. Massat, P. et al. Charge-induced nematicity in FeSe. *Proc. Natl Acad. Sci. USA* **113**, 9177–9181 (2016).
30. Sulewski, P. E., Fleury, P. A., Lyons, K. B. & Cheong, S.-W. Observation of chiral spin fluctuations in insulating planar cuprates. *Phys. Rev. Lett.* **67**, 3864 (1991).
31. Muschler, B. et al. Electron interactions and charge ordering in $\mathrm{CuO_2}$ compounds. *Eur. Phys. J. Spec. Top.* **188**, 131 (2010).
32. Knoll, P., Thomsen, C., Cardona, M. & Murugaraj, P. Temperature-dependent lifetime of spin excitations in $\mathrm{RBa_2Cu_3O_6}$ (R = Eu, Y). *Phys. Rev. B* **42**, 4842–4845 (1990).
33. Choi, K.-Y. et al. Lattice and electronic anomalies of $\mathrm{CaFe_2As_2}$ studied by Raman spectroscopy. *Phys. Rev. B* **78**, 212503 (2008).
34. Gallais, Y. et al. Observation of incipient charge nematicity in $\mathrm{Ba(Fe}_{1-x}\mathrm{Co}_x)_2\mathrm{As}_2$. *Phys. Rev. Lett.* **111**, 267001 (2013).
35. Kretzschmar, F. et al. Critical spin fluctuations and the origin of nematic order in $\mathrm{Ba(Fe_{1-x}Co_x)_2As_2}$. *Nat. Phys.* **12**, 560–563 (2016).
36. Burrard-Lucas, M. et al. Enhancement of the superconducting transition temperature of fese by intercalation of a molecular spacer layer. *Nat. Mater.* **12**, 15–19 (2013).
37. Zhang, A.-M. et al. Superconductivity at 44 K in K intercalated FeSe system with excess Fe. *Sci. Rep.* **3**, 1216 (2013).
38. Ge, J.-F. et al. Superconductivity above 100 K in single-layer FeSe films on doped $\mathrm{SrTiO_3}$. *Nat. Mater.* **14**, 285–289 (2015).

39. Medvedev, S. et al. Electronic and magnetic phase diagram of β-$Fe_{1.01}Se$ with superconductivity at 36.7 K under pressure. *Nat. Mater.* **8**, 630 (2009).
40. Canali, C. M. & Girvin, S. M. Theory of Raman scattering in layered cuprate materials. *Phys. Rev. B* **45**, 7127–7160 (1992).
41. Weidinger, S. A. & Zwerger, W. Higgs mode and magnon interactions in 2D quantum antiferromagnets from Raman scattering. *Eur. Phys. B* **88**, 237 (2015).
42. Chelwani, N. et al. Magnetic excitations and amplitude fluctuations in insulating cuprates. *Phys. Rev. B* **97**, 024407 (2018).
43. Fleury, P. A. & Loudon, R. Scattering of light by one- and two-magnon excitations. *Phys. Rev.* **166**, 514 (1968).
44. Chauvière, L. et al. Impact of the spin-density-wave order on the superconducting gap of $Ba(Fe_{1-x}Co_x)_2As_2$. *Phys. Rev. B* **82**, 180521 (2010).
45. Yildirim, T. Frustrated magnetic interactions, giant magneto-elastic coupling, and magnetic phonons in iron-pnictides. *Phys. C.* **469**, 425 (2009).
46. Böhmer, A. E. et al. Lack of coupling between superconductivity and orthorhombic distortion in stoichiometric single-crystalline FeSe. *Phys. Rev. B* **87**, 180505 (2013).
47. Sorensen, D., Lehoucq, R. & Yang, C. *ARPACK Users' Guide: Solution of Large-Scale Eigenvalue Problems with Implicitly Restarted Arnoldi Methods.* (Siam, Philadelphia, 1998).
48. Gretarsson, H. et al. Revealing the dual nature of magnetism in iron pnictides and iron chalcogenides using x-ray emission spectroscopy. *Phys. Rev. B* **84**, 100509 (2011).
49. Dagotto, E. Correlated electrons in high-temperature superconductors. *Rev. Mod. Phys.* **66**, 763 (1994).
50. Ruiz, H., Wang, Y., Moritz, B. & Devereaux, T. P. Frustrated magnetism from local moments in FeSe. Preprint at https://arxiv.org/abs/1812.09609 (2018).

Acknowledgements

The work was supported by the German Research Foundation (DFG) via the Priority Program SPP 1458 (grant-no. Ha2071/7) and the Transregional Collaborative Research Center TRR80 and by the Serbian Ministry of Education, Science and Technological Development under Project III45018. We acknowledge support by the DAAD through the bilateral project between Serbia and Germany (grant numbers 57142964 and 57335339). The collaboration with Stanford University was supported by the Bavaria California Technology Center BaCaTeC (grant-no. A5 [2012-2]). Work in the SIMES at Stanford University and SLAC was supported by the U.S. Department of Energy, Office of Basic Energy Sciences, Division of Materials Sciences and Engineering, under Contract No. DE-AC02-76SF00515. Computational work was performed using the resources of the National Energy Research Scientific Computing Center supported by the U.S. Department of Energy, Office of Science, under Contract No. DE-AC02-05CH11231.

Author contributions

A.B., T.B. and R.H. conceived the experiment. B.M. and T.P.D. conceived the ED analysis. P.A. and T.W. synthesized and characterized the samples. A.B., N.L., T.B. and R.H. A. performed the Raman scattering experiment. H.N.R. and Y.W. coded and performed the ED calculations. A.B., H.N.R., N.L., B.M. and R.H. analyzed and discussed the data. A.B., H.N.R., N.L., Z.P., B.M., T.P.D. and R.H. wrote the paper. All authors commented on the manuscript.

Additional information

Supplementary information accompanies this paper at https://doi.org/10.1038/s42005-019-0107-y.

Competing interests: The authors declare no competing interests.

www.pss-a.com

Temperature-Dependent Raman Study of Nanostructured and Multifunctional Materials

Maja Šćepanović, Mirjana Grujić-Brojčin, Nenad Lazarević, and Zoran V. Popović*

The scope of this paper is temperature dependence of Raman spectra in several nanocrystalline materials and iron-based single-crystals. The Raman results presented and analyzed here are related to TiO_2 nanopowders (with dominant anatase and brookite phase) and $Zn_xCd_{1-x}Se$ single layers measured at different temperatures. Temperature-dependent Raman spectra of iron-based sulphides and selenides ($BaFe_2S_3$ and $BaFe_2Se_3$), as well as alkali-doped iron selenides ($K_xFe_{2-y}Se_2$ and $K_{0.8}Fe_{1.8}Co_{0.2}Se_2$) are also analyzed. A physical model, including thermal expansion as well as three- and four-phonon anharmonic effects, is used to quantitatively analyze temperature evolution of the characteristic Raman mode self-energies for the materials of interest. It is demonstrated how this model can be used as a tool for predicting the temperature of structural and phase transitions, with critical scrutany of its limitations.

1. Introduction

Variable-temperature Raman scattering measurements provide great assistance in the analysis of structural, electronic, and magnetic properties, as well as phase transitions, in large number of materials currently in the focus of modern research in condensed matter physics. Two important classes of materials are in the scope of the present paper – nanomaterials and iron-based compounds. Temperature-dependent Raman spectra of nanomaterials is a significant source of information on their thermal stability and other properties (such as phase composition, nanocrystallite size distribution, strain, defects, and non-stoichiometry) strongly depended on the temperature and affecting the shape, shift, and linewidth of characteristic Raman modes.[1–4] The obtained Raman results are related to titanium dioxide (TiO_2) nanopowders (with dominant anatase or brookite phase) and $Zn_xCd_{1-x}Se$ single layers. In addition the influence of the antiferromagnetic order, ferromagnetism, and magnetic fluctuations on the Raman scattering spectra of several iron-based compounds measured in wide temperature range were also analyzed. These materials may have not only superconducting but also low-dimensional magnetic properties (forming spin chains, spin ladders, spin dimers, etc.).[5] The temperature dependent Raman spectra of iron-based sulphides and selenides ($BaFe_2S_3$ and $BaFe_2Se_3$, belonging to the family of the iron-based $S=2$ two-leg spin-ladder compounds),[5] together with alkali-doped iron selenides (superconducting $K_xFe_{2-y}Se_2$ and non-superconducting $K_{0.8}Fe_{1.8}Co_{0.2}Se_2$)[6] are analyzed. A physical model, including thermal expansion, as well as three- and four-phonon anharmonic effects, is used to quantitatively analyze experimentally obtained temperature dependence of energy and linewidth of the Raman modes characteristic for investigated materials. We have shown that this simplified model could be successfully used to predict the temperature of microstructural phase trasitions, but its limitations have also been indicated.

2. Theoretical Background

Lattice vibrations are strongly related to crystalline, thermodynamical, and transport properties of materials, including phase stability at finite temperatures, lattice thermal conductivity, and superconducting critical temperature of phonon-mediated superconductors.[7] In order to interpret experimental vibrational spectra some computational methods based on density functional theory have been developed. These methods use the first-principles calculations of phonons and other related properties, but it appears that their performance is always limited by chosen approximations and assumptions. The harmonic approximation, assuming independent phonons, is usually adopted in calculations of phonon properties at low temperatures; it is a method of choice when describing the phonon spectra of the metals and insulators, valid and useful for obtaining phonon dispersion curves and studying phase stability. However, harmonic approximation is not successful in describing phonon behavior at high temperatures, where phonon-phonon interactions must be considered, together with properties related to the lattice anharmonicity (thermal expansion, lattice thermal conductivity, temperature, and volume dependences of phonon frequencies). The anharmonic effects can be successfully treated by the many-body perturbation theory.[8,9] However, this theory seems to be inadequate, when the cubic and higher-order anharmonic terms of the phonon energies are larger than the harmonic one, or when the harmonic solution shows dynamical instability. In order to overcome these limitations, some advanced methods have been

---

Dr. M. Šćepanović, Dr. M. Grujić-Brojčin, Dr. N. Lazarević,
Prof. Z. V. Popović
Center for Solid State Physics and New Materials
Institute of Physics
University of Belgrade
Pregrevica 118, 11080 Belgrade, Serbia
E-mail: maja@ipb.ac.rs

DOI: 10.1002/pssa.201800763

developed, such as the self-consistent phonon theory,[10] or ab-initio molecular dynamics method,[11,12] both treating anharmonic effects in solids nonperturbatively.[7] However, all these calculations require significant computer resources, rapidly increasing with the size of the system. This may be the reason why the first-principles calculations of phonons are usually performed at low temperatures, and the results related to the temperature dependence of phonon properties are, to the best of our knowledge, still unavailable for materials studied here.

The analysis of experimentally obtained temperature dependence of phonon frequency and lifetime in the materials presented in this paper includes quasiharmonic and anharmonic contribution to the lattice potential, which both contribute to nonharmonic lattice dynamics. The phonon modes in the quasiharmonic model behave harmonically with infinite lifetimes, but their frequencies are influenced by the effects of lattice volume on the interatomic potential,[13] whereas explicit anharmonicity originates from phonon-phonon interactions increasing with temperature.

Frequency shift and broadening of phonon mode can be described as real and imaginary part of phonon self-energy[6,14,15]:

$$\Sigma_{\mathrm{i}}(T) = \Delta_{\mathrm{i}}(T) + \mathrm{i}\Gamma_{\mathrm{i}}(T) \tag{1}$$

where $\Delta_i(T)$ corresponds to the energy of i-th Raman mode and $\Gamma_i(T)$ to its linewidth, defined as inverse value of phonon lifetime τ. Temperature dependence of Raman shift can be defined by the real part of self-energy:

$$\omega_i(T) = \omega_{0,i} + \Delta_i(T) \tag{2}$$

where $\omega_{0,\iota}$ is temperature independent contribution to phonon mode energy. Temperature dependent term may be written as

$$\Delta_i(T) = \Delta_i^V + \Delta_i^A \tag{3}$$

The first term, Δ_i^V, corresponds to the frequency shift from the volume thermal expansion or quasiharmonicity, and can be expressed as

$$\Delta_i^V = -\omega_{0,i}\left(e^{-\gamma_i \int_0^T \alpha_V(T')dT'} - 1\right) \tag{4}$$

with Grüneisen parameter γ_i of given mode and volume thermal expansion coefficient $\alpha_V(T)$ of investigated material.[15] The Grüneisen model assumes that the Grüneisen parameter correlates the temperature dependence of vibrational frequencies with the unit cell volume. At constant pressure the Grüneisen constant is defined by

$$\gamma_i = \frac{\partial \ln \omega_i}{\partial \ln V}\bigg|_P = -\frac{1}{\alpha_V}\frac{\partial \ln \omega_i}{\partial T}|_P \tag{5}$$

where ω_i is the frequency of i-th vibrational mode, V the unit cell volume and α_V the volumetric thermal expansion given by

$$\alpha_V = \frac{1}{V}\frac{\partial V}{\partial T}|_P \tag{6}$$

Maja Šćepanović received her PhD from the School of Electrical Engineering, University of Belgrade. She is employed as a Research Professor at the Center for Solid State Physics and New Materials, Institute of Physics Belgrade. She has contributed greatly to the understanding of a number of problems in the experimental study and simulation of intense ns laser pulse-matter interaction, Raman, infrared and photoluminescence spectroscopy, and spectroscopic ellipsometry. In recent years, she has been primarily concerned with the experimental and theoretical studies, as well as development of numerical models, related to the investigation of nanostructured and iron-based related materials.

Mirjana Grujić-Brojčin, PhD (School of Electrical Engineering, University of Belgrade). Employed, as a Research Professor at the Center for Solid State Physics and New Materials, Institute of Physics Belgrade. She is engaged in experimental study and development of numerical models in Raman, infrared and photoluminescence spectroscopy, and spectroscopic ellipsometry of nanomaterials. In recent years she has been involved in application of spectroscopic techniques in Cultural Heritage.

Nenad Lazarević is Research Associate professor employed at the Canter for Solid State Physics and Materials, Institute of Physics, University of Belgrade. His main research interest is focused on optical spectroscopy of strongly correlated electron systems with particular emphasis on Raman spectroscopy. In the last years, his activities were mostly focused on the iron-based superconductors and related materials. Other activities include work on devising new experimental setups for Raman spectroscopy.

Hence, when the temperature dependence of vibrational modes is known, the Grüneisen parameter (which varies significantly from one mode to the other) can be determined from the known thermal expansion (or vice-versa).

The second term, Δ_i^A, in the Equation (3) describes the frequency shift caused by the anharmonic phonon-phonon coupling, that is, the explicit anharmonicity or pure temperature effect. The anharmonic decay of phonons includes the leading, three-phonon and four-phonon processes, cubic $\Delta_i^{(3)}$ and quartic $\Delta_i^{(4)}$ components of the anharmonicity term Δ_i^A and it should be determined for each Raman mode. The explicit anharmonicity for frequency shift may be simplified by the model proposed by Klemens[16] and extended by Balkanski et al.[17] where phonon-phonon interactions include only overtone processes (one optical phonon at the Γ point decays into two or three phonons of equal energy on the same branch), specifying the contributions of three-phonon and four-phonon processes to the frequency shift in the following form[17]:

$$\begin{aligned}\Delta_i^A &= \Delta_i^{(3)} + \Delta_i^{(4)} \\ &= C_i\left(1 + \frac{2}{\mathrm{e}^{\frac{\hbar\omega_i}{2k_BT}} - 1}\right) + D_i\left(1 + \frac{3}{\mathrm{e}^{\frac{\hbar\omega_i}{3k_BT}} - 1} + \frac{3}{\left(\frac{\hbar\omega_i}{e^{3k_BT}-1}\right)^2}\right)\end{aligned} \tag{7}$$

where C_i and D_i are so-called anharmonic constants. It should be noted that the parameters which exist in the simplified Klemens model are treated as independent, which is not quite physically correct. In general, the exact interdependence of these parameters is very hard to determine. In order to obtain the relationship between the parameters, when the anharmonic effect can be defined only by three phonon processes, the model of a damped oscillator is adopted,[15] and phonon-phonon scattering contribution to energy of Raman mode is represented as:

$$\Delta_\mathrm{i}^\mathrm{A} = \mathrm{C_i}\left(1 + \frac{4\lambda_{\mathrm{ph-ph,i}}}{\frac{\hbar\omega_\mathrm{i}}{\mathrm{e}^{2\mathrm{k}}\mathrm{B}^\mathrm{T}-1}}\right) \tag{8}$$

with phonon-phonon interaction constant $\lambda_{ph\text{-}ph}$ introduced as fitting parameter to represent phonon-phonon coupling strength.

Unlike the phonon energy, the phonon linewidth is not affected by the thermal expansion of crystal lattice. Two main contributions to the phonon linewidth are the anharmonic decay of the phonons and the perturbation of the crystal translational symmetry, due to the presence of impurities and defects. According to Klemens model, temperature dependence of Raman mode linewidth can be described by

$$\begin{aligned}\Gamma_i(T) = \Gamma_{0,i} &+ A_i\left(1 + \frac{2}{\mathrm{e}^{\hbar\omega_i/2k_BT} - 1}\right) \\ &+ B_i\left(1 + \frac{3}{\mathrm{e}^{\hbar\omega_i/3k_BT} - 1} + \frac{3}{(\mathrm{e}^{\hbar\omega_i/3k_BT} - 1)^2}\right)\end{aligned} \tag{9}$$

where $\Gamma_{0,i}$ is the temperature-independent linewidth, which originates mainly from the presence of impurities and defect (nonstoichiometry), whereas A_i and B_i are the three- and four-phonon anharmonic constants, respectively. According to the model of a damped oscillator, if four-phonon processes turned out to be negligible, Raman mode linewidth could be written as[15]:

$$\Gamma_i(T) = \Gamma_{0,\mathrm{i}}\left(1 + \frac{2\lambda_{\mathrm{ph-ph,i}}}{\mathrm{e}^{\frac{\hbar\omega_i}{2k_BT}} - 1}\right) \tag{10}$$

with $\Gamma_{0,i}$ as anharmonic constant, which could be related to the phonon-phonon interaction constant $\lambda_{ph\text{-}ph}$ and the anharmonic parameter C_i from relation (8), given as[15]:

$$C_i = \frac{\Gamma_{0,i}^2}{2\omega_{0,i}} \tag{11}$$

It should be noted that more general calculations, including asymmetric decay channels, result in a better agreement with experiment, especially in some semiconductors.[15]

3. Temperature-Dependent Raman Spectra of Nanomaterials

The Raman scattering provides important information on the nature of the solid on a scale of few lattice constants. Therefore, this technique can be used to study the correlation between the change in vibrational properties on one, and structural and/or morphological changes in nanostructured material on the other side.

The Raman spectra of nanocrystalline materials are usually simulated by phenomenological phonon confinement model (PCM).[18,19] In this model several independent factors, like phonon confinement, strain, non-homogeneity of the size distribution, defects, and variations in phonon relaxation with crystallite size decreasing, contribute to the changes in the position and linewidth of calculated Raman mode.[18–21] Due to the crystallite size decrease, the phonons are confined and optical phonons over the entire Brillouin zone (BZ) contribute to the first-order Raman spectra. The Raman intensity $I(\omega)$ for crystallite size L, according to Richter et al.[22] and Campbell and Fauchet,[23] is presented as a superposition of weighted Lorentzian contributions over the whole BZ, by the equation[3,4,18–23]:

$$I(\omega) = \sum\nolimits_{i=1}^{m} \int_0^\infty \rho(L)dL$$

$$\left(\int_{BZ} \frac{\exp\left(\frac{-q^2L^2}{8\beta}\right)d^3q}{[\omega - (\omega_i(q) + \Delta\omega_i(q, L, T))]^2 + \left(\frac{\Gamma_{0i}(T)}{2}\right)^2}\right) \tag{12}$$

where ρ (L) defines crystallite size distribution, q is expressed in units of π/a_L (a_L – effective unit cell parameter), β – strength of confinement (varies from $\beta = 1$ in the Richter's confinement model to $\beta = 2\pi^2$ in the Campbell's confinement model, depending on the confinement boundary conditions in different nanomaterials), $\omega_i(q)$ – phonon dispersion, $\Gamma_{0i}(T)$ – the intrinsic linewidth of Raman mode dependent on temperature T, as well as nonstoichiometry, disorder, and defects state.

The change of the lattice parameters (lattice volume) with nanocrystallite size decrease is registered in nanomaterials due to effect of microstrain and may affect the Raman mode position. The influence of strain on Raman shift $\Delta\omega_i(q, T, L)$ of particular mode is included into PCM through the term given by[4,20,24]:

$$\Delta\omega_i(q,T,L) = -\gamma_i\omega_i(q,T)\frac{V(L)}{V_0} \tag{13}$$

The unit cell volume variation of nanocrystallite size L can be written as

$$V(L) = V_0 \pm \Delta V(L) \tag{14}$$

where signs "+" and "–" correspond to tensile and compressive strain, respectively.

3.1. TiO_2 Based Nanomaterials

Titanium dioxide is material of great importance in modern materials science. It is probably the most characterised oxide in different areas, such as defect chemistry, phase transitions, surface structure, surface chemistry, optical properties, and electronic structure.[2] Also, it is widely used nowadays, with a variety of achieved and potential applications: as a pigment, in photocatalysis, as electron transport layer in solar cells, as self-cleaning material, etc.[25] Only three of TiO_2 several polymorphs (rutile, anatase, and brookite) are considered to be its naturally occurring phases. Although extensively studied during past decades, there are still some unresolved questions related to vibrational and thermal properties of these phases, especially those originated from their nanocrystalline structure.

3.1.1. Anatase Nanocrystalline Powders

The Raman spectroscopy of nanocrystalline anatase (the TiO_2 phase most commonly synthesized at ambient conditions), has been established as a very sensitive tool for detecting nano-structural changes in this material, associated with phonon confinement effect, non-stoichiometry, internal stress/surface tension effects and/or the anharmonicity effects due to temperature variations.[1–4]

In this review we present our experimental results related to the temperature dependence of the most intense anatase E_g Raman mode, taken from laser-synthesized and commercial anatase nanopowder samples, published in our earlier papers.[1,2] The interpretation of these results is slightly modified here, in accordance with recent experimental and theoretical findings related to the variation of nanostructural properties of anatase with temperature.[26–30]

The results of a detailed study of the most intense E_g mode in the Raman spectra of anatase nanopowder synthesized by laser-induced pyrolysis, with crystallite size about 12.3 nm, are presented in the **Figure 1**. The spectra in the temperature range from 25 to 300 K were taken in closed cryostat coupled with Jobin Yvon U1000 macro-Raman system. Other spectra were obtained in the same Raman system, but under conditions of local heating of the sample due to laser radiation, with the temperature estimation based on the intensity ratio between the Stokes and anti-Stokes Raman spectra.[1]

As can be seen from the Figure 1a, very good agreement between the experimental and calculated spectra of anatase

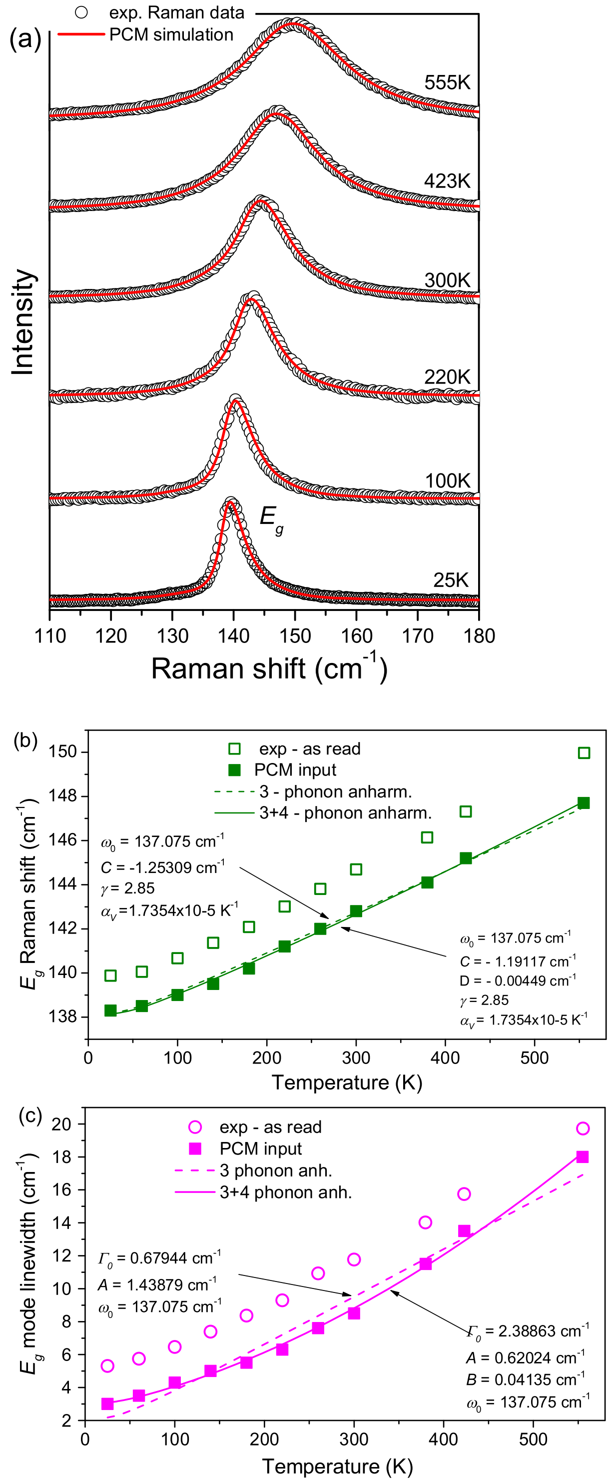

Figure 1. a) The Raman spectra of laser-synthesized TiO_2 nanopowder measured at different temperatures (circles) simulated by PCM (lines). Temperature dependence of the E_g Raman (b) shift and (c) linewidth fitted by three- (dashed lines) and four-phonon (full lines) anharmonic model with the corresponding parameters specified in the figures.

nanopowder has been obtained at all given temperatures, by using the PCM (Equation (12)) with anisotropic dispersion relations[31] and temperature dependent parameters.[1] It has also been demonstrated that the frequency shift (Figure 1b) and mode broadening (Figure 1c) of the E_g Raman mode were induced by both phonon confinement due to the nanocrystalline size and effect of heating. In order to analyze only heating effects on E_g Raman shift and linewidth, their as-read experimental values (shown with open symbols in the Figure 1b and c) have been corrected to exclude the effects of phonon confinement. Thereafter the corresponding temperature dependences of the E_g Raman shift and linewidth (closed symbols in Figures 1b and c) were fitted according to the Equations (7) and (9), respectively. The obtained results show that the contribution of explicit anharmonicity overpowers the effect of quasiharmonicity in the E_g frequency shift. Namely, the volume thermal expansion due to the heating, in combination with the positive value of Grüneisen parameter for E_g mode, should lead to a decreasing in E_g Raman frequency with temperature, contrary to experimental observation. It also has been shown that the curves (full line) corresponding to the contributions of both three- and four-phonon processes were better matched to the experimental results, than those calculated with the assumption of three-phonon processes only (dashed line). This effect is particularly pronounced in linewidth temperature dependence of E_g Raman mode.

Raman spectra of commercial anatase TiO_2 nanocrystals (Aldrich 637254, 99.7%) with a declared average crystallite size of about 5 nm were measured in the temperature range from 22 to 900 °C using Linkam TS 1500 heating stage coupled with Jobin Yvon T64000 micro-Raman system.[2] The temperature dependences of Raman shift and broadening of the lowest frequency E_g mode were analyzed by using PCM and anharmonic model. Comparison between experimental spectra and those calculated by PCM (Equation (12)) at several chosen temperatures is shown in the **Figure 2**a. In this case PCM included not only the effects of phonon confinement and nonstoichiometry, but also the strain. Namely, recently published results have revealed that the strain in anatase particles varied with temperature[26,27,29,30]: at some medium-high temperatures, the strain could be released, but at high temperatures, close to the transformations from anatase to rutile phase, the strain could strengthen again. Also, in situ x-ray diffraction study of the anatase microstructure evolution as a function of temperature has confirmed that anatase nanoparticle size increased with temperature. But it should be pointed out that the temperature at which the particles size begin to increase depends on their initial size,[32] and that for smaller anatase nanoparticles the increase starts at higher temperature. This was the reason for modification of our previous calculations by including the strain in PCM, which led to the increase of calculated temperature at which the anatase nanoparticles begin to grow from previously estimated 500 °C to currently specified 600 °C.[2] Different calculated results are the consequence of following assumption: the discrepancy of experimental temperature dependences of E_g Raman shift and linewidth from those predicted by anharmonic model (Equations (7) and (9)), observed at about 500 °C, originates from strain relaxation, and nanoparticle growth starts at higher temperatures (about 600 °C). Also, nanoparticles growth with temperature, estimated

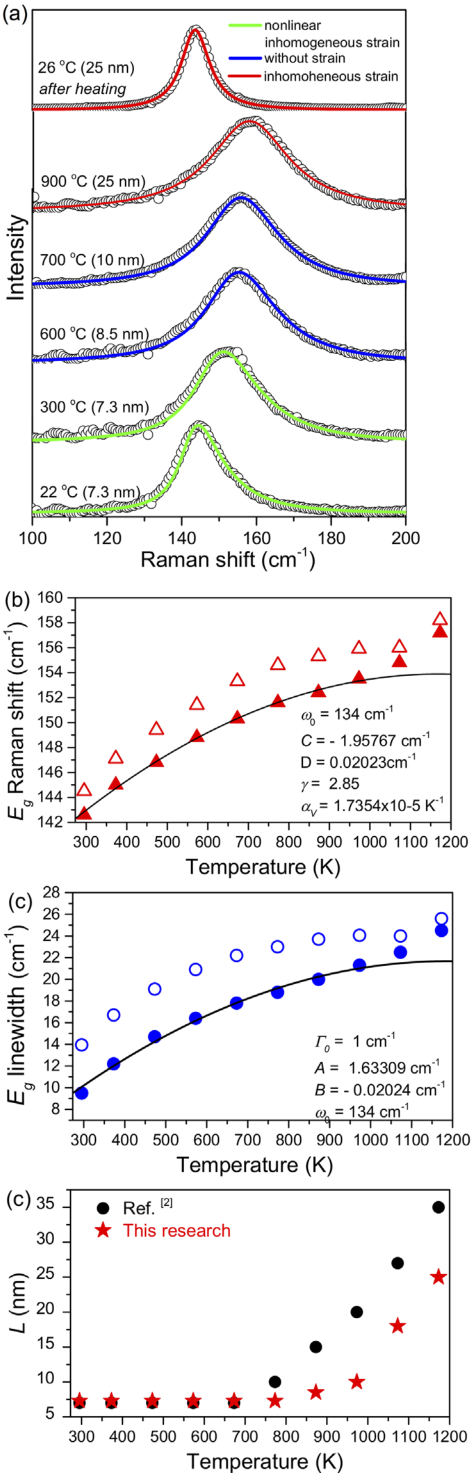

Figure 2. a) The Raman spectra of commercial anatase TiO_2 nanopowder measured at different temperatures (circles) simulated by PCM (lines). Temperature dependence of the E_g Raman (b) shift and (c) linewidth fitted by four-phonon anharmonic model (full lines) with the corresponding parameters specified in the figures. d) Nanocrystallite size L estimated by using PCM with (circles) and without (asterisks) included strain.

by using PCM with strain effect, is less steep than that obtained with strain effect neglected,[2] which is much more consistent with the published XRD results for very small anatase nanoparticles.[32] Note that we assume anatase nanocrystallites to obey a log-normal size distribution with average crystallite size of about 7 nm, previously estimated by the procedure based on the low frequency Raman scattering measurements.[2]

3.1.2. Brookite Nanocrystalline Powders

Unlike the anatase phase, the variation of Raman spectra of TiO_2 brookite phase with temperature has not yet been reported, to the best of our knowledge. The Raman spectra of hydrothermally synthesized spindle-like brookite nanoparticles with mean crystallite size of $\approx$33 nm (according to XRD results[33]) were measured in the temperature range from 80 to 860 K using Linkam THMS 600 heating stage coupled with Jobin Yvon T64000 micro-Raman system. The Raman spectra of brookite taken at several temperatures are shown in the **Figure 3**a. It can be seen that a great number of observed modes, characteristic for this orthorhombic structure (36 Raman active modes are expected according to symmetry considerations),[34] broadens and shifts towards lower frequencies with the temperature increase. The temperature dependence of Raman shift (squares) and linewidth (circles) of the most intensive brookite A_{1g} mode, collected from experimental spectra is presented in the Figure 3b. The PCM has not been used to analyze the spectra of brookite nanopowder, because of relatively large mean crystallite size, as well as quite flat phonon dispersion curves theoretically predicted for this brookite Raman mode.[35] Even the application of the anharmonic model in this analysis is not simple, due to lack of experimental and calculated data on the brookite thermal expansion coefficients, as well as the pressure dependence of brookite vibrational properties, needed for determination of mode Grüneisen parameter. Therefore, the value of volume thermal expansion coefficient for brookite is assumed in the range limited by expansion coefficients of anatase and rutile, as indicated by published experimental results related to polyhedral thermal expansion in these TiO_2 polymorphs.[36] The value of Grüneisen parameter is taken as fitting parameter in the calculation of quasiharmonic contribution to A_{1g} Raman shift according to Equations (4). The curves calculated as described above start to deviate from experimental temperature dependence of A_{1g} Raman shift on temperature already at 450 K, whereas the discrepancy of the values predicted according to Equation (9) from experimental linewidth appears above 600 K. The experimental A_{1g} linewidth at higher temperatures, narrower than predicted by the model, can be explained by the strain relaxation and increase of the brookite crystallite size with temperature. Note that gradual increase of brookite crystallite size due to thermal treatment of TiO_2 nanopowders has been documented in the literature.[37] The comparison between brookite Raman spectra measured at 80 K, before and after heating the sample at 873 K (Figure 3a), indicates that some modes become better defined, narrower, and shifted to lower frequencies after the thermal treatment, thus supporting the assumptions of defect relaxation and partial consolidation of small particles into larger. On the other hand, the deviation of temperature dependence of A_{1g} Raman shift from those predicted by model, could be not only a consequence of microstructural changes in brookite nanopowder due to heating, but also a result of the changes in the thermal properties of

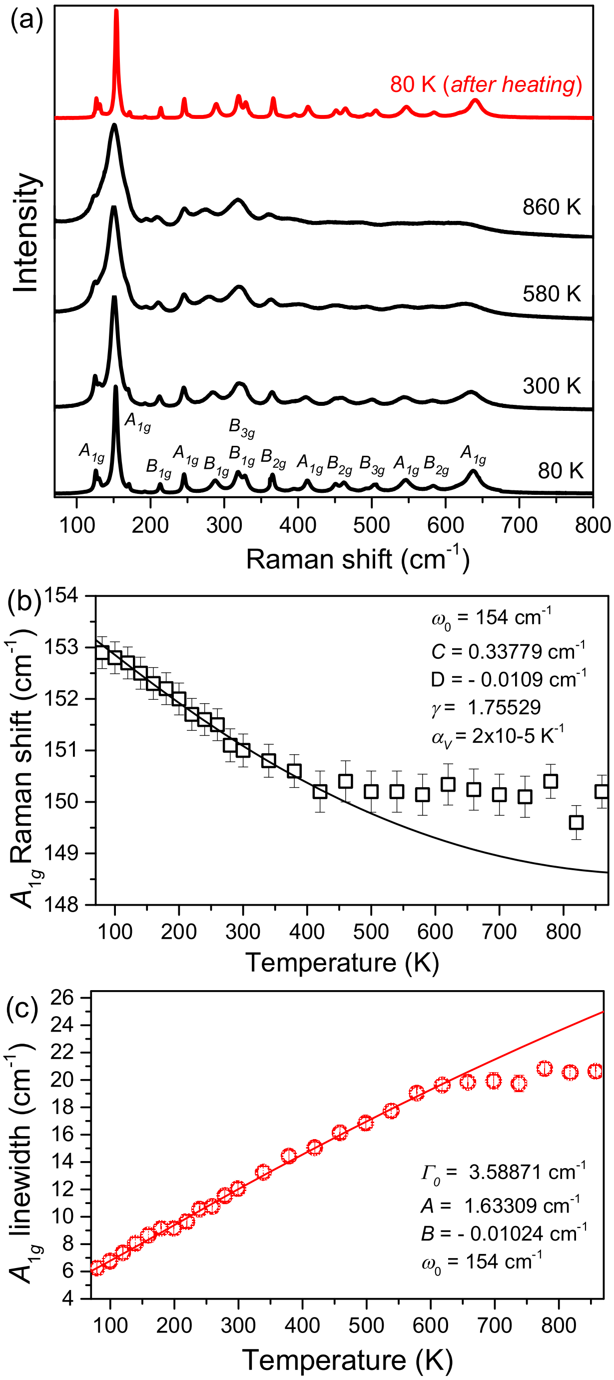

Figure 3. a) The Raman spectra of brookite TiO_2 nanopowder measured at different temperatures with characteristic modes assigned. Temperature dependence of the A_{1g} Raman mode (b) shift and (c) linewidth; experimental as read values (symbols) are fitted by four-phonon (full lines) anharmonic model with the corresponding parameters specified in the figures.

brookite with temperature. These changes are not taken into account because, despite some indications, precise data about these phenomena still are not available.

3.2. $Zn_xCd_{1-x}Se$ Single Layers

The examination of vibrational properties of $Zn_{1-x}Cd_xSe$ is a matter of special interest due to structural phase transition observed in this material with variation of composition x and temperature.[38] There are also the strong indications that vibration properties of thin layers are not identical to those for bulk $Zn_{1-x}Cd_xSe$ mixed crystal.[39] The Raman spectra of microcrystalline $Zn_xCd_{1-x}Se$ single layer (with composition $x = 0.59$ and thickness of 400 nm), prepared by thermal vacuum evaporation, through alloying of ultrathin ZnSe and CdSe films with equivalent thickness,[40] were measured in the temperature range from 20 to 600 °C using Linkam THMS 600 heating stage coupled with Jobin Yvon T64000 micro-Raman system. Some of these spectra, obtained with 514.5 nm line of mixed Ar/Kr laser, are presented in the **Figure 4**a. The temperature dependences of Raman shift and linewidth of the most intensive Raman mode, ascribed to the scattering from 1LO phonons of the $Zn_xCd_{1-x}Se$,[38,41,42] are shown in the Figure 4b for chosen temperatures. We have decided to analyze temperature dependence of 1LO mode because of the change of the LO-phonon spectrum versus crystal composition, which has been described as one-mode type. On the other side, the TO-phonon dependence appeared to be much more complicated, with rather anomalous features in the line shape and mode frequency versus crystal composition, as well as the temperature, due to the anharmonic coupling between TO-mode and two-phonon states.[42] To simulate this dependence by the model described in Section 2, values for thermal expansion coefficient and Grüneisen parameter have been taken from recently calculated pressure and temperature dependence of $Zn_{0.5}Cd_{0.5}Se$ thermodynamic properties.[43] It is obvious that at the temperatures higher than 700 K, there are some discrepancies between experimentally obtained values and those predicted by the model, more pronounced for the mode frequencies. Such discrepancies are most probably the consequence of the change in the film composition at higher temperatures. Namely, it is well known that frequency of 1LO Raman mode of $Zn_xCd_{1-x}Se$ increases with the increase in composition x, which arises here due to the evaporation of Cd at higher temperatures.[41]

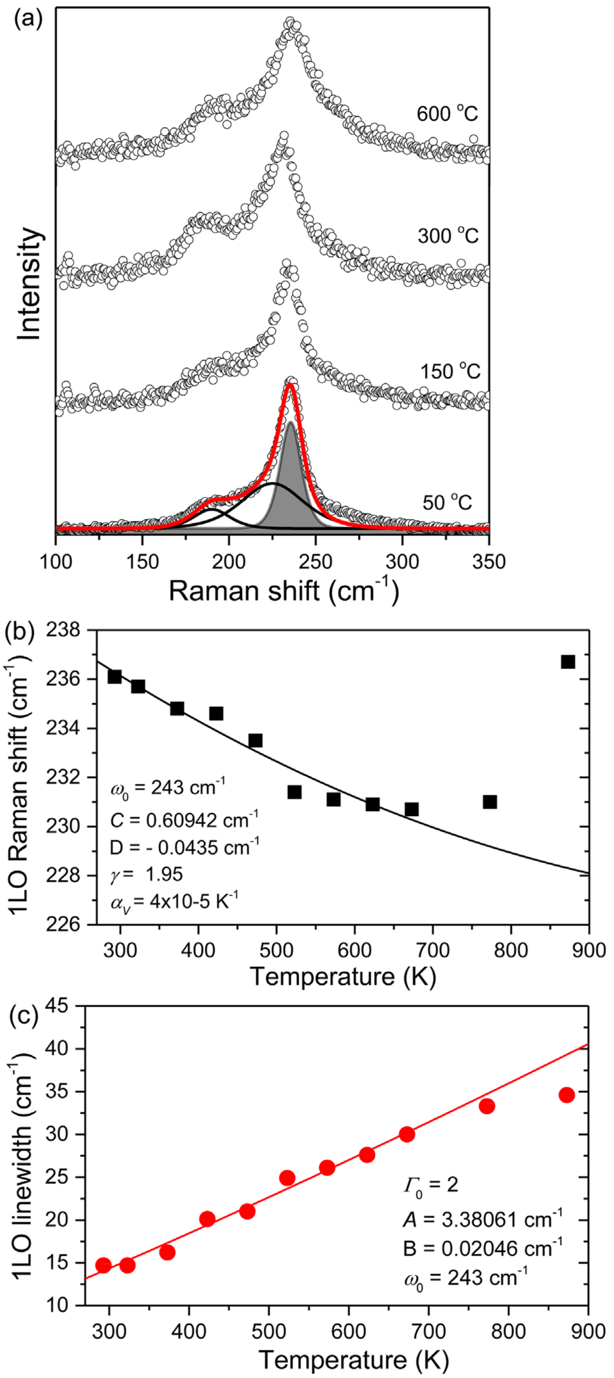

Figure 4. a) Experimental Raman spectra of $Zn_xCd_{1-x}Se$ single layers measured at different temperatures; Lorentzian fit correspond to the 1LO mode of $Zn_xCd_{1-x}Se$ is pointed out. Temperature dependence of the 1LO Raman mode (b) shift and (c) linewidth; symbols represent as-read experimental values, whereas full lines correspond to the results calculated by model described in the text with the parameters specified in the figures.

4. Temperature Dependence of Raman Spectra of Iron-Based Materials

The discovery of superconductivity in iron-based materials has attracted a great attention of the solid state community. During the last decade many new classes of iron-based materials with reach phase diagrams have been reported, featuring a variety of the (competing) phases,[44] and their phonon properties have been extensively studied by using temperature-dependent Raman spectroscopy.[5,6,45–64] In order to demonstrate the ability of inelastic light scattering to probe a number of structural and/or magnetic properties of iron-based materials, an overview of some published results is presented.[5,6] The Raman scattering experiments shown here were performed in backscattering micro-Raman configuration using 514.5 nm line of an Ar^+/Kr^+ mixed laser. Low-temperature measurements were taken using KONTI CryoVac continuous flow cryostat coupled with JY T64000 or TriVista 557 Raman systems, whereas the Raman scattering measurements at higher

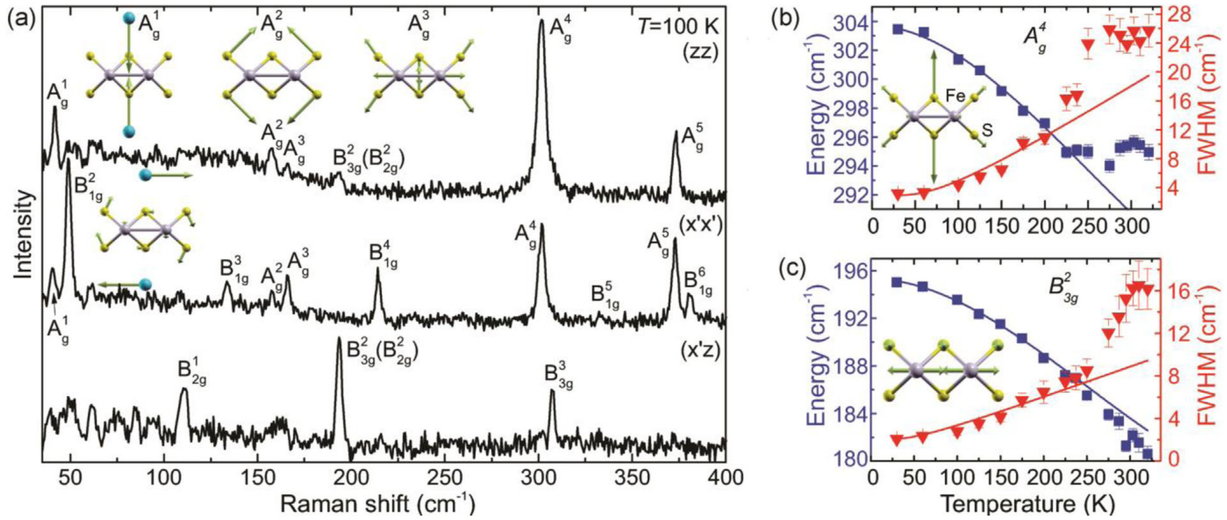

Figure 5. a) The polarized Raman scattering spectra of $BaFe_2S_3$ single crystal measured at 100 K. Insets: the normal modes of the A_g^1, A_g^2, A_g^3, and B_{2g}^1 vibrations. $x = [110]$, $y = [1\bar{1}0]$, and $z = [001]$. Experimental values (symbols) and calculated temperature dependence (solid lines) of the energies and broadenings of (b) A_g^4 and (c) B_{3g}^2 Raman modes of $BaFe_2S_3$, with the normal modes of corresponding vibrations graphically represented in the insets. Reproduced with permission.[5] Copyright 2015, American Physical Society.

temperatures were done using a Linkam THMS600 heating stage.

4.1. Temperature-Dependent Raman Spectra of $BaFe_2S_3$ and $BaFe_2Se_3$

The crystal structures of the $BaFe_2S_3$ and $BaFe_2Se_3$, representatives of the iron-based $S = 2$ two-leg spin-ladder compound family, are isomorphic, but not isostructural.[5] They can be described as alternate stacking of Fe-S(Se) layers and Ba cations along the crystallographic *a* axis (*b* axis), whereas in the Fe-S(Se) plane, only one-dimensional (1D) double chains of edge-shared $[FeS(Se)]_4$ tetrahedra propagate along these axes.

The $BaFe_2S_3$ is a quasi-one-dimensional semiconductor with orthorhombic crystal symmetry, with space group *Cmcm* and $Z = 4$. Based on the factor group analysis, the 18 Raman active modes are expected to be registered in the spectra of single-

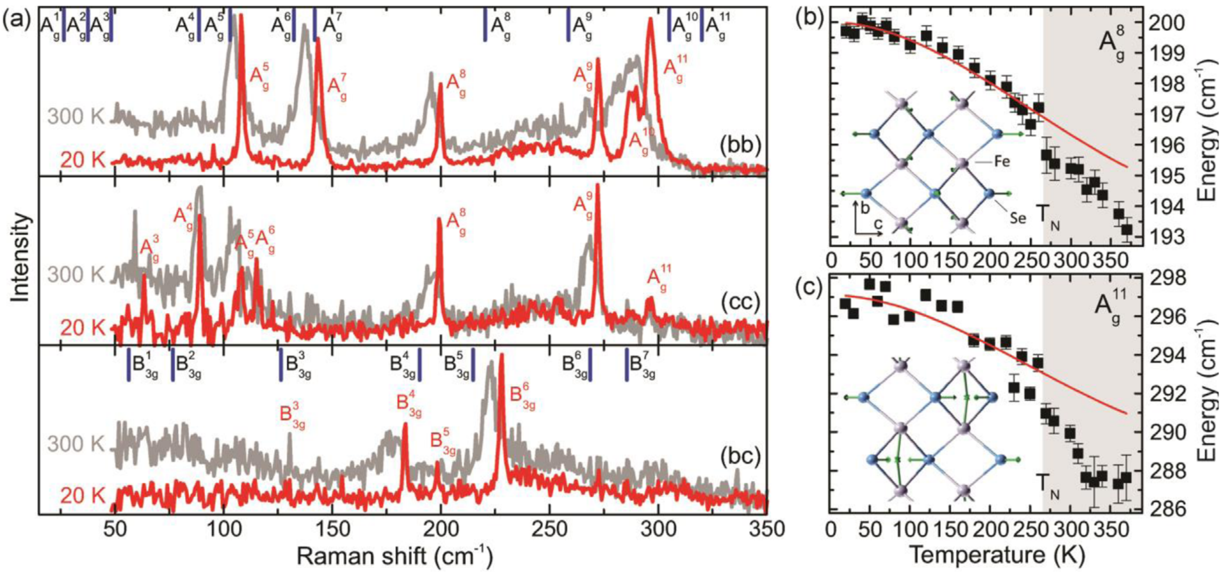

Figure 6. a) The $x(yy)\bar{x}$, $x(zz)\ \bar{x}$, and $x(yz)\bar{x}$ polarized Raman scattering spectra of $BaFe_2Se_3$ single crystals measured at room temperature and at 20 K. Vertical bars are calculated values of the A_g and the B_{3g} symmetry Raman active vibrations. Experimental values (symbols) and calculated temperature dependence (solid lines) of $BaFe_2Se_3$ (b) A_g^8 and (c) A_g^{11} Raman mode energies with normal modes of corresponding vibrations graphically represented in the insets. Reproduced with permission.[5] Copyright 2015, American Physical Society.

crystal with (110) orientation.[5] Most of these modes are observed in polarized Raman scattering spectra of $BaFe_2S_3$ investigated here (**Figure** 5a).

Experimental values and temperature dependence of the energy and broadening of A_g^4 and B_{3g}^2 Raman modes of $BaFe_2S_3$, calculated by Equations (3), (4), (8) and (10), are shown in the Figures 5b and c, respectively. The change in the slope of temperature dependence of these modes linewidth (energy), as well as deviations of simulated anharmonic behavior from experimental values, is observed at about 275 K. This could be related to the spin and charge, because of a hump in the inverse molar magnetic susceptibility, and a change of slope of the electrical resistivity temperature dependence, which have been observed in $BaFe_2S_3$ at similar temperature.

The antiferromagnetic ordering of spins within the ladder legs could change from short-range to the long-range state, without 3D antiferromagnetic spin ordering (the Néel state) of the whole $BaFe_2S_3$ crystal, followed by the change of electronic structure, which could explain the abrupt increase of the resistivity at this temperature. Note that 3D-antiferromagnetic phase transition is registered in many of iron-based spin-ladder materials at about 260 K.

The $BaFe_2Se_3$ also has an orthorhombic structure (*Pmna*) with unit cell consisting of four formula units containing 24 atoms. However, unlike the $BaFe_2S_3$, there is an alternation of the Fe–Fe distances along the chain direction in $BaFe_2Se_3$. The 36 Raman active modes are predicted in the $BaFe_2Se_3$ spectra by the factor group analysis, but only modes of A_g and B_{3g} symmetry are observed in the spectra measured from the (100) plane of the sample (the crystallographic *a* axis is perpendicular to the plane of the single crystal), as shown in the **Figure** 6a.

The energies of A_g^8 and A_g^{11} Raman modes of $BaFe_2Se_3$ change abruptly at temperatures below $T_N = 255$ K, when this compound becomes antiferromagneticaly long-range ordered (Figure 6b and c, respectively). It appears that the spin-phonon (magnetoelastic) coupling is responsible for Raman mode energy change in the antiferromagnetic phase, due to significant local lattice distortion (Fe atom displacement along the *b* axis of ≈0.001 nm) driven by the magnetic order. Moreover, local displacements in the Fe atoms at T_N have a significant impact on the electronic structure due to rearrangement of electrons near the Fermi level, and, consequently, the change in the phonon energy and broadening.

4.2. Temperature-Dependent Raman Spectra of Superconducting $K_xFe_{2-y}Se_2$ and Non-Superconducting $K_{0.8}Fe_{1.8}Co_{0.2}Se_2$

According to the selection rules, two Raman modes in the spectra of $K_xFe_{2-y}Se_2$ can be ascribed to high symmetry ($I4/mmm$), whereas 18 phonon modes could originate from low-symmetry ($I4/m$) phase, out of which 16 has been observed in this phase-separated sample.[6,50] Polarized Raman scattering

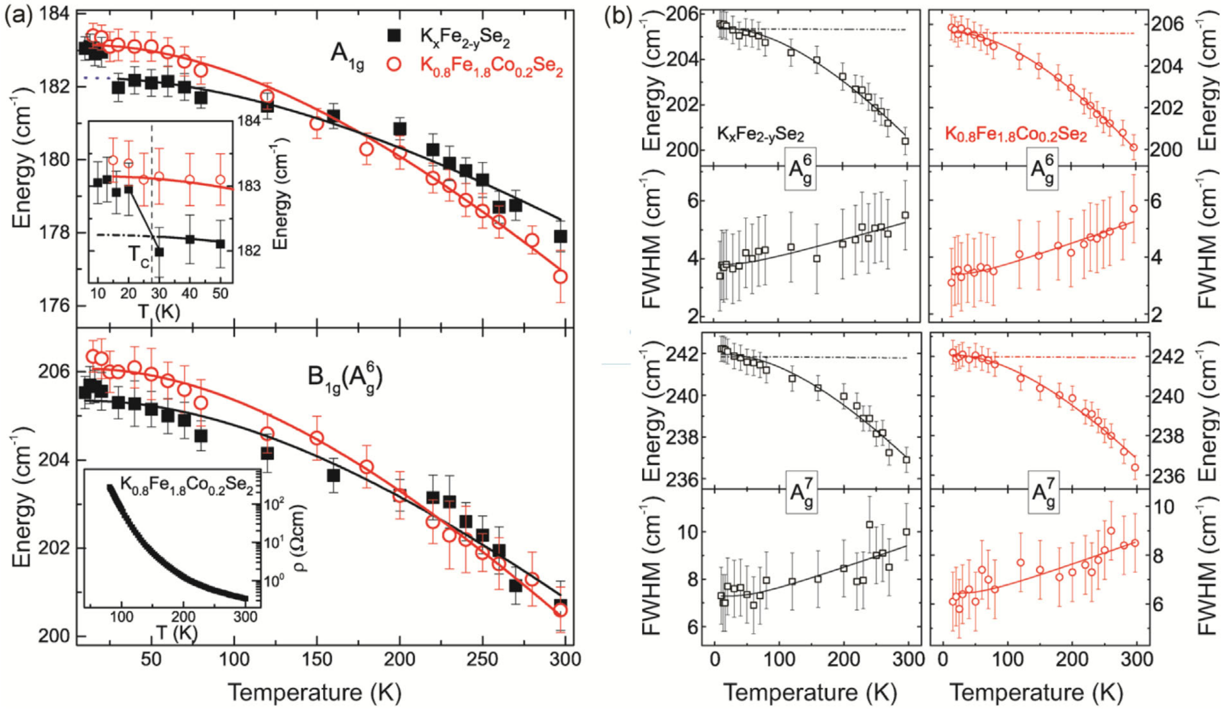

Figure 7. a) Temperature dependence of the energy for the A_{1g} and $B_{1g}(A_g^6)$ Raman modes of $K_xFe_{2-y}Se_2$ and $K_{0.8}Fe_{1.8}Co_{0.2}Se$ single crystals. Upper inset: Enlarged view of the dependence of the A_{1g} mode energy on temperature in a low-temperature region near T_C for $K_xFe_{2-y}Se_2$. Lower inset: the temperature dependence of the electrical resistivity for $K_{0.8}Fe_{1.8}Co_{0.2}Se_2$ shows the nonmetallic behaviour of this single crystal. b) Temperature dependence of energy and linewidth for some A_g modes of $K_xFe_{2-y}Se_2$ (left panel) and $K_{0.8}Fe_{1.8}Co_{0.2}Se$ (right panel). Solid lines take into account only the volume contribution to the phonon mode energy. Reproduced with permission.[6] Copyright 2015, IOP Publishing.

spectra of $K_{0.8}Fe_{1.8}Co_{0.2}Se_2$ single crystals, measured from the (001) plane of the sample at various temperatures, have shown that the energies of Raman active phonons are close to the energies of the corresponding modes in $K_xFe_{2-y}Se_2$. The same number of Raman modes observed in both compounds, with similar corresponding energies, suggests that phase separation is also present in $K_{0.8}Fe_{1.8}Co_{0.2}Se_2$, and that doping of a $K_xFe_{2-y}Se_2$ single crystal with a small amount of Co does not have a significant impact on the phonon spectrum in the normal state.[6]

The temperature dependences of A_{1g} and $B_{1g}(A_g^6)$ modes of $K_xFe_{2-y}Se_2$ and $K_{0.8}Fe_{1.8}Co_{0.2}Se_2$ single crystals are shown in the **Figure 7**a. These dependences are analyzed using Equation (3) with Δ_i^V therm only, knowing that the calculated values of parameters C_i in the anharmonic term Δ_i^A are negligible. The temperature dependence of the $B_{1g}(A_g^6)$ mode energy in both samples in the whole temperature range under investigation is well described by the proposed model. However, A_{1g} mode energy is well fitted by this model only in the case of non-superconducting Co-doped sample, whereas an abrupt change in A_{1g} mode energy around T_C in the superconducting sample is observed. It may be concluded that the hardening of A_{1g} mode around Tc (observed for superconducting sample and absent for non-superconducting one; see the inset in the Figure 7a) is caused by the superconductivity induced phonon renormalization. Note that sudden change in the energy near T_C is registered only for the mode corresponding to vibration of high-symmetry ($I4/mmm$) phase in the superconducting $K_xFe_{2-y}Se_2$ and could be related to the rearrangement of the electronic states to which this mode couples, as the superconducting gap opens.

On the other side, the temperature dependence of the Raman energy and linewidth of A_g^6 and A_g^7 modes (Figure 7b), registered in the spectra of $K_xFe_{2-y}Se_2$ and $K_{0.8}Fe_{1.8}Co_{0.2}Se_2$ single crystals, and ascribed to non-superconducting low-symmetry phase ($I4/m$), are well described by the proposed lattice anharmonic model only with the contribution of the lattice thermal expansion.

5. Conclusion

The results presented in this paper have shown how temperature-dependent Raman scattering measurements could be used to analyze the variation of structural, morphological, compositional, electronic, and/or magnetic material properties with the temperature. It was demonstrated that physical model, including quasiharmonical and anharmonical contributions, used to quantitatively analyze experimentally obtained temperature dependence of energy and linewidth of the characteristic Raman modes, could serve as predictive tool for determining the temperatures at which significant changes occur in studied materials. Temperature-dependent Raman spectra of nanomaterials have given information about their thermal stability and allowed tracking changes in phase composition, nanocrystallite size, strain and non-stoichiometry with temperature. In addition to thermal expansion and three-phonon anharmonic contribution, usually the four-phonon anharmonic contribution must be included in order to describe the temperature dependence of the shift and linewidth of Raman modes in nanomaterials. However, it should be noted that, although this approach provides good fits to experimental Raman data of investigated nanomaterials, some results may not have a complete physical meaning, due to oversimplified approximations (too large cubic anharmonicity in comparison to the quartic, a negative fitting parameter for the quartic anharmonicity in some cases, which is unreasonable). However, if asymmetric phonon decays and four phonon processes turn out to be negligible, the Klemens model provides a reasonable fit to the Raman shift and linewidth of all studied phonons in iron-based single crystals, making this model very convenient for investigated iron-based materials. Thermal expansion and three-phonon anharmonic contributions are usually sufficient to describe temperature dependence of shift and linewidth of Raman modes characteristic for iron-based materials, whereas deviation of experimental values from those predicted by the model has indicated structural and phase transitions and has allowed determining the temperature at which they occurred. The influence of antiferromagnetic order, ferromagnetism, and magnetic fluctuations on the Raman scattering spectra of iron-based compounds depending on temperature can show, not only superconducting, but also a low-dimensional magnetic properties of these materials.

Acknowledgements

This work was financially supported by the Ministry of Education, Science and Technological Development, Republic of Serbia, under the Project No. III45018. We would like to express our very great appreciation to dr Diana Nesheva (Institute of Solid State Physics, Bulgarian Academy of Sciences), dr Cedomir Petrovic (Condensed Matter Physics & Materials Science Department Brookhaven National Laboratory), and dr Nataša Tomić (Institute of Physics, University of Belgrade), who provided us with valuable sample materials and participated in discussing experimental results. The assistance provided by dr Marko Opačić (Institute of Physics, University of Belgrade) is always greatly appreciated.

Conflict of Interest

The authors declare no conflict of interest.

Keywords

iron-based compounds, nanomaterials, quasiharmonic and anharmonic effects, Raman spectra

Received: September 30, 2018
Revised: January 21, 2019

[1] M. J. Šćepanović, M. Grujić-Brojčin, Z. D. Dohčević-Mitrović, Z. V. Popović, *Appl. Phys. A* **2007**, *86*, 365.
[2] M. J. Šćepanović, M. Grujić-Brojčin, Z. D. Dohčević-Mitrović, Z. V. Popović, *Sci. Sinter.* **2009**, *41*, 67.
[3] M. Šćepanović, M. Grujić-Brojčin, Z. Dohčević-Mitrović, Z. V. Popović, *J. Phys. Conf. Ser.* **2010**, *253*, 012015.
[4] M. Grujić-Brojčin, M. J. Šćepanović, Z. D. Dohčević-Mitrović, Z. V. Popović, *Acta Phys. Pol. A* **2009**, *116*, 51.

[5] Z. V. Popović, M. Šćepanović, N. Lazarević, M. Opačić, M. M. Radonjić, D. Tanasković, H. Lei, C. Petrovic, *Phys. Rev. B* **2015**, *91*, 064303.
[6] M. Opačić, N. Lazarević, M. Šćepanović, H. Ryu, H. Lei, C. Petrovic, Z. V. Popović, *J. Phys. –Condens. Mat.* **2015**, *27*, 485701.
[7] T. Tadano, S. Tsuneyuki, *J. Phys. Soc. Jpn.* **2018**, *87*, 041015.
[8] A. A. Maradudin, R. F. Wallis, *Phys. Rev.* **1960**, *120*, 442; A. A. Maradudin, P. A. Flinn, R. A. Coldwell-Horsfall, *Ann. Phys-New York* **1961**, *15*, 337; A. A. Maradudin, P. A. Flinn, R. A. Coldwell-Horsfall, *Ann. Phys-New York* **1961**, *15*, 360; A. A. Maradudin, I. P. Ipatova, *J. Math. Phys.* **1968**, *9*, 525.
[9] I. P. Ipatova, A. A. Maradudin, R. F. Wallis, *Phys. Rev.* **1967**, *155*, 882.
[10] I. Errea, M. Calandra, F. Mauri, *Phys. Rev B* **2014**, *89*, 064302.
[11] T. Sun, D.-B. Zhang, R. M. Wentzcovitch, *Phys. Rev. B* **2014**, *89*, 094109.
[12] T. Lan, X. Tang, B. Fultz, *Phys. Rev B* **2012**, *85*, 094305; T. Lan, C. W. Li, O. Hellman, D. S. Kim, J. A. Munoz, H. Smith, D. L. Abernathy, B. Fultz, *Phys. Rev B* **2015**, *92*, 054304; T. Lan, Z. Zhu, *Adv. Cond. Matter Phys.* **2016**, 2714592.
[13] Z. Zhao, J. Elwood, M. A. Carpenter, *J. Phys. Chem. C* **2015**, *119*, 23094.
[14] J. Menéndez, M. Cardona, *Phys. Rev. B* **1984**, *29*, 2051.
[15] H-M. Eiter, P. Jaschke, R. Hackl, A. Bauer, M. Gangl, C. Pfleiderer, *Phys. Rev. B* **2014**, *90*, 024411.
[16] P. G. Klemens, *Phys. Rev.* **1966**, *148*, 845.
[17] M. Balkanski, R. F. Wallis, E. Haro, *Phys. Rev. B* **1983**, *28*, 1928.
[18] A. K. Arora, M. Rajalakshmi, T. R. Ravindran, V. Sivasubramanian, *J. Raman Spectrosc.* **2007**, *38*, 604.
[19] M. Fernandez-Garcıa, A. Martınez-Arias, J. C. Hanson, J. A. Rodriguez, *Chem. Rev.* **2004**, *104*, 4063.
[20] J. E. Spanier, R. D. Robinson, F. Zhang, S.-W. Chan, I. P. Herman, *Phys. Rev B* **2001**, *64*, 245407.
[21] S. Kelly, F. H. Pollak, M. Tomkiewicz, *J. Phys. Chem. B* **1997**, *101*, 2730.
[22] H. Richter, Z. P. Wang, L. Ley, *Solid State Commun.* **1981**, *39*, 625.
[23] I. I. Campbell, P. M. Fauchet, *Solid State Commun.* **1986**, *58*, 739.
[24] K.-R. Zhu, M.-S. Zhang, Q. Chen, Z. Yin, *Phys. Lett. A* **2005**, *340*, 220.
[25] A. C. Breeson, G. Sankar, G. K. Liang Goh, R. G. Palgrave, *Phys. Chem. Chem. Phys* **2016**, *18*, 24722.
[26] H. M. Moghaddam, S. Nasirian, *Nanosci. Methods* **2012**, *1*, 201.
[27] B. Choudhury, A. Choudhury, *Int Nano Lett* **2013**, *3*, *55*.
[28] W. Naffouti, T. B. Nasr, H. Meradji, N. Kamoun-Turki, *J. Electron. Mater* **2016**, *45*, 5096.
[29] M. K. Hossain, M. F. Pervez, M. N. H. Mia, S. Tayyaba, M. J. Uddin, R. Ahamed, R. A. Khan, M. Hoq, M. A. Khan, F. Ahmed, *Mater. Sci. –Poland* **2017**, *35*, 868.
[30] A. Verma, A. K. Yadav, N. Khatun, S. Kumar, C-M. Tseng, S. Biring, S. Sen, *J. Mater. Sci.: Mater. Electron* **2017**, *28*, 19017.
[31] M. Mikami, S. Nakamura, O. Kitao, H. Arakawa, *Phys. Rev. B* **2002**, *66*, 1552131.
[32] S. Patra, C. Davoisne, H. Bouyanfif, D. Foix, F. Sauvage, *Sci. Rep. –UK* **2016**, *5*, 10928.
[33] N. Tomić, M. Grujić-Brojčin, N. Finčur, B. Abramović, B. Simović, J. Krstić, B. Matović, M. Šćepanović, *Mater. Chem. Phys.* **2015**, *163*, 518.
[34] M. N. Iliev, V. G. Hadjiev, A. P. Litvinchuk, *Vib. Spectrosc.* **2013**, *64*, 148.
[35] E. Shojaee, M. Abbasnejad, M. Saeedian, M. R. Mohammadizadeh, *Phys. Rev. B* **2011**, *83*, 174302.
[36] E. P. Meagher, G. A. Lager, *Can. Mineral.* **1979**, *17*, 77.
[37] N. S. Allen, N. Mahdjoub, V. Vishnyakov, P. J. Kelly, R. J. Kriek, *Polym. Degrad. Stabil.* **2018**, *150*, 31.
[38] L. K. Vodopyanov, E. A. Vinogradov, V. S. Vinogradov, I. V. Kucherenko, B. N. Mavrin, N. N. Novikova, P. V. Shapkin, *phys. stat. sol. (c)* **2004**, *1*, 3162.
[39] L. K. Vodopyanov, *J. Alloy Compd.* **2004**, *371*, 72.
[40] D. Nesheva, Z. Aneva, M. J. Šćepanović, I. Bineva, Z. Levi, Z. V. Popović, B. Pejova, *J. Phys. Conf. Ser.* **2010**, *253*, 012035.
[41] D. Nesheva, Z. Aneva, M. J. Scepanovic, Z. Levi, I. Iordanova, Z. V. Popovic, *J. Phys. D: Appl. Phys.* **2011**, *44*, 415305.
[42] M. Y. Valakh, M. P. Lisitsa, G. S. Pekar, G. N. Polysskii, V. I. Sidorenko, A. M. Yaremko, *Phys. Stat. Sol. (b)* **1982**, *113*, 635.
[43] N. ul Aarifeen, A. Afaq, *Mater. Res. Express* **2017**, *4*, 095901.
[44] G. R. Stewart, *Rev. Mod. Phys.* **2011**, *83*, 1589.
[45] Z. V. Popović, M. Šćepanović, N. Lazarević, M. M. Radonjić, D. Tanasković, H. Lei, C. Petrovic, *Phys. Rev. B* **2014**, *89*, 014301.
[46] Z. V. Popović, N. Lazarević, S. Bogdanović, M. M. Radonjić, D. Tanasković, R. Hu, H. Lei, C. Petrovic, *Solid State Commun.* **2014**, *193*, 51.
[47] N. Lazarević, M. Radonjić, M. Šćepanović, H. Lei, D. Tanasković, C. Petrovic, Z. V. Popović, *Phys. Rev. B* **2013**, *87*, 144305.
[48] N. Lazarević, H. Lei, C. Petrovic, Z. V. Popović, *Phys. Rev. B* **2011**, *84*, 214305.
[49] N. Lazarević, M. M. Radonjić, D. Tanasković, R. Hu, C Petrovic, Z. V. Popović, *J. Phys.: Condens. Matter* **2012**, *24*, 255402.
[50] N. Lazarević, M. Abeykoon, P. W. Stephens, H. Lei, E. S. Bozin, C. Petrovic, Z. V. Popović, *Phys. Rev. B* **2012**, *86*, 054503.
[51] R. Hu, H. Lei, C. Petrovic, *Solid State Commun.* **2014**, *193*, 51.
[52] M. R. Opačić, N. Ž. Lazarević, *J. Serb. Chem. Soc.* **2017**, *82*, 1.
[53] M. Opačić, N. Lazarević, D. Tanasković, M. M. Radonjić, A. Milosavljević, Y. Ma, C. Petrovic, Z. V. Popović, *Phys. Rev. B* **2017**, *96*, 174303.
[54] A. Baum, Ying Li, M. Tomić, N. Lazarević, D. Jost, F. Löffler, B. Muschler, T. Böhm, J.-H. Chu, I. R. Fisher, R. Valentí, I. I. Mazin, R. Hackl, *Phys. Rev. B* **2018**, *98*, 075113.
[55] A. Baum, A. Milosavljević, N. Lazarević, M. M. Radonjić, B. Nikolić, M. Mitschek, Z. Inanloo Maranloo, M. Šćepanović, M. Grujić-Brojčin, N. Grujić-Brojčin, M. Opel, Aifeng Wang, C. Petrovic, Z. V. Popović, R. Hackl, *Phys. Rev. B* **2018**, *97*, 054306.
[56] A. P. Litvinchuk, V. G. Hadjiev, M. N. Iliev, Bing Lv, A. M. Guloy, C. W. Chu, *Phys. Rev. B* **2008**, *78*, 060503(R).
[57] V. Gnezdilov, Y. G. Pashkevich, P. Lemmens, D. Wulferding, T. Shevtsova, A. Gusev, D. Chareev, A. Vasiliev, *Phys. Rev. B* **2013**, *87*, 144508.
[58] V. Gnezdilov, Yu. Pashkevich, P. Lemmens, A. Gusev, K. Lamonova, T. Shevtsova, I. Vitebskiy, O. Afanasiev, S. Gnatchenko, V. Tsurkan, J. Deisenhofer, A. Loidl, *Phys. Rev. B* **2011**, *83*, 245127.
[59] L. Chauvière, Y. Gallais, M. Cazayous, A. Sacuto, M. A. Méasson, D. Colson, A. Forget, *Phys. Rev. B* **2009**, *80*, 094504.
[60] Y. Gallais, A. Sacuto, M. Cazayous, P. Cheng, L. Fang, H. H. Wen, *Phys. Rev. B* **2008**, *78*, 132509.
[61] A. M. Zhang, K. Liu, J. H. Xiao, J. B. He, D. M. Wang, G. F. Chen, B. Normand, Q. M. Zhang, *Phys. Rev. B* **2012**, *85*, 024518.
[62] T.-L. Xia, D. Hou, S. C. Zhao, A. M. Zhang, G. F. Chen, J. L. Luo, N. L. Wang, J. H. Wei, Z.-Y. Lu, Q. M. Zhang, *Phys. Rev. B* **2009**, *79*, 140510(R).
[63] A. Ignatov, A. Kumar, P. Lubik, R. H. Yuan, W. T. Guo, N. L. Wang, K. Rabe, G. Blumberg, *Phys. Rev. B* **2012**, *86*, 134107.
[64] Y. J. Um, A. Subedi, P. Toulemonde, A. Y. Ganin, L. Boeri, M. Rahlenbeck, Y. Liu, C. T. Lin, S. J. E. Carlsson, A. Sulpice, M. J. Rosseinsky, B. Keimer, M. Le Tacon, *Phys. Rev. B* **2012**, *85*, 064519.

Evidence of spin-phonon coupling in CrSiTe$_3$

A. Milosavljević,[1] A. Šolajić,[1] J. Pešić,[1] Yu Liu (刘育),[2] C. Petrovic,[2] N. Lazarević,[1,*] and Z. V. Popović[1,3]
[1] *Center for Solid State Physics and New Materials, Institute of Physics Belgrade, University of Belgrade, Pregrevica 118, 11080 Belgrade, Serbia*
[2] *Condensed Matter Physics and Materials Science Department, Brookhaven National Laboratory, Upton, New York 11973-5000, USA*
[3] *Serbian Academy of Sciences and Arts, Knez Mihailova 35, 11000 Belgrade, Serbia*

(Received 12 July 2018; published 18 September 2018)

We present Raman scattering results on the layered semiconducting ferromagnetic compound CrSiTe$_3$. Four Raman-active modes, predicted by symmetry, are observed and assigned. The experimental results are supported by density functional theory calculations. The self-energies of the A_g^3 and the E_g^3 symmetry modes exhibit unconventional temperature evolution around 180 K. In addition, the doubly degenerate E_g^3 mode shows a clear change of asymmetry in the same temperature region. The observed behavior is consistent with the presence of the previously reported short-range magnetic order and strong spin-phonon coupling.

DOI: 10.1103/PhysRevB.98.104306

I. INTRODUCTION

Trichalcogenides CrXTe$_3$ (X = Si, Ge) belong to a rare class of quasi-two-dimensional semiconducting materials with a ferromagnetic order, band gaps of 0.4 eV for Si and 0.7 eV for Ge compounds, and Curie temperatures (T_C) of 32 and 61 K, respectively [1–6]. Because of their layered structure, due to van der Waals bonding, they can be exfoliated to mono- and few-layer nanosheets, which, together with their semiconducting and magnetic properties, make an ideal combination for applications in optoelectronics and nanospintronics [7–11]. This was further supported by the observation of giant resistivity modulation of CrGeTe$_3$-based devices [12].

From an x-ray diffraction study [1], it was revealed that CrSiTe$_3$ crystals are twined along c axes, the thermal expansion is negative at low temperatures, and the thermal conductivity shows strong magnon-phonon scattering effects. A very small single-ion anisotropy favoring magnetic order along c axes and spin waves was found in CrSiTe$_3$ by elastic and inelastic neutron scattering [13]. Spin-wave measurements suggest the absence of three-dimensional correlations above T_C, whereas in-plane dynamic correlations are present up to 300 K. First-principles calculations suggested the possibility of graphenelike mechanical exfoliation for CrXTe$_3$ (X = Si, Ge) single crystals with conserved semiconducting and ferromagnetic properties [14]. The exfoliation of CrSiTe$_3$ bulk to mono- and few-layer two-dimensional crystals onto a Si/SiO$_2$ substrate has been achieved [15] with a resistivity between 80 and 120 K, depending on the number of layers. Critical exponents for CrSiTe$_3$ were also determined from theoretical analysis [16].

Spin-phonon coupling in CrGeTe$_3$ was investigated in Raman scattering experiments [17]. Splitting of the two lowest-energy E_g modes in the ferromagnetic phase has been observed and ascribed to time-reversal symmetry breaking by the spin ordering. Furthermore, the significant renormalization of the three higher-energy modes' self-energies below T_C provided additional evidence of spin-phonon coupling [17]. The external pressure-induced effect on lattice dynamics and magnetization in CrGeTe$_3$ has also been studied [18].

The Raman spectrum of CrSiTe$_3$ single crystals was reported in Ref. [1], where three Raman-active modes have been observed. Similar results have also been presented in Ref. [15] for ultrathin nanosheets of CrSiTe$_3$. Here, we report a Raman scattering study of CrSiTe$_3$ single crystals, with the main focus on phonon properties in the temperature range between 100 and 300 K. Our experimental results are qualitatively different from those previously reported [1,15] but consistent with the results obtained for CrGeTe$_3$ [17,18]. Furthermore, our data reveal the asymmetry of the E_g^3 mode, which is suppressed at higher temperatures. The A_g^3 and E_g^3 symmetry modes exhibit nonanharmonic self-energy temperature dependence in the region around 180 K, related to the strong spin-lattice interaction due to short-range magnetic order [1]. Energies and symmetries of the observed Raman-active modes are in good agreement with theoretical calculations.

II. EXPERIMENT AND NUMERICAL METHOD

Single crystals of CrSiTe$_3$ and CrGeTe$_3$ were grown as described previously [19]. For a Raman scattering experiment, a Tri Vista 557 spectrometer was used in the backscattering micro-Raman configuration with a 1800/1800/2400 grooves/mm diffraction grating combination. A coherent Verdi G solid-state laser with a 532-nm line was used as the excitation source. The direction of the incident (scattered) light coincides with a crystallographic c axis. Right before being placed in the vacuum, the samples were cleaved in the air. All measurements were performed in a high vacuum (10^{-6} mbar) using a KONTI CryoVac continuous-helium-flow cryostat with a 0.5-mm-thick window. Laser-beam focusing was achieved through a microscope objective with ×50 magnification, a spot size of approximately 8 μm, and a power

---

[*] nenadl@ipb.ac.rs

TABLE I. Calculated and experimental crystallographic lattice parameters for $\mathrm{CrSiTe_3}$ ($|a| = |b|$), bond lengths, interlayer distance (d), and van der Waals (vdW) gap.

$\mathrm{CrSiTe_3}$	Calculation (Å)	Experiment (Å) [20]
a	6.87	6.76
c	19.81	20.67
Si-Si	2.27	2.27
Si-Te	2.52	2.51
Cr-Te	2.77	2.78
d	6.86	6.91
vdW gap	3.42	3.42

<2 mW on the surface of a sample. All spectra were corrected for the Bose factor.

Density functional theory calculations were performed in the Quantum Espresso software package [21], using the PBE exchange-correlation functional [22], PAW pseudopotentials [23,24], and energy cutoffs for wave functions and the charge density of 85 and 425 Ry, respectively. For k-point sampling, the Monkhorst-Pack scheme was used, with a Γ-centered $8 \times 8 \times 8$ grid. Optimization of the atomic positions in the unit cell was performed until the interatomic forces were minimized down to 10^{-6} Ry/Å. In order to obtain the parameters accurately, treatment of the van der Waals interactions was included using the Grimme-D2 correction [25]. Phonon frequencies were calculated at the Γ point within the linear response method implemented in Quantum Espresso. Calculated crystallographic properties obtained by relaxing the structures are in good agreement with x-ray diffraction measurements [20]. A comparison between our, calculated, and experimental results is presented in Table I.

III. RESULTS AND DISCUSSION

A. Polarization dependence

$\mathrm{CrSiTe_3}$ crystallizes in the rhombohedral crystal structure, described by $R\bar{3}$ (C_{3i}^2) [26]. Wyckoff positions of atoms, together with each site's contribution to phonons at the Γ point and corresponding Raman tensors, are listed in Table II. The phonon mode distribution obtained by factor-group analysis for the $R\bar{3}$ space group is as follows:

$$\begin{aligned}\Gamma_{\text{Raman}} &= 5A_g + 5E_g,\\ \Gamma_{\text{IR}} &= 4A_u + 4E_u,\\ \Gamma_{\text{Acoustic}} &= A_u + E_u.\end{aligned}$$

Since the plane of incidence is ab, where $|a| = |b|$ [$\measuredangle(a, b) = 120°$], and the direction of light propagation is along c axes, from the selection rules, it is possible to observe all Raman-active modes, i.e., five A_g modes and five doubly degenerate E_g modes. According to the Raman tensors presented in Table II, A_g symmetry modes are observable only in the parallel polarization configuration, whereas E_g symmetry

TABLE II. (a) Type of atoms, Wyckoff positions, each site's contribution to the phonons at the Γ point, and corresponding Raman tensors for the $R\bar{3}$ space group of $\mathrm{CrSiTe_3}$. (b) Phonon symmetry, calculated optical phonon frequencies at 0 K, and experimental values for Raman-active (at 100 K) and infrared (IR)-active (at 110 K) [1] $\mathrm{CrSiTe_3}$ phonons.

(a) Space group $R\bar{3}$ (No. 148)

Atom(s) (Wyckoff positions)	Irreducible representations
Cr, Si (6c)	$A_g + E_g + A_u + E_u$
Te (18f)	$3A_g + 3E_g + 3A_u + 3E_u$

(b) Raman tensors

$$A_g = \begin{pmatrix} a & 0 & 0 \\ 0 & b & 0 \\ 0 & 0 & c \end{pmatrix} \qquad E_g^1 = \begin{pmatrix} c & d & e \\ d & -c & f \\ e & f & 0 \end{pmatrix} \qquad E_g^2 = \begin{pmatrix} d & -c & -f \\ -c & -d & e \\ -f & e & 0 \end{pmatrix}$$

Raman active			IR active [1]		
Symmetry	Calc. (cm^{-1})	Expt. (cm^{-1})	Symmetry	Calc. (cm^{-1})	Expt. (cm^{-1})
A_g^1	88.2	–	A_u^1	91.8	91.0
E_g^1	93.5	88.9	E_u^1	93.7	–
E_g^2	96.9	–	A_u^2	116.8	–
E_g^3	118.3	118.2	E_u^2	117.1	–
A_g^2	122.0	–	A_u^3	202.4	–
A_g^3	148.0	147.4	E_u^3	206.2	207.9
A_g^4	208.7	–	A_u^4	243.7	–
E_g^4	219.5	217.2	E_u^4	365.8	370.4
E_g^5	357.4	–			
A_g^5	508.8	–			

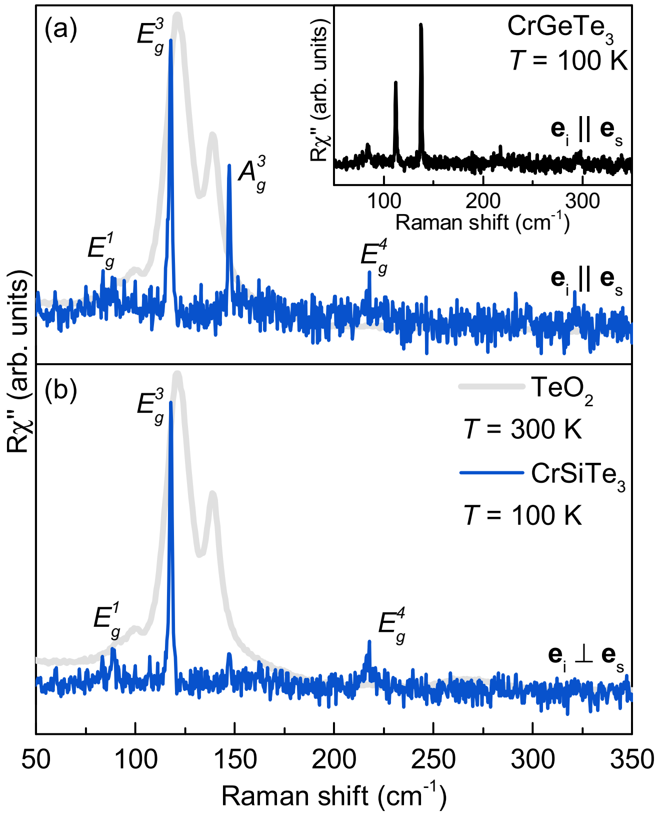

FIG. 1. Raman spectra of CrSiTe$_3$ single crystals measured at 100 K in (a) parallel and (b) cross polarization configurations. The gray line represents the TeO$_2$ spectrum measured at 300 K. Inset: Raman spectrum of CrGeTe$_3$ in the parallel polarization configuration measured at 100 K.

modes can be expected to appear for both in-parallel and cross polarization configurations.

The Raman spectra of CrSiTe$_3$ for two main linear polarization configurations, at 100 K, are shown in Fig. 1. Four peaks can be observed in the spectra, at energies of 88.9, 118.2, 147.4, and 217.2 cm^{-1}. Since only the peak at 147.4 cm^{-1} vanishes in the cross polarization configuration, it corresponds to the A_g symmetry mode. The other three modes appear in both parallel and cross polarization configurations and, thereby, can be assigned as E_g symmetry modes (Fig. 1).

In order to exclude the possibility that any of the observed features originate from the TeO$_2$ [17,27], its Raman spectrum is also presented in Fig. 1. It can be noted that no TeO$_2$ contribution is present in our CrSiTe$_3$ data. Furthermore, the observed CrSiTe$_3$ Raman spectra are also consistent with the CrGeTe$_3$ Raman spectra (see inset in Fig. 1), isostructural to CrSiTe$_3$. Five Raman-active modes have been observed for CrGeTe$_3$, two A_g modes, at 137.9 and 296.6 cm^{-1}, and three E_g modes, at 83.5, 112.2, and 217.5 cm^{-1}, in agreement with the previously published data [17,18]. The main difference in the spectra of CrSiTe$_3$ and CrGeTe$_3$ arises from the change in mass and lattice parameter effects that cause the peaks to shift.

Calculated and observed Raman-active phonon energies are compiled in Table II, together with the experimental energies of the infrared (IR)-active phonons [1], and are found to be in good agreement. Displacement patterns of the A_g and E_g symmetry modes are presented in Fig. 4, in the Appendix.

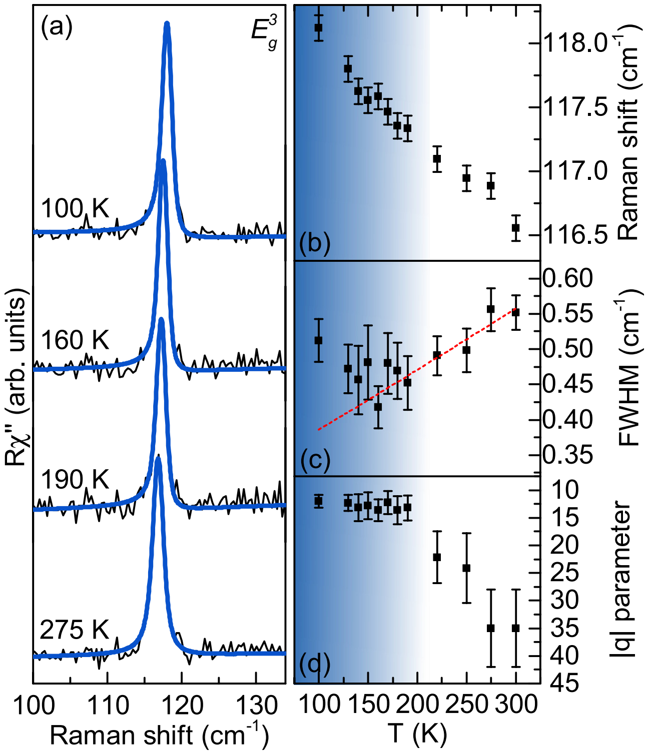

FIG. 2. (a) The E_g^3 mode Raman spectra of CrSiTe$_3$ at four temperatures measured in the cross polarization configuration. Blue lines represent line shapes obtained as a convolution of the Fano line shape and Gaussian, calculated to fit the experimetal data. Temperature dependence of (b) the energy, (c) the line width, and (d) the Fano parameter q of the E_g^3 mode. The dashed red line represents standard anharmonic behavior [28,29]. All the parameters show a change in tendency around 180 K.

B. Temperature dependence

After proper assignment of all the observed CrSiTe$_3$ Raman-active modes we proceeded with temperature evolution of their properties, focusing on the most prominent ones, E_g^3 and A_g^3. Figure 2(a) shows the spectral region of the doubly degenerate E_g^3 mode at an energy of 118.2 cm^{-1}, at four temperatures. Closer inspection of the 100 K spectra revealed clear asymmetry of the peak on the low-energy side. The presence of defects may result in the appearance of the mode asymmetry [30], however, they would also contribute to the mode line width and, possibly, the appearance of phonons from the edge of the Brillouin zone in the Raman spectra [29]. The very narrow lines and absence of additional features in the Raman spectra of CrSiTe$_3$ do not support this scenario. The asymmetry may also arise when the phonon is coupled to a continuum [31]. Such a coupling of the E_g^3 phonon mode would result in a line shape given by the convolution of a Fano function and a Gaussian, the latter representing the resolution of the spectrometer [29]. Comparison between the Fano line shape convoluted with a Gaussian, the Voigt line shape, and the experimental data at 100 K is presented in Fig. 5, in the

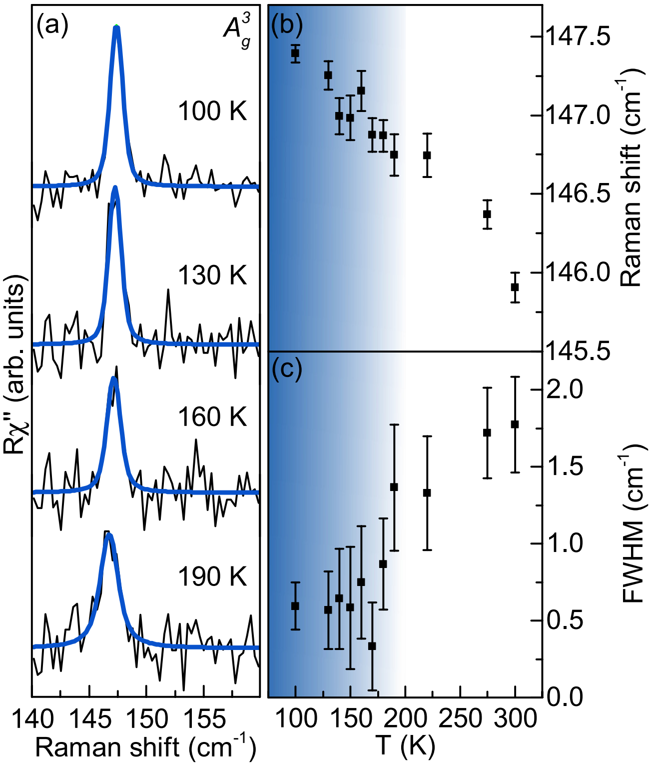

FIG. 3. (a) A_g^3 mode Raman spectra of CrSiTe$_3$ at four temperatures measured in the parallel polarization configuration. Blue lines represent Voigt line shapes. (b) Energy and (c) line-width temperature dependence of the A_g^3 mode.

Appendix, with the former yielding better agreement with the experimental data. Furthermore, it fully captures the E_g^3 mode line shape at all temperatures under investigation [Figs. 2(a) and 6].

Upon cooling of the sample, the E_g^3 mode energy hardens [Fig. 2(b)] with a very small discontinuity in the temperature range around 180 K. Down to the same temperature, the line width monotonically narrows in line with the standard anharmonic behavior [dashed red line in Fig. 2(c)]. Upon further cooling, the line width increased, deviating from the expected anharmonic tendency. This indicates activation of an additional scattering mechanism, e.g., spin-phonon interaction. Figure 2(d) shows the evolution of the Fano parameter, $|q|$. Whereas in the region below 180 K, it increases slightly but continuously, at higher temperatures it promptly goes to lower values and the mode recovers a symmetric line shape. We believe that the observed behavior of the E_g^3 mode can be traced back to the short-range magnetic correlations, which, according to Ref. [1], persist up to 150 K, and the strong spin-phonon coupling in CrSiTe$_3$. Similar behavior of the energy and line width, which differs from the conventional anharmonic, as well as the E_g mode Fano-type line shape, was recently reported in α-RuCl$_3$ and was interpreted as a consequence of the spin-phonon interaction [32].

Unlike the E_g^3 mode, no pronounced asymmetry was observed for the A_g^3 mode. As can be seen from Figs. 3(b) and 3(c) both the energy and the line width of the A_g^3 mode showed a similar change in tendency in the same temperature region as the E_g^3 mode, most likely due to the spin-phonon coupling.

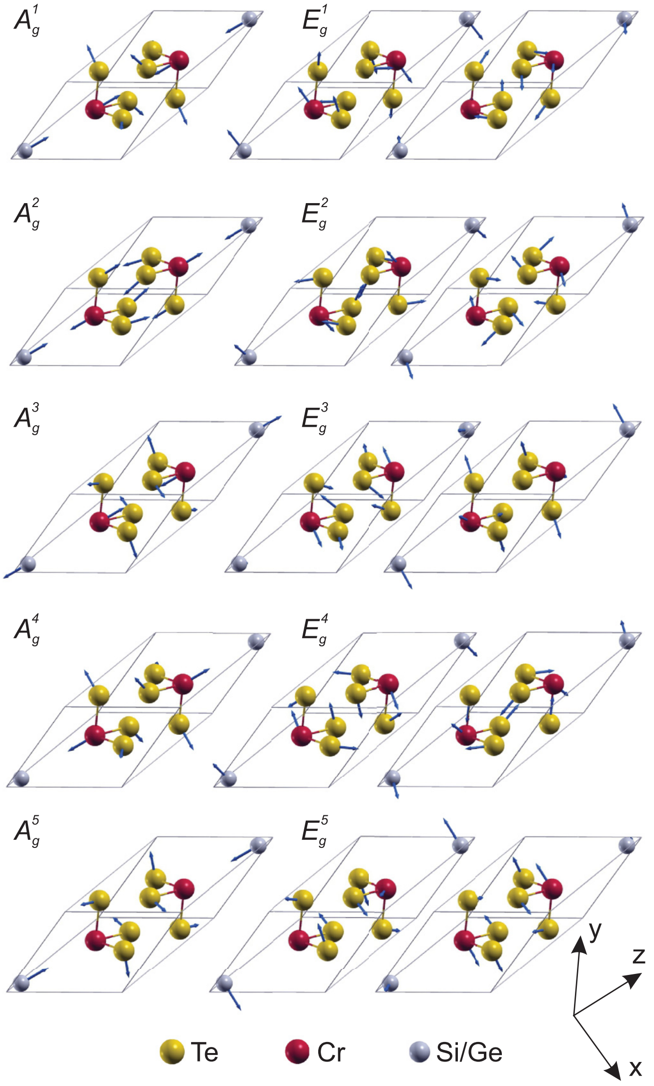

FIG. 4. Unit cell of a CrSiTe$_3$ single crystal (solid lines) with the displacement patterns of the A_g and E_g symmetry modes. Arrow lengths are proportional to the square root of the interatomic forces.

IV. CONCLUSION

The lattice dynamics of CrSiTe$_3$, a compound isostructural to CrGeTe$_3$, is presented. An A_g and three E_g modes were observed and assigned. The experimental results are well supported by theoretical calculations. The temperature dependences of the energies and line widths of the A_g^3 and E_g^3 modes deviate from the conventional anharmonic model in the temperature range around 180 K. In addition, the E_g^3 mode shows clear Fano resonance at lower temperatures. This can be related to the previously reported short-range magnetic correlations at temperatures up to 150 K [1] and the strong spin-phonon coupling.

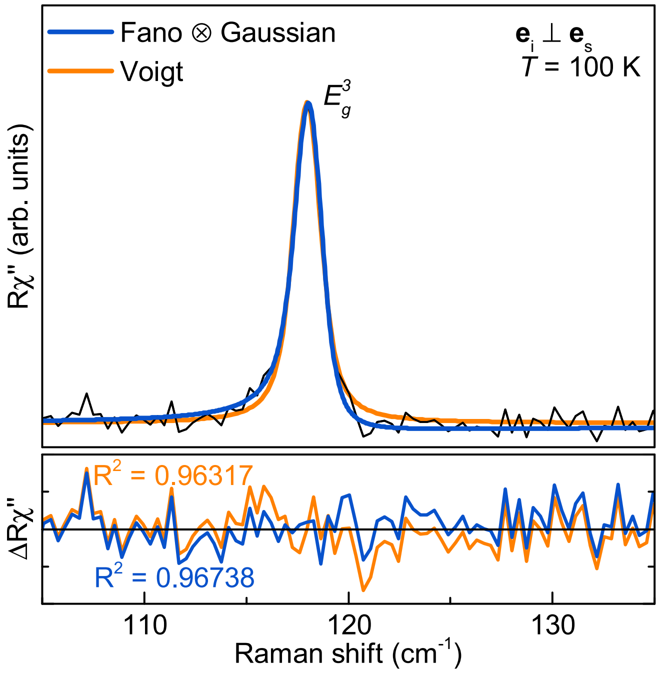

FIG. 5. Analysis of the E_g^3 asymmetry. Measured data are shown as the black line. The solid blue line represents the line shape obtained as a convolution of the Fano line shape and a Gaussian, whereas the orange line represents a Voigt line shape, both calculated to fit the experimental data. The Voigt profile deviates from the experimental data at the peak flanks.

ACKNOWLEDGMENTS

The work was supported by the Serbian Ministry of Education, Science and Technological Development under Projects III45018 and OI171005. DFT calculations were performed using computational resources at Johannes Kepler University, Linz, Austria. Work at Brookhaven is supported by the U.S. DOE under Contract No. DE-SC0012704.

A.M. and N.L. conceived and performed the experiment, analyzed and discussed data, and wrote the paper; A.S. and J.P. calculated phonon energies, analyzed and discussed data, and wrote the paper; Y.L. and C.P. synthesized and characterized the samples; Z.V.P. analyzed and discussed data and wrote the paper. All authors commented on the manuscript.

APPENDIX

1. Eigenvectors of Raman-active modes

Figure 4 summarizes the A_g and E_g symmetry mode displacement patterns of a CrSiTe$_3$ single crystal ($R\overline{3}$ space group). Arrow lengths are proportional to the square root of the interatomic forces.

2. Asymmetry of the E_g^3 line

The peak at 118.2 cm^{-1}, which we assigned as the E_g^3 symmetry mode, at low temperatures shows a significant asymmetry towards lower energies. The possibility of additional defect-induced features in Raman spectra can be excluded, since the modes are very narrow, suggesting high crystallinity of the sample. Also, the theoretical calculations do not predict additional Raman-active modes in this energy region. On the other hand, coupling of the phonon mode to a continuum may result in an asymmetric line shape described with the Fano function. Due to the finite resolution of the spectrometer it has to be convoluted with a Gaussian ($\Gamma_G = 1$ cm^{-1}). In Fig. 5 we present a comparison of the line obtained as a convolution of the Fano line shape and a Gaussian (blue line) and a Voigt line shape (orange line) fitted to the experimental data. Whereas the Voigt line shape deviates at the peak flanks, excellent agreement has been achieved for convolution of the Fano line shape and a Gaussian.

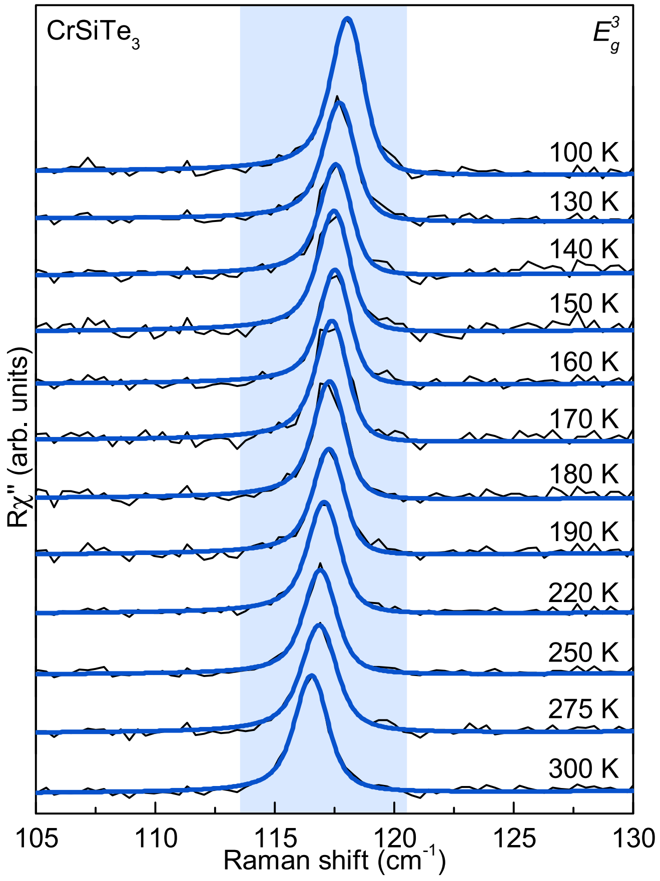

FIG. 6. The E_g^3 mode Raman spectra of CrSiTe$_3$ at all temperatures measured in the cross polarization configuration. Blue lines represent calculated spectra obtained as the convolution of the Fano line shape and Gaussian.

3. E_g^3 mode temperature dependence

Figure 6 shows Raman spectra of CrSiTe$_3$ in the region of the E_g^3 mode in the cross polarization configuration at various temperatures. Solid blue lines represent the convolution of the Fano line shape and Gaussian fitted to the experimental data. The asymmetry is the most pronounced below 190 K. Above this temperature, the asymmetry is decreasing, and at high temperatures the peak recovers the fully symmetric line shape.

[1] L. D. Casto, A. J. Clune, M. O. Yokosuk, J. L. Musfeldt, T. J. Williams, H. L. Zhuang, M.-W. Lin, K. Xiao, R. G. Hennig, B. C. Sales, J.-Q. Yan, and D. Mandrus, Strong spin-lattice coupling in $CrSiTe_3$, APL Mater. **3**, 041515 (2015).

[2] X. Zhang, Y. Zhao, Q. Song, S. Jia, J. Shi, and W. Han, Magnetic anisotropy of the single-crystalline ferromagnetic insulator $Cr_2Ge_2Te_6$, Jpn. J. Appl. Phys. **55**, 033001 (2016).

[3] T. Leineweber and H. Kronmuller, Micromagnetic examination of exchange coupled ferromagnetic nanolayers, J. Magn. Magn. Mater. **176**, 145 (1997).

[4] G. Ouvrard, E. Sandre, and R. Brec, Synthesis and crystal structure of a new layered phase: The chromium hexatellurosilicate $Cr_2Si_2Te_6$, J. Solid State Chem. **73**, 27 (1988).

[5] B. Siberchicot, S. Jobic, V. Carteaux, P. Gressier, and G. Ouvrard, Band structure calculations of ferromagnetic chromium tellurides $CrSiTe_3$ and $CrGeTe_3$, J. Phys. Chem. **100**, 5863 (1996).

[6] V. Carteaux, F. Moussa, and M. Spiesser, 2D Ising-like ferromagnetic behaviour for the lamellar $Cr_2Si_2Te_6$ compound: A neutron scattering investigation, Europhys. Lett. **29**, 251 (1995).

[7] N. Sivadas, M. W. Daniels, R. H. Swendsen, S. Okamoto, and D. Xiao, Magnetic ground state of semiconducting transition-metal trichalcogenide monolayers, Phys. Rev. B **91**, 235425 (2015).

[8] K. S. Novoselov, A. K. Geim, S. V. Morozov, D. Jiang, Y. Zhang, S. V. Dubonos, I. V. Grigorieva, and A. A. Firsov, Electric field effect in atomically thin carbon films, Science **306**, 666 (2004).

[9] Q. H. Wang, K. Kalantar-Zadeh, A. Kis, J. N. Coleman, and M. S. Strano, Electronics and optoelectronics of two-dimensional transition metal dichalcogenides, Nat. Nanotechnol. **7**, 699 (2012), review Article.

[10] C. Gong, L. Li, Z. Li, H. Ji, A. Stern, Y. Xia, T. Cao, W. Bao, C. Wang, Y. Wang, Z. Q. Qiu, R. J. Cava, S. G. Louie, J. Xia, and X. Zhang, Discovery of intrinsic ferromagnetism in two-dimensional van der Waals crystals, Nature **546**, 265 (2017).

[11] B. Huang, G. Clark, E. Navarro-Moratalla, D. R. Klein, R. Cheng, K. L. Seyler, D. Zhong, E. Schmidgall, M. A. McGuire, D. H. Cobden, W. Yao, D. Xiao, P. Jarillo-Herrero, and X. Xu, Layer-dependent ferromagnetism in a van der Waals crystal down to the monolayer limit, Nature **546**, 270 (2017).

[12] W. Xing, Y. Chen, P. M. Odenthal, X. Zhang, W. Yuan, T. Su, Q. Song, T. Wang, J. Zhong, S. Jia, X. C. Xie, Y. Li, and W. Han, Electric field effect in multilayer $Cr_2Ge_2Te_6$: A ferromagnetic 2D material, 2D Mater. **4**, 024009 (2017).

[13] T. J. Williams, A. A. Aczel, M. D. Lumsden, S. E. Nagler, M. B. Stone, J.-Q. Yan, and D. Mandrus, Magnetic correlations in the quasi-two-dimensional semiconducting ferromagnet $CrSiTe_3$, Phys. Rev. B **92**, 144404 (2015).

[14] X. Li and J. Yang, $CrXTe_3$ ($X = Si, Ge$) nanosheets: Two dimensional intrinsic ferromagnetic semiconductors, J. Mater. Chem. C **2**, 7071 (2014).

[15] M.-W. Lin, H. L. Zhuang, J. Yan, T. Z. Ward, A. A. Puretzky, C. M. Rouleau, Z. Gai, L. Liang, V. Meunier, B. G. Sumpter, P. Ganesh, P. R. C. Kent, D. B. Geohegan, D. G. Mandrus, and K. Xiao, Ultrathin nanosheets of $CrSiTe_3$: A semiconducting two-dimensional ferromagnetic material, J. Mater. Chem. C **4**, 315 (2016).

[16] B. Liu, Y. Zou, S. Zhou, L. Zhang, Z. Wang, H. Li, Z. Qu, and Y. Zhang, Critical behavior of the van der Waals bonded high T_C ferromagnet Fe_3GeTe_2, Sci. Rep. **7**, 6184 (2017).

[17] Y. Tian, M. J. Gray, H. Ji, R. J. Cava, and K. S. Burch, Magneto-elastic coupling in a potential ferromagnetic 2D atomic crystal, 2D Mater. **3**, 025035 (2016).

[18] Y. Sun, R. C. Xiao, G. T. Lin, R. R. Zhang, L. S. Ling, Z. W. Ma, X. Luo, W. J. Lu, Y. P. Sun, and Z. G. Sheng, Effects of hydrostatic pressure on spin-lattice coupling in two-dimensional ferromagnetic $Cr_2Ge_2Te_6$, Appl. Phys. Lett. **112**, 072409 (2018).

[19] Y. Liu and C. Petrovic, Critical behavior of quasi-two-dimensional semiconducting ferromagnet $Cr_2Ge_2Te_6$, Phys. Rev. B **96**, 054406 (2017).

[20] G. T. Lin, H. L. Zhuang, X. Luo, B. J. Liu, F. C. Chen, J. Yan, Y. Sun, J. Zhou, W. J. Lu, P. Tong, Z. G. Sheng, Z. Qu, W. H. Song, X. B. Zhu, and Y. P. Sun, Tricritical behavior of the two-dimensional intrinsically ferromagnetic semiconductor $CrGeTe_3$, Phys. Rev. B **95**, 245212 (2017).

[21] P. Giannozzi, S. Baroni, N. Bonini, M. Calandra, R. Car, C. Cavazzoni, D. Ceresoli, G. L. Chiarotti, M. Cococcioni, I. Dabo, A. D. Corso, S. de Gironcoli, S. Fabris, G. Fratesi, R. Gebauer, U. Gerstmann, C. Gougoussis, A. Kokalj, M. Lazzeri, L. Martin-Samos, N. Marzari, F. Mauri, R. Mazzarello, S. Paolini, A. Pasquarello, L. Paulatto, C. Sbraccia, S. Scandolo, G. Sclauzero, A. P. Seitsonen, A. Smogunov, P. Umari, and R. M. Wentzcovitch, Quantum espresso: A modular and open-source software project for quantum simulations of materials, J. Phys.: Condens. Matter **21**, 395502 (2009).

[22] J. P. Perdew, K. Burke, and M. Ernzerhof, Generalized Gradient Approximation Made Simple, Phys. Rev. Lett. **77**, 3865 (1996).

[23] P. E. Blöchl, Projector augmented-wave method, Phys. Rev. B **50**, 17953 (1994).

[24] G. Kresse and D. Joubert, From ultrasoft pseudopotentials to the projector augmented-wave method, Phys. Rev. B **59**, 1758 (1999).

[25] G. Stefan, Semiempirical GGA-type density functional constructed with a long-range dispersion correction, J. Comput. Chem. **27**, 1787 (2006).

[26] R. E. Marsh, The crystal structure of $Cr_2Si_2Te_6$: Corrigendum, J. Solid State Chem. **77**, 190 (1988).

[27] N. Lazarević, E. S. Bozin, M. Šćepanović, M. Opačić, Hechang Lei, C. Petrovic, and Z. V. Popović, Probing $IrTe_2$ crystal symmetry by polarized Raman scattering, Phys. Rev. B **89**, 224301 (2014).

[28] M. Opačić, N. Lazarević, M. Šćepanović, H. Ryu, H. Lei, C. Petrovic, and Z. V. Popović, Evidence of superconductivity-induced phonon spectra renormalization in alkali-doped iron selenides, J. Phys.: Condens. Matter **27**, 485701 (2015).

[29] A. Baum, A. Milosavljević, N. Lazarević, M. M. Radonjić, B. Nikolić, M. Mitschek, Z. Inanloo Maranloo, M. Šćepanović, M. Grujić-Brojčin, N. Stojilović, M. Opel, Aifeng Wang, C. Petrovic, Z. V. Popović, and R. Hackl, Phonon anomalies in FeS, Phys. Rev. B **97**, 054306 (2018).

[30] N. Lazarević, M. Radonjić, M. Šćepanović, Hechang Lei, D. Tanasković, C. Petrovic, and Z. V. Popović, Lattice dynamics of KNi_2Se_2, Phys. Rev. B **87**, 144305 (2013).

[31] N. Lazarević, Z. V. Popović, Rongwei Hu, and C. Petrovic, Evidence for electron-phonon interaction in $Fe_{1-x}M_xSb_2$ ($M =$ Co and Cr; $0 \leqslant x \leqslant 0.5$) single crystals, Phys. Rev. B **81**, 144302 (2010).

[32] L. J. Sandilands, Y. Tian, K. W. Plumb, Y.-J. Kim, and K. S. Burch, Scattering Continuum and Possible Fractionalized Excitations in α-$RuCl_3$, Phys. Rev. Lett. **114**, 147201 (2015).

PHYSICAL REVIEW B **98**, 104307 (2018)

Lattice dynamics and phase transition in CrI_3 single crystals

S. Djurdjić-Mijin,[1] A. Šolajić,[1] J. Pešić,[1] M. Šćepanović,[1] Y. Liu (刘育),[2] A. Baum,[3,4] C. Petrovic,[2]
N. Lazarević,[1] and Z. V. Popović[1,5]
[1] *Center for Solid State Physics and New Materials, Institute of Physics Belgrade, University of Belgrade, Pregrevica 118, 11080 Belgrade, Serbia*
[2] *Condensed Matter Physics and Materials Science Department, Brookhaven National Laboratory, Upton, New York 11973-5000, USA*
[3] *Walther Meissner Institut, Bayerische Akademie der Wissenschaften, 85748 Garching, Germany*
[4] *Fakultät für Physik E23, Technische Universität München, 85748 Garching, Germany*
[5] *Serbian Academy of Sciences and Arts, Knez Mihailova 35, 11000 Belgrade, Serbia*

(Received 9 July 2018; published 18 September 2018)

The vibrational properties of CrI_3 single crystals were investigated using Raman spectroscopy and were analyzed with respect to the changes of the crystal structure. All but one mode are observed for both the low-temperature $R\bar{3}$ and the high-temperature $C2/m$ phase. For all observed modes the energies and symmetries are in good agreement with DFT calculations. The symmetry of a single layer was identified as $p\bar{3}1/m$. In contrast to previous studies we observe the transition from the $R\bar{3}$ to the $C2/m$ phase at 180 K and find no evidence for coexistence of both phases over a wide temperature range.

DOI: 10.1103/PhysRevB.98.104307

I. INTRODUCTION

Two-dimensional layered materials have gained attention due to their unique properties, the potential for a wide spectrum of applications, and the opportunity for the development of functional van der Waals heterostructures. CrI_3 is a member of the chromium-trihalide family which are ferromagnetic semiconductors [1]. Recently they have received significant attention as candidates for the study of magnetic monolayers. The experimental realization of CrI_3 ferromagnetic monolayers [1] motivated further efforts towards their understanding. CrI_3 features electric field controlled magnetism [2] as well as a strong magnetic anisotropy [3,4]. With the main absorption peaks lying in the visible part of the spectrum, it is a great candidate for low-dimensional semiconductor spintronics [5]. In its ground state, CrI_3 is a ferromagnetic semiconductor with a Curie temperature of 61 K [1,6] and a band gap of 1.2 eV [6]. It was demonstrated that the magnetic properties of CrI_3 mono- and bilayers can be controlled by electrostatic doping [2]. Upon cooling, CrI_3 undergoes a phase transition around 220 K from the high-temperature monoclinic ($C2/m$) to the low-temperature rhombohedral ($R\bar{3}$) phase [3,7]. Although the structural phase transition is reported to be first order, it was suggested that the phases may coexist over a wide temperature range [3]. Raman spectroscopy can be of use here due to its capability to simultaneously probe both phases in a phase-separated system [8–10].

A recent theoretical study predicted the energies of all Raman active modes in the low-temperature and high-temperature structure of CrI_3 suggesting a near degeneracy between the A_g and B_g modes in the monoclinic ($C2/m$) structure. Their energies match the energies of E_g modes in the rhombohedral ($R\bar{3}$) structure [7].

In this article we present an experimental and theoretical Raman scattering study of CrI_3 lattice dynamics. In both phases all but one of the respective modes predicted by symmetry were observed. The energies for all modes are in good agreement with the theoretical predictions for the assumed crystal symmetry. Our data suggest that the first-order transition occurs at $T_s \approx 180$ K without evidence for phase coexistence over a wide temperature range.

II. EXPERIMENT AND NUMERICAL METHOD

The preparation of the single crystal CrI_3 sample used in this study is described elsewhere [11]. The Raman scattering experiment was performed using a Tri Vista 557 spectrometer in backscattering micro-Raman configuration with a 1800/1800/2400 groves/mm diffraction grating combination. The 532 nm line of a Coherent Verdi G solid state laser was used for excitation. The direction of the incident light coincides with the crystallographic c axis. The sample was oriented so that its principal axis of the $R\bar{3}$ phase coincides with the x axis of the laboratory system. A KONTI CryoVac continuous helium flow cryostat with a 0.5-mm-thick window was used for measurements at all temperatures under high vacuum (10^{-6} mbar). The sample was cleaved in air before being placed into the cryostat. The obtained Raman spectra were corrected by the Bose factor and analyzed quantitatively by fitting Voigt profiles to the data whereby the Gaussian width $\Gamma_{\mathrm{Gauss}} = 1\ \mathrm{cm}^{-1}$ reflects the resolution of the spectrometer.

The spin polarized density functional theory (DFT) calculations have been performed in the Quantum Espresso (QE) software package [12] using the Perdew-Burke-Ernzehof (PBE) exchange-correlation functional [13] and PAW pseudopotentials [14,15]. The energy cutoffs for the wave functions and the charge density were set to be 85 and 425 Ry, respectively, after convergence tests. For k-point sampling, the Monkhorst-Pack scheme was used with a $8 \times 8 \times 8$ grid centered around the Γ point. Optimization of the atomic positions in the unit cell was performed until the interatomic forces were smaller than 10^{-6} Ry/Å. To treat the van der Waals (vdW) interactions a Grimme-D2 correction [16] is used in order to include long-ranged forces between the layers, which are not properly captured within LDA or GGA functionals. This way, the parameters are obtained more accurately, especially the interlayer distances. Phonon frequencies were calculated at the Γ point using the linear response method implemented in QE. The phonon energies are compiled in Table III together with the experimental values. The eigenvectors of the Raman active modes for both the low- and high-temperature phase are depicted in Fig. 5 of the Appendix.

III. RESULTS AND DISCUSSION

CrI_3 adopts a rhombohedral $R\bar{3}$ (C_{3i}^2) crystal structure at low temperatures and a monoclinic $C2/m$ (C_{2h}^3) crystal structure at room temperature [3], as shown in Fig. 1. The main difference between the high- and low-temperature crystallographic space groups arises from different stacking sequences with the CrI_3 layers being almost identical. In the rhombohedral structure the Cr atoms in one layer are placed above the center of a hole in the Cr honeycomb net of the two adjacent layers. When crossing the structural phase transition at T_s to the monoclinic structure the layers are displaced along the a direction so that every fourth layer is at the same place as the first one. The interatomic distances, mainly the interlayer distance, and the vdW gap, are slightly changed by the structural transition. The crystallographic parameters for both phases are presented in Table I. The numerically obtained values are in good agreement with reported x-ray diffraction data [11].

The vibrational properties of layered materials are typically dominated by the properties of the single layers composing the crystal. The symmetry of a single layer can be described by one of the 80 diperiodic space groups (DG) obtained by lifting translational invariance in the direction perpendicular to the layer [17]. In the case of CrI_3, the symmetry analysis revealed that the single layer structure is fully captured by the $p\bar{3}1/m$ (D_{3d}^1) diperiodic space group DG71, rather than by $R\bar{3}2/m$ as proposed in Ref. [7].

TABLE I. Calculated and experimental [11] parameters of the crystallographic unit cell for the low-temperature $R\bar{3}$ and high-temperature $C2/m$ phase of CrI_3.

	Space group $R\bar{3}$		Space group $C2/m$	
T (K)	Calc.	Expt. [11]	Calc.	Expt. [11]
a (Å)	6.87	6.85	6.866	6.6866
b (Å)	6.87	6.85	11.886	11.856
c (Å)	19.81	19.85	6.984	6.966
α (deg)	90	90	90	90
β (deg)	90	90	108.51	108.68
γ (deg)	120	120	90	90

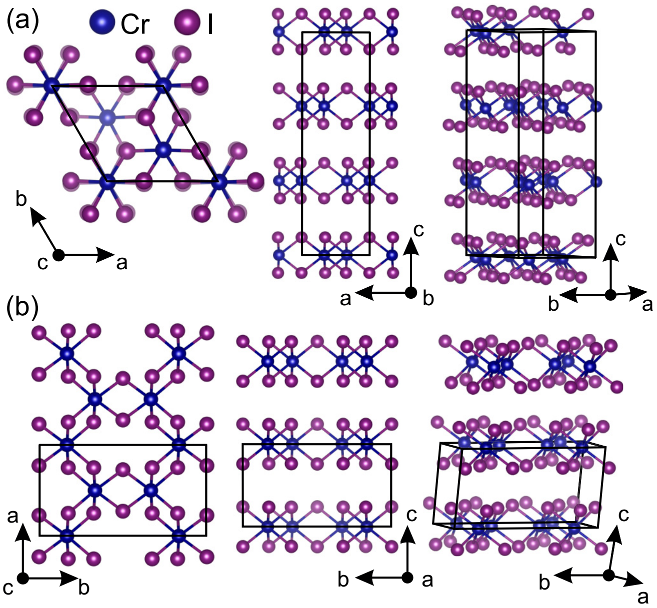

FIG. 1. Schematic representation of (a) the low-temperature $R\bar{3}$ and (b) the high-temperature $C2/m$ crystal structure of CrI_3. Black lines represent unit cells.

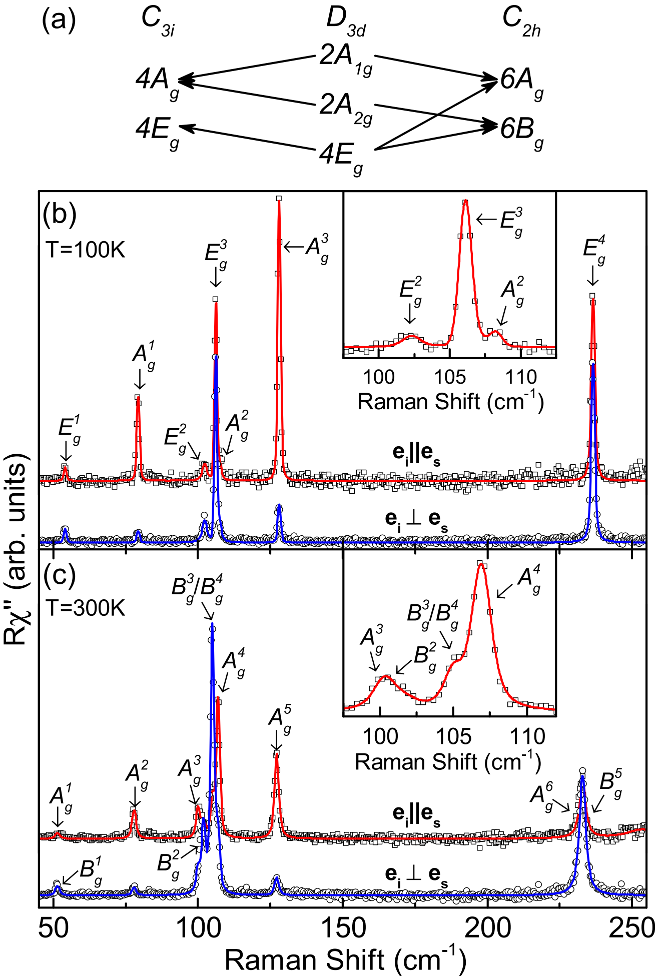

FIG. 2. (a) Compatibility relations for the CrI_3 layer and the crystal symmetries. Raman spectra of (b) the low-temperature $R\bar{3}$ and (c) the high-temperature $C2/m$ crystal structure measured in parallel (open squares) and crossed (open circles) polarization configurations at 100 and 300 K, respectively. Red and blue solid lines represent fits of Voigt profiles to the experimental data.

TABLE II. Wyckoff positions of the two types of atoms and their contributions to the Γ-point phonons for the $R\bar{3}$ and $C2/m$ as well as the $p\bar{3}1/m$ diperiodic space group. The second row shows the Raman tensors for the corresponding space groups.

Space group $R\bar{3}$		Diperiodic space group $p\bar{3}1/m$		Space group: C2/m	
Atoms	Irreducible representations	Atoms	Irreducible representations	Atoms	Irreducible representations
Cr (6c)	$A_g+A_u+E_g+E_u$	Cr (2c)	$A_{2g}+A_{2u}+E_g+E_u$	Cr (4g)	$A_g+A_u+2B_g+2B_u$
I (18f)	$3A_g+3A_u+3E_g+3E_u$	I (6k)	$2A_{1g}+A_{1u}+A_{2g}$ $+2A_{2u}+3E_g+3E_u$	I (4i) I (8j)	$2A_g+2A_u+B_g+B_u$ $3A_g+3A_u+3B_g+3B_u$
$A_g = \begin{pmatrix} a & & \\ & a & \\ & & b \end{pmatrix}$		$A_{1g} = \begin{pmatrix} a & & \\ & a & \\ & & b \end{pmatrix}$		$A_g = \begin{pmatrix} a & & d \\ & c & \\ d & & b \end{pmatrix}$	
${}^1E_g = \begin{pmatrix} c & d & e \\ d & -c & f \\ e & f & \end{pmatrix}$ ${}^2E_g = \begin{pmatrix} d & -c & -f \\ -c & -d & e \\ -f & e & \end{pmatrix}$		${}^1E_g = \begin{pmatrix} c & & \\ & -c & d \\ & d & \end{pmatrix}$ ${}^2E_g = \begin{pmatrix} & -c & -d \\ -c & & \\ -d & e & \end{pmatrix}$		$B_g = \begin{pmatrix} & e & \\ e & & f \\ & f & \end{pmatrix}$	

According to the factor group analysis (FGA) for a single $\mathrm{CrI_3}$ layer, six modes $(2A_{1g}+4E_g)$ are expected to be observed in the Raman scattering experiment (see Table II). By stacking the layers the symmetry is reduced and, depending on the stacking sequence, FGA yields a total of eight Raman active modes $(4A_g+4E_g)$ for the $R\bar{3}$ and 12 Raman active modes $(6A_g+6B_g)$ for the $C2/m$ crystal symmetry. The correlation between layer and crystal symmetries for both cases is shown in Fig. 2(a) [18,19].

Figure 2(b) shows the $\mathrm{CrI_3}$ single crystal Raman spectra measured at 100 K in two scattering channels. According to the selection rules for the rhombohedral crystal structure (Table II) the A_g modes can be observed only in the parallel polarization configuration, whereas the E_g modes appear in both parallel and crossed polarization configurations. Based on the selection rules the peaks at about 78, 108, and 128 $\mathrm{cm^{-1}}$ were identified as A_g symmetry modes, whereas the peaks at about 54, 102, 106, and 235 $\mathrm{cm^{-1}}$ are assigned as E_g symmetry. The weak observation of the most pronounced A_g modes in crossed polarizations [Fig. 2(b)] is attributed to the leakage due to a slight sample misalignment and/or the presence of defects in the crystal. The energies of all observed modes are compiled in Table III together with the energies predicted by our calculations and by Ref. [7], and are found to be in good agreement for the E_g modes. The discrepancy is slightly larger for the low energy A_g modes. Our calculations in general agree with those from Ref. [7]. The A_g^4 mode of the rhombohedral phase, predicted by calculation to appears at about 195 $\mathrm{cm^{-1}}$, was not observed in the experiment, most likely due to its low intensity.

When the symmetry is lowered in the high-temperature monoclinic $C2/m$ phase [Fig. 2(c)] the E_g modes split into an A_g and a B_g mode each, whereas the rhombohedral A_g^2 and A_g^4 modes are predicted to switch to the monoclinic B_g symmetry. The correspondence of the phonon modes across the phase transition is indicated by the arrows in Table III. The selection rules for $C2/m$ (see Table II) predict that A_g and B_g modes can be observed in both parallel and crossed polarization configurations. Additionally, the sample forms three types of domains which are rotated with respect to each other. We

TABLE III. Phonon symmetries and phonon energies for the low-temperature $R\bar{3}$ and high-temperature $C2/m$ phase of $\mathrm{CrI_3}$. The experimental values were determined at 100 and 300 K, respectively. All calculations were performed at zero temperature. Arrows indicate the correspondence of the phonon modes across the phase transition.

Space group $R\bar{3}$					Space group C2/m			
Symm.	Expt. ($\mathrm{cm^{-1}}$)	Calc. ($\mathrm{cm^{-1}}$)	Calc. ($\mathrm{cm^{-1}}$) [7]		Symm.	Expt. ($\mathrm{cm^{-1}}$)	Calc. ($\mathrm{cm^{-1}}$)	Calc. [7] ($\mathrm{cm^{-1}}$)
E_g^1	54.1	59.7	53	$\rightrightarrows$	B_g^1 A_g^1	52.0 53.6	57.0 59.8	52 51
A_g^1	73.33	89.6	79	$\longrightarrow$	A_g^2	78.6	88.4	79
E_g^2	102.3	99.8	98	$\rightrightarrows$	A_g^3 B_g^2	101.8 102.4	101.9 101.8	99 99
E_g^3	106.2	112.2	102	$\rightrightarrows$	B_g^3 A_g^4	106.4[a] 108.3	108.9 109.3	101 102
A_g^2	108.3	98.8	88	$\longrightarrow$	B_g^4	106.4[a]	97.8	86
A_g^3	128.1	131.1	125	$\longrightarrow$	A_g^5	128.2	131.7	125
A_g^4	–	195.2	195	$\longrightarrow$	B_g^5	–	198.8	195
E_g^4	236.6	234.4	225	$\rightrightarrows$	A_g^6 B_g^6	234.6 235.5	220.1 221.1	224 225

[a] Observed as two peak structure.

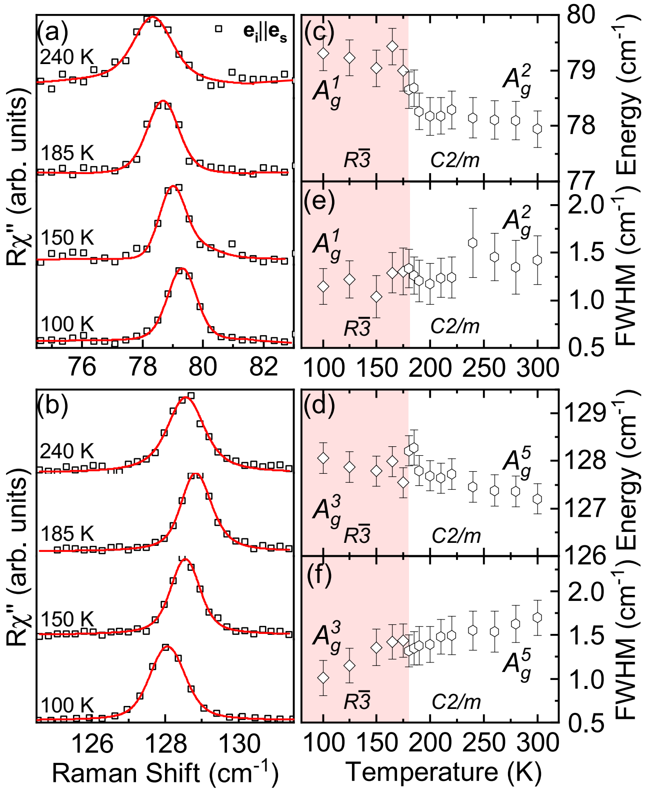

FIG. 3. Temperature dependence of the A_g^1 and A_g^3 phonon modes of the rhombohedral structure and the corresponding A_g^2 and A_g^5 modes of the monoclinic structure, respectively. (a) and (b) Raman spectra at temperatures as indicated. The spectra are shifted for clarity. Solid red lines represent Voigt profiles fitted to the data. (c) and (d) and (e) and (f) Temperature dependence of the phonon energies and linewidths, respectively. Both modes show an abrupt change in energy at the phase transition at 180 K.

therefore identify the phonons in the $C2/m$ phase in relation to the calculations and find again good agreement of the energies. The B_g^3 and B_g^4 modes overlap and therefore cannot be resolved separately. As can be seen from the temperature dependence shown below [Fig. 4(b)] the peak at 106 cm^{-1} broadens and gains spectral weight in the monoclinic phase in line with the expectance that two modes overlap. The missing rhombohedral A_g^4 mode corresponds to the monoclinic B_g^5 mode, which is likewise absent in the spectra.

The temperature dependence of the observed phonons is shown in Figs. 3 and 4. In the low-temperature rhombohedral phase all four E_g modes as well as A_g^1 and A_g^2 soften upon warming, whereas A_g^3 hardens up to $T \approx 180$ K before softening again. Crossing the first-order phase transition from $R\bar{3}$ to $C2/m$ crystal symmetry is reflected in the spectra as a symmetry change and/or renormalization for the nondegenerate modes and lifting of the degeneracy of the E_g modes as shown in Table II. In our samples, this transition is observed at $T_s \approx 180$ K. The splitting of the E_g phonons into A_g and B_g modes at the phase transition is sharp (Fig. 4). The rhombohedral A_g^1 and A_g^3 phonons show a jump in energy and a small discontinuity in the linewidth at T_s (Fig. 3). Our spectra were taken during warming in multiple runs after cooling to 100 K each time. We found that the temperature dependence for the phonon modes obtained this way was smooth in each phase. McGuire *et al.* [3,20] reported T_s in the range of 220 K, a coexistence of both phases and a large thermal hysteresis. However, they also noted that the first and second warming cycle showed identical behavior and only found a shift of the transition temperature to higher values for cooling cycles. We therefore consider the difference between the reported transition around 220 K and our $T_s \approx 180$ K significant. To some extent this difference may be attributed

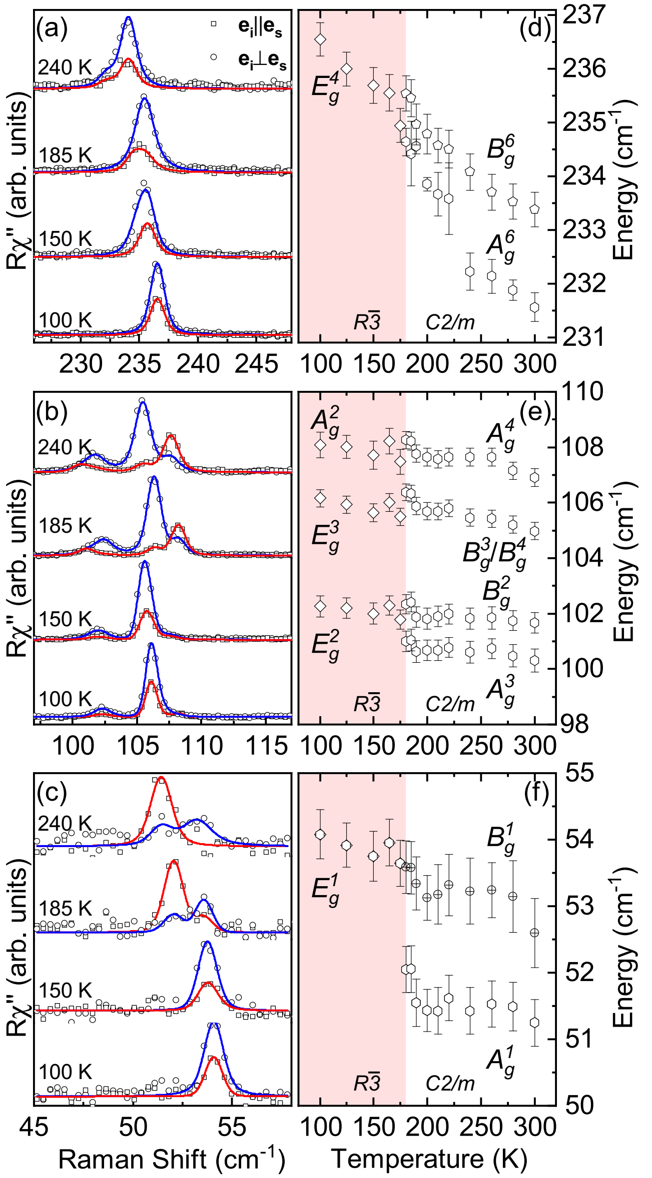

FIG. 4. Temperature dependence of the rhombohedral A_g^4 and E_g modes. (a)–(c) Raman spectra in parallel (open squares) and crossed (open circles) light polarizations at temperatures as indicated. The spectra are shifted for clarity. Blue and red solid lines are fits of Voigt profiles to the data. Two spectra were analyzed simultaneously in two scattering channels with the integrated intensity as the only independent parameter. (d)–(f) Phonon energies obtained from the Voigt profiles. Each E_g mode splits into an A_g and a B_g mode above 180 K.

to local heating by the laser. More importantly, we find no signs of phase coexistence in the observed temperature range. The spectra for the low-temperature and high-temperature phases are distinctly different (Fig. 2) and the E_g modes exhibit a clearly resolved splitting which occurs abruptly at T_s. We performed measurements in small temperature steps (see Figs. 3 and 4). This limits the maximum temperature interval where the phase coexistence could occur in our samples to approximately 5 K, much less than the roughly 30 to 80 K reported earlier [3,20]. We cannot exclude the possibility that a small fraction of the low-temperature phase could still coexist with the high-temperature phase over a wider temperature range, whereby weak peaks corresponding to the remains of the low-temperature $R\bar{3}$ phase might be hidden under the strong peaks of the $C2/m$ phase.

IV. CONCLUSION

We studied the lattice dynamics in single crystalline CrI_3 using Raman spectroscopy supported by numerical calculations. For both the low-temperature $R\bar{3}$ and the high-temperature $C2/m$ phase, all except one of the predicted

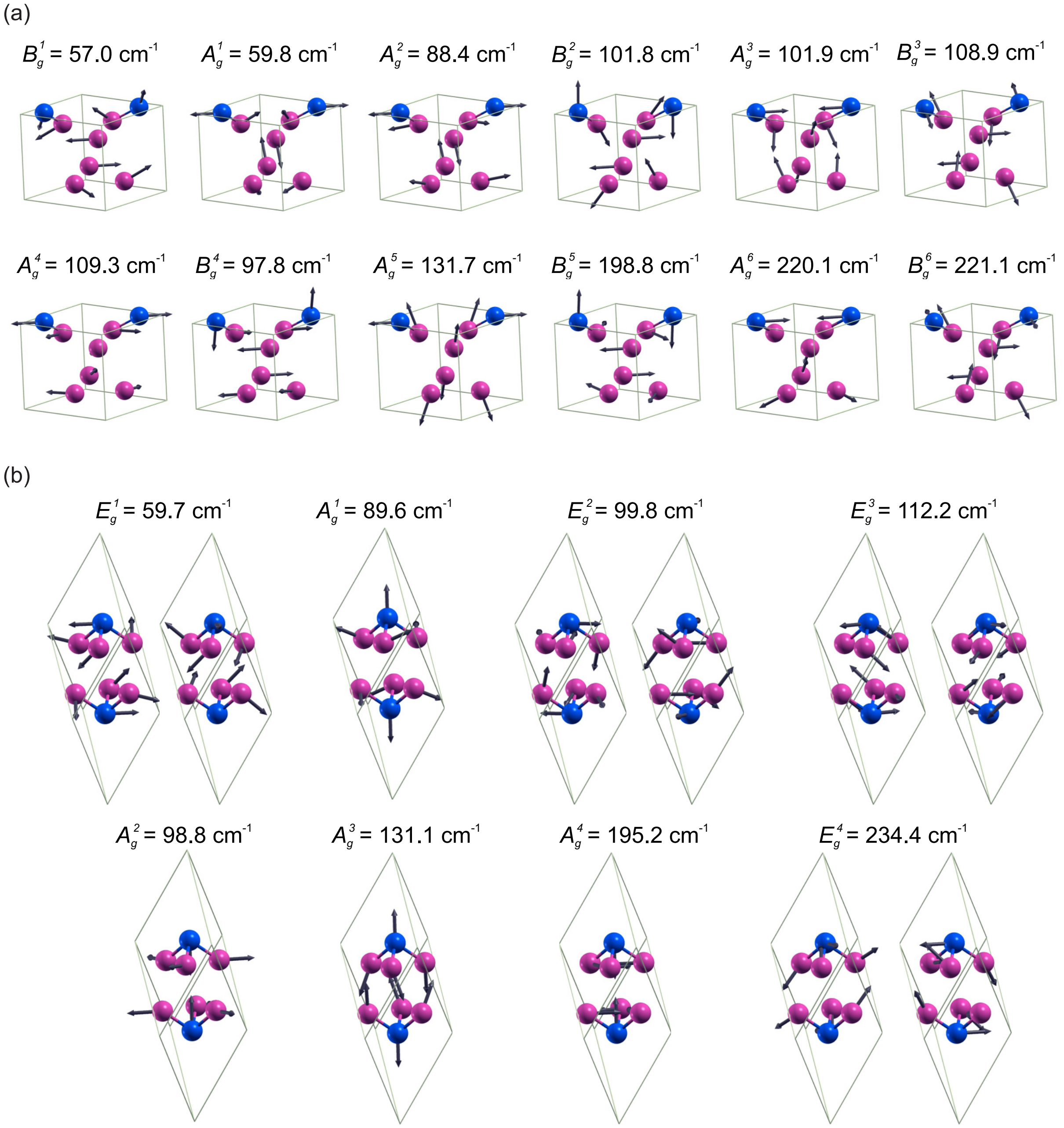

FIG. 5. Raman-active phonons in CrI_3 for (a) the monoclinic phase hosting A_g and B_g modes and for (b) the rhombohedral phase hosting A_g and E_g modes. Blue and violet spheres denote Cr and I atoms, respectively. Solid lines represent primitive unit cells. Arrow lengths are proportional to the square root of the interatomic forces. The given energies are calculated for zero temperature.

phonon modes were identified and the calculated and experimental phonon energies were found to be in good agreement. We determined that the symmetry of the single CrI_3 layers is $p\bar{3}1/m$. Abrupt changes to the spectra were found at the first-order phase transition which was located at $T_s \approx 180$ K, lower than in previous studies. In contrast to the prior reports we found no sign of phase coexistence over temperature ranges exceeding 5 K.

ACKNOWLEDGMENTS

The work was supported by the Serbian Ministry of Education, Science and Technological Development under Projects No. III45018 and No. OI171005. DFT calculations were performed using computational resources at Johannes Kepler University, Linz, Austria. Work at Brookhaven is supported by the U.S. DOE under Contract No. DE-SC0012704.

S.Dj.M. and N.L. conceived the experiment, performed the experiment, analyzed and discussed the data, and wrote the paper. A.Š. and J.P. calculated the phonon energies, analyzed and discussed the data, and wrote the paper. Y.L. and C.P. synthesized and characterized the samples. M.Š. performed the experiment and analyzed and discussed the data. A.B. and Z.V.P. analyzed and discussed the data and wrote the paper. All authors commented on the manuscript.

APPENDIX: EIGENVECTORS

In addition to the phonon energies we also calculated the phonon eigenvectors which are shown in Fig. 5(a) for the high-temperature monoclinic phase and in Fig. 5(b) for the low-temperature rhombohedral phase. The energies, as given, are calculated for zero temperature. The relative displacement of the atoms is denoted by the length of the arrows.

[1] E. Navarro-Moratalla, B. Huang, G. Clark *et al.*, Layer-dependent ferromagnetism in a van der Waals crystal down to the monolayer limit, Nature (London) **546**, 270 (2017).

[2] S. Jiang, L. Li, Z. Wang, K. F. Mak, and J. Shan, Controlling magnetism in 2D CrI_3 by electrostatic doping, Nat. Nanotechnol. **13**, 549 (2018).

[3] M. A. McGuire, H. Dixit, V. R. Cooper, and B. C. Sales, Coupling of crystal structure and magnetism in the layered, ferromagnetic insulator CrI_3, Chem. Mater. **27**, 612 (2015).

[4] J. L. Ladno and J. Fernández-Rossier, On the origin of magnetic anisotropy in two dimensional CrI_3, 2D Mater. **4**, 035002 (2017).

[5] W.-B. Zhang, Q. Qu, P. Zhu, and C.-H. Lam, Robust intrinsic ferromagnetism and half semiconductivity in stable two-dimensional single-layer chromium trihalides, J. Mater. Chem. C **3**, 12457 (2015).

[6] J. F. Dillon, Jr. and C. E. Olson, Magnetization, resonance, and optical properties of the ferromagnet CrI_3, J. Appl. Phys. **36**, 1259 (1965).

[7] D. T. Larson and E. Kaxiras, Raman Spectrum of CrI_3: An *ab initio* study, Phys. Rev. B **98**, 085406 (2018).

[8] N. Lazarević, M. Abeykoon, P. W. Stephens, H. Lei, E. S. Bozin, C. Petrovic, and Z. V. Popović, Vacancy-induced nanoscale phase separation in $\mathrm{K}_x\mathrm{Fe}_{2-y}\mathrm{Se}_2$ single crystals evidenced by Raman scattering and powder x-ray diffraction, Phys. Rev. B **86**, 054503 (2012).

[9] H. Ryu, M. Abeykoon, K. Wang, H. Lei, N. Lazarevic, J. B. Warren, E. S. Bozin, Z. V. Popovic, and C. Petrovic, Insulating and metallic spin glass in Ni-doped $\mathrm{K}_x\mathrm{Fe}_{2-y}\mathrm{Se}_2$ single crystals, Phys. Rev. B **91**, 184503 (2015).

[10] H. Ryu, K. Wang, M. Opacic, N. Lazarevic, J. B. Warren, Z. V. Popovic, E. S. Bozin, and C. Petrovic, Sustained phase separation and spin glass in Co-doped $\mathrm{K}_x\mathrm{Fe}_{2-y}\mathrm{Se}_2$ single crystals, Phys. Rev. B **92**, 174522 (2015).

[11] Y. Liu and C. Petrovic, Three-dimensional magnetic critical behavior in CrI_3, Phys. Rev. B **97**, 014420 (2018).

[12] P. Giannozzi, S. Baroni, N. Bonini, M. Calandra, R. Car, C. Cavazzoni, D. Ceresoli, G. L. Chiarotti, M. Cococcioni, I. Dabo, A. D. Corso, S. de Gironcoli, S. Fabris, G. Fratesi, R. Gebauer, U. Gerstmann, C. Gougoussis, A. Kokalj, M. Lazzeri, L. Martin-Samos, N. Marzari, F. Mauri, R. Mazzarello, S. Paolini, A. Pasquarello, L. Paulatto, C. Sbraccia, S. Scandolo, G. Sclauzero, A. P. Seitsonen, A. Smogunov, P. Umari, and R. M. Wentzcovitch, Quantum espresso: A modular and open-source software project for quantum simulations of materials, J. Phys. Condens. Matter **21**, 395502 (2009).

[13] J. P. Perdew, K. Burke, and M. Ernzerhof, Generalized Gradient Approximation Made Simple, Phys. Rev. Lett. **77**, 3865 (1996).

[14] P. E. Blöchl, Projector augmented-wave method, Phys. Rev. B **50**, 17953 (1994).

[15] G. Kresse and D. Joubert, From ultrasoft pseudopotentials to the projector augmented-wave method, Phys. Rev. B **59**, 1758 (1999).

[16] S. Grimme, Semiempirical GGA-type density functional constructed with a long-range dispersion correction, J. Comput. Chem. **27**, 1787 (2006).

[17] E. A. Wood, The 80 diperiodic groups in three dimensions, Bell Syst. Tech. J. **43**, 541 (1964).

[18] W. G. Fateley, N. T. McDevitt, and F. F. Bentley, Infrared and raman selection rules for lattice vibrations: The correlation method, Appl. Spectrosc. **25**, 155 (1971).

[19] N. Lazarević, Z. V. Popović, R. Hu, and C. Petrovic, Evidence of coupling between phonons and charge-density waves in ErTe_3, Phys. Rev. B **83**, 024302 (2011).

[20] M. A. McGuire, G. Clark, S. KC, W. M. Chance, G. E. Jellison, V. R. Cooper, X. Xu, and B. C. Sales, Magnetic behavior and spin-lattice coupling in cleavable van der Waals layered CrCl_3 crystals, Phys. Rev. Mater. **1**, 014001 (2017).

Interplay of lattice, electronic, and spin degrees of freedom in detwinned $BaFe_2As_2$: A Raman scattering study

A. Baum,[1,2] Ying Li,[3] M. Tomić,[3] N. Lazarević,[4] D. Jost,[1,2] F. Löffler,[1,2] B. Muschler,[1,2,*] T. Böhm,[1,2,†] J.-H. Chu,[5,6,7]
I. R. Fisher,[5,6] R. Valentí,[3] I. I. Mazin,[8] and R. Hackl[1,‡]
[1]*Walther Meissner Institut, Bayerische Akademie der Wissenschaften, 85748 Garching, Germany*
[2]*Fakultät für Physik E23, Technische Universität München, 85748 Garching, Germany*
[3]*Institut für Theoretische Physik, Goethe-Universität Frankfurt, Max-von-Laue-Straße 1, 60438 Frankfurt am Main, Germany*
[4]*Center for Solid State Physics and New Materials, Institute of Physics Belgrade, University of Belgrade,*
Pregrevica 118, 11080 Belgrade, Serbia
[5]*Stanford Institute for Materials and Energy Sciences, SLAC National Accelerator Laboratory, 2575 Sand Hill Road,*
Menlo Park, California 94025, USA
[6]*Geballe Laboratory for Advanced Materials & Dept. of Applied Physics, Stanford University, California 94305, USA*
[7]*Department of Physics, University of Washington, Seattle, Washington 98195, USA*
[8]*Code 6393, Naval Research Laboratory, Washington, DC 20375, USA*

(Received 13 June 2018; revised manuscript received 18 July 2018; published 7 August 2018)

We report results of Raman scattering experiments on twin-free $BaFe_2As_2$ with the main focus placed on understanding the influence of electronic and spin degrees of freedom on the lattice dynamics. In particular, we scrutinize the E_g modes and the As A_{1g} mode. Each of the two E_g phonons in the tetragonal phase is observed to split into a B_{2g} and a B_{3g} mode upon entering the orthorhombic stripe-magnetic phase. The splitting amounts to approximately 10 cm^{-1} and less than 5 cm^{-1} for the low- and the high-energy E_g mode, respectively. The detailed study of the fully symmetric As mode using parallel incident and outgoing photon polarizations along either the antiferromagnetic or the ferromagnetic Fe-Fe direction reveals an anisotropic variation of the spectral weight with the energy of the exciting laser indicating a polarization-dependent resonance effect. Along with the experiments we present results from density functional theory calculations of the phonon eigenvectors, the dielectric function, and the Raman tensor elements. The comparison of theory and experiment indicates that (i) orbital-selective electronic correlations are crucial to understand the lattice dynamics and (ii) all phonon anomalies originate predominantly from the magnetic ordering and the corresponding reconstruction of the electronic bands at all energies.

DOI: 10.1103/PhysRevB.98.075113

I. INTRODUCTION

One of the most debated issues in Fe-based superconductors is the interplay of spin, orbital, and lattice degrees of freedom at the onset of magnetism, nematicity, and superconductivity [1–5], particularly interplay between phonons and magnetic degrees of freedom. For instance, soon after the discovery of Fe-based superconductors, the magnetic moment was predicted to couple to the As position [6]. Zbiri *et al.* found a modulation of the electronic density of states (DOS) at the Fermi energy E_F by the two E_g and the A_{1g} modes [7]. Various anomalies were observed experimentally using neutron, Raman, and optical spectroscopy [8–15] but are not fully understood yet.

One particular effect is the observation of substantial Raman scattering intensity of the As phonon below the magnetostructural transition in crossed polarizations with the electric fields oriented along the axes of the pseudo-tetragonal 2 Fe unit cell [9] [for the definition of the axes see Fig. 1(a)]. From the weak coupling point of view, it has been argued that the formation of a spin-density wave (SDW) modifies the low-energy electronic structure near the Fermi level, and this modification leads to the anomalous intensity [16]. On the other hand, recent experiments were interpreted by introducing a phenomenological coupling between the phonon and the particle-hole continuum scaling with the amplitude of ordered magnetic moment [17] being on the order of 1 μ_B. This approach is clearly beyond the weak-coupling regime. Density functional (DFT) calculations and general considerations suggest that substantial modifications of the electronic structure occur in a broad energy range of order $J_{\mathrm{Hund}} \gtrsim 1$ eV, corresponding to the Raman *photon* (as opposed to phonon) energy scale. This raises suspicion that a quantitative description of the modifications in the Raman spectra upon magnetic ordering should take into account the broad energy range covering the entire $d-$electron band widths. Unfortunately, previous studies were done either in twinned samples or using only a single excitation energy, which limited the scope of experimental data being, as

---

[*] Present address: Zoller & Fröhlich GmbH, Simoniusstrasse 22, 88239 Wangen im Allgäu,Germany

[†] Present address: TNG Technology Consulting GmbH, Beta-Straße, 85774 Unterföhring, Germany

[‡] hackl@wmi.badw.de

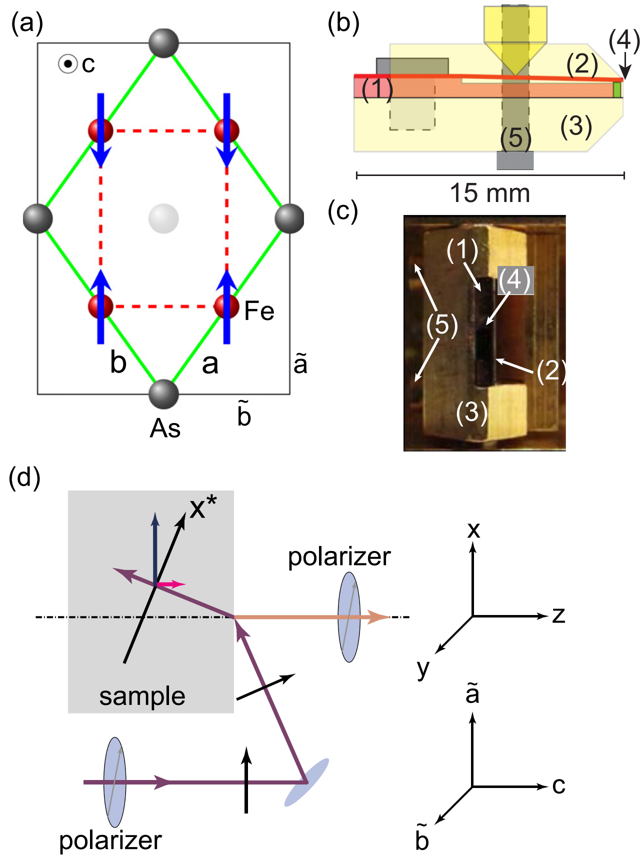

FIG. 1. FeAs layer of $BaFe_2As_2$ and detwinning clamp. (a) The As-atoms (grey) in the center and at the edges are below and, respectively, above the Fe plane (red). For this reason, the 2 Fe unit cell with the axes a and b (green) is determined by the As atoms. In the orthorhombic phase, the Fe-Fe distances become inequivalent with the distortion strongly exaggerated here. The magnetic unit cell is twice as large as the 2 Fe unit cell and has the axes $\tilde{a}$ and $\tilde{b}$. (b) Schematic sketch and (c) photograph of the detwinning clamp. The sample (4) is glued on the copper plate (1), which is in good thermal contact with the sample holder (3). Upon tightening the screws (5), the force exerted by the copper-beryllium cantilever (2) can be adjusted. (d) Schematic representation of the geometry of our Raman scattering experiment. All incoming light polarizations $\mathbf{e}_\mathrm{I}$ which are not parallel to y have finite projections on the c axis (red arrow).

a result, not sufficiently restrictive to different, maybe even contradictory, interpretations.

In this paper, we systematically address this issue experimentally, using detwinned samples and resonant Raman scattering, and interpret the results quantitatively, not on a phenomenological or model level, but using DFT calculations. Our two most vital conclusions are that (i) magnetism affects *all* Fe bands in an essential way and that has to be accounted for in explaining Raman efficiencies and (ii) the fact that Fe d states are correlated on a moderate, but considerable level, while As p states are not, is not just quantitatively, but qualitatively important in understanding the resonant behavior.

A key issue hindering straightforward DFT calculations is the fact that the *high-temperature tetragonal* phase is paramagnetically disordered, and cannot be simulated by calculations with suppressed local magnetism [18]. As explained in detail below, we circumvented this problem by assuming a magnetic order that preserves the large (albeit probably still somewhat underestimated) magnetic moment but respects the tetragonal symmetry. Yet another issue was to account for the correlation-driven renormalization of the $d-$band width. To this end, we separated the energy bands into two windows, a high-energy one dominated by As and a low-energy one derived predominantly from Fe. The Fe states were then uniformly renormalized. With these two assumptions, we could reproduce (i) the positions of the Raman-active phonons and their splitting and evolution in the detwinned orthorhombic antiferromagnetic state and (ii) Raman intensities, including the $\tilde{a}-\tilde{b}$ anisotropy as well as the complex resonant evolution with the laser light energy $\hbar\omega_\mathrm{I}$. While it is not clear *a priori* that the two computational tricks described above are sufficiently accurate, even being physically motivated, the results provide an experimental justification and convincingly substantiate the underlying physical concepts: the pivotal role of local moments in the lattice dynamics of Fe-based superconductors, and the importance of band renormalizations for d-electrons. This said, further calculations avoiding these approximations, such as full-scale dynamical mean-field theory (DMFT) computations, are quite desirable but are beyond the scope of this work.

II. METHODS

A. Samples

The $BaFe_2As_2$ crystal was prepared using a self-flux technique. Details of the crystal growth and characterization are described elsewhere [19]. $BaFe_2As_2$ is a parent compound of double-layer iron-based superconductors and orders in a stripelike SDW below $T_\mathrm{SDW} \approx 135$ K. Superconductivity can be obtained by substituting any of the ions or by pressure [20]. In $Ba(Fe_{1-x}Co_x)_2As_2$ $(0 < x \lesssim 0.06)$, the SDW is preceded by a structural phase transition from a tetragonal $(I4/mmm)$ to an orthorhombic $(Fmmm)$ lattice at $T_\mathrm{s} > T_\mathrm{SDW}$ [19]. It remains a matter of debate as to whether or not T_SDW and T_s coincide in $BaFe_2As_2$ [19,21].

Figure 1(a) shows the relation of the various axes. The axes of the tetragonal crystal ($T > T_\mathrm{s}$, green lines) are denoted a and b with $a = b$. The axes of the magnetically ordered structure (4 Fe per unit cell, black lines), $\tilde{a}$ and $\tilde{b}$, differ by approximately 0.7% below T_SDW [22] and the Fe-Fe distance along the $\tilde{b}$ axis becomes shorter than along the $\tilde{a}$ axis as sketched in Fig. 1(a). As a result, the angle between a and b differs from 90° by approximately 0.4°.

Below T_SDW, the spins order ferromagnetically along $\tilde{b}$ and antiferromagnetically along $\tilde{a}$. Due to the small difference between $\tilde{a}$ and $\tilde{b}$, the crystals are twinned below T_s, and the orthogonal $\tilde{a}$ and $\tilde{b}$ axes change roles at twin boundaries running along the directions of the tetragonal a and b axes. The orthorhombic distortion makes the proper definition of the axes important as has been shown for twin-free crystals by longitudinal and optical transport as well as by ARPES [23–28]. To obtain a single-domain orthorhombic crystal, we constructed a sample holder for applying uniaxial pressure parallel to the Fe-Fe direction.

B. Detwinning clamp

The detwinning clamp is similar to that used by Chu *et al.* [23]. Figures 1(b) and 1(c) show, respectively, a schematic drawing and a photograph of the clamp. The sample is attached to a thermally sinked copper block (1) with GE varnish, which remains sufficiently elastic at low temperatures and maintains good thermal contact between the holder (3) and the sample (4). The stress is applied using a copper-beryllium cantilever (2), which presses the sample against the body of the clamp. Upon tightening the screws (5), the force on the sample can be adjusted. In our experiment, the pressure is applied along the Fe-Fe bonds. The c axis of the sample is perpendicular to the force and parallel to the optical axis. The uniaxial pressure can be estimated from the rate of change of the tetragonal-to-orthorhombic phase transition at T_s. Using the experimentally derived rate of 1 K per 7 MPa [29,30], we find approximately 35 MPa for our experiment to be sufficient to detwin the sample.

C. Light scattering

The experiment was performed with a standard light scattering setup. We used two ion lasers (Ar^+ Coherent Innova 304C and Kr^+ Coherent Innova 400) and two diode pumped solid state lasers (Coherent Genesis MX SLM, Laser Quantum Ignis) providing a total of 14 lines ranging from 407 nm to 676 nm, corresponding to incident energies $\hbar\omega_\mathrm{I}$ between 3.1 and 1.8 eV. Due to this wide range, the raw data have to be corrected. The quantity of interest is the response function $R\chi''(\Omega)$ where $\Omega = \omega_\mathrm{I} - \omega_\mathrm{S}$ is the Raman shift, ω_S is the energy of the scattered photons and R is an experimental constant. Details of the calibration are described in Appendix A.

Application of the Raman selection rules requires well-defined polarizations for the exciting and scattered photons. The polarizations are given in Porto notation with the first and the second symbol indicating the directions of the incoming and scattered photons' electric fields $\mathbf{e}_\mathrm{I}$ and $\mathbf{e}_\mathrm{S}$, respectively. We use xyz for the laboratory system [see Fig. 1(d)]. The xz plane is vertical and defines the plane of incidence, yz is horizontal, xy is the sample surface, and the z axis is parallel to the optical axis and to the crystallographic c axis. For the sample orientation used here (see Fig. 1), the Fe-Fe bonds are parallel to x and y, specifically $\tilde{a} = (1, 0, 0) \parallel x$ and $\tilde{b} = (0, 1, 0) \parallel y$. Since the orthorhombicity below T_s is small, the angle between a and $\tilde{a}$ deviates only by 0.2° from 45°. It is therefore an excellent approximation to use $a \parallel x' = 1/\sqrt{2}(x + y) \equiv 1/\sqrt{2}(1, 1, 0)$ and $b \parallel y' = 1/\sqrt{2}(y - x) \equiv 1/\sqrt{2}(1, \bar{1}, 0)$.

As the angle of incidence of the exciting photons is as large as 66° in our setup [see Fig. 1(d)], the orientations of $\mathbf{e}_\mathrm{I}$ parallel and perpendicular to the xz plane are inequivalent. In particular, $\mathbf{e}_\mathrm{I}$ has a projection on the c axis for $\mathbf{e}_\mathrm{I} \parallel xz$. This effect was used before [8] and allows one to project out the E_g phonons in the x^*x and x^*y configurations, where $x^* \parallel (x + \alpha z)$ inside the crystal [see Fig. 1(d)]. For $\mathrm{BaFe_2As_2}$, the index of refraction is $n' = 2.2 + 2.1i$ at 514 nm, resulting in $\alpha \approx 0.4$ for an angle of incidence of 66°. The corresponding intensity contribution is then 0.16. As a consequence, x^*x and yy are inequivalent whereas $\mathbf{e}_\mathrm{I} = x'^* \parallel (x' + \alpha\, z/\sqrt{2})$ and $\mathbf{e}_\mathrm{I} = y'^* \parallel (y' + \alpha\, z/\sqrt{2})$ are equivalent for having the same projection on the c direction. Upon comparing x^*y and yx, the leakage of the c-axis polarized contributions to the electronic continuum can be tested. In the case here, they are below the experimental sensitivity. The effect of the finite angle of acceptance of the collection optics (±15° corresponding to a solid angle $\tilde{\Omega}$ of 0.21 sr) on the projections of the scattered photons can be neglected.

D. Theoretical calculations

The phonon eigenvectors $Q^{(\nu)}$ (displacement patterns of the vibrating atoms in the branch ν) and the energies of all Raman-active phonons of $\mathrm{BaFe_2As_2}$ in the tetragonal ($I4/mmm$) and the orthorhombic ($Fmmm$) phases were obtained from *ab initio* DFT calculations within the Perdew-Burke-Ernzerhof parametrization [31] of the generalized gradient approximation. The phonon frequencies were calculated by diagonalizing the dynamical matrices using the *phonopy* package [32,33]. The dynamical matrices were constructed from the force constants determined from the finite displacements in 2 × 2 × 1 supercells [34]. We used the projector augmented wave approximation [35], as implemented in the Vienna package (VASP) [36–38]. The Brillouin zone for one unit cell was sampled with a 10 × 10 × 10 **k** point mesh, and the plane wave cutoff was set at 520 eV. For the tetragonal phase, we used a Néel-type magnetic order to relax the structure and to obtain the experimental lattice parameters.[1] For the orthorhombic phase, we used the stripelike magnetic order shown in Fig. 1(a).

We have then calculated the complex Raman tensor $\alpha^{(\nu)}_{jk}(\omega_\mathrm{I}) = \alpha^{(\nu)\prime}_{jk}(\omega_\mathrm{I}) + i\alpha^{(\nu)\prime\prime}_{jk}(\omega_\mathrm{I})$, defined as the derivative of the dielectric tensor elements $\varepsilon_{jk}(\omega_\mathrm{I}) = \varepsilon'_{jk}(\omega_\mathrm{I}) + i\varepsilon''_{jk}(\omega_\mathrm{I})$ with respect to the normal coordinate of the respective phonon, $Q^{(\nu)}$. Since we are interested only in the resonance behavior of the As phonon, we only needed the derivatives with respect to $Q^{(\mathrm{As})}$,

$$\alpha^{(\mathrm{As})}_{ll}(\omega_\mathrm{I}) = \frac{\partial\varepsilon'_{ll}(\omega_\mathrm{I})}{\partial Q^{(\mathrm{As})}} + i\,\frac{\partial\varepsilon''_{ll}(\omega_\mathrm{I})}{\partial Q^{(\mathrm{As})}}. \tag{1}$$

To calculate the dielectric (tensor) function $\hat{\varepsilon}$ we used the *optics* code package [39] implemented in WIEN2k [40] with the full-potential linearized augmented plane-wave basis. The Perdew-Burke-Ernzerhof generalized gradient approximation [31] was employed as the exchange correlation functional and the basis-size controlling parameter $\mathrm{RK_{max}}$ was set to 8.5. A mesh of 400 **k** points in the first Brillouin zone for the self-consistency cycle was used. The DOS and dielectric tensors were computed using a 10 × 10 × 10 **k** mesh. For the dielectric tensor, a Lorentzian broadening of 0.1 eV was introduced.

III. RESULTS AND DISCUSSION

A. Lattice dynamics

The energies and symmetries as obtained from lattice dynamical calculations for tetragonal and orthorhombic

---

[1] The local correlations in the tetragonal phase are of the stripe type; however, we had to use a pattern that does not break the symmetry, and it is known [18] that the difference in the elastic properties calculated within different magnetic orders is much smaller than between magnetic and nonmagnetic calculations.

TABLE I. Raman-active phonons in $BaFe_2As_2$. The experimental and theoretically determined energies are given in cm^{-1}. In addition, the symmetry correlations between the tetragonal ($I4/mmm$) and orthorhombic ($Fmmm$) structures are shown.

$I4/mmm$				$Fmmm$		
	Exp. (140 K)	Theory			Exp. (60 K)	Theory
A_{1g}	180	168	→	A_g	180	172
B_{1g}	215	218	→	B_{1g}	215	221
$E_g^{(1)}$	130	140	↗	$B_{2g}^{(1)}$	125	110
			↘	$B_{3g}^{(1)}$	135	133
$E_g^{(2)}$	268	290	↗	$B_{2g}^{(2)}$	270	272
			↘	$B_{3g}^{(2)}$	273	287

$BaFe_2As_2$ are compiled in Table I. The four modes in tetragonal $I4/mmm$ symmetry obey $A_{1g} + B_{1g} + 2\ E_g$ selection rules. The eigenvectors are depicted in Fig. 2. In the orthorhombic $Fmmm$ phase, the two E_g modes are expected to split into B_{2g} and B_{3g} modes. Thus, there are six nondegenerate modes in the orthorhombic phase, $A_g + B_{1g} + 2\ B_{2g} + 2\ B_{3g}$. Table I shows the symmetry relations between the tetragonal and orthorhombic phonons.

Since the A_g and B_{1g} eigenvectors remain unchanged upon entering the orthorhombic phase, only those of the B_{2g} and B_{3g} phonons are shown in Fig. 3. For the B_{2g} and B_{3g} phonons, the As and Fe atoms move perpendicular to the c axis and perpendicular to each other. The calculated phonon vibrations agree with previous results for $BaFe_2As_2$ [7], however our energies differ slightly from those reported by Zbiri *et al.* [7]. In particular, we find a splitting between the $B_{2g}^{(1)}$ and $B_{3g}^{(1)}$ phonons.

B. E_g phonons

Table I displays the experimental phonon energies above and below the magneto-structural transition, along with the theoretical values. The $E_g^{(1)}$ phonon found at 130 cm^{-1} above T_s splits into two well-separated lines as predicted (Table I) and shown in Fig. 4. The splitting of the $E_g^{(2)}$ mode at 268 cm^{-1} is small, and the $B_{2g}^{(2)}$ and $B_{3g}^{(2)}$ modes are shifted to higher energies by 2 cm^{-1} and 5 cm^{-1}, respectively.

The theoretical and experimental phonon energies are in agreement to within 14% for both crystal symmetries. The splitting between the B_{2g} and B_{3g} modes is overestimated in the calculations.

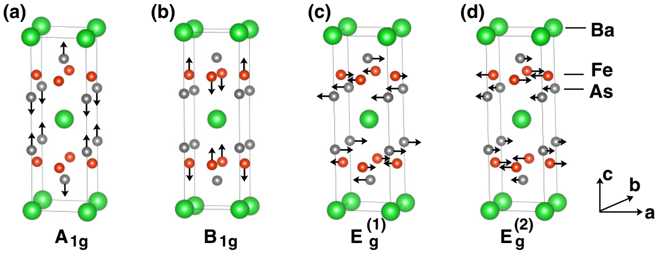

FIG. 2. Raman-active phonons in $BaFe_2As_2$ with the symmetry assignments in the tetragonal crystallographic unit cell abc.

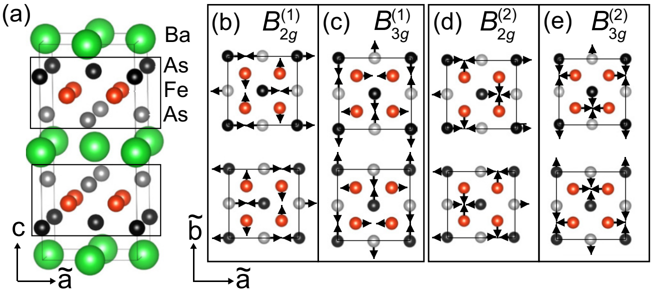

FIG. 3. B_{2g} and B_{3g} phonon modes in $BaFe_2As_2$ with the symmetry assignments in the orthorhombic crystallographic unit cell $\tilde{a}\tilde{b}c$.

Previous experiments were performed on twinned crystals [8,41,42] and the B_{2g} and B_{3g} modes were observed next to each other in a single spectrum. An equivalent result can be obtained in detwinned samples by using x'^*y', x'^*x', or RR polarizations where the x and y axes are simultaneously projected (along with the z axis). In neither case can the symmetry of the B_{2g} and B_{3g} phonons be pinned down. Only in a detwinned sample where the xz and yz configurations are projected separately, the B_{2g} and B_{3g} modes can be accessed independently.

Uniaxial pressure along the Fe-Fe direction, as shown by the black arrows in the insets of Fig. 4, determines the orientation of the shorter $\tilde{b}$ axis. This configuration enables us to observe the $B_{2g}^{(1)}$ mode at 125 cm^{-1} and the $B_{3g}^{(1)}$ mode at 135 cm^{-1} in x^*x and, respectively, x^*y polarization configurations, thus augmenting earlier work. With the shorter axis determined by

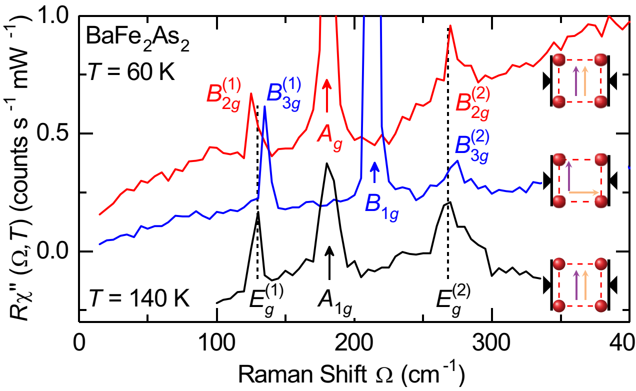

FIG. 4. Phonons in detwinned $BaFe_2As_2$. The spectra at 60 K (red and blue) are displayed with the experimental intensity. The spectrum at 140 K (black) is downshifted by 1.4 counts s^{-1} mW^{-1} for clarity. Each of the two tetragonal E_g phonons (vertical dashed lines) splits into two lines below T_s. The $B_{2g}^{(1)}$ and $B_{3g}^{(1)}$ lines appear at distinct positions for polarizations of the scattered light parallel (blue) and perpendicular (red) to the applied pressure as indicated in the insets. The $B_{2g}^{(2)}$ and $B_{3g}^{(2)}$ phonons are shifted only slightly upward with respect to the $E_g^{(2)}$ mode. Violet and orange arrows indicate the polarizations of the incident and scattered photons, respectively. The black triangles indicate the direction of the applied pressure. The shorter $\tilde{b}$ axis is parallel to the stress.

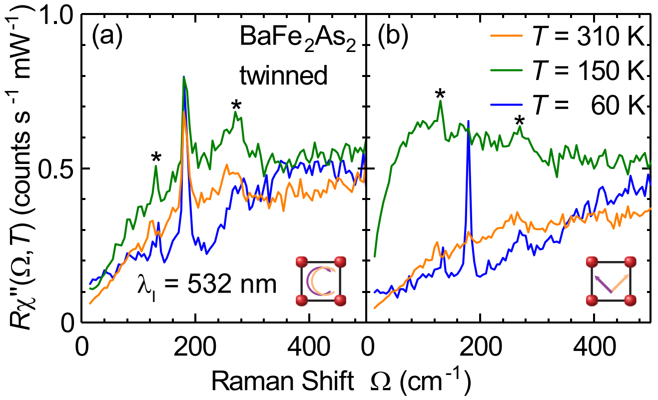

FIG. 5. Raman spectra of twinned BaFe$_2$As$_2$ at temperatures as indicated. The spectra were measured using $\hbar\omega_I = 2.33$ eV (532 nm). (a) In parallel RR polarization configuration (see inset), the As phonon appears at all temperatures. (b) For crossed light polarizations (ab), the As phonon is present only below the magnetostructural transition at $T_s = 135$ K as reported before [8]. Asterisks mark the E_g modes discussed in Sec. III B.

the direction of the stress (insets of Fig. 4) the assignment of the B_{2g} and B_{3g} modes is unambiguous. Since the x^*x spectrum (red) comprises $\tilde{a}\tilde{a}$ and $c\tilde{a}$ polarizations both the A_g and the B_{2g} phonons appear. The x^*y spectrum (blue) includes the B_{1g} ($\tilde{a}\tilde{b}$) and B_{3g} ($c\tilde{b}$) symmetries.

The calculated splitting between the B_{2g} and B_{3g} modes is smaller for the $E_g^{(2)}$ than for the $E_g^{(1)}$ mode, qualitatively agreeing with the experiment. However, in the calculations this difference is entirely due to the different reduced masses for these modes since the $E_g^{(1)}$ and $E_g^{(2)}$ phonon are dominated by As and Fe motions, respectively. In the experiment the splitting for the $E_g^{(2)}$ mode is close to the spectral resolution, indicating an additional reduction of the splitting below that obtained in the calculation. The source of this additional reduction is unclear at the moment.

C. As phonon line intensity

Figure 5 shows low-energy spectra of twinned BaFe$_2$As$_2$ for (a) RR and (b) ab polarization configurations at 310 (orange), 150 (green), and 60 K (blue). The As phonon at 180 cm^{-1} is the strongest line in the RR spectra at all temperatures as expected and gains intensity upon cooling. In ab polarizations, there is no contribution from the As mode above T_s. Below T_s (blue spectrum), the As phonon assumes a similar intensity as in the RR polarization as reported earlier [8,17]. Due to a finite projection of the incident light polarizations onto the c axis [see Fig. 1(d)] in both RR and ab configurations, the E_g phonons appear in all spectra (asterisks). The electronic continuum has been extensively discussed in previous works [43–47] and is not a subject of the study here.

To understand the appearance of the As line in the crossed ab polarizations, it is sufficient to consider the in-plane components of the A_g Raman tensor,

$$\hat{\alpha}^{(Ag)} = \begin{pmatrix} \alpha_{11} & 0 \\ 0 & \alpha_{22} \end{pmatrix}. \tag{2}$$

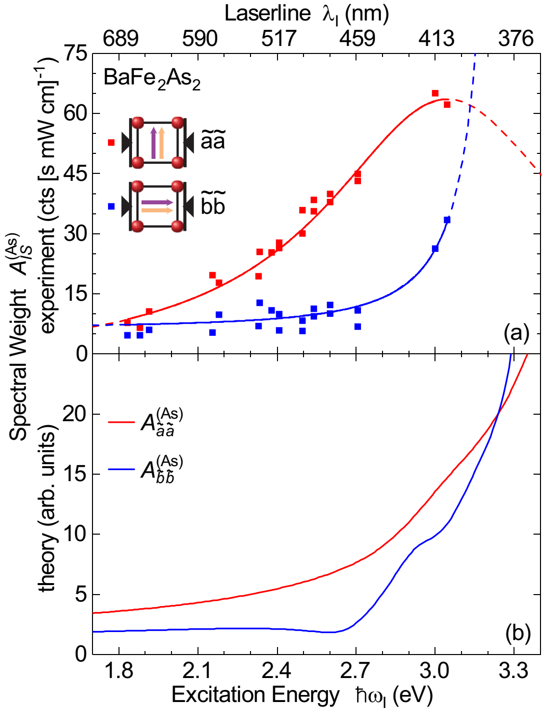

FIG. 6. Spectral weight $A_{IS}^{(As)}(\omega_I)$ of the As phonon as a function of excitation energy and polarization. The top axis shows the corresponding wavelength of the exciting photons. (a) Experimental data. The intensity for parallel light polarizations along the ferromagnetic axis ($\tilde{b}\tilde{b}$, blue squares) is virtually constant for $\hbar\omega_I < 2.7$ eV and increases rapidly for $\hbar\omega_I > 2.7$ eV. For light polarizations along the antiferromagnetic axis ($\tilde{a}\tilde{a}$, red squares), the phonon intensity increases monotonically over the entire range studied. The solid lines are Lorentzian functions whose extrapolations beyond the measured energy interval are shown as dashed lines. (b) Theoretical prediction of $A_{\tilde{a}\tilde{a}}^{(As)}$ (red) and $A_{\tilde{b}\tilde{b}}^{(As)}$ (blue). The curves qualitatively reproduce the experimental data shown in panel (a).

The response of this phonon for the polarization configuration ($\mathbf{e}_I$,$\mathbf{e}_S$) is given by $\chi_{IS}^{\prime\prime(As)} \propto |\mathbf{e}_S^* \cdot \hat{\alpha}^{(Ag)} \cdot \mathbf{e}_I|^2$ (where * means conjugate transposed). In the tetragonal (A_{1g}) case, the two elements are equal, $\alpha_{11} = \alpha_{22}$, and the phonon appears only for $\mathbf{e}_S \parallel \mathbf{e}_I$. In the orthorhombic phase the tensor elements are different, and one can expect the phonon to appear for $\mathbf{e}_S \perp \mathbf{e}_I$ since then the intensity depends on the difference between α_{11} and α_{22}.

In detwinned samples, α_{11} and α_{22} can be accessed independently by using parallel polarizations for the incident and scattered light oriented along either the $\tilde{a}$ or the $\tilde{b}$ axis. In addition, putative imaginary parts of α_{ii} may be detected by analyzing more than two polarization combinations as discussed in Appendix C. Spectra for $\tilde{a}\tilde{a}$ and $\tilde{b}\tilde{b}$ configurations are shown in Fig. 7 of Appendix B and we proceed here directly with the analysis of the phonon spectral weight $A_{IS}^{(As)}(\omega_I)$ as a function of the incident photon excitation energy ($\hbar\omega_I$) and polarization.

Figure 6(a) shows $A_{IS}^{(As)}(\omega_I)$ as derived by fitting the peak with a Voigt function, after subtracting a linear background. Measurements were repeated several times to check the reproducibility. The variation of the spectral weight between different measurements can be taken as an estimate of the experimental error. For light polarizations parallel to the antiferromagnetic $\tilde{a}$ axis, $A^{(\mathrm{As})}_{\tilde{a}\tilde{a}}(\omega_{\mathrm{I}})$ (red squares) increases continuously with increasing $\hbar\omega_{\mathrm{I}}$ whereas $A^{(\mathrm{As})}_{\tilde{b}\tilde{b}}$ (blue squares) stays virtually constant for incident photons in the red and green spectral range, $\hbar\omega_{\mathrm{I}} < 2.7$ eV, and increases rapidly for $\hbar\omega_{\mathrm{I}} > 2.7$ eV. For all wavelengths, the spectral weight is higher for the $\tilde{a}\tilde{a}$ than for the $\tilde{b}\tilde{b}$ configuration.

The variations of $A^{(\mathrm{As})}_{\tilde{a}\tilde{a}}(\omega_{\mathrm{I}})$ and $A^{(\mathrm{As})}_{\tilde{b}\tilde{b}}(\omega_{\mathrm{I}})$ display a typical resonance behavior [48], which is expected when the intermediate state of the Raman scattering process is an eigenstate of the electronic system. Then, in second-order perturbation theory, the intensity diverges as $|\hbar\omega_{\mathrm{I}} - E_0|^{-2}$, where E_0 is the energy difference between an occupied and an unoccupied electronic Bloch state. In real systems having a finite electronic lifetime, a Lorentzian profile is expected. We therefore approximated $A^{(\mathrm{As})}_{IS}(\omega_{\mathrm{I}})$ with Lorentzians centered at $E_{0,IS}$ as shown by solid lines in Fig. 6(a). From these model functions we determine $E_{0,\tilde{a}\tilde{a}} = 3.1$ eV and $E_{0,\tilde{b}\tilde{b}} = 3.3$ eV.

As discussed in the Introduction, the band structure needs to be renormalized so as to account for correlation effects (for details, see Appendix D). To this end, we differentiated three regions: (i) the unoccupied Fe 3d bands near the Fermi energy that we rescale uniformly, (ii) the occupied bands below −2.7 eV of predominantly As 4p character that remain unchanged, and (iii) the occupied bands between −2.7 eV and the Fermi level derived from hybridized Fe 3d and As 4p orbitals. Due to this hybridization, the renormalization of the latter bands cannot be performed by simple rescaling. One can anticipate that the optical absorption would set in at energies below 1.8 eV, smaller than our minimal laser energy, if the occupied Fe bands would have been renormalized prior to hybridization with the As bands. Due to the small DOS of the As bands in the range from −2.7 eV to E_{F}, their contribution to the dielectric function would be small. With this in mind, we simply excluded all occupied bands in this range from the calculations. The effect of these bands, although small, could be accounted for using the DMFT method, which, however, is beyond the scope of our present work.

The results obtained as described above are presented in Fig. 6(b). One can see that the resonances lie in the range $\hbar\omega_{\mathrm{I}} > 2.7$ eV, and our calculations capture both the intensities and the $\tilde{a} - \tilde{b}$ anisotropy in this range rather well. Note that the antiferromagnetic ordering along the $\tilde{a}$ axis entails a backfolding of the electronic bands; we tentatively ascribe the much larger width of the resonance in the $\tilde{a}\tilde{a}$ configuration to this backfolding.

A corollary of our analysis is that resonance effects are the main source of the anomalous intensity of the As phonon in crossed polarizations. The main experimental argument is based on the anisotropic variation of the phonon intensities with $\hbar\omega_{\mathrm{I}}$ in $\tilde{a}\tilde{a}$ and $\tilde{b}\tilde{b}$ polarization configurations that comes about because of band reconstruction at higher energies. As proposed previously [16], magnetism appears to be the origin of the anisotropy. However, the intensity anisotropy cannot be explained without taking into account the high-energy electronic states.

Finally, we briefly look into the cross-polarization anomaly and find further support for its magnetic origin. In $\mathrm{Ba(Fe_{1-x}Co_x)_2As_2}$, the transition temperature T_{SDW} is several degrees below T_{s} for a finite x, and one observes that the anomaly of the As phonon does not appear at T_{s}, but rather at the magnetic transition. For $x = 0.025$, the phonon assumes intensity in crossed polarizations only below T_{SDW} (see supplementary information of Ref. [46]). For $x = 0.051$, the anomaly appears at T_{s}, as displayed in Fig. 10 in the Appendix but the spectral weight does not show an order-parameter-like temperature dependence. The increase is nearly linear and saturates below T_{SDW} at a value which is smaller by approximately a factor of 7 than that in the RR polarization projecting A_g/A_{1g} symmetry. In FeSe, with a structural transition at $T_{\mathrm{s}} = 89.1$ K but no long-range magnetism [49], the anomalous intensity can also be observed below T_{s} but the intensity relative to that in the A_g projection is only 1%, as shown in Fig. 11. Similar to $\mathrm{Ba(Fe_{0.949}Co_{0.051})_2As_2}$, the spectral weight increases approximately linearly but does not saturate, presumably because FeSe does not develop a long-ranged magnetic order.

IV. CONCLUSION

We studied the Raman scattering for three As phonons, the two E_g, and the one fully symmetric modes, in twin-free $\mathrm{BaFe_2As_2}$, accompanied by DFT calculations of Raman intensities, with the goal of clarifying the impact of magnetism on electrons and phonons.

The tetragonal E_g phonons at 130 cm^{-1} ($E_g^{(1)}$) and 268 cm^{-1} ($E_g^{(2)}$) were studied with the laser line at 532 nm and found to split into two modes in the orthorhombic phase. The detwinning allows us to identify the modes at 125 cm^{-1} and 135 cm^{-1} as the $B_{2g}^{(1)}$ and $B_{3g}^{(1)}$ phonons, respectively. DFT calculations predict the symmetries correctly and show that the splitting occurs because of the stripe magnetic order (and not because of the orthorhombic distortion).

The As A_g phonon was studied for various laser lines in the range 1.8 to 3.1 eV. In the ordered phase, the spectral weight of the phonon resonates for an excitation energy of (3.2 ± 0.1) eV. The resonance energy is almost the same for the light polarized along the ferro- or antiferromagnetic directions $\tilde{b}$ and $\tilde{a}$ [for the definition of the axes see Fig. 1(a)], whereas the variation of the spectral weight with the energy of the incident photon is rather different for the $\tilde{b}\tilde{b}$ and $\tilde{a}\tilde{a}$ configurations. The larger width of the resonance in $\tilde{a}\tilde{a}$ configuration can be understood qualitatively in terms of band backfolding along the antiferromagnetic direction.

Our DFT calculations reproduce the anisotropy and the resonance very well for energies above 2.7 eV if we include both the effects of the magnetism and of the correlations-induced renormalization of Fe 3d bands. Due to DFT limitations, for energies below 2.7 eV, where correlated Fe 3d bands are strongly hybridized with the As bands, our approximation is only semiquantitative. Further studies based, for instance, on DMFT or other many-body methods are needed to test this approximation, apart from experimental verification. As in the case of the E_g phonons, all effects are strongly linked to magnetism. However, in the case of the As phonon, the inclusion of electronic states at high energies is essential because of the observed resonance behavior. Weak-coupling, low-energy physics with magnetism-induced anisotropic electron-phonon coupling [16] appears insufficient for explaining the anomalous intensity in crossed polarizations.

More generally, our experimental observations and theoretical studies indicate the importance of orbital-dependent band renormalizations and of (nearly) localized ordered spins on the electronic properties at all energy scales.

ACKNOWLEDGMENTS

We gratefully acknowledge discussions with L. Degiorgi and thank him for providing us with raw and analyzed IR data of BaFe$_2$As$_2$. The work was supported by the Deutsche Forschungsgemeinschaft (DFG) via the Priority Program No. SPP 1458, the Transregional Collaborative Research Centers TRR 80 and TRR 49, and by the Serbian Ministry of Education, Science and Technological Development under Project No. III45018. We acknowledge support by the DAAD through the bilateral project between Serbia and Germany (Grants No. 56267076 and No. 57142964). The collaboration with Stanford University was supported by the Bavaria California Technology Center BaCaTeC (Grant No. A5 [2012-2]). Work in the SIMES at Stanford University and SLAC was supported by the U.S. Department of Energy, Office of Basic Energy Sciences, Division of Materials Sciences and Engineering, under Contract No. DE-AC02-76SF00515. Y.L. and R.V. acknowledge the allotment of computer time at the Centre for Scientific Computing (CSC) in Frankfurt. I.I.M. was supported by ONR through the NRL basic research program and by the Alexander von Humboldt-Stiftung.

APPENDIX A: CALIBRATION OF THE SENSITIVITY

Scattering experiments performed over a wide energy range necessitate an appropriate correction of the data. The quantity of interest is the response function $R\chi''_{IS}(\Omega)$ where $\Omega = \omega_\mathrm{I} - \omega_\mathrm{S}$ is the Raman shift, and ω_S is the energy of the scattered photons. R includes all experimental constants and units in a way that $R\chi''_{IS}(\Omega)$ is as close as possible to the count rate $\dot{N}^*_{I,S}$, measured for a given laser power $P_\mathrm{I} = I_\mathrm{I}\hbar\omega_\mathrm{I}$ absorbed by the sample. I_I is the number of incoming photons per unit time and I, S refer to both photon energies and polarizations. With A_f, the (nearly) energy-independent area of the laser focus the cross section is given by [50]

$$\frac{\dot{N}^*_{IS}(\Delta\omega_\mathrm{S},\Delta\tilde{\Omega})}{P_I}\hbar\omega_\mathrm{I}A_\mathrm{f} = R^* r(\omega_\mathrm{S})\frac{d^2\sigma}{d\omega_\mathrm{S}d\tilde{\Omega}}\Delta\omega_\mathrm{S}\Delta\tilde{\Omega}. \qquad \text{(A1)}$$

R^* and $r(\omega_\mathrm{S})$ are a constant and the relative sensitivity, respectively. $r(\omega_\mathrm{S})$ is assumed to be dimensionless and includes energy-dependent factors such as surface losses, penetration depth, and the monochromatic efficiency of the setup. $\Delta\omega_\mathrm{S}$ and $\Delta\tilde{\Omega}$ are the bandwidth and the solid angle of acceptance, respectively, and depend both on ω_S. $r(\omega_\mathrm{S})\Delta\omega_\mathrm{S}\Delta\tilde{\Omega}$ is determined by calibration and used for correcting the raw data. The resulting rate $\dot{N}_{IS}$ is close to $\dot{N}^*_{IS}$ in the range $\Omega \leqslant 1,000\,\mathrm{cm}^{-1}$ but increasingly different for larger energy transfers mainly for the strong variation of $\Delta\omega_\mathrm{S}$. Applying the fluctuation-dissipation theorem, one obtains

$$\begin{aligned}\frac{\dot{N}_{IS}}{P_I}\hbar\omega_\mathrm{I}A_\mathrm{f} &= R'\frac{d^2\sigma}{d\omega_\mathrm{S}d\tilde{\Omega}}\\ &= R'\frac{\hbar}{\pi}r_0^2\frac{\omega_\mathrm{S}}{\omega_\mathrm{I}}\{1+n(\Omega,T)\}\chi''(\Omega),\end{aligned} \qquad \text{(A2)}$$

where R' is another constant, which is proportional to $\Delta\omega_\mathrm{S}(\omega_0)\Delta\tilde{\Omega}(\omega_0), n(\Omega,T) = [\exp(\frac{\hbar\Omega}{k_BT}) - 1]^{-1}$ is the thermal Bose factor and r_0 is the classical electron radius. Finally, after collecting all energy-independent factors in R we obtain

$$R\chi''_{IS}(\Omega) = \frac{\dot{N}_{IS}}{P_\mathrm{I}}\frac{\omega_\mathrm{I}^2}{\omega_0\omega_\mathrm{S}}\left\{1-\exp\left(-\frac{\hbar\Omega}{k_BT}\right)\right\}. \qquad \text{(A3)}$$

Here, $\omega_0 = 20,000\,\mathrm{cm}^{-1}$ is inserted for convenience to get a correction close to unity. Therefore, the spectra shown reflect the measured number of photon counts per second and mW absorbed power as closely as possible, thus approximately obeying counting statistics as intended. Since the spectra are taken with constant slit width the spectral resolution depends on energy, and narrow structures such as phonons may change their shapes but the spectral weight is energy independent.

APPENDIX B: A_g SPECTRA

Figure 7 shows the complete set of the A_g spectra we measured for detwinned BaFe$_2$As$_2$ and used for deriving the spectral weights $A^{(\mathrm{As})}_{\tilde{a}\tilde{a}}(\omega_\mathrm{I})$ and $A^{(\mathrm{As})}_{\tilde{b}\tilde{b}}(\omega_\mathrm{I})$ displayed in Fig. 6(a). All spectra were corrected as described in Appendix A. For all spectra, the same constant width of 550 μm of the intermediate slit of the spectrometer was used. This results in an energy-dependent resolution varying between approximately 12 cm^{-1} at 24,630 cm^{-1} (3.05 eV or 406 nm) and 3 cm^{-1} at 14,793 cm^{-1} (1.83 eV or 676 nm). Accordingly, the width of the peak changes as a function of the excitation wavelength and does not reflect the intrinsic line width of the phonon, in particular

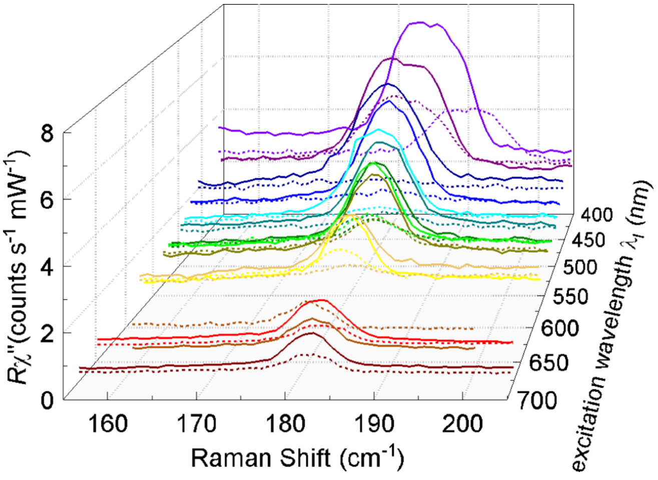

FIG. 7. (Color online.) A_g spectra of detwinned BaFe$_2$As$_2$ at various laser wavelengths λ_I. We used laser lines between 406 and 676 nm and parallel polarizations of incoming and outgoing photons along the antiferromagnetic ($\tilde{a}\tilde{a}$, solid lines) and the ferromagnetic ($\tilde{b}\tilde{b}$, dashed lines) direction.

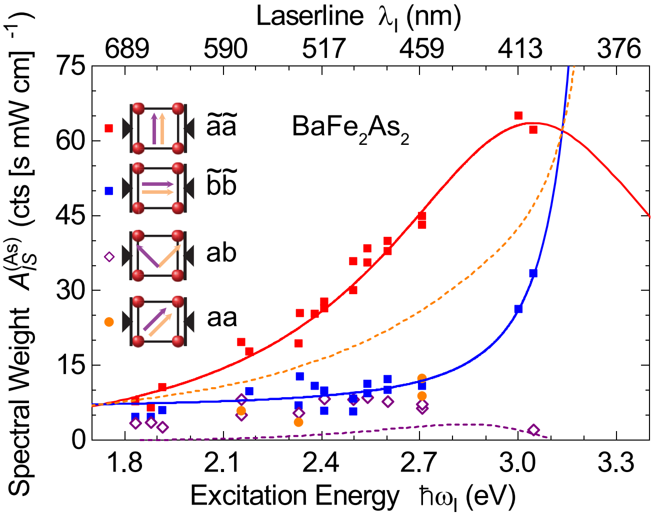

FIG. 8. Spectral weight $A_{IS}^{(\mathrm{As})}(\omega_\mathrm{I})$ of the As phonon as a function of excitation energy and polarization. The top axis shows the corresponding wavelength of the exciting photons. The data for $\tilde{a}\tilde{a}$ (red squares) and $\tilde{b}\tilde{b}$ (blue squares) polarizations as well as the Lorentzian model functions (red and blue solid lines) are identical to Fig. 6(a). The intensity for crossed (*ab*, purple diamonds) and for *aa* polarizations (orange dots) is comparable to the intensity found for $\tilde{b}\tilde{b}$ polarization. The purple dashed line is the intensity for *ab* polarization calculated from the fitted resonance profiles (solid lines) assuming a Raman tensor with real elements. The orange dashed line shows the same calculation for *aa* polarization.

not for blue photons. The intensity of the peak monotonically increases towards short wavelengths for the $\tilde{a}\tilde{a}$ spectra (solid lines). For light polarized parallel to the ferromagnetic axis ($\tilde{b}\tilde{b}$, dashed lines), the intensity is low for $\lambda_\mathrm{I} > 450$ nm, but strongly increases for $\lambda_\mathrm{I} < 450$ nm. The underlying electronic continuum, which is not a subject of this paper, also changes in intensity as a function of the excitation wavelength. From the spectra, the spectral weight $A_{IS}^{(\mathrm{As})}(\omega_\mathrm{I})$ of the phonon can be derived by fitting a Voigt function to the phonon peak after subtracting a linear background. The width of the Gaussian part of the Voigt function is given by the known resolution of the spectrometer while that of the Lorentzian part reflects the line width of the phonon.

APPENDIX C: SPECTRAL WEIGHT FOR *aa* AND *ab* POLARIZATIONS

Since the ratio $A_{ab}^{(\mathrm{As})}/A_{aa}^{(\mathrm{As})}$ was not in the main focus of our work, Fig. 6(a) displays only part of the data we collected. We also measured spectra in *aa* and *ab* configurations (cf. Figs. 1(a) and 8 for the definitions) and find them instructive for two reasons. The *aa* and *ab* data (i) can be compared directly with results presented recently [17] and (ii) indicate that the Raman tensor has large imaginary parts which can result only from absorption processes. Figure 8 shows the spectral weights of the As phonon mode for *aa* and *ab* polarizations, $A_{aa}^{(\mathrm{As})}(\omega_\mathrm{I})$ (orange circles) and $A_{ab}^{(\mathrm{As})}(\omega_\mathrm{I})$ (open purple diamonds), respectively, for selected wavelengths together with the data and model functions from Fig. 6(a) of the main text. Given the experimental error, the respective intensities for *aa* and *ab* polarizations are rather similar and are also comparable to $A_{\tilde{b}\tilde{b}}^{(As)}(\omega_\mathrm{I})$ (blue squares) in the range $1.9 < \hbar\omega_\mathrm{I} \leqslant 2.7$ eV. For $\hbar\omega_\mathrm{I} = 3.05$ eV (406 nm), $A_{ab}^{(As)}(\omega_\mathrm{I})$ is very small, for the yellow-green spectral range $A_{ab}^{(As)}(\omega_\mathrm{I})$ may be even larger than $A_{aa}^{(\mathrm{As})}(\omega_\mathrm{I})$ in qualitative agreement with Ref. [17].

If the elements of the Raman tensor $\hat{\alpha}^{(\mathrm{Ag})}$ [Eq. (2) of the main text] would be strictly real, they could be derived directly from the experimental data as $\alpha_{11} = \sqrt{A_{\tilde{a}\tilde{a}}^{(As)}}$ and $\alpha_{22} = \sqrt{A_{\tilde{b}\tilde{b}}^{(As)}}$. Then, the phonon's spectral weight expected for all other polarizations could be calculated right away, and $A_{aa}^{(As)}$ is just the average of $A_{\tilde{a}\tilde{a}}^{(As)}$ and $A_{\tilde{b}\tilde{b}}^{(As)}$ (dashed orange line in Fig. 8). Obviously, there is no agreement with the experimental values for $A_{aa}^{(As)}$ (orange circles).

$A_{ab}^{(As)}$ can be determined in a similar fashion. In Fig. 8, we show the expected spectral weight as purple dashed line. The dependence on ω_I is again derived from the model functions describing the resonance (full red and blue lines). Also for $A_{ab}^{(As)}$, the mismatch between experiment (open purple diamonds) and expectation (purple dashed line) is statistically significant, and one has to conclude that the assumption of real tensor elements in the orthorhombic phase is not valid.

This effect is not particularly surprising in an absorbing material and was in fact discussed earlier for the cuprates [51,52]. For the Fe-based systems, the possibility of complex Raman tensor elements for the As phonon was not considered yet. Our experimental observations show that the complex nature of $\hat{\alpha}^{(\mathrm{Ag})}$ is crucially important and that the imaginary parts of α_{11} and α_{22} must have opposite sign to explain the observed enhancement of $A_{ab}^{(\mathrm{As})}(\omega_\mathrm{I})$ and the suppression of $A_{aa}^{(\mathrm{As})}(\omega_\mathrm{I})$ with respect to the values expected for real tensor elements (dashed orange and purple lines in Fig. 8).

In summary, the results for $A_{aa}^{(As)}(\omega_\mathrm{I})$ and $A_{ab}^{(As)}(\omega_\mathrm{I})$ along with those for $A_{\tilde{a}\tilde{a}}^{(As)}(\omega_\mathrm{I})$ and $A_{\tilde{b}\tilde{b}}^{(As)}(\omega_\mathrm{I})$ support our point of view that absorption processes are important for the proper interpretation of the Raman data. Currently, we cannot imagine anything else but resonance effects due to interband transitions as the source.

APPENDIX D: BAND STRUCTURE

The DFT band structure is shown in Fig. 9. Bands above E_F stem predominantly from Fe $3d$ orbitals (brown) while for $E < -2.7$ eV As $4p$ orbitals prevail (black). For a suitable comparison to the experiment these Fe bands are renormalized by a factor between 2 and 3 [53–56] while no renormalization is needed for the As bands. The bands between -2.7 eV and E_F are of mixed Fe/As character and are left out when calculating the dielectric tensor as is illustrated by the grey shade in Fig. 9. Only transitions between the ranges [-5.5 eV,-2.7 eV] and [0,2.6 eV], highlighted by turquoise rectangles, are taken into account. Thus for photon energies below 2.7 eV, the absorption in our calculations originates predominantly from the Drude response whereas for $\hbar\omega_\mathrm{I} > 2.7$ eV the results become increasingly realistic since they include interband absorption. In either case, we use a phenomenological damping of 0.1 eV. We determine the dielectric tensor and the Raman tensor as described in Sec. II D on the basis of this renormalized

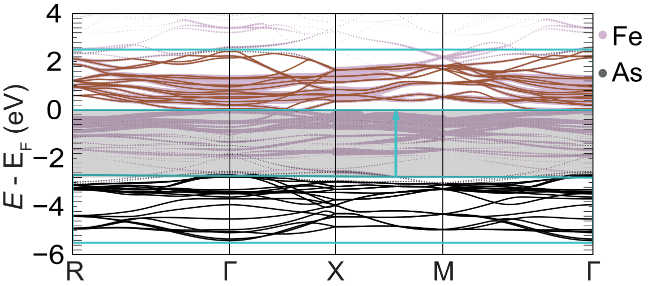

FIG. 9. DFT band structure. Bands predominantly from Fe states are shown in brown, bands predominantly from As states in black. The shaded region from −2.7 eV to E_F contains bands of mixed character and is blacked out for the calculation of the dielectric tensor. Only transitions between the bands within the turquoise frames are included.

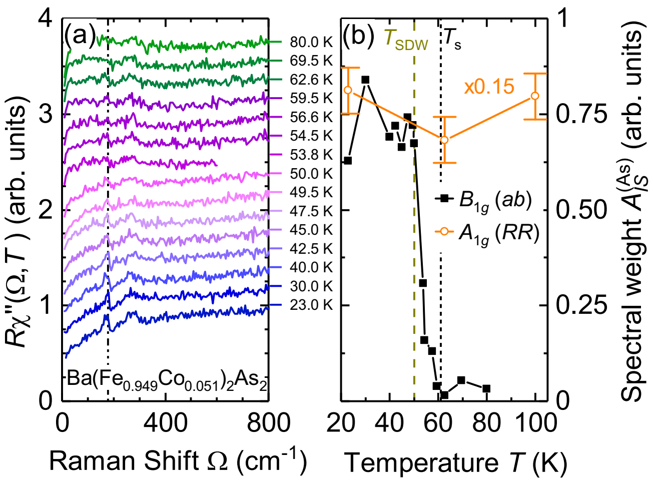

FIG. 10. As phonon in crossed polarizations for Ba(Fe$_{1-x}$Co$_x$)$_2$As$_2$ at $x = 0.051$. (a) Raw data for temperatures as indicated. The phonon position is shown as a vertical dash-dotted line. The spectra are shifted vertically for clarity. (b) Temperature dependence of the spectral weight. The spectral weight in A_{1g} symmetry (orange circles) was multiplied by 0.15. T_s and T_SDW are indicated as vertical dashed lines.

band structure. While the $\tilde{a} - \tilde{b}$ anisotropy is qualitatively reproduced for all energies ω_I as shown in Fig. 6(b) of the main text, the two other experimental quantities, $A_{ab}^{(\mathrm{As})}(\omega_\mathrm{I})$ (purple) and $A_{aa}^{(\mathrm{As})}(\omega_\mathrm{I})$ (orange) shown in Fig. 8 here, are not captured properly simply because the imaginary parts of the theoretically determined tensor elements $\alpha_{ii}^{(\mathrm{As})\prime\prime}$ become very small below 2.7 eV. To describe $A_{aa}^{(\mathrm{As})}(\omega_\mathrm{I})$ and $A_{ab}^{(\mathrm{As})}(\omega_\mathrm{I})$, absorption processes which lead to imaginary parts of the Raman tensor are necessary. Upon phenomenologically introducing imaginary parts of $\hat{\alpha}$ for low energies, which cut off at 2.7 eV where the correct absorption takes over, full agreement can be achieved. However, a solution on a microscopic basis becomes possible only by using schemes that include many-body effects beyond DFT.

APPENDIX E: INTERRELATION OF THE A_g PHONON ANOMALY AND MAGNETISM IN Ba(Fe$_{1-x}$Co$_x$)$_2$As$_2$ AND FeSe

Similarly as in BaFe$_2$As$_2$, the anomalous intensity of the A_g phonon in crossed polarizations is also linked to magnetic order in other Fe-based systems as shown for Ba(Fe$_{1-x}$Co$_x$)$_2$As$_2$ at $x = 0.025$ a while ago [46] and more recently for EuFe$_2$As$_2$, NaFeAs, LaFeAsO, and FeSe [17]. Here, we add a few more results which support our interpretation. Figure 10(a) shows Raman spectra in *ab* polarization of Ba(Fe$_{1-x}$Co$_x$)$_2$As$_2$ with $x = 5.1\%$ having $T_\mathrm{s} = 60.9\,\mathrm{K}$ and $T_\mathrm{SDW} = 50.0\,\mathrm{K}$. The As mode appears below T_s and gains strength upon cooling. Figure 10(b) shows the corresponding spectral weight as a function of temperature. In the nematic phase $T_\mathrm{SDW} < T < T_\mathrm{s}$, the phonon spectral weight increases almost linearly upon cooling (rather than order-parameter-like), becomes constant in the magnetic phase for $T < T_\mathrm{SDW}$ and reaches approximately 15% of that in the fully symmetric channel (A_g/A_{1g}).

In FeSe, the Se phonon appears also in the *ab* spectra as shown in Fig. 11(a) when the temperature is lowered below the structural phase transition at $T_\mathrm{s} \approx 90\,\mathrm{K}$. Upon cooling [Fig. 11(b)], the spectral weight of the phonon increases almost linearly for crossed polarizations (*ab*, black squares), but stays virtually constant across the phase transition for parallel light polarizations [*RR*, orange circles in Fig. 11(b)]. As opposed to Ba(Fe$_{1-x}$Co$_x$)$_2$As$_2$, no saturation of the spectral weight in *ab* polarizations is found, likely because FeSe shows no long-range magnetic order down to the lowest temperatures [49]. Only about 1% of the spectral weight of the A_{1g} spectra (*RR*) is found in crossed polarizations here, in contrast to BaFe$_2$As$_2$ and Ba(Fe$_{1-x}$Co$_x$)$_2$As$_2$, where the spectral weight of the phonon is larger (Figs. 5 and 10).

The nearly linear temperature dependence in both FeSe and Ba(Fe$_{1-x}$Co$_x$)$_2$As$_2$ and the larger saturation value in magnetically ordered Ba(Fe$_{1-x}$Co$_x$)$_2$As$_2$ indicate that the anomalous intensity is more likely related to magnetism than to the orthorhombic distortion.

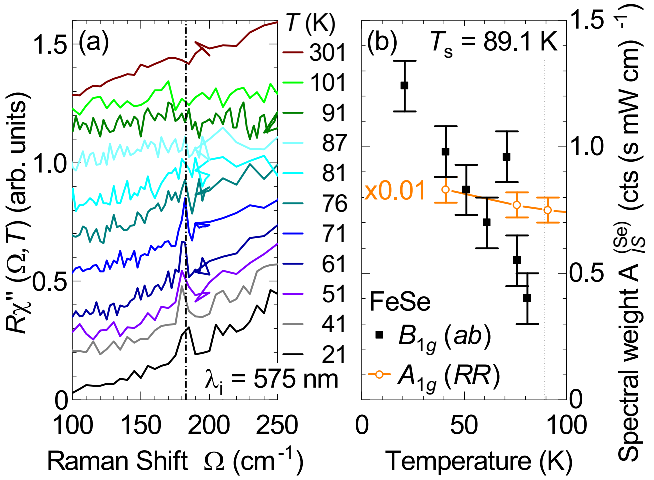

FIG. 11. Se phonon in crossed polarization for FeSe. (a) Raw data for temperatures as indicated. The phonon position is shown as dash-dotted line. The spectra are shifted vertically for clarity. (b) Temperature dependence of the spectral weight. The spectral weight in A_{1g} symmetry (orange circles) was multiplied by 0.01. T_s is indicated as vertical dotted line.

[1] A. S. Sefat and D. J. Singh, Chemistry and electronic structure of iron-based superconductors, MRS Bull. **36**, 614 (2011).

[2] F. Wang, S. A. Kivelson, and D.-H. Lee, Nematicity and quantum paramagnetism in FeSe, Nat. Phys. **11**, 959 (2015).

[3] Y. Gallais and I. Paul, Charge nematicity and electronic Raman scattering in iron-based superconductors, C. R. Phys. **17**, 113 (2016).

[4] M. Yi, Y. Zhang, Z.-X. Shen, and D. Lu, Role of the orbital degree of freedom in iron-based superconductors, npj Quantum Mater. **2**, 57 (2017).

[5] A. E. Böhmer and A. Kreisel, Nematicity, magnetism and superconductivity in FeSe, J. Phys.: Condens. Matter **30**, 023001 (2018).

[6] T. Yildirim, Strong Coupling of the Fe-Spin State and the As-As Hybridization in Iron-Pnictide Superconductors from First-Principle Calculations, Phys. Rev. Lett. **102**, 037003 (2009).

[7] M. Zbiri, H. Schober, M. R. Johnson, S. Rols, R. Mittal, Y. Su, M. Rotter, and D. Johrendt, Ab initio lattice dynamics simulations and inelastic neutron scattering spectra for studying phonons in $BaFe_2As_2$: Effect of structural phase transition, structural relaxation, and magnetic ordering, Phys. Rev. B **79**, 064511 (2009).

[8] L. Chauvière, Y. Gallais, M. Cazayous, A. Sacuto, M. A. Méasson, D. Colson, and A. Forget, Doping dependence of the lattice dynamics in $Ba(Fe_{1-x}Co_x)_2As_2$ studied by Raman spectroscopy, Phys. Rev. B **80**, 094504 (2009).

[9] L. Chauvière, Y. Gallais, M. Cazayous, M. A. Méasson, A. Sacuto, D. Colson, and A. Forget, Raman scattering study of spin-density-wave order and electron-phonon coupling in $Ba(Fe_{1-x}Co_x)_2As_2$, Phys. Rev. B **84**, 104508 (2011).

[10] M. Rahlenbeck, G. L. Sun, D. L. Sun, C. T. Lin, B. Keimer, and C. Ulrich, Phonon anomalies in pure and underdoped $R_{1-x}K_xFe_2As_2$ (R = Ba, Sr) investigated by Raman light scattering, Phys. Rev. B **80**, 064509 (2009).

[11] P. Kumar, A. Kumar, S. Saha, D. V. S. Muthu, J. Prakash, S. Patnaik, U. V. Waghmare, A. K. Ganguli, and A. K. Sood, Anomalous Raman scattering from phonons and electrons of superconducting $FeSe_{0.82}$, Solid State Commun. **150**, 557 (2010).

[12] R. Mittal, L. Pintschovius, D. Lamago, R. Heid, K.-P. Bohnen, D. Reznik, S. L. Chaplot, Y. Su, N. Kumar, S. K. Dhar, A. Thamizhavel, and T. Brueckel, Measurement of Anomalous Phonon Dispersion of $CaFe_2As_2$ Single Crystals Using Inelastic Neutron Scattering, Phys. Rev. Lett. **102**, 217001 (2009).

[13] V. Gnezdilov, Y. G. Pashkevich, P. Lemmens, D. Wulferding, T. Shevtsova, A. Gusev, D. Chareev, and A. Vasiliev, Interplay between lattice and spin states degree of freedom in the FeSe superconductor: Dynamic spin state instabilities, Phys. Rev. B **87**, 144508 (2013).

[14] V. Gnezdilov, Y. Pashkevich, P. Lemmens, A. Gusev, K. Lamonova, T. Shevtsova, I. Vitebskiy, O. Afanasiev, S. Gnatchenko, V. Tsurkan, J. Deisenhofer, and A. Loidl, Anomalous optical phonons in FeTe chalcogenides: Spin state, magnetic order, and lattice anharmonicity, Phys. Rev. B **83**, 245127 (2011).

[15] A. Akrap, J. J. Tu, L. J. Li, G. H. Cao, Z. A. Xu, and C. C. Homes, Infrared phonon anomaly in $BaFe_2As_2$, Phys. Rev. B **80**, 180502 (2009).

[16] N. A. García-Martínez, B. Valenzuela, S. Ciuchi, E. Cappelluti, M. J. Calderón, and E. Bascones, Coupling of the As A_{1g} phonon to magnetism in iron pnictides, Phys. Rev. B **88**, 165106 (2013).

[17] S.-F. Wu, W.-L. Zhang, V. K. Thorsmølle, G. F. Chen, G. T. Tan, P. C. Dai, Y. G. Shi, C. Q. Jin, T. Shibauchi, S. Kasahara, Y. Matsuda, A. S. Sefat, H. Ding, P. Richard, and G. Blumberg, Magneto-elastic coupling in Fe-based superconductors (2017), arXiv:1712.01896 [cond-mat.supr-con].

[18] I. I. Mazin, M. D. Johannes, L. Boeri, K. Koepernik, and D. J. Singh, Problems with reconciling density functional theory calculations with experiment in ferropnictides, Phys. Rev. B **78**, 085104 (2008).

[19] J.-H. Chu, J. G. Analytis, C. Kucharczyk, and I. R. Fisher, Determination of the phase diagram of the electron-doped superconductor $Ba(Fe_{1-x}Co_x)_2As_2$, Phys. Rev. B **79**, 014506 (2009).

[20] S. A. J. Kimber, A. Kreyssig, Y.-Z. Zhang, H. O. Jeschke, R. Valentí, F. Yokaichiya, E. Colombier, J. Yan, T. C. Hansen, T. Chatterji, R. J. McQueeney, P. C. Canfield, A. I. Goldman, and D. N. Argyriou, Similarities between structural distortions under pressure and chemical doping in superconducting $BaFe_2As_2$, Nat. Mater. **8**, 471 (2009).

[21] M. G. Kim, R. M. Fernandes, A. Kreyssig, J. W. Kim, A. Thaler, S. L. Bud'ko, P. C. Canfield, R. J. McQueeney, J. Schmalian, and A. I. Goldman, Character of the structural and magnetic phase transitions in the parent and electron-doped $BaFe_2As_2$ compounds, Phys. Rev. B **83**, 134522 (2011).

[22] M. Rotter, M. Tegel, and D. Johrendt, Superconductivity at 38 K in the Iron Arsenide $(Ba_{1-x}K_x)Fe_2As_2$, Phys. Rev. Lett. **101**, 107006 (2008).

[23] J.-H. Chu, J. G. Analytis, K. D. Greve, P. L. McMahon, Z. Islam, Y. Yamamoto, and I. R. Fisher, In-plane resistivity anisotropy in an underdoped iron arsenide superconductor, Science **329**, 824 (2010).

[24] J. J. Ying, X. F. Wang, T. Wu, Z. J. Xiang, R. H. Liu, Y. J. Yan, A. F. Wang, M. Zhang, G. J. Ye, P. Cheng, J. P. Hu, and X. H. Chen, Measurements of the Anisotropic in-Plane Resistivity of Underdoped FeAs-Based Pnictide Superconductors, Phys. Rev. Lett. **107**, 067001 (2011).

[25] A. Dusza, A. Lucarelli, F. Pfuner, J.-H. Chu, I. R. Fisher, and L. Degiorgi, Anisotropic charge dynamics in detwinned $Ba(Fe_{1-x}Co_x)_2As_2$, Europhys. Lett. **93**, 37002 (2011).

[26] A. Dusza, A. Lucarelli, A. Sanna, S. Massidda, J.-H. Chu, I. R. Fisher, and L. Degiorgi, Anisotropic in-plane optical conductivity in detwinned $Ba(Fe_{1-x}Co_x)_2As_2$, New J. Phys. **14**, 023020 (2012).

[27] M. Nakajima, T. Liang, S. Ishida, Y. Tomioka, K. Kihou, C. H. Lee, A. Iyo, H. Eisaki, T. Kakeshita, T. Ito, and S. Uchida, Unprecedented anisotropic metallic state in undoped iron arsenide $BaFe_2As_2$ revealed by optical spectroscopy, Proc. Natl. Acad. Sci. USA **108**, 12238 (2011).

[28] M. Yi, D. Lu, J.-H. Chu, J. G. Analytis, A. P. Sorini, A. F. Kemper, B. Moritz, S.-K. Mo, R. G. Moore, M. Hashimoto, W.-S. Lee, Z. Hussain, T. P. Devereaux, I. R. Fisher, and Z.-X. Shen, Symmetry-breaking orbital anisotropy observed for detwinned $Ba(Fe_{1-x}Co_x)_2As_2$ above the spin density wave transition, Proc. Natl. Acad. Sci. USA **108**, 6878 (2011).

[29] T. Liang, M. Nakajima, K. Kihou, Y. Tomioka, T. Ito, C. H. Lee, H. Kito, A. Iyo, H. Eisaki, T. Kakeshita, and S. Uchida, Effects of uniaxial pressure and annealing on the resistivity of $Ba(Fe_{1-x}Co_x)_2As_2$, J. Phys. Chem. Solids **72**, 418 (2011).

[30] E. C. Blomberg, A. Kreyssig, M. A. Tanatar, R. M. Fernandes, M. G. Kim, A. Thaler, J. Schmalian, S. L. Bud'ko, P. C. Canfield,

A. I. Goldman, and R. Prozorov, Effect of tensile stress on the in-plane resistivity anisotropy in $BaFe_2As_2$, Phys. Rev. B **85**, 144509 (2012).

[31] J. P. Perdew, K. Burke, and M. Ernzerhof, Generalized Gradient Approximation Made Simple, Phys. Rev. Lett. **77**, 3865 (1996).

[32] A. Togo, F. Oba, and I. Tanaka, First-principles calculations of the ferroelastic transition between rutile-type and $CaCl_2$-type SiO_2 at high pressures, Phys. Rev. B **78**, 134106 (2008).

[33] A. Togo and I. Tanaka, First principles phonon calculations in materials science, Scr. Mater. **108**, 1 (2015).

[34] K. Parlinski, Z. Q. Li, and Y. Kawazoe, First-Principles Determination of the Soft Mode in Cubic ZrO_2, Phys. Rev. Lett. **78**, 4063 (1997).

[35] P. E. Blöchl, Projector augmented-wave method, Phys. Rev. B **50**, 17953 (1994).

[36] G. Kresse and J. Hafner, Ab initio molecular dynamics for liquid metals, Phys. Rev. B **47**, 558 (1993).

[37] G. Kresse and J. Furthmüller, Efficient iterative schemes for ab initio total-energy calculations using a plane-wave basis set, Phys. Rev. B **54**, 11169 (1996).

[38] G. Kresse and J. Furthmüller, Efficiency of ab-initio total energy calculations for metals and semiconductors using a plane-wave basis set, Comput. Mater. Sci. **6**, 15 (1996).

[39] C. Ambrosch-Draxl and J. O. Sofo, Linear optical properties of solids within the full-potential linearized augmented planewave method, Comput. Phys. Commun. **175**, 1 (2006).

[40] P. Blaha, K. Schwarz, G. K. H. Madsen, D. Kvasnicka, and J. Luitz, WIEN2k: *An Augmented Plane Wave Plus Local Orbitals Program for Calculating Crystal Properties* (Technische Universität Wien, Wien, 2001).

[41] X. Ren, L. Duan, Y. Hu, J. Li, R. Zhang, H. Luo, P. Dai, and Y. Li, Nematic Crossover in $BaFe_2As_2$ under Uniaxial Stress, Phys. Rev. Lett. **115**, 197002 (2015).

[42] W.-L. Zhang, A. S. Sefat, H. Ding, P. Richard, and G. Blumberg, Stress-induced nematicity in $EuFe_2As_2$ studied by Raman spectroscopy, Phys. Rev. B **94**, 014513 (2016).

[43] K.-Y. Choi, D. Wulferding, P. Lemmens, N. Ni, S. L. Bud'ko, and P. C. Canfield, Lattice and electronic anomalies of $CaFe_2As_2$ studied by Raman spectroscopy, Phys. Rev. B **78**, 212503 (2008).

[44] L. Chauvière, Y. Gallais, M. Cazayous, M. A. Méasson, A. Sacuto, D. Colson, and A. Forget, Impact of the spin-density-wave order on the superconducting gap of $Ba(Fe_{1-x}Co_x)_2As_2$, Phys. Rev. B **82**, 180521 (2010).

[45] S. Sugai, Y. Mizuno, R. Watanabe, T. Kawaguchi, K. Takenaka, H. Ikuta, Y. Takayanagi, N. Hayamizu, and Y. Sone, Spin-density-wave gap with Dirac nodes and two-magnon Raman scattering in $BaFe_2As_2$, J. Phys. Soc. Jpn. **81**, 024718 (2012).

[46] F. Kretzschmar, T. Böhm, U. Karahasanović, B. Muschler, A. Baum, D. Jost, J. Schmalian, S. Caprara, M. Grilli, C. Di Castro, J. H. Analytis, J.-H. Chu, I. R. Fisher, and R. Hackl, Critical spin fluctuations and the origin of nematic order in $Ba(Fe_{1-x}Co_x)_2As_2$, Nat. Phys. **12**, 560 (2016).

[47] V. K. Thorsmølle, M. Khodas, Z. P. Yin, C. Zhang, S. V. Carr, P. Dai, and G. Blumberg, Critical quadrupole fluctuations and collective modes in iron pnictide superconductors, Phys. Rev. B **93**, 054515 (2016).

[48] M. Cardona, *Resonance Phenomena*, 1st ed. (Springer-Verlag, Berlin, Heidelberg, 1982) Chap. 2, pp. 19–178.

[49] S.-H. Baek, D. V. Efremov, J. M. Ok, J. S. Kim, J. van den Brink, and B. Büchner, Orbital-driven nematicity in FeSe, Nat. Mater. **14**, 210 (2014).

[50] B. Muschler, W. Prestel, L. Tassini, R. Hackl, M. Lambacher, A. Erb, S. Komiya, Y. Ando, D. C. Peets, W. N. Hardy, R. Liang, and D. A. Bonn, Electron interactions and charge ordering in CuO_2 compounds, Eur. Phys. J. Special Topics **188**, 131 (2010).

[51] T. Strach, J. Brunen, B. Lederle, J. Zegenhagen, and M. Cardona, Determination of the phase difference between the Raman tensor elements of the A_{1g}-like phonons in $SmBa_2Cu_3O_{7-\delta}$, Phys. Rev. B **57**, 1292 (1998).

[52] C. Ambrosch-Draxl, H. Auer, R. Kouba, E. Y. Sherman, P. Knoll, and M. Mayer, Raman scattering in $yba_2cu_3o_7$: A comprehensive theoretical study in comparison with experiments, Phys. Rev. B **65**, 064501 (2002).

[53] S. L. Skornyakov, A. V. Efremov, N. A. Skorikov, M. A. Korotin, Y. A. Izyumov, V. I. Anisimov, A. V. Kozhevnikov, and D. Vollhardt, Classification of the electronic correlation strength in the iron pnictides: The case of the parent compound $BaFe_2As_2$, Phys. Rev. B **80**, 092501 (2009).

[54] Y. X. Yao, J. Schmalian, C. Z. Wang, K. M. Ho, and G. Kotliar, Comparative study of the electronic and magnetic properties of $BaFe_2As_2$ and $BaMn_2As_2$ using the Gutzwiller approximation, Phys. Rev. B **84**, 245112 (2011).

[55] J. Ferber, K. Foyevtsova, R. Valentí, and H. O. Jeschke, LDA + DMFT study of the effects of correlation in LiFeAs, Phys. Rev. B **85**, 094505 (2012).

[56] S. Backes, H. O. Jeschke, and R. Valentí, Microscopic nature of correlations in multiorbital $AFe_2As_2(A = \mathrm{K, Rb, Cs})$: Hund's coupling versus Coulomb repulsion, Phys. Rev. B **92**, 195128 (2015).

PHYSICAL REVIEW B **98**, 020504(R) (2018)

Rapid Communications

Indication of subdominant d-wave interaction in superconducting $CaKFe_4As_4$

D. Jost,[1,2] J.-R. Scholz,[1,2] U. Zweck,[1,2] W. R. Meier,[3,4] A. E. Böhmer,[4,*] P. C. Canfield,[4,3] N. Lazarević,[5] and R. Hackl[1]

[1] *Walther Meissner Institut, Bayerische Akademie der Wissenschaften, 85748 Garching, Germany*
[2] *Fakultät für Physik E23, Technische Universität München, 85748 Garching, Germany*
[3] *Department of Physics and Astronomy, Iowa State University, Ames, Iowa 50011, USA*
[4] *Division of Materials Science and Engineering, Ames Laboratory, Ames, Iowa 50011, USA*
[5] *Center for Solid State Physics and New Materials, Institute of Physics Belgrade, University of Belgrade, Pregrevica 118, 11080 Belgrade, Serbia*

(Received 31 May 2018; revised manuscript received 26 June 2018; published 13 July 2018)

We report inelastic light scattering results on the stoichiometric and fully ordered superconductor $CaKFe_4As_4$ as a function of temperature and light polarization. In the energy range between 10 and 315 cm^{-1} (1.24 and 39.1 meV) we observe the particle-hole continuum above and below the superconducting transition temperature T_c and seven of the eight Raman active phonons. The main focus is placed on the analysis of the electronic excitations. Below T_c all three symmetries projected with in-plane polarizations display a redistribution of spectral weight characteristic for superconductivity. The energies of the pair-breaking peaks in A_{1g} and B_{2g} symmetry are in approximate agreement with the results from photoemission studies. In B_{1g} symmetry the difference between the normal and superconducting state is most pronounced, and the feature is shifted downwards with respect to those in A_{1g} and B_{2g} symmetry. The maximum peaking at 134 cm^{-1} (16.6 meV) has a substructure on the high-energy side. We interpret the peak at 134 cm^{-1} in terms of a collective Bardasis-Schrieffer (BS) mode and the substructure as a remainder of the pair-breaking feature on the electron bands. There is a very weak peak at 50 cm^{-1} (6.2 meV) which is tentatively assigned to another BS mode.

DOI: 10.1103/PhysRevB.98.020504

$CaKFe_4As_4$ is among the few iron-based compounds which are superconducting at a high transition temperature T_c at stoichiometry [1] since the Ca and K atoms form alternating intact layers, as shown in Fig. 1. The high degree of order allows one to get as close to the intrinsic properties of the material class as possible since the effects of disorder are expected to be negligible or at least significantly smaller than in solid solutions such as $Ba_{1-x}K_xFe_2As_2$ or $Ba(Fe_{1-x}Co_x)_2As_2$. For instance, the residual resistivity ratio (RRR) reaches 15 and is much higher than for $Ba(Fe_{1-x}Co_x)_2As_2$ and is comparable to or better than that for $Ba_{1-x}K_xFe_2As_2$ [2]. Other transport and thermodynamic properties [2] highlight the similarities to optimally or overdoped $Ba_{1-x}K_xFe_2As_2$.

These similarities include the electronic structure, in particular, the Fermi surfaces [Fig. 1(c)] and the superconducting energy gaps [3]. The gaps were found to be rather isotropic on the individual bands having values of $2\Delta_\alpha = 21$ meV, $2\Delta_\beta = 24$ meV, $2\Delta_\gamma = 16$ meV, and $2\Delta_\delta = 24$ meV on the three hole bands (α,β,γ) and the electron band (δ), respectively. The good nesting observed between the β and δ bands was considered to support s-wave interband pairing [3–5], as proposed earlier for the iron-based materials in general [6].

Since there is also nesting among the electron bands, one can expect a competing pairing interaction with d-wave symmetry as a subleading instability [7]. Indications thereof were found recently in Raman scattering experiments on $Ba_{1-x}K_xFe_2As_2$ [8–10]. The subleading channel manifests itself as a narrow line below the gap edge given that the gap is as clean as, e.g., in $Ba_{1-x}K_xFe_2As_2$ [11–13]. The bound state has its origin in a phase fluctuation of the condensate of Cooper pairs. The experimental identification of this excitation as a Bardasis-Schrieffer (BS) exciton rests on the shape of the line, its temperature dependence, and the spectral weight transfer from the pair-breaking feature to the in-gap mode, as described in detail in Refs. [9,10].

Given its nearly clean gap and high crystal quality, $CaKFe_4As_4$ is an excellent candidate for scrutinizing the superconducting properties of hole-doped 122 systems. We aim at answering the question as to whether or not subleading channels can also be observed in systems other than $Ba_{1-x}K_xFe_2As_2$ and whether they can be identified as generic.

Calibrated Raman scattering equipment was used for the experiments. The sample was attached to the cold finger of a He-flow cryostat. For excitation, a diode-pumped solid state laser emitting at 575 nm (Coherent GENESIS MX-SLM 577-500) was used. The polarization of the incoming light was adjusted in such a way that the light inside the sample had the proper polarization state. The absorbed power (inside the sample) was set at typically $P_a = 2$ mW, independent of polarization. By setting the polarizations of the incident and scattered photons, the four symmetries A_{1g}, A_{2g}, B_{1g}, and B_{2g} of the D_{4h} space group can be accessed. For the symmetry assignment we use the 1-Fe unit cell [see Figs. 1(b) and 1(c)] since the density of states at the Fermi energy E_F is nearly entirely derived from Fe orbitals. The related projections in the first Brillouin zone (BZ) are visualized in Fig. S1 of the

---

[*] Present address: Karlsruher Institut für Technologie, Institut für Festkörperphysik, 76021 Karlsruhe, Germany.

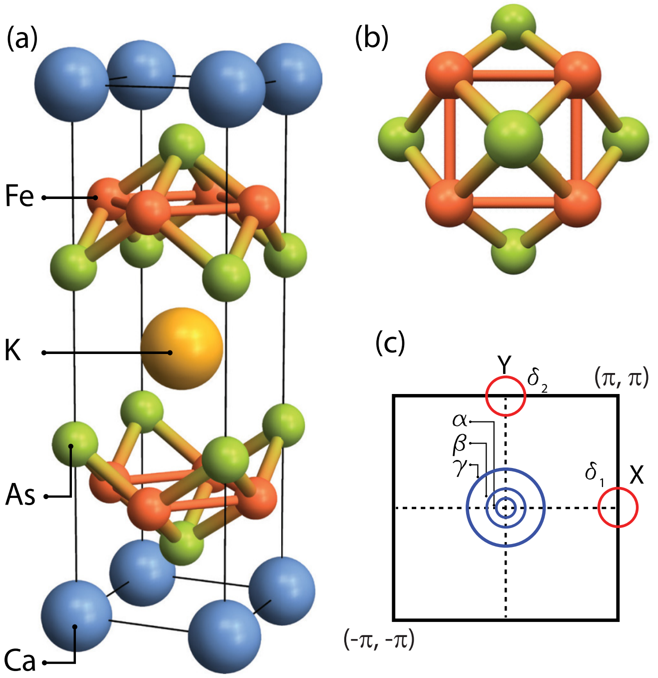

FIG. 1. Structure and Fermi surface of CaKFe$_4$As$_4$. (a) Tetragonal unit cell with the Ca, K, Fe, and As atoms shown in blue, gold, red, and green, respectively [1]. (b) Quasi-two-dimensional (2D) Fe$_2$As$_2$ layer with the solid orange line depicting the 1-Fe unit cell. (c) Brillouin zone of the 1-Fe cell. The three hole bands labeled α, β, and γ (blue) encircle the Γ point. The electron bands δ_1 and δ_2 (red) are centered at the X and Y points, respectively (adopted from Mou *et al.* [3]).

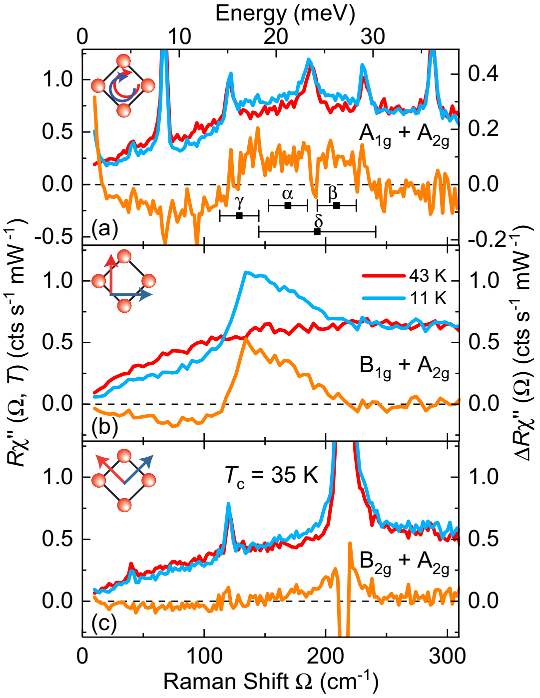

FIG. 2. Raman response in CaKFe$_4$As$_4$ at symmetries and polarizations as indicated. Shown are raw data for $T \ll T_c$ (blue), $T > T_c$ (red), and difference spectra (orange). Phonon modes are present in the A_{1g} and B_{2g} spectra. (a) The pair-breaking maximum extends from $\Omega_0^{(A_{1g})} = 120 \pm 5$ cm^{-1} to $\Omega_\mathrm{m} \approx 230$ cm^{-1}. The gap energies $2\Delta_i$ for the four bands i observed by ARPES [3] are reproduced as horizontal bars. Note that the right vertical axis is expanded by a factor of 2.5 with respect to the left one. (b) The B_{1g} pair-breaking peak is well defined and sets on at $\Omega_0^{(B_{1g})} = 116 \pm 5$ cm^{-1}. (c) The weak B_{2g} pair-breaking peak is located slightly above $2\Delta_\beta$. The intersection of the normal and superconducting spectra is close to $\Omega_0^{(B_{2g})} = 130 \pm 5$ cm^{-1}.

Supplemental Material [14]. In this Rapid Communication, the focus is placed on low energies, where A_{2g} is negligibly small. The polarization combinations RR, xy, and $x'y'$ almost exclusively project the A_{1g}, B_{2g}, and B_{1g} symmetries, as desired. Here, x and y are horizontal and vertical, respectively, in the laboratory system. Note that the out-of-phase vibration of the Fe atoms appears in B_{2g} symmetry in the 1-Fe unit cell rather than in B_{1g} symmetry of the crystallographic unit cell hosting two Fe atoms per Fe$_2$As$_2$ plane [14]. The spectra are represented as response functions $R\chi''(T,\Omega)$ which are obtained by dividing the measured cross section by the thermal Bose factor $\{1 + n(\Omega,T)\} = \{1 + [\exp(\hbar\omega/k_BT) - 1]^{-1}\}$. R is an experimental constant.

The CaKFe$_4$As$_4$ single crystals were grown from the FeAs flux and characterized thoroughly as described by Meier and co-workers [2,15]. The T_c value of 35.21 ± 0.10 K we found here is in the range 35.0 ± 0.2 K determined by Meier *et al.* (see Fig. S3 in the Supplemental Material [14]). The crystal structure of CaKFe$_4$As$_4$ is very similar to that of AFe$_2$As$_2$ systems [cf. Fig. 1(a)] and belongs to the tetragonal D_{4h} space group. Since CaKFe$_4$As$_4$ has alternating Ca and K planes between the Fe$_2$As$_2$ layers, the point group is simple tetragonal ($P4/mmm$) [1] rather than the body-centered tetragonal ($I4/mmm$) as BaFe$_2$As$_2$ [16].

Figure 2 shows the normal (red) and superconducting (blue) Raman spectra of CaKFe$_4$As$_4$ at the three polarization configurations (a) RR, (b) xy, and (c) $x'y'$. The sample is rotated by 45° with respect to the orientation in Fig. 1 in order to suppress any c-axis projection in the B_{1g} spectra (xy in the laboratory system). Superimposed on the particle-hole continua we observe six and four phonons in RR and $x'y'$ polarization, respectively [17], which will be discussed in the Supplemental Material [14]. As intended, there are no phonons in the xy configuration, and the spectrum in the normal state is completely smooth to within the experimental error. The structureless shape indicates that there is no polarization leakage and, more importantly, that there is no defect-induced scattering from phonons, highlighting the high crystal quality.

We focus now exclusively on the electronic continua. To this end we also plot the difference spectra,

$$\Delta R\chi''(\Omega) = R\chi''(T = 11\text{ K},\Omega) - R\chi''(T = 43\text{ K}) \quad (1)$$

(orange in Fig. 2), along with the raw data of each polarization configuration. In the difference spectra $\Delta R\chi''(\Omega)$ temperature-independent structures such as (most of) the phonons and the presumably weak and temperature-independent luminescence contributions are eliminated. In this way the changes induced by superconductivity are highlighted.

All spectra show the typical changes upon entering the superconducting state: (i) The opening of the gap induces a suppression of the intensity below a crossover energy of

$\Omega_0 = 125, 115$, and $130\ \mathrm{cm}^{-1}$ for A_{1g}, B_{1g}, and B_{2g} symmetry, respectively. In this range, $\Delta R\chi''(\Omega)$ (orange) is negative. (ii) The intensity piles up above Ω_0 due to a coherent superposition of pair-breaking and Bogoliubov quasiparticle excitations across the gap 2Δ. The amplitude of the redistribution is small in A_{1g} and B_{2g} symmetry (Figs. 2(a) and 2(c) and Figs. S4 and S6 of Ref. [14]) but pronounced in B_{1g} symmetry. (Fig. 2(b) and Fig. S5 of Ref. [14]). In the A_{1g} response [Fig. 2(a)] the signal at $\Omega \rightarrow 0$ is enhanced because of the surface layers of accumulating residual gas molecules at low temperature (see Fig. S4 of Ref. [14]) and the insufficient suppression of the elastically scattered light in the case of parallel light polarizations (RR here).

The first striking observation is the nearly symmetry-independent crossover energy Ω_0 where the normal (red) and superconducting (blue) spectra intersect each other or where $\Delta R\chi''(\Omega)$ changes sign. Yet, the intensity for $\Omega < \Omega_0$ does not vanish entirely as expected for a clean gap, but is only reduced. No additional structures are observed in the A_{1g} and B_{2g} spectra while a weak hump appears at approximately $50\ \mathrm{cm}^{-1}$ [see Fig. 2(b) and asterisks in Figs. 3(c)–3(e)] in B_{1g} symmetry, as can also be seen in Fig. S5 of Ref. [14].

Second, whereas the normal and the superconducting spectra merge at similar energies close to $\Omega_\mathrm{m} = 230\ \mathrm{cm}^{-1}$ in all symmetries the distribution of spectral weight in the range $\Omega_0 < \Omega < \Omega_\mathrm{m}$ varies substantially. In none of the symmetries do the pair-breaking features display the typical shape. The pair-breaking maximum in B_{2g} symmetry is found at approximately $215\ \mathrm{cm}^{-1}$ right underneath the Fe phonon. The negative intensity at $215\ \mathrm{cm}^{-1}$ shows that the phonon is renormalized below T_c, and an influence of this renormalization on the electronic features cannot be excluded. However, the gap below $130\ \mathrm{cm}^{-1}$ indicates the presence of an intensity redistribution below T_c. In A_{1g} symmetry a wide plateau is observed between Ω_0 and Ω_m. Finally, in B_{1g} symmetry, a pronounced peak is found at $135\ \mathrm{cm}^{-1}$, above which the intensity decays. Upon studying various temperatures, a secondary maximum at about $165\ \mathrm{cm}^{-1}$ can be resolved, as shown in Fig. S5 of Ref. [14].

For the discussion below we additionally plot in Fig. 2(a) the gap energies $2\Delta_i$ as horizontal bars, according to a recent photoemission study [3], where i is the band index [cf. Fig. 1(c)]. The width of the bars corresponds to the error bars of order ±10% indicated there.

We now discuss the possible interpretations of the electronic Raman spectra presented above. Can the spectra be interpreted exclusively in terms of pair breaking, or are collective modes, similarly as in $\mathrm{Ba}_{1-x}\mathrm{K}_x\mathrm{Fe}_2\mathrm{As}_2$, necessary for a more consistent explanation?

Using yellow excitation we find a strong redistribution of spectral weight in B_{1g} symmetry, similarly as in a simultaneous Raman study using red photons [18]. (Note that B_{1g} and B_{2g} are interchanged in the two studies.) With yellow photons we observe the redistribution in all three symmetry channels. As already noticed earlier, this difference in the experimental results may be traced back to orbital-dependent resonance effects [10]. In contrast to Zhang and co-workers [18], we find finite intensity in the range below the maximal gap at approximately $215\ \mathrm{cm}^{-1}$, similar as in $\mathrm{Ba}_{1-x}\mathrm{K}_x\mathrm{Fe}_2\mathrm{As}_2$. We attribute this intensity predominantly to the multigap structure in both compounds. Since there is an intensity redistribution below T_c in all channels we do not believe that there is a strong background at low energies from, e.g., luminescence, which has an intensity comparable to that of particle-hole excitations.

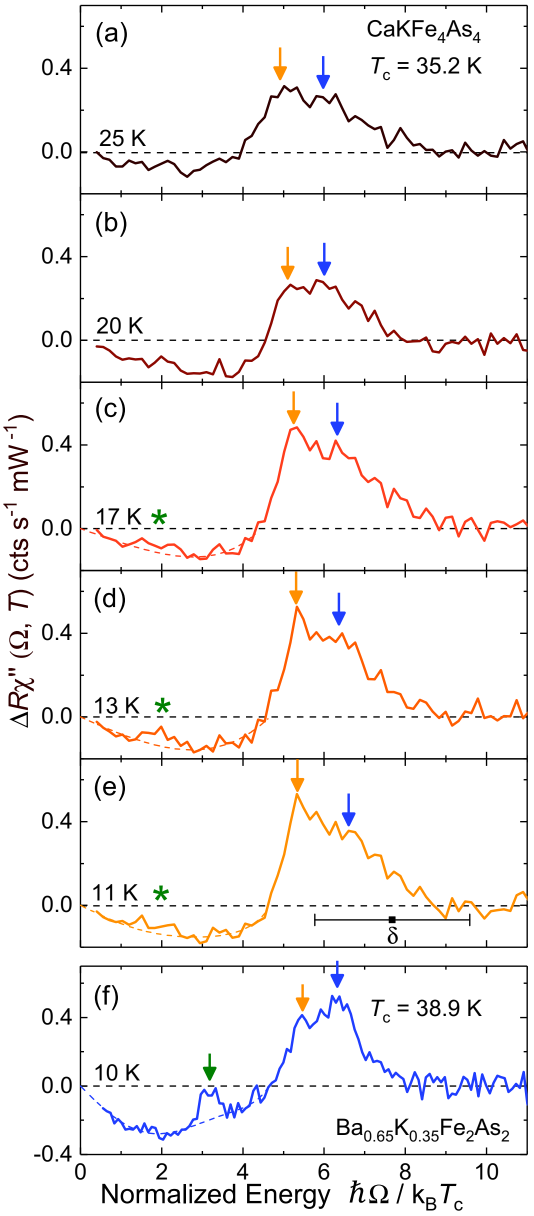

FIG. 3. Difference spectra of the B_{1g} Raman response in $\mathrm{CaKFe_4As_4}$ and $\mathrm{Ba}_{1-x}\mathrm{K}_x\mathrm{Fe}_2\mathrm{As}_2$ for temperatures as indicated. For raw data, cf. Fig. 2 and S5 of Ref. [14]. The main peak exhibits a double structure (orange and blue arrows). A second hump is visible in the spectra at 11, 13, and 17 K (asterisks) above the spectral shape expected for a clean gap (colored dashes). (f) Difference spectrum of $\mathrm{Ba_{0.65}K_{0.35}As_2Fe_2}$. From Ref. [10]. The arrows show two Bardasis-Schrieffer modes at $3.1k_BT_c$ (green arrow) and $5.2k_BT_c$ (orange arrow). The remainder of the pair-breaking peak is located at $6.2k_BT_c$ (blue arrow) since the high-energy part is drained into the BS modes.

The highest pair-breaking energy in our study is observed in B_{2g} symmetry, implying a maximal gap energy of $2\Delta_\mathrm{max} \approx 215\ \mathrm{cm}^{-1}$. This energy corresponds to $\Delta_\mathrm{max} = 13.3$ meV, which is slightly higher than the largest gaps derived for the β

and δ bands, $\Delta_{\beta,\delta} = 12$ meV, using angle-resolved photoemission spectroscopy (ARPES) [3]. The value 215 cm^{-1} coincides with the edge of the A_{1g} pair-breaking feature (see Fig. 2), and we conclude that the ARPES data slightly underestimate the gap energies found by Raman scattering, as already observed for $\mathrm{Ba}_{1-x}\mathrm{K}_x\mathrm{Fe}_2\mathrm{As}_2$ [8,9]. Similarly, the lowest gap energy of $\Delta_\gamma = 8$ meV is below 9.3 meV, as expected from the lower edge in the A_{1g} spectra. There are no structures in the A_{1g} and B_{2g} spectra which one could associate with the gap energy on the α band, $\Delta_\alpha = 10.5$ meV, obtained from ARPES. On this basis we conclude that the maximal gap energies derived from the A_{1g} and B_{2g} Raman spectra are in the same range of approximately $9k_BT_c$ as in $\mathrm{Ba}_{1-x}\mathrm{K}_x\mathrm{Fe}_2\mathrm{As}_2$ close to optimal doping [9].

The question arises whether ARPES and Raman results are compatible with the selection rules. As shown in Fig. S1 of Ref. [14], all bands should be visible in A_{1g} symmetry with comparable weight upon neglecting the resonance effects. In fact, all energies are represented in the spectra shown in Fig. 2(a). Even if a Leggett mode contributes to the A_{1g} spectra, as suggested recently [19], this conclusion survives since the Leggett modes are expected to be close to the maximal gap energies in the Fe-based systems. The B_{2g} spectra are less easily reconciled with this scenario since the gaps on the hole bands should be projected with a similar spectral weight as that of the electron band. Yet, we find only a contribution from the largest gap. Although the overall intensity is very weak, here the absence of contributions from the γ band cannot be explained by the variation of the peak height with $|\Delta|^2$ [20] or by applying the symmetry selection rules. Either a phenomenological treatment as for $\mathrm{Ba}_{1-x}\mathrm{K}_x\mathrm{Fe}_2\mathrm{As}_2$ [9] or a detailed resonance study needs to be performed which, however, is beyond the scope of this work.

Given that the single-particle gap energies are by and large reproduced in the A_{1g} and B_{2g} spectra, it is important to understand the B_{1g} spectra. As shown in Fig. 2(c), the energies appearing there are well below those of the A_{1g} and B_{2g} spectra. This is particularly surprising as the δ bands are expected to be projected fully (and not marginally) in B_{1g} symmetry (see Fig. S1 of Ref. [14]) as opposed to all hole bands. Thus, the argument that the strongest peak in the B_{1g} spectra results from the γ band can be discarded. Since in contrast to $\mathrm{Ba}(\mathrm{Fe}_{1-x}\mathrm{Co}_x)_2\mathrm{As}_2$ [21,22], $\mathrm{NaFe}_{1-x}\mathrm{Co}_x\mathrm{As}$ [23], or FeSe [24,25] there is no nematic phase and related fluctuations in $\mathrm{CaKFe}_4\mathrm{As}_4$, an interpretation of the observation in B_{1g} symmetry in terms of nematic fluctuations would be far fetched.

As a consequence, there remains only one scenario which reconciles the results observed in the three Raman active symmetries and the ARPES results: The B_{1g} spectra do not directly reflect gap energies but rather are shifted downward by a final state interaction, as discussed for $\mathrm{Ba}_{1-x}\mathrm{K}_x\mathrm{Fe}_2\mathrm{As}_2$ in earlier work [8–10]. The similarity can be observed directly by comparing the data in Fig. 3. The difference spectra as a function of temperature indicate that the B_{1g} peak has a robust shoulder on the high-energy side. The overall shape is surprisingly similar to the spectra of $\mathrm{Ba}_{0.65}\mathrm{K}_{0.35}\mathrm{Fe}_2\mathrm{As}_2$.

Following this reasoning we identify the maximum of the B_{1g} spectra at 134 cm^{-1} with a collective mode pulled off of the maximal gap energy on the δ band due to a $d_{x^2-y^2}$-wave subleading interaction among the two electron bands, as predicted theoretically [13] and observed in $\mathrm{Ba}_{1-x}\mathrm{K}_x\mathrm{Fe}_2\mathrm{As}_2$. The hump at approximately 165 cm^{-1} is then the remaining intensity of the pair-breaking peak on the δ band after switching on the final state interaction, which induces a transfer of intensity from the pair-breaking peak into the bound state [9,12,13]. The missing intensity in the range of $2\Delta_\delta$ can only be explained consistently in this way.

It is tempting, yet a bit speculative, to explain the faint peak close to 50 cm^{-1} ($2k_BT_c$) in terms of a second BS mode in a similar fashion as in $\mathrm{Ba}_{1-x}\mathrm{K}_x\mathrm{Fe}_2\mathrm{As}_2$ [10]. This would mean that the subdominant coupling is already very strong, and $\mathrm{CaKFe}_4\mathrm{As}_4$ is on the brink of a d-wave instability. The very weak intensity of the peak argues in this direction since the BS mode is expected to vanish when d-wave pairing wins [10]. Yet, the vanishingly small intensity is also the Achilles' heel of the argument, and we refrain from going beyond pointing out this possibility. A robust statement is possible only on the basis of improved counting statistics and a microscopic model, which includes the derivation of the eigenvectors of the subdominant pairing channels, as proposed for $\mathrm{Ba}_{1-x}\mathrm{K}_x\mathrm{Fe}_2\mathrm{As}_2$ [10]. Such an expensive theoretical treatment is beyond the scope of this experimental study.

In summary, we investigated the recently discovered superconductor $\mathrm{CaKFe}_4\mathrm{As}_4$ with inelastic light scattering as a function of photon polarization and temperature. Using yellow light (575 nm), superconducting features were found in A_{1g}, B_{1g}, and B_{2g} symmetry.

A weak but well-defined pair-breaking feature is found at 215 cm^{-1} (corresponding to $\Delta = 13.3$ meV) in B_{2g} symmetry, which is slightly above the largest gaps observed by ARPES for the β and the δ bands [3] and close to the energy Ω_m where the normal and the superconducting spectra merge in all symmetry projections. This feature is also present in the A_{1g} spectra. In addition to the high-energy feature, the A_{1g} intensity displays a plateaulike shape down to $\Omega_0^{(A_{1g})} = 125\ \mathrm{cm}^{-1}$. Given the small discrepancies between the gap energies derived from the ARPES data and the Raman spectra, one can conclude that the A_{1g} spectra reflect the entire range of gap energies of $\mathrm{CaKFe}_4\mathrm{As}_4$ even though the individual gap energies cannot be resolved.

In B_{1g} symmetry, the superconducting feature is centered at a lower energy than in the two other symmetries. We interpret the sharp maximum at 134 cm^{-1} as a collective Bardasis-Schrieffer mode pulled off of the maximal gap on the δ band, similarly as in the sister compound $\mathrm{Ba}_{0.65}\mathrm{K}_{0.35}\mathrm{Fe}_2\mathrm{As}_2$. The shoulder at approximately 165 cm^{-1} is a remainder of the pair-breaking peak losing most of its intensity to the collective mode [9,13]. Whether or not the weak structure at 50 cm^{-1} is another BS mode with even stronger coupling cannot be decided with certainty because of the fading intensity. If this interpretation could be supported further, $\mathrm{CaKFe}_4\mathrm{As}_4$ would be closer to a d-wave instability than $\mathrm{Ba}_{1-x}\mathrm{K}_x\mathrm{Fe}_2\mathrm{As}_2$. The smaller T_c of $\mathrm{CaKFe}_4\mathrm{As}_4$ argues in this direction since a strong d-pairing channel frustrates the s-wave ground state and reduces T_c. Even without dwelling on the peak at 50 cm^{-1}, we may conclude that $\mathrm{CaKFe}_4\mathrm{As}_4$ is a true sibling of $\mathrm{Ba}_{1-x}\mathrm{K}_x\mathrm{Fe}_2\mathrm{As}_2$ [10], thus demonstrating that pairing fingerprints can be observed preferably in materials with clean gaps.

We acknowledge valuable discussions with G. Blumberg. The work was supported by the Friedrich-Ebert-Stiftung, the Deutsche Forschungsgemeinschaft (DFG) via the Transregional Collaborative Research Center TRR 80, and the Serbian Ministry of Education, Science and Technological Development under Project No. III45018. We acknowledge support by the Deutscher Akademischer Austauschdienst (DAAD) through the bilateral project between Serbia and Germany (Grants No. 56267076 and No. 57142964). Work at Ames Laboratory was supported by the U.S. Department of Energy, Office of Basic Energy Sciences, Division of Materials Sciences and Engineering under Contract No. DE-AC02- 07CH11358. W.R.M. was supported by the Gordon and Betty Moore Foundation's EPiQS Initiative through Grant No. GBMF4411.

---

[1] A. Iyo, K. Kawashima, T. Kinjo, T. Nishio, S. Ishida, H. Fujihisa, Y. Gotoh, K. Kihou, H. Eisaki, and Y. Yoshida, New-structure-type Fe-based superconductors: $CaAFe_4As_4$ (A = K, Rb, Cs) and $SrAFe_4As_4$ (A = Rb, Cs), J. Am. Chem. Soc. **138**, 3410 (2016).

[2] W. R. Meier, T. Kong, U. S. Kaluarachchi, V. Taufour, N. H. Jo, G. Drachuck, A. E. Böhmer, S. M. Saunders, A. Sapkota, A. Kreyssig, M. A. Tanatar, R. Prozorov, A. I. Goldman, F. F. Balakirev, A. Gurevich, S. L. Bud'ko, and P. C. Canfield, Anisotropic thermodynamic and transport properties of single-crystalline $CaKFe_4As_4$, Phys. Rev. B **94**, 064501 (2016).

[3] D. Mou, T. Kong, W. R. Meier, F. Lochner, L.-L. Wang, Q. Lin, Y. Wu, S. L. Bud'ko, I. Eremin, D. D. Johnson, P. C. Canfield, and A. Kaminski, Enhancement of the Superconducting Gap by Nesting in $CaKFe_4As_4$: A New High Temperature Superconductor, Phys. Rev. Lett. **117**, 277001 (2016).

[4] P. K. Biswas, A. Iyo, Y. Yoshida, H. Eisaki, K. Kawashima, and A. D. Hillier, Signature of multigap nodeless superconductivity in $CaKFe_4As_4$, Phys. Rev. B **95**, 140505 (2017).

[5] R. Yang, Y. Dai, B. Xu, W. Zhang, Z. Qiu, Q. Sui, C. C. Homes, and X. Qiu, Anomalous phonon behavior in superconducting $CaKFe_4As_4$: An optical study, Phys. Rev. B **95**, 064506 (2017).

[6] I. I. Mazin, D. J. Singh, M. D. Johannes, and M. H. Du, Unconventional Superconductivity with a Sign Reversal in the Order Parameter of $LaFeAsO_{1-x}F_x$, Phys. Rev. Lett. **101**, 057003 (2008).

[7] P. J. Hirschfeld, Using gap symmetry and structure to reveal the pairing mechanism in Fe-based superconductors, C. R. Phys. **17**, 197 (2016).

[8] F. Kretzschmar, B. Muschler, T. Böhm, A. Baum, R. Hackl, H.-H. Wen, V. Tsurkan, J. Deisenhofer, and A. Loidl, Raman-Scattering Detection of Nearly Degenerate s-Wave and d-Wave Pairing Channels in Iron-Based $Ba_{0.6}K_{0.4}Fe_2As_2$ and $Rb_{0.8}Fe_{1.6}As_2$ Superconductors, Phys. Rev. Lett. **110**, 187002 (2013).

[9] T. Böhm, A. F. Kemper, B. Moritz, F. Kretzschmar, B. Muschler, H.-M. Eiter, R. Hackl, T. P. Devereaux, D. J. Scalapino, and H.-H. Wen, Balancing Act: Evidence for a Strong Subdominant d-Wave Pairing Channel in $Ba_{0.6}K_{0.4}Fe_2As_2$, Phys. Rev. X **4**, 041046 (2014).

[10] T. Böhm, F. Kretzschmar, A. Baum, M. Rehm, D. Jost, R. Hosseinian Ahangharnejhad, R. Thomale, C. Platt, T. A. Maier, W. Hanke, B. Moritz, T. P. Devereaux, D. J. Scalapino, S. Maiti, P. J. Hirschfeld, P. Adelmann, T. Wolf, H.-H. Wen, and R. Hackl, Microscopic pairing fingerprint of the iron-based superconductor $Ba_{1-x}K_xFe_2As_2$, arXiv:1703.07749.

[11] A. Bardasis and J. R. Schrieffer, Excitons and plasmons in superconductors, Phys. Rev. **121**, 1050 (1961).

[12] H. Monien and A. Zawadowski, Theory of Raman scattering with final-state interaction in high-T_c BCS superconductors: Collective modes, Phys. Rev. B **41**, 8798 (1990).

[13] D. J. Scalapino and T. P. Devereaux, Collective d-wave exciton modes in the calculated Raman spectrum of Fe-based superconductors, Phys. Rev. B **80**, 140512 (2009).

[14] See Supplemental Material at http://link.aps.org/supplemental/10.1103/PhysRevB.98.020504 for details on selection rules, phonons, samples, and for additional raw data.

[15] W. R. Meier, T. Kong, S. L. Bud'ko, and P. C. Canfield, Optimization of the crystal growth of the superconductor $CaKFe_4As_4$ from solution in the $FeAs$-$CaFe_2As_2$-KFe_2As_2 system, Phys. Rev. Mater. **1**, 013401 (2017).

[16] M. Rotter, M. Tegel, and D. Johrendt, Superconductivity at 38 K in the Iron Arsenide $(Ba_{1-x}K_x)Fe_2As_2$, Phys. Rev. Lett. **101**, 107006 (2008).

[17] J.-R. Scholz, Raman scattering study of the superconducting pairing in $CaKFe_4As_4$, Master's thesis, Technische Universität München, 2017.

[18] W.-L. Zhang, W. R. Meier, T. Kong, P. C. Canfield, and G. Blumberg, High T_c superconductivity in $CaKFe_4As_4$ in absence of nematic fluctuations, arXiv:1804.06963.

[19] T. Cea and L. Benfatto, Signature of the Leggett mode in the A_{1g} Raman response: From MgB_2 to iron-based superconductors, Phys. Rev. B **94**, 064512 (2016).

[20] T. P. Devereaux and R. Hackl, Inelastic light scattering from correlated electrons, Rev. Mod. Phys. **79**, 175 (2007).

[21] Y. Gallais, R. M. Fernandes, I. Paul, L. Chauvière, Y.-X. Yang, M.-A. Méasson, M. Cazayous, A. Sacuto, D. Colson, and A. Forget, Observation of Incipient Charge Nematicity in $Ba(Fe_{1-x}Co_x)_2As_2$, Phys. Rev. Lett. **111**, 267001 (2013).

[22] F. Kretzschmar, T. Böhm, U. Karahasanović, B. Muschler, A. Baum, D. Jost, J. Schmalian, S. Caprara, M. Grilli, C. Di Castro, J. H. Analytis, J.-H. Chu, I. R. Fisher, and R. Hackl, Critical spin fluctuations and the origin of nematic order in $Ba(Fe_{1-x}Co_x)_2As_2$, Nat. Phys. **12**, 560 (2016).

[23] V. K. Thorsmølle, M. Khodas, Z. P. Yin, C. Zhang, S. V. Carr, P. Dai, and G. Blumberg, Critical quadrupole fluctuations and collective modes in iron pnictide superconductors, Phys. Rev. B **93**, 054515 (2016).

[24] P. Massat, D. Farina, I. Paul, S. Karlsson, P. Strobel, P. Toulemonde, M.-A. Méasson, M. Cazayous, A. Sacuto, S. Kasahara, T. Shibauchi, Y. Matsuda, and Y. Gallais, Charge-induced nematicity in FeSe, Proc. Natl. Acad. Sci. USA **113**, 9177 (2016).

[25] A. Baum, H. N. Ruiz, N. Lazarević, Y. Wang, T. Böhm, R. Hosseinian Ahangharnejhad, P. Adelmann, T. Wolf, Z. V. Popović, B. Moritz, T. P. Devereaux, and R. Hackl, Frustrated spin order and stripe fluctuations in FeSe, arXiv:1709.08998.

PHYSICAL REVIEW B **97**, 054306 (2018)

Phonon anomalies in FeS

A. Baum,[1,2] A. Milosavljević,[3] N. Lazarević,[3] M. M. Radonjić,[4] B. Nikolić,[5] M. Mitschek,[1,2,*] Z. Inanloo Maranloo,[1,†]
M. Šćepanović,[3] M. Grujić-Brojčin,[3] N. Stojilović,[3,6] M. Opel,[1] Aifeng Wang (王爱峰),[7] C. Petrovic,[7]
Z. V. Popović,[3,8] and R. Hackl[1]
[1]*Walther Meissner Institut, Bayerische Akademie der Wissenschaften, 85748 Garching, Germany*
[2]*Fakultät für Physik E23, Technische Universität München, 85748 Garching, Germany*
[3]*Center for Solid State Physics and New Materials, Institute of Physics Belgrade, University of Belgrade, Pregrevica 118, 11080 Belgrade, Serbia*
[4]*Scientific Computing Laboratory, Center for the Study of Complex Systems, Institute of Physics Belgrade, University of Belgrade, Pregrevica 118, 11080 Belgrade, Serbia*
[5]*Faculty of Physics, University of Belgrade, Studentski trg 12, Belgrade, Serbia*
[6]*Department of Physics and Astronomy, University of Wisconsin Oshkosh, Oshkosh, Wisconsin 54901, USA*
[7]*Condensed Matter Physics and Materials Science Department, Brookhaven National Laboratory, Upton, New York 11973-5000, USA*
[8]*Serbian Academy of Sciences and Arts, Knez Mihailova 35, 11000 Belgrade, Serbia*

(Received 12 December 2017; published 12 February 2018)

We present results from light scattering experiments on tetragonal FeS with the focus placed on lattice dynamics. We identify the Raman active A_{1g} and B_{1g} phonon modes, a second order scattering process involving two acoustic phonons, and contributions from potentially defect-induced scattering. The temperature dependence between 300 and 20 K of all observed phonon energies is governed by the lattice contraction. Below 20 K the phonon energies increase by 0.5–1 cm^{-1}, thus indicating putative short range magnetic order. Along with the experiments we performed lattice-dynamical simulations and a symmetry analysis for the phonons and potential overtones and find good agreement with the experiments. In particular, we argue that the two-phonon excitation observed in a gap between the optical branches becomes observable due to significant electron-phonon interaction.

DOI: 10.1103/PhysRevB.97.054306

I. INTRODUCTION

In the iron based superconductors (IBS) magnetic order, structure, nematicity, and superconductivity are closely interrelated. Upon substituting atoms in the parent compounds the properties change in a way that the shape of the Fermi surface is generally believed to play a crucial role. Yet, the magnetic properties were found recently to be more complex and to depend also on the degree of correlation in the individual *d* orbitals contributing to the density of states close to the Fermi surface [1–3].

The influence of correlation effects seems to increase from the 122 systems such as BaFe$_2$As$_2$ to the 11 chalcogenides FeTe, FeSe, and FeS [4,5]. Surprisingly, the properties of the 11 class members differ substantially although they are isostructural and isoelectronic [3,6]: FeSe undergoes a structural transition at $T_s \sim 90$ K and displays electronic nematicity [7]. While long-range magnetic order cannot be observed down to the lowest temperatures [7–10] the thermodynamic properties and the Raman spectra strongly support the presence of short-ranged magnetism [11,12]. Below $T_c \sim 9$ K superconductivity is observed [13] in pristine FeSe. In mono-layer FeSe T_c can reach values close to 100 K [14,15].

The replacement of Se by Te leads to slightly off-stoichiometric Fe$_{1+y}$Te which exhibits a simultaneous magnetostructural transition near 67 K [16] but is not superconducting [17,18]. Finally, FeS having a superconducting transition at $T_c \sim 5$ K [19] remains tetragonal down to the lowest temperatures [20]. It is still an open question whether tetragonal FeS hosts magnetic order. Obviously, the iron-chalcogenides are at the verge of various neighboring phases and very susceptible to small changes in the lattice and electronic structure. Yet direct access to the competing phases is still very difficult in FeTe and FeS because of the variation of the crystal quality across the families.

Here, we choose a slightly different approach and do not look directly at the electronic but rather at the lattice properties in FeS close to potential instabilities and use the Raman-active phonons as probes. We identify the A_{1g} and B_{1g} modes, a two-phonon scattering process, and a fourth mode from either defect-induced scattering or second-order scattering as well. These results are in good agreement with numerical calculations. Furthermore the temperature dependence of all phononic modes supports the results reported in Refs. [21,22], where emerging short range magnetic order at approximately 20 K was reported.

II. EXPERIMENT

Single crystals of FeS were synthesized as described elsewhere [23]. Before the experiment the samples were cleaved in air.

---

[*] Present address: Physikalisches Institut, Goethe Universität, 60438 Frankfurt am Main, Germany.

[†] Present address: Fakultät für Physik E21, Technische Universität München, 85748 Garching, Germany.

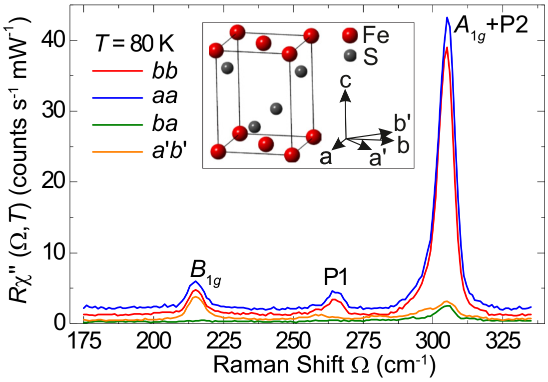

FIG. 1. Raman spectra of FeS at $T = 80$ K measured with light polarizations as indicated. The inset shows the crystal structure of FeS and the polarization directions with respect to the crystal orientation.

Calibrated customized Raman scattering equipment was used for the experiment. The samples were attached to the cold finger of a He-flow cryostat having a vacuum of approximately 5×10^{-5} Pa. For excitation we used a diode-pumped solid state laser emitting at 575 nm (Coherent GENESIS). Polarization and power of the incoming light were adjusted in a way that the light inside the sample had the proper polarization state and, respectively, a power of typically $P_a = 3$ mW independent of polarization. The samples were mounted as shown in the inset of Fig. 1. The crystallographic axes are a and b with $|a| = |b|$. The c axis is parallel to the optical axis. a' and b' are rotated by 45° with respect to a and b. The laser beam reached the sample at an angle of incidence of 66° and was focused to a spot of approximately 50 μm diameter. The plane of incidence is the bc plane. By choosing proper in-plane polarizations of the incident and scattered light the four symmetry channels A_{1g}, A_{2g}, B_{1g}, and B_{2g} of the D_{4h} space group can be accessed. Additionally, for the large angle of incidence, exciting photons being polarized along the b axis have a finite c-axis projection and the E_g symmetry can also be accessed. For the symmetry assignment we use the 2 Fe unit cell (crystallographic unit cell).

The observed phonon lines were analyzed quantitatively. Since the phonon lines are symmetric and $\Gamma_L(T) \ll \omega(T)$ the intrinsic line shape can be described by a Lorentz function with a central temperature dependent energy $\omega(T)$ and a width $\Gamma_L(T)$ (FWHM). The widths turn out to be comparable to the resolution σ of the spectrometer. Therefore, the Lorentzian needs to be convoluted with a Gaussian having width $\Gamma_G \equiv \sigma$.

III. THEORY

The electronic structure and the phonon dispersion were calculated using density functional theory (DFT) and density functional perturbation theory (DFPT), respectively, [24] within the QUANTUM ESPRESSO package [25]. The calculations were performed with the experimental unit cell parameters $a = 3.6735$ Å, $c = 5.0328$ Å, and $z = 0.2602$, where z is the height of the sulfur atoms above the Fe plane in units of the c axis [26]. We used the Vanderbilt ultrasoft pseudopotentials with the Becke-Lee-Yang-Parr (BLYP) exchange-correlation functional and s and p semicore states included in the valence for iron. The electron-wave-function and density energy cutoffs were 70 Ry and 560 Ry, respectively, chosen to ensure stable convergence of the phonon modes. We used a Gaussian smearing of 0.01 Ry. The Brillouin zone was sampled with a $16 \times 16 \times 16$ Monkhorst-Pack k-space mesh. Our electronic structure and phonon calculations are in agreement with previously reported results [27,28].

The experimental positions of the S atoms entail a nonzero z component of the force of 6×10^{-2} Ry/a_B acting on them with a_B the Bohr radius. However, the relaxation of the z positions of the S atoms would result in a large discrepancy between the calculated and experimental energies of the optical branches [28], whereas the phonon frequencies calculated from experimental structure parameters are in good agreement with the experiment (see Table II). When using the measured lattice parameters, including atomic positions, some of the acoustic phonons are unstable and do not have a linear dispersion at small **k**. Upon relaxing the atomic positions the acoustic dispersion becomes linear and the energies at the zone boundary decrease slightly. The energies of the optical branches, on the other hand, increase by some 10%. Having all this in mind, we choose to use the experimental lattice parameters stated above. In this sense our calculations should be understood as a compromise.

The phonon dispersion and the density of states were calculated on a $6 \times 6 \times 6$ Monkhorst-Pack k-point mesh, and the dispersion is interpolated along the chosen line. The calculated phonon dispersions of the experimental and relaxed structures qualitatively coincide and display similar shapes and a gap. Discrepancies only appear in the absolute energies.

The selection rules for two-phonon processes were calculated using the modified group projector technique (MGPT) [29], which avoids summing over an infinite set of space group elements.

IV. RESULTS AND DISCUSSION

A. Polarization dependence

Raman spectra of FeS for four linear polarization configurations at a sample temperature of $T = 80$ K are shown in Fig. 1. Three peaks can be identified at 215, 265, and 305 cm^{-1}. The symmetric peak at 215 cm^{-1} shows up for aa, bb, and $a'b'$ polarizations, but vanishes for ba polarization. Hence the excitation obeys B_{1g} selection rules and can be identified as the out-of-phase vibration of iron atoms along the c axis. The strongest slightly asymmetric peak at 305 cm^{-1} obeys A_{1g} selection rules with contributions of order 5% in ba and $a'b'$ polarizations from either leakage or defect-induced scattering. An asymmetric Fano-type line shape can be acquired by coupling a phonon to an electronic continuum. However, as shown in Fig. 6 in the Appendixes, we find that the superposition of two symmetric, yet spectrally unresolved peaks gives a better agreement with the data than the description in terms of a Fano function. The stronger peak at 305 cm^{-1} has A_{1g} symmetry with some remaining leakage. We therefore identify this mode with the in-phase vibration of sulfur atoms along the c axis. The second peak, labeled P2, appears in spectra with parallel light polarizations and vanishes in ba, but has some contribution in $a'b'$ polarizations, suggesting mixed A_{1g} and B_{1g} symmetry. The third peak, labeled P1, is symmetric and appears only in

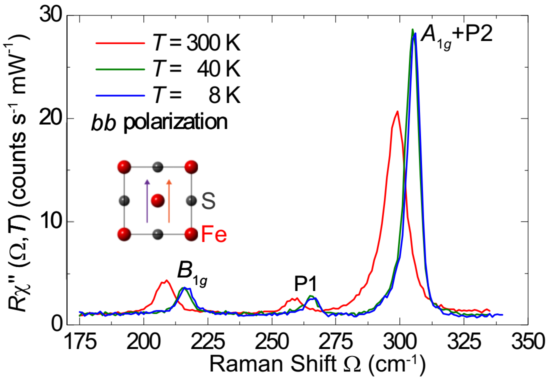

FIG. 2. Raman spectra of FeS in *bb* polarization projecting $A_{1g} + B_{1g} + E_g$ symmetries measured at temperatures given in the legend. The inset shows the light polarizations with respect to the crystal orientation.

spectra with parallel light polarizations and thus has pure A_{1g} symmetry.

B. Temperature dependence

For properly assigning all observed modes and for getting access to putative phase transitions we studied the temperature dependence. Figure 2 shows Raman spectra in *bb* polarization at 8, 40, and 300 K. The three peaks shift to higher energies upon cooling. The fourth peak P2 cannot be resolved in the raw data and can only be analyzed after a fitting procedure (see Appendix B). The peak energies $\omega(T)$ and the (intrinsic) linewidths $\Gamma_L(T)$ were determined as described at the end of Sec. II. All four modes show a monotonous increase in energy and decrease in linewidth upon cooling as shown in Fig. 3. Below 20 K the increase in the energies accelerates. We first address this overall behavior and disregard the anomaly around 50 K for the moment.

The shift and narrowing of all modes can be explained in terms of lattice contraction using a constant Grüneisen parameter γ and anharmonic decay into other phonon modes, respectively. The change in the (Lorentzian) linewidth $\Gamma_L(T)$ is given by [30]

$$\Gamma_L(T) = \Gamma_{L,0}\left(1 + \frac{2\lambda_{\text{ph-ph}}}{\exp\left(\frac{\hbar\omega_0}{2k_B T}\right) - 1}\right). \tag{1}$$

The zero temperature limits $\Gamma_{L,0}$ and ω_0 were obtained by extrapolating the respective experimental points of $\Gamma_L(T)$ and $\omega(T)$ in the range $20 \leqslant T \leqslant 50$ K to $T = 0$ (Fig. 3). With the phonon-phonon coupling $\lambda_{\text{ph-ph}}$ being the only free parameter the temperature dependence of $\Gamma_L(T)$ can be described as shown by red dashed lines in Fig. 3. The phonon energy $\omega(T)$ contains contributions from both the anharmonic decay and the lattice contraction, which depends essentially on the thermal occupation of the phonons, and can be written as [31]

$$\omega(T) = \omega_0\left[1 - \gamma\frac{V(T) - V_0}{V_0} - \left(\frac{\Gamma_{L,0}}{\sqrt{2}\omega_0}\right)^2\left(1 + \frac{4\lambda_{\text{ph-ph}}}{\exp\left(\frac{\hbar\omega_0}{2k_B T}\right) - 1}\right)\right]. \tag{2}$$

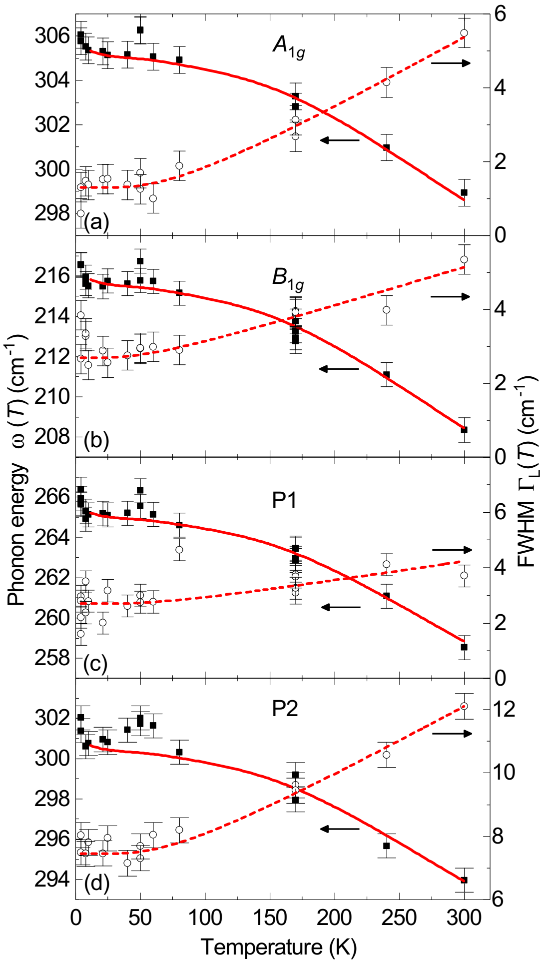

FIG. 3. Temperature dependence of energy and width of the four observed phonon modes in FeS. Black squares show the phonon energies ω; open circles denote the phonon linewidths Γ_L. The red dashed and solid lines represent the temperature dependencies of the phonon linewidths and energies according to Eqs. (1) and (2), respectively. For better visualizing the low-temperature part, the data of this figure are plotted on a logarithmic temperature scale in Fig. 8 of Appendix D.

$V(T)$ and V_0 are the volumes of the unit cell at temperatures T and $T \to 0$, respectively. The numbers for the calculations are taken from Ref. [20]. The second term describes the effect of phonon damping on the line position in the harmonic approximation. Using $\lambda_{\text{ph-ph}}$ from Eq. (1), the Grüneisen parameter γ is the only free parameter and is assumed to be constant. The temperature dependencies $\omega(T)$ resulting from the fits are plotted in Fig. 3 as solid red lines. The numerical values for parameters γ and $\lambda_{\text{ph-ph}}$ obtained from the T-dependent energy and linewidth are compiled in Table I.

Below 20 K and around 50 K anomalies are found in the experimental data as follows:

(i) At 50 K the peak energies of all four modes deviate significantly from the otherwise smooth temperature dependence. The nearly discontinuous increase in energy could be reproduced for the A_{1g} phonon and peak P2 in multiple measurements. For the B_{1g} phonon and mode P1 the anomaly is not as clearly reproducible. The energy anomalies do not

TABLE I. Symmetry, Grüneisen constant γ, and phonon-phonon coupling parameter $\lambda_{\text{ph-ph}}$ of the four experimentally observed modes.

Mode	Symmetry	γ	$\lambda_{\text{ph-ph}}$
S	A_{1g}	2.2	1.68
Fe	B_{1g}	3.4	0.31
P1	A_{1g}	2.4	0.25
P2	$A_{1g} + B_{1g}$	2.2	0.31

have a correspondence in the linewidth. As there is neither an abrupt change in the lattice constants [20] nor any other known phase transition close to 50 K the origin of this anomaly remains unexplained although we consider it significant.

(ii) Upon cooling from 20 K to 4 K all four modes exhibit sudden, yet small, increases in energy. The changes in width are heterogeneous in that the A_{1g} mode narrows and the B_{1g} mode broadens. No clear tendencies can be derived for modes P1 and P2. Sudden changes in the temperature dependence typically indicate phase transitions. Yet, no phase transition has been identified so far. However, the anomaly at 20 K coincides with the emergence of short range magnetic order as inferred from two μSR studies [21,22]. Susceptibility measurements on a sample from the same batch were inconclusive. On the other hand, the XRD data show a small anomaly in the lattice parameters and the unit cell volume does not saturate at low temperature but rather decreases faster between 20 K and 10 K than above 20 K [20]. This volume contraction by and large reproduces the change in the phonon energies as can be seen by closely inspecting the low-temperature parts of Fig. 3 (see also Fig. 8). Hence the indications of short-range magnetism in FeS found by μSR have a correspondence in the temperature dependence of the volume and the phonon energies.

Clear phonon anomalies were observed at the onset of the spin density wave (SDW) phases in 122 systems [32–34] and of the more localized magnetic phase in FeTe [35], whereas continuous temperature dependence of the phonons was found in systems without long-range magnetism [36,37]. Upon entering the SDW state in the 122 systems the A_{1g} (As) mode softens abruptly and narrows by a factor of 3, whereas the B_{1g} (Fe) mode stays pinned and narrows only slightly [32]. The strong coupling of the As mode to magnetism was traced back to the interaction of the Fe magnetic moment with the Fe-As tetrahedra angle [38], which goes along with a change of the c-axis parameter. In Fe_{1+y}Te the roles of the B_{1g} and A_{1g} modes are interchanged [35,39,40]. In contrast, all four modes observed here in FeS harden below $T^* \approx 20$ K being indicative of a type of magnetic ordering apparently different from that in the other Fe-based systems.

Very recently, commensurate magnetic order with a wave vector of $\mathbf{q} = (0.25,0.25,0)$ was found in FeS below $T_{\text{N}} = 116$ K using neutron powder diffraction [41]. In the Raman spectra no anomalies can be seen around 120 K even if the range is studied with fine temperature increments of 10 K as shown in Appendix C. However, a small change in the temperature dependence of the c-axis parameter is observed around 100 K by XRD [20], which could be related to this type of magnetic order. Since the influence on the volume is small there is no detectable impact on the phonons.

TABLE II. Raman active phonon modes in t-FeS. Shown are the symmetries, the theoretical predictions for the experimental lattice parameters at $T = 0$, and the atoms involved in the respective vibrations. The experimental energies in the third column are extrapolations to $T = 0$ of the points measured between 20 K and 50 K.

	Phonon energy (cm^{-1})		
Symmetry	Calculation	Experiment	Atomic displacement
A_{1g}	316.1	305.3	S
B_{1g}	220.4	215.8	Fe
E_g	231.6		Fe, S
E_g	324.8		Fe, S

C. Analysis of the modes P1 and P2

Based on the energies, the selection rules, and the temperature dependence we first clarify the phononic nature of the two lines P1 and P2, which cannot as straightforwardly be identified as lattice vibrations as the in-phase sulfur and out-of-phase iron vibrations at 305.3 and 215.8 cm^{-1}. Second we derive their origin from the phonon density of states (PDOS) calculated for the zero-temperature limit.

All experimental energies for $T \to 0$ were derived from the points at low temperature as described in Sec. IV B (see also Fig. 3). The results for the modes at the Γ point are summarized in Table II and can be directly compared to the results of the calculations. The discrepancies between the experimental and theoretical energies for the Raman-active phonons are smaller than 4%. The price for this accuracy in the optical energies is an instability and possibly too high energies in the acoustical branches at small and, respectively, large momentum (see Sec. III).

The unidentified peaks P1 and P2 appear in the spectra measured with aa polarization, where none of the electric fields has a projection on the c axis. Thus they cannot have E_g symmetry obeying ca and cb selection rules. In addition, the observed energies would be relatively far off of the calculated energies (see Table II). Both peaks exhibit temperature dependencies similar to those of the two Raman-active phonons and the Grüneisen parameters are close to the typical value [42] of 2 and similar to those of the Raman-active phonons. The phonon-phonon coupling parameters $\lambda_{\text{ph-ph}}$ derived from the temperature dependence of the linewidths are close to 0.3 similar to that of the B_{1g} phonon. $\lambda_{\text{ph-ph}}$ of the A_{1g} phonon is roughly five times bigger for reasons we address later. Yet, because of the small prefactor $(\Gamma_{\text{L},0}/\sqrt{2}\omega_0)^2 = O(10^{-3})$, the contribution of phonon-phonon coupling to the temperature dependence of $\omega(T)$ remains negligible in all cases and the phonon energies are essentially governed by the lattice contraction. These considerations demonstrate the phononic origin of the peaks P1 and P2.

In the second step we try to identify the phonon branches to which P1 and P2 can be related. To this end the full phonon dispersion and density of states (PDOS) were derived as described in Sec. III and are plotted in Fig. 4.

Independent of using the relaxed or experimental structure, P1 is located in the gap of the (theoretical) PDOS and cannot result from first order defect-induced Raman scattering. What

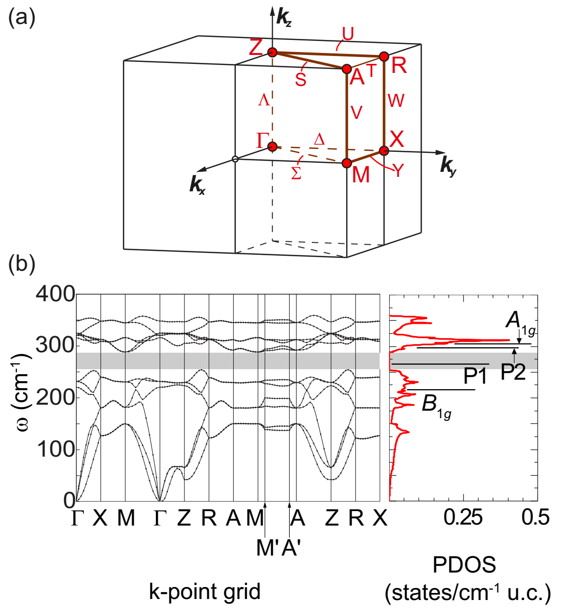

FIG. 4. Phonon dispersion of t-FeS. (a) Brillouin zone with high symmetry points and lines [43]. (b) Phonon dispersion along the directions as indicated and phonon density of states (PDOS). The gray-shaded area marks the gap in the phonon dispersion. The dispersion shown here is derived using experimental lattice parameters. For this reason some of the acoustic phonons are unstable and do not have a linear dispersion around the Γ point. Upon relaxing the structure the acoustic dispersion becomes linear at Γ, and the energies at the zone boundary decrease slightly. The energies of the optical branches, on the other hand, increase by some 10%. $M' = (0.4{,}0.4{,}0.0)$ and $A' = (0.4{,}0.4{,}0.5)$. The experimental energies of the four observed modes are shown as black lines.

alternatives exist for explaining P1? If we exclude exotic explanations such as a collective mode for the reasons given above the energy of $\omega_{\mathrm{P1}} = 265\ \mathrm{cm}^{-1}$ can only be obtained by the sum of two phonon modes having equal energy $\omega_{\mathrm{P1}}/2$ and momenta $\mathbf{k}$ and $-\mathbf{k}$ (for maintaining the $q \approx 0$ selection rule). As shown for various transition metal compounds including TiN, ZrN, or NbC second-order phonon Raman scattering can occur in the presence of defects [44]. Then first-order scattering being proportional to the PDOS (modulo energy and symmetry dependent weighting factors) is expected to be also substantial if not stronger. Although our crystals are slightly disordered there is no indication of substantial intensity at energies with high PDOS as can be seen by directly comparing Figs. 1 and 4(b). Alternatively, second-order scattering can originate in enhanced electron-phonon coupling [45]. In either case the energies of two phonons add up as they get excited in a single scattering process. Generally, no selection rules apply for second order Raman scattering and the resulting peak would appear in all symmetry channels [46]. Exceptions exist if the phonon wave vectors coincide with high-symmetry points or lines of the Brillouin zone.

From the phonon dispersion alone several phonon branches having $\mathbf{k}$ and $-\mathbf{k}$ and energies in the range around $\omega_{\mathrm{P1}}/2$ could add up to yield $265\ \mathrm{cm}^{-1}$ (see Fig. 4). However, as explained in Appendix F and shown in Table III for the space group P4/nmm of t-FeS, the A_{1g} selection rules of P1 exclude all nonsymmetric combinations of branches (right column of Table III). On the other hand, all symmetric combinations include A_{1g} selection rules for the two-phonon peak (left column of Table III) and one has to look essentially for a high PDOS in the range $\omega_{\mathrm{P1}}/2$. As shown in Fig. 4(b) the PDOS has a maximum in the right energy range. Since the maximum results from momenta away from the high-symmetry points or lines (see Fig. 4) which alone lead to pure A_{1g} symmetry one expects also intensity in B_{1g} and E_g symmetry as opposed to the experiment. For exclusive A_{1g} selection rules only seven possibilities exist. Since phase space arguments favor modes having a flat dispersion in extended regions of the Brillouin zone the Γ, M, and/or A points are unlikely to give rise to P1, and only the lines $S = A - Z$, $\Sigma = \Gamma - M$, and $V = A - M$ remain. The dispersion along the S or Σ branch contributes very little to the PDOS. On the high-symmetry line V a doubly degenerate branch would have a flat dispersion [see Fig. 4(b)] and contributes substantially to the PDOS but the energy of $150\ \mathrm{cm}^{-1}$ differs by 13% from the expected energy of $132.5\ \mathrm{cm}^{-1}$. Instead of arguing about the accuracy of the theoretical phonon energies (see Sec. III) we looked at the dispersion close to but not strictly on V where the contribution to B_{1g} and E_g symmetries is expected to be still very small, e.g., along $M' - A'$ [Fig. 4(b)]. A detailed inspection shows that the maximum of the PDOS between 130 and $140\ \mathrm{cm}^{-1}$ comes from there. This explains both the selection rules and the energy of P1 to within a few percent.

Peak P2 cannot be explained in terms of one of the two E_g phonons either. As opposed to P1 it is not inside the gap of the PDOS and thus can originate from either first or second order scattering. If P2 originates in second order scattering in the same fashion as P1 there are five possibilities yielding $A_{1g} + B_{1g}$ but not E_g selection rules. As explained in the last paragraph only the branches $\Delta = \Gamma - X$ and $U = Z - R$ may contribute. For the low PDOS there we consider also first order defect-induced scattering for P2 to originate from. In fact, the PDOS possesses its strongest maximum $5\ \mathrm{cm}^{-1}$ below the (theoretical) A_{1g} phonon exactly where P2 is found. In spite of the very high PDOS here, the peak is weak explaining the negligible contributions from first order defect-induced scattering at lower energies. The high PDOS between 300 and $325\ \mathrm{cm}^{-1}$ may also be an alternative yet less likely explanation for the weak contributions in crossed polarizations in the energy range of the A_{1g} phonon (Fig. 1).

Finally, we wish to clarify whether the large phonon-phonon coupling $\lambda_{\text{ph-ph}}^{A1g}$ found for the A_{1g} Raman-active mode (see Table I) is related to the appearance of P1. Due to the close proximity of the energies the A_{1g} mode apparently decays into states close to those adding up to yield P1. The decay is less restricted by symmetry leaving more options. For both processes the phonon-phonon coupling has to be substantial with the order of magnitude given by $\lambda_{\text{ph-ph}}^{A1g} \approx 1.7$. Phonon-phonon coupling is present in any type of material because of the anharmonic potential. Defects enhance this effect [44]. Since FeS is a metal the phonon-phonon coupling goes at least partially through electronic states and may be indicative of enhanced electron-phonon coupling, $\lambda_{\text{el-ph}}$, as described, e.g., in Ref. [45]. The related contribution to $\lambda_{\text{ph-ph}}$ is then expected

TABLE III. Two-phonon processes in FeS. The symmetry group of the FeS system is the space group $P4/nmm$. For products of irreducible representations (IRs) in the left column Raman active modes (RM) in decomposition are given in the right one. Raman active modes of FeS are Γ_1^+ (A_{1g}), Γ_2^+ (B_{1g}), and two double degenerate Γ_5^+ (E_g). Γ_1^+ comes from vibrations of S atoms, Γ_2^+ from Fe ones, and both atom types contribute with one pair of Γ_5^+ modes. For complex representations ($V_{1,2,3,4}$ and all W) the double index indicates that the real representation is used, for example, $V_{13} = V_1 \oplus V_1^* = V_1 \oplus V_3$. Irreducible representations of the space group given in Ref. [53] are used.

Overtones		Combinations	
IR products (phonon states)	RM in decomposition	IR products (phonon states)	RM in decomposition
$[(\Gamma_i^\pm)^2]$ $(i = 1,2,3,4)$	A_{1g}	$\Gamma_1^h \otimes \Gamma_2^h, \Gamma_3^h \otimes \Gamma_4^h$ $(h = \pm)$	B_{1g}
$[(\Gamma_5^\pm)^2]$	A_{1g}, B_{1g}	$\Gamma_i^h \otimes \Gamma_5^h$ $(i = 1,2,3,4, h = \pm)$	E_g
$[(X_i)^2]$ $(i = 1,2)$	A_{1g}, B_{1g}, E_g	$X_1 \otimes X_2$	E_g
$[(M_i)^2]$ $(i = 1,2,3,4)$	A_{1g}	$M_1 \otimes M_2, M_3 \otimes M_4$	B_{1g}
$[(\Sigma_i)^2]$ $(i = 1,2,3,4)$	A_{1g}	$M_1 \otimes M_3, M_1 \otimes M_4, M_2 \otimes M_3, M_2 \otimes M_4$	E_g
$[(\Delta_i)^2]$ $(i = 1,2,3,4)$	A_{1g}, B_{1g}	$\Sigma_1 \otimes \Sigma_2, \Sigma_3 \otimes \Sigma_4$	B_{1g}
$[(V_{13})^2], [(V_{24})^2], [(V_5)^2]$	A_{1g}	$\Sigma_1 \otimes \Sigma_3, \Sigma_1 \otimes \Sigma_4, \Sigma_2 \otimes \Sigma_3, \Sigma_2 \otimes \Sigma_4$	E_g
$[(W_{13})^2], [(W_{24})^2]$	A_{1g}, B_{1g}, E_g	$\Delta_1 \otimes \Delta_2, \Delta_1 \otimes \Delta_3, \Delta_2 \otimes \Delta_4, \Delta_3 \otimes \Delta_4$	E_g
$[(Y_1)^2]$	A_{1g}, B_{1g}, E_g	$V_{13} \otimes V_{24}$	Γ_2^+
$[(Z_i^\pm)^2]$ $(i = 1,2,3,4)$	A_{1g}	$V_{13} \otimes V_5, V_{24} \otimes V_5$	Γ_5^+
$[(Z_5^\pm)^2]$	A_{1g}, B_{1g}	$W_{13} \otimes W_{24}$	Γ_5^+
$[(A_i)^2]$ $(i = 1,2,3,4)$	A_{1g}	$Z_1^h \otimes Z_2^h, Z_3^h \otimes Z_4^h$ $(h = \pm)$	B_{1g}
$[(R_i)^2]$ $(i = 1,2)$	A_{1g}, B_{1g}, E_g	$Z_i^h \otimes Z_5^h$ $(i = 1,2,3,4, h = \pm)$	E_g
$[(S_i)^2]$ $(i = 1,2,3,4)$	A_{1g}	$A_1 \otimes A_2, A_3 \otimes A_4$	B_{1g}
$[(U_i)^2]$ $(i = 1,2,3,4)$	A_{1g}, B_{1g}	$A_1 \otimes A_3, A_1 \otimes A_4, A_2 \otimes A_3, A_2 \otimes A_4$	E_g
$[(\Lambda_i)^2]$ $(i = 1,2,3,4)$	A_{1g}	$R_1 \otimes R_2$	E_g
$[(\Lambda_5)^2]$	A_{1g}, B_{1g}	$S_1 \otimes S_2, S_3 \otimes S_4$	B_{1g}
$[(T_1)^2]$	A_{1g}, B_{1g}, E_g	$S_1 \otimes S_3, S_1 \otimes S_4, S_2 \otimes S_3, S_2 \otimes S_4$	E_g
		$U_1 \otimes U_2, U_1 \otimes U_3, U_2 \otimes U_4, U_3 \otimes U_4$	E_g
		$\Lambda_1 \otimes \Lambda_2, \Lambda_3 \otimes \Lambda_4$	B_{1g}
		$\Lambda_i \otimes \Lambda_5$ $(i = 1,2,3,4)$	E_g

to be proportional to $\lambda_{\text{el-ph}}^2$. This conclusion is compatible with early results on the branch-dependent electron-phonon coupling in LaFeAsOF, where the strongest effects are reported for some Γ-point modes and the acoustic branches with intermediate to large momenta [47]. $\lambda_{\text{ph-ph}}^{A1g} > 1$ and the two-phonon peak P1 indicate that the electron-phonon coupling is possibly larger than in the other Fe-based systems and reaches values up to unity. In BaFe_2As_2, as an example from the pnictide family, $\lambda_{\text{el-ph}}^2 \approx (1–4) \times 10^{-2} < \lambda_{\text{ph-ph}} \approx 0.1$ is reported [32,48,49]. On the other hand, one finds $\lambda_{\text{el-ph}}^2 \approx 0.4 < \lambda_{\text{ph-ph}} \approx 0.9$ for the E_g phonon in MgB_2, being generally believed to be a conventional superconductor [50,51]. Thus one may speculate whether $\lambda_{\text{el-ph}}$ might be even large enough in FeS to account for a T_c in the 5 K range.

V. CONCLUSION

We have studied and identified phonons in tetragonal FeS by Raman scattering. For the A_{1g} sulfur and B_{1g} iron mode the DFT and DFPT calculations agree to within a few percent with the experiment. A third observed peak within a gap in the theoretical phonon density of states can be identified as a second order scattering process involving two phonons. Both the selection rules, based on the modified group projector technique, and the energy are in agreement with the experiment. A fourth mode identified close to the A_{1g} sulfur phonon can be traced back to the biggest maximum of the PDOS and is most likely activated by a small amount of defects.

The temperature dependence of all four modes is governed by the contraction of the lattice, but shows anomalies at 50 K and below 20 K. The anomaly observed at 20 K has a correspondence in the thermal expansion [20] and μSR experiments [21,22], which indicate short-range magnetic order. The long-range magnetic order observed recently by neutron diffraction experiments [41] below $T_N = 116$ K has no correspondence in the Raman spectra.

The appearance of two-phonon scattering indicates strong phonon-phonon scattering, which is likely to originate from an electron-phonon interaction being enhanced in comparison to other pnictides and chalcogenides. We argue that in FeS the T_c can in principle entirely result from electron-phonon interaction.

ACKNOWLEDGMENTS

We acknowledge valuable discussions with T. Böhm and D. Jost. The work was supported by the German Research Foundation (DFG) via the Priority Program SPP 1458 (Grant No. Ha2071/7) and the Serbian Ministry of Education, Science

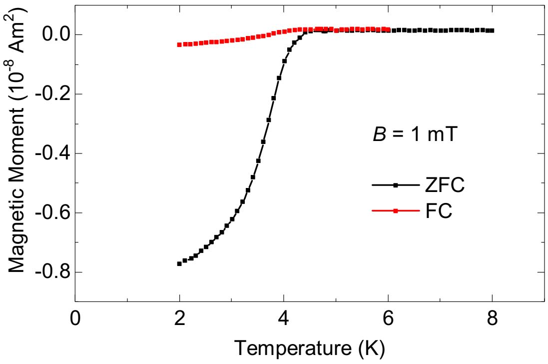

FIG. 5. Magnetization measurements of t-FeS at an applied field of $B = 1$ mT cooled to 2 K with (red curve) and without applied field (black curve).

and Technological Development under Projects No. III45018 and No. ON171017. Numerical simulations were run on the PARADOX supercomputing facility at the Scientific Computing Laboratory of the Institute of Physics Belgrade. We acknowledge support by the DAAD through the bilateral project between Serbia and Germany (Grants No. 56267076 and No. 57142964). Work carried out at the Brookhaven National Laboratory was primarily supported by the Center for Emergent Superconductivity, an Energy Frontier Research Center funded by the U.S. DOE, Office of Basic Energy Sciences (A.W. and C.P.). N.S. was supported by UW Oshkosh FDS498 grant.

A.B. and A.M. have contributed equally to this work.

APPENDIX A: MAGNETIZATION MEASUREMENTS

Figure 5 shows magnetization measurements on a t-FeS sample from the batch studied in small applied fields. Measurements were done on a Quantum Design MPMS XL-7 SQUID magnetometer by cooling the sample to 2 K and sweeping the temperature at 0.1 K/min. When cooled without applied field (ZFC, black curve) the sample shows a superconducting transition with onset at 4.5 K and a center of the transition at 3.6 K. When cooled in an applied field the magnetization decreases only weakly in the superconducting state indicating strong pinning.

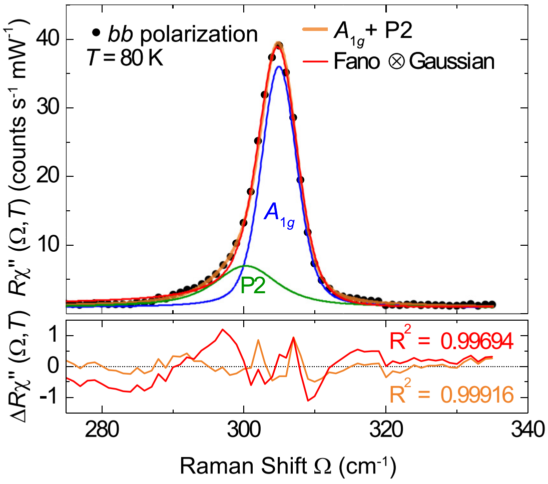

FIG. 6. Decomposition of the asymmetric phonon peak at 305 cm^{-1}. Measured data are shown as black dots. The orange line shows the sum of two Voigt profiles shown as blue and green lines, respectively. The convolution of Fano and Gaussian (red line) deviates in the peak flanks and the nearby continuum.

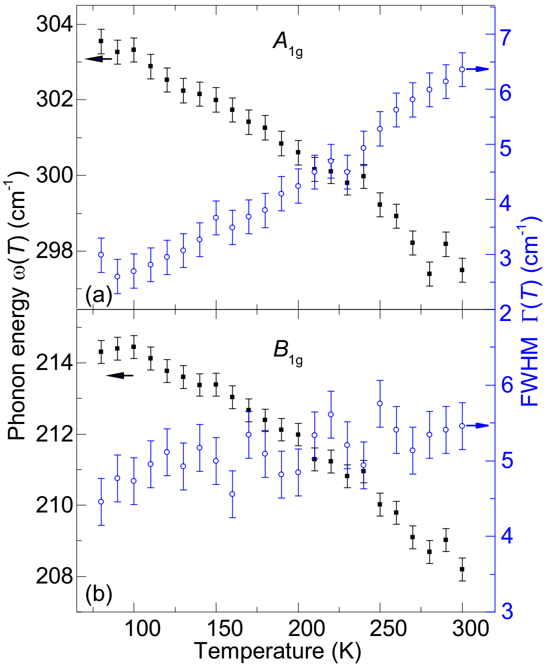

FIG. 7. Temperature dependence of A_{1g} and B_{1g} phonon modes in the temperature range between 80 K and 300 K. Black squares denote the phonon energies; open circles denote the phonon linewidths.

APPENDIX B: DECOMPOSITION OF THE LINE AT 305 cm^{-1}

The peak at 305 cm^{-1} at low temperatures shows a significant asymmetry towards lower energies (see also Fig. 1). Coupling of the A_{1g} phonon mode to an electronic continuum by strong electron-phonon coupling would result in a line shape given by the convolution of a Fano function and a Gaussian, the latter representing the resolution of the spectrometer. We find, however, that this does not yield a satisfactory description of the measured line shape as can be seen from the red curve in Fig. 6, and thus conclude that the asymmetry of the peak stems from the overlap of two peaks which cannot be resolved separately. The corresponding line shape is the sum of two Lorentzians convoluted with a Gaussian which governs the resolution of the setup. Due to the distributivity of the convolution this is identical to the sum of two Voigt functions sharing the same width Γ_G of the Gaussian part. The overall spectral shape is shown in Fig. 6 as an orange line and agrees excellently with the data. The two contributing lines are shown in blue and green. From the selection rules (see Fig. 1) we identify the blue curve as the in-phase vibration of sulfur atoms in A_{1g} symmetry. The green line denotes a second mode P2, the origin of which is discussed in the main text.

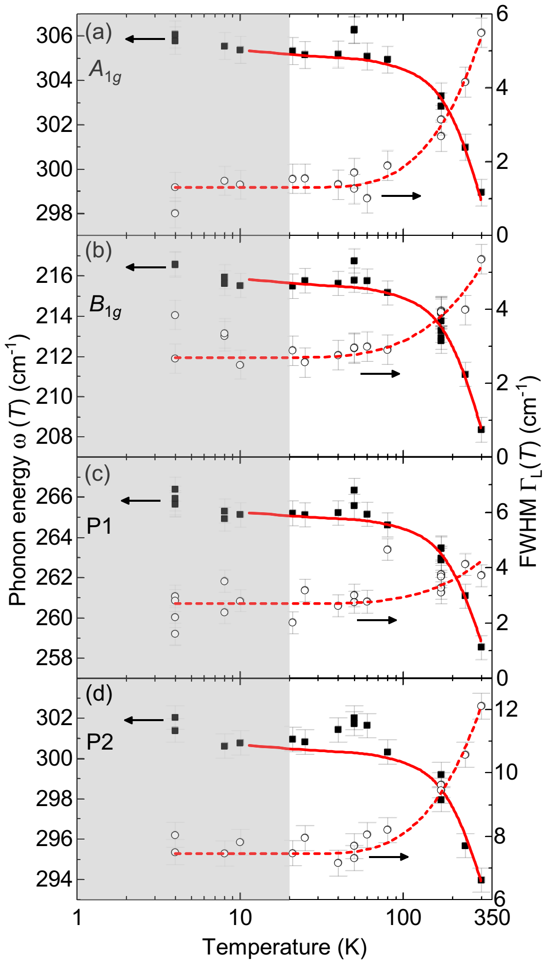

FIG. 8. Temperature dependence of energy and width of the four observed phonon modes in FeS on a logarithmic scale. The data is identical to Fig. 3 of the main text. Black squares show the phonon energies ω; open circles denote the phonon linewidths Γ_L. The red dashed and full lines represent the temperature dependence of the phonon linewidths and energies according to Eqs. (1) and (2), respectively. The region below 20 K is shaded light gray. Since the data for the volume are limited to the range above 10 K the theoretical curves for the phonon energies (full red lines) end at 10 K.

APPENDIX C: DETAILED TEMPERATURE DEPENDENCE FOR $80 \leqslant T \leqslant 300$ K

Figure 7 shows the temperature dependence of the energies ω and linewidths $\Gamma(T)$ (FWHM) from 80 K to 300 K measured in temperature increments of 10 K. Raman scattering measurements were performed using a Jobin Yvon T64000 Raman system in micro-Raman configuration. A solid state laser with 532 nm line was used as an excitation source. Measurements were performed in high vacuum (10^{-6} mbar) using a KONTI CryoVac continuous helium flow cryostat with 0.5 mm thick window. Laser beam focusing was accomplished using a microscope objective with ×50 magnification. The samples were cleaved right before being placed in the vacuum. As can be seen from Fig. 7, there is no deviation from the standard temperature behavior around 120 K.

APPENDIX D: TEMPERATURE DEPENDENCE ON A LOGARITHMIC SCALE

To better illustrate the behavior of the phonons at low temperatures Fig. 8 shows the experimental data and the theoretical curves from Fig. 3 of the main text on a logarithmic temperature scale. The region below 20 K is shaded light gray. As explained in Sec. IV B all four modes show an increase in energy below 20 K instead of the expected saturation, indicative of the putative onset of short range magnetic order. This effect manifests itself also in an incipient decrease of the unit cell volume [20] and is visible in the theoretical results for the phonon energies (full red lines). No clear tendency can be seen for the linewidths. The energy anomaly found around 50 K is discussed in the same section.

APPENDIX E: SECOND SAMPLE BATCH

Figure 9 shows Raman spectra on a t-FeS sample from a different batch (E256) taken at $T = 310$ K. The sample was oriented the same way as described in the main text. All three modes are visible for parallel light polarizations (*bb*), but vanish for crossed polarizations (*ba*), confirming the selection rules observed in the sample described in the main text. The inset shows magnetization measurements on a sample from batch E256 similar to the ones described in Appendix A. The superconducting transition sets in at 4.1 K.

APPENDIX F: SELECTION RULES FOR TWO-PHONON PROCESSES AND MGPT

In the multiphonon scattering process the system goes from an initial vibrational state (ground vibrational state) $|0,0,\ldots\rangle$ to a final multiphonon state $|n_\mu,n_{\mu'},\ldots\rangle$, where n_μ is the number of phonons in the same state μ and μ stands for the entire set of quantum numbers (quasimomentum k, angular momentum quantum number m, etc.). For two-phonon processes the final vibrational state is the state with two phonons in the same quantum state (double-phonon or the first overtone state) or with two phonons in different states (combination state). The corresponding matrix element for

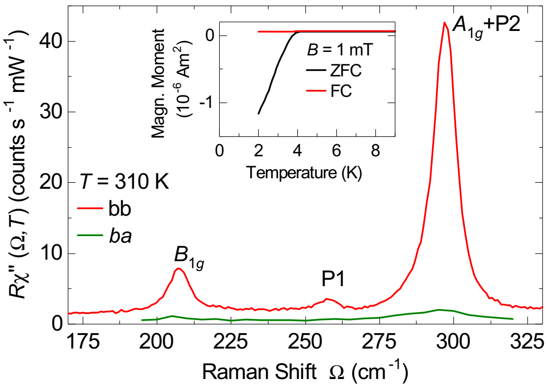

FIG. 9. Raman spectra of a t-FeS sample from a different batch taken at $T = 310$ K in polarizations as given in the legend. The inset shows magnetization measurements on a sample from this batch similar to Appendix A.

two-phonon Raman scattering is

$$\begin{aligned}&\langle 0,\ldots,n_\mu,0,\ldots|\mathcal{R}|0,0,\ldots\rangle, n_\mu = 2, \text{overtones},\\ &\langle 0,\ldots,n_\mu,0,\ldots,n_{\mu'},\ldots|\mathcal{R}|0,0,\ldots\rangle,\\ &n_\mu = n_{\mu'} = 1, \text{combinations},\end{aligned} \tag{F1}$$

where $\mathcal{R}$ is the Raman tensor. This matrix element should be a scalar or should transform as unit representation of the system space group $\mathcal{S}$. The standard approximation for the Raman tensor in infinite wavelength-light approximation for the nonresonant case is the polarizability tensor, which transforms as the (symmetrized) square of the vector representation, $D^{\mathcal{R}}(\mathcal{S})$. Decomposition of $D^{\mathcal{R}}(\mathcal{S})$ gives irreducible representations of the Raman active modes. The ground vibrational state transforms as unit representation, whereas the final two-phonon state transforms as symmetrized square, $[(D^\mu(\mathcal{S}))^2]$, of the corresponding irreducible representation $D^\mu(\mathcal{S})$ (overtones) or the direct product of two irreducible representations $D^\mu(\mathcal{S}) \otimes D^{\mu'}(\mathcal{S})$ (combinations). Symmetrization in the case of overtones comes from the bosonic nature of phonons. The matrix element [Eq. (F1)] transforms as reducible representation

$$\begin{aligned}&[(D^\mu(\mathcal{S}))^2] \otimes D^{\mathcal{R}}(\mathcal{S}), \quad \text{for overtones, or}\\ &D^\mu(\mathcal{S}) \otimes D^{\mu'}(\mathcal{S}) \otimes D^{\mathcal{R}}(\mathcal{S}), \quad \text{for combinations.}\end{aligned} \tag{F2}$$

It is a scalar if the decomposition of the representations shown above contains the unit representation or, equivalently, if the intersection of decompositions of $[(D^\mu(\mathcal{S}))^2]$ or $D^\mu(\mathcal{S}) \otimes D^{\mu'}(\mathcal{S})$ and $D^{\mathcal{R}}(\mathcal{S})$ is a nonempty set. To obtain selection rules for two-phonon processes, following Birman's original method [52], it is enough to find the decomposition of $[(D^\mu(\mathcal{S}))^2]$ (for overtones) and $D^\mu(\mathcal{S}) \otimes D^{\mu'}(\mathcal{S})$ (for combinations) for all irreducible representations. If there is any representation of the Raman active mode in those decompositions then that overtone or two-phonon combination is symmetrically allowed in the Raman scattering process. The decomposition of the (symmetrized) square of the vector representation is straightforward and is actually a finite dimensional point group problem. On the other hand, decomposition of $[(D^\mu(\mathcal{S}))^2]$ or $D^\mu(\mathcal{S}) \otimes D^{\mu'}(\mathcal{S})$ for any irreducible representation could be a difficult task because space groups are infinite. In the standard method based on character theory summation over all group elements is used and it is a problem in the infinite case. Therefore, it is necessary to apply a method which avoids summation over group elements. As is proven in Ref. [29] the modified group projector technique (MGPT) uses only group generators and finite dimensional matrices. Actually, the decomposition $D(\mathcal{S}) = \oplus_\mu f_D^\mu D^{(\mu)}(\mathcal{S})$ of the arbitrary reducible representation $D(\mathcal{S})$ into irreducible representations is effectively a determination of the frequency numbers f_D^μ. The MGPT expression for frequency numbers involves group generators s_i only:

$$f_D^\mu = \mathrm{Tr}\,F\left(\prod_{i=1}^{S} F(D(s_i) \otimes D^{(\mu)^*}(s_i))\right). \tag{F3}$$

Here S is the number of group generators, $F(X)$ is the projector on the subspace of the fixed points of the operator X, and Tr is the matrix trace (sum of the diagonal matrix elements). Consequently, the problem is reduced to calculation of the $S+1$ projector to the fixed points. Technically, one looks for the eigenspaces for the eigenvalue 1 of each of the operators $D(s_i) \otimes D^{(\mu)^*}(s_i)$, finding projectors on them, then multiplies the corresponding projectors, and repeats the procedure for the whole product from Eq. (F3). The trace of the final projector gives the corresponding frequency number.

[1] Z. P. Yin, K. Haule, and G. Kotliar, Magnetism and charge dynamics in iron pnictides, Nat. Phys. **7**, 294 (2011).

[2] Q. Si, R. Yu, and E. Abrahams, High-temperature superconductivity in iron pnictides and chalcogenides, Nat. Rev. Mater. **1**, 16017 (2016).

[3] I. Leonov, S. L. Skornyakov, V. I. Anisimov, and D. Vollhardt, Correlation-Driven Topological Fermi Surface Transition in FeSe, Phys. Rev. Lett. **115**, 106402 (2015).

[4] C. Tresca, G. Giovannetti, M. Capone, and G. Profeta, Electronic properties of superconducting FeS, Phys. Rev. B **95**, 205117 (2017).

[5] J. Miao, X. H. Niu, D. F. Xu, Q. Yao, Q. Y. Chen, T. P. Ying, S. Y. Li, Y. F. Fang, J. C. Zhang, S. Ideta, K. Tanaka, B. P. Xie, D. L. Feng, and F. Chen, Electronic structure of FeS, Phys. Rev. B **95**, 205127 (2017).

[6] S. L. Skornyakov, V. I. Anisimov, D. Vollhardt, and I. Leonov, Effect of electron correlations on the electronic structure and phase stability of FeSe upon lattice expansion, Phys. Rev. B **96**, 035137 (2017).

[7] T. M. McQueen, A. J. Williams, P. W. Stephens, J. Tao, Y. Zhu, V. Ksenofontov, F. Casper, C. Felser, and R. J. Cava, Tetragonal-to-Orthorhombic Structural Phase Transition at 90 K in the Superconductor $\mathrm{Fe}_{1.01}\mathrm{Se}$, Phys. Rev. Lett. **103**, 057002 (2009).

[8] Y. Mizuguchi, T. Furubayashi, K. Deguchi, S. Tsuda, T. Yamaguchi, and Y. Takano, Mössbauer studies on FeSe and FeTe, Physica C (Amsterdam) **470**, S338 (2010).

[9] M. Bendele, A. Amato, K. Conder, M. Elender, H. Keller, H.-H. Klauss, H. Luetkens, E. Pomjakushina, A. Raselli, and R. Khasanov, Pressure Induced Static Magnetic Order in Superconducting FeSe_{1-x}, Phys. Rev. Lett. **104**, 087003 (2010).

[10] S.-H. Baek, D. V. Efremov, J. M. Ok, J. S. Kim, J. van den Brink, and B. Büchner, Orbital-driven nematicity in FeSe, Nat. Mater. **14**, 210 (2015).

[11] M. He, L. Wang, F. Hardy, L. Xu, T. Wolf, P. Adelmann, and C. Meingast, Evidence for short-range magnetic order in the nematic phase of FeSe from anisotropic in-plane magnetostriction and susceptibility measurements, arXiv:1709.03861 [cond-mat.supr-con].

[12] A. Baum, H. N. Ruiz, N. Lazarević, Y. Wang, T. Böhm, R. Hosseinian Ahangharnejhad, P. Adelmann, T. Wolf, Z. V. Popović, B. Moritz, T. P. Devereaux, and R. Hackl, Frustrated spin order and stripe fluctuations in FeSe, arXiv:1709.08998 [cond-mat.str-el].

[13] F.-C. Hsu, J.-Y. Luo, K.-W. Yeh, T.-K. Chen, T.-W. Huang, P. M. Wu, Y.-C. Lee, Y.-L. Huang, Y.-Y. Chu, D.-C. Yan, and M.-K.

Wu, Superconductivity in the PbO-type structure α-FeSe, Proc. Natl. Acad. Sci. U.S.A. **105**, 14262 (2008).

[14] S. He, J. He, W. Zhang, L. Zhao, D. Liu, X. Liu, D. Mou, Y.-B. Ou, Q.-Y. Wang, Z. Li, L. Wang, Y. Peng, Y. Liu, C. Chen, L. Yu, G. Liu, X. Dong, J. Zhang, C. Chen, Z. Xu, X. Chen, X. Ma, Q. Xue, and X. J. Zhou, Phase diagram and electronic indication of high-temperature superconductivity at 65 K in single-layer FeSe films, Nat. Mater. **12**, 605 (2013).

[15] J.-F. Ge, Z.-L. Liu, C. Liu, C.-L. Gao, D. Qian, Q.-K. Xue, Y. Liu, and J.-F. Jia, Superconductivity above 100 K in single-layer FeSe films on doped $SrTiO_3$, Nat. Mater. **14**, 285 (2014).

[16] S. Li, C. de la Cruz, Q. Huang, Y. Chen, J. W. Lynn, J. Hu, Y.-L. Huang, F.-C. Hsu, K.-W. Yeh, M.-K. Wu, and P. Dai, First-order magnetic and structural phase transitions in $Fe_{1+y}Se_xTe_{1-x}$, Phys. Rev. B **79**, 054503 (2009).

[17] M. H. Fang, H. M. Pham, B. Qian, T. J. Liu, E. K. Vehstedt, Y. Liu, L. Spinu, and Z. Q. Mao, Superconductivity close to magnetic instability in $Fe(Se_{1-x}Te_x)_{0.82}$, Phys. Rev. B **78**, 224503 (2008).

[18] K.-W. Yeh, T.-W. Huang, Y.-l. Huang, T.-K. Chen, F.-C. Hsu, P. M. Wu, Y.-C. Lee, Y.-Y. Chu, C.-L. Chen, J.-Y. Luo, D.-C. Yan, and M.-K. Wu, Tellurium substitution effect on superconductivity of the α-phase iron selenide, Europhys. lett. **84**, 37002 (2008).

[19] X. Lai, H. Zhang, Y. Wang, X. Wang, X. Zhang, J. Lin, and F. Huang, Observation of superconductivity in tetragonal FeS, J. Am. Chem. Soc. **137**, 10148 (2015).

[20] U. Pachmayr, N. Fehn, and D. Johrendt, Structural transition and superconductivity in hydrothermally synthesized FeX (X = S, Se), Chem. Commun. **52**, 194 (2016).

[21] S. Holenstein, U. Pachmayr, Z. Guguchia, S. Kamusella, R. Khasanov, A. Amato, C. Baines, H.-H. Klauss, E. Morenzoni, D. Johrendt, and H. Luetkens, Coexistence of low-moment magnetism and superconductivity in tetragonal FeS and suppression of T_c under pressure, Phys. Rev. B **93**, 140506 (2016).

[22] F. K. K. Kirschner, F. Lang, C. V. Topping, P. J. Baker, F. L. Pratt, S. E. Wright, D. N. Woodruff, S. J. Clarke, and S. J. Blundell, Robustness of superconductivity to competing magnetic phases in tetragonal FeS, Phys. Rev. B **94**, 134509 (2016).

[23] A. Wang, L. Wu, V. N. Ivanovski, J. B. Warren, J. Tian, Y. Zhu, and C. Petrovic, Critical current density and vortex pinning in tetragonal $FeS_{1-x}Se_x$ ($x = 0,0.06$), Phys. Rev. B **94**, 094506 (2016).

[24] S. Baroni, S. de Gironcoli, A. Dal Corso, and P. Giannozzi, Phonons and related crystal properties from density-functional perturbation theory, Rev. Mod. Phys. **73**, 515 (2001).

[25] P. Giannozzi, S. Baroni, N. Bonini, M. Calandra, R. Car, C. Cavazzoni, D. Ceresoli, G. L. Chiarotti, M. Cococcioni, I. Dabo, A. D. Corso, S. de Gironcoli, S. Fabris, G. Fratesi, R. Gebauer, U. Gerstmann, C. Gougoussis, A. Kokalj, M. Lazzeri, L. Martin-Samos, N. Marzari, F. Mauri, R. Mazzarello, S. Paolini, A. Pasquarello, L. Paulatto, C. Sbraccia, S. Scandolo, G. Sclauzero, A. P. Seitsonen, A. Smogunov, P. Umari, and R. M. Wentzcovitch, QUANTUM ESPRESSO: a modular and open-source software project for quantum simulations of materials, J. Phys.: Condens. Matter **21**, 395502 (2009).

[26] A. R. Lennie, S. A. T. Redfern, P. F. Schofield, and D. J. Vaughan, Synthesis and Rietveld crystal structure refinement of mackinawite, tetragonal FeS, Mineral. Mag. **59**, 677 (1995).

[27] A. Subedi, L. Zhang, D. J. Singh, and M. H. Du, Density functional study of FeS, FeSe, and FeTe: Electronic structure, magnetism, phonons, and superconductivity, Phys. Rev. B **78**, 134514 (2008).

[28] Y. El Mendili, B. Minisini, A. Abdelouas, and J.-F. Bardeau, Assignment of Raman-active vibrational modes of tetragonal mackinawite: Raman investigations and *ab initio* calculations, RSC Adv. **4**, 25827 (2014).

[29] M. Damnjanović and I. Milošević, Full symmetry implementation in condensed matter and molecular physics–Modified group projector technique, Phys. Rep. **581**, 1 (2015).

[30] P. G. Klemens, Anharmonic decay of optical phonons, Phys. Rev. **148**, 845 (1966).

[31] H.-M. Eiter, P. Jaschke, R. Hackl, A. Bauer, M. Gangl, and C. Pfleiderer, Raman study of the temperature and magnetic-field dependence of the electronic and lattice properties of MnSi, Phys. Rev. B **90**, 024411 (2014).

[32] M. Rahlenbeck, G. L. Sun, D. L. Sun, C. T. Lin, B. Keimer, and C. Ulrich, Phonon anomalies in pure and underdoped $R_{1-x}K_xFe_2As_2$ (R = Ba, Sr) investigated by Raman light scattering, Phys. Rev. B **80**, 064509 (2009).

[33] L. Chauvière, Y. Gallais, M. Cazayous, A. Sacuto, M. A. Measson, D. Colson, and A. Forget, Doping dependence of the lattice dynamics in $Ba(Fe_{1-x}Co_x)_2As_2$ studied by Raman spectroscopy, Phys. Rev. B **80**, 094504 (2009).

[34] L. Chauvière, Y. Gallais, M. Cazayous, M. A. Méasson, A. Sacuto, D. Colson, and A. Forget, Raman scattering study of spin-density-wave order and electron-phonon coupling in $Ba(Fe_{1-x}Co_x)_2As_2$, Phys. Rev. B **84**, 104508 (2011).

[35] Y. J. Um, A. Subedi, P. Toulemonde, A. Y. Ganin, L. Boeri, M. Rahlenbeck, Y. Liu, C. T. Lin, S. J. E. Carlsson, A. Sulpice, M. J. Rosseinsky, B. Keimer, and M. Le Tacon, Anomalous dependence of *c*-axis polarized Fe B_{1g} phonon mode with Fe and Se concentrations in $Fe_{1+y}Te_{1-x}Se_x$, Phys. Rev. B **85**, 064519 (2012).

[36] Y. J. Um, J. T. Park, B. H. Min, Y. J. Song, Y. S. Kwon, B. Keimer, and M. Le Tacon, Raman scattering study of the lattice dynamics of superconducting LiFeAs, Phys. Rev. B **85**, 012501 (2012).

[37] V. Gnezdilov, Y. G. Pashkevich, P. Lemmens, D. Wulferding, T. Shevtsova, A. Gusev, D. Chareev, and A. Vasiliev, Interplay between lattice and spin states degree of freedom in the FeSe superconductor: Dynamic spin state instabilities, Phys. Rev. B **87**, 144508 (2013).

[38] T. Yildirim, Strong Coupling of the Fe-Spin State and the As-As Hybridization in Iron-Pnictide Superconductors from First-Principle Calculations, Phys. Rev. Lett. **102**, 037003 (2009).

[39] V. Gnezdilov, Yu. Pashkevich, P. Lemmens, A. Gusev, K. Lamonova, T. Shevtsova, I. Vitebskiy, O. Afanasiev, S. Gnatchenko, V. Tsurkan, J. Deisenhofer, and A. Loidl, Anomalous optical phonons in FeTe chalcogenides: Spin state, magnetic order, and lattice anharmonicity, Phys. Rev. B **83**, 245127 (2011).

[40] Z. V. Popović, N. Lazarević, S. Bogdanović, M. M. Radonjić, D. Tanasković, R. Hu, H. Lei, and C. Petrovic, Signatures of the spin-phonon coupling in $Fe_{1+y}Te_{1-x}Se_x$ alloys, Solid State Commun. **193**, 51 (2014).

[41] S. J. Kuhn, M. K. Kidder, D. S. Parker, C. dela Cruz, M. A. McGuire, W. M. Chance, L. Li, L. Debeer-Schmitt, J. Ermentrout, K. C. Littrell, M. R. Eskildsen, and A. S. Sefat, Structure and property correlations in FeS, Physica C (Amsterdam) **534**, 29 (2017).

[42] R. A. MacDonald and W. M. MacDonald, Thermodynamic properties of fcc metals at high temperatures, Phys. Rev. B **24**, 1715 (1981).

[43] M. I. Aroyo, D. Orobengoa, G. de la Flor, E. S. Tasci, J. M. Perez-Mato, and H. Wondratschek, Brillouin-zone database on the *Bilbao Crystallographic Server*, Acta Crystallogr. A **70**, 126 (2014).

[44] W. Spengler and R. Kaiser, First and second order Raman scattering in transition metal compounds, Solid State Commun. **18**, 881 (1976).

[45] W. Spengler, R. Kaiser, A. N. Christensen, and G. Müller-Vogt, Raman scattering, superconductivity, and phonon density of states of stoichiometric and nonstoichiometric TiN, Phys. Rev. B **17**, 1095 (1978).

[46] W. Hayes and R. Loudon, *Scattering of Light by Crystals* (John Wiley and Sons, New York, 1978).

[47] L. Boeri, O. V. Dolgov, and A. A. Golubov, Is $LaFeAsO_{1-x}F_x$ an Electron-Phonon Superconductor? Phys. Rev. Lett. **101**, 026403 (2008).

[48] B. Mansart, D. Boschetto, A. Savoia, F. Rullier-Albenque, F. Bouquet, E. Papalazarou, A. Forget, D. Colson, A. Rousse, and M. Marsi, Ultrafast transient response and electron-phonon coupling in the iron-pnictide superconductor $Ba(Fe_{1-x}Co_x)_2As_2$, Phys. Rev. B **82**, 024513 (2010).

[49] L. Rettig, R. Cortés, H. S. Jeevan, P. Gegenwart, T. Wolf, J. Fink, and U. Bovensiepen, Electron-phonon coupling in 122 Fe pnictides analyzed by femtosecond time-resolved photoemission, New J. Phys. **15**, 083023 (2013).

[50] H. Martinho, C. Rettori, P. G. Pagliuso, A. A. Martin, N. O. Moreno, and J. L. Sarrao, Role of the E_{2g} phonon in the superconductivity of MgB_2: a Raman scattering study, Solid State Commun. **125**, 499 (2003).

[51] Y. Wang, T. Plackowski, and A. Junod, Specific heat in the superconducting and normal state (2–300 K, 0–16 T), and magnetic susceptibility of the 38 K superconductor MgB_2: evidence for a multicomponent gap, Physica C (Amsterdam) **355**, 179 (2001).

[52] J. L. Birman, Theory of infrared and Raman processes in crystals: Selection rules in diamond and zincblende, Phys. Rev. **131**, 1489 (1963).

[53] M. I. Aroyo, A. Kirov, C. Capillas, J. M. Perez-Mato, and H. Wondratschek, Bilbao Crystallographic Server. II. Representations of crystallographic point groups and space groups, Acta Crystallogr. A **62**, 115 (2006).

PHYSICAL REVIEW B **96**, 174303 (2017)

Small influence of magnetic ordering on lattice dynamics in $TaFe_{1.25}Te_3$

M. Opačić,[1] N. Lazarević,[1] D. Tanasković,[2] M. M. Radonjić,[2] A. Milosavljević,[1] Yongchang Ma,[3,4]
C. Petrovic,[3] and Z. V. Popović[1,5]

[1]*Center for Solid State Physics and New Materials, Institute of Physics Belgrade, University of Belgrade, Pregrevica 118, 11080 Belgrade, Serbia*

[2]*Scientific Computing Laboratory, Center for the Study of Complex Systems, Institute of Physics Belgrade, University of Belgrade, Pregrevica 118, 11080 Belgrade, Serbia*

[3]*Condensed Matter Physics and Materials Science Department, Brookhaven National Laboratory, Upton, New York 11973-5000, USA*

[4]*School of Materials Science and Engineering, Tianjin University of Technology, Tianjin 300384, People's Republic of China*

[5]*Serbian Academy of Sciences and Arts, Knez Mihailova 35, 11000 Belgrade, Serbia*

(Received 12 September 2017; published 16 November 2017)

Raman scattering spectra of zigzag spin chain $TaFe_{1.25}Te_3$ single crystal are presented in a temperature range from 80 to 300 K. Nine Raman active modes of A_g and B_g symmetry are clearly observed and assigned by probing different scattering channels, which is confirmed by lattice dynamics calculations. Temperature dependence of the Raman modes linewidth is mainly governed by the lattice anharmonicity. The only deviation from the conventional behavior is observed for A_g symmetry modes in a vicinity of the magnetic phase transition at $T_N \approx 200$ K. This implies that the electron-phonon interaction weakly changes with temperature and magnetic ordering, whereas small changes in the spectra near the critical temperature can be ascribed to spin fluctuations.

DOI: 10.1103/PhysRevB.96.174303

I. INTRODUCTION

The discovery of superconductivity in $La(O_{1-x}F_x)FeAs$ in 2008 [1] initiated an intensive search for new iron-based superconducting materials, in order to obtain better understanding of their physical properties and the mechanism of high-T_c superconductivity [2–4]. Novel iron-based materials, however, are not only superconducting, but can also exhibit various types of magnetic ordering. In some cases the magnetic phase transition is continuous [5–8], whereas in others it is accompanied by structural changes [9–15], or even by a nanoscale coexistence of antiferromagnetic (AFM) and superconducting domains [16–18].

$TaFe_{1+y}Te_3$ was synthesized and characterized about 25 years ago [19,20]. It is a layered system consisting of FeTe chains, along the *b* axis, separated by a Ta/Te network in between; see Fig. 1. These layers are parallel to the natural cleavage plane. There are also additional Fe ions, Fe2, randomly occupying interstitial sites [21–23]. $TaFe_{1+y}Te_3$ features anisotropic charge transport with metallic resistivity within the plane and insulating in the direction normal to the FeTe layers [23]. The first study of magnetic structure implies that $TaFe_{1+y}Te_3$ is composed of double zigzag spin chains with antiferromagnetic ordering of Fe1 spins [22]. The newest neutron diffraction measurements suggest that spin ordering within zigzag chains is ferromagnetic, whereas these zigzag chains couple antiferromagnetically [23], as shown in Fig. 1(b). However, the exact interaction mechanism is not clearly resolved.

There is a similarity between $TaFe_{1+y}Te_3$ and the extensively studied $Fe_{1+y}Te$ compound since they are correlated bad metals which order antiferromagnetically below $T_N \approx$ 200 K and 70 K, respectively [10,23], both having rather large magnetic moments on Fe ions, $\approx 2\ \mu_B$/Fe. $TaFe_{1+y}Te_3$, however, forms ferromagnetic (FM) zigzag spin chains which couple antiferromagnetically between the layers, whereas the Fe spins in $Fe_{1+y}Te$ form a bicollinear AFM structure. The magnetic phase transition in $Fe_{1+y}Te$ is accompanied by the structural change from a tetragonal to a monoclinic, as opposed to $TaFe_{1+y}Te_3$ where a continuous transition to the AFM phase is observed in thermodynamic and transport measurements [22]. Just like in $Fe_{1+y}Te$, interest in spin chain and ladder materials [24] stems not only from their block-AFM states similar to parent compounds of iron-based superconductors [25], but also from superconductivity. It is worth noting that spin 1/2 copper oxide ladder structures host a spin gap and superconductivity upon doping [26–28]. In contrast to superconductivity in copper oxide ladder materials that was rather rare and with critical temperatures rather small when compared to highest achieved in copper square lattices [29,30], iron-ladder materials feature T_c's similar to the highest found in Fe-based superconductors [31].

Raman spectra provide additional information on magnetic ordering and electron-phonon coupling. There exist several Raman studies of the phonon spectra of iron based materials near the superconducting or magnetic phase transition [32,33]. While no anomalies were observed in 1111 compounds [34,35], the Raman spectra show anomalous behavior near the spin density wave (SDW) transition in some of the 122 and 11 compounds [15,36–38], which was ascribed to the phonon renormalization due to the opening of the SDW or superconducting gap, or to the structural transition. Large anomalies were observed also in ferromagnetic $K_xCo_{2-y}Se_2$ [5], which was ascribed to the effect of electron-phonon coupling and spin fluctuations. $Fe_{1+y}Te$ phonon spectra feature unusually large anomalies near the magnetic phase transition, as seen in sudden changes in the phonon frequencies and linewidths, due to the phonon modulation of magnetic interactions and structural phase transition [11–13]. Therefore, it is of interest to examine lattice dynamics in the normal state of iron-spin chain and ladder materials and compare it to materials like $Fe_{1+y}Te$. To the best of our knowledge, there are no published data on lattice dynamics of $TaFe_{1+y}Te_3$.

In this paper we present polarized Raman scattering spectra of $TaFe_{1.25}Te_3$ single crystal measured in a temperature range from 80 to 300 K. Nine out of 15 Raman active modes are

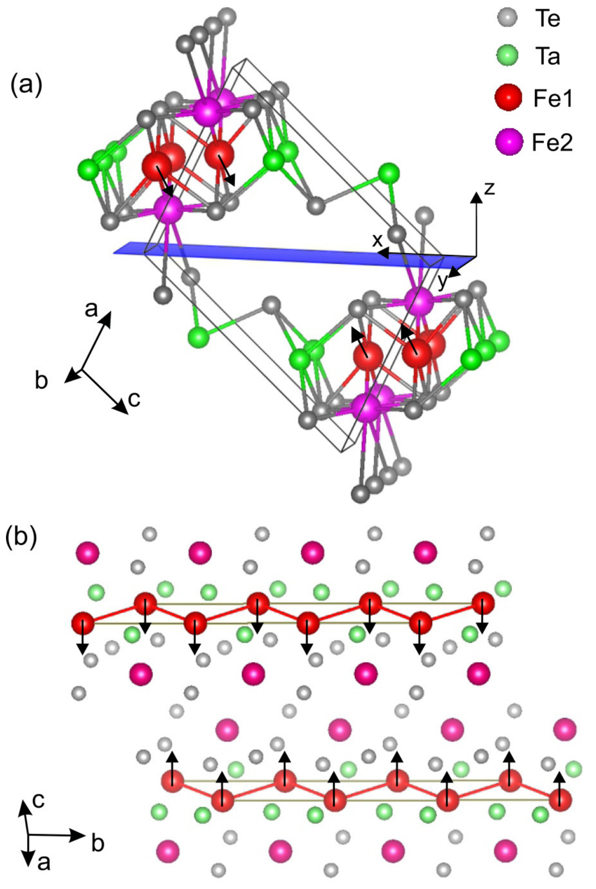

FIG. 1. (a) Structure of the $\mathrm{TaFe_{1.25}Te_3}$ single crystal together with the natural cleavage plane $[\bar{1}01]$. $\mathbf{x} = 1/\sqrt{2}(\bar{1}0\bar{1})$ and $\mathbf{y} = (010)$ correspond to our laboratory system. (b) A view of the $\mathrm{TaFe_{1.25}Te_3}$ structure along the b axis. Two neighboring chains of Fe1 spins point in a parallel direction, forming a ferromagnetic zigzag chain, whereas spins of neighboring zigzag chains order antiferromagnetically. One should note that Fe2 is present with occupancy of 0.25.

observed and assigned using the selection rules for different polarization configurations and lattice dynamics calculations. In a sharp contrast to the related FeTe compound, $\mathrm{TaFe_{1.25}Te_3}$ Raman spectra do not show significant changes near $T_N \approx 200$ K, which clearly indicates that the phase transition is continuous. Temperature dependence of the frequency and linewidth is conventional, driven by the anharmonicity effects, except very near T_N where some of phonon lines slightly broaden which should be the consequence of spin fluctuations near the critical temperature. These results indicate very small changes in the electron-phonon coupling and in the Fermi surface in the measured temperature range.

II. EXPERIMENT AND NUMERICAL METHOD

Single crystals were grown using the self-flux method, as described elsewhere [19]. Raman scattering measurements were performed on freshly cleaved $(\bar{1}01)$-oriented samples, using Jobin Yvon T64000 Raman system, equipped with a nitrogen-cooled CCD detector, in the backscattering micro-Raman configuration. The 532 nm line of a solid state laser was used as an excitation source. A microscope objective with 50× magnification was used for focusing the laser beam. All measurements were performed at low laser power, to reduce local heating of the sample. For low temperature measurements KONTI CryoVac continuous flow cryostat with 0.5 mm thick window was used. All spectra were corrected for the Bose factor. For extracting the data from the Raman spectra, phonon modes were fitted with a Lorentzian profile.

The electronic structure is calculated for stoichiometric $\mathrm{TaFeTe_3}$ in the paramagnetic phase within the density functional theory (DFT), and the phonon frequencies at the Γ-point are obtained within the density functional perturbation theory (DFPT) [39], using the QUANTUM ESPRESSO package [40]. We have used projector augmented wave (PAW) pseudopotentials with Perdew-Burke-Ernzerhof (PBE) exchange-correlation functional with nonlinear core correction and Gaussian smearing of 0.01 Ry. The electron wave function and the density energy cutoffs were 64 Ry and 782 Ry, respectively. The Brillouin zone is sampled with $8 \times 8 \times 8$ Monkhorst-Pack k-space mesh. The phonon frequencies were calculated with the unit cell size taken from the experiments and the relaxed positions of atoms within the unit cell. The forces acting on individual atoms in the relaxed configuration were smaller than 10^{-4} Ry/a.u.

III. RESULTS AND DISCUSSION

$\mathrm{TaFe_{1+y}Te_3}$ crystallizes in the monoclinic crystal structure, which is shown in Fig. 1. The space group is $P2_1/m$ (unique axis b), with two formula units per unit cell [19,20]. The experimental values of the unit cell parameters are $a = 7.436$ Å, $b = 3.638$ Å, $c = 10.008$ Å, and $\beta = 109.17°$. All atoms (including the excess Fe), are at $2e$ Wyckoff positions, with fractional coordinates given in Table I.

The factor group analysis (FGA) for $P2_1/m$ space group yields the following normal mode distribution at the Γ point:

$$\begin{aligned}\Gamma_{\mathrm{Raman}} &= 10A_g + 5B_g,\\ \Gamma_{\mathrm{IR}} &= 4A_u + 8B_u,\\ \Gamma_{\mathrm{acoustic}} &= A_u + 2B_u.\end{aligned}$$

The Raman spectra were measured from the $(\bar{1}01)$ plane of the sample, which is the natural cleavage plane [23,42]. From the Raman tensors given in Table II, the A_g phonon modes are expected to be observable in the (xx) and (yy) scattering configurations. The B_g modes can be observed only in (xy) polarization configuration.

TABLE I. Experimental fractional coordinates of $\mathrm{TaFe_{1.25}Te_3}$ taken from Ref. [19]. In the parentheses are the calculated values for $\mathrm{TaFeTe_3}$.

Atom type	x	y	z
Ta	0.8340 (0.8331)	0.25	0.3007 (0.2987)
Fe1	0.6147 (0.6223)	−0.25	0.0890 (0.0988)
Fe2	0.7686	0.25	−0.0047
Te1	0.4392 (0.4326)	0.25	0.1860 (0.1637)
Te2	0.9835 (0.9842)	−0.25	0.1589 (0.1584)
Te3	0.2179 (0.2192)	0.25	0.4970 (0.5028)

TABLE II. Upper panel: atomic species (all of them are at $2e$ Wyckoff positions) and the contribution of each atom to the Γ-point phonons, the corresponding Raman tensors for the $TaFeTe_3$ single crystal ($P2_1/m$ space group) [41]. Lower panel: the calculated (for the stoichiometric $TaFeTe_3$) and experimental phonon energies at 100 K (for the $TaFe_{1.25}Te_3$ single crystal).

Atoms	Irreducible representations
Ta, Fe1, Te1, Te2, Te3	$2A_g + A_u + B_g + 2B_u$

Raman tensors

$$\hat{R}_{A_g} = \begin{pmatrix} a & 0 & d \\ 0 & b & 0 \\ d & 0 & c \end{pmatrix} \qquad \hat{R}_{B_g} = \begin{pmatrix} 0 & e & 0 \\ e & 0 & f \\ 0 & f & 0 \end{pmatrix}$$

Raman active			Infrared active		
Symmetry	Calc. (cm^{-1})	Expt. (cm^{-1})	Symmetry	Calc. (cm^{-1})	Expt. (cm^{-1})
A_g^1	36.2		A_u^1	42.8	
B_g^1	43.8		B_u^1	54.9	
B_g^2	57.9	61.6	B_u^2	94.4	
A_g^2	63.8	62.3	A_u^2	101.4	
A_g^3	75.3	68.5	B_u^3	111.3	
A_g^4	104.4	90	A_u^3	131.1	
B_g^3	105.1		B_u^4	143.2	
A_g^5	124.6		B_u^5	160.4	
B_g^4	127.2	130.4	B_u^6	188.6	
A_g^6	149.8	155	B_u^7	227.9	
A_g^7	164.9	165	A_u^4	231.1	
A_g^8	191		B_u^8	289.4	
B_g^5	217.1	222.3			
A_g^9	241.9	223.9			
A_g^{10}	276.22				

Raman scattering spectra of $TaFe_{1.25}Te_3$ single crystals, measured at 100 K in three different polarization configurations, are presented in Fig. 2. By using the selection rules, we assign the Raman peaks appearing in the (xx) and (yy) polarization configuration as the A_g ones. This conclusion is supported by the lattice dynamics calculations, given in Table II. By comparing the calculated values of A_g mode energies with those of the peaks appearing in the (xx) and (yy) spectra, we can unambiguously assign four Raman modes (A_g^4, A_g^6, A_g^7, and A_g^9). The broad structure around 65 cm^{-1} probably originates from the A_g^2 and A_g^3 modes, although the contribution of the A_g^1 mode (with calculated energy of 42.7 cm^{-1}) cannot be excluded. The peaks at 57.9 cm^{-1} and 130 cm^{-1} that are clearly visible in (xy) but absent in (yy) configuration are assigned as B_g^2 and B_g^4 modes, respectively. The low intensity peak at $\approx$220 cm^{-1}, that becomes clearly observable at low temperatures, is tentatively assigned as B_g^5 mode, although the contribution from the leakage of A_g^9 mode cannot be excluded. The origin of the two very broad structures at about 70 cm^{-1} and 160 cm^{-1}, which are pronounced in the (xy) configuration, is not completely clear. Aside from providing additional charge, Fe2 atoms may contribute to momentum transfer scattering, in line with the pronounced quasielastic continuum, present in all the scattering configurations. Consequently, contribution from single-phonon scattering away from Γ point becomes observable, which is theoretically predicted [43,44] and experimentally observed [45,46]. Although we cannot exclude the possibility of two- and, in particular, double-phonon contributions, we believe it is less likely due to the nature of the processes and since they usually have more pronounced contribution to A channel (for arbitrary irreducible symmetry μ of C_{2h} holds $\mu \otimes \mu \ni A$).

The normal modes of the selected A_g and B_g vibrations, as obtained by the lattice dynamics calculations, are shown in Fig. 3. The low energy B_g^2 mode represents vibrations of Te and Ta atoms which tend to elongate the (Ta,Fe)Te tetrahedra in the xy plane. B_g^4 phonon originates mainly from Ta and Te atom vibrations in directions opposite to each other, whereas A_g^4 mode represents dominantly vibrations of another Te atom in the xy plane. A_g^7 and A_g^9 modes originate from the vibrations of Fe and Te atoms which tend to rotate the tetrahedra around the x axis.

The DFT calculations are in very good agreement with the measured Raman spectra, specially having in mind the strength of electronic correlations in iron based compounds and the presence of additional Fe2 atoms in the measured sample. We restricted to the nonmagnetic DFT calculations. This is because small changes in the phonon energies due to the magnetic ordering cannot be reliably captured since the DFT does not treat strong correlation and spin-fluctuations effects. Our DFT calculations for the electronic band structure agree with the results from Ref. [42]. The calculated electronic dispersions are in rather good agreement with the ARPES measurements [42], which indicates that the main effect of the interstitial Fe2 ion is to provide additional charge and shift

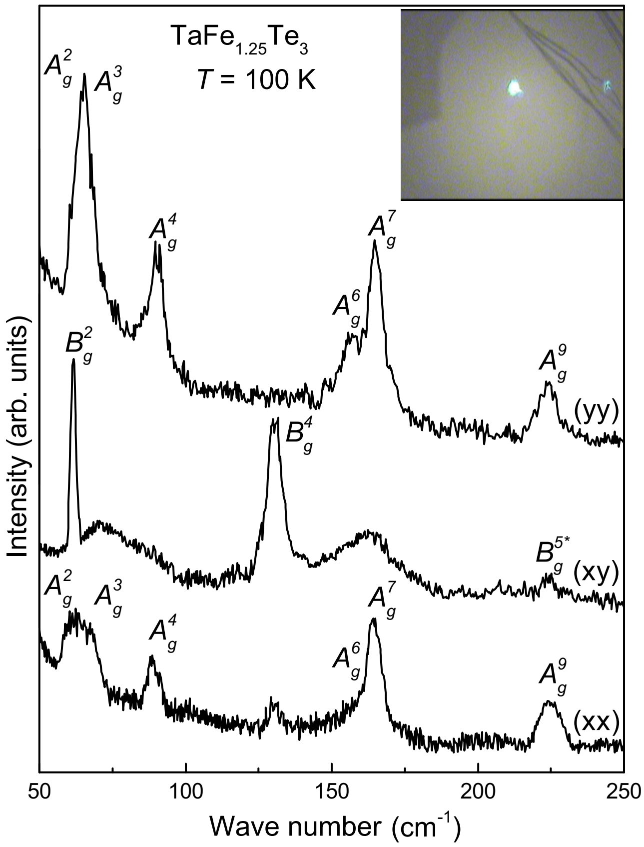

FIG. 2. Polarized Raman scattering spectra of $TaFe_{1.25}Te_3$ single crystal measured at 100 K in various polarizations. The notation in parentheses indicates the polarization directions of the incident and scattered light according to Fig. 1(a). Inset: surface of the probed $TaFe_{1.25}Te_3$ single crystal.

the Fermi level. This conclusion is supported with a small difference between the relaxed and experimental fractional coordinates; see Table I.

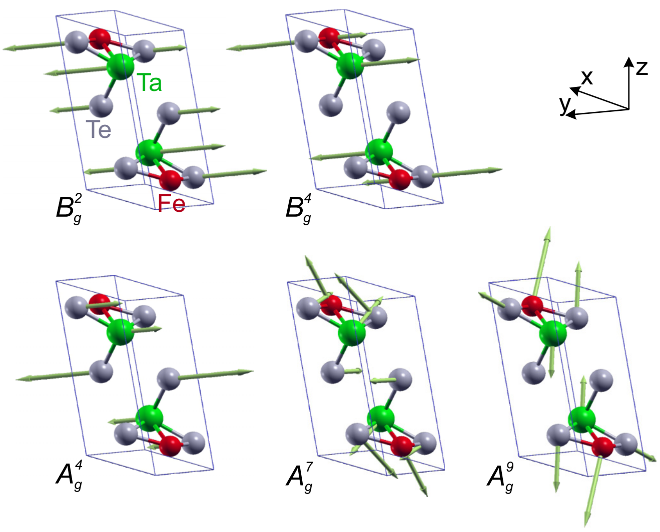

FIG. 3. Unit cell of $TaFeTe_3$ single crystal with the displacement patterns of several A_g and B_g Raman modes. Arrow lengths are proportional to the square root of the interatomic forces.

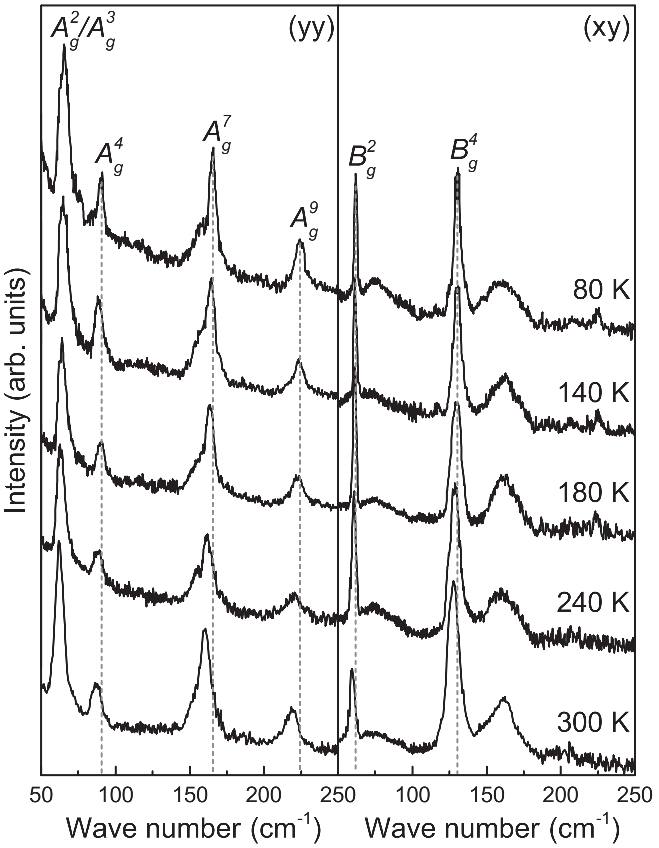

FIG. 4. Temperature dependent Raman scattering spectra of $TaFe_{1.25}Te_3$ single crystal in the (yy) (left panel) and (xy) (right panel) polarization.

In order to analyze the changes of the Raman spectra near the AFM transition at $T_N \approx 200$ K, we have performed measurements in a temperature range from 80 K up to 300 K. Raman spectra of $TaFe_{1.25}Te_3$ single crystal, measured at different temperatures in the (yy) and (xy) scattering configurations, are given in Fig. 4. In the following, we perform the temperature analysis of the energy and the linewidth for five most clearly observed modes.

The temperature dependence of the Raman mode energy is usually described with [47,48]

$$\omega_i(T) = \omega_{0,i} + \Delta_i^V(\gamma_i, \alpha_i(T)) + \Delta_i^A(C_i), \tag{1}$$

where $\omega_{0,i}$ is a temperature independent contribution to the Raman mode energy. The second term represents a change of the phonon energy induced by the lattice thermal expansion and depends on the Grüneisen parameter γ_i and the thermal expansion coefficient $\alpha_i(T)$. The term Δ_i^A describes the anharmonicity induced change of the Raman mode energy which is a function of the anharmonic constant C_i. Both Δ_i^V and Δ_i^A have qualitatively the same temperature dependence. Since there are no reported experimental data on the temperature dependence of the lattice parameters for $TaFe_{1+y}Te_3$, we didn't attempt to fit the data, and the black dotted lines in Figs. 5 and 6 are guides to the eye. The $\omega_i(T)$ curves follow the "standard" [5,15,37,49,50] continuous decrease in energy with temperature, with very small anomalies near T_N except for the A_g^4 mode.

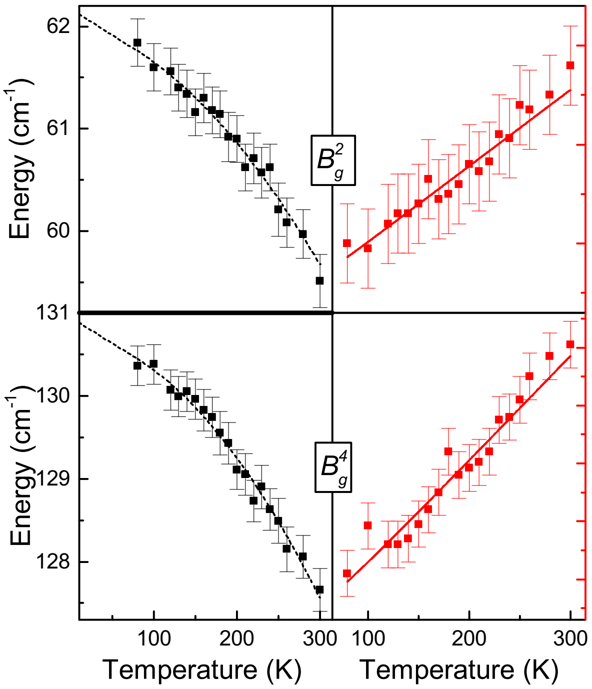

FIG. 5. Temperature dependence of the energy and linewidth for the B_g^2 and B_g^4 Raman modes of the TaFe$_{1.25}$Te$_3$ single crystal. The red lines are fitted according to Eq. (2), whereas black lines are guides to the eye.

The temperature dependences of the linewidth of selected B_g and A_g modes are given in the right panels of Figs. 5 and 6, respectively. While the B_g^2 and B_g^4 phonon modes do not show significant deviation from the usual behavior due to the anharmonicity effects, with gradual broadening with increasing temperature, the A_g^4, A_g^7, and A_g^9 modes exhibit moderate additional broadening above 200 K. The red lines present a fit to the standard formula for the temperature dependent linewidth due to the anharmonicity [11,47,51]:

$$\Gamma_i(T) = \Gamma_{0,i}\left(1 + \frac{2}{e^{\hbar\omega_{0,i}/2k_BT} - 1}\right) + A_i, \tag{2}$$

where $\Gamma_{0,i}$ is the anharmonic constant and A_i is the constant term due to the disorder and electron-phonon interaction [52]. The deviation from these anharmonicity curves is most pronounced around T_N (see the insets of Fig. 6).

We can observe that all Raman modes have moderate linewidth and exhibit small anomalies near T_N. This shows that the phase transition is continuous, in agreement with the thermodynamic and transport measurements [22]. Small anomalies in the phonon spectra, which are restricted only to the vicinity of the phase transition, imply that the electron-phonon interaction of Raman active modes does not change with temperature. This is in agreement with the recent ARPES measurements which show negligible change of the Fermi surface across the AFM transition [42], indicating that the magnetic transition is not driven by the Fermi surface instability. The anomalies in the linewidth of some phonon modes near T_N are likely the signature of the increased scattering by spin fluctuations near the phase transition [51,53].

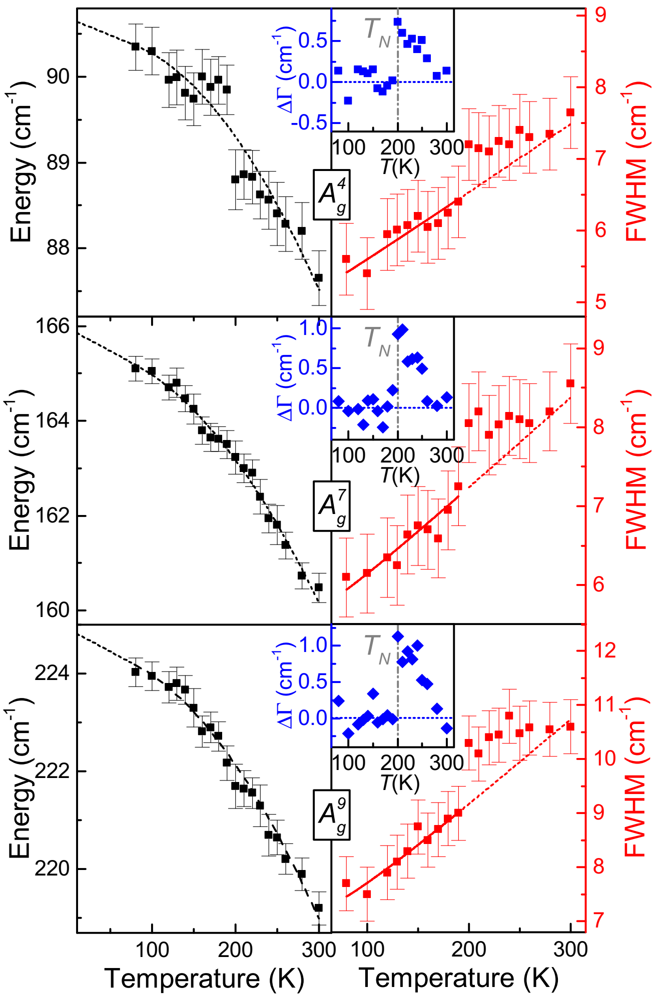

FIG. 6. Energy and linewidth of the A_g^4, A_g^7, and A_g^9 Raman modes of the TaFe$_{1.25}$Te$_3$ single crystal as a function of temperature. The red lines are plotted according to Eq. (2), and the black dotted lines are guides to the eye. The insets represent deviations of the Raman mode linewidth from the anharmonic form.

The density of states (DOS) at the Fermi level is not large. This can be concluded from the ARPES experiments [42] which have shown three bands crossing the Fermi level but with strong dispersion, while several relatively flat bands are found only well below the Fermi level. The DFT calculations also give moderate values for the DOS, $N(E_F) \approx 1\ \mathrm{eV}^{-1}$/f.u., after the Fermi level is shifted due to the additional charge provided by the Fe2 atoms. This value for the DOS also suggests that the electron-phonon coupling is not strong in TaFe$_{1.25}$Te$_3$, since it is proportional to $N(E_F)$.

TaFe$_{1.25}$Te$_3$ has a similar moment size as Fe$_{1+y}$Te, $\approx 2\mu_B$/Fe. However, the differences in the magnetic ordering and crystal structure cause different phonon properties of these two compounds. Namely, the phonon lines in the Raman spectra of Fe$_{1+y}$Te have very large linewidth and pronounced anomalies both in the frequency and in the linewidth near the first order phase transition [11,13]. Small anomalies in the Raman spectra of TaFe$_{1.25}$Te$_3$ as compared to Fe$_{1+y}$Te can be ascribed to the continuous, second order nature of the AFM transition and smaller electron-phonon coupling due to lower DOS at the

Fermi level. Also, the monoclinic angle β in the $TaFe_{1.25}Te_3$ unit cell significantly differs from 90° and therefore the form of the vibrational modes is different.

IV. CONCLUSION

In summary, we have performed the Raman scattering study of the zigzag spin chain $TaFe_{1.25}Te_3$ single crystal, together with the lattice dynamics calculations of $TaFeTe_3$. By analyzing the Raman spectra in different polarization configurations and using numerical calculations we have assigned nine Raman active modes predicted by the FGA. Very good agreement between the experimental frequencies and those calculated for the stoichiometric compound shows that the excess iron atoms weakly influence the phonon energies but provide momentum conservation for the phonon scattering away from Γ point. The temperature dependence of the frequency and the linewidth of the B_g Raman modes looks conventional, governed by the anharmonicity effects. While in a broad temperature range the behavior of the A_g modes is also conventional, there are clear anomalies near the AFM transition. The anomalies in the frequency and the linewidth are in the form of small kinks near T_N. This implies that the electron-phonon interaction and the DOS at the Fermi level are approximately constant in the measured temperature range. The increase in the linewidth near T_N is likely due to the coupling of spin fluctuations and vibration near the second order phase transition.

ACKNOWLEDGMENTS

We thank D. Stepanenko for useful discussions. This work was supported by the Serbian Ministry of Education, Science and Technological Development under Projects No. ON171032, No. III45018, and No. ON171017, and by the European Commission under H2020 project VI-SEEM, Grant No. 675121. Work at Brookhaven is supported by the Center for Emergent Superconductivity, an Energy Frontier Research Center funded by the U.S. DOE, Office for Basic Energy Science (C.P. and Y.M.). Numerical calculations were performed on the PARADOX supercomputing facility at the Scientific Computing Laboratory of the Institute of Physics Belgrade.

---

[1] Y. Kamihara, T. Watanabe, M. Hirano, and H. Hosono, J. Am. Chem. Soc. **130**, 3296 (2008).
[2] L. Ma, G. F. Ji, J. Dai, X. R. Lu, M. J. Eom, J. S. Kim, B. Normand, and W. Yu, Phys. Rev. Lett. **109**, 197002 (2012).
[3] B. Wei, H. Qing-Zhen, C. Gen-Fu, M. A. Green, W. Du-Ming, H. Jun-Bao, and Q. Yi-Ming, Chin. Phys. Lett. **28**, 086104 (2011).
[4] G. R. Stewart, Rev. Mod. Phys. **83**, 1589 (2011).
[5] M. Opačić, N. Lazarević, M. M. Radonjić, M. Šćepanović, H. Ryu, A. Wang, D. Tanasković, C. Petrovic, and Z. V. Popović, J. Phys.: Condens. Matter **28**, 485401 (2016).
[6] Z. S. Gönen, P. Fournier, V. Smolyaninova, R. Greene, F. M. Araujo-Moreira, and B. Eichhorn, Chem. Mater. **12**, 3331 (2000).
[7] H. Lei, H. Ryu, A. I. Frenkel, and C. Petrovic, Phys. Rev. B **84**, 214511 (2011).
[8] F. Han, X. Wan, B. Shen, and H.-H. Wen, Phys. Rev. B **86**, 014411 (2012).
[9] M. H. Fang, H. M. Pham, B. Qian, T. J. Liu, E. K. Vehstedt, Y. Liu, L. Spinu, and Z. Q. Mao, Phys. Rev. B **78**, 224503 (2008).
[10] S. Li, C. de la Cruz, Q. Huang, Y. Chen, J. W. Lynn, J. Hu, Y.-L. Huang, F.-C. Hsu, K.-W. Yeh, M.-K. Wu, and P. Dai, Phys. Rev. B **79**, 054503 (2009).
[11] V. Gnezdilov, Y. Pashkevich, P. Lemmens, A. Gusev, K. Lamonova, T. Shevtsova, I. Vitebskiy, O. Afanasiev, S. Gnatchenko, V. Tsurkan, J. Deisenhofer, and A. Loidl, Phys. Rev. B **83**, 245127 (2011).
[12] Y. J. Um, A. Subedi, P. Toulemonde, A. Y. Ganin, L. Boeri, M. Rahlenbeck, Y. Liu, C. T. Lin, S. J. E. Carlsson, A. Sulpice, M. J. Rosseinsky, B. Keimer, and M. Le Tacon, Phys. Rev. B **85**, 064519 (2012).
[13] Z. V. Popović, N. Lazarević, S. Bogdanović, M. M. Radonjić, D. Tanasković, R. Hu, H. Lei, and C. Petrovic, Solid State Commun. **193**, 51 (2014).
[14] K.-Y. Choi, D. Wulferding, P. Lemmens, N. Ni, S. L. Bud'ko, and P. C. Canfield, Phys. Rev. B **78**, 212503 (2008).
[15] M. Rahlenbeck, G. L. Sun, D. L. Sun, C. T. Lin, B. Keimer, and C. Ulrich, Phys. Rev. B **80**, 064509 (2009).
[16] F. Chen, M. Xu, Q. Q. Ge, Y. Zhang, Z. R. Ye, L. X. Yang, J. Jiang, B. P. Xie, R. C. Che, M. Zhang, A. F. Wang, X. H. Chen, D. W. Shen, J. P. Hu, and D. L. Feng, Phys. Rev. X **1**, 021020 (2011).
[17] W. Li, H. Ding, P. Deng, K. Chang, C. Song, K. He, L. Wang, X. Ma, J.-P. Hu, P. Chen, and Q.-K. Xue, Nat. Phys. **8**, 126 (2012).
[18] N. Lazarević, M. Abeykoon, P. W. Stephens, H. Lei, E. S. Bozin, C. Petrovic, and Z. V. Popović, Phys. Rev. B **86**, 054503 (2012).
[19] M. Badding, J. Li, F. DiSalvo, W. Zhou, and P. Edwards, J. Solid State Chem. **100**, 313 (1992).
[20] J. Neuhausen, E. Potthoff, W. Tremel, J. Ensling, P. Gütlich, and R. Kremer, Z. Naturforsch. B **48**, 797 (1993).
[21] C. Perez Vicente, M. Womes, J. C. Jumas, L. Sanchez, and J. L. Tirado, J. Phys. Chem. B **102**, 8712 (1998).
[22] R. H. Liu, M. Zhang, P. Cheng, Y. J. Yan, Z. J. Xiang, J. J. Ying, X. F. Wang, A. F. Wang, G. J. Ye, X. G. Luo, and X. H. Chen, Phys. Rev. B **84**, 184432 (2011).
[23] X. Ke, B. Qian, H. Cao, J. Hu, G. C. Wang, and Z. Q. Mao, Phys. Rev. B **85**, 214404 (2012).
[24] E. Dagotto, Rev. Mod. Phys. **85**, 849 (2013).
[25] W. Li, C. Setty, X. H. Chen, and J. Hu, Front. Phys. **9**, 465 (2014).
[26] E. Dagotto, J. Riera, and D. Scalapino, Phys. Rev. B **45**, 5744 (1992).
[27] E. Dagotto and T. M. Rice, Science **271**, 618 (1996).
[28] E. Dagotto, Rep. Prog. Phys. **62**, 1525 (1999).
[29] M. Uehara, T. Nagata, J. Akimitsu, H. Takahashi, N. Môri, and K. Kinoshita, J. Phys. Soc. Jpn. **65**, 2764 (1996).
[30] A. Hisada, K. Matsubayashi, Y. Uwatoko, N. Fujiwara, G. Deng, E. Pomjakushina, K. Conder, D. M. Radheep, R. Thiyagarajan, S. Esakkimuthu, and S. Arumugam, J. Phys. Soc. Jpn. **83**, 073703 (2014).

[31] H. Takahashi, A. Sugimoto, Y. Nambu, T. Yamauchi, Y. Hirata, T. Kawakami, M. Avdeev, K. Matsubayashi, F. Du, C. Kawashima, H. Soeda, S. Nakano, Y. Uwatoko, Y. Ueda, T. J. Sato, and K. Ohgushi, Nat. Mater. **14**, 1008 (2014).

[32] A.-M. Zhang and Q.-M. Zhang, Chin. Phys. B **22**, 087103 (2013).

[33] M. Opačić and N. Lazarević, J. Serb. Chem. Soc. **82**, 957 (2017).

[34] L. Zhang, T. Fujita, F. Chen, D. L. Feng, S. Maekawa, and M. W. Chen, Phys. Rev. B **79**, 052507 (2009).

[35] Y. Gallais, A. Sacuto, M. Cazayous, P. Cheng, L. Fang, and H. H. Wen, Phys. Rev. B **78**, 132509 (2008).

[36] V. Gnezdilov, Y. G. Pashkevich, P. Lemmens, D. Wulferding, T. Shevtsova, A. Gusev, D. Chareev, and A. Vasiliev, Phys. Rev. B **87**, 144508 (2013).

[37] A. P. Litvinchuk, B. Lv, and C. W. Chu, Phys. Rev. B **84**, 092504 (2011).

[38] K.-Y. Choi, P. Lemmens, I. Eremin, G. Zwicknagl, H. Berger, G. L. Sun, D. L. Sun, and C. T. Lin, J. Phys.: Condens. Matter **22**, 115802 (2010).

[39] S. Baroni, S. de Gironcoli, A. Dal Corso, and P. Giannozzi, Rev. Mod. Phys. **73**, 515 (2001).

[40] P. Gianozzi, S. Baroni, N. Bonini, M. Calandra, R. Car, C. Cavazzoni, D. Ceresoli, G. L. Chiarotti, M. Cococcioni, I. Dabo, A. D. Corso, S. de Gironcoli, S. Fabris, G. Fratesi, R. Gebauer, U. Gerstmann, C. Gougoussis, A. Kokalj, M. Lazzeri, L. Martin-Samos, N. Marzari, F. Mauri, R. Mazzarello, S. Paolini, A. Pasquarello, L. Paulatto, C. Sbraccia, S. Scandolo, G. Sclauzero, A. P. Seitsonen, A. Smogunov, P. Umari, and R. M. Wentzcovitch, J. Phys.: Condens. Matter **21**, 395502 (2009).

[41] D. L. Rousseau, R. P. Bauman, and S. P. S. Porto, J. Raman Spectrosc. **10**, 253 (1981).

[42] X. Min, W. Li-Min, P. Rui, G. Qing-Qin, C. Fei, Y. Zi-Rong, Z. Yan, C. Su-Di, X. Miao, L. Rong-Hua, M. Arita, K. Shimada, H. Namatame, M. Taniguchi, M. Matsunami, S. Kimura, S. Ming, C. Xian-Hui, Y. Wei-Guo, K. Wei, X. Bin-Ping, and F. Dong-Lai, Chin. Phys. Lett. **32**, 027401 (2015).

[43] R. Shuker and R. W. Gammon, Phys. Rev. Lett. **25**, 222 (1970).

[44] P. Benassi, O. Pilla, V. Mazzacurati, M. Montagna, G. Ruocco, and G. Signorelli, Phys. Rev. B **44**, 11734 (1991).

[45] H. Ryu, M. Abeykoon, K. Wang, H. Lei, N. Lazarevic, J. B. Warren, E. S. Bozin, Z. V. Popovic, and C. Petrovic, Phys. Rev. B **91**, 184503 (2015).

[46] B.-B. Zhang, N. Zhang, S.-T. Dong, Y. Lv, Y. B. Chen, S. Yao, S.-T. Zhang, Z.-B. Gu, J. Zhou, I. Guedes, D. Yu, and Y.-F. Chen, AIP Adv. **5**, 087111 (2015).

[47] J. Menéndez and M. Cardona, Phys. Rev. B **29**, 2051 (1984).

[48] H.-M. Eiter, P. Jaschke, R. Hackl, A. Bauer, M. Gangl, and C. Pfleiderer, Phys. Rev. B **90**, 024411 (2014).

[49] N. Lazarević, M. Radonjić, M. Šćepanović, H. Lei, D. Tanasković, C. Petrovic, and Z. V. Popović, Phys. Rev. B **87**, 144305 (2013).

[50] M. Opačić, N. Lazarević, M. Šćepanović, H. Ryu, H. Lei, C. Petrovic, and Z. V. Popović, J. Phys.: Condens. Matter **27**, 485701 (2015).

[51] M. N. Iliev, A. P. Litvinchuk, H.-G. Lee, C. W. Chu, A. Barry, and J. M. D. Coey, Phys. Rev. B **60**, 33 (1999).

[52] N. Lazarević, Z. V. Popović, R. Hu, and C. Petrovic, Phys. Rev. B **81**, 144302 (2010).

[53] M. N. Iliev, A. P. Litvinchuk, H.-G. Lee, C. L. Chen, M. L. Dezaneti, C. W. Chu, V. G. Ivanov, M. V. Abrashev, and V. N. Popov, Phys. Rev. B **59**, 364 (1999).

Journal of the Serbian Chemical Society
eVersion electronic

JSCS-info@shd.org.rs • www.shd.org.rs/JSCS

J. Serb. Chem. Soc. *82*(9) 957–983 (2017)
JSCS–5016
UDC 546.721’221:548.313:544.174.5:66–977
Review

REVIEW

Lattice dynamics of iron chalcogenides: Raman scattering study

MARKO R. OPAČIĆ[1,2]* and NENAD Ž. LAZAREVIĆ[2]

[1]*Faculty of Electrical Engineering, Bulevar Kralja Aleksandra 73, University of Belgrade, Belgrade, Serbia and* [2]*Center for Solid State Physics and New Materials, Institute of Physics, Pregrevica 118, University of Belgrade, Belgrade, Serbia*

(Received 21 March, revised 2 June, accepted 5 June 2017)

Abstract: The discovery of superconductivity in FeSe led to a new subclass of high-temperature superconductors – iron chalcogenides. Materials from this group exhibit variety of specific features, from superconductivity with relatively high critical temperatures to low-dimensional magnetic properties. This review presents the most important results regarding the iron chalcogenides, with special emphasis on their vibrational properties investigated by means of Raman spectroscopy. Temperature- and/or doping-dependent Raman scattering spectra of iron chalcogenides provide a valuable insight into the complex relationships between the vibrational, electronic and magnetic properties of these materials. The results presented in this review demonstrated that Raman spectroscopy provides new insights which may significantly improve our understanding of the fundamental properties of iron chalcogenides.

Keywords: superconductors; phonons; energy; linewidth.

CONTENTS

---

* Corresponding author. E-mail: marko.opacic@ipb.ac.rs

https://doi.org/10.2298/JSC170321077O

1. INTRODUCTION

Superconductivity (SC) is one of the greatest and the most striking phenomena discovered so far in the materials science. The history of SC began in 1911, when Kamerlingh-Onnes observed it in mercury below 4 K.[1] Since then, researchers made a great effort in searching for materials with as high as possible superconducting critical temperature T_c.

The breakthrough in the development of SC materials happened with the discovery of SC in oxide compounds. In 1975, $Ba(Pb,Bi)O_3$ was reported with $T_c \approx 13$ K,[2] which motivated further intensive studies. These investigations resulted in the discovery of SC in $La_{2-x}Ba_xCuO_2$ system (T_c = 35 K) – the first high-temperature superconductor,[3] as well as in $YBa_2Cu_3O_{7-x}$ compound (T_c = 92 K).[4] Numerous SC materials from this class were found in quick succession, from which $HgBa_2Ca_2Cu_3O_8$ (T_c = 134 K) should be mentioned.[5] All cuprate superconductors have distorted, oxygen-deficient, multi-layered perovskite structure. The most important property is an alternating multi-layer of CuO_2 planes, with intercalated layers containing Y, Ba, La, Sr,..., which act to stabilize the structure and to dope the carriers onto the CuO_2.[6–8] This structure causes a large anisotropy in normal conducting and superconducting properties.[6,8] Parent (undoped) compounds are Mott insulators, with long range antiferromagnetic (AFM) order at low temperatures.[7,8] Similarities between the AFM state of the undoped materials and doping-induced SC state indicate that the electron–electron interaction is more significant than electron-phonon interaction, making the SC unconventional.[9,10] It was argued that cuprates have *d*-wave pairing symmetry and one Fermi surface sheet.[11]

The first iron-based superconductor was discovered in 2006 (LaFePO, T_c = = 5 K).[12] However, until 2008, when Kamihara *et al.*[13] found SC in $LaFeAsO_{1-x}F_x$ with T_c = 26 K (43 K under high pressure), it was widely believed that only cuprates belong to the class of unconventional high-T_c superconductors. This discovery led to a new class of the so-called iron pnictide SC which includes several types of materials, denoted according to their crystal structure: 1111--compounds (LaFePO, LaFeAsO, $SmFeAsO_{1-x}$ with T_c = 56 K[14]), 122-family ($Ba_{0.6}K_{0.4}Fe_2As_2$ with T_c = 38 K[15]), 111-compounds (MFeAs, T_c = 18 K[16]), *etc.* Crystal structure of these superconductors is given in Fig. 1. All these materials crystallize into the [FeAs]-layered structure, with spacer or charge reservoir blocks between the FeAs-layers.[17,18] The parent compounds are poor metals and it is widely believed that proximity to the magnetically ordered states induces SC, making them unconventional, like in the cuprates.[17,18] However, in iron pnictides SC and AFM order can coexist, contrary to the cuprates, where SC state emerges only after the AFM order is destroyed by doping.[18,19] Symmetry of the pairing wave function can be of the $s^{\pm}$-type,[20,21] although this is still under intensive debate.

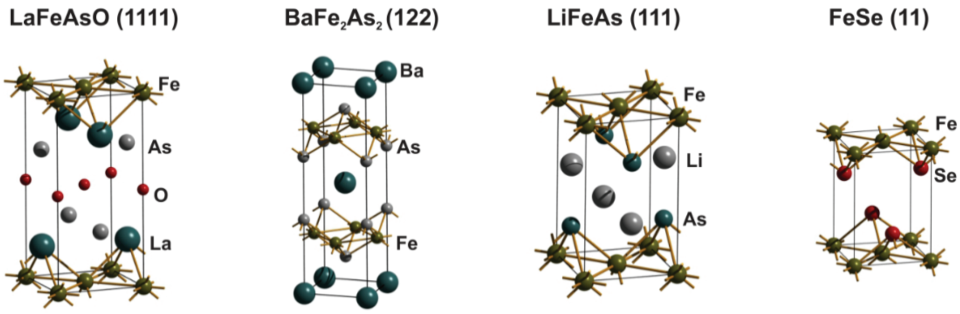

Fig. 1. Crystal structure of the representative iron-based superconductors.

FeSe is the first discovered material from one of the newest subclasses of iron-based superconductors – iron chalcogenides.[22] Its physical properties are extremely sensitive to doping on the chalcogen site, as well as to the Fe concentration, and T_c can be enhanced by applying pressure.[23,24] Intercalation of alkali metal between the FeSe layers led to the formation of $A_xFe_{2-y}Se_2$ (A = alkali metal) crystals with the defect 122* structure.[25] These materials exhibit very interesting properties, including the presence of AFM phase with ordered vacancies and vacancy-free SC/semiconducting phase, unconventional superconductivity with $T_c > 30$ K and large iron magnetic moments.[25–28] Absence of hole pockets at the Fermi surface suggests that the pairing mechanism may differ from the one in the pnictides. By cutting the layers of $FeSe_4$ tetrahedra, *e.g.*, removing every third Fe atom from these layers, one obtains a basic building block of the so-called spin-ladder compounds $BaFe_2Se_3$ ($BaFe_2S_3$).[29] These compounds have low-dimensional magnetic properties, which opened a new field in searching for new iron-based materials.[30–33]

In this article an overview of iron-chalcogenides is presented, but instead of a comprehensive review of their features, we focus our attention on the vibrational properties studied by Raman spectroscopy, as a suitable technique for investigating lattice and magnetic excitations of crystalline solids. It can also provide valuable information about coupling of phonons with electrons and charge-density waves and might even serve as a useful tool for probing the crystal symmetry.[34–36]

2. 11-TYPE MATERIALS

2.1. *Crystal structure*

Materials with the general formula FeCh (Ch = Se or Te), belonging to this group, have the simplest structure among all iron chalcogenides. They are built of edge-sharing $FeCh_4$ tetrahedra stacked along the crystallographic *c*-axis, see Fig. 1. At room temperature, they adopt the tetragonal crystal structure of the PbO type, space group *P4/nmm*.[22,37,38]

The crystal structure of FeSe at low temperatures is orthorombic, space group *Cmma*,[24,37,39] although it was initially proposed that $FeSe_{0.88}$ below $T_s \approx$ ≈ 100 K changes symmetry into triclinic, space group $P\text{-}\overline{1}$.[22] Structural transition temperature T_s for FeSe differs between various papers, depending strongly on the strain and sample stoichiometry.[37,40,41] Based on the temperature evolution of synchrotron X-ray diffraction profiles of $FeSe_{0.92}$,[37] it is concluded that T_s is about 70 K, whereas elsewhere[40] is showed that the phase transition in SC $Fe_{1.01}Se$ occurs at 90 K.

With Te-doping of FeSe crystals, the tetragonal-to-orthorombic structural transition moves toward lower temperatures and finally disappears for $FeTe_{0.507}Se_{0.493}$.[42] For low Te-content a miscible region with the local phase separation between two phases emerges.[23,43] These two phases have the same space group (*P4/nmm*) but different lattice parameters. With further increasing Te-concentration, the monoclinic structure appears at low temperatures (space group $P2_1/m$), instead of orthorombic.[38] Martinelli e*t al.*[38] reported tetragonal-to-monoclinic phase transition in $Fe_{1+y}Te_{1-x}Se_x$ crystals for $x \leq 0.1$, with increasing T_s as x decreases. For the end member $Fe_{1+y}Te$, the structural transition occurs around 70 K.

2.2. Physical properties

FeSe exhibits metallic behavior of electrical resistivity (ρ) from room temperature down to $T_c \approx 8$ K, where a sharp drop to zero resistance occurs.[22,23,43] Some authors[22] noticed a weak anomaly at about 100 K, which coincide with the anomaly in magnetic susceptibility $\chi(T)$, and attributed them to the structural transition. They observed almost temperature independent magnetic susceptibility for $T > T_c$, which led them to conclude that FeSe does not order magnetically.[22] However, recent inelastic neutron scattering experiments revealed stripe and Neel spin fluctuations over a wide energy range.[44] Susceptibility measurements also showed SC transition at about 8 K.[22,43] Temperature dependence of resistivity under various pressures is analyzed,[24] and the SC transition was noticed below 13.4 K for low pressures. With the increasing pressure, T_c rapidly increases and reaches maximal value of 37 K at about 6.6 GPa. With further pressurization, T_c decreases and at 13.9 GPa $T_c \approx 6$ K.[24] It was recently shown that an electronic nematic state develops below T_s,[45,46] suggesting that structural transition in FeSe may be driven by the orbital, magnetic and/or charge instability.

FeTe does not exhibit the SC transition.[38,43] Its resistivity weakly increases with decreasing temperature and exhibits an upturn at about 77 K, with rapid drop. Below the structural phase transition temperature $T_s = 70$ K FeTe has metallic behaviour.[38,43] Structural transition is followed by the AFM spin ordering, with $T_N \approx T_s$.[42] For $FeTe_{0.82}$ single crystals, magnetic susceptibility curve $\chi(T)$ exhibits two anomalies, at 65 and 125 K. Anomalous peak in $\rho(T)$ also appears at 65 K.[23] It was later shown that this behaviour is connected with the structural and

AFM phase transition.[47] Hall constant, R_H, is negative in the temperature range 10 K ≤ T ≤160 K, indicating that charge carriers are dominantly electrons.[23]

Comprehensive study of physical properties of $Fe(Se_{1-x}Te_x)_{0.82}$, $0 \leq x \leq 1$, alloys is performed.[23] Maximal T_c of about 14 K is achieved for the sample with $x = 0.6$, and SC disappears in the end member ($x = 1$). Anomaly in the susceptibility at 125 K, similar to that in $FeTe_{0.82}$, persists for all samples with $x > 0.4$. It was shown that,[47] for the $(FeSe_{0.4}Te_{0.6})_{0.82}$ sample, short range magnetic correlations appear below 75 K and rapidly enhance below 40 K, which coincide with anomalous temperature dependence of R_H in this temperature range, indicating the strong interplay between spin and charge degrees of freedom.[23] Samples with $0 \leq x \leq 0.15$ have metallic resistivity from room temperature down to T_c, whereas samples with $0.3 \leq x \leq 1$ have a weak upturn before approaching the SC transition temperature.[23] This is consistent with the results for $FeTe_{1-x}Se_x$, $0< x \leq 0.2$, alloys,[38] where all samples show an upturn in $\rho(T)$ below 100 K, which weakens and shifts to lower temperature as x increases, and metallic behavior at lower temperatures. For $x \geq 0.05$, material become SC, and T_c increases with increasing Se content.[38] Similar resistivity curves were also obtained for $FeSe_{1-x}Te_x$ samples with low Se content, where it was found that T_c increases with x for $x \leq 0.75$, and $T_{c,max} = 15.3$ K for $x = 0.25$.[43]

2.3. Raman scattering studies

According to the factor group analysis (FGA) for the *P4/nmm* space group, four Raman active modes ($A_{1g}+B_{1g}+2E_g$) could be observed in the room-temperature Raman spectra of FeCh (Ch = Se or Te) materials. A_{1g} mode represents vibrations of the Ch-ions, whereas B_{1g} one represents Fe-ion vibrations along the z-axis. Twofold degenerate E_g modes originate from Fe- and Ch-ion vibrations within the *ab*-plane.[39,48]

Vibrational properties of 11-iron chalcogenides were extensively studied by means of Raman spectroscopy.[48–52] Almost all authors observed and assigned, at room temperature, two Raman active modes, of A_{1g} and B_{1g} symmetry, allowed by the selection rules when measuring from the (001)-plane of the sample. The A_{1g} mode was not observed in $Fe_{1.03}Se_{0.3}Te_{0.7}$ sample,[49] although in $FeTe_{0.92}$ sample it is present; it was suggested that it may be due to the vacancies introduced into the system with Se doping, or slightly different excess of Fe-ions. Energies of the A_{1g} and B_{1g} modes for different samples are compared in Table I. As can be seen, they are rather close. However, temperature dependence of Raman mode energy, $\omega(T)$, and linewidth, $\Gamma(T)$, differs substantially between various papers. The spectrum of FeSe single crystal,[39] is shown in Fig. 2.

Magnetic transition that exists in FeTe leaves a clear fingerprint on the behavior of B_{1g} mode energy and linewidth.[48,50,52] Namely, the B_{1g} mode exhibits significant softening and narrowing below $T_N \approx 70$ K (where it changes the symmetry to A_g[52]) for all samples except $Fe_{1.09}Te$. Besides that, both the B_{1g} mode energy and linewidth decrease with decreasing temperature[48,50,52] (Fig. 3) and it was shown[52] that they scales well with the normalized magnetic susceptibility, confirming that spin-phonon coupling substantially influence the behaviour of the B_{1g}(Fe) mode.

TABLE I. Experimentally obtained energies of the A_{1g} and B_{1g} Raman modes at room temperature (except for FeSe,[51] for which data are shown at $T = 5$ K) for some FeCh single crystals

Wave number	$Fe_{1.05}Te$[48]	$Fe_{1.07}Te$[52]	$FeTe_{0.92}$[49]	$FeTe_{0.6}Se_{0.4}$[51]	FeSe[39]
$\bar{\nu}$ (A_{1g}) / cm^{-1}	155.2	156	159.1	161	179.8
$\bar{\nu}$ (B_{1g}) / cm^{-1}	201.4	198	196.3	202	193.9

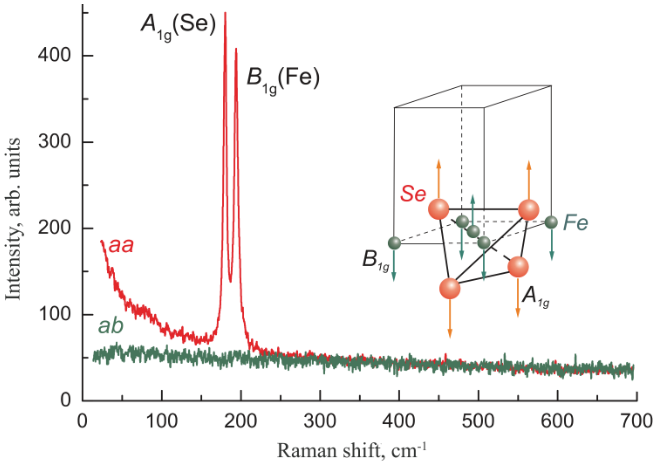

Fig. 2. Polarized Raman scattering spectra of FeSe, room temperature. The inset shows the displacement patterns of the observed modes.[39] (Reprinted with permission from Ref. 39, copyright (2013) by the American Physical Society).

Absence of the B_{1g} phonon softening below T_N for $Fe_{1.09}Te$ single crystal[50] was ascribed to the significant Fe excess, which contributes to the filling up the gap in the spin-wave excitation spectrum with the low-energy spin fluctuations. Unlike the B_{1g} one, behaviour of the A_{1g} symmetry mode differs substantially. The only common feature is the large intrinsic linewidth, which is attributed[48] to the spin-orbital frustration, whereas elsewhere[52] is suggested that electron–phonon interaction may also play an important role.

The A_{1g} mode for $Fe_{1.051}Te$[48] hardens and broadens with decreasing temperature, showing a weak anomaly in $\omega(T)$ at T_s, followed by more rapid increase of $\Gamma(T)$ below T_s. Authors believe that the A_{1g} mode energy renormalization is caused by the phonon modulation of the magnetic interactions and by the anti-phase motion of Te-ions surrounding Fe-ions, which modulates exchange interaction. Rapid increase of the A_{1g} mode linewidth is attributed to the spin-orbital frustration. Energy and linewidth of the A_{1g} mode for $Fe_{1.02}Te$ and $Fe_{1.09}Te$[50] remains almost constant at the temperatures up to 300 K. The A_{1g} mode energy and linewidth were analyzed[52] using phonon anharmonicity model and good agreement is obtained between experimental data and calculated spectra, indicating that they follow anharmonic temperature dependence.

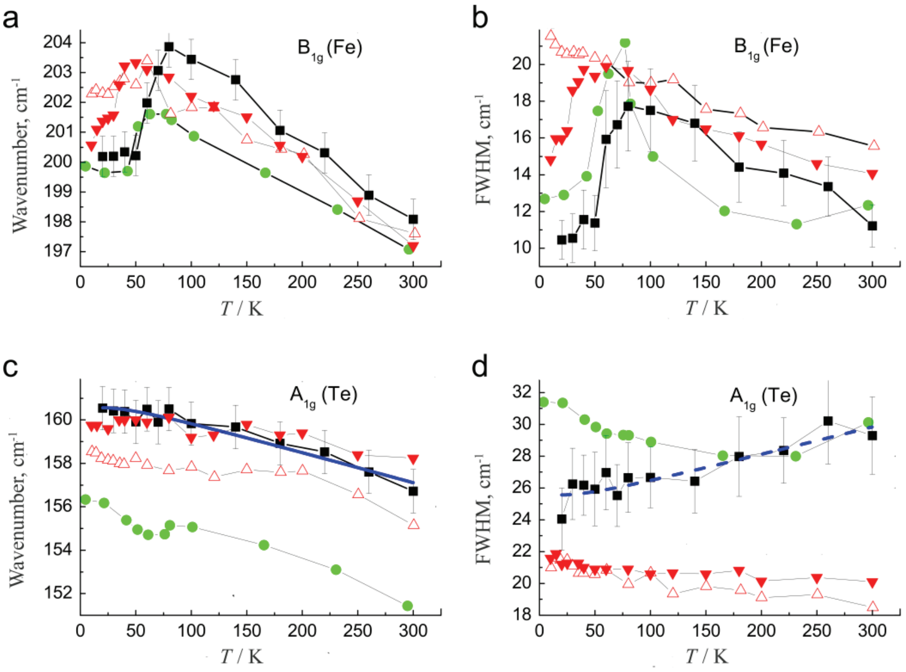

Fig. 3. Comparison of energy and linewidth temperature dependence for A_{1g} and B_{1g} Raman active modes of $Fe_{1+y}Te$ crystals. Filled circles represent data from Ref. 48, open triangles data from Ref. 50, $y = 0.09$, filled triangles data from Ref. 50, $y = 0.02$, and filled squares data from Ref. 52. Solid and dashed lines are calculated spectra using phonon anharmonicity model. (Reprinted from Ref. 52, copyright (2017) with permission from Elsevier).

Effect of Se doping on FeTe Raman spectra has also been investigated.[49,50,52] Um *et al.*[50] analyzed Raman spectra of Se-doped FeTe single crystals and showed that in the sample with the highest Se content ($Fe_{0.95}Te_{0.56}Se_{0.44}$) change of the A_{1g} and B_{1g} mode energy and linewidth with temperature is in agreement with the anharmonic picture: the phonon energy increases and the linewidth decreases with the decreasing temperature. By decreasing Se content, the energy and the linewidth of these modes gradually moves away from the conventional behaviour and for the $Fe_{1.00}Te_{0.78}Se_{0.22}$ crystal the B_{1g} phonon even broadens with decreasing temperature (Fig. 4). Absence of phonon renormalization at T_c for these SC samples is expected because their energies are much larger than the energy of the SC gap.[50]

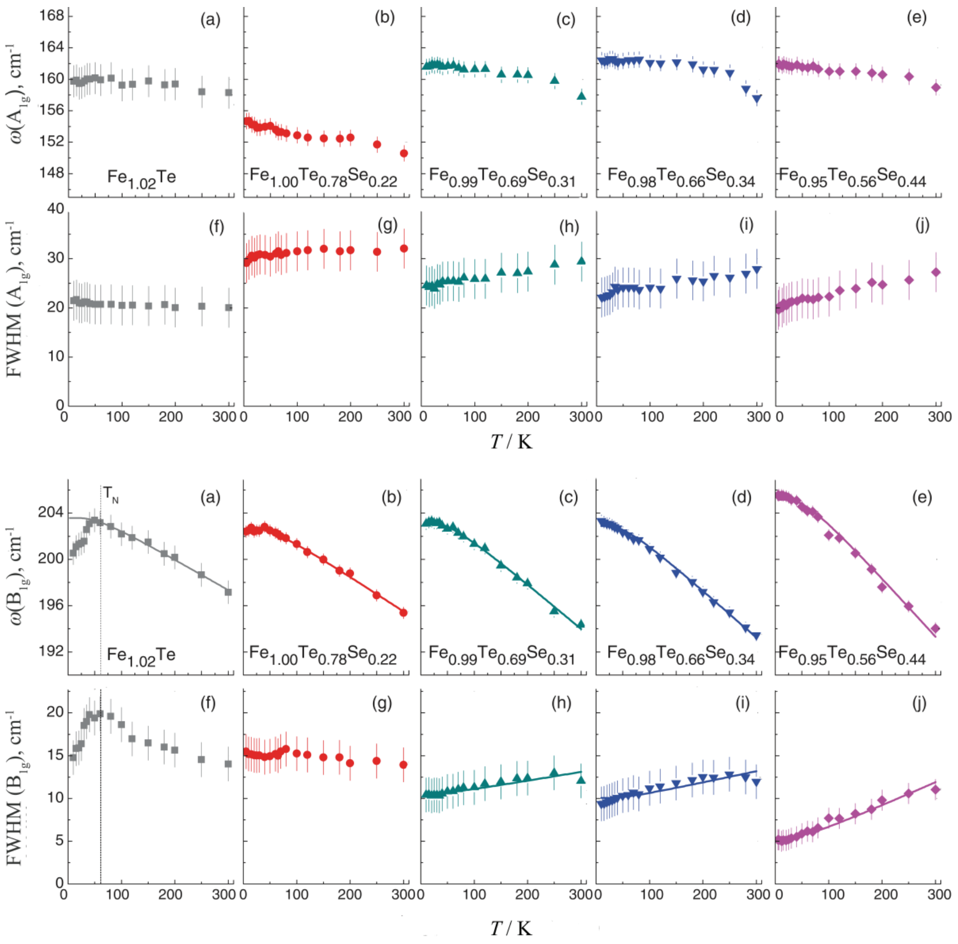

Fig. 4. Temperature dependence of the A_{1g} and B_{1g} mode frequency (ω) and f linewidth (FWHM) of the $Fe_{1.02}Te$, $Fe_{1.00}Te_{0.78}Se_{0.22}$, $Fe_{0.99}Te_{0.69}Se_{0.31}$, $Fe_{0.98}Te_{0.66}Se_{0.34}$ and $Fe_{0.95}Te_{0.56}Se_{0.44}$ samples.[50] (Reprinted with permission from Ref. 50, copyright (2012) by the American Physical Society).

More detailed analysis of the B_{1g} mode linewidth temperature dependence for Se-doped samples revealed that with decreasing Se content its intrinsic linewidth increases, which is attributed to the influence of the spin-phonon coupling, since lower Se (higher Te) content means stronger magnetic interactions. Raman spectra of Se-doped $Fe_{1+y}Te$ crystals were analyzed[52] with respect to the undoped case. It was observed that the A_{1g} and B_{1g} modes have opposite behaviour of energy and linewidth with Se doping: A_{1g} mode hardens and narrows whereas the B_{1g} one softens and broadens with increasing Se content. A_{1g} mode hardening is explained by the mass effect, whereas decreased linewidth is attributed to the lower electron–phonon interaction and/or to the excess Fe-ions. On the other hand, B_{1g} mode broadening in $Fe_{1.02}Te_{0.6}Se_{0.4}$ compared with $Fe_{1.07}Te$ authors ascribed to the induced structural disorder, whereas phonon softening could be explained with the change in excess iron in these two single crystals. Qualitatively similar behaviour is presented[50] for the A_{1g} mode, whereas for the B_{1g} one the situation is almost opposite.

Temperature-dependent phonon Raman spectra of FeSe were analyzed in detail.[39] Room-temperature spectra consist of A_{1g} and B_{1g} modes, as expected from the selection rules. Due to the structural transition into the ortorhombic phase (*e.g.*, lowering of the rotational symmetry from C4 to C2), A_{1g} mode changes symmetry becoming A_g one, but without energy change, and three new modes appearing at higher energies can be of B_{2g}/B_{3g} symmetry, according to the *Cmma* space group. They emerge due to the splitting of E_g mode from the tetragonal phase. Both A_{1g} and B_{1g} mode energies vary smoothly with temperature, and large B_{1g} mode hardening with decreasing temperature is argued to be a consequence of the dynamical crossover from Fe spin state $S = 2$ to $S = 0$ with the lowering of temperature.[39] They suggested that smooth temperature dependence of the phonon linewidth at T_s indicates that orbital fluctuations do not have significant impact on the behavior of Raman modes. Highly polarized quasi-elastic response emerging in Raman spectra of the tetragonal phase, with maximal intensity at T_s, is considered as a fingerprint of electronic nematic fluctuations.[39,53] E_g mode splitting to $B_{2g}+B_{3g}$ phonons in FeSe, as a consequence of C4-symmetry breaking, is found to be only about 2.6 cm^{-1}, which is small in comparison to $Ba(Fe_{1-x}Co_x)_2As_2$, probably due to the lack of the magnetic order (Fig. 5).[54] This

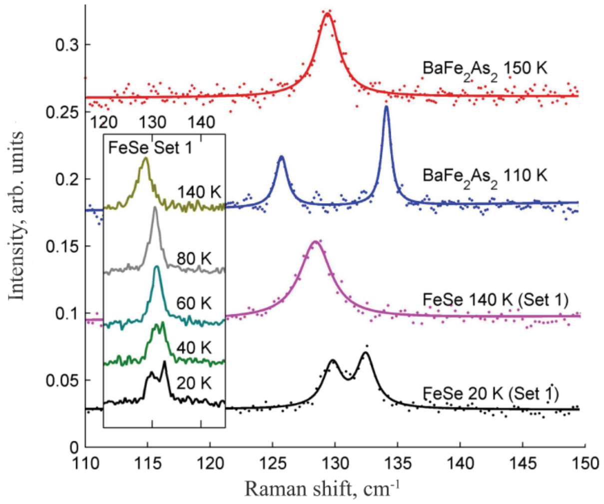

Fig. 5. Raman spectra of $BaFe_2As_2$ and FeSe single crystals. The inset shows temperature dependence of the FeSe Raman spectrum near 130 cm^{-1}, vertically offset for clarity.[54] (Reprinted with permission from Ref. 54, copyright (2016) by the American Physical Society).

splitting sets in below 65 K, where the spin-lattice relaxation rate is found to increase, which led to the conclusion that spin correlations have stronger influence to the lattice than the orbital interactions.[46]

3. 122*-TYPE MATERIALS

3.1. Crystal structure

The SC in this class was firstly discovered in a sample with the nominal composition $K_{0.8}Fe_2Se_2$, with the proposed tetragonal crystal structure of the $ThCr_2Si_2$-type, space group *I4/mmm*.[25] It consists of FeSe layers and K atoms stacked alternatively along the *z*-axis (Fig. 6a). Intercalation of the K atoms between the FeSe slabs significantly increases the lattice parameter *c* (decreasing

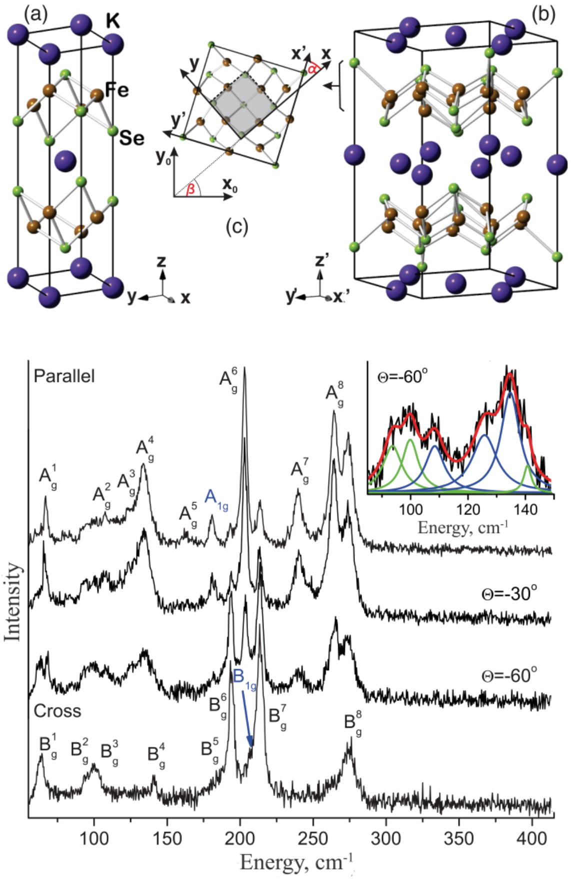

Fig. 6. Crystal structure of $K_xFe_{2-y}Se_2$ within: a) *I4/mmm* and b) *I4/m* unit cells; c) FeSe layer in the (001)-plane of the sample. The solid line represents *I4/m*, whereas shaded square illustrates *I4/mmm* unit cell. Angle between principal axes of the two phases is around 26.6°. Parallel: Raman spectra of $K_xFe_{2-y}Se_2$ measured at 85 K in various polarization configuration ($\Theta = \measuredangle(\mathbf{e_i},\mathbf{e_s})$).[28]

dimensionality of the system), as well as the interlayer Fe–Fe spacing. $(Fe_2Se_2)^{\delta-}$ layers serve as conducting layers, whereas K^+ are charge carriers. Fe–Se–Fe bond angle is very close to the angle of the ideal tetrahedra (109.47°).[25]

However, the appearance of additional peaks in the neutron powder diffraction (NPD) spectra indicated that symmetry lowering to *I4/m* phase occurs, due to the Fe vacancies ordered into the $\sqrt{5}\times\sqrt{5}$ superlattice in the FeSe plane (Fig. 6b).[26] Zavalij *et al.*[55] and Wang *et al.*[56] also suggested $\sqrt{5}\times\sqrt{5}$ order of the iron vacancies. Fe vacancy order disappears at very high temperature (500 K $\leq T_s \leq$ $\leq$ 578 K), depending on the sample composition,[26,57] and *I4/mmm* symmetry is achieved.

The application of the transmission electron microscopy, Chen *et al.*[58] showed that $K_xFe_{2-y}Se_2$ single crystals exhibit a mesoscopic phase separation between an insulating phase with $\sqrt{5}\times\sqrt{5}$ vacancy order and SC/semiconducting phase free of vacancies (*i.e.*, with composition KFe_2Se_2, space group *I4/mmm*). This is also seen by Li e*t al.*[27] on $K_xFe_{2-y}Se_2$ thin films. PXRD measurements confirmed[28] the phase separation: experimental data were well described with the mixture of *I4/m* and *I4/mmm* space groups. Presence of both phases was also confirmed by Raman scattering measurements.[28,59–61] On the other hand, Bao *et al.*[62] reported phase separation between three phases (*I4/m*, *I4/mmm* and *Pmna*) in $K_xFe_{2-y}Se_2$ samples for $1.4 \leq 2-y \leq 1.6$ and $x > 0.85$ (the samples have general formula $K_2Fe_3Se_4$) between T_s and $T^* \approx 350$ K, whereas below T^* only *I4/m* phase with ordered Fe vacancies persists. For Fe content $1.6 \leq 2-y \leq 1.7$ the sample composition is described with $K_2Fe_4Se_5$ and below T_s their space group is *I4/m*.[62]

Doping of $K_xFe_{2-y}Se_2$ crystals on either chalcogen or transition metal site significantly affects their properties. It was recently shown[60] that the phase separation persists in Co-doped $K_xFe_{2-y}Se_2$ single crystals. However, when Co content is significant ($z \geq 0.92$ in $K_xFe_{2-y-z}Co_zSe_2$), vacancy order was not observed and these samples belong to the *I4/mmm* space group.[60,63,64] Doping of $K_xFe_{2-y}Se_2$ with small Ni content also preserves the phase separation.[59] Similarly to the Co-doped case, in $K_xFe_{2-y-z}Ni_zSe_2$ samples with $z \geq 0.73$ low symmetry *I4/m* phase disappears.[59] Pure $K_xNi_{2-y}Se_2$ crystallizes in the tetragonal crystal structure with *I4/mmm* space group, without any indications of vacancy ordering,[65–67] as well as his Co-counterpart. $K_xFe_{2-y}Se_2$ samples doped with S on chalcogen site exhibit iron vacancy order for all doping levels.[68,69]

3.2. Physical properties

Detailed investigations revealed that the physical properties of $K_xFe_{2-y}Se_2$ strongly depend on the sample composition, *i.e.*, K- and Fe-stoichiometry. Bao *et al.*[62] systematically studied few samples having general formula $K_xFe_{2-y}Se_2$ and obtained different properties for various sample compositions. Two samples with higher Fe and lower K content exhibit SC with $T_c \approx 30$ K and large resistivity just above T_c. These samples show poor diamagnetic response below T_c. With the gradually increasing K content, a bump in $\rho(T)$ appears, which is attributed to the metal–insulator crossover, similarly to the results presented elsewhere:[25] above the peak, samples show semiconducting behaviour, whereas below the bump down to T_c, $\rho(T)$ has typical metallic character. Peak position is strongly dependent on the sample composition.[25,62] With the further increasing of K and the decreasing of Fe content, the gradual opening of transport activation gap was observed in the resistivity.[62]

Early studies of the magnetic properties of alkali metal iron selenides revealed that AFM order appears at $T_N \approx 560$ K, slightly below the Fe vacancy ordering temperature T_s.[26,62] The four magnetic moments from the nearest neighbouring Fe atoms order ferromagnetically (FM), whereas these FM blocks form the block-checkerboard AFM order, with very high magnetic moment (3.31 μ_B/Fe at 11 K).[26] SC transition strongly affects the magnetic order parameter, suggesting significant interaction between SC and AFM order.[26]

Recent studies indicated that SC in $K_xFe_{2-y}Se_2$ was highly influenced by the connectivity between SC phases and the proximity effects.[70,71] Three $K_xFe_{2-y}Se_2$ samples with different microstructure exhibited different T_c,[71] although they all have approximately the same fractional ratio of the SC area and similar resistive and magnetic properties. Huang *et al.*[71] showed that proximity effects, that is, the interlayer hopping and interlayer spin coupling, reduce T_c from the theoretically predicted 65 K to the experimentally observed 32 K. On the other hand, large AFM order results in a large SC order, thus explaining relatively high T_c.[71]

The chemical doping is an appropriate way to tune and control physical properties of materials, since it introduces changes in the structure and carrier density. Doping on the Fe site with other transition metals is detrimental for SC.[72] Namely, Cr-, Co- and Zn-doping rapidly suppresses SC in the $K_{0.8}Fe_{2-y}Se_2$, by inducing a large effective magnetic moment, thus destroying SC *via* a magnetic pair-breaking effect.[72] Recently reported study of Ni-doped $K_xFe_{2-y}Se_2$ single crystals[59] shows that small Ni content destroys SC, leading to the insulating behaviour, whereas with further Ni-doping metallic character of crystals gradually increases. It was also shown that these materials exhibit spin glass behaviour below critical temperature T_f of 10–50 K, depending on the Ni concentration.[59] $K_xNi_{2-y}Se_2$ have a local charge-density-wave state persisting up to 300 K.[65] Some authors[66] reported the metallic resistivity of $K_xNi_{2-y}Se_2$ single crystal up to the room temperature, without SC transition or bump in the $\rho(T)$, unlike the $K_xFe_{2-y}Se_2$. SC is suppressed probably due to the K and Ni deficiency, indicating the strong sensitivity to the sample composition. Magnetic measurements revealed that this material is Pauli paramagnet, with local magnetic moments much lower than in $K_xFe_{2-y}Se_2$.[66] Co-doped $K_xFe_{2-y}Se_2$ single crystals behave similarly to its Ni-counterparts.[60] Preliminary analysis of $K_xCo_{2-y}Se_2$ single crystals indicate the FM phase transition at 74 K and absence of SC.[73] When S completely replaces Se in $K_xFe_{2-y}Se_2$, single crystal becomes a small-gap semiconductor, which is ascribed to the random scattering potential introduced by the Fe deficiency, and exhibits a spin glass behaviour below 32 K.[68,69]

3.3. Raman scattering studies

FGA for the *I4/m* space group predicts $9A_g$, $9B_g$ and $9E_g$ modes to be observed in the Raman scattering experiments,[28,61] whereas for the *I4/mmm* space group only four phonon modes ($A_{1g}+B_{1g}+2E_g$) are expected to be observed.[28,61,64,67] In most of the Raman scattering studies of $K_xFe_{2-y}Se_2$ single crystals, the phonon spectra with large number of modes are obtained, confirming the fact that Fe vacancy order reduces locally the symmetry to *I4/m*.[28,61,74–76] These spectra are very similar to each other; characteristic $K_xFe_{2-y}Se_2$ Raman spectrum is shown in Fig. 6. However, the symmetry analysis of the phonon spectra was performed assuming the different space groups in various papers. Temperature analysis of Raman spectra, as well as the line shape of some modes, also differs, as will be discussed.

First Raman study of $K_xFe_{2-y}Se_2$ was done by Zhang *et al*.[74] They assumed the *I4/m* space group for the single phase and thus assigned phonons which appeared in the parallel polarization configuration only as A_g symmetry modes, whereas those modes appearing in both polarization configurations were assigned as B_g ones. In that way 6 A_g and 5 B_g modes were assigned, with energies coinciding well with the lattice dynamics calculations. The most intriguing fact is a frequency jump at T_c for the Raman mode appearing at about 180 cm^{-1} in parallel polarization configuration, of unknown origin, since its energy did not match with any of the calculated A_g mode energies. Authors interpreted this behaviour as an evidence of specific connection between phonons and SC. This hardening was also observed,[75] where Raman spectra of three SC ($K_{0.8}Fe_{1.6}Se_2$, $Tl_{0.5}K_{0.3}Fe_{1.6}Se_2$ and $Tl_{0.5}Rb_{0.3}Fe_{1.6}Se_2$) and one non-SC sample ($KFe_{1.5}Se_2$) were analyzed in terms of *I4/m* space group (Fig. 7). It is suggested that this mode is local, originating from the nanoscopic region of filled Fe vacancies. By comparing the Raman spectra of $K_{0.8}Fe_{1.6}Se_2$ and $KFe_{1.5}Se_2$ single crystals, frequency shift of the Raman modes originating from Fe- and Se-ion vibrations was observed, due to the differences in the FeSe plane induced by the change of Fe content. Doping on the K site did not influence phonon spectra above 60 cm^{-1}, but induces additional modes in the low energy range, attributed to the change of local symmetry in the K layer.[75] *I4/m* space group is assumed also for $K_xFe_{2-y}Se_2$.[76] 16 Raman modes at room temperature was observed, some of them with Fano line shape, attributed to the coupling of the vibrations with AFM spin fluctuations. Authors agreed that three new phonon modes appear below 250 K, due to the structural transition, *i.e.* symmetry lowering from the *I4/m* to the *I4* phase.[76]

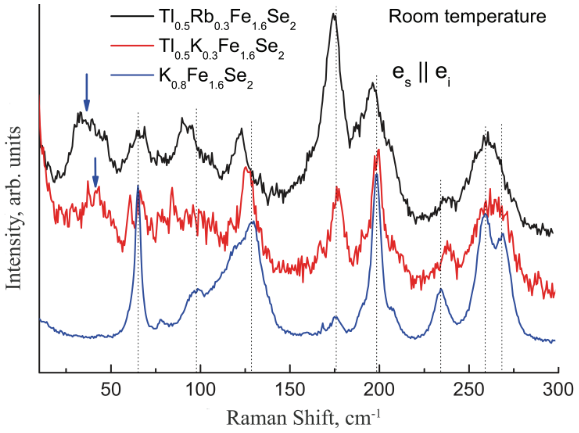

Fig. 7. Raman spectra of the three superconducting crystals measured at room temperature. Additional modes, appearing below 60 cm^{-1} in the Tl- and Rb-substituted samples, are denoted by blue arrows. Dotted lines are guides indicating the peak positions.[75] (Reprinted with permission from Ref. 75, copyright (2012) by the American Physical Society).

Unlike to the presentations by some authors,[74–76] Raman spectra of $K_xFe_{2-y}Se_2$ were analyzed[28,61] in terms of both *I4/m* and *I4/mmm* space groups. Raman modes from the *I4/mmm* space group were assigned.[28] It was determined that the A_{1g} mode appears at about 180 cm^{-1}, whereas energy of the B_{1g} mode is 207 cm^{-1}. It is interesting to note that this A_{1g} phonon is probably the same Raman mode as that of the unknown origin,[74,75] with frequency jump at T_c. Large number of modes from the low symmetry *I4/m* phase were assigned[28] by means of detailed symmetry analysis and measurements in various polarization configurations. A_g and B_g mode energies coincide with other data,[74] which can be seen from Table II. Detailed temperature-dependent Raman scattering study of SC $K_xFe_{2-y}Se_2$ and non-SC $K_xFe_{1.8}Co_{0.2}Se_2$ is given.[61] Similar spectra of the two crystals indicate that phase separation is preserved with small amount of Co doped at the Fe-site. Analysis of the temperature-dependent Raman spectra revealed the phonon energies temperature dependence is dominantly driven by the lattice thermal expansion, whereas the impact of phonon anharmonicity is negligible. The renormalization of the A_{1g} phonon energy below T_c was observed only for the SC sample (Fig. 8), which led to the conclusion that it is induced by the SC gap opening, in line with the theoretically expected behaviour.[77]

Room temperature Raman spectra of Ni- and Co-doped $K_xFe_{2-y}Se_2$ crystals give valuable insight into the structural changes of $K_xFe_{2-y}Se_2$ with doping. Recent Raman studies[59,60] revealed that increasing Co and Ni content have similar influence on phonon spectra of these materials. When Ni (Co) content is low, large number of modes are present in Raman spectra (Fig. 9), in accordance with the symmetry lowering due to the Fe-vacancy ordering, *i.e.*, presence of *I4/m* phase,

TABLE II. Comparison of experimentally observed wavenumbers (in cm^{-1}) at room temperature for the selected A_g and B_g symmetry modes of $K_xFe_{2-y}Se_2$ single crystals[28,74]

Ref.	A_g^4	A_g^6	A_g^8	B_g^7	B_g^8
28	134	203	264	214	274
74	134.6	202.9	264.6	214.3	274.9

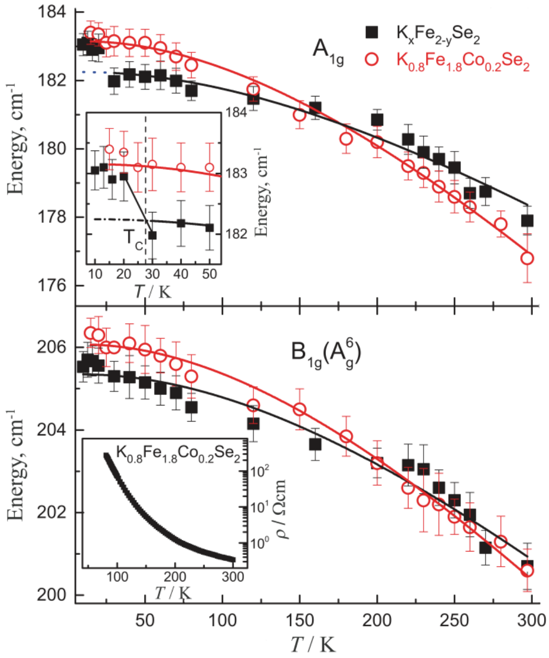

Fig. 8. Temperature dependence of A_{1g} and B_{1g} mode energy in $K_xFe_{2-y}Se_2$ and $K_{0.8}Fe_{1.8}Co_{0.2}Se_2$ single crystals. Inset: An enlarged view of A_{1g} temperature dependence in a low temperature region near T_c.[61]

as in pure $K_xFe_{2-y}Se_2$.[28] Broad asymmetric structures, appearing in Raman spectra of both series of samples for the intermediate Ni (Co) concentrations, were attributed to the large structural disorder. At high Ni (Co) concentrations, as well as for pure $K_xNi_{2-y}Se_2$[67] and $K_xCo_{2-y}Se_2$,[64] only two modes can be observed in Raman spectra, confirming the lack of any vacancy order. Appearance of the A_{1g} mode in the whole series gives a clear evidence that *I4/mmm* phase persists for all Ni (Co) concentrations.[59,60] Detailed Raman scattering studies of $K_xNi_{2-y}Se_2$[67] and $K_xCo_{2-y}Se_2$ single crystals[64] support the findings given elsewhere.[59,60] As opposed to the A_{1g} phonon that appears at similar energies in these two compounds,[64,67] the B_{1g} phonon energy (representing vibrations of the transition metal ions) differs substantially (Table III). Besides that, by measuring from the (010)-plane of $K_xNi_{2-y}Se_2$, one E_g mode is clearly observed (Fig. 10) whereas the other, low intensity E_g mode, was confirmed by numerical calculations. Large intrinsic line-

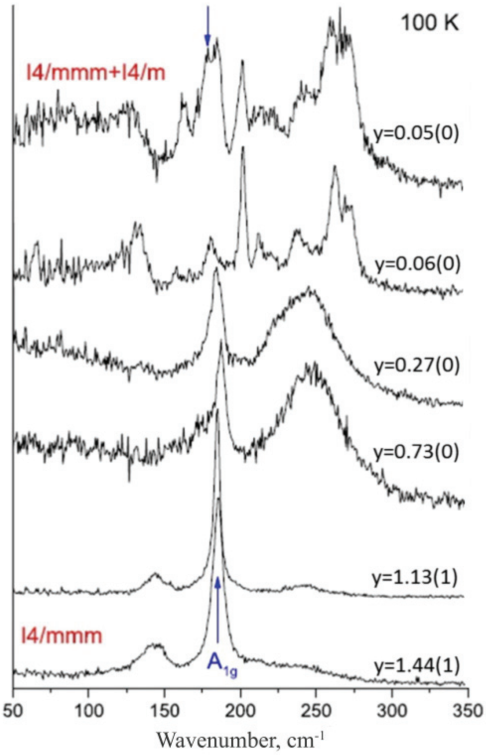

Fig. 9. Raman spectra of $K_xFe_{2-x-y}Ni_ySe_2$ single crystal series measured from the (001)-plane at 100 K.[59]

width of the B_{1g} phonon, together with the mode asymmetry, is believed to originate from the structural disorder, although the impact of the electron–phonon interaction cannot be excluded.[67] Similar features of the B_{1g} phonon are also observed in $K_xCo_{2-y}Se_2$, where it was argued that they are mainly caused by the spin fluctuations coupled to the electronic structure *via* lattice vibrations.[64] Temperature dependence of A_{1g} and B_{1g} mode energy in $K_xCo_{2-y}Se_2$ in the paramagnetic phase is governed by the lattice thermal expansion and phonon anharmonicity, whose relative importance is not yet firmly established. Change of phonon linewidths is well described with the lattice anharmonicity model. Both phonon modes have energy jump below the FM transition temperature T_c, but the A_{1g} mode exhibits sharpening with further cooling, whereas the B_{1g} mode broadens (Fig. 11). Sudden frequency change of the observed Raman mode energies as the sample gets magnetized can occur due to the magnetostriction effects, spin-phonon coupling and/or changes in the electron–phonon interaction caused by the spin polarization and changes in the electronic spectrum.[64]

As opposed to $K_x(Co, Ni)_{2-y}Se_2$, phonon spectra of $K_{0.88}Fe_{1.63}S_2$ consists of large number of modes, originating from the *I4/m* phase. This confirms symmetry lowering due to the Fe-vacancy order, but without phase separation, unlike the

$K_xFe_{2-y}Se_2$.[78] 6 A_g and 8 B_g modes were assigned by measuring the spectra from the (001)-plane of the sample.

TABLE III. Experimentally obtained energies of the A_{1g} and B_{1g} Raman modes (in cm^{-1}) at room temperature for $K_xM_{2-y}Se_2$ single crystals (M = Fe, Co or Ni)

Wave number	$K_xFe_{2-y}Se_2$[28]	$K_xCo_{2-y}Se_2$[64]	$K_xNi_{2-y}Se_2$[67]
$\omega(A_{1g})$	180	197	178
$\omega(B_{1g})$	207	187	134

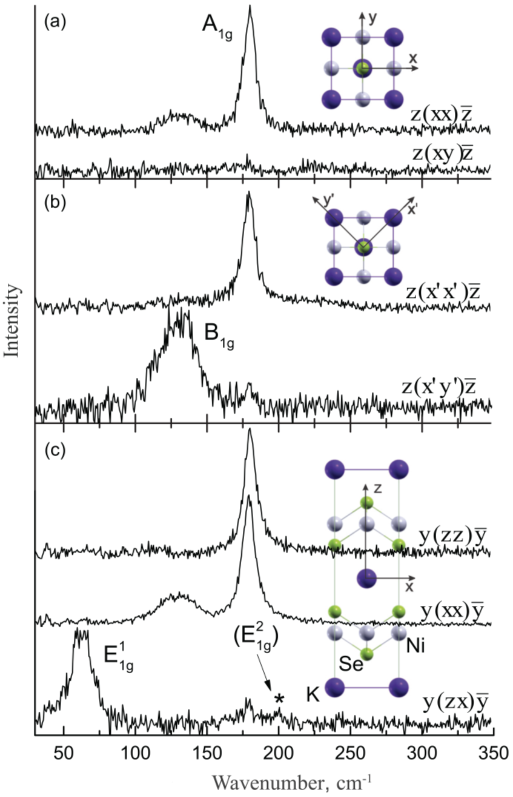

Fig. 10. Room temperature Raman spectra of $K_{0.95}Ni_{1.86}Se_2$ single crystals measured in various scattering configurations (**x** = [100], **y** = [010], **x'** = $1/\sqrt{2}$ [110], **y'** = $1\sqrt{2}$/[1 1 0], **z** = b[001]).[67]

4. IRON-BASED SPIN-LADDER MATERIALS

4.1. Crystal structure

The most studied materials among the iron-containing spin-ladder compounds with the general formula AFe_2X_3 (A = K, Rb, Cs, Ba and X = Ch) are barium–iron-chalcogenides, $BaFe_2(S,Se)_3$. The ladder structure of these compounds can be considered as obtained by cutting the layers of edge-sharing $FeSe_4$ tetrahedra of the two-dimensional 11-iron chalcogenides, *i.e.*, removing every third Fe atom from the FeSe layers. $BaFe_2(S,Se)_3$ crystals consists of one-dimensional

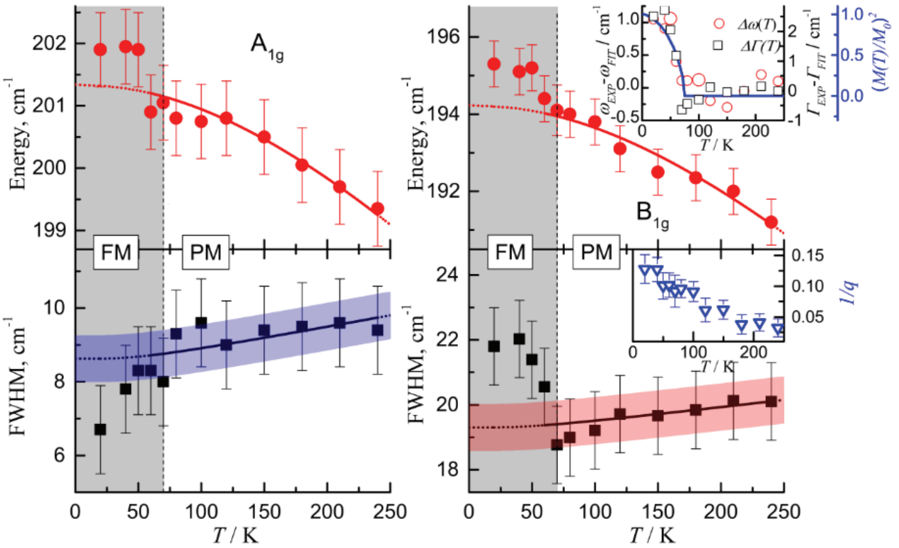

Fig. 11. Temperature dependence of the energy and linewidth (FWHM) for the A_{1g} and B_{1g} Raman modes of $K_xCo_{2-y}Se_2$ single crystal. Solid lines are the theoretical fits which take into account lattice thermal expansion and phonon–phonon scattering for energy and linewidth temperature dependence, respectively. The dotted lines are the extrapolation to 0 K. Shaded area denotes temperature range of the ferromagnetic phase. Inset of B_{1g} energy: temperature dependence of the B_{1g} mode frequency, compared with $(M(T)/M(0))^2$ curve. Inset of B_{1g} FWHM: measure of the electron–phonon coupling $(1/q)$ of the B_{1g} mode as a function of temperature.[64]

$[Fe_2(S,Se)_3]^{2-}$ double chains, propagating along the long ladder direction („lag'') and Ba^{2+} as separators (Fig. 12). In $BaFe_2S_3$ the double chains extend along the *a*-axis, whereas in $BaFe_2Se_3$ the ladder lag is along the *b*-axis.[33,79] There are two important structural differences between these two materials. Namely, two different Fe–Fe distances along the ladder lag exist in $BaFe_2Se_3$, whereas in $BaFe_2S_3$ all Fe–Fe distances are the same. Moreover, $[Fe_2Se_3]^{2-}$ double chains are tilted off the *bc*-plane, with opposite tilting directions of the two neighbouring layers, whereas in $BaFe_2S_3$ there is no tilting. Due to the slight structural differences, $BaFe_2Se_3$ and $BaFe_2S_3$crystals, although both orthorombic, are not isostructural. $BaFe_2S_3$ has *Cmcm* space group, whereas space group of $BaFe_2Se_3$ is *Pnma*, both with four formula units per unit cell.[79]

$BaFe_2Se_2O$ is the first layered iron-oxychalcogenide with alkali earth metal. It consists of Fe–Se(O) layers and Ba^{2+}, stacked alternatively along the *c*-axis, similar with $BaFe_2Se_3$ and $BaFe_2S_3$. Fe–Se(O) double chains are bridged by the oxygen atoms along the *a*-axis and propagate along the *b*-axis. However, the intralayer structure differs from those in previously described spin-ladder materials. Different Fe–Se and Fe–O distances cause Fe atoms to be located in highly distorted (asymmetric) tetrahedra, whose angle significantly deviates from the ideal value. Crystal structure is orthorombic (*Pmmn* space group), with two formula units per unit cell.[80]

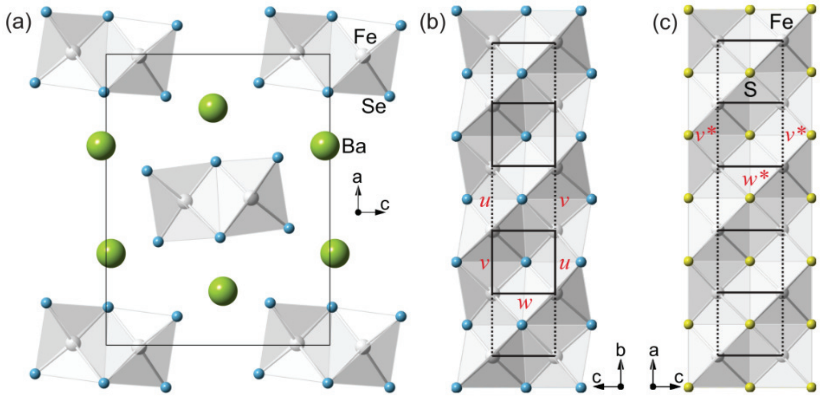

Fig. 12. Crystal structure of $BaFe_2Se_3$ and $BaFe_2S_3$.. a) Projection of the $BaFe_2Se_3$ crystal in the (010)-plane; b) double chain of $[Fe_2Se_3]^{2-}$ tetrahedra propagating along the *b*-axis; c) $[Fe_2S_3]^{2-}$ double chain in the (010) plane. *w* and w^* denote Fe–Fe distances along short ladder directions ("rungs"), whereas *u*, *v* and v^* represent Fe–Fe distances along the ladder legs.[81]

4.2. Physical properties

$BaFe_2S_3$ has semiconducting $\rho(T)$, with very low resistivity.[82,83] The change of slope in resistivity occurs at about 275 K,[82] where inverse molar magnetic susceptibility has a broad hump.[83] This material also exhibits negative magnetoresistive effect of about 10 % at low temperatures. The divergence between ZFC (zero field-cooled) and and FC (field-cooled) magnetic susceptibility below 25 K points out to the spin-glass behaviour, which is confirmed by other measurements.[83] Strong intrachain AFM coupling of the ions, together with the additional crystal field splitting due to the neighbouring Fe atoms and direct Fe–Fe interactions cause ground state with $S = 0$.[83] Takahashi *et al.*[30] recently measured the resistivity of $BaFe_2S_3$ single crystals under various pressures and found the gradual suppression of insulating behaviour with increasing pressure, with metal–insulator transition at about 11 GPa. With further increasing pressure, this material exhibits SC below T_c = 14 K. The increased metallicity of the sample at higher pressures is caused by the anisotropic compression of the crystal.[30] NPD measurements indicate the stripe-type magnetic order, with magnetic moment 1.2 μ_B (at 4 K) per Fe site. These moments form FM units along the rung direction, whereas these units order antiferromagnetically along the lag direction.[30]

$BaFe_2Se_3$ single crystal also has semiconducting $\rho(T)$ properties, similar to $BaFe_2S_3$, but without magnetoresistive effect.[33] Large diversity of susceptibilities for different field directions indicatesmagnetic anisotropy.[29,33] The transition in magnetic susceptibility at 255 K for all field directions is attributed to the crossover from short-range to long-range AFM order.[33] This transition was not observed,[29] since a divergence of ZFC and FC magnetic susceptibilities is attributed to the spin-glass behavior with $T_\mathrm{f} \approx 50$ K.

Resistivity measurements on $BaFe_2Se_2O$ single crystals revealed the insulating behaviour. At $T_\mathrm{a} = 240$ K, there is anomaly in resistivity, allowing their fitting below T_a with the relation $\rho = \rho_0\exp\{(E_\mathrm{a}/k_\mathrm{B}T)^\alpha\}$, $\alpha < 1$, which means that thermal activation is less effective at low temperatures and the other mechanism is responsible for electron trapping.[80] Authors proposed the existence of long range AFM order below 240 K, which is confirmed by the strong peak in differential magnetic susceptibility $\partial\chi/\partial T$ at T_a. Anisotropy in the magnetic susceptibility indicates that the easy axis of magnetization is in the *ab*-plane. Besides that, a sudden decrease of susceptibility below 115 K, with much less anisotropy, was attributed to the spin-singlet dimers, believed to be formed at low temperatures.[80] All iron ions in $BaFe_2Se_2O$ are in Fe^{2+} state and high spin state, and this compound can be considered as $S = 2$ spin-ladder system, with the dominant AFM superexchange interaction along the ladder rungs.[32]

4.3. Raman scattering studies

Raman spectra of $BaFe_2Se_2O$ were analysed.[31] In the optical part of the spectra 6 (of 6) A_g modes and 2 out of 2 B_{1g} modes were observed and assigned (Fig. 13) whereas the remaining modes (of B_{2g} and B_{3g} symmetry) could not be observed by measuring from the (001)-plane of the sample. Three new modes appearing below $T_\mathrm{N} = 240$ K are attributed to the crystal structure and/or crystal symmetry change. Analysis of the Raman mode energy and linewidth depend-

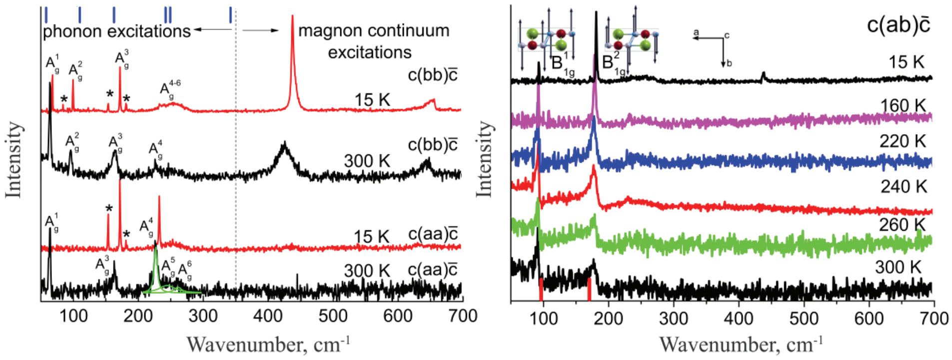

Fig. 13. Left: the (*aa*) and (*bb*) polarized Raman spectra of $BaFe_2Se_2O$ single crystals measured at room temperature and at 15 K. Vertical bars denote calculated values of the A_g Raman active modes. New modes appearing below 240 K are denoted by asterisks. Right: the (*ab*) polarized Raman spectra of $BaFe_2Se_2O$ single crystals measured at various temperatures. Vertical bars denote calculated values of the B_{1g} symmetry modes. Insets show normal modes of the two B_{1g} symmetry vibrations.[31]

ence on temperature showed significant hardening and narrowing of A_g modes below T_N. B_{1g} modes asymmetry above T_N (persisting in the region of short-range magnetic order) is believed to originate from the spin fluctuations.[31]

Besides the optical phonon modes, two broad and asymmetric structures appear in the Raman spectra of $BaFe_2Se_2O$ single crystals at higher energies, in $c(bb)\bar{c}$ polarization only (which coincides with the spin orientations). Therefore, they are assigned as two-magnon continuum modes.[31] These structures are shown in Fig. 14. From the ratio $T_N/T_{max} = 0.53$ (where T_{max} denotes temperature where magnetic susceptibility has a maximum), it was concluded that $BaFe_2Se_2O$ is a quasi-2D magnetic system. From the onset of the magnetic continuum, which should correspond to $2\Delta_S$ (where Δ_S is a spin gap energy), it was estimated $\Delta_S \approx$ $\approx$ 27 meV. Magnon modes disappear above 623 K, *e.g.*, 2.6 T_N[31] in agreement with the other results indicating that the short-range magnetic order in oxychalcogenides persists at least up to 2 T_N.[84]

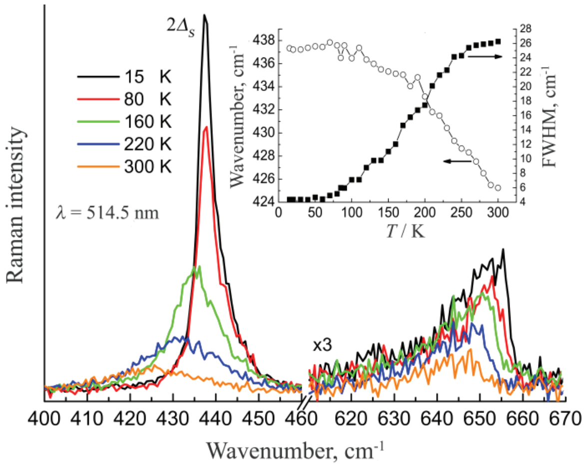

Fig. 14. Raman scattering spectra of $BaFe_2Se_2O$ single crystals measured at various temperatures between 15 and 300 K in $c(bb)\bar{c}$ polarization configuration. Only 400–670 cm^{-1} spectral range is shown. Inset: energy (circles) and linewidth (squares) of the $2\Delta_S$ (spin gap) mode as a function of temperature.[31]

Phonon properties of $BaFe_2S_3$ and $BaFe_2Se_3$ were analysed.[81] By measuring from the (110)-plane of the $BaFe_2S_3$ sample, in parallel polarization configurations 5 (of 5) A_g symmetry modes and 5 out of 6 B_{1g}, the symmetry modes were clearly observed. In crossed polarization configuration B_{2g} and B_{3g} modes could appear in the Raman spectra; therefore, the assignation was done with the help of lattice dynamics calculations. Three such modes were observed in phonon spectra.

On the other hand, lower symmetry of $BaFe_2Se_3$ single crystals compared to $BaFe_2S_3$, caused more Raman active modes to be observed in the phonon spectra. Indeed, by measuring from the (100)-plane of the sample, 9 (of 11) A_g symmetry modes were observed in parallel polarization configuration, whereas in the crossed one three additional modes were assigned as of B_{3g} symmetry.[81]

The temperature analysis of phonon energy and linewidth was performed in terms of lattice thermal expansion and phonon anharmonicity for both $BaFe_2S_3$ and $BaFe_2Se_3$ single crystals. It turned out that the contribution of the phonon–phonon scattering to the Raman mode energy temperature dependence is negligible. The sudden change of slope of energy and linewidth temperature dependence of the A_g^4 mode at about 275 K (where the hump in inverse molar magnetic susceptibility and change of slope in resistivity also occur) in $BaFe_2S_3$ is attributed to the AFM spin ordering within the ladder lag from the short-range to the long-range state, without spin ordering of the whole crystal, followed by the change in the electronic structure. The energies of the all analyzed modes in $BaFe_2Se_3$ sharply increase below T_N, which was ascribed to the spin–phonon coupling. This mechanism is also responsible for the deviation from the usual anharmonic behaviour of the phonon linewidth.[81]

5. SUMMARY AND CONCLUSIONS

The results discussed in this review clearly demonstrate that Raman spectroscopy is a very powerful technique for investigating the vibrational properties of iron chalcogenides. Moreover, almost all structural and magnetic transitions leave a clear fingerprint on the vibrational spectra of 11, 122* and spin-ladder iron-based superconductors, reviewed in this article, through the appearance of new phonon modes or a sudden change in the phonon energy and/or linewidth.

Raman spectra of Fe(Te, Se) single crystals measured from the *ab*-plane consist of two modes, assigned as A_{1g} and B_{1g} ones. Magnetic transition in FeTe causes softening and narrowing of the B_{1g} (Fe) mode. With Se doping of FeTe crystals the A_{1g} mode hardens and narrows, whereas the B_{1g} ones softens and broadens, compared to the pure FeTe. Large B_{1g} mode hardening observed for FeSe is explained as a consequence of the dynamical crossover between different Fe spin states. Electronic nematic fluctuations leave a fingerprint through highly polarized quasielastic response in the Raman spectra of FeSe in the tetragonal phase.

Vibrational spectra of $K_xFe_{2-y}Se_2$ single crystals have large number of phonon peaks. Some authors assigned them according only to the *I4/m* space group, whereas the others assume the existence of *I4/mmm* and *I4/m* phases, which is confirmed by the other techniques. Renormalization of the A_{1g} mode energy at T_c in SC $K_xFe_{2-y}Se_2$ and the absence of renormalization in non-SC isostructural $K_xFe_{1.8}Co_{0.2}Se_2$ indicates that it is induced by the opening of SC gap, confirming that this mode indeed represents the *I4/mmm* phase vibration. Raman studies also revealed that doping of $K_xFe_{2-y}Se_2$ single crystals with different amount of Co and Ni significantly affects their crystal structure. When Ni (Co) content is low, large number of modes points out to the presence of both *I4/mmm* and *I4/m* phases. At high dopant concentrations, as well as for pure $K_x(Co, Ni)_{2-y}Se_2$, only two modes, of A_{1g} and B_{1g} symmetry, appear in phonon spectra, confirming the lack of ordered vacancies. Spin-dependent electron-phonon coupling and magnetostriction effects leave a clear fingerprint on the vibrational spectra of $K_xCo_{2-y}Se_2$, through a strong deviations of the phonon energy and the linewidth temperature dependence from the anharmonic behaviour.

The magnetic ordering manifests itself through the impact on energy, linewidth and lineshape of the observed phonon modes of spin-ladder iron-based systems $BaFe_2S_3$, $BaFe_2Se_3$ and $BaFe_2Se_2O$. Besides that, the analysis of the two-magnon continuum modes of $BaFe_2Se_2O$ allows the estimation of the spin gap energy and classification of this material as a quasi-2D magnetic system.

Future work could be concentrated on the high pressure Raman scattering studies, as well as on the investigations of possible new materials from this class that will be produced by the doping of the existing ones. The results presented in this paper show that Raman spectroscopy is an invaluable tool which can expand our knowledge of the fundamental properties of iron chalcogenides.

Acknowledgements. This work was supported by the Serbian Ministry of Education, Science and Technological Development under Projects ON171032 and III45018.

ИЗВОД

ДИНАМИКА РЕШЕТКЕ ГВОЖЂЕ-ХАЛКОГЕНИДА – ИСПИТИВАЊА МЕТОДОМ РАМАНОВЕ СПЕКТРОСКОПИЈЕ

МАРКО Р. ОПАЧИЋ[1,2] и НЕНАД Ж. ЛАЗАРЕВИЋ[2]

[1]*Електротехнички факултет Универзитета у Београду, Булевар краља Александра 73, Београд*
и[2]*Центар за физику чврстог стања и нове материјале, Институт за физику, Прегревица 118, Београд*

Откриће суперпроводног кристала FeSe значило је појаву нове подкласе високотемпературских суперпроводника – гвожђе-халкогенида. Материјали из ове групе имају разна специфична својства, од суперпроводљивости са релативно високим критичним температурама до нискодимензионалних магнетних особина. Овај прегледни рад приказује најважније резултате везане за гвожђе-халкогениде, са посебним нагласком на њихове вибрационе особине, испитиване методом Раманове спектроскопије. Раманови спектри гвожђе-халкогенида у зависности од температуре и допирања пружају значајан увид у комплексне везе између вибрационих, електронских и магнетних особина ових материјала. Резултати приказани у овом прегледном раду показују да Раманова спектроскопија пружа нове информације које могу значајно побољшати разумевање фундаменталних својстава гвожђе-халкогенида.

(Примљено 21. марта, ревидирано 2.јуна, прихваћено 5. јуна 2017)

REFERENCES

1. H. Kamerlingh Onnes, *Commun. Phys. Lab. Univ. Leiden* **120b** (April 1911), reprinted in *Proc. K. Ned. Akad. Wet.***13** (1911) 1274
2. A. W. Sleight, J. L. Gillson, P. E. Bierstedt, *Solid State Commun.* **17** (1975) 27
3. J. G. Bednorz, K. A. Müller, *Z. Angew. Phys., B* **64** (1986) 189

4. C. W. Chu, P. H. Hor, R. L. Meng, L. Gao, Z. J. Huang, Y. Q. Wang, *Phys. Rev. Lett.* **58** (1987) 908
5. C. W. Chu, P. H. Hor, R. L. Meng, L. Gao, Z. J. Huang, *Science* **235** (1987) 567
6. M. A. Kastner, R. J. Birgeneau, G. Shirane, Y. Endoh, *Rev. Mod. Phys.* **70** (1998) 897
7. P. A. Lee, N. Nagaosa, X.-G. Wen, *Rev. Mod. Phys.* **78** (2006) 17
8. E. Dagotto, *Rev. Mod. Phys.* **66** (1994) 763
9. P. Monthoux, A. V. Balatsky, D. Pines, *Phys. Rev. Lett.* **67** (1991) 3448
10. D. J. Scalapino, *Phys. Rep.* **250** (1995) 329
11. C. C. Tsuei, J. R. Kirtley, C. C. Chi, Lock-See Yu-Jahnes, A. Gupta, T. Shaw, J. Z. Sun, M. B. Ketchen, *Phys. Rev. Lett.* **73** (1994) 593
12. Y. Kamihara, H. Hiramatsu, M. Hirano, R. Kawamura, H. Yanagi, T. Kamiya, H. Hosono, *J. Am. Chem. Soc.* **128** (2006) 10012
13. Y. Kamihara, T. Watanabe, M. Hirano, H. Hosono, *J. Am. Chem. Soc.* **130** (2008) 3296
14. Z.-A. Ren, G.-C. Che, X.-L. Dong, J. Yang, W. Lu, W. Yi, X.-L. Shen, Z.-C. Li, L.-L. Sun, F. Zhou, *Europhys. Lett.* **83** (2008) 17002
15. M. Rotter, M. Tegel, D. Johrendt, *Phys. Rev. Lett.* **101** (2008) 107006
16. X. C. Wang, Q. Q. Liu, Y. X. Lv, W. B. Gao, L. X. Yang, R. C. Yu, F. Y. Li, C. Q. Jin, *Solid State Commun.* **148** (2008) 538
17. M. D. Lumsden, A. D. Christianson, *J. Phys.: Condens. Matter* **22** (2010) 203203
18. D. C. Johnston, *Adv. Phys.* **59** (2010) 803
19. H. Chen, Y. Ren, Y. Qiu, Wei Bao, R. H. Liu, G. Wu, T. Wu, Y. L. Xie, X. F. Wang, Q. Huang, X. H. Chen, *Europhys. Lett.* **85** (2009) 17006.
20. I. I. Mazin, D. J. Singh, M. D. Johannes, M. H. Du, *Phys. Rev. Lett.* **101** (2008) 057003
21. A. D. Christianson, E. A. Goremychkin, R. Osborn, S. Rosenkranz, M. D. Lumsden, C. D. Malliakas, I. S. Todorov, H. Claus, D. Y. Chung, M. G. Kanatzidis, R. I. Bewley, T. Guidi, *Nature* **456** (2008) 930
22. F.-C. Hsu, J.-Y. Luo, K.-W. Yeh, T.-K. Chen, T.-W. Huang, P.-M. Wu, Y.-C. Lee, Y.-L. Huang, Y.-Y.Chu, D.-C. Yan, M.-K. Wu, *Proc. Natl. Acad. Sci. U.S.A.* **105** (2008) 14262
23. M. H. Fang, H. M. Pham, B. Qian, T. J. Liu, E. K. Vehstedt, Y. Liu, L. Spinu, Z. Q. Mao, *Phys. Rev., B* **78** (2008) 224503
24. S. Margadonna, Y. Takabayashi, Y. Ohishi, Y. Mizuguchi, Y. Takano, T. Kagayama, T. Nikagawa, M. Takata, K. Prassides, *Phys. Rev., B* **80** (2009) 064506
25. J. Guo, S. Jin, G. Wang, S. Wang, K. Zhu, T. Zhou, M. He, X. Chen, *Phys. Rev., B* **82**(2010) 180520
26. W. Bao, Q. Huang, G. F. Chen, M. A. Green, D. M. Wang, J. B. He, X. Q. Wang, Y. Qiu, *Chin. Phys. Lett.* **28** (2011) 086104
27. W. Li, H. Ding, P. Deng, K. Chang, C. Song, K. He, L. Wang, X. Ma, J.-P. Hu, X. Chen, Q.-K. Xue, *Nat. Phys*. **8** (2012) 126
28. N. Lazarević, M. Abeykoon, P. W. Stephens, H. Lei, E. S. Bozin, C. Petrovic, Z. V. Popović, *Phys. Rev., B* **86** (2012) 054503
29. B. Saparov, S. Calder, B. Sipos, H. Cao, S. Chi, D. J. Singh, A. D. Christianson, M. D. Lumsden, A. S. Sefat, *Phys. Rev., B* **84** (2011) 180409
30. H. Takahashi, A. Sugimoto, Y. Nambu, T. Yamauchi, Y. Hirata, T. Kawakami, M. Avdeev, K. Matsubayashi, F. Du, C. Kawashima, H. Soeda, S. Nakano, Y. Uwatoko, Y. Ueda, T. J. Sato, K. Ohgushi, *Nat. Mater.* **14** (2015) 1008
31. Z. V. Popović, M. Šćepanović, N. Lazarević, M. M. Radonjić, D. Tanasković, H. Lei, C. Petrovic, *Phys. Rev., B* **89** (2014) 014301

32. H. Kabbour, E. Janod, B. Corraze, M. Danot, C. Lee, M. H. Whangbo, L. Cario, *J. Am. Chem. Soc.* **130** (2008) 8261
33. H. Lei, H. Ryu, A. I. Frenkel, C. Petrovic, *Phys. Rev., B* **84** (2011) 214511
34. N. Lazarević, E. S. Bozin, M. Šćepanović, M. Opačić, H. Lei, C. Petrovic, Z. V. Popović, *Phys. Rev., B* **89** (2015) 224301
35. N. Lazarević, Z. V. Popović, R. Hu, C. Petrovic, *Phys. Rev., B* **83** (2011) 024302
36. N. Lazarević, Z. V. Popović, R. Hu, C. Petrovic, *Phys. Rev., B* **81** (2010) 144302
37. S. Margadonna, Y. Takabayashi, M. T. McDonald, K. Kasperkiewicz, Y. Mizuguchi, Y. Takano, A. N. Fitch, E. Suarde, K. Prassides, *Chem. Commun.* (2008) 5607
38. A. Martinelli, A. Palenzona, M. Tropeano, C. Ferdeghini, M. Putti, M. R. Cimberle, T. D. Nguyen, M. Affronte, C. Ritter, *Phys. Rev., B* **81** (2010) 094115
39. V. Gnezdilov, Y. G. Pashkevich, P. Lemmens, D. Wulferding, T. Shevtsova, A. Gusev, D. Chareev, A. Vasiliev, *Phys. Rev., B* **87** (2013) 114305
40. T. M. McQueen, A. J. Williams, P. W. Stephens, J. Tao, Y. Zhu, V. Ksenofontov, F. Casper, C. Felser, R. J. Cava, *Phys. Rev. Lett.* **103** (2009) 057002
41. S.-H. Baek, D.V. Efremov, J. M. Ok, J. S. Kim, Jeroen van den Brink, B. Büchner, *Phys. Rev., B* **93** (2016) 180502(R)
42. S. Li, C. de la Cruz, Q. Huang, Y. Chen, J. W. Lynn, J. Hu, Y.-L. Huang, F.-C. Hsu, K.-W. Yeh, M.-K. Wu, P. Dai, *Phys. Rev., B* **79** (2009) 054503
43. Y.Mizuguchi, F.Tomioka, S.Tsuda, T.Yamaguchi, and Y.Takano, *J. Phys. Soc. Jpn.* **78** (2009) 074712
44. Qisi Wang, Yao Shen, Bingying Pan, Xiaowen Zhang, K. Ikeuchi, K. Iida, A. D. Christianson, H. C. Walker, D. T. Adroja, M. Abdel-Hafiez, Xiaojia Chen, D. A. Chareev, A. N. Vasiliev, Jun Zhao, *Nat. Commun.* **7** (2016) 12182
45. S-H. Baek, D. V. Efremov, J. M. Ok, J. S. Kim, Jeroen van den Brink, B. Büchner, *Nat. Mater.* **14** (2015) 210
46. M. D. Watson, T. K. Kim, A. A. Haghighirad, N. R. Davies, A. McCollam, A. Narayanan, S. F. Blake, Y. L. Chen, S. Ghannadzadeh, A. J. Schofield, M. Hoesch, C. Meingast, T. Wolf, A. I. Coldea, *Phys. Rev., B* **91** (2015) 155106
47. W. Bao, Y. Qiu, Q. Huang, M. A. Green, P. Zajdel, M. R. Fitzsimmons, M. Zhernenkov, S. Chang, M. H. Fang, B. Qian, E. K. Vehstedt, J. Yang, H. M. Pham, L. Spinu, Z. Q. Mao, *Phys. Rev. Lett.* **102** (2009) 247001
48. V. Gnezdilov, Y. Pashkevich, P. Lemmens, A. Gusev, K. Lamonova, T. Shevtsova, I. Vitebskiy, O. Afanasiev, S. Gnatchenko, V. Tsurkan, J. Deisenhofer, A. Loidl, *Phys. Rev., B* **83** (2011) 245127
49. T.-L. Xia, D. Hou, S. C. Zhao, A. M. Zhang, G. F. Chen, J. L. Luo, N. L. Wang, J. H. Wei, Z.-Y. Lu, Q. M. Zhang, *Phys. Rev., B* **79** (2009) 140510
50. Y. J. Um, A. Subedi, P. Toulemonde, A. Y. Ganin, L. Boeri, M. Rahlenbeck, Y. Liu, C. T. Lin, S. J. E. Carlsson, A. Sulpice, M. J. Rosseinsky, B. Keimer, M. Le Tacon, *Phys. Rev., B* **85**(2012) 064519
51. K. Okazaki, S. Sugai, S. Niitaka, H. Takagi, *Phys. Rev., B* **83** (2011) 035103
52. Z. V. Popović, N. Lazarević, S. Bogdanović, M. M. Radonjić, D. Tanasković, Rongwei Hu, Hechang Lei, C. Petrovic, *Solid State Commun.* **193** (2014) 51
53. P. Massat, D. Farina, I. Paul, S. Karlsson, P. Strobel, P. Toulemonde, M.-A. Measson, M. Cazayous, A. Sacuto, S. Kasahara, T. Shibauchi, Y. Matsuda, Y. Gallais, *Proc. Natl. Acad. Sci. U.S.A.* **113** (2016) 9177

54. Yuwen Hu, Xiao Ren, Rui Zhang, Huiqian Luo, Shigeru Kasahara, Tatsuya Watashige, Takasada Shibauchi, Pengcheng Dai, Yan Zhang, Yuji Matsuda, Yuan Li, *Phys. Rev., B* **93** (2016) 060504(R)
55. P. Zavalij, W. Bao, X. F. Wang, J. J. Ying, X. H. Chen, D. M. Wang, J. B. He, X. Q. Wang, G. F. Chen, P.-Y. Hsieh, Q. Huang, M. A. Green, *Phys. Rev., B* **83** (2011) 132509
56. Z. Wang, Y. J. Song, X. L. Shi, Z. W. Wang, Z. Chen, H. F. Tian, G. F. Chen, J. G. Guo, H. X. Yang, J. Q. Li, *Phys. Rev., B* **83** (2011) 140505(R)
57. F. Ye, S. Chi, W. Bao, X. F. Wang, J. J. Ying, X. H. Chen, H. D. Wang, C. H. Dong, M. H. Fang, *Phys. Rev. Lett.* **107** (2011) 137003
58. F. Chen, M. Xu, Q. Q. Ge, Y. Zhang, Z. R. Ye, L. X. Yang, Juan Jiang, B. P. Xie, R. C. Che, M. Zhang, A. F. Wang, X. H. Chen, D. W. Shen, J. P. Hu, D. L. Feng, *Phys. Rev. X* **1** (2011) 021020
59. Hyejin Ryu, Milinda Abeykoon, Kefeng Wang, Hechang Lei, N. Lazarević, J. B. Warren, E. S. Bozin, Z. V. Popović, C. Petrovic, *Phys. Rev., B* **91** (2015) 184503
60. Hyejin Ryu, Kefeng Wang, M. Opačić, N. Lazarević, J. B. Warren, Z. V. Popović, C. Petrovic, *Phys. Rev., B* **92** (2015) 174522
61. M. Opačić, N. Lazarević, M. Šćepanović, H. Ryu, H. Lei, C. Petrovic, Z. V. Popović, *J. Phys.: Cond. Matter* **27** (2015) 485701
62. W. Bao, G. N. Li, Q. Huang, G. F. Chen, J. B. He, M. A. Green, Y. Qiu, D. M. Wang, J. L. Luo, M. M. Wu, *Chin. Phys. Lett.* **30** (2013) 027402
63. G. Huan, M. Greenblatt, *J. Less-Common Met.* **156** (1989) 247
64. M. Opačić, N. Lazarević, M. M. Radonjić, M. Šćepanović, H. Ryu, A. Wang, D. Tanasković, C. Petrovic, Z. V. Popović, *J. Phys.: Cond. Matter* **28** (2016) 485401
65. J. R. Neilson, A. Llobet, A. V. Stier, L. Wu, J. Wen, J. Tao, Y. Zhu, Z. B. Tesanovic, N. P. Armitage, T. M. McQueen, *Phys. Rev., B* **86** (2012) 054512
66. H. Lei, M. Abeykoon, K. Wang, E. S. Bozin, H. Ryu, D. Graf, J. B. Warren, C. Petrovic, *J. Phys.: Cond. Matter* **26** (2014) 015701
67. N. Lazarević, M. Radonjić, M. Šćepanović, H. Lei, D. Tanasković, C. Petrovic, Z. V. Popović, *Phys. Rev., B* **87** (2013) 144305
68. H. Lei, M. Abeykoon, E. S. Bozin, K. Wang, J. B. Warren, C. Petrovic, *Phys. Rev. Lett.* **107** (2011) 137002
69. H. Lei, M. Abeykoon, E. S. Bozin, C. Petrovic, *Phys. Rev., B* **83** (2011) 180503(R)
70. X. Ding, D. Fang, Z. Wang, H. Yang, J. Liu, Q. Deng, G. Ma, C. Meng, Y. Hu, H.-H. Wen, *Nat. Commun.* **4** (2013) 1897
71. S.-M. Huang, C.-Y. Mou, T.-K. Lee, *Phys. Rev., B* **88** (2013) 174510
72. D. Tan, C. Zhang, C. Xi, L. Ling, L. Zhang, W. Ton, Y. Yu, G. Feng, H. Yu, L. Pi, Z. Yang, S. Tan, Y. Zhang, *Phys. Rev., B* **84** (2011) 014502
73. J. Yang, B. Chen, H. Wang, Q. Mao, M. Imai, K. Yoshimura, M. Fang, *Phys. Rev., B* **88** (2013) 064406
74. A. M. Zhang, K. Liu, J. H. Xiao, J. B. He, D. M. Wang, G. F. Chen, B. Normand, Q. M. Zhang, *Phys. Rev., B* **85** (2012) 024518
75. A. M. Zhang, K. Liu, J. B. He, D. M. Wang, G. F. Chen, B. Normand, Q. M. Zhang, *Phys. Rev., B* **86** (2012) 134502
76. A. Ignatov, A. Kumar, P. Lubik, R. H. Yuan, W. T. Guo, N. L. Wang, K. Rabe, G. Blumberg, *Phys. Rev., B* **86** (2012) 134107
77. M. Cardona, *NATO ASI Ser., B* **372** (2002) 257.
78. N. Lazarević, H. Lei, C. Petrovic, Z. V. Popović, *Phys. Rev., B* **84** (2011) 214305
79. H. Hong, H. Steinfink, *J. Solid State Chem.* **5** (1972) 93

80. H. Lei, H. Ryu, V. Ivanovski, J. B. Warren, A. I. Frenkel, B. Cekic, W.-G. Yin, C. Petrovic, *Phys. Rev., B* **86** (2012) 195133
81. Z. V. Popović, M. Šćepanović, N. Lazarević, M. Opačić, M. M. Radonjić, D. Tanasković, H. Lei, C. Petrovic, *Phys. Rev., B* **91** (2015) 064303
82. W. Reiff, I. Grey, A. Fan, Z. Eliezer, H. Steinfink, *J. Solid State Chem.* **13** (1975) 32
83. Z. S. Gönen, P. Fournier, V. Smolyaninova, R. Greene, F. M. Araujo-Moreira, B. Eichhorn, *Chem. Mater.* **12** (2000) 3331
84. J. B. He, D. M. Wang, H. L. Shi, H. X. Yang, J. Q. Li, G. F. Chen, *Phys. Rev., B* **84** (2011) 205212.

Journal of Drug Delivery Science and Technology 39 (2017) 467–474

Contents lists available at ScienceDirect

Journal of Drug Delivery Science and Technology

journal homepage: www.elsevier.com/locate/jddst

Application of the melt granulation technique in development of lipid matrix tablets with immediate release of carbamazepine

Marko Krstic [a], *, Jelena Djuris [a], Ognjen Petrovic [a], Nenad Lazarevic [b], Sandra Cvijic [a], Svetlana Ibric [a]

[a] Department of Pharmaceutical Technology and Cosmetology, University of Belgrade - Faculty of Pharmacy, Vojvode Stepe 450, 11221 Belgrade, Serbia
[b] Center for Solid State Physics and New Materials, Institute of Physics Belgrade, University of Belgrade, Pregrevica 118, 11080 Belgrade, Serbia

ARTICLE INFO

Article history:
Received 4 March 2017
Received in revised form
17 April 2017
Accepted 18 April 2017
Available online 19 April 2017

Keywords:
Carbamazepine
Lipid matrix tablets
Neusilin® UFL2
Immediate release tablets
Melt granulation
Experimental design

ABSTRACT

The aim was to develop immediate-release carbamazepine lipid matrix tablets by using the melt granulation technique, application of Quality by design. The first set of screening experiments investigated the influence of six parameters (meltable binder type; amounts of meltable binder, carbamazepine and crospovidone; carrier type, and compression force) on carbamazepine release rate from tablets, using fractional factorial experimental design. In the second set of experiments, amounts of meltable binder and Cremophor® RH40 were varied according to the central composite design. The optimal formulation which showed the fastest release rate (more than 80% in first 30 min) was identified (compression force of 8 kN, 20% of Labrafil® 2130CS, 10% of Cremophor® RH40, 30% of carbamazepine, 5% of crospovidone NP and Neusilin® UFL2 used as the carrier). Different analytical techniques (DSC, PXRD, FT-IR, Raman spectroscopy) confirmed the maintenance of carbamazepine in its therapeutically active polymorph form III in the optimal formulation. Raman spectroscopy was used to demonstrate the stability of the optimal formulation during the two months stability study (25°C, RH 40%). It can be concluded that melt granulation technique can be used in development of lipid matrix tablets with immediate-release of the drug.

1. Introduction

Poor solubility is one of the key reasons for the poor absorption and bioavailability of drugs [1]. There are many approaches for increasing dissolution rate of a drug, with one of them being a formulation of lipid drug delivery systems [2].

The use of lipid formulations for enhancing gastrointestinal absorption of poorly water soluble drugs is well-documented in the literature. It was observed that the food which contains high amounts of lipids increases absorption, as well as bioavailability of poorly water-soluble drugs, when taken together [3–7]. Lipids and lipid excipients increase bioavailability by the following mechanisms: drug solubilization in intestinal fluid, modification of transport mechanisms in enterocytes, modification of drug distribution into systemic circulation (portal bloodstream vs. lymphatic system) [8]. Solid lipid delivery systems combine the advantages of lipid formulation (i.e., enhanced solubility and bioavailability) with those of solid dosage forms (e.g., low production cost, convenience of process control, high stability and reproducibility, better patient compliance). Also, a combination of lipid formulation and adsorbents with great specific surface results in the increase of release rate for poorly water-soluble drugs such as griseofulvin, lansoprazole, tacrolimus, celecoxib, gentamicin and carbamazepine [3–7].

One of the techniques for prepared solid lipid formulations is the melt granulation. Melt granulation is a procedure in which granules are obtained through the addition of either a molten binder or a solid binder which melts during the process. The advantages of the melt granulation over wet or dry granulation are that solvents are not needed and fewer processing steps are required [9]. Traditionally, lipid matrix systems are prepared by adsorption of the liquid forms onto the appropriate carrier. Frequently used carriers include magnesium aluminometasilicate (Neusilin®), porous silica (Sylysia®) or microcrystalline cellulose (Avicel®) [10,11]. On the other hand, the melt granulation technique enables one-step preparation of lipid matrix whereby selected multifunctional lipophilic excipient acts as the molten binder and a

---

* Corresponding author.
E-mail address: mkrstic109@gmail.com (M. Krstic).

http://dx.doi.org/10.1016/j.jddst.2017.04.024
1773-2247/© 2017 Published by Elsevier B.V.

Table 1
Varied parameters in the first set of experiment.

Parameter	Parameter mark	Low level (-1)	High level (+1)
Type of meltable binder	X_1	Labrafil® 2130CS	Gelucire® 44/14
Amount of meltable binder (%)	X_2	20	30
Amount of carbamazepine (%)	X_3	20	30
Amount of crospovidone NP (%)	X_4	2	5
Type of carrier	X_5	Neusilin®UFL2	Vivapur® Type 101
Compression force (kN)	X_6	7	8

component of the formulation [12].

Quality by Design (QbD) is a modern, scientific approach that ensures the quality of the final product by developing a thorough understanding of the influence of the critical materials attributes (CMA, such as the melting point, flowability) and the critical process parameters (CPP, such as the processing temperature, mixing rate) on the critical quality attributes (CQAs) of the product, such as the drug release rate and stability [13].

The aim of the present study was to develop lipid matrix system, in the form of tablets, for immediate release of carbamazepine using the melt granulation technique. Carbamazepine is a model drug with poor water solubility (0.17 mg mL^{-1} at 24 °C) and high permeability [4]. Formulation development was guided by experimental design for determination of the critical materials attributes influencing the carbamazepine release rate. The melt granulation technique was used, with self-emulsifying lauroylmacrogol glycerides as binders, whereas magnesium aluminometasilicate and microcrystalline cellulose were used as carriers for preparation of the lipid matrix tablets.

2. Materials and methods

2.1. Materials

In the experiment, carbamazepine was used as a model drug (Ph. Eur. 8.0), Neusilin® UFL2 (magnesium aluminometasilicate, Fuji Chemical Industry Co., Toyama, Japan) and microcrystalline cellulose (Vivapur® Type 101, Ph. Eur. 8.0) were used as carriers. Gelucire® 44/14 (lauroyl macrogol-32 glycerides, Gattefose, France) and Labrafil® 2130CS (lauroyl macrogol-6 glycerides, Gattefose, France) were used as meltable binder and components of lipid matrix systems. Cremophor® RH 40 (macrogolglycerol hydroxystearate, BASF, Germany) was used as a non-ionic surfactant, and Crospovidone NP (Ph. Eur. 8.0) as superdisintegrant, and magnesium-stearate (Ph. Eur. 8.0) as lubricant in the tablets.

2.2. Experimental plan

The experimental part can be divided into two phases. In the first phase, the feasibility of one-step procedure for preparation of lipid matrix tablets of carbamazepine was investigated through the screening study. Potential critical material attributes (CMAs), namely the type and amount of meltable binder, the amount of carbamazepine and superdisintegrant, as well as the type of carrier were analyzed, accompanied with the investigation of the influence of the compression force as the potential critical processing parameter (CPP) influencing carbamazepine release rate (CQA). Factors $X_1 - X_6$ were varied on two levels (Table 1), according to the 2^{6-3} fractional factorial design. Experimental plan is represented in Table 2.

Table 2
Experimental plan according to the fractional factorial design 2^{6-3}.

Formulation	Input					
	X_1	X_2	X_3	X_4	X_5	X_6
F-I-1	+1	−1	+1	−1	+1	−1
F-I-2	+1	−1	−1	−1	−1	+1
F-I-3	−1	−1	+1	+1	−1	−1
F-I-4	+1	+1	−1	+1	−1	−1
F-I-5	+1	+1	+1	+1	+1	+1
F-I-6	−1	−1	−1	+1	+1	+1
F-I-7	−1	+1	−1	−1	+1	−1
F-I-8	−1	+1	+1	−1	−1	+1

In the second phase, the optimization of immediate-release carbamazepine tablets (lipid matrix tablets) was performed. The amount of the meltable binder Labrafil® 2130CS (A) and the amount of Cremophor® RH 40 (B) were varied according to the central composite experimental design (CCD), as represented in Table 3, in order to identify the optimal formulation. Cremophor® RH 40 was added in order to further improve the drug release rate. Nine different formulations were prepared, with four replications in the central point of the design space.

For the both phases of the study percentages of carbamazepine released after 10, 20, 30, 45, 60 and 120 min ($Y_1–Y_6$) were monitored as output parameters (CQAs). Granules and tablets obtained in the first phase were also tested for flowability, density and resistance to crushing. Design Expert software (version 7.0.0; Stat-Ease, Inc., Minneapolis, MN, USA) was used for the data analysis.

Afterwards, characterization of carbamazepine solid state in the optimal formulation (tablets that provided the highest dissolution rate) was performed using the differential scanning calorimetry (DSC), powder X-ray diffraction (PXRD), and Fourier transform infrared spectroscopy (FT-IR). Stability of the optimal formulation was monitored for two months, by application of Raman spectroscopy.

2.3. Methods

2.3.1. Preparation of granules and tablets

Carbamazepine lipid matrix tablets were made by using the melt granulation technique, in both phases. The experimental plan

Table 3
Experimental plan according to the central composite design.

Formulation	Varied parameter	
	A - Labrafil® 2130CS (%)	B - Cremophor® RH 40 (%)
F-II-1	15.00	7.93
F-II-2	15.00	15.00
F-II-3	10.00	10.00
F-II-4	20.00	10.00
F-II-5	10.00	20.00
F-II-6	20.00	20.00
F-II-7	15.00	22.07
F-II-8	22.07	15.00
F-II-9	7.93	15.00
F-II-10	15.00	15.00
F-II-11	15.00	15.00
F-II-12	15.00	15.00
F-II-13	15.00	15.00

and composition of the formulations were presented in Tables 1–3. Carbamazepine, crospovidone NP and the carrier (Neusilin® UFL2 or Vivapur®) were mixed in a mortar with pestle. After that, Cremophor® RH 40 was added to the formulations which contained it (in the second phase, Table 3). The meltable binder (Gelucire® 44/14 or Labrafil® 2130CS), which was melted at 50 °C, was added to the mixture of carbamazepine, superdisintegrant and the diluent, mixed well and granulated using a 300 μm sieve. Prior to tablet compression, 0.5% of magnesium-stearate was added as a glidant. Tablets were prepared by compression of granules on an excenter tablet press (Ek0 Korsch, Hamburg, Germany). The mass of the tablets was kept constant at 500 mg.

2.3.2. *Characterization of granules*

Flowability, bulk and tapped density were determined for the obtained granules, and Hausner ratio and Carr index were calculated (according to the Ph. Eur. 8.0 procedure), before compression of the tablet mixtures.

Granules flowability was determined by the official method (European Pharmacopoeia, 2014). A 50 g sample of granules was transferred to the flow testing device (Flowmeter GDT, Erweka, Germany), and the time needed for sample flowing through an orifice of 12 mm in diameter was measured. Flowability was expressed as a flow rate which was calculated from the ratio of sample mass and measured time. The results are expressed as the mean value of three replicates.

Bulk density was determined in the graduated 50 mL cylinder. 15 g of the sample was measured and poured into the cylinder. Bulk density was calculated as the ratio of granule's mass and read volume. Tapped density was calculated as the ratio of granules mass and read volume after agitation according to the compendial procedure.

Hausner ratio and Carr index were calculated using the following formulas [14]:

$$\text{Hausner ratio} = \text{tapped density}/\text{bulk density} \quad (1)$$

$$\text{Carr index} = (\text{tapped density} - \text{bulk density})/\text{tapped density} \quad (2)$$

2.3.3. *Resistance to crushing of tablets*

Resistance to crushing of tablets (tablet hardness) was determined on the Erweka TBH 125 (Erweka, Germany) device, which measures the force that leads to the tablet fracture. Results are expressed as the mean value of 10 replicates.

2.3.4. *In vitro drug release studies*

Dissolution profiles were determined using a rotating paddle apparatus (Erweka DT70, Germany). The dissolution conditions were: water as the medium; 37 ± 0.5 °C; 900 mL and 50 rpm. Aliquots of 4 mL were withdrawn from the medium at fixed times (10, 20, 30, 45, 60 and 120 min). The sink conditions were maintained at all times. All samples were filtered through a 0.45 μm MF-Millipore® membrane filter (Millipore Corporation, Bedford, USA). The carbamazepine concentration was determined spectrophotometrically at λ = 287 nm (Evolution 300 spectrophotometer, Thermo Fisher Scientific, UK). The dissolution experiments were performed in triplicate and the data is expressed as a mean value.

2.4. *Characterization of the carbamazepine solid phase*

2.4.1. *Differential scanning calorimetry (DSC)*

DSC analyses were carried out on a computer-interfaced differential scanning calorimeter (DSC Q2000, TA Instruments). DSC was used to determine the polymorphic form of crystalline carbamazepine in samples (pure carbamazepine and the optimal formulation). The samples were accurately weighed (1–2 mg) and heated from 20 to 200 °C at a rate of 10 °C/min, under a nitrogen purge gas flow of 50 mL/min. The presence of an endothermic and/or exothermic peak was used as a marker of the crystalline form of carbamazepine.

2.4.2. *Fourier transform infrared spectroscopy (FT-IR)*

FT-IR spectra in the region of 600–4000 cm^{-1} for both starting materials and solid formulations were obtained using a Shimadzu IR-Prestige-21 FT-IR spectrometer coupled with a horizontal Golden Gate MKII single-reflection ATR system (Specac, 214 Kent, UK) equipped with a Zn Se lens, after appropriate background subtraction. Sixteen scans over the selected wave number range at a resolution of 4 cm^{-1} were averaged for each sample.

2.4.3. *Powder X-ray diffraction (PXRD)*

Powder X–ray diffraction patterns were measured in order to evaluate the crystalline/amorphous character of the prepared samples. Measurements were performed using a Bruker AXS D8 Advance powder diffractometer, equipped with copper cathode ($\lambda = 0.15418$ nm, 40 kV, 40 mA). Patterns were obtained with a step width of 0.02° and a detector in 2θ between 4° and 40° at ambient temperature. Samples, ground into powders with an agate mortar and pestle, were measured on a low background quartz plate in an aluminum holder.

2.4.4. *Raman spectroscopy*

The chosen optimal formulation was being held under controlled environmental conditions for the two months (25 °C, 40% RH). Raman spectra for the optimal formulation were recorded at the first day and after the first and second month.

Raman scattering measurements were performed using JY T64000 Raman system with 1800/1800/1800 grooves/mm gratings in a backscattering micro-Raman configuration. The 514.5 nm line of a mixed Ar^+/Kr^+ gas laser was used as an excitation source. In order to reduce the local heating, laser power density was kept at low levels.

3. Results and discussion

3.1. *The first set of experiments (screening study)*

3.1.1. *Flowability*

Flowability is one of the critical materials attributes that influences the process of tableting and quality of the obtained dosage form. Values for flowability of prepared granules are represented in Table 4 and ranged from 0.42 (F-I-2) to 3.96 (F-I-5) g/s. Granules that showed poor flowability (F-I-2, F-I-3, F-I-4 and F-I-8), were prepared using Neusilin® UFL2 as a carrier, whereas the flowability

Table 4
Flowability, Hausner's ratio and Carr's index values for the granules obtained in the first set of the experiments; Tablet hardness values.

	Flowability (g/s)	Hausner's ratio	Carr'sindex (%)	Hardness (N)
F-I-1	2.50	1.33	25	42.1
F-I-2	0.42	1.47	32	108.3
F-I-3	0.43	1.37	27	117.0
F-I-4	0.46	1.35	26	104.4
F-I-5	3.96	1.21	17	52.7
F-I-6	2.29	1.33	25	17.5
F-I-7	2.77	1.33	25	13.7
F-I-8	0.57	1.50	33	83.4

of granules containing microcrystalline cellulose can be classified as passable (according to the Ph. Eur. 8.0 classification for the Carr index and Hausner ratio). Statistical significance of the selected carrier influence on granules flowability was confirmed through ANOVA analysis ($p = 0.0007$) of the screening experimental design. The influence of carrier is positive, which means that the flowability is better if microcrystalline cellulose (high level of the studied factor) is used instead of Neusilin® UFL2. A possible explanation of these results lays in the fact that the diameter of Neusilin® UFL2 particles is 5 μm, and the specific surface of this very voluminous substance is 300–310 m^2/g, [3]. Strong adhesive and cohesive forces exhibited during the powder flow, combined with the mentioned properties, enable better “packing” of the particles, resulting in the poor flowability of these granules. Poor flowability of granules can be improved by addition of a glidant or by increasing the amount of the molten binder.

3.1.2. Resistance to crushing of tablets

Tablets with Neusilin® UFL2 as the carrier showed greater strength than those which were made with microcrystalline cellulose. This is expected, considering the above mentioned properties of Neusilin® UFL2. Also, particles of this constituent are spherical, porous, and free from rough edges [3], which allows them to consolidate better. Stronger tablets were made using greater compression force, which was also expected. Table 4 shows values that represent the force that leads to tablet fracture. The firmest tablets were made with F-I-3 (117.0 N), and the most fragile tablets were those made with F-I-7 (13.7 N) granules. The influence of the selected carrier on tablets hardness was proven to be statistically significant ($p = 0.0011$) and negative, meaning that the hardness of tablets is greater if Neusilin® UFL2 (low level of the studied factor) is used instead of microcrystalline cellulose.

These encouraging results show that Neusilin® UFL2, a constituent which is not yet fully explored, especially when it comes to compression and compactable features, can be used for tableting [15]. Lipid matrix tablets made with the Neusilin® UFL2, following the melt granulation procedure, have an acceptable hardness, in comparison to tablets containing microcrystalline cellulose which is known for its compressibility and compactibility [16]. Also, due to a large specific surface, Neusilin® UFL2 can absorb a significant amount of melted lipid excipients, resulting in dry a powder form. This is very important for tableting and the possibilities of using lipid matrix tablets [3]. Our preliminary studies revealed that Neusilin® UFL2 could absorb significantly higher amounts of liquid content in comparison to microcrystalline cellulose (results not shown).

3.1.3. In vitro drug release studies

Profiles of drug release rate for formulations F-I-1 to F-I-8 are represented in Fig. 1. None of the formulations had an acceptable percentage of the released drug, which is more than 80% of the released drug in 30 min, according to the USP 38 - NF 33 requirement for immediate release tablets. The formulation with the highest drug release rate was F-I-3 (58.67% of carbamazepine released after 30 min). This is also the formulation in which the powder mixture had poor flowability, and from which the strongest tablets were produced.

Influence of the varied input parameters are shown in Table 5, as the regression coefficients in the coded values, in order to be able to compare the magnitude of different parameters influence. It was determined that the type of the meltable binder (X_1) has the highest influence on the drug realese rate (CQA). This influence is negative, which indicates that a greater release rate is obtained by using Labrafil® 2130CS (lower coded value) instead of Gelucire® 44/14 (higher coded value). This also means that selection of the meltable binder is crucial for the lipid matrix formulation development, making it a CMA.

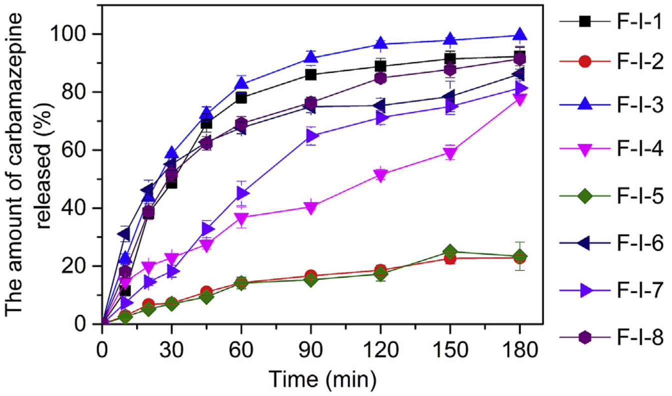

Fig. 1. Dissolution profiles of the formulations prepared in the first set of experiment.

The amount of the meltable binder (X_2) also reported negative influence on the carbamazepine release rate, and is therefore recognized as a CMA. Negative influence means that this parameter should be kept at its lower value (20%) to achieve increased drug release rate. Greater percentage of meltable binder can result in a more hydrophobic system and lead to decreased drug release rate.

The impact of the amount of carbamazepine (X_3) in the formulation is positive, meaning that the increase of carbamazepine amount from 20% to 30% results in greater drug release rate. This finding served the purpose of the experiment, since it shows that formulations with greater percentage of the model substance (30%) can be used in the second phase of the experiment. By increasing the amount of the active substance in the formulation, the drug could be administrated less often during the day, which would cause better compliance of the patient. Also, due to the decrease in the surfactant content in the formulation there is less potential for gastrointestinal irritation.

Crospovidone NP (X_4) leads to the increase in the initial amount of carbamazepine released, which was expected. Crospovidone NP accelerates disintegration of the tablet, which, therefore, allows quicker release of carbamazepine [17].

The impact of the selected carrier (X_5) on carbamazepine release rate was not proven to be statistically significant.

The effect of compression force (X_6) on carbamazepine release rate is negative. Less hard tablets were made using lower compression force, resulting in faster disintegration of tablets and subsequent carbamazepine release. Significant interaction occurred between the two examined parameters, the type of the binder and compression force (X_1 and X_6) (Table 5). It was also noticed that the tablets obtained by using Gelucire® 44/14 as the meltable binder and a higher compression force (8 kN) had very slow and incomplete carbamazepine release.

Parameters that increase the release rate of the drug were determined and used in the second set of experiments:

Table 5
Regression coefficients from the first set of the experiment.

	X_1	X_2	X_3	X_4	X_5	X_6	X_1 X_6
Y_1	−6.02	−3.25	/	+3.80	−0.64	/	−6.02
Y_2	−9.25	−7.13	/	/	/	/	−9.25
Y_3	−12.37	−8.81	+7.95	/	/	/	−12.37
Y_4	−14.26	−10.58	+10.05	/	/	−6.94	−14.26
Y_5	−15.33	−9.87	+10.21	/	/	−9.49	−15.33
Y_6	−19.20	−7.05	+9.10	/	/	−13.75	−19.20

compression force of 8 kN, 20% of Labrafil® 2130CS, 30% of carbamazepine, 5% of crospovidone NP and Neusilin® UFL2 as a diluent. The purpose of the first set of experiments was achieved considering acceptable flowability properties and strength of tablets, and increased amount of the active substance with poor solubility and high drug loading in the formulation.

3.2. *The second set of experiments (optimization study)*

Formulation of tablets with immediate-release of carbamazepine using central composite experimental design was the aim of the second set of experiments, as an extension of the first set. After compaction, tablets were subjected to the dissolution testing.

3.2.1. *In vitro drug release studies*

Fig. 2 shows profiles of carbamazepine release rates from tablets prepared in the second set of experiments. Two out of nine formulations (F-II-1 and F-II-4) demonstrated adequate release rates which was in accordance with USP 38 - NF 33 (more than 80% of drug released in first 30 min).

Multiple regression analysis and ANOVA test was applied for all output responses (amount of carbamazepine released in different time periods, Y_1-Y_6) and quadratic models were obtained. Gained mathematical models, which describe correlation between the input and output parameters, are statistically significant, based on values of p ($p < 0.05$) and, based on relatively high value of coefficient of correlation ($R^2 > 0.922$), can be used to interpret relationships between the parameters. Fig. 3 shows 2D contur diagrams, which describe dependence between input (Cremophor® RH40 and Labrafil® 2130CS amounts) and output parameters (amounts of carbamazepine released after 30 and 120 min). It can be concluded that the greatest (negative) impact on carbamazepine release rate, has the amount of Cremophor® RH40 ($p < 0,0001$; Table 6). Negative value indicates that increase in the amount of Cremophor® RH40 would result in decrease of release rate of carbamazepine, which is unexpected. Even though the addition of Cremophor® RH40 has improved carbamazepine release rate (by comparing formulations that did or did not contain this non-ionic surfactant), results of this study demonstrate that the level of surface active ingredients in the formulations need to be carefully selected. Table 6 shows that the influence of Labrafil® 2130CS amount on the release rate of carbamazepine is statistically significant at the level of 0.1. With the increase of Labrafil® 2130CS amount, release rate of carbamazepine increases. Furthermore, interaction between the influences of Cremophor® RH40 and Labrafil® 2130CS amounts on carbamazepine release rate is negative and statistically significant. Quadratic effects of the studies factors also have significant impact on carbamazepine release rate. In order to achieve immediate release of carbamazepine from tablets, the amount of Labrafil® 2130CS should be close to 20% and the amount of Cremophor® RH40 should be close to 10%. Formulation with greatest release rate of carbamazepine (88.49% of carbamazepine released after 30 min), F-II-4, which has 20% of Labrafil® 2130CS, and 10% of Cremophor® RH40, confirmes mentioned impacts. It is clear that experimental design techniques are reliable and can be used for assesment of formulation factors influences on selected drug release rate. Formulation F-II-4 has been chosen as optimal for further characterization and monitoring of stability, since it was determined that after 30 min percentage of released carbamazepine was 88%, which was in accordance with USP 38 - NF 33 for preparations with immediate release.

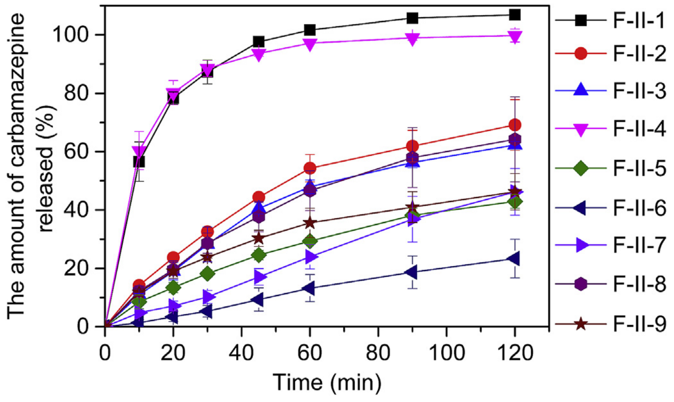

Fig. 2. Dissolution profiles of the formulations prepared in the second set of experiment.

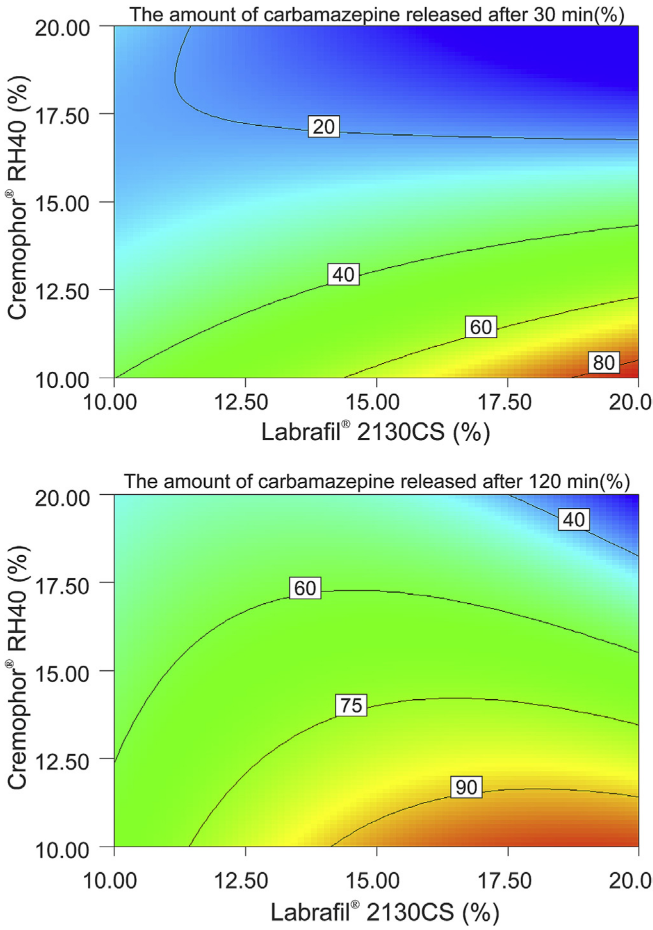

Fig. 3. 2D contour diagrams that describe the influence of input parameters on carbamazepine release rate after: a) 30 min; b) 120 min.

3.3. *Characterization of the solid phase*

3.3.1. *Differential scanning calorimetry (DSC)*

Based on the characteristic peaks which are present in DSC curves of pure carbamazepine (Fig. 4), it can be concluded that carbamazepine was in the polymorphous form III [18,19].

The DSC curves of the tested sample of optimal formulation showed an endothermic peak at 52.36 °C which derives from melting of Labrafil® 2130CS [20]. Endothermic peak at 161.26 °C indicates a melting process of polymorph form III of carbamazepine. Exothermic peak at 187.36 °C represents recrystallization of

Table 6
Regression coefficients that connect varied input parameters in the second set of experiments (A- Labrafil® 2130CS; B-Cremophor® RH 40) with response (Y_1–Y_6 – amount of released carbamazepine after 10, 20, 30, 45, 60 and 120 min).

	Y_1		Y_2		Y_3		Y_4		Y_5		Y_6	
		F-value p- value		F- value p- value		F- value p- value		F- value p- value		F- value p- value		F- value p- value
Regression intercept/ Model significance	+14.18	16.48 0.0009	+23.69	18.04 0.0007	+32.53	24.87 0.0003	+44.37	39.15 <0.0001	+54.33	59.57 <0.0001	+69.15	101.15 <0.0001
A	+4.86	4.09 0.0830	+5.72	3.61 0.0991	+5.55	4.08 0.0830	+4.62	4.19 0.0799	+4.81	7.04 0.0328	+4.35	12.36 0.0098
B	−17.07	50.48 0.0002	−23.19	59.45 0.0001	−25.67	87.49 <0.0001	−27.24	145.42 <0.0001	−27.04	222.62 <0.0001	−23.04	365.26 <0.0001
AB	−13.65	16.12 0.0051	−17.16	16.28 0.0050	−17.51	20.34 0.0028	−16.17	25.63 0.0015	−15.36	35.91 0.0005	−13.56	65.76 <0.0001
A^2	/	/	/	/	/	/	−8.32	11.80 0.0109	−9.98	26.41 0.0013	−10.82	51.29 0.0002
B^2	+8.40	9.97 0.0160	+9.26	8.24 0.0240	+7.88	7.18 0.0316	+6.01	6.16 0.0421	/	/	+1.82	5.62 0.0496
R^2	0.9220		0.9280		0.9467		0.9655		0.9770		0.9863	

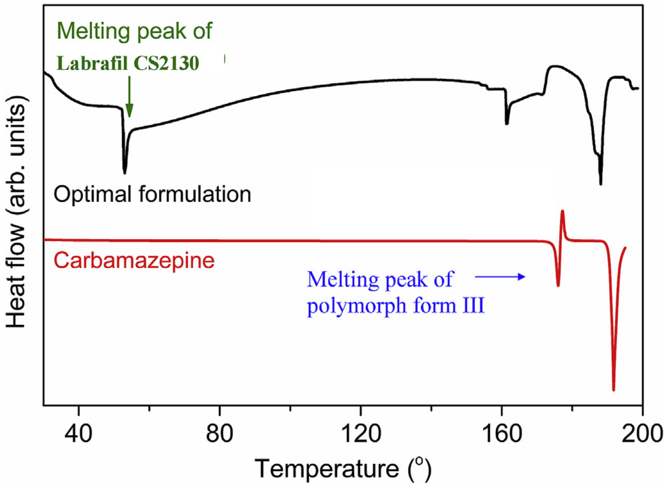

Fig. 4. DSC curve of carbamazepine and optimal formulation of immediate-release carbamazepine tablets.

polymorph form III into polymorph form I. Melting of polymorph form I is indicated by the peak that occurs at 187.91 °C. Characteristic melting peaks from polymorphous form III in the temperature range of 150–175.8 °C were noticed in DSC curves of tested sample of optimal formulation [18,19]. These results correspond to those previously stated for the polymorph form III of pure carbamazepine which indicates that carbamazepine in optimal formulation retained polymorph form III.

3.3.2. Fourier transform infrared spectroscopy (FT-IR)

The FT-IR spectra of carbamazepine and the optimal formulation are given in (Fig. 5). Characteristic peaks (3462 cm^{-1}, 1674 cm^{-1}, 1593 cm^{-1} and 1605 cm^{-1}) of both carbamazepine and optimal formulation spectra correspond to those previously reported for the polymorph form III [4,10]. Low-intensity peaks in FT-IR spectra of optimal formulation are explained by the fact that the optimal formulation had smaller quantity of carbamazepine compared to the pure carbamazepine. These peaks were apparent in FT-IR spectra of the optimal formulation and carbamazepine, which implies that significant interactions between carbamazepine and all of the excipients, and transition of the carbamazepine into the amorphous form, did not occur.

3.3.3. Powder X-ray diffraction (PXRD)

PXRD diffractogram of pure carbamazepine and the optimal formulation are illustrated in Fig. 6. The PXRD diffractogram of pure carbamazepine and optimal formulation exhibit characteristic high-intensity diffraction peaks at 13.02°, 15.22°, 15.78°, 19.40°, 24.92°, 27.50° and 31.86 2θ, which is in accordance with diffractograms previously reported for crystal form III [18,19]. This confirms that carbamazepine did not transform into the amorphous form

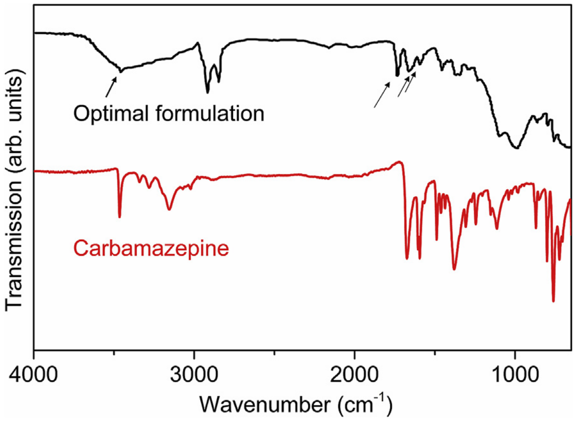

Fig. 5. FT-IR specter of pure carbamazepine and optimal formulation of immediate-release carbamazepine tablets.

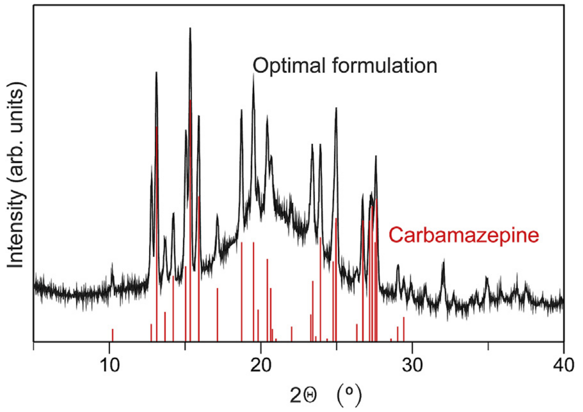

Fig. 6. The PXRD diffractogram of pure carbamazepine and optimal formulation of immediate-release carbamazepine tablets.

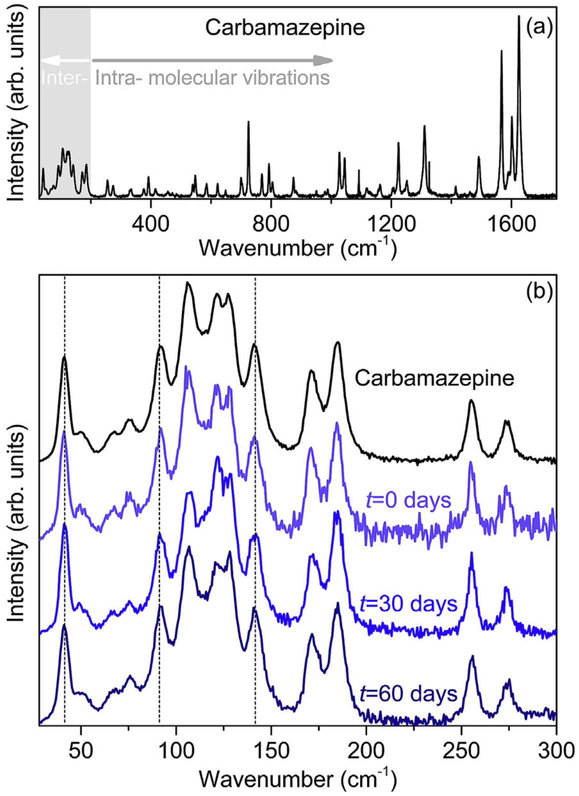

Fig. 7. (a) Raman scattering spectra of carbamazepine (b) Low-energy Raman spectra of carbamazepine and optimal formulation after $t = 0$, 30 and 60 days.

and it kept polymorph form III. These peaks have a somewhat lower intensity in comparison to pure carbamazepine samples, because the ratio of carbamazepine in the mixture is 30%. All diffractograms of the samples have a characteristic shape of amorphous form, as a consequence of a high adsorbens ratio. This is in accordance with results obtained by other analysis (DSC and FT-IR) that were conducted.

3.3.4. *Raman spectroscopy*

Fig. 7 (a) shows Raman scattering spectra of carbamazepine. In molecular crystal, in general, one can distinguish two separate regions of the Raman scattering spectra. The high energy (conventional) region, comprising of intramolecular vibrations, and low energy region (below 200 cm^{-1}) dominated by the intermolecular vibrations (Fig. 7 (a)) [21]. Although the high energy region also bears the information regarding the crystal structure, observable changes between different polymorphs are usually rather small and restricted to change in Raman modes relative intensities. Investigation of the low energy region offers more direct approach because the intermolecular vibrations distribution directly corresponds to the crystal structure of the material. The low-energy Raman spectra of carbamazepine and optimal formulation after $t = 0$, 30 and 60 days are shown at Fig. 7 (b). All the form III characteristic Raman modes with the emphasis on peaks at about 40, 91 and 141 cm^{-1} which are absent for other carbamazepine polymorphs, can be observed in the carbamazepine spectrum [22]. These modes are also present in the optimal formulation samples, thereby confirming the preservation of the polymorphic form after 30 and 60 days.

4. Conclusion

The first set of experiments demonstrated that the type of meltable binder (defined as CMA) has the most significant influence on the drug release rate (CQA). Through application of the QbD approach, critical process parameters and critical quality attributes were determined, and their influence on CQA was analyzed by fractional and central composite design of experiments. Optimal formulation of lipid matrix tablets (prepared using compression force of 8 kN, 20% of Labrafil® 2130CS, 10% of Cremophor® RH 40, 30% of carbamazepine, 5% of crospovidone NP and Neusilin® UFL2 as the carrier) demonstrated an immediate release of carbamazepine with more than 80% of the drug being released in the first 30 min of the dissolution testing. Different analytical techniques (DSC, PXRD, FT-IR) were used for assessment and confirmation of the presence of carbamazepine polymorph form III. Raman spectroscopy was applied in order to assess the stability of the optimal sample, demonstrating that it maintained carbamazepine form III after the 2 months stability study.

This work demonstrated advantages of lipid matrices as drug carriers, especially for drug with poor solubility such as carbamazepine. Also, tablets prepared with Neusilin® UFL2 demonstrated an enhancement of mechanical properties in terms of greater resistance to crushing, which is encouraging considering that this constituent is not yet fully explored, especially when it comes to compression and compaction features. Making granules by melt granulation technique improves drug stability, while it does not affect immediate-release properties of formulation. Further study should be performed in order to evaluate permeability (*in vitro*) and bioavailability (*in vivo*) of carbamazepine when incorporated in lipid matrix tablets.

Acknowledgements

This work was done under the project No. TR 34007 supported by the Ministry of Education, Science and Technological Development, Republic of Serbia.

References

[1] L.X. Yu, G.L. Amidon, J.E. Polli, H. Zhao, M.U. Mehta, D.P. Conner, V.P. Shah, L.J. Lesko, M.L. Chen, V.H. Lee, A.S. Hussain, Biopharmaceutics classification system: the scientific basic for biowaiver extensions, Pharm. Res. 19 (2002) 921–925.
[2] C.W. Pouton, Formulation of poorly water-soluble drugs for oral administration: physicochemical and physiological issues and the lipid formulation classification system, Eur. J. Pharm. Sci. 29 (2006) 278–287.
[3] V. Agarwal, A. Siddiqui, H. Ali, S. Nazzal, Dissolution and powder flow characterization of solid self-emulsified drug delivery system (SEDDS), Int. J. Pharm. 366 (2009) 44–52.
[4] M. Krstic, S. Razic, D. Vasiljevic, Dj. Spasojevic, S. Ibric, Application of experimental design in examination of the dissolution rate of carbamazepine from formulations. Characterization of the optimal formulation by DSC, TGA, FT-IR and PXRD analysis, J. Serb. Chem. Soc. 80 (2) (2015) 209–222.
[5] M. Krstic, S. Razic, L. Djekic, V. Dobricic, M. Momcilovic, D. Vasiljevic, S. Ibric, Application of a mixture experimental design in the optimization of the formulation of solid self-emulsifying drug delivery systems containing carbamazepine, Lat. Am. J. Pharm. 34 (5) (2015) 885–894.
[6] D.R. Lee, Y.H. Kim, K.W. Park, M.J. Ho, H.J. Jung, H.R. Cho, J.S. Park, Y.S. Choi, D.W. Yeom, Y.W. Choi, M.J. Kang, Fujicalin®-based solid supersaturable self-emulsifying drug delivery system (S-SEDDS) of tacrolimus for enhanced dissolution rate and oral absorption, J. Pharm. Investig. 45 (7) (2015) 651–658.
[7] R.B. Chavan, S.R. Modi, A.K. Bansal, Role of solid carriers in pharmaceutical performance of solid supersaturable SEDDS of celecoxib, Int. J. Pharm. 495 (1) (2015) 374–384.
[8] C.J.H. Porter, C.W. Pouton, J.F. Cuine, W.N. Charman, Enhancing intestinal drug solubilisation using lipid-based delivery systems, Adv. Drug Deliv. Rev. 60 (6) (2008) 673–691.
[9] S. Shanmugam, Granulation techniques and technologies: recent progresses, Bioimpacts 5 (1) (2015) 55–63.
[10] M. Krstić, M. Popović, V. Dobričić, S. Ibrić, Influence of solid drug delivery

system formulation on poorly water-soluble drug dissolution and permeability, Molecules 20 (2015) 14684–14698.

[11] N.R. Jadhav, P.V. Irny, U.S. Patil, Solid state behavior of progesterone and its release from Neusilin US2 based liquisolid compacts, J. Drug Deliv. Sci. Tech. 38 (2017) 97–106.

[12] B. Tang, G. Cheng, J.C. Gu, C.H. Xu, Development of solid self-emulsifying drug delivery systems: preparation techniques and dosage forms, Drug Discov. Today 13 (13) (2008) 606–612.

[13] L.X. Yu, Pharmaceutical quality by design: product and process development, understanding, and control, Pharm. Res. 25 (4) (2008) 781–791.

[14] Council of Europe, European Pharmacopoeia, eighth ed., Council of Europe, Strasbourg, France, 2014.

[15] S.G. Gumaste, D.M. Dalrymple, A.T. Serajuddin, Development of solid SEDDS, V: compaction and drug release properties of tablets prepared by adsorbing lipid-based formulations onto Neusilin® US2, Pharm. Res. 30 (12) (2013) 3186–3199.

[16] G. Shlieout, K. Arnold, G. Müller, Powder and mechanical properties of microcrystalline cellulose with different Degrees of Polymerization, AAPS Pharm. Sci. Tech. 3 (2) (2002) 45–54.

[17] S.K. Battu, M.A. Repka, S. Majumdar, Y.M. Rao, Formulation and evaluation of rapidly disintegrating fenoverine tablets: effect of superdisintegrants, Drug Dev. Ind. Pharm. 33 (2007) 1225–1232.

[18] A.L. Grzesiak, M. Lang, K. Kim, A.J. Matzeger, Comparison of the four anhydrous polymorphs of carbamazepine and the crystal structure of form, Int. J. Pharm. Sci. 92 (2003) 2260–2271.

[19] L. Yu, S.M. Reutzel-Edens, C.A. Mitchell, Crystallization and polymorphism of conformationally flexible molecules: problems, patterns, and strategies, Org. Process Res. Dev. 4 (2000) 396–402.

[20] J. Akbari, R. Enayatifard, M. Saeedi, K. Morteza-Semnani, S. Rajabi, Preparation, characterization, and dissolution studies of naproxen solid dispersions using polyethylene glycol 6000 and labrafil M2130, Pharm. Biomed. Res. 1 (2) (2015) 44–53.

[21] J. Lazarević, S. Uskoković-Marković, M. Jelikić-Stankov, M. Radonjić, D. Tanasković, N. Lazarević, Z.V. Popović, Intermolecular and low-frequency intramolecular Raman scattering study of racemic ibuprofen, Spectrochim. Acta A 126 (2014) 301–305.

[22] R. Saikat, B. Chamberlin, A.J. Matzger, Polymorph discrimination using low wavenumber raman spectroscopy, Org. Process Res. Dev. 17 (7) (2013) 976–980.

Čvrste disperzije sa karbamazepinom: optimizacija formulacija, karakterizacija i ispitivanje dugoročne stabilnosti

Marko Krstić[1], **Igor Lukić**[2], **Alma Bušatlić**[3], **Nenad Lazarević**[4], **Dragana Vasiljević**[1]

[1]*Farmaceutski fakultet, Katedra za farmaceutsku tehnologiju i kozmetologiju, Univerzitet u Beogradu,*
Vojvode Stepe 450, 11221 Beograd, Srbija
[2]*ASV Beograd d.o.o., Kumodraška 380, 11221 Beograd, Srbija*
[3]*Adoc d. o. o., Milorada Jovanovića 11, 11030 Beograd, Srbija*
[4]*Centar za fiziku čvrstog stanje i nove materijale, Institut za fiziku, Univerzitet u Beogradu, Pregrevica 118,*
11080 Beograd, Srbija

Izvod

U ovom radu je izvršena optimizacija formulacija čvrstih disperzija sa karbamazepinom, primenom metode D-optimalnog eksperimentalnog dizajna smeše, u cilju povećanja brzine rastvaranja navedene teško rastvorljive aktivne supstance. Primenom metode eksperimentalnog dizajna smeše, formulisane su čvrste disperzije variranjem udela karbamazepina (30-50 %), *Gelucire*® *44/14* (20-40 %) i polimera *Soluplus*® (30-50 %) (ulazni parametri). Izrađeno je 16 formulacija, iz kojih je ispitana *in vitro* brzina rastvaranja karbamazepina. Kao izlazni parametri praćeni su procenti rastvorenog karbamazepina, nakon 10, 20, 30, 45 i 60 minuta. Najveći udeo oslobođenog karbamazepina iz čvrstih disperzija (preko 80 % za 30 minuta) se postiže pri udelima aktivne supstance od oko 40 %, *Soluplus*® oko 45 % i *Gelucire*® 44/14 oko 25%. Nakon obrade podataka i optimizacije, iz različitih delova optimizacione oblasti odabrane su 3 formulacije za dalja ispitivanja. Rezultati ispitivanja odabranih optimizovanih uzoraka čvrstih disperzija nakon izrade, kao i nakon skladištenja 24 meseca pod ambijentalnim uslovima (25 °C, 40 % RH), dobijeni primenom metoda diferencijalne skenirajuće kalorimetrije (DSC), infracrvene spektroskopije sa Furijeovom transformacijom (FT-IR) i Ramanske spektoskopije potvrdili su njihovu stabilnost i očuvanje karbamazepina u polimrfnom obliku III, jedinom farmakološki aktivnom obliku. Primenom PAMPA (*eng.* Parallel Artificial-Membrane Permeability Assay) testa pokazano je da je u dve, od tri ispitivane optimizovane čvrste disperzije očuvana, odnosno blago povećana permeabilnost karbamazepina.

Ključne reči: *čvrste disperzije, karbamazepin, optimizacija formulacija, eksperimentalni dizajn, in vitro oslobađanje, fizička stabilnost.*

NAUČNI RAD

UDC 615.015.14:004.896(043.3)

Hem. Ind. **72 (4)** 191–204 (2018)

1. UVOD

Čvrste disperzije se definišu kao disperzije jedne ili više lekovitih supstanci u inertnom nosaču (matriksu), u čvrstom stanju, dobijene metodom topljenja, metodom rastvaranja ili kombinacijom ove dve metode. Lekovite supstance u čvrstim disperzijama mogu biti dispergovane kao odvojene molekule, amorfne ili kristalne čestice, dok nosač može biti u kristalnom ili amorfnom stanju. Glavni razlog izrade čvrstih disperzija je povećanje rastvorljivosti/brzine rastvaranja teško rastvorljivih lekovitih supstanci, a sledstveno tome i njihova biološka raspoloživost [1]. Mehanizmi, kojima se to postiže su: rastvaranje lekovite supstance u inertnom matriksu, smanjenje veličine čestica i smanjenje aglomeracije, poboljšano kvašenje i solubilizacija lekovite supstance molekulima nosača, povećana poroznost sistema, kao i prelazak lekovite supstance iz kristalnog u amorfni oblik [2 - 4].

Uprkos brojnim prednostima čvrstih disperzija sa teško rastvorljivim lekovitim supstancama, broj komercijalnih preparata tipa čvrstih disperzija na tržištu je mali, zbog problema koji se mogu javiti tokom procesa izrade/proizvodnje i skladištenja. Ovi problemi uključuju termičku nestabilnost lekovitih supstanci i nosača pri izradi čvrstih disperzija

---

Korespodencija: Marko Krstić, Farmaceutski fakultet, Katedra za farmaceutsku tehnologiju i kozmetologiju, Univerzitet u Beogradu,
Vojvode Stepe 450, 11221 Beograd, Srbija
E-mail: mkrstic109@gmail.com; telefon : +381 11 3951-356

Rad primljen: 25. oktobra 2017.
Rad prihvaćen: 25. juna 2018.
https://doi.org/10.2298/HEMIND171025013K

metodom topljenja, ostatke rastvarača, primenom metode rastvaranja, rekristalizaciju lekovitih supstanci pri očvršćavanju, taloženje lekovite supstance posle rastvaranja u vodi zbog prezasićenja [2]. Takođe, može doći do razdvajanja lekovite supstance od matriksa, što ima za posledicu njenu neravnomernu raspodelu u čvrstoj disperziji, što se može odraziti na nepravilno doziranje lekovite supstance. Takođe, u toku procesa usitnjavanja izrađene čvrste disperzije može doći do prelaska amorfnog oblika lekovite supstance u kristalni. Veliki broj tehnoloških operacija u farmaceutskoj industriji, koji se sprovodi u toku proizvodnje čvrstih disperzija je takođe ograničavajući faktor za njihovu širu proizvodnju i primenu [5].

Razvoj formulacije predstavlja složen proces i često se između sastava formulacija i njenih karakterisitka ne može uspostaviti jasna, a gotovo nikada linearna korelacija. Iz tog razloga, sve češće se u razvoju formulacija koriste tehnike eksperimentalnog dizajna, kako bi se uz što manji broj eksperimenata došlo do optimalne formulacije. Dizajn smeše predstavlja vrstu eksperimentalnog dizajna, koji se koristi kada se optimizuju formulacije koje imaju više različitih sastojaka, čiji je zbir udela stalan. Jedna od često korišćenih metoda eksperimentalnog dizajna smeše je D-optimalni dizajn, koji omogućava da se na osnovu najmanjeg broja eksperimenata sa velikom pouzdanošću dođe do formulacije željenih karakteristika. Poslednjih godina je uspešno korišćen u razvoju tečnih i čvrstih samo-emulgujućih sistema, kao i čvrstih disperzija [6 - 8].

Tokom izrade formulacija u kojima se povećava rastvorljivost teško rastvorljive lekovite supstance, njena permeabilnost se može smanjiti, povećati ili ostati nepromenjena [9]. Sa ciljem da se proceni uticaj različitih faktora na resorpciju lekovite supstance, kao i da se smanji broj ispitivanja na ljudima i životinjama, stalno se razvijaju i unapređuju *in vitro* metode za procenu resorpcije lekovite supstance [10,11]. PAMPA (*eng*. Parallel Artificial-Membrane Permeability Assay) test je brz, jeftin i jednostavan metod, kojim se može ispitati permeabilnost lekovitih supstanci pasivnom difuzijom. Simulacija bioloških membrana postiže se odgovarajućim odabirom rastvarača i supstanci od kojih se formira veštačka membrana. Dugi niz godina se PAMPA test koristio u proceni permeabilnosti novosintetisanih lekovitih susptanci, a tek poslednjih godina se koristi za ispitivanje permeabilnosti lekovite supstance iz različitih farmaceutskih oblika i savremenih nosača [8,9,12,13].

Cilj rada bio je razvoj i optimizacija formulacija čvrstih disperzija sa karbamazepinom, primenom metode D-optimalnog eksperimentalnog dizajna, radi povećanja brzine rastvaranja navedene lekovite supstance. Takođe, cilj rada je bio i karakterizacija i ispitivanje dugoročne stabilnosti optimizovanih formulacija čvrstih disperzija, nakon skladištenja uzoraka 24 meseca pod ambijentalnim uslovima.

2. MATERIJALI I METODE

2. 1. Materijal

U eksperimentalnom radu korišćen je karbamazepin (Ph. Eur. 8.0), kao model lekovita supstanca. Lauroil makrogol-32 gliceridi (*Gelucire® 44/14*; Gattefosse, Francuska) i makrogol 6000-poli(vinilkaprolaktam)-poli(vinilacetat) kalemljeni (*eng*. graft) polimer (*Soluplus®*; BASF ChemTrade GmbH, Nemačka) su korišćeni kao ekscipijensi za izradu čvrstih disperzija. Za rastvaranje polimera za izradu čvrstih disperzija korišćen je etanol (99,5 % *V/V*).

Dodekan (Sigma-Aldrich Chemie GmbH, Nemačka) i lecitin jajeta (Lipoid GmbH, Nemačka) korišćeni su u PAMPA testu. Svi drugi reagensi, koji su korišćeni za HPLC analizu, bili su analitičke čistoće.

2. 2. Metode

2. 2. 1. Formulacija čvrstih disperzija

Primenom optimizacione tehnike, uz pomoć kompjuterskog programa *Design Expert®* (version 8.0.7.1, Stat-Ease, SAD), definisan je D-optimalni eksperimentalni dizajn smeše, koju čine tri komponente, sastojci čvrstih disperzija: A –karbamazepin (koncentracija 30 – 50 %), B –*Gelucire® 44/14* (koncentracija 20-40 %) i C –*Soluplus®* (koncentracija 30-50 %). Ove tri komponente predstavljaju ulazne parametre i njihov ukupan udeo je 100 %. Granične vrednosti udela komponenti postavljene su na osnovu literaturnih podataka i prethodnih ispitivanja. Kao izlazni parametri (odgovori sistema) praćeni su procenti rastvorenog karbamazepina nakon 10, 20, 30, 45 i 60 minuta, označeni sa R_1 - R_5.

Primenom D-optimalnog eksperimentalnog dizajna dobijen je eksperimentalni plan (Tabela 1.), koji se sastojao od 16 formulacija čvrstih disperzija, od kojih su 11 različitih i 5 ponovljenih, radi smanjenja eksperimentalne greške.

2. 2. 2. Izrada čvrstih disperzija

Čvrste disperzije su izrađene kombinacijom metoda topljenja i rastvaranja. *Gelucire® 44/14* se otopi na temperaturi od 50 °C i dodaje, uz stalno mešanje, u patenu sa karbamazepinom. U disperziju karbamazepina i *Gelucire® 44/14* dodaje se etanolni rastvor *Soluplus®*, uz neprekidno mešanje. Dobijena smeša se ostavi 72 h na sobnoj temperaturi, da etanol ispari. Izrađene čvrste disperzije su usitnjavane i prosejavane kroz sito 600 (Ph. Eur. 9.0).

Tabela 1. Eksperimentalni plan
Table 1. Experimental plan

Redni broj formulacije	Ulazni parametri		
	A - Sadržaj karbamazepina, %	B - Sadržaj *Gelucire® 44/14*, %	C - Sadržaj *Soluplus®*, %
F1	34,22	33,59	32,19
F2	33,54	23,93	42,53
F3	50,00	20,00	30,00
F4	30,00	20,01	49,99
F5	41,07	20,00	38,93
F6	30,00	31,48	38,52
F7	43,84	23,32	32,84
F8	30,00	36,08	33,92
F9	40,59	29,41	30,00
F10	36,44	27,30	36,26
F11	30,01	39,99	30,00
F12	50,00	20,00	30,00
F13	41,07	20,00	38,93
F14	30,01	39,99	30,00
F15	40,59	29,41	30,00
F16	30,00	20,01	49,99

2. 2. 3. *In vitro* procena brzine rastvaranja karbamazepina iz čvrstih disperzija

Ispitivanje brzine rastvaranja karbamazepina iz čvrstih disperzija (prašak, veličine čestica ≤ 600 µm) i komercijalnih tableta sa trenutnim oslobađanjem (ravne površine, prečnika 10 mm), kao i čiste lekovite supstance, izvedeno je u aparaturi sa rotirajućom lopaticom (Erweka DT70, Nemačka). Prilikom ispitivanja, masa čvrstih disperzija je sadržala 200 mg karbamazepina, kao i komercijalne tablete. Kao akceptorski medijum je korišćena prečišćena voda (900 ml), zagrejana na 37 °C, a brzina obrtanja rotirajuće lopatice bila je 50 obrtaja/min. Po 4 ml uzorka je uzimano nakon 10, 20, 30, 45 i 60 minuta, uz nadoknađivanje medijuma. U uzorcima je, nakon filtriranja, spektrofotometrijski (spektrofotometar Evolution 300, Termo Fisher Scientific, Engleska) određena količina rastvorenog karbamazepina na 287 nm. Kalibraciona kriva za određivanje karbamazepina data je u prilogu, na slici S1, pri čemu je postignuta visoka vrednost koeficijenta korelacije $r^2 = 0,999$, kao i visoka preciznost metode, pri merenju apsorbancije za svaki standardni rastvor 10 puta RSD nije prelazila 0,61%. Dobijeni rezultati predstavljaju srednju vrednost merenja procenta oslobođenog karbamazepina iz tri uzorka, ± SD.

2. 2. 4. Modelovanje uticaja ulaznih na izlazne parametre primenom metode dizajna smeše

D-optimalnim eksperimentalnim dizajnom smeše moguće je dobiti odgovarajući regresioni model, koji, u ovom slučaju, opisuje uticaj udela komponenata čvrstih disperzija, kao nezavisno promenljivih, na procenat rastvorenog karbamazepina nakon 10, 20, 30, 45 i 60 minuta, kao zavisno promenljivih. Modeli, koje je najčešće moguće dobiti pri ovakvim ispitivanjima su:

specijalni kubni: $Y= b_1A + b_2B + b_3C + b_{12}AB + b_{13}AC + b_{23}BC + b_{123}ABC$ (1)

kubni: $Y= b_1A + b_2B + b_3C + b_{12}AB + b_{13}AC + b_{23}BC + b_{123}ABC + \gamma_{12}AB(A - B) + \gamma_{13}AC(A - C) + \gamma_{23}BC(B - C)$, (2)

gde su b_1-b_{123} i γ_{12}-γ_{23} koeficijenti, koji pokazuju uticaj nezavisno promenljivih, kao i njihovih međusobnih interakcija na vrednost zavisno promenljive. Vrednosti koeficijenata izračunavane su regresionom analizom, korišćenjem programa *Design Expert®*.

Regresioni model, tj. finalna jednačina, razmatra L-Pseudo vrednosti ulaznih parametara (A, B, C), koje se kreću od 0 do 1. Vrednost 0 se dodeljuje donjoj granici, a vrednost 1 gornjoj granici ulaznih parametara, dok se sve ostale vrednosti izračunavaju iz sledećih jednačina:

Karbamazepin: $A_{1(\text{L-Pseudo})}=(A_1 - 30)/20$ (3)

Gelucire® 44/14: $B_{1(\text{L-Pseudo})}=(B_1 - 20)/20$ (4)

Soluplus®: $C_{1(\text{L-Pseudo})}=(C_1 - 30)/20$ (5)

gde su A_1, B_1 i C_1 bilo koje vrednosti koncentracija karbamazepina, *Gelucire® 44/14* i *Soluplus®*, u okviru postavljenih granica.

Regresioni model, koji najbolje opisuje vezu između ulaznih i izlaznih parametara bira se na osnovu poređenja nekoliko statističkih parametara, uključujući standardnu devijaciju (SD), koeficijent višestruke korelacije (R^2), prilagođen koeficijent višestruke korelacije (prilagođeni R^2) i predvidiv ostatak zbira kvadrata (PRESS). PRESS pokazuje koliko se podaci dobro uklapaju u model i za izabrani model njegova vrednost treba da bude manja, u poređenju sa drugim modelima. Za razliku od vrednosti PRESS, vrednosti za R^2 i prilagođeni R^2 treba da budu veće u odnosu na druge modele, dok vrednost standardne devijacije treba da bude manja. Kompromisom između postavljenih zahteva vrši se odabir najpogodnijeg regresionog modela.

2. 2. 5. Optimizacija formulacija čvrstih disperzija

Nakon dobijanja regresionih modela, izvršena je optimizacija formulacija čvrstih disperzija sa sledećim zahtevima za procenat oslobođenog karbamazepina: $60\,\% < R_1 < 75\,\%$, $75\,\% < R_2 < 85\,\%$, $85\,\% < R_3 < 95\,\%$, $90\,\% < R_4 < 95\,\%$, $90\,\% < R_5 < 100\,\%$. Iz različitih delova optimizacione oblasti odabrane su 3 formulacije čvrstih disperzija, koje su izrađene i iz kojih je ispitana *in vitro* brzina oslobađanja karbamazepina, na prethodno opisan način. Radi procene uspešnosti predviđanja, predviđeni i eksperimentalno dobijeni profili brzine oslobađanja su upoređeni računanjem faktora sličnosti (f_1) i faktora razlike (f_2) [14].

2. 2. 6. Ispitivanja optimizovanih formulacija čvrstih disperzija

Iz tri optimizovane formulacije čvrstih disperzija izvršeno je *in vitro* ispitivanje brzine rastvaranja karbamazepina, kao i ispitivanje permeabilnosti karbamazepina, primenom PAMPA testa. Diferencijalna skenirajuća kalorimetrija (DSC), infracrvena spektroskopija sa Furijevom transformacijom (FT-IR) i Ramanska spektroskopija su sprovedene nakon izrade, kao i nakon 24 meseca čuvanja uzoraka pod ambijentalnim uslovima (25 °C, 40 % RH), u cilju procene dugoročne stabilnosti čvrstih disperzija.

2. 2. 7. Procena permeabilnosti karbamazepina

Procena permeabilnosti karbamazepina iz odabranih formulacija i čistog karbamazepina izvršena je korišćenjem PAMPA testa.

Prilikom izvođenja PAMPA testa, kao nosač veštačke membrane i akceptorski panel korišćen je filtracioni panel sa 96 bazena, izrađen od hidrofilnog poliviniliden difluorida (PVDF) (Millipore, SAD). U bazene akceptorske ploče naneto je po 5 µl rastvora lecitina jajeta u dodekanu (1 %, m/V) i ostavljeno 2 h na sobnoj temperaturi, da rastvarač potpuno ispari. Na ovaj način je dno akceptorske ploče impregnirano lecitinom i formirana je veštačka membrana, koja u kontaktu sa rastvorom pufera formira multilamelarni lipidni dvosloj između pora filtera. Akceptorska ploča je postavljena na donorsku, u čije je bazene prethodno naneto po 300 µl suspenzije čistog karbamazepina i odabranih formulacija u fosfatnom puferu pH 5,5. Istovremeno je u bazene akceptorske ploče naneto po 300 µl fosfatnog pufera pH 5,5. Akceptorska ploča je prekrivena folijom, kako bi se sprečilo isparavanje rastvarača. Ispitivanje za svaki uzorak je vršeno u triplikatu, a rezultat je predstavljen kao srednja vrednost ±SD. Nakon inkubacije od 2 h na sobnoj temperaturi, koncentracija karbamazepina u bazenima akceptorske ploče određivana je prethodno razvijenom i validiranom HPLC metodom [8,13].

Koeficijenti permeabilnosti (P_{app}) izračunati su primenom sledećih jednačina [15]:

$$T/\% = 100\frac{A_{\mathrm{R}}V_{\mathrm{R}}}{A_{\mathrm{D0}}V_{\mathrm{D}}} \tag{6}$$

$$P_{\mathrm{app}} = \frac{V_D V_R}{\left(V_{\mathrm{D}}+V_{\mathrm{R}}\right)St}\ln\frac{100V_{\mathrm{D}}}{100V_{\mathrm{D}} - T\left(V_{\mathrm{D}}+V_{\mathrm{R}}\right)} \tag{7}$$

gde su:

V_{D} i V_{R} – zapremine donorskog i akceptorskog rastvora (ml);
A_{D0} i A_{R} – HPLC površine pikova pripremljenog rastvora ispitivanog uzorka i akceptorskog rastvora;
S – površina membrane između komora (0,28 cm^2);
t – vreme inkubacije (s).

2. 2. 8. Diferencijalna skenirajuća kalorimetrija (DSC)

DSC merenja izvršena su na Mettler–Toledo AG termalnom analizatoru (Mettler–Toledo AG, Analytical, Švajcarska). Precizno odmerena masa uzorka (2–5 mg) stavljana je u T-Zero® aluminijumske posude, koje su potom hermetički zatvarane, a merenja vršena na temperaturama od 20 do 200 °C, pri brzini zagrevanja od 10 °C/min, u struji azota, sa protokom od 100 ml/min.

2. 2. 9. Infracrvena spektroskopija sa Furijevom transformacijom (FT-IR)

FT-IR spektri u regionu od 600–4000 cm^{-1}, čistog karbamazepina i tri optimizovane formulacije, dobijeni su korišćenjem Shimadzu IR-Prestige-21 FT-IR spektrometra spojenog sa horizontalnim Golden Gate MKII jednoreflektnim ATR sistemom (Specac, 214 Kent, Velika Britanija) i opremljenog sa Zn-Se sočivom. Nakon odgovarajuće pripreme uzorka urađeno je šesnaest snimanja za svaki uzorak.

2. 2. 10. Ramanska spektroskopija

Merenje Ramanskih spektra je izvedeno korišćenjem JY T64000 Ramanskog spektrometra (Horiba Scientific, Nemačka) sa 1800/1800/1800 zareza/mm kombinacijom rešetki i Symphony detektorom hlađenim tečnim azotom. Sistem je postavljen u mikro-konfiguraciju sa objektivom x100. Ulazni slit je postavljen na 100 μm. Za ekscitaciju je korišćen čvrstotelni laser, talasne dužine 532 nm.

3. REZULTATI I DISKUSIJA

3. 1. *In vitro* procena brzine rastvaranja karbamazepina iz čvrstih disperzija

Rezultati *in vitro* brzine rastvaranja karbamazepina iz 16 izrađenih čvrstih disperzija, komercijalnih tabelta i čiste supstance, prikazani su u tabeli 2 (i na slici S2., Prilog rada).

Tabela 2. Procenti rastvorenog karbamazepina iz čvrstih disperzija, komercijalnih tabelta i čiste lekovite supstance, u funkciji vremena
Table 2. Percentages of dissolved carbamazepine from solid dispersions, a commercial tablet and pure drug, as a function of time

Uzorak	Količina rastvorenog karbamazepina u funkciji vremena, %						
	10 min	20 min	30 min	45 min	60 min	90 min	120 min
F1	56,20±1,24	80,60±3,21	90,60±1,24	96,00±0,37	95,60±0,21	96,70±0,43	98,80±0,21
F2	67,70±1,06	85,40±1,74	92,00±1,21	96,80±0,65	98,30±0,23	98,70±0,37	98,20±0,09
F3	60,60±0,86	78,30±1,27	85,30±2,29	90,30±1,57	93,30±0,33	94,80±0,54	96,50±0,71
F4	62,50±1,94	85,04±0,68	93,62±0,71	98,26±1,02	99,30±0,09	99,61±0,23	99,81±0,15
F5	65,00±0,33	90,40±0,23	95,60±0,17	97,50±0,06	97,70±0,38	99,00±0,16	99,20±0,25
F6	31,00±2,21	49,20±3,21	62,80±3,24	83,10±1,16	83,50±1,53	94,50±0,34	93,90±0,11
F7	53,48±0,97	73,86±1,12	78,92±0,86	83,33±0,14	83,01±0,21	84,36±0,21	87,32±1,23
F8	48,37±1,46	76,99±2,23	82,92±2,96	89,71±0,32	90,53±0,45	92,65±0,23	94,87±0,87
F9	42,26±2,14	61,53±1,32	70,87±1,31	83,19±0,96	83,23±0,14	89,42±1,54	90,61±0,37
F10	63,28±1,32	79,26±0,78	87,40±0,65	91,11±0,32	92,14±0,85	94,77±1,09	96,23±1,23
F11	52,77±2,87	70,39±2,21	79,14±0,33	87,15±0,39	87,69±0,65	92,10±1,12	94,58±2,22
F12	60,60±0,86	78,30±1,27	85,30±2,29	90,30±1,57	93,30±0,33	94,80±0,54	96,50±0,71
F13	65,00±0,33	90,40±0,23	95,60±0,17	97,50±0,06	97,70±0,38	99,00±0,16	99,20±0,25
F14	52,77±2,87	70,39±2,21	79,14±0,33	87,15±0,39	87,69±0,65	92,10±1,12	94,58±2,22
F15	42,26±2,14	61,53±1,32	70,87±1,31	83,19±0,96	83,23±0,14	89,42±1,54	90,61±0,37
F16	62,50±1,94	85,04±0,68	93,62±0,71	98,26±1,02	99,30±0,09	99,61±0,23	99,81±0,15
Karbamazepin	4,91±0,09	26,42±0,87	41,56±0,24	41,89±0,11	48,85±0,98	53,00±0,21	59,41±1,04
Tablete*	13,99±1,02	22,52±1,21	30,36±0,76	38,08±0,34	46,45±1,98	50,98±2,36	55,63±0,47

*Komercijalne tablete karbamazepina sa trenutnim oslobađanjem lekovite susptance

Najveće razlike u procentu rastvorenog karbamazepina iz ispitivanih čvrstih disperzija primećene su posle 10 minuta (od 31,00 % do 67,70 %). Kod većine ispitivanih formulacija (F1 – F5, F8, F10, F12 - F14; Tabela 2.) nakon 30 minuta dolazi do oslobađanja više od 80% karbamazepina, što odgovara zahtevima Američke farmakopeje (USP 38/NF33) za preparate sa trenutnim oslobađanjem aktivne supstance. Može se smatrati da je povećanje brzine oslobađanja karbamazepina iz ispitivanih čvrstih diperzija posledica površinske aktivnosti korišćenih ekscipijenasa. Procenti oslobođenog karbamazepina nakon 30 minuta iz uzoraka F6, F9 i F16, znatno manji od 80%, ukazuju da udeli tj. međusobni odnosi karbamazepina i ekscipijenasa (*Gelucire® 44/14* i *Soluplus®*) nisu odgovarajući, jer ne dovode do željenog oslobađanja aktivne supstance. I pored toga, procenti oslobođenog karbamazepina iz čvrstih disperzija su veći u poređenju sa čistom supstancom (41,56 %, nakon 30 min) i komercijalnim tabletama (30,36 %, nakon 30 min). Nakon 90 i 120 minuta se ne uočavaju značajne razlike u brzini rastvaranja karbamazepina (Tabela 2.), pa se vrednosti procenta oslobođenog karbamazepina nakon 60-og minuta nisu koristile kao izlazni parametri za modelovanje u eksperimenatalnom dizajnu.

3. 2. Modelovanje uticaja ulaznih na izlazne parametre primenom metode dizajna smeše

Primenom metode D-optimalnog eksperimentalnog dizajna smeše, izvršen je izbor regresionog modela, koji prema statističkim parametrima najbolje opisuje vezu između ulaznih i izlaznih parametara. Na osnovu poređenja statističkih parametara (pomenutih u delu: Materijali), odabran je kubni model, koji je najviše odgovarao zahtevima za izlazni parametar R_1 (procenat rastvorenog karbamazepina nakon 10 minuta) (Tabela 3.). Prilikom primene regresionih modela isprobane su linearna i kvadratna funkcija, međutim na osnovu dobijenih profila brzine rastvaranja karbamazepina iz čvrstih disperzija nije ni bilo očekivano dobro uklapanje u ove modele, na šta ukazuju i niske vrednosti koeficijenata determinacije za ova dva modela (Tabela 3.).

Tabela 3. Prikaz statističkih parametara za izbor regresionog modela za R_1 (procenat rastvorenog karbamazepina nakon 10 minuta)
Table 3. Presentation of statistical parameters for selecting a regression model for R_1 (percentage of dissolved carbamazepine after 10 minutes)

Model	Standardna devijacija	R^2	Prilagođeni R^2	PRESS
Linearni	8,93	0,3365	0,2344	1402,84
Kvadratni	7,96	0,5941	0,3911	1814,92
Specijalni kubni	4,67	0,8743	0,7905	723,03
Kubni	**1,59**	**0,9903**	**0,9757**	**1368,88**

Nakon dobijanja regresionog modela vršeno je isključivanje parametara, koji nemaju statističku značajnost ($p>0,05$). Za izlazni parametar R_1 (procenat oslobođenog karbamazepina nakon 10 minuta) isključen je koeficijent uz parametar AB(A-B), čiji je $p=0,7204$. Uticaj svih ostalih parametara je bio statistički značajan. U tabeli S1 (Prilog) prikazana je statistička značajnost parametara pre i nakon isključivanja parametra AB(A-B) koji nema statistički značaj.

Nakon toga je dobijena jednačina, na osnovu koje je moguće za bilo koje vrednosti ulaznih parametara, a u okviru postavljenih graničnih vrednosti, predvideti procenat rastvorenog karbamazepina nakon 10 minuta. Statistički parametri ove jednačine su $p<0,0001$ i $F=87,06$, a ona glasi:

$$R_1 = 60{,}76A+53{,}03B+62{,}69C-57{,}81AB+39{,}90AC-124{,}23BC+639{,}92ABC-235{,}24AC(A-C)+132{,}67BC(B-C) \tag{8}$$

Na slici 1. prikazan je 2D trokomponentni dijagram, koji opisuje uticaj ulaznih parametara na izlazni parametar R_1. Sa ovog dijagrama se može uočiti da se udelima *Soluplus®* u formulaciji od oko 45% i *Gelucire® 44/14* od oko 25 % povećava procenat rastvorenog karbamazepina nakon 10 minuta.

Najveći procenat rastvorenog karbamazepina, nakon 10 minuta, dobija se sa udelom ove supstance od oko 40 % u formulaciji, dok je pri udelima karbamazepina od oko 30 % ili oko 50 % manji procenat rastvorene supstance (Slika 1.). Ovakava zavisnost uočava se i nakon 20, 30, 45 i 60 minuta. Povećanje brzine rastvaranja karbamazepina iz čvrstih disperzija koje sadrže *Soluplus®* i *Gelucire® 44/14*, verovatno je posledica boljeg kvašenja lekovite supstance, kao i njene solubilizacije ekscipijensima [16].

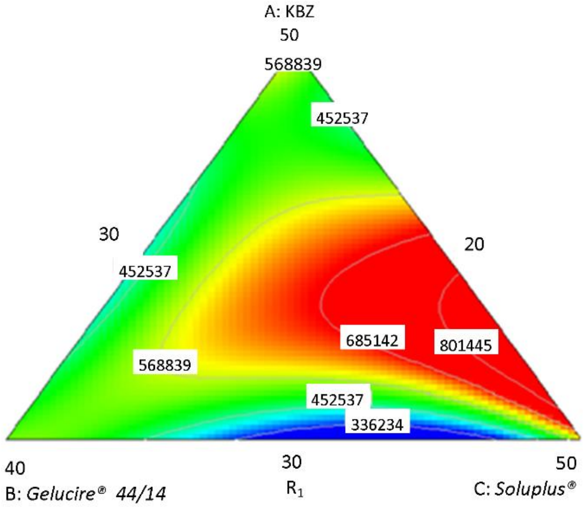

Slika 1. 2D trokomponentni dijagram koji opisuje uticaj ulaznih parametara na R_1. Na temena trouglova predstavljene su maksimalne vrednosti ispitivanih parametara, dok se na sredinama naspramnih stranica nalaze minimalne vrednosti. Crveni, žuti, zeleni, svetlo plavi i tamno plavi regioni predstavljaju regione u kojima su postignuti različiti procenti oslobođenog karbemazepina, od najvišeg (crveni) ka najnižem (tamno plavi)
Figure 1. 2D ternary diagram which describes the effect of input parameters on R_1. The maximum values of the tested parameters are presented on the triangle vertex, while the minimal values are presented in the center of the contrary sides. Red, yellow, green, light blue and dark blue regions represent regions where different percentages of released carbamazepine have been achieved, from the highest (red) to the lowest value (dark blue), respectively.

Za ostale izlazne parametre (R_2 - R_5) odabrani regresioni model bio je takođe kubni, a dobijene su jednačine, čije su vrednosti faktorskih efekata i njihovi statistički parametri prikazani u tabeli 4.

Tabela 4. Vrednosti faktorskih efekata i njihovi statistički parametri za izlazne parametre $R_2 – R_5$
Table 4. Values of factor effects, and their statistical parameters for output parameters $R_2 – R_5$

	R_2	**R_3**	**R_4**	**R_5**
A	+78,67	+85,30	+90,43	+93,41
B	+70,95	+79,57	+87,31	+87,81
C	+85,42	+93,88	+98,38	+99,41
AB	-50,59	-42,78	-16,71	-24,49
AC	+68,08	+54,49	+25,77	+21,22
BC	-146,39	-127,33	-44,88	-47,95
ABC	+573,90	+504,94	+130,63	+155,06
AB(A-B)	/	/	-88,81	-82,33
AC(A-C)	-281,97	-259,30	-99,20	-130,66
BC(B-C)	+261,15	+228,41	+71,52	+79,88
Statistički parametri odabranih (kubnih) modela				
p	0,0003	0,0003	0,0001	<0,0001
F	21,38	20,84	41,19	75,98

Na slici 2. prikazani su 2D trokomponentni dijagrami, koji opisuju uticaj ulaznih parametara na R_2, R_3, R_4 i R_5 (procenat rastvorenog karbamazepina nakon 20, 30, 45 i 60 minuta).

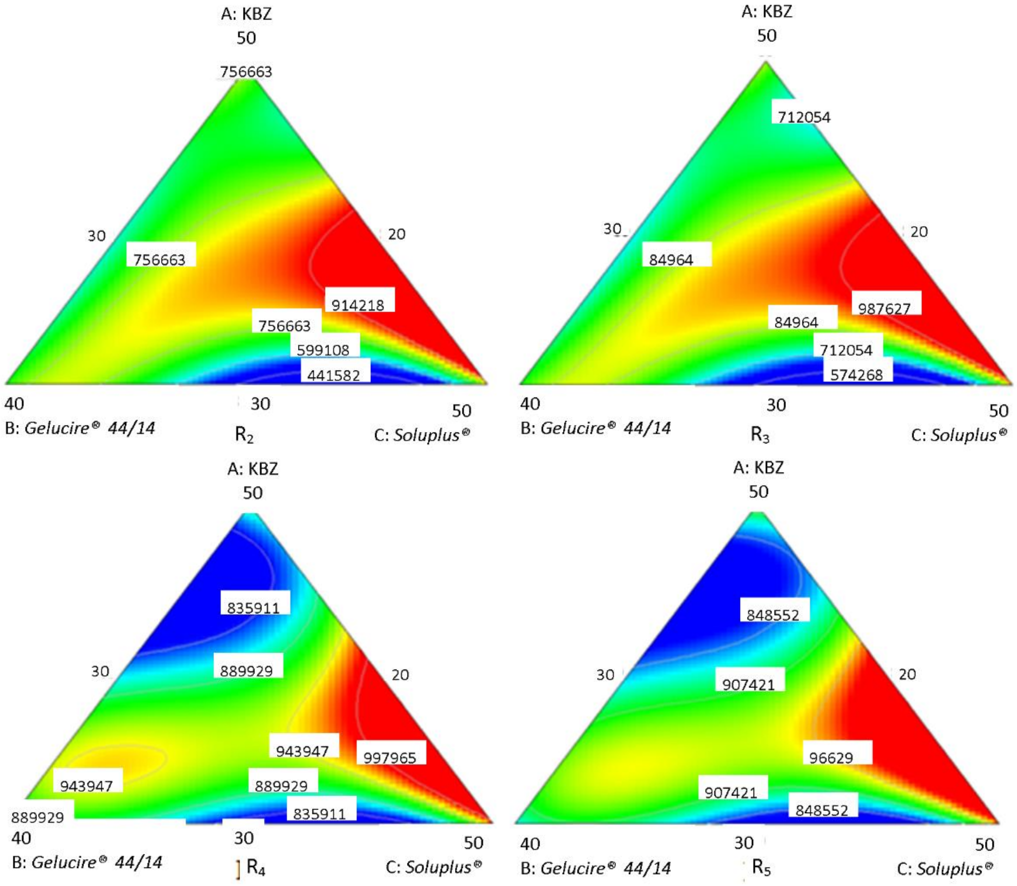

Slika 2. 2D trokomponentni dijagrami koji opisuju uticaj ulaznih parametara na R_2 (gore levo), R_3 (gore desno), R_4 (dole levo) i R_5 (dole desno). Na temena trouglova predstavljene su maksimalne vrednosti ispitivanih parametara, dok se na sredinama naspramnih stranica nalaze minimalne vrednosti. Crveni, žuti, zeleni, svetlo plavi i tamno plavi regioni predstavljaju regione u kojima su postignuti različiti procenti oslobođenog karbemazepina, od najvišeg (crveni) ka najnižem (tamno plavi)

Figure 2. 2D ternary diagram which describes the effect of input parameters on R_2 (up left), R_3 (up right), R_4 (down left) i R_5 (down right). The maximum values of the tested parameters are presented on the triangle vertex, while the minimal values are presented in the center of the contrary sides. Red, yellow, green, light blue and dark blue regions represent regions where different percentages of released carbamazepine have been achieved, from the highest (red) to the lowest value (dark blue), respectively

3. 3. Optimizacija formulacija čvrstih disperzija

Trokomponentni dijagram (Slika 3.) pokazuje oblast u kojoj se ukrštaju zadate vrednosti odgovora, postavljene tokom optimizacije. Kompjuterski program *Design Expert®* je u okviru ove oblasti predvideo 22 formulacije, čiji su sastavi (udeli komponenti) i predviđene vrednosti izlaznih parametara prikazani u tabeli 5.

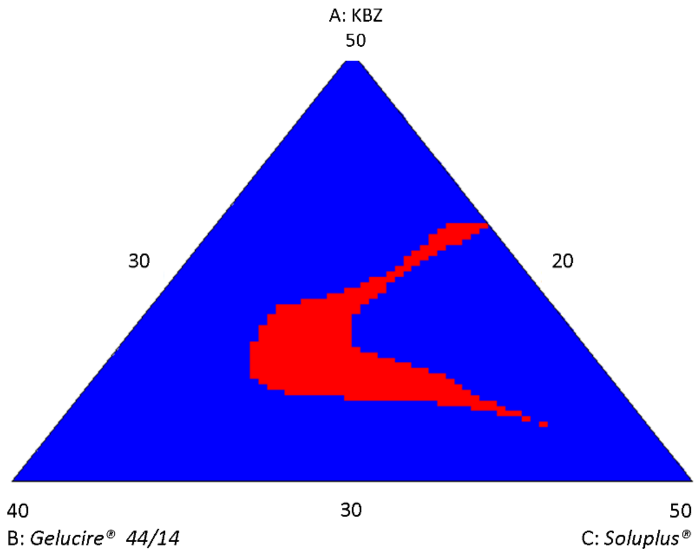

Slika 3. 2D trokomponentni dijagram sa regionom (označenom crvenom bojom) u okviru koga se nalaze optimalne formulacije. Na temena trouglova predstavljene su maksimalne vrednosti ispitivanih parametara, dok se na sredinama naspramnih stranica nalaze minimalne vrednosti.

Figure 3. 2D ternary diagram with the region (marked in red) indicating optimal formulations. The maximum values of the tested parameters are presented on the triangle vertex, while the minimal values are presented in the center of the contrary sides.

Tabela 5. Formulacije čvrstih disperzija predložene kompjuterskim programom Design Expert® (sastav i vrednosti izlaznih parametara)

Table 5. Formulations of optimal solid dispersions proposed by computer program Design Expert® (the composition and values of the output parameters)

Oznaka formulacije	Ulazni parametri			Izlazni parametri				
	Sadržaj karbamzepina, %	Sadržaj *Gelucire®* 44/14, %	Sadržaj *Soluplus®*, %	R_1	R_2	R_3	R_4	R_5
O1	33,92	26,24	39,84	62,80	78,63	87,07	93,35	94,56
O2	36,90	27,13	35,97	65,55	84,47	91,32	92,40	92,95
O3	39,15	24,59	36,26	65,67	84,39	90,69	90,59	90,96
O4	35,30	30,33	34,37	60,53	81,84	89,23	93,80	94,10
O5	38,66	25,11	36,23	66,08	84,72	91,12	90,97	91,41
O6	37,91	25,99	36,10	66,13	84,78	91,37	91,54	92,04
O7	33,56	25,39	41,05	62,44	77,39	86,16	93,52	94,91
O8	35,69	26,77	37,54	66,64	84,69	91,84	93,64	94,54
O9	40,94	21,62	37,44	63,68	84,90	90,49	92,46	92,49
O10	36,20	27,60	36,20	65,28	84,28	91,30	93,02	93,64
O11	34,52	29,84	35,64	61,16	81,79	89,37	93,85	94,41
O12	34,67	28,71	36,62	62,66	81,95	89,56	93,57	94,29
O13	36,87	26,85	36,28	66,15	84,89	91,71	92,57	93,18
O14	35,28	29,64	35,08	61,85	82,51	89,86	93,67	94,11
O15	36,27	29,03	34,70	62,27	82,55	89,72	92,81	93,15
O16	35,90	29,77	34,33	61,09	81,94	89,23	93,23	93,50
O17	37,22	26,81	35,97	65,75	84,58	91,35	92,11	92,65
O18	33,78	24,83	41,39	61,82	80,18	88,61	94,48	96,01
O19	35,49	29,28	35,23	62,45	82,80	90,08	93,49	93,96
O20	34,12	29,08	36,80	61,02	80,40	88,29	93,43	94,17
O21	41,56	21,32	37,12	61,05	82,32	88,01	91,67	91,45
O22	37,98	27,44	34,58	62,53	81,91	88,85	90,56	90,81

R_1, R_2, R_3, R_4, R_5: procenat rastvorenog karbamazepina nakon 10, 20, 30, 45, 60 minuta.

3. 4. Ispitivanja odabranih optimizovanih formulacija čvrstih disperzija

Radi procene uspešnosti predviđanja, iz različitih delova optimizacione oblasti odabrane su tri formulacije čvrstih disperzija (O2, O4 i O21; Tabela 5.), koje su izrađene na prethodno opisan način i iz kojih je ispitana *in vitro* brzina rastvaranja karbamazepina.

Predviđeni i eksperimentalno dobijeni procenti rastvorenog karbamazepina iz odabranih čvrstih disperzija prikazani su u tabeli 6. Na osnovu poređenja eksperimentalno dobijenih i predviđenih profila brzine rastvaranja karbamazepina iz izrađenih čvrstih disperzija i izračunatih vrednosti za faktore razlike f_1 i faktore sličnosti f_2 (Tabela 6.), uočava se veliko slaganje između predviđenih i dobijenih profila brzine rastvaranja lekovite supstance i zaključuje se da se ovi profili mogu smatrati sličnim, jer je $f_1<15$ i $f_2>50$ [14], kao i da nema statistički značajne razlike među njima.

Tabela 6. Dobijeni i predviđeni sadrža jrastvorenog karbamazepina iz čvrstih disperzija, faktori razlike (f_1) i faktori sličnosti (f_2)
Table 6. Obtained and predicted percentages of dissolved carbamazepine from solid dispersions, the difference factors (f_1) and the similarity factors (f_2)

	Sadržaj rastvorenog karbamazepina, %					
	Formulacija O2		Formulacija O4		Formulacija O21	
	dobijeno	predviđeno	dobijeno	predviđeno	dobijeno	predviđeno
10	59,21	63,19	61,61	61,12	54,55	60,17
20	78,22	81,97	75,82	75,81	78,74	80,57
30	88,70	89,60	85,90	85,30	88,18	87,84
45	93,42	93,52	96,45	94,86	94,21	91,65
60	96,55	94,31	98,76	96,56	96,19	91,78
f_1	2,64		1,17		3,58	
f_2	88,12		96,02		83,93	

3. 5. Procena permeabilnosti karbamazepina

Rezultati ispitivanja permeabilnosti karbamazepina (PAMPA test) iz ispitivanih formulacija i čistog karbamazepina dati su na slici 4. Dobijena vrednost koeficijenta permeabilnosti za čist karbamazepin ($14,52 \pm 1,50\times10^{-6}$ cm/s) bila je u skladu sa prethodno dobijenim rezultatima u sličnim ispitivanjima [8, 13, 15]. Rezultati PAMPA testa pokazuju da je postignuto izvesno povećanje permeabilnosti karbamazepina iz formulacije O2 ($16,18 \pm 3,17\times10^{-6}$ cm/s), dok je permeabilnost neznatno smanjena u slučaju uzorka O4 ($12,41 \pm 1,88\times10^{-6}$ cm/s), ali ove razlike nisu statistički značajne ($p>0,05$). Permeabilnost karbamazepina iz formulacije O21 je značajno smanjena ($9,71 \pm 0,61\times10^{-6}$ cm/s) ($p<0,05$), što može biti posledica najnižeg udela *Gelucire® 44/14* u ovoj formulaciji. Ovaj ekscipijens verovatno stupa u interakciju sa veštačkom membranom, pa se može pretpostaviti da se sa smanjenjem njegove koncentracije smanjuje i propustljivost membrane, a sa tim i permeabilnost karbamazepina iz navedenog uzoraka čvrste disperzije [17].

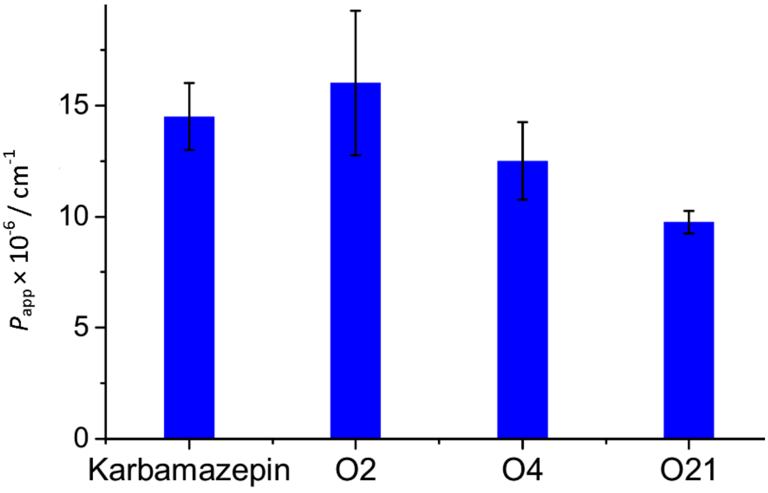

Slika 4. Rezultati PAMPA testa za prašak karbamazepina i tri odabrane optimizovane formulacije (O_2, O_4 i O_{21}) (P_{app} - koeficijent permeabilnosti)
Figure 4. Results of the PAMPA test for carbamazepine powder and three selected optimized formulations (O_2, O_4 i O_{21}) (P_{app} - permeability coefficient)

Rezultati ove studije idu u prilog osnovnoj pretpostavci da prilikom razvoja formulacija sa teško rastvorljivom lekovitom supstancom treba postići kompromis između brzine rastvaranja, sa jedne, i permeabilnosti, sa druge strane. Dobra rastvorljivost lekovite supstance u vodenoj sredini gastrointestinalnog trakta je skoro uvek preduslov za dobru bioraspoloživost lekovite supstance nakon peroralne primene. Međutim, tokom izrade formulacija u kojima se povećava rastvorljivost lekovitih supstanci, može doći do promene permeabilnosti, odnosno uticaja na resorpciju [12]. Prilikom povećanja brzine rastvaranja lekovite supstance, najčešće dolazi do formiranja struktura koje su veće od molekula same lekovite supstance. Veličina čestica je važan faktor koji utiče na resorpciju lekovite supstance, naročito onih koje su teško rastvorljive u vodi ili biološkim tečnostima. Kao posledica formiranja struktura koje su veće od molekula same lekovite supstance, može nastati problem sa permeabilnošću aktivne supstance iz ovakvih formulacija. Takođe, primena površinski aktivnih materija za povećanje rastvorljivosti lipofilnih lekovitih supstanci, koje pokazuju visoku permeabilnost, kakav je i sam karbamazepin (BSK klasa II), usled solubilizacije lekovite supstance primenom površinski aktivne materije može doći do smanjenja slobodne frakcije lekovite supstance, što posledično vodi smanjenju permeabilnosti, što verovatno jeste još jedan od razloga za smanjenje permeabilnosti iz formulacije O21. Iz svega navedenog, može se smatrati da su formulacije čvrstih disperzija O2 i O4 prihvatljive, jer je postignuta ravnoteža između brzine rastvaranja i permeabilnosti karbamazepina [13,18].

3. 6. Diferencijalna skenirajuća kalorimetrija

Na DSC krivoj čistog karbamazepina (Slika 5), na osnovu karakterističnih pikova, može se zaključiti da je karbamezepin u polimorfnom obliku III, jedinom farmakološki aktivnom obliku [19-21]. Na to ukazuje endotermni pik na oko 178 °C, koji je posledica topljenja polimorfnog oblika III karbamazepina, a egzotermni pik na oko 181 °C predstavlja rekristalizaciju polimorfnog oblika III karbamazepina u polimorfni oblik I. Topljenje polimorfnog oblika I je verovatno uzrok pojave endotermnog pika na 194 °C. Karakteristični pikovi topljenja polimorfnog oblika III karbamazepina u temperaturnom opsegu od 150 do 180 °C [7,19,20] su uočeni na DSC krivama svih ispitivanih formulacija, kako u trenutku izrade, tako i nakon 24 meseca čuvanja pod ambijentalnim uslovima. Uočavaju se na gotovo svim DSC krivama i endotermni pikovi topljenja polimorfnog oblika I, međutim rekristalizacioni egzotermni pikovi prelaska polimorfnog oblika III u polimorfni oblik I nisu uočeni na svim DSC krivama. Izostajanje egzoterminh pikova prelaska karbamazepina iz polimorfnog oblika III u polimorfni oblik I su verovatno posledica malog udela lekovite supstance u uzorku i prisustva ekscipijenasa u formulaciji. Takođe, na DSC krivama ispitivanih formulacija uočavaju se i endotermni pikovi topljenja u opsegu temperatura od 40 do 50 °C, koji su verovatno posledica topljenja *Gelucire® 44/14*, prisutnog u formulacijama. Rezultati DSC analize ukazuju da je karbamazepin u svim ispitivanim formulacijama prisutan u polimorfnom obliku III i da su uzorci stabilni tokom dvogodišnjeg čuvanja.

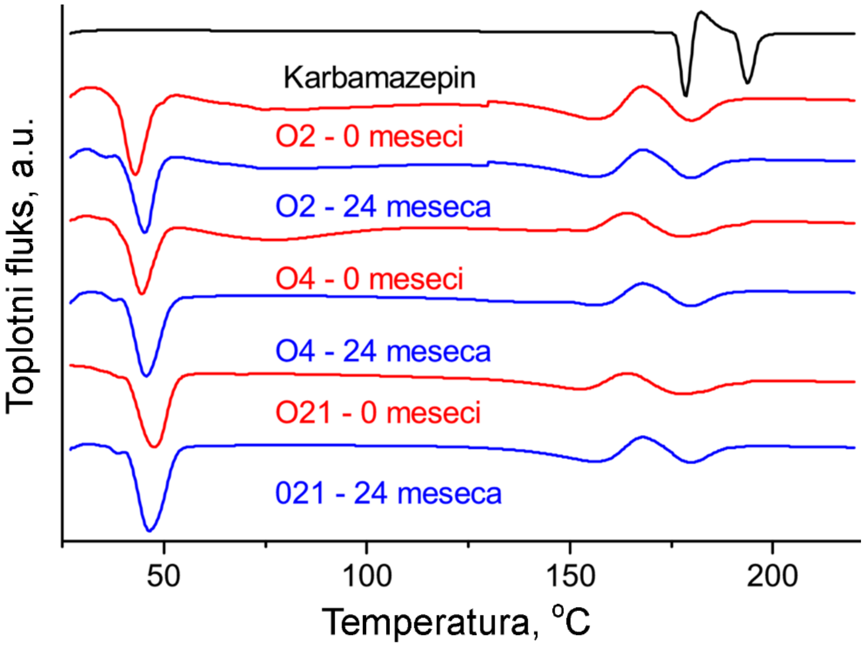

Slika 5. DSC krive karbamazepina i ispitivanih uzoraka O2, O4 i O21 nakon izrade i nakon 24 meseca

Figure 5. DSC curve of carbamazepine and investigated samples O2, O4 i O21 initially after preparation and after 24 months

3. 7. Infracrvena spektroskopija sa Furjeovom transformacijom

Na spektru čistog karbamazepina (Slika 6.) se uočavaju karakteristične trake na 3462 cm^{-1} (–NH valenciona vibracija), 1674 cm^{-1} (–CO–R vibracija), 1593 cm^{-1} i 1605 cm^{-1} (opseg za –C=C– i –C=O vibraciju i –NH deformaciju), što takođe ukazuje da je on u polimorfnom obliku III [22, 23]. U tri izrađene optimizovane formulacije se takođe uočavaju ove karakteristične trake, što ukazuje da nije došlo do interakcije između karbamazepina i ekscipijenasa i da je karbamazepin ostao u polimorfnom obliku III. Nakon čuvanja uzoraka 24 meseca pod ambijentalnim uslovima, takođe se uočavaju karakteristične trake na spektru ovih formulacija. I ovi rezultati idu u prilog tome da je karbamazepin i nakon navedenog vremenskog perioda ostao u kristalnom polimorfnom obliku III.

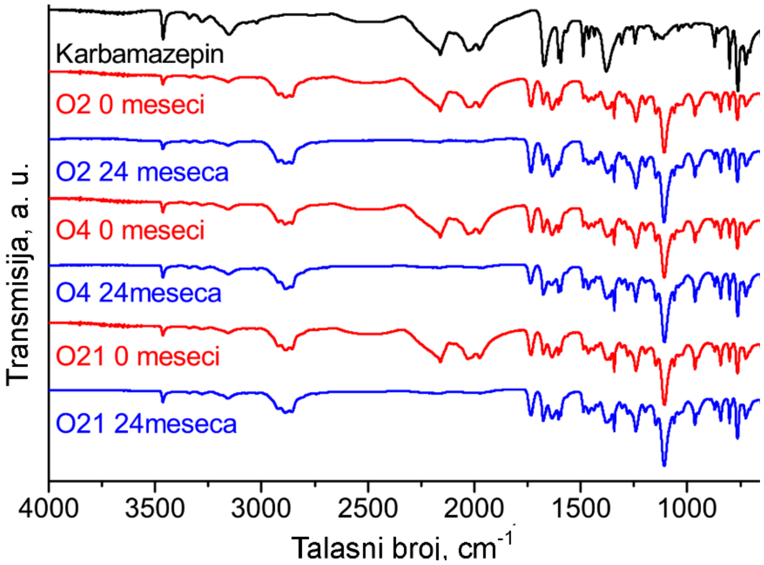

Slika 6. FT-IR spektri karbamazepina i ispitivanih uzoraka O2, O4 i O21 nakon izrade i nakon 24 meseca

Figure 6. FT-IR spectra of pure carbamazepine and investigated samples O2, O4 i O21 initially after preparation and after 24 months

3. 8. Ramanska spektroskopija

Na slici 7. prikazani su spektri Ramanovog rasejanja karbamazepina i tri odabrane optimizovane formulacije, nakon izrade i nakon 24 meseca čuvanja pod ambijentalnim uslovima.

U molekularnom kristalu, generalno, mogu se razlikovati dva spektralna opsega Ramanovog rasejanja, visoko energetski (konvencionalni) opseg, koji se sastoji od intramolekulskih vibracija i nisko energetski opseg (ispod 200 cm^{-1}) u kojem dominiraju intermolekulske vibracije (Slika 7) [24]. Iako visoko energetski opseg takođe može nositi informaciju vezanu za kristalnu strukturu, uočene promene između različitih polimorfnih oblika su obično male i često ograničene na varijacije u intenzitetu Ramanskih pikova. Istraživanje nisko energetskog opsega pruža direktan uvid u kristalnu strukturu materijala [24]. U Ramanskim spektrima prisutni su svi karakteristični pikovi polimorfnog oblika III karbamazepina, sa naglaskom na pikove na oko 40, 91 i 141 cm^{-1} [25, 26]. Isti pikovi su prisutni i u uzorcima nakon 24 meseca, čime se potvrđuje očuvanje polimorfnog oblika III i stabilnost izrađenih formulacija nakon 24 meseca čuvanja. Varijacije u relativnim intenzitetima Ramanskih pikova posledica su različite orijentacije kristalita.

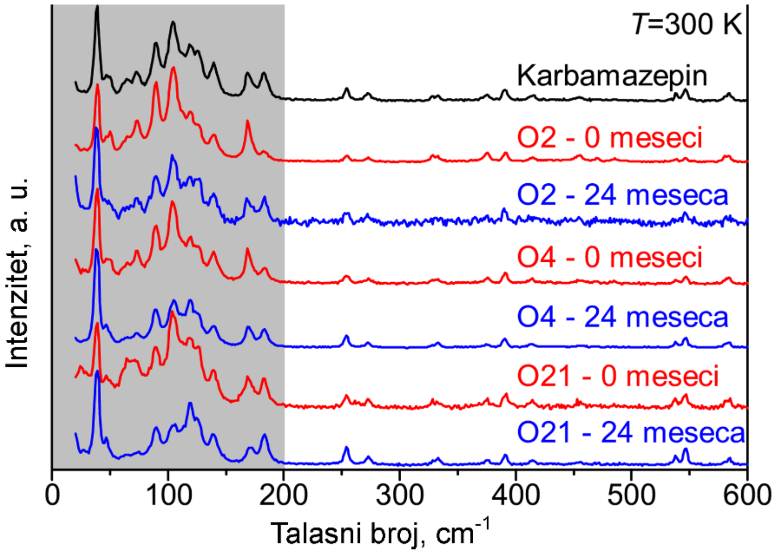

Slika 7. Ramanski spekti karbamazepina i ispitivanih uzoraka O2, O4 i O21 nakon izrade i nakon 24 meseca

Figure 7. Raman scattering spectra of carbamazepine and investigated samples O2, O4 i O21 initially after preparation and after 24 months

Rezultati ispitivanja, dobijeni primenom tri tehnike karakterizacije (DSC, FT-IR i Ramanska spektoskopija) su u saglasnosti i potvrđuju da je karbamazepin u uzorcima ostao u polimorfnom obliku III, kao i da su tri odabrane formulacije stabilne nakon 24 meseca čuvanja pod ambijentalnim uslovima.

4. ZAKLJUČAK

Primenom metode eksperimentalnog dizajna smeše, formulisane su čvrste disperzije variranjem udela karbamazepina, *Gelucire® 44/14* i polimera *Soluplus®*. Rezultati ispitivanja *in vitro* brzine rastvaranja karbamazepina iz čvrstih disperzija su pokazali da je postignuto povećanje procenta rastvorenog karbamazepina iz čvrstih disperzija, u odnosu na čistu supstancu i komercijalne tablete sa trenutnim oslobađanjem. Najveće vrednosti procenta oslobođenog karbamazepina dobijene su pri udelima karbamazepina od oko 35 – 40 %, *Gelucire® 44/14* od oko 25 – 30 % i *Soluplus®* od oko 35 – 40 %. Na osnovu dobijenih rezultata matematičke regresije, sa velikom tačnošću se može predvideti procenat rastvorenog karbamazepina, za bilo koju kombinaciju ulaznih parametara, u ispitivanom opsegu.

Poređenjem eksperimentalno dobijenih i predviđenih profila brzine rastvaranja karbamazepina iz tri izrađene optimizovane formulacije čvrstih disperzija, uočava se veliko slaganje (f_1<15; f_2>50).

Primenom PAMPA testa je pokazano da je u dve, od tri ispitivane optimizovane čvrste disperzije očuvana, odnosno blago povećana permeabilnost karbamazepina.

Rezultati ispitivanja uzoraka čvrstih disperzija nakon izrade, kao i nakon skladištenja 24 meseca, dobijeni primenom metoda DSC, FT-IR i Ramanske spektroskopije su potvrdili njihovu stabilnost i očuvanje karbamazepina u polimorfnom obliku III, jedinom farmakološki aktivnom obliku.

Zahvalnica: *Ovaj rad je realizovan u okviru projekata TR34007 i ON171032, koje finansira Ministarstvo prosvete, nauke i tehnološkog razvoja Rebuplike Srbije.*

LITERATURA

[1] Potta S, Minemi S, Nukala N, Peinado C, Lamprou DA, Urquhart A, Douroumis D. Development of solid lipid nanoparticles for enhanced solubility of poorly soluble drugs. *J Biomed Nanotechnol.* 2010; 6: 634–640.

[2] Leuner C, Dressman J. Improving drug solubility for oral delivery using solid dispersions. *Eur J Pharm Biopharm.* 2000; 50: 47–60.

[3] Damian F, Blaton N, Naesens L, Balzarini J, Kinget R, Augustijns P, Vanden Mooter G. Physicochemical characterization of solid dispersions of the antiviral agent UC-781 with polyethylene glycol 6000 and Gelucire 44/14. *Eur J Pharm Sci.* 2000; 10: 311–322.

[4] Kalivoda A, Fischbach M, Kleinebudde P. Application of mixtures of polymeric carriers for dissolution enhancement of oxeglitazar using hotmelt extrusion. *Int J Pharmaceut*. 2012; 439: 145–156.

[5] Serajuddin A. Solid dispersion of poorly water-soluble drugs: early promises, subsequent problems, and recent breakthroughs. *J Pharm Sci-US.* 1999; 88(10): 1058-1066.

[6] Djuris J, Ioannis N, Ibric S, Djuric Z, Kachrimanis K. Effect of composition in the development of carbamazepine hot-melt extruded solid dispersions by application of mixture experimental design. *J Pharm Pharmacol.* 2014; 66 (2):232-243.

[7] Krstić M, Ibrić S. Primena dizajna smeše u formulaciji i karakterizaciji čvrstih samo-nanoemulgujućih terapijskih sistema sa karbamazepinom. *Hem Ind.* 2016; 70(5): 525-537. (in Serbian)

[8] Krstić M, Ražić S, Đekić Lj, Dobričić V, Momčilović M, Vasiljević D, Ibrić S. Application of a mixture experimental design in the optimization of the formulation of solid self-emulsifying drug delivery systems containing carbamazepine. *Lat Am J Pharm.* 2015; 34 (5): 885-894.

[9] Dahan A, Miller MJ, Hoffman A, Amidon EG, Amidon LG. The solubility - permeability interplay in using cyclodextrins as pharmaceutical solubilizers: mechanistic modeling and application to progesterone. *J Pharm Sci-US*. 2010; 99(6): 2739-2749.

[10] Kataoka M, Tsuneishi S, Maeda Y, Masaoka Y, Sakuma S, Yamashita S. A new in vitro system for evaluation of passive intestinal drug absorption: Establishment of a double artificial membrane permeation assay. *Eur J Pharm Biopharm*. 2014; 88(3): 840-846.

[11] Kostewicz ES, Aarons L, Bergstrand M, Bolger MB, Galetin A, Hatley O, Jamei M, Lloyd R, Pepin X, Rostami-Hodjegan A, Sjögren E, Tannergren C, Turner DB, Wagner C, Weitschies W, Dressman J. PBPK models for the prediction of in vivo performance of oral dosage forms. *Eur J Pharm Sci*. 2014; 57: 300-321.

[12] Dahan A, Miller JM. The solubility-permeability interplay and its implications in formulation design and development for poorly soluble drugs. *AAPS J.* 2012; 14(2): 244-251.

[13] Krstić M, Popović M, Dobričić V, Ibrić S. Influence of Solid Drug Delivery System Formulation on Poorly Water-Soluble Drug Dissolution and Permeability. *Molecules.* 2015; 20: 14684-14698.

[14] Moore JW, Flanner HH. Mathematical Comparison of curves with an emphasis on in vitro dissolution profiles. *Pharm Tech.* 1996; 20(6): 64-74.

[15] Zhu C, Jiang L, Chen TM, Hwang KK. A comparative study of artificial membrane permeability assay for high-throughput profiling of drug absorption potential. *Eur J Med Chem.* 2002; 37: 399-407.

[16] Shamma RN, Basha M. Soluplus®: A novel polymeric solubilizer for optimization of Carvedilol solid dispersion: Formulation design and effect of method of preparation. *Powder Technol*. 2013; 29(1): 161-165.

[17] Porter C, Trevaskis N, Charman W. Nature Lipids and lipid-based formulations: optimizing the oral delivery of lipophilic drugs. *Nat Rev Drug Discov*. 2007; 6: 231-248.

[18] Löbenberg R, Amidon GL. Modern bioavailability, bioequivalence and biopharmaceutics classifcation system. New scientifc approaches to international regulatory standards. *Eur J Pharm Biopharm*. 2000; 50: 3-12.

[19] Grzesiak A, Lang M, Kim K, Matzger A. Comparison of the four anhydrous polymorphs of carbamazepine and the crystal structure of form I. *J Pharm Sci-US*. 2003; 92: 2261-2271.

[20] Yu L, Reutzel-Edens SM, Mitchell CA. Crystallization and Polymorphism of Conformationally Flexible Molecules: Problems, Patterns, and Strategies. *Org Process Res Dev*. 2000; 4(5): 396-402.

[21] Krstić M, Ražić S, Vasiljević D, Spasojević Đ, Ibrić S. Application of experimental design in the examination of the dissolution rate of carbamazepine from formulations. Characterization of the optimal formulation by DSC, TGA, FT-IR and PXRD analysis. *J Serb Chem Soc*. 2015; 80(2): 209-222.

[22] Rustichelli C, Gamberini G, Ferioli V, Gamberini MC, Ficarra R, Tommasini S. Solid-state study of polymorphic drugs: Carbamazepine. *J Pharm Biomed Anal*. 2000; 23(1): 41-54.

[23] Kobayashi Y, Ito S, Itai S, Yamamoto K. Physicochemical properties and bioavailability of carbamazepine polymorphs and dihydrate. *Int J Pharm.* 2000; 193: 137-146.

[24] Lazarević J, Uskoković-Marković S, Jelikić-Stankov M, Radonjić M, Tanasković D, Lazarević N, Popović Z. Intermolecular and low-frequency intramolecular Raman scattering study of racemic ibuprofen. *Spectrochim Acta A.* 2014; 126: 301-305.

[25] Saikat R, Chamberlin B, Matzger A. Polymorph Discrimination Using Low Wavenumber Raman Spectroscopy. *Org Process Res Dev*. 2013;17(7): 976-980.

[26] Krstic M, Djuris J, Petrovic O, Lazarevic N, Cvijic S, Ibric S. Application of the melt granulation technique in development of lipid matrix tablets with immediate release of carbamazepine. *J Drug Deliv Sci Tech*. 2017; 39: 467-474.

SUMMARY

Solid dispersions with carbamazepine: optimization of formulation, characterization and examination of long-term stability

Marko Krstić[1], Igor Lukić[2], Alma Bušatlić[3], Nenad Lazarević[4], Dragana Vasiljević[1]

[1]*Department of Pharmaceutical Technology and Cosmetology, University of Belgrade - Faculty of Pharmacy,*
Vojvode Stepe 450, 11221 Belgrade, Serbia
[2]*ASV Beograd d.o.o., Kumodraška 380, 11221 Belgrade, Serbia*
[3]*Adoc d. o. o., Milorada Jovanovića 11, 11030 Belgrade, Serbia*
[4]*Center for Solid State Physics and New Materials, Institute of Physics Belgrade, University of Belgrade,*
Pregrevica 118, 11080 Belgrade, Serbia

(Scientific paper)

Solid dispersions are defined as dispersions of one or more active pharmaceutical ingredients in inert solid-state carriers. They are made with the aim to increase solubility and the dissolution rate of low solubility active pharmaceutical ingredients, with the subsequent increase in their bioavailability.

The aim of this study was the development and optimization of solid dispersion formulations with carbamazepine, using D-optimal experimental design, in order to increase the dissolution rate of the selected model drug. By using the method of experimental mixture design, solid dispersions were formulated by varying the ratio of carbamazepine (30-50 %), *Gelucire® 44/14* (20-40 %) and *Soluplus®* polymer (30-50 %) (input parameters). Sixteen formulations were made and used for in vitro testing of the carbamazepine dissolution rate. The observed output parameters were the percentages of carbamazepine released after 10, 20, 30, 45, and 60 minutes. After the data analysis, three test formulations were chosen from different parts of the optimization area. They were prepared and the carbamazepine dissolution rate was determined, followed by stability assessment for 24 months under ambient conditions (25 °C, 40 % RH).

The highest dissolution rate of carbamazepine from solid dispersions (more than 80 % in 30 minutes) was achieved at the carbamazepine mass fraction of about 40 %, *Soluplus®* of about 45 % and *Gelucire® 44/14* of about 25 %. Comparing the predicted and the experimental obtained release rate profiles of carbamazepine from the three prepared optimized formulations, a significant compliance of the results was observed (f_1<15; f_2>50). The application of the PAMPA (Parallel Artificial-Membrane Permeability Assay) test has shown that carbamazepine premeability was maintained and mildly increased in two out of the three tested optimzed solid state formulations. Raman spectroscopy, FT-IR and DSC analyes showed that in the three optimized solid dispersions, after preparation and 24 months of storage, interactions between carbamazepine and the excipients were not present and that carbamazepine remained in the single pharmacologically active crystal polymorph form III.

Proper selection of solid dispersion proportions of carbamazepine, *Gelucire® 44/14* and *Soluplus®* may significantly increase the dissolution rate of the active substance, and the method of experimental mixture design can be successfully used for optimization of these formulations.

Keywords: solid dispersions, carbamazepine, formulation optimization, experimental design, in vitro release, physical stability

Vortex 2019

Antwerp, 20.05.2019.

Certificate of Attendance

I herewith certify that

Nenad Lazarević

from

Institute of Physics Belgrade, Serbia

has delivered an invited contribution at the

17th International Workshop on Vortex Matter
May 20-25, 2019, Antwerp
BELGIUM

For additional information, I refer to the official website of the conference - http://vortex2019.org.

Conference chairman

Milorad V. Milošević
University of Antwerp, Belgium

Vortex 2019

XVII INTERNATIONAL WORKSHOP ON
Vortex Matter in Superconductors

Antwerp, Belgium
20-25 May, 2019

ABSTRACT BOOK

cost
EUROPEAN COOPERATION
IN SCIENCE & TECHNOLOGY

This conference is organized within the framework of

EU-COST **Action CA16218**:

Nanoscale Coherent Hybrid Devices for Superconducting Quantum Technologies

NANOSCALE COHERENT
HYBRID DEVICES
FOR SUPERCONDUCTING
QUANTUM TECHNOLOGIES

Frustration and fluctuations in FeSe: A Raman scattering study

Nenad LAZAREVIĆ[1], Andreas BAUM[2,3], Harrison N RUIZ[4], Yao WANG[4,6,10], Thomas BÖHM[2,3,11], R Hosseinian AHANGHAMEJHAD[2,3,12], Peter ADELMANN[7], Thomas WOLF[7], Zoran V POPOVIĆ[1,8], Brian MORITZ[4], Thomas P DEVEREAUX[4,9], Rudi HACKL[2]

[1]Center for Solid State Physics and New Materials, Institute of Physics Belgrade, University of Belgrade, Pregrevica 118, 11080 Belgrade, Serbia.
[2]Walther Meissner Institut, Bayerische Akademie der Wissenschaften, 85748 Garching, Germany.
[3]Fakultät für Physik E23, Technische Universitä München, 85748 Garching, Germany.
[4]Stanford Institute for Materials and Energy Sciences, SLAC National Accelerator Laboratory, 2575 Sand Hill Road, Menlo Park, CA 94025, USA.
[5]Department of Physics, Stanford University, Stanford, CA 94305, USA.
[6]Department of Applied Physics, Stanford University, Stanford, CA 94305, USA.
[7]Karlsruher Institut für Technologie, Institut für Festkörperphysik, 76021 Karlsruhe, Germany.
[8]Serbian Academy of Sciences and Arts, Knez Mihailova 35, 11000 Belgrade, Serbia.
[9]Geballe Laboratory for Advanced Materials, Stanford University, Stanford, CA 94305, USA.
[10]Present address: Lyman Laboratory 336, Harvard University, 17 Oxford St. Cambridge, 02138 MA, USA.
[11]Present address: TNG Technology Consulting GmbH, Beta-Straße,85774 Unterföhring, Germany.
[12]Present address: School of Solar and Advanced Renewable Energy, Department of Physics and Astronomy, University of Toledo, Toledo, OH 43606, USA.

FeSe, the simplest of the iron based superconductors, is a puzzling material. As opposed to the related iron pnictides and FeTe, no long range magnetic order is found down to lowest temperatures. Here, we use Raman scattering as a function of temperature and polarization to probe charge and spin dynamics in FeSe. In agreement with numerical simulations of a spin-1 Heisenberg model several peaks in all Raman active symmetries can be assigned to spin excitations. The dominating feature is a peak in B_{1g} symmetry around 500 cm^{-1} which shows distinct temperature dependence. Further comparison of the simulations to neutron scattering data furnishes evidence for FeSe hosting nearly frustrated stripe order of local spins.

References

[1] A. Baum, H. N. Ruiz, N. Lazarević, Yao Wang, T. Böhm, R. Hosseinian Ahangharnejhad, P. Adelmann, T. Wolf, Z. V. Popović, B. Moritz, T. P. Devereaux & R. Hackl, Communications Physics **2**, 14 (2019).
[2] H. Ruiz, Yao Wang, B. Moritz, A. Baum, R. Hackl & T. P. Devereaux, Phys. Rev. B **99**, 125130 (2019).

E-mail: nenad.lazarevic@ipb.ac.rs

MATERIALS RESEARCH SOCIETY OF SERBIA
INSTITUTE OF TECHNICAL SCIENCES OF SASA

Programme and the Book of Abstracts

EIGHTEENTH YOUNG RESEARCHERS' CONFERENCE
MATERIALS SCIENCE AND ENGINEERING

Belgrade, December 4–6, 2019

http://www.mrs-serbia.org.rs/index.php/young-researchers-conference

EIGHTEENTH YOUNG RESEARCHERS' CONFERENCE

MATERIALS SCIENCE AND ENGINEERING

December 4-6, 2019, Belgrade, Serbia

Program and the Book of Abstracts

Materials Research Society of Serbia
&
Institute of Technical Sciences of SASA

November 2019, Belgrade, Serbia

Book title:
Eighteenth Young Researchers’ Conference - Materials Science and Engineering:
Program and the Book of Abstracts

Publisher:
Institute of Technical Sciences of SASA
Knez Mihailova 35/IV, 11000 Belgrade, Serbia
Tel: +381-11-2636994, 2185263, http://www.itn.sanu.ac.rs

Editor:
Dr. Smilja Marković

Technical Editor:
Aleksandra Stojičić

Cover page: Aleksandra Stojičić and Milica Ševkušić
Cover: Modified Photo by Miloš Stošić; Wikimedia Commons
(https://commons.wikimedia.org/wiki/File:Бедеми_-_поглед_на_Ушће.jpg); Creative
Commons Attribution-Share Alike 3.0 Unported license

Printer:
Gama digital centar
Autoput No. 6, 11070 Belgrade, Serbia
Tel: +381-11-6306992, 6306962
http://www.gdc.rs

Edition:
130 copies

CIP - Каталогизација у публикацији

Народна библиотека Србије, Београд

66.017/.018(048)

YOUNG Researchers Conference Materials Sciences and Engineering (18 ; 2019 ; Beograd)
Program ; and the Book of abstracts / Eighteenth Young Researchers' Conference Materials Sciences and Engineering, December 4-6, 2019, Belgrade, Serbia ; [organized by] Materials Research Society of Serbia & Institute of Technical Sciences of SASA ; [editor Smilja Marković]. - Belgrade : Institute of Technical Sciences of SASA, 2019 (Belgrade : Gama digital centar). - XX, 102 str. : ilustr. ; 23 cm

Tiraž 130. - Registar.

ISBN 978-86-80321-35-6 (ITSSASA)

а) Наука о материјалима -- Апстракти б) Технички материјали – Апстракти

COBISS.SR-ID 281006348

1-7

Single cell Raman scattering study of mesenchymal stem cells

Jasmina. J. Lazarević[1], Tamara Kukolj[2], Uroš Ralević[1], Diana Bugarski[2],
Nenad Lazarević[1], Branko Bugarski[3], and Zoran V. Popović[1,4]
[1]Center for Solid State Physics and New Materials, Institute of Physics Belgrade, University of Belgrade, Pregrevica 118, Belgrade 11080, Serbia, [2]Laboratory for Experimental Hematology and Stem Cells, Institute for Medical Research, University of Belgrade, Belgrade, Serbia, [3]Department of Chemical Engineering, Faculty of Technology and Metallurgy, University of Belgrade, Karnegijeva 4, Belgrade 11060, Serbia, [4]Serbian Academy of Science and Arts, Knez Mihailova 35, Belgrade 11000, Serbia

Mesenchymal stem cells (MSCs) are multipotent adult stem cells present in tissues throughout organism. The International Society for Cell Therapy defines MSCs by three characteristics: adhesion to plastic, expression of specific set of membrane molecules with lack of hematopoietic markers and human leukocyte antigen-DR, and ability to differentiate towards three lineages: osteogenic, chondrogenic, and adipogenic. Having in mind that the isolation process of these cells is not related to ethical issues of any kind, they are potent cell source for tissues engineering and regenerative medicine, meaning that in the near future currently incurable illnesses could be eradicated. Due to various culture conditions, different tissues of origin, donor age, etc. MSCs present heterogenic group of cells. Moreover, before any manipulation, they have to be adequately characterized and purified. Numerous methods and techniques are used for these purposes, but most of them are time-consuming and demanding in terms of sample preparation. Most importantly, many of these techniques are invasive and destructive. Owing to its features, Raman spectroscopy is ideal candidate to become the method of choice for characterization and monitoring of changes occurring in cells, on a single cell level. It overcomes all above mentioned issues. We utilized Raman spectroscopy for tracing changes in MSCs during the fixation process performed with fixatives witch have different chemical mechanism of action, formaldehyde and methanol. Furthermore, this optical technique was employed for probing differentiation status of MSCs after the differentiation was induced towards osteogenic, adipogenic, and chondrogenic lineages.

References:

1. Lazarević *et al. Spectrochim Acta A Mol Biomol Spectrosc.* **213**, 384-390 (2019).
2. Lazarević *et al.Spectrochim Acta A Mol Biomol Spectrosc.* **216**, 173-178 (2019).

7-5

Probing subsequent charge density waves in 1T-TaS$_2$ by inelastic light scattering

S. Djurdjić-Mijin,[1] J. Bekaert,[2] A. Šolajić,[1] J. Pešić,[1] Y. Liu,[3]
M. V. Milosevic, [2] C. Petrovic,[3] N. Lazarević,[1] and Z. V. Popović [1,4]
[1]*Center for Solid State Physics and New Materials, Institute of Physics Belgrade, University of Belgrade, Pregrevica 118, 11080 Belgrade, Serbia,* [2]*Department of Physics, University of Antwerp, Groenenborgerlaan 171, B-2020 Antwerp, Belgium,* [3]*Condensed Matter Physics and Materials Science Department, Brookhaven National Laboratory, Upton, New York 11973-5000, USA,* [4]*Serbian Academy of Sciences and Arts, Knez Mihailova 35, 11000 Belgrade, Serbia*

Two-dimensional layered transition-metal dichalcogenides (TMDs) have attracted attention for over 30 years mostly due to multiple charge-density wave (CDW) states that had been observed. Prime candidate is 1T-TaS$_2$ because of its unique and opulent electronic phase diagram. It experiences various phase transitions at high temperature, starting from the normal metallic to the incommensurate charge-density wave (IC-CDW) phase transition, at T= 554 K. At T=355 K 1T-TaS$_2$ CDW state changes to nearly-commensurate CDW (NC-CDW) phase, eventually leading to commensurate CDW (C-CDW) phase at approximately T= 180 K. Recent discoveries indicate the possibility of yet another phase transition in 1T-TaS$_2$ at T= 80 K. The new state is identified as hidden CDW (H-CDW) state, and can be induced using ultra-fast laser pulse. We present a detailed Raman spectroscopy study on CDW transitions. Our data indicate the coexistence of different CDW states, as well as strong electron-phonon interaction in the IC-CDW state. The experimental results presented in this work are supported by density functional theory (DFT) calculations.

10-6

Spin-phonon coupling in $CrSiTe_3$ and $CrSi_{0.8}Ge_{0.1}Te_3$

Ana Milosavljević[1], A. Šolajić[1], J. Pešić[1], B. Višić[1], M. Opačić[1],
Yu Liu[2], C. Petrovic[2], N. Lazarević[1], Z. V. Popović[1,3]
[1]Center for Solid State Physics and New Materials, Institute of Physics Belgrade, University of Belgrade, Pregrevica 118, 11080 Belgrade, Serbia, [2]Condensed Matter Physics and Materials Science Department, Brookhaven National Laboratory, Upton, NY 11973-5000, USA, [3]Serbian Academy of Sciences and Arts, Knez Mihailova 35, 11000 Belgrade, Serbia

Trichalcogenides $CrXTe_3$ (X = Si, Ge) are semiconducting representatives of the van der Waals materials, with ferromagnetic order and band gap of 0.4 eV for Si and 0.7 eV for Ge compound, and Curie temperatures of 32 K and 61 K, respectively. Their layered structure provided exfoliation to mono and few-layer nanosheets, due to the weak van der Waals inter-layer bonding. This possibility togeather with their semiconducting and magnetic properties makes them ideal candidates for applications in optoelectronics and nano-spintronics.

Here we present temperature dependent Raman scattering study on $CrSiTe_3$ and $CrSi_{0.8}Ge_{0.1}Te_3$. Four and eight out of ten Raman active modes were assigned and observed for pure and slightly doped compound, respectively. The self-energies of A_g^3 and E_g^3 symmetry modes of $CrSiTe_3$ compound exhibit unconventional temperature evolution around 180 K. In addition, doubly degenerate E_g^3 mode shows a clear change of asymmetry in the same temperature region. The observed behavior is consistent with the previously reported presence of short-range magnetic order and strong spin-phonon coupling. Changing the concentrations of elements in parent compounds and doping plays a significant role in semiconducting physics and can lead to surprising physical properties, like considerable change in magnetic transition temperature or structural modifications. SEM measurements performed on our CrSi0.8Ge0.1Te3 single crystals revealed the 10% concentration of Ge atoms and the same amount of vacancies. Inelastic scattering results on CrSi0.8Ge0.1Te3 in addition to symmetry predicted modes, shows the presence of one mode attributed to the inhomogeneous distribution of Ge atoms, and two overtones, all obeying pure A_g selection rules. All analyzed modes display unconventional behavior, but in a difference from the pure compound on a higher temperature of 210 K.

MATERIALS RESEARCH SOCIETY OF SERBIA
INSTITUTE OF TECHNICAL SCIENCES OF SASA

Programme and the Book of Abstracts

SEVENTEENTH YOUNG RESEARCHERS' CONFERENCE MATERIALS SCIENCE AND ENGINEERING

Belgrade, December 5–7, 2018

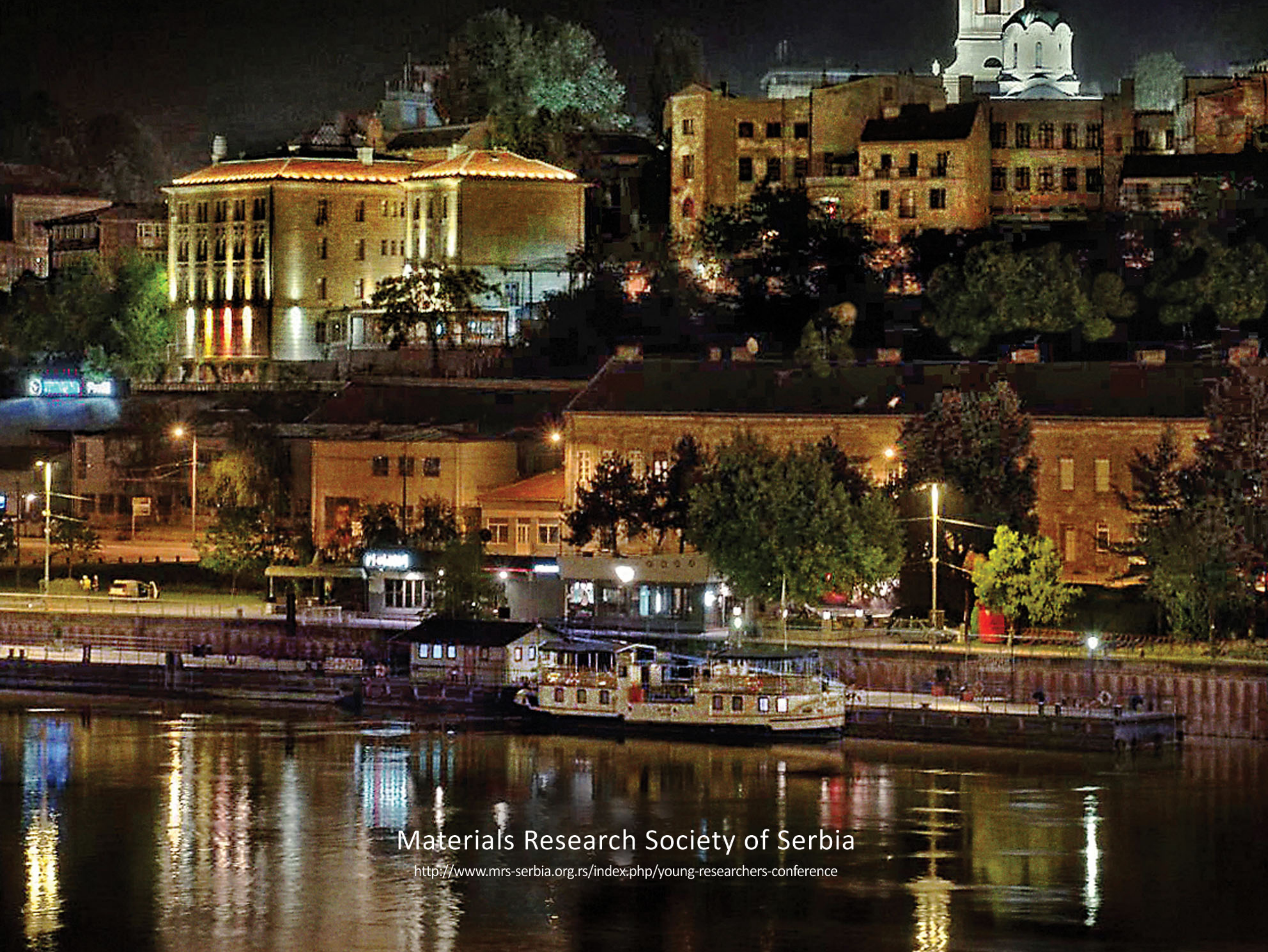

Materials Research Society of Serbia
http://www.mrs-serbia.org.rs/index.php/young-researchers-conference

10-6

Raman Spectroscopy Study on phase transition in CrI_3 single crystals

Sanja Đurđić[1], Andrijana Šolajić[1], Jelena Pešić[1], Maja Šćepanović[1], Y. Liu[2],
Andreas Baum[3,4], Čeda Petrović[2], Nenad Lazarević[1], Zoran V. Popović[1,5]
[1]Institute of Physics, Pregrevica 118, Belgrade, Serbia, [2]Brookhaven National Laboratory, Upton, New York 11973-5000, USA, [3]Walther Meissner Institut, Bayerische Akademie der Wissenschaften, 85748 Garching, Germany, [4]Fakultät für Physik E23, Technische Universität München, 85748 Garching, Germany, [5]Serbian Academy of Sciences and Arts, Knez Mihailova 35, 11000 Belgrade, Serbia

By virtue of their unique properties and the potential for a wide spectrum of applications, such as the development of functional van derWaals heterostructures, CrI_3 among the other two dimensional materials, has received significant attention in the most recent studies on the ferromagnetic semiconductors. In this study we represent the vibrational properties of CrI_3 single crystals investigated using Raman spectroscopy together with the density functional theory (DFT) calculations. Experimental results show that first-order phase transition from the low-temperature ($R\bar{3}$) to the high-temperature ($C2/m$) phase occurs at 180K with no evidence of the two-phase coexistence. All observed modes, in both phases, are in good agreement with DFT calculations.

MATERIALS RESEARCH SOCIETY OF SERBIA
INSTITUTE OF TECHNICAL SCIENCES OF SASA

Programme and the Book of Abstracts

SIXTEENTH YOUNG RESEARCHERS' CONFERENCE MATERIALS SCIENCE AND ENGINEERING

Belgrade, December 6–8, 2017

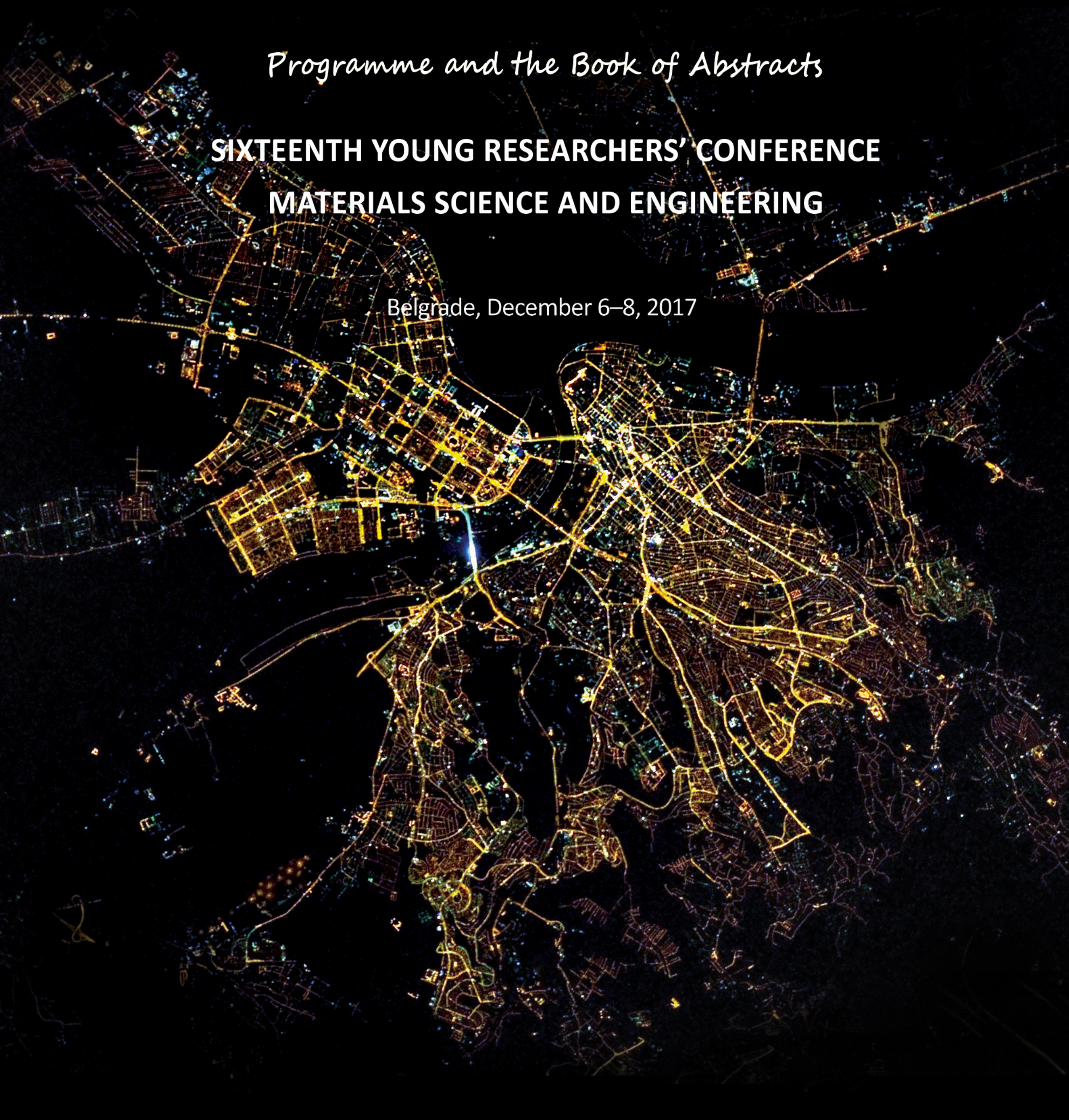

9-3

Small influence of magnetic ordering on lattice dynamics in $TaFe_{1.25}Te_3$

Marko Opačić,[1] Nenad Lazarević,[1] Darko Tanasković,[2] Miloš Radonjić,[2]
Ana Milosavljević,[1] Yongchang Ma,[3,4] Čedomir Petrović,[3] Zoran V. Popović[1,5]
[1]Center for Solid State Physics and New Materials, Institute of Physics Belgrade, University of Belgrade, Pregrevica 118, 11080 Belgrade, Serbia, [2]Scientific Computing Laboratory, Center for the Study of Complex Systems, Institute of Physics Belgrade, University of Belgrade, Pregrevica 118, 11080 Belgrade, Serbia, [3]Condensed Matter Physics and Materials Science Department, Brookhaven National Laboratory, Upton, New York 11973-5000, USA, [4]School of Materials Science and Engineering, Tianjin University of Technology, Tianjin 300384, People's Republic of China, [5]Serbian Academy of Sciences and Arts, Knez Mihailova 35, 11000 Belgrade, Serbia

The $TaFe_{1+y}Te_3$ single crystal is a layered system with monoclinic crystal structure, composed of FeTe chains along the b-axis, separated by a Ta/Te network, with additional Fe ions randomly situated on interstitial sites. It is a correlated bad metal which orders antiferromagnetically at T_N\approx 200 K. The magnetic structure consists of double zigzag spin chains, although the type of intra- and interchain magnetic interactions is still under debate. We present polarized Raman scattering spectra of $TaFe_{1.25}Te_3$ single crystal in a wide temperature range. Nine out of 15 Raman active modes are observed and assigned using measured spectra in different polarization configurations and lattice dynamics calculations. Unlike the case of related FeTe compound, $TaFe_{1.25}Te_3$ do not show significant changes near magnetic transition temperature T_N, which lead us to conclude that the phase transition is continuous. Temperature dependence of energy and linewidth is conventional, with the only exception in the vicinity of T_N, where some of phonon modes broaden. This is probably the consequence of spin fluctuations near the critical temperature. Our results suggest very small changes in the electron-phonon coupling and density of states at the Fermi level in the investigated temperature range.

9-5

Phonon anomalies in FeS

Ana Milosavljević[1], Andreas Baum[2,3], Nenad Lazarević[1], Miloš M. Radonjić[4], Božidar Nikolić[5], Merlin Mitschek[2,3], Zahra Inanloo Maranloo[2], Maja Šćepanović[1], Nenad Stojilović[1], Matthias Opel[2], Aifeng Wang[6], Čedomir Petrović[6], Zoran V. Popović[1], Rudi Kackl[2]

[1]Center for Solid State Physics and New Materials, Institute of Physics Belgrade, University of Belgrade, Pregrevica 118, 11080 Belgrade, Serbia, [2]Walther Meissner Institut, Bayerische Akademie der Wissenschaften, 85748 Garching, Germany, [3]Fakultat fur Physik E23, Technische Universitat Munchen, 85748 Garching, Germany, [4]Scientific Computing Laboratory, Center for the Study of Complex Systems, Institute of Physics Belgrade, University of Belgrade, Pregrevica 118, 11080 Belgrade, Serbia, [5]Faculty of Physics, University of Belgrade, Studentski trg 12, Belgrade, Serbia, [6]Condensed Matter Physics and Materials Science Department, Brookhaven National Laboratory, Upton, NY 11973-5000, USA

In the iron-based superconductors (IBS) magnetic order, structure, nemacity and superconductivity are closely interrelated. Influence of correlation effects seems to increase from 122 systems, such as $BaFe_2As_2$, to the 11 chalcogenides FeTe, FeSe and FeS. Although, isostructural and isoelectronic, 11 class members differ significantly. FeSe undergoes a structural transition at 90 K, shows electronic nemacity, with no long range magnetic ordering down to lowest temperatures, and superconductivity at 9 K. On the other hand, FeTe exhibits magneto-structural transition at 67 K, but no superconductivity. FeS has a superconducting transition at 5 K, but it does not show structural transition. Magnetic ordering in FeS still remains an open question.

Here we present light scattering data on phonons in tetragonal FeS. We identified two out of four Raman-active phonon modes, and a second order scattering process involving two acoustic phonons. Additionally, DFT calculations verify experimentally obtained results. Calculated phonon density of states and selection rules for two-phonon process based on the modified group projector technique confirm second order scattering process within a gap in the projected density of states. Low temperature experiments revealed that temperature dependence of all modes is mainly governed by lattice contraction, except for deviations at 50 K and below 20 K. The anomaly below 20 K coincides with the observation of the possible short range magnetic order.

Book of abstracts

PHOTONICA2019

The Seventh International School and Conference on Photonics, 26 August – 30 August 2019, Belgrade, Serbia

& Machine Learning with Photonics Symposium (ML-Photonica 2019)

AiPT MULTIPLY CARDIALLY FONTE

& ESUO Regional Workshop

ESUO
EUROPEAN
SYNCHROTRON
AND FEL USER
ORGANISATION

& COST action CA16221

AtomQT cost

Editors: Milica Matijević, Marko Krstić and Petra Beličev

Belgrade, 2019

Lattice dynamics of iron-based superconductors and related compounds

M. Opacic[1], N. Lazarevic[1], D. Tanaskovic[2], C. Petrovic[3] and Z.V.Popovic[1,4]
[1]*Center for Solid State Physics and New Materials, Institute of Physics Belgrade, University of Belgrade, Serbia*
[2]*Scientific Computing Laboratory, Center for the Study of Complex Systems,*
Institute of Physics Belgrade University of Belgrade, Serbia
[3]*Condensed Matter Physics and Materials Science Department,*
Brookhaven National Laboratory, Upton, New York, USA
[4]*Serbian Academy of Sciences and Arts, Belgrade, Serbia*
e-mail: marko.opacic@ipb.ac.rs

The lecture focuses on vibrational properties of some unconventional iron-based superconductors and related compounds by means of Raman spectroscopy. In the measured phonon spectra of superconducting $K_xFe_{2-y}Se_2$ and nonsuperconducting $K_{0.8}Fe_{1.8}Co_{0.2}Se_2$ single crystals there are phonon modes originating from metallic/superconducting *I4/mmm* phase and insulating *I4/m* phase with ordered Fe vacancies. Temperature analysis of energy and linewidth of the vibrational modes were done using the model which takes into account lattice thermal expansion and anharmonic effects. The modes originating from the *I4/m* phase are well described by that model. On the other hand, A_{1g} mode energy in the superconducting sample exhibits sudden jump, which was ascribed to the change in the electronic structure when entering the superconducting state. By investigating Raman spectra of $K_xFe_{2-y}Se_2$ single crystals doped with various Co concentrations, the evolution of phase separation was followed. With increasing cobalt content phonon modes from the *I4/m* phase disappear and in Raman spectra remain only two phonon modes originating from the high symmetry *I4/mmm* phase. Broad asymmetric structure in the samples with intermediate Co concentrations was interpreted as a fingerprint of strong crystalline disorder. The presence of only two phonon modes in the end member of this sequence - $K_xCo_{2-y}Se_2$ - excludes the possibility of ordered vacancies. Measured Raman spectra show that ferromagnetic phase transition around 74 K in this single crystal has significant impact on phonon mode behavior. Namely, above the ferromagnetic transition, temperature dependence of phonon energy and linewidth looks conventional. On the other hand, below critical temperature both modes exhibit sudden hardening, A_{1g} mode narrows and B_{1g} one significantly broadens, which is ascribed to the spin-phonon and electron-phonon interaction. Large linewidth of the Raman modes originates from the electron-phonon coupling enhanced by the crystal disorder and spin fluctuation effects.

7-11th October 2019
Belgrade, Serbia

http://www.sfkm.ac.rs/

The 20th Symposium on Condensed Matter Physics

BOOK OF ABSTRACTS

University of Belgrade,
Faculty of Physics

Institute of Physics Belgrade

Vinca Institute
of Nuclear Sciences

Serbian Academy
of Sciences and Arts

Ministry of Education, Science and
Technological Development,
Republic of Serbia

Nematic Fluctuations In Iron Based Systems

A. Baum[ab], F. Kretzschmar[ab], D. Jost[ab], T. Böhm[ab], L. Peis[ab],
U. Karahasanović[c], B. Muschler[ab], J. Schmalian[c], S. Caprara[d], M. Grilli[d],
C. Di Castro[d], J. G. Analytis[e], J.-H. Chu[e], I. R. Fisher[e], P. Gegenwart[f],
J. Maiwald[f], R. Hosseinian Ahangharnejhad[ab], P. Adelmann[c], T. Wolf[c],
N. Lazarević[g], Z. Popović[gh] and R. Hackl[a]

[a] *Walther Meissner Institut, Bayerische Akademie der Wissenschaften, Garching*
[b] *Fakultät für Physik E23, Technische Universität München*
[c] *Karlsruhe Institute of Technology (KIT)*
[d] *Department of Physics, University of Rome "Sapienza"*
[e] *SIMES, SLAC National Accelerator Laboratory, and Geballe Laboratory for Advanced Materials & Department of Applied Physics, Stanford University*
[f] *Experimentalphysik VI, Universität Augsburg*
[g] *Center for Solid State Physics and New Materials, Institute of Physics, University of Belgrade*
[h] *Serbian Academy of Sciences and Arts, Belgrade*

Abstract. The origin and interplay of nematicity, magnetism, and superconductivity in iron based materials are still a subject of current research. The fluctuations which precede the ordered phases provide an additional probe for these phenomena. Using Raman spectroscopy we study fluctuations in $Ba(Fe_{1-x}Co_x)_2As_2$ (x = 0-0.051) as a function of temperature, symmetry, and doping. Our results provide evidence for critical spin fluctuations, suggesting a spin driven mechanism of the nematic and magnetic order. We discuss similarities with related systems such as $EuFe_2As_2$ and FeSe.

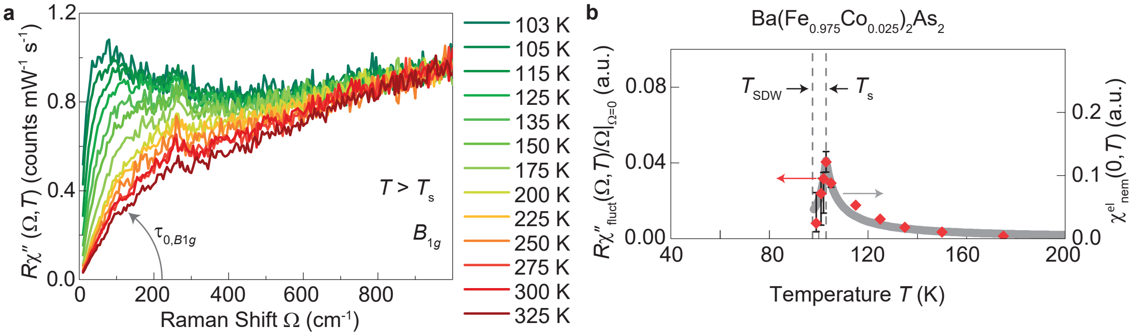

FIGURE 1. Fluctuations in $Ba(Fe_{0.975}Co_{0.025})_2As_2$. **a** Due to the response from fluctuations above the structural phase transition at $T_s \approx 103\,K$ the spectral weight at low energies and the initial slope $\tau_{0,B1g}$ increase upon cooling. **b** The initial slope (red diamonds) exhibits a maximum at T_s, but the fluctuations only vanish at the magnetic ordering temperature T_{SDW}. The maximum is reflected in the temperature dependence of the electronic nematic susceptibility χ^{el}_{nem} (grey) when the fluctuations couple to the lattice.

REFERENCES

1. Kretzschmar *et al.*, *Nat. Phys.* **12**, 560-563 (2016)

The vibrational properties of CrI_3 single crystals

S. Djurdjić-Mijin,[1] A. Šolajić,[1] J. Pešić,[1] M. Šćepanović,[1] Y. Liu,[2] A. Baum,[3,4] C. Petrovic,[2]
N. Lazarević,[1] and Z. V. Popović [1,5]

[1]*Center for Solid State Physics and New Materials, Institute of Physics Belgrade, University of Belgrade,Pregrevica 118, 11080 Belgrade, Serbia*
[2]*Condensed Matter Physics and Materials Science Department, Brookhaven National Laboratory,Upton, New York 11973-5000, USA*
[3]*Walther Meissner Institut, Bayerische Akademie der Wissenschaften, 85748 Garching, Germany*
[4]*Fakultät für Physik E23, Technische Universität München, 85748 Garching, Germany*
[5]*Serbian Academy of Sciences and Arts, Knez Mihailova 35, 11000 Belgrade, Serbia*

Abstract. CrI_3 is a two-dimensional layered material and a ferromagnetic [1] with Curie temperature of 61K [1,2] and first order phase transition that occurs at 220K [3,4]. This class of materials has recently gained a lot of intention due to numerous potential applications. Here we represent our work consisting of both experimental and theoretical Raman scattering study of CrI_3 lattice dynamics. Based on our results we can distinguish two different phases for CrI_3 with monoclinic (*C2/m*) being the high-temperature and rhombohedral ($\bar{R}3$) phase being the low-temperature phase. Abrupt changes to the spectra were found at the first order phase transition which was located at $T_S \approx$ 180 K, lower than in previous studies. In contrast to the prior reports we found no sign of phase coexistence over temperature range exceeding 5 K [5].

REFERENCES

[1] E. Navarro-Moratalla, B. Huang, G. Clark *et al.*, Layer dependent ferromagnetism in a van der Waals crystal down to the monolayer limit, Nature (London) **546**, 270 (2017).

[2] J. F. Dillon, Jr. and C. E. Olson, Magnetization, resonance, and optical properties of the ferromagnet CrI3, J. Appl. Phys. **36**, 1259 (1965).

[3] M. A. McGuire, H. Dixit, V. R. Cooper, and B. C. Sales, Coupling of crystal structure and magnetism in the layered, ferromagnetic insulator CrI3, Chem. Mater. **27**, 612 (2015).

[4] D. T. Larson and E. Kaxiras, Raman Spectrum of CrI3: An *ab initio* study, Phys. Rev. B **98**, 085406 (2018).

[5] S. Djurdjić-Mijin, A. Šolajić, J. Pešić, M. Šćepanović, Y. Liu, A. Baum, C. Petrovic, N. Lazarević, and Z. V. Popović, Lattice dynamics and phase transition in CrI3 single crystals, Phys. Rev. B **98**, 104307 (2018.)

Nanostructured $BiFeO_3$ thin films

B. Colson[a], V. Fuentes[a], Z. Konstantinovic[b], C. Frontera[a], D. Colson[c], A. Forget[c], N. Lazarevic[b], M. Scepanovic[b], Z. V. Popovic[b], Ll. Balcells[a], B. Martinez[a], A. Pomar[a]

[a]ICMAB-CSIC, Campus UAB, 08193 Bellaterra, Spain
[b]CSSPNM, Institute of Physics Belgrade, University of Belgrade, Serbia
[c]SPEC/IRASMIS/ DSM, CEA-Saclay, Gif-sur Yvette, France

Abstract. Well defined structures at nanometric scale of multiferroic materials present an increasing interest due to their unique physical properties and potential applications. Fabrication of artificial nanostructures requires sophisticated technology and has been recognized as a hard-attainable issue. For these reasons the fabrication of ordered nanostructures, via spontaneous self-organization, is a topic of major relevance. Complex oxide thin films are often elastically strained and this lattice strain can, in some cases, select preferential growth modes leading to the appearance of different self-organized morphologies. In this work we report on the controlled fabrication of a self-assembled network of nanostructures (pits and grooves) in highly epitaxial $BiFeO_3$ thin films. As previously shown in the case of manganite thin films [1-2], the remarkable degree of ordering is achieved using vicinal substrates with well-defined step-terrace morphology. Nanostructured $BiFeO_3$ thin films show mixed-phase morphology, exhibiting the giant ferroelectric polarization close to the theoretical limit. These particular microstructures open a huge playground for future applications in multiferroic nanomaterials.

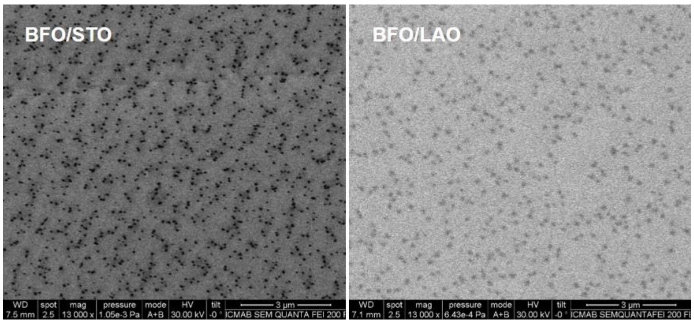

FIGURE 1. Scanning Electron Microscopy of nanostructured $BiFeO_3$ films grown on top of $SrTiO_3$ and $LaAlO_3$ substrates.

REFERENCES

1. Z. Konstantinovic et al., Small 5, 265 (2009)
2. Z. Konstantinovic et al., Nanoscale, 5, 1001 (2013).

Raman Spectroscopy Study of Primary Mesenchymal Stem Cells

J. J. Lazarević[a], T. Kukolj[b], U. Ralević[a], D. Bugarski[b], N. Lazarević[a], B. Bugarski[c], and Z.V. Popović[a,d]

[a]Center for Solid State Physics and New Materials, Institute of Physics Belgrade, University of Belgrade, Pregrevica 118, Belgrade 11080, Serbia
[b]Laboratory for Experimental Hematology and Stem Cells, Institute for Medical Research, University of Belgrade, Belgrade, Serbia
[c]Department of Chemical Engineering, Faculty of Technology and Metallurgy, University of Belgrade, Karnegijeva 4, Belgrade 11060, Serbia
[d]Serbian Academy of Science and Arts, Knez Mihailova 35, Belgrade 11000, Serbia

Abstract. Cells possess specific dynamic biochemical structure and by analyzing (inter)molecular vibrations with Raman spectroscopy, correlation between biochemical composition to specific cell lineages is established, as well as to disorders of their physiologic state. In regenerative medicine and tissue engineering, mesenchymal stem cells, as adult stem cells, are of crucial importance, due to self-renewal, multi-lineage differentiation potential and undemanding isolation procedure. These cells are widespread in the adult organism and no ethical issues are related to their isolation. However, they need to be well characterized and purified before further application, having in mind their intrinsic heterogeneity. Raman spectroscopy was used for analyzing the influence of two most frequently used chemical fixatives, methanol and formaldehyde, on Raman spectra of primary mesenchymal stem cells isolated from periodontal ligament. Further, this vibrational spectroscopy technique was applied for probing differentiation status of these cells, after stimulating towards chondrogenic, adipogenic, and osteogenic lineages.

REFERENCES

1. Lazarević J.J., Kukolj T., Bugarski D., Lazarević N., Bugarski B., and Popović Z.V., *Spectrochim Acta A Mol Biomol Spectrosc.* **213**, 384-390 (2019).
2. Lazarević J.J., Ralević U., Kukolj T., Bugarski D., Lazarević N., Bugarski B., and Popović, Z.V., *Spectrochim Acta A Mol Biomol Spectrosc.* **216**, 173-178 (2019).

Frustrated Spin Order and Fluctuations in FeSe: A Raman Scattering Study

N. Lazarević[a], A. Baum[b,c], H. N. Ruiz[d.e], Yao Wang[d,f,j], T. Böhm[b,c,k], R. H. Ahanghamejhad[b,c,l], P. Adelmann[g], T. Wolf[g], Z. V. Popović[a,h], B. Moritz[d], T. P. Devereaux[d,i], R. Hackl[b]

[a] *Center for Solid State Physics and New Materials, Institute of Physics Belgrade, University of Belgrade, Pregrevica 118, 11080 Belgrade, Serbia.*
[b] *Walther Meissner Institut, Bayerische Akademie der Wissenschaften, 85748 Garching, Germany.*
[c] *Fakultät für Physik E23, Technische Universitä München, 85748 Garching, Germany.*
[d] *Stanford Institute for Materials and Energy Sciences, SLAC National Accelerator Laboratory, 2575 Sand Hill Road, Menlo Park, CA 94025, USA.*
[e] *Department of Physics, Stanford University, Stanford, CA 94305, USA.*
[f] *Department of Applied Physics, Stanford University, Stanford, CA 94305, USA.*
[g] *Karlsruher Institut für Technologie, Institut für Festkörperphysik, 76021 Karlsruhe, Germany.*
[h] *Serbian Academy of Sciences and Arts, Knez Mihailova 35, 11000 Belgrade, Serbia.*
[i] *Geballe Laboratory for Advanced Materials, Stanford University, Stanford, CA 94305, USA.*
[j] *Present address: Lyman Laboratory 336, Harvard University, 17 Oxford St. Cambridge, 02138 MA, USA.*
[k] *Present address: TNG Technology Consulting GmbH, Beta-Straße,85774 Unterföhring, Germany.*
[l] *Present address: School of Solar and Advanced Renewable Energy, Department of Physics and Astronomy, University of Toledo, Toledo, OH 43606, USA.*

Abstract. FeSe is the simplest and yet the most controversial member of the iron based superconductors whose charge and spin dynamics may hold key information on the physics of high temperature superconductors. As opposed to the related iron pnictides and FeTe, no long range magnetic order is found down to lowest temperatures. Here, we present the results of the inelastic light scattering experiments on FeSe as a function of temperature and polarization. In agreement with numerical simulations of a spin-1 Heisenberg model, several peaks in all Raman active symmetries can be assigned to spin excitations. The dominating feature is a peak in B_{1g} symmetry around 500 cm^{-1} which shows distinct temperature dependence. Further comparison of the simulations to neutron scattering data furnishes evidence for FeSe hosting nearly frustrated stripe order of local spins.

REFERENCES

1. A. Baum, H. N. Ruiz, N. Lazarević, Yao Wang, T. Böhm, R. Hosseinian Ahangharnejhad, P. Adelmann, T. Wolf, Z. V. Popović, B. Moritz, T. P. Devereaux & R. Hackl, *Communications Physics* **2**, 14 (2019).
2. H. Ruiz, Yao Wang, B. Moritz, A. Baum, R. Hackl & T. P. Devereaux, *Phys. Rev. B* **99**, 125130 (2019).

Lattice dynamics and phonon anomalies in FeS

A. Baum[a,b], A. Milosavljević[c], N. Lazarević[c], M.M. Radonjić[d], B. Nikolić[e], M. Mitschek[a,b], Z. Inanloo Maranloo[a], M. Šćepanović[c], M. Grujić – Brojčin[c], N. Stojilović[f], M. Opel[a], Aifeng Wang[g], C. Petrovic[g], Z.V. Popović[c,h] and R. Hackl[a]

[a]*Walther Meissner Institut, Bayerische Akademie der Wissenschaften, 85748 Garching, Germany*
[b]*Fakultät für Physik E23, Technische Universität München, 85748 Garching, Germany*
[c]*Center for Solid State Physics and New Materials, Institute of Physics Belgrade, University of Belgrade, Pregrevica 118, 11080 Belgrade, Serbia*
[d]*Scientific Computing Laboratory, Center for the Study of Complex Systems, Institute of Physics Belgrade, University of Belgrade,Pregrevica 118, 11080 Belgrade, Serbia*
[e]*Faculty of Physics, University of Belgrade, Studentski trg 12, Belgrade, Serbia*
[f]*Department of Physics and Astronomy, University of Wisconsin Oshkosh, Oshkosh, Wisconsin 54901, USA*
[g]*Condensed Matter Physics and Materials Science Department, Brookhaven National Laboratory, Upton, New York 11973-5000, USA*
[h]*Serbian Academy of Sciences and Arts, Knez Mihailova 35, 11000 Belgrade, Serbia*

Abstract. Crystal structure, magnetic ordering and nematic phase are closely interrelated in the iron-based superconductors. Although isostructural and isoelectronic, properties of 11 chacogenides, FeSe, FeTe and FeS, differ significantly. Whereas FeSe undergoes a nematic and structural phase transition at 90 K, togeather with superconductivity below 9 K, and no traces of long-range magnetic ordering, FeTe is not superconducting but exhibits magnetostructural phase transition at temperature of 67 K. The last member of the familly, FeS, have a superconducting transition at 5 K, and remains tetragonal down to lowest temperatures.

Here, we present results of Raman scattering experiment on tetragonal FeS, and analysis of vibrational properties close to potential instabilities [1]. Besides A_{1g} and B_{1g} modes assignation, which is in a good agreement with DFT calculations, third peak whitin a gap of calculated phonon density of states can be indentified as a result of second order scattering process. Both, selection rules for two-phonon processes, based on modified group projector technique and energy are in a good agreement with the experiment. A fourth mode, close to A_{1g} could originate from either deffect-induced scattering or second order scattering as well. The temperature dependence of all four modes is governed by the contraction of the lattice, with anomalies at 50 K and below 20 K. The anomaly observed at 20 K has a correspondence with previously reported results of short-range magnetic ordering. The presence of two-phonon scattering indicates strong phonon-phonon scattering, which is likely to originate from an electron-phonon interaction being enhanced in comparison to other pnictides and chalcogenides.

REFERENCES

1. A. Baum, A. Milosavljević, N. Lazarević, M. M. Radonjić, B. Nikolić, M. Mitschek, Z. I. Maranloo, M. Šćepanović, M. Grujić-Brojčin, N. Stojilović, M. Opel, A. Wang, C.Petrovic, Z.V.Popović, and R. Hackl, Phonon anomaliesin FeS, *Phys.Rev.B* **97**, 054306 (2018).

Lattice dynamics and phase transitions in $Fe_{3-x}GeTe_2$

A. Milosavljević[a], A. Šolajić[a], S. Djurdjić Mijin[a], J. Pešić[a], B. Višić[a], Y. Liu[b], C. Petrovic[b], N. Lazarević[a] and Z. V. Popović[c]

[a] *Center for Solid State Physics and New Materials, Institute of Physics Belgrade, University of Belgrade, Pregrevica 118, 11080 Belgrade, Serbia*
[b] *Condensed Matter Physics and Materials Science Department, Brookhaven National Laboratory, Upton, New York 11973-5000, USA*
[c] *Center for Solid State Physics and New Materials, Institute of Physics Belgrade, University of Belgrade, Pregrevica 118, 11080 Belgrade, Serbia and Serbian Academy of Sciences and Arts, Knez Mihailova 35, 11000 Belgrade, Serbia*

Abstract. A new class of magnetic van der Waals bonded materials has recently become of great interest, as a suitable candidates for various applications. Whereas $CrXTe_3$ (X = Si, Ge, Sn) and CrX_3 (X = Cl, Br, I) classes maintain low phase transition temperatures even in a monolayer regime, $Fe_{3-x}GeTe_2$ has a high bulk transition temperature, between 220 and 230 K, making it a promising applicant.

Here we present DFT calculations of lattice dynamics and Raman spectroscopy measurements of the van der Waals bonded ferromagnet $Fe_{3-x}GeTe_2$ [1]. Four out of eight Raman active modes are observed and assigned, in agreement with numerical calculations. The energies and linewidths of the observed modes display an unconventional temperature dependence at about 150 and 220 K, followed by the nonmonotonic evolution of the Raman continuum. Whereas the former can be related to the magnetic phase transition, the origin of the latter anomaly remains an open question.

REFERENCES

1. A. Milosavljević, A. Šolajić, S. Djurdjić-Mijin, J. Pešić, B. Višić, Yu Liu, C. Petrovic, N. Lazarević, and Z. V. Popović. "Lattice dynamics and phase transitions in $Fe_{3-x}GeTe_2$." Physical Review B 99, no. 21 (2019): 214304.

XIX Symposium on Condensed Matter Physics
SFKM 2015

Book of Abstracts

7 – 11 September 2015
Belgrade, Serbia

Raman Scattering in Iron-Based Superconductors and Related Materials

N. Lazarevic[a], M. Opačić[a], M. Šćepanović[a], Hechang Lei[1b], Hyejin Ryu[b], C. Petrovic[b] and Z. V. Popović[a]

[a] *Center for Solid State Physics and New Materials, Institute of Physics Belgrade, University of Belgrade, Pregrevica 118, 11080 Belgrade, Serbia*
[b] *Condensed Matter Physics and Materials Science Department, Brookhaven National Laboratory, Upton, New York 11973-5000, USA*

Abstract. The discovery of superconductivity in F -doped LaFeAsO in 2008 brought a new excitement to the field of superconductivity. In the months following the initial report, numerous superconducting iron-based compounds have been found and categorized into several sub-classes. The class of iron-chalcogenide superconductors shows an exceptional variety of features, such as the existence of the excess Fe atoms or Fe vacancies, different types of magnetic order in the normal state, intrinsic phase separation and, possibly, a novel paring mechanism. We present the results of a comprehensive polarization and temperature dependent Raman scattering study of iron-chalcogenide superconductors and related materials. Special emphasis will be placed on the intrinsic phase separation in the alkali-doped iron-selenides. Clear evidence of phonon modes renormalization due to electron-phonon and spin-phonon interactions is presented.

REFERENCES

1. N. Lazarević, M. Abeykoon, P. W. Stephens, Hechang Lei, E. S. Bozin, C. Petrovic, and Z. V. Popović *Phys. Rev. B* **86**, 054503, (2012).
2. N. Lazarević, M. Radonjić, M. Šćepanović, Hechang Lei, D. Tanasković, C. Petrovic, and Z. V. Popović *Phys. Rev. B* **87**, 144305, (2013).
3. Z. V. Popović, M. Šćepanović, N. Lazarević, M. M. Radonjić, D. Tanasković, Hechang Lei, and C. Petrovic *Phys. Rev. B* **89**, 014301, (2014).
4. Z. V. Popović, M. Š ćepanović, N. Lazarević, M. Opačić, M. M. Radonjić, D. Tanasković, Hechang Lei, and C. Petrovic, *Phys. Rev. B* **91**, 064303, (2015).

---

[1] Present address: Department of Physics, Renmin University of China, 59 Zhongguancun Street, Haidian District, Beijing 100872, China

Charge Density Wave in $CeTe_3$ – A Scanning Tunneling Microscopy Study

U. Ralević[a], N.Lazarević[a], R. Hu[b], C. Petrović[b], R. Gajić[a], Z. V. Popović[a]

[a]*Center for Solid State Physics and New Materials, Institute of Physics Belgrade, University of Belgrade, Pregrevica 118, 11080 Belgrade, Serbia*
[b]*Condensed Matter Physics and Materials Science Department, Brookhaven National Laboratory, Upton, New York 11973-5000, USA*

Abstract. Charge density waves (CDW) are a type of coupled electronic-lattice instability found in quasi-low dimensional materials. The rare-earth tritellurides, $ReTe_3$, represent an excellent model system for systematic study of CDW physics. They are layered quasi-2D materials with a weakly orthorhombic crystal structure of the *Cmcm* space group.[1] The layers are composed of a corrugated ReTe slab sandwiched between two planar Te layers and connected together along the crystalline b axis via weak van der Waals forces. The planar Te atomic layers (*ac* plane) are weakly hybridized with the ReTe slab atoms. Hence, the physical properties of $ReTe_3$ are dominantly determined by the Te planes and consequently the CDW state is formed in Te atomic layers.[2] Here we present a scanning tunneling microscopy study of CDW in $CeTe_3$ at room temperature. We demonstrate that $CeTe_3$ hosts an unidirectional incommensurate CDW with a characteristic wave vector, $k_{cdw}=3.9\ nm^{-1}$, which is in a good agreement with theoretically predicted value, $k_{cdw}=2/7\cdot2\pi/c=4.1\ nm^{-1}$. Using scanning tunneling spectroscopy we estimate the CDW gap to be approximately 380 meV, which is in good agreement with previously reported values.[3]

We are grateful to the Serbian Ministry of Education, Science and Technological Development for financial support through projects Nos. OI 171005, III45018.

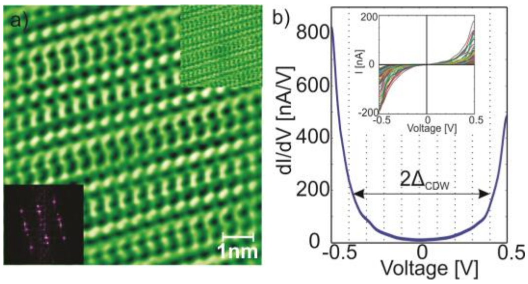

FIGURE 1. (a) STM topography of CDW in CeTe3. (b) dI/dV curve showing 380 meV CDW gap

REFERENCES

1. B. K. Norling and H. Steinfnk, *Inorg. Chem.* **5**, 1488 (1966).
2. E. DiMasi, B. Foran, M. C. Aronson, and S. Lee, *Chem. Mater.* **6**, 1867 (1994).
3. N. Ru and I. R. Fisher, *Phys. Rev. B* **73**, 033101 (2006).

Bulletin of the American Physical Society

APS March Meeting 2019
Volume 64, Number 2
Monday–Friday, March 4–8, 2019; Boston, Massachusetts

Session S62: Nematic Order and Correlated Electrons in Iron Pnictides and Chalcogenides

11:15 AM–2:15 PM, Thursday, March 7, 2019
BCEC Room: 258C

Sponsoring Unit: DCMP
Chair: Ming Yi

Abstract: S62.00003 : Orbital selective magnetism, nematicity, and fluctuations in FeSe*

12:27 PM–1:03 PM

← Abstract →

Presenter:
Rudolf Hackl
(Walther Meissner Institute, Bavarian Academy of Sciences and Humanities)

Authors:
Rudolf Hackl
(Walther Meissner Institute, Bavarian Academy of Sciences and Humanities)

Andreas Baum
(Walther Meissner Institute, Bavarian Academy of Sciences and Humanities)

Harrison N Ruiz
(Stanford University)

Nenad Lazarevic
(Institute of Physics Belgrade)

Yao Wang
(Harvard University)

Thomas U Boehm
(Walther Meissner Institute, Bavarian Academy of Sciences and Humanities)

Thomas Wolf
(Karlsruhe Institute of Technology)

Brian Moritz
(Stanford University)

Thomas Devereaux
(Stanford University)

Iron pnictides and chalcogenides have rich phase diagrams displaying superconductivity, nematic and spin density wave order, fluctuations and short-range magnetism. Yet, the magnetism observed in FeSe, for instance, is not necessarily of the same type as that in the pnictides since the typical nesting conditions of the Fermi surfaces are much less robust in the chalcogenides and the question as to strong *versus* weak coupling magnetism arises. Raman scattering experiments afford a window into the type of ordering and allow one to distinguish between itinerant and localized magnetism. We show how the response from a weakly coupled itinerant system can be distinguished from that of a Heisenberg-type localized magnet. We present results of light scattering experiments as a function of polarization and temperature. In the pnictides the Raman spectra display all features of a spin density wave while the spectra of FeSe the are similar to those of systems with localized spins such as the cuprates. Our numerical simulations using exact diagonalization of a 4x4 cluster reproduce the experiments semi-quantitatively in the limit of a nearly frustrated spin-1 Heisenberg model (localized spins), in particular the low energy peak in B_{1g} symmetry. The results indicate that the electrons in some of the orbitals are more localized in FeSe than in the pnictides and reopen the discussion on the type of nematic fluctuations observed recently.

*Work in Europe was supported by the DFG via SPP 1458 and TRR80, by the Serbian Ministry of Education, Science and Technological Development (Project III45018), by the DAAD, and by BaCaTeC. Work in the SIMES at Stanford University and SLAC was supported by the U.S. DOE, Office of Basic Energy Sciences (DE-AC02-76SF00515) and Office of Science (DE-AC02-05CH11231).

Bulletin of the American Physical Society

APS March Meeting 2020
Volume 65, Number 1
Monday–Friday, March 2–6, 2020; Denver, Colorado

Session L61: Fe-Based Superconductors - Nematicity IV
8:00 AM–11:00 AM, Wednesday, March 4, 2020
Room: Mile High Ballroom 4B

Sponsoring Units: DMP DCMP DCOMP
Chair: Benjamin Frandsen, Brigham Young Univ - Provo

Abstract: L61.00009 : Exploring the electronic structure of $BaFe_2As_2$ using resonant Raman scattering*

View Presentation

Abstract

Presenter:
Rudolf Hackl
(Walther Meissner Institute, Bavarian Academy of Sciences and Humanities)

Authors:
Rudolf Hackl
(Walther Meissner Institute, Bavarian Academy of Sciences and Humanities)

Andreas Baum
(Walther Meissner Institute, Bavarian Academy of Sciences and Humanities)

Ying Li
(Institute for Theoretical Physics, Goethe University Frankfurt)

Nenad Lazarevic
(Center for Solid State Physics and New Materials, Institute of Physics Belgrade)

Daniel Jost
(Walther Meissner Institute, Bavarian Academy of Sciences and Humanities)

Jiun-Haw Chu
(Department of Physics, University of Washington)

Ian Fisher
(Geballe Laboratory for Advanced Materials & Dept. of Applied Physics, Stanford University)

Roser Valenti
(Institute for Theoretical Physics, Goethe University Frankfurt)

Igor Mazin
(Code 6393, Naval Research Laboratory)

Iron-based materials are characterized by the competition of various phases including magnetism, nematicity, and superconductivity. The interrelation of these instabilities is a key question of both materials science and theoretical modelling. In this study we present light scattering data on twin-free $BaFe_2As_2$ as a function of the energy of the incident photons. The phonon intensities display an anisotropy for the polarizations oriented along either the ferro- or the antiferromagnetically ordered direction. This anisotropy makes the fully symmetric As phonon to appear in crossed polarizations. The anomalous intensity and the anisotropy of the spectral weight increase substantially in the blue-green spectral range. The experimental results are analyzed using density functional theory. Qualitative agreement between model calculations and experiment is found if the magnetic order is properly taken into account. The anomalies are fully developed only in the presence of long range magnetic order and are not directly linked to nematicity. Rather they are a high-energy phenomenon indicating that magnetism and nematicity are interrelated.

*We acknowledge support by the DFG, the Serbian Ministry of Education, the DAAD , by BaCaTeC, the DOE, the NRL and by the AvH Foundation.

Bulletin of the American Physical Society

APS March Meeting 2020
Volume 65, Number 1

Monday–Friday, March 2–6, 2020; Denver, Colorado

Session M61: Fe-Based Superconductors - Mostly FeSe & FeTe
11:15 AM–2:15 PM, Wednesday, March 4, 2020
Room: Mile High Ballroom 4B

Sponsoring Units: DMP DCMP DCOMP
Chair: Leonardo Civale, Los Alamos Natl Lab

Abstract: M61.00002 : Frustrated spin order in FeSe*

View Presentation

Abstract

Presenter:
Andreas Baum
(Walther Meissner Institute, Bavarian Academy of Sciences and Humanities)

Authors:
Andreas Baum
(Walther Meissner Institute, Bavarian Academy of Sciences and Humanities)

Harrison N Ruiz
(Stanford University)

Nenad Lazarević
(Institute of Physics Belgrade)

Yao Wang
(Harvard University)

Thomas U Boehm
(Walther Meissner Institute, Bavarian Academy of Sciences and Humanities)

Ramez Hosseinian Ahangharnejhad
(Walther Meissner Institute, Bavarian Academy of Sciences and Humanities)

Thomas Wolf
(Karlsruhe Institute of Technology)

Brian Moritz
(Stanford University)

Thomas Devereaux
(Stanford University)

Rudolf Hackl
(Walther Meissner Institute, Bavarian Academy of Sciences and Humanities)

Magnetism in the structurally simplest iron based superconductor, FeSe, poses a challenge. Unlike in the related iron pnictide compounds, no magnetic order was found down to lowest temperatures in FeSe. However, recent theoretical and experimental studies point towards frustration quenching long range order. Here we demonstrate that inelastic light scattering can distinguish between itinerant and localized magnetism. We find the Raman response from FeSe to be more similar to localized systems such as cuprates. Together with simulations of a spin-1 Heisenberg model this furnishes evidence that FeSe hosts an almost fully frustrated system of essentially localized moments.

*Work in Europe was supported by the DFG via SPP 1458 and TRR80, by the Serbian Ministry of Education, Science and Technological Development (Project III45018), by the DAAD, and by BaCaTeC. Work in the SIMES at Stanford University and SLAC was supported by the U.S. DOE, Office of Basic Energy Sciences (DE-AC02-76SF00515) and Office of Science (DE-AC02-05CH11231).

Bulletin of the American Physical Society

APS March Meeting 2018
Volume 63, Number 1
Monday–Friday, March 5–9, 2018; Los Angeles, California

Session A14: Fe-based Superconductors -- Spectroscopy

8:00 AM–11:00 AM, Monday, March 5, 2018
LACC Room: 304B

Sponsoring Unit: DMP
Chair: Jinguang Cheng, Chinese Academy of Sciences (CAS)

Abstract ID: BAPS.2018.MAR.A14.11

Abstract: A14.00011 : Spin order and fluctuations in FeSe*

10:24 AM–10:36 AM

← Abstract →

Presenter:
Rudolf Hackl
(Walther Meissner Institut)

Authors:
Rudolf Hackl
(Walther Meissner Institut)

Andreas Baum
(Walther Meissner Institut)

Harrison Ruiz
(Stanford Institute for Materials and Energy Sciences, SLAC National Accelerator Laboratory)

Nenad Lazarevic
(Institute of Physics Belgrade, University of Belgrade)

Yao Wang
(Stanford Institute for Materials and Energy Sciences, SLAC National Accelerator Laboratory)

Thomas Boehm
(Walther Meissner Institut)

Ramez Hosseinian Ahangharnejhad
(Walther Meissner Institut)

Peter Adelmann
(Karlsruhe Institute of Technology)

Thomas Wolf
(Karlsruhe Institute of Technology)

Zoran Popovic
(Institute of Physics Belgrade, University of Belgrade)

Brian Moritz
(Stanford Institute for Materials and Energy Sciences, SLAC National Accelerator Laboratory)

Thomas Devereaux
(Stanford Institute for Materials and Energy Sciences, SLAC National Accelerator Laboratory)

FeSe is the simplest Fe-based system. Depending on the environment, the superconducting transition temperature ranges between 9 and approximately 100 K. As opposed to the Fe pnictides, long range magnetic order is not found in FeSe. Yet, the charge and spin dynamics of FeSe may hold key information on the physics of high temperature superconductors in general. We report results of light scattering experiments as a function of polarization and temperature and simulate the spectra using exact diagonalization. With the parameters of a frustrated spin 1 Heisenberg model the experiment can be reproduced for all Raman active symmetries. We find a low energy peak in B_{1g} symmetry and assign this feature to excitations of nearly localized spins. Comparable agreement between theory and experiment can be achieved for neutron scattering data. The study furnishes evidence for nearly frustrated spin order and critical fluctuations of spin stripes with an ordering vector close to or at (π,0).

*German Research Foundation (DFG): SPP1458 (HA2071/7), HA2071/8, Transregional Collaborative Research Center TRR80; Bavarian Californian Technology Center (BaCaTeC).

To cite this abstract, use the following reference: http://meetings.aps.org/link/BAPS.2018.MAR.A14.11

INTERNATIONAL WORKSHOP ON **IRON-BASED SUPERCONDUCTORS**

MUNICH, GERMANY | SEPTEMBER 13-16, 2016

P5:
Spin order and fluctuations in FeSe

A.Baum[1,2], N. Lazarević[3], T. Böhm[1,2], R. Hosseinian Ahangharnejhad[1,2], P. Adelmann[4], T. Wolf[4], Z. Popović[3], R. Hackl[1]

[1]*Walther Meissner Institut, Bayerische Akademie der Wissenschaften, 85748 Garching, Germany*
[2]*Fakultät für Physik E23, Technische Universität München, 85748 Garching, Germany*
[3]*Center for Solid State Physics and New Materials, Institute of Physics Belgrade, University of Belgrade, Pregrevica 118, 11080 Belgrade, Serbia*
[4]*Karlsruher Institut für Technologie, Institut für Festkörperphysik, 76021 Karlsruhe, Germany*

In the ferro-pnictides and chalcogenides superconductivity and magnetism are in close proximity and believed to be intertwined. Whereas stripe-like antiferromagnetism prevails in the pnictides FeSe does not order magnetically down to the lowest temperatures. However, similarly as in Co-substituted $BaFe_2As_2$ a nematic phase accompanied by a structural transformation appears in the 100 K range. The question arises as to the origin of the nematic order and possible related fluctuations in FeSe. FeSe is a model system for such type of studies since magnetic order [1], fluctuations, and superconductivity can be tuned in wide ranges using pressure as a control parameter [2]. We started the studies in FeSe at ambient pressure and performed Raman experiments on single crystalline FeSe as a function of temperature and polarization. In B_{1g} symmetry an intense weakly peaked response in the 60 meV range is observed at room temperature which piles up upon cooling. In addition, a narrow mode close to 5 meV emerges below 150 K which gradually fades away below the structural transition at T_S. In B_{2g} symmetry a broad band is found above 100 meV. The high-energy response in B_{1g} and B_{2g} symmetry can be identified with frustrated magnetic order of either stripe or checkerboard-like antiferromagnetism. The low-energy mode is similar to those in the $BaFe_2As_2$ family [3] and is therefore interpreted in terms of incipient $(\pi,0)$ spin order.

[1] Bendele et al., Phys. Rev. Lett. 104, 087003 (2010)
[2] Mizuguchi et al., Appl. Phys. Lett. 93, 152505 (2008)
[3] Kretzschmar et.al., Nat. Phys. 12, 560 (2016)

P23:
Vacancies and phase separation in pure and transitional metal doped $K_xFe_{2-y}Se_2$

N. Lazarevic[1], M. Opacic[1], M. Radonjic[2,3], D Tanaskovic[3], Hyejin Ryu[4], M. Scepanovic[1], C. Petrovic[4], Z.V. Popovic[1]

[1]*Center for Solid State Physics and New Materials, Institute of Physics Belgrade, University of Belgrade, Pregrevica 118, 11080 Belgrade, Serbia*
[2]*Center for Electronic Correlations and Magnetism, Theoretical Physics III, Institute of Physics, University of Augsburg, D-86135 Augsburg, Germany*
[3]*Scientific Computing Laboratory, Institute of Physics Belgrade, University of Belgrade, Pregrevica 118, 11080 Belgrade, Serbia*
[4]*Condensed Matter Physics and Materials Science Department, Brookhaven National Laboratory, Upton, New York 11973-5000, USA*

Understanding the origin and mechanism of superconductivity in iron-based materials pose one of the main challenges in the condensed matter physics today. The presence of vacancies and intrinsic phase separation in alkali-doped iron-selenides make these questions even more challenging. We present the results of a comprehensive polarization and temperature dependent Raman scattering study of pure and transitional metals (Co and Ni) doped $K_xFe_{2-y}Se_2$. The Raman modes, originating from both the high symmetry (superconducting) and low symmetry (antiferromagnetic) domains, have been identified [1]. By analyzing these modes we were able to follow the phase separation evolution throughout the series in the full doping range [2]. The $K_xFe_{2-y}Se_2$ temperature dependent Raman scattering study revealed the sudden change of the A_{1g} mode energy near superconducting transition temperature due to the rearrangement of the electronic states [3]. The phonon modes renormalization due to the electron-phonon and spin-phonon interactions around Curie temperature in $K_xCo_{2-y}Se_2$ has also been discussed [4].

[1] N. Lazarević et al. Phys. Rev. B 86, 054503 (2012).
[2] Hyejin Ryu et al. Phys. Rev. B, 91, 184503 (2015); Phys. Rev. B, 91, 184503 (2015).
[3] M. Opačić et al. J. Phys. Cond. Matt 27, 485701 (2015).
[4] M. Opačić et al. arXiv:1605.05871 (2016).

Abstract

SNS 2019

Spectroscopies in Novel Superconductors

June 16 – 21, 2019 Tokyo, Japan

Ito International Research Center Conference, The University of Tokyo
ISSP International Workshop

『松の栄』を改変（東京大学総合図書館所蔵）

伊藤国際学術研究センター
ITO INTERNATIONAL RESEARCH CENTER

THE INSTITUTE FOR SOLID STATE PHYSICS
THE UNIVERSITY OF TOKYO

東京大学 低温センター
CRYOGENIC RESEARCH CENTER, THE UNIVERSITY OF TOKYO

CHIVAC Co., Ltd.

Inoue Foundation for Science

OXIDE

R-DEC Co.,Ltd.

scientaomicron

mks
Spectra-Physics®

OXFORD INSTRUMENTS
The Business of Science®

株式会社 東京インスツルメンツ
TOKYO INSTRUMENTS, INC.

UNISOKU
TII Group

SNS 2019

Spectroscopies in Novel Superconductors

June 16 – 21, 2019 Tokyo, Japan
Ito International Research Center Conference, The University of Tokyo
ISSP International Workshop

P-Tu-17: Frustrated spin order and orbital selectivity in FeSe

A. Baum[1,2], H. N. Ruiz[3,4], N. Lazarević[5], Yao Wang[3,6], T. Böhm[1,2],
R. Hosseinian Ahangharnejhad[1,2], P. Adelmann[7], T. Wolf[7], Z. V. Popović[5,8], B. Moritz[3],
T. P. Devereaux[3,9], and R. Hackl[1]

[1] *Walther Meissner Institut, BAdW, 85748 Garching, Germany.*
[2] *Fakultät für Physik E23, Technische Universität München, 85748 Garching, Germany.*
[3] *SIMES, SLAC National Accelerator Laboratory, CA 94025, USA.*
[4] *Department of Physics, Stanford University, Stanford, CA 94305, USA.*
[5] *Institute of Physics Belgrade, University of Belgrade, 11080 Belgrade, Serbia.*
[6] *Department of Applied Physics, Stanford University, Stanford, CA 94305, USA.*
[7] *KIT, Institut für Festkörperphysik, 76021 Karlsruhe, Germany.*
[8] *Serbian Academy of Sciences and Arts, 11000 Belgrade, Serbia.*
[9] *Geballe Laboratory for Advanced Materials, Stanford University, Stanford, CA 94305, USA.*

The separation of nematic and magnetic order in FeSe creates a unique opportunity to study these phenomena. We use Raman spectroscopy [1] and exact diagonalization of a spin-1 Heisenberg model [2] and show that the dominating response above 50 meV originates from localized spins. Our simulations create a link to neutron scattering and provide evidence for nearly frustrated stripe-order. We argue that these results indicate the important role of Hund-type physics in FeSe inducing orbital selective localization.

[1] A. Baum *et al.*, Commun. Phys. **2**, 14 (2019)
[2] H. N Ruiz *et al.*, Phys. Rev. B**99**, 125130 (2019)

P-Tu-18: Substitution Effects in Ultrathin Iron-based Superconductor Films Studied by High-Resolution ARPES

K. Nakayama[1], K. Shigekawa[1], K. Owada[1], G. N. Phan[1], T. Takahashi[1,2,3], and T. Sato[1,2,3]

[1] *Department of Physics, Tohoku University, Sendai 980-8578, Japan*
[2] *WPI-AIMR, Tohoku University, Sendai 980-8577, Japan*
[3] *CSRN, Tohoku University, Sendai 980-8577, Japan*

The discovery of high-temperature (T_c) superconductivity above 65 K in monolayer FeSe film on $SrTiO_3$ substrate [1] has generated tremendous attention because the T_c value is surprisingly high and the material is an atomically thin (a few angstrom thick) film. To search for higher T_c and also to clarify the mechanism of high-T_c superconductivity, further studies on monoalyer films of other iron-based superconductors are highly required. In this study, we have grown chalcogen-substituted monolayer films on $SrTiO_3$ by molecular-beam epitaxy and determined the electronic structure by high-resolution angle-resolved photoemission spectroscopy. We observed substitution-induced changes in the T_c value, Fermi-surface shape, and band width. We also found a signature of interfacial electron-phonon coupling. We discuss the implications of our results in relation to the high-T_c mechanism of atomically-thin iron-based superconductors.

[1] Q.-Y. Wang *et al.*, Chin. Phys. Lett. **29**, 037402 (2012).